UNIVERSITAT DE BARCELONA

Giant caloric and multicaloric effects in magnetic alloys

Adrià Gràcia Condal

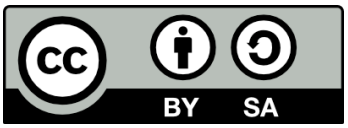

Giant caloric and multicaloric effects in magnetic alloys

– Doctoral thesis–

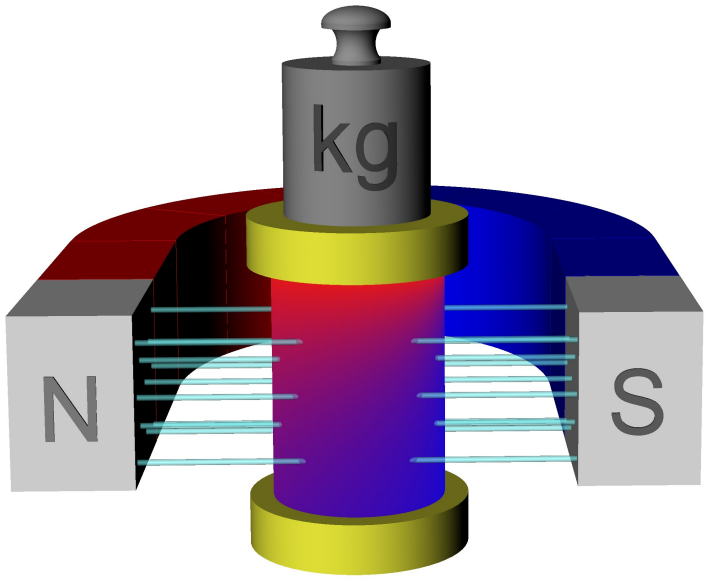

Adrià Gràcia Condal

UNIVERSITAT DE BARCELONA

Giant caloric and multicaloric effects in magnetic alloys

Programa de Doctorat en Física

Autor: **Adrià Gràcia Condal**
Department de Física de la Matèria Condensada

Director: Dr. Lluís Mañosa Carrera

Tutor: Dr. Giancarlo Franzese

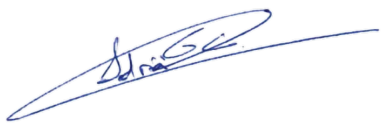

UNIVERSITAT DE BARCELONA

Associeu-vos i sereu forts;
instruïu-vos i sereu lliures;
estimeu-vos i sereu feliços.

— Josep Anselm Clavé i Camps

A la memòria d'en José, l'Antonio i la tieta Pilar:
perquè el seu record segueixi ben present.

Agraïments

La redacció d'aquest llibre ha estat la culminació d'un camí que va començar fa cinc anys. No ha estat una tasca senzilla, però sí molt enriquidora, i m'emporto la certesa d'haver crescut tan científicament com personalment. Així mateix, cal dir que si he pogut arribar fins aquí és gràcies a l'empenta, l'energia, la complicitat i l'empatia de moltes (moltissimes!) persones que, d'una manera o altra, hi han deixat la seva empremta. Per tant, vull utlitzar aquestes pàgines de la meva tesi doctoral per fer-los arribar el meu més sentit i profund agraïment per formar part d'aquesta història.

En primer lloc, m'agradaria destacar l'importantissim paper que ha jugat en Lluís Mañosa com a director d'aquesta tesi doctoral. Sempre que ho he necessitat ha tingut la porta del seu despatx ben oberta per parlar del que calgués. N'he après moltissim gràcies a ell (i en continuo aprenent!) tan d'aspectes purament científics com d'altres que van més enllà de la recerca. Lluís, m'has deixat espai créixer i avançar, i sense el teu mestratge, ni jo ni aquest treball haguéssim arribat fins aquí. Així mateix, també es mereixen un lloc ben destacat en aquests agraïments els altres membres del grup de recerca: l'Antoni Planes, l'Eduard Vives i la Teresa Castán. Durant aquests anys han compartit la seva enorme experiència amb mi en incomptables ocasions, tot donant-me un cop de mà sempre que ho he necessitat per tirar endavant. Tots ells formen, en conjunt, més que un grup de recerca. Formen un equip que transmet passió per la investigació a les noves generacions.

Durant aquests cinc anys, he compartit moltes hores amb varis investigadors i investigadores (tant doctorals com postdoctorals) al grup de recerca. En aquest sentit m'agradaria destacar a en Daniel Soto, i els seus aperitius mexicans (tots ells ben picants!), en Tino Gottschall, i la seva inesgotable font de coneixements (i paciència!), en Lukas Pfeuffer, i la seva ajuda tant al laboratori com amb la meva mudança, i a la Michela Romanini, per tantes estones compartides entre experiments inacabables. De la mateixa menera, m'agradaria tenir una menció especial per l'Enric Stern, amb qui vaig tenir el plaer de compartir els primers mesos del meu doctorat (que justament van ser els últims mesos del seu doctorat). Tots ells, a la seva manera, m'han permès créixer a llarg de les diferents etapes d'aquest camí. Sempre disposats a discutir i ajudar-me desinteressadament a solucionar un i mil contratemps, només desitjo que jo també hagi estat capaç d'ajudar-los a solucionar uns quants dels seus.

Seguint dins de la Facultat de Física, hi ha una sèrie de persones que m'han simplificat el meu dia a dia una infinitat de vegades. Als tècnics del taller mecànic, i en especial al Javier, per totes les hores dedicades a construir i redissenyar les

nostres màquines. A l'Oriol, el Miquel i al personal de la secretaria de la planta 6 (Isabel, Rosa i Dolors), per la vostra ajuda desinteressada i els valuosos consells que m'heu donat al llarg dels anys. A la Miriam, i en general a tot el personal de neteja, per la vostra feina ben visible de cada dia i per fer-nos possible tornar a la facultat malgrat la pandèmia. Des del meu punt de vista, tots vosaltres formeu part del selecte grup d'imprescindibles de la facultat ja que si no hi estiguéssiu, aquesta no seria la que molts coneixem i ens estimem. Així mateix, també m'agradaria fer extensius aquests agraïments a en Félix Mata, del CCiTUB, per demostrar la seva paciència amb mi, la polidora i la serra una i altra vegada (sempre acompanyada de bon humor).

Durant aquests anys, he tingut el plaer de poder col·laborar amb diversos grups i laboratoris de recerca punters. Als companys de ciutat del Grup de Caracterització de Materials de la Universitat Politècnica de Catalunya, i en concret a en Josep Lluís Tamarit, en Pol Lloveras i a l'Araceli Aznar. Per obrir-me les portes dels seus laboratoris i per totes les hores compartides (i amenitzades) entre mesures al sincrotró ALBA. Al grup de Functional Materials de la Technische Universität Darmstadt, i en concret a l'Oliver Gutfleisch, en Tino Gottschall i en Lukas Pfeuffer. Per les seves mostres excepcionals i les profitoses discussions. Així mateix, m'agradaria posar en especial valor la hospitalitat en terres germàniques que em van brindar en Lukas, durant una estada breu a Darmstadt, i en Tino i l'Eduard Bykov, a Dresden, durant la meva estada al Helmholtz-Zentrum Dresden-Rossendorf a finals del 2019.

El doctorat no només és feina, també són estones compartides entre amigues i amics (alguns nous i d'altres no tan nous). A la facultat, he compartit una infinitat de converses durant l'hora de dinar amb la Clàudia, l'Albert, el Javi, els Marcs (Illa i Oncins), l'Iván, la Glòria, l'Àlex o el Chiru. I la llista, sorprenetment, no acaba aquí! A l'Andreu (l'original), la Carol, la Pam, els Joseps (l'1 i el 2), l'Helena, l'Antonio, el Raúl, la Carla, el Mattia, el Gaspard, el Sergio, la Irina, l'Eric, l'Andreu i el Joan. Tots vosaltres heu posat llum al dia a dia del doctorat, que no és poca cosa. Així mateix, també vull tenir un record per a les companyes i companys que vam reflotar l'associació D-Recerca Precària allà al 2018, amb l'objectiu de fer sentir el col·lectiu d'investigadors i investigadores predoctorals dins la universitat.

No menys importants són els amics que ja arrosegava abans de començar aquest camí. Al barri sempre hi he comptat amb la Gina, el Gerard, l'Albert, la Noe, el Marcel i l'Andrea. Per tants i tants vespres (i els que vindràn!) que hem compartit entre cerveses, vins (a vegades gintònics), billars o jocs de taula. Per altra banda, com oblidar-me de l'Ignasi, la Cris (i el petitó o petitona que està de camí), el Joan, la Judit, el Victor, el Max i els Marcs (Font i Ferrer). Tots ben diferents. Potser, aquest es el ciment que ens ha mantingut junts, i n'estic segur que ho continuarà sent per molts i molts anys. Finalment, a la bona colla d'amics i amigues que vaig fer durant el grau de Física, i els que hem anat sumant durant el camí: el Sergi, el Pérez, el Monty, el Fran, la Gemma, el Grau, la Raquel, l'Adri (i al León tambe! un físic de segona generació), les Albes (la Física i la "Bollera"), la Irene, l'Isma, el Joan, el Toni, el Grau i el Popep. Tinc una llista tan larga de bons records amb

aquesta gent que en fi...només espero i desitjo que segueixi creixent!

Durant tots aquests anys, i en especial al llarg del procés complicat d'escriptura de la tesi, he comptat amb el suport incondicional de la meva família, i en especial dels meus pares: en Lluís i la Esther. Sempre han estat al meu costat, tant als dies bons com als no tant bons, i mai els hi ho podré agraïr prou. Així mateix, bona part d'aquesta última etapa l'he pogut compartir també amb l'Andrea (i el Bowie i el Vader). Vam compartir molts moments, i em vau donar energia en dies que estava esgotat.

Per acabar, agraeixo el finançament rebut per part de la Universitat de Barcelona, en forma d'un contracte APIF, durant bona part del meu doctorat. Així mateix, vull utilitzar les últimes linies per desitjar que el futur ens porti una millora dels recursos destinats a la recerca i la investigació, especialment per millorar les condicions de treball de les persones que ens hi dediquem en un o altre moment de la nostra vida.

Barcelona, febrer de 2022

Contents

Resum en català

La refrigeració artificial és fonamental i omnipresent a les societats dels països desenvolupats, i l'escalfament global degut al canvi climàtic n'està impulsant una demanda creixent a nivell planetari. Actualment, la tecnologia emprada en els sistemes de refrigeració es basa en l'expansió i compressió de gasos que són nocius pel medi ambient i contribueixen de manera molt rellevant a l'efecte hivernacle i a l'escalfament global. Tenint en compte la creixent necessitat de reduir les emissions de gasos d'efecte hivernacle, és urgent i imprescindible desenvolupar nous sistemes de refrigeració que siguin eficients i respectuosos amb el medi ambient.

En aquest sentit, els dispositius basats en materials que presenten efectes calòrics gegants representen avui en dia una de les millors alternatives a la tecnologia actual. L'origen físic dels efectes calòrics gegants és una transició de fase ferroica que s'indueix en el material quan se li aplica un determinat camp extern. Són especialment interessants els materials que presenten una transició de fase de primer ordre, on l'alliberament o absorció de la calor latent en la transició dóna lloc a un canvi d'entropia de gran magnitud en el cas que el camp s'apliqui de manera isoterma, o a un canvi de temperatura important si el camp s'aplica de manera adiabàtica. En funció de la natura del camp aplicat, poden donar-se els següents efectes calòrics: magnetocalòric, electrocalòric i mecanocalòric si els camps aplicats són magnètic, elèctric o mecànic, respectivament. Pel cas de l'efecte mecanocalòric, n'hi ha de dos tipus: elastocalòric si s'aplica un esforç uniaxial i barocalòric si s'aplica una pressió hidrostàtica.

Degut al seu gran interès tecnològic, l'estudi de materials amb efectes calòrics gegants és, avui dia, un dels temes de recerca punters en la Física de Materials. Tot i així, encara hi ha una sèrie d'obstacles a superar per tal que aquests materials puguin ser utilitzats en sistemes de refrigeració comercials. En primer lloc, es necessiten camps intensos per induir efectes calòrics grans. En segon lloc, la histèresi inherent a les transicions de fase de primer ordre pot reduir dràsticament la reversibilitat de l'efecte calòric i la seva eficiència.

Curiosament, la transició de fase que està en l'origen dels efectes calòrics gegants de molts materials involucra canvis en més d'un paràmetre d'ordre, com ara el magnètic, l'elèctric o l'estructural. De fet, degut al fort acoblament entre els diferents graus de llibertat, aquests materials presenten una resposta creuada als camps aplicats i és possible induir canvis en una propietat física mitjançant camps externs que no són els conjugats d'aquesta propietat. Per exemple, és possible canviar la imantació d'un material magnètic aplicant un esforç o una pressió hidrostàtica. Aquests materials, que presenten transicions de fase mutiferròiques, possibiliten que

la seva resposta tèrmica s'indueixi mitjançant l'aplicació simultània o seqüencial de diversos camps, donant lloc als anomenats efectes multicalòrics.

L'interès en l'estudi dels efectes multicalòrics és molt recent malgrat que s'ha predit que l'aplicació de més d'un camp pot ser la solució a alguns dels problemes que s'han posat de manifest en els diferents efectes calòrics. A més a més, encara hi ha molt pocs estudis experimentals basats en mesures directes ja que requereixen l'ús de dispositius que no són comercials. La recerca que s'ha desenvolupat durant el doctorat ha intentat donar-hi resposta, centrant-se en l'estudi dels efectes calòrics i multicalòrics en materials que presenten transicions magnetoestructurals de primer ordre amb un fort acoblament entre els graus de llibertat magnètic i estructural. S'han dissenyat i calibrat diversos dispositius experimentals que permeten realitzar mesures calorimètriques o termomètriques sota la influència de camp magnètic i esforç uniaxial. Al llarg del doctorat, aquests dispositius experimentals s'han emprat en la caracterització de materials que pertanyen a dues famílies diferents: el Fe-Rh i els aliatges tipus Heusler de base Ni-Mn. La recerca realitzada n'ha caracteritzat els efectes calòrics i multicalòrics, tot discutint en detall els avantatges dels efectes multicalòrics respecte els efectes calòrics (magnetocalòric i elastocalòric). En concret, s'ha demostrant que la combinació de diversos camps permet reduir-ne la seva intensitat per induir una resposta tèrmica gran, que permeten expandir el rang de temperatura de treball dels materials i que proporcionen estratègies per controlar o fins i tot aprofitar la histèresi associada a la transició de fase.

Abstract

The urgent need to reduce our footprint on the earth environment is leading to ever more stringent commitments to decrease greenhouse gases emissions, which entails one of the greatest challenges that mankind has to tackle. As a direct consequence, it is of utmost importance to develop novel, energy-efficient and environmentally-friendly refrigeration technologies that do not require the use of climate-damaging substances. In this regard, solid-state refrigerants based on the large thermal response exhibited by a variety of materials when field-inducing a ferroic phase transition are among the best alternatives. Specifically, materials undergoing a first-order phase transition are of particular interest as the latent heat associated with the phase transition contributes on enhancing the magnitude of the thermal response. Depending on the nature of the external field that drives the phase transition one distinguishes between magnetocaloric, electrocaloric, elastocaloric or barocaloric effects. In spite of all the intensive research devoted to the study of the diverse caloric effects, there are still a series of bottlenecks to overcome. Firstly, they require the application of strong external fields in order to induce a large thermal response. Secondly, the hysteresis associated with the phase transition can drastically reduce the efficiency and compromises its reversibility. A way out of such issues can be provided by materials exhibiting a strong coupling between the structural, magnetic or electronic degrees of freedom, denoted as multicaloric materials, which allow to drive their phase transition by the combination of diverse external fields, giving rise to multicaloric effects. Despite the high potential they exhibit, the research on multicaloric materials is germinal as it requires the use of non-commercial experimental systems. In this dissertation, we have focused on the study of materials displaying a magnetostructural first-order phase transition with a strong coupling between the structural and magnetic degrees of freedom. For such purpose, we have used distinct purpose-built calorimetric and adiabatic thermometry systems to investigate their caloric and multicaloric effects by direct methods. We have concentrated on two distinct families of multicaloric materials: Fe-Rh and Ni-Mn-based Heusler alloys. Our research is aimed at thoroughly characterizing the diverse advantages of multicaloric effects: showing that lower driving fields are required, that the operating temperature windows of the materials can be enlarged and discussing how their inherent hysteresis can be mastered or even exploited.

1 Introduction

The effects of global warming, resulting from the increasing levels of heat-trapping greenhouse gases on the atmosphere due to human activities, are changing the world as we know it today. With the passage of time, its effects are becoming more evident all around the globe, and this is happening at an unprecedented pace [1]. The evidence is compelling: from the global temperature rise to the shrinking ice sheets, the rising sea level or the increase of extreme weather events. [1] Global warming affects us all, but it particularly worsens the living conditions of those that are more vulnerable. In this regard, according to the United Nations High Commissioner for Refugees (UNHCR), [2] extreme weather events during the last decade triggered on average 21.5 million displacements per year worldwide (which is more than double of the average displaced by armed conflicts during the same period). [3]

Since the late nineteenth century, the earth surface temperature has risen about $1.2°C$ [1] and undoubtedly, global warming represents one of the greatest challenges that mankind has to tackle during this century. Based on the scientific evidence, the need to reduce greenhouse gases emissions has been on the agenda since the Kyoto Protocol (1997), and even more stringent commitments have been adopted on the Paris agreement (2015) [2] and at the COP26 (2021) held in Glasgow. [4]

Among the diverse contributors to global warming, the refrigeration sector plays an important role. Cooling systems are ubiquitous in developed countries, they are used in countless sectors of our society (from households to industry, agriculture or healthcare) and nowadays they consume about 20 % of the electricity generated all over the world [3]. Current cooling systems are based on a vapour-compression cycle using HFCs as refrigerants, which are climate-damaging substances that exhibit a strong global warming potential [4].

The impact of refrigeration on global warming is expected to drastically increase during the next decades, particularly driven by the soaring growth of emerging economies, such as China or India. For instance, as illustrated in Figure 1.1, while refrigerators are common in the households of western countries, they are much less common in the households of emerging economies [5]. Therefore, following the economic prosperity and the improvement of living conditions in emerging economies,

[1] NASA, Climate change evidence: https://climate.nasa.gov/evidence/

[2] UNHCR website: https://www.unhcr.org/

[3] UNHCR, Displaced on the frontlines of the climate emergency: https://storymaps.arcgis.com/stories/065d18218b654c798ae9f360a626d903

[4] COP26 agreements: https://ukcop26.org/the-conference/cop26-outcomes/

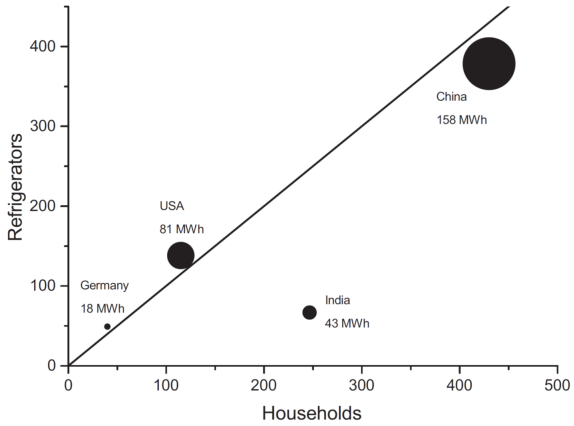

Figure 1.1: *Number of refrigerators versus the number of households (in million units) for selected countries. The seize of each data point indicates the amount of energy spent per country on domestic refrigeration. This figure has been taken from [6].*

it is expected that millions of households will install a refrigerator for the first time during the next decades. The same holds true for air conditioning systems, which is expected to multiply the worldwide energy demand for refrigeration during this century, even surpassing the energy demand for heating [5, 6]. Furthermore, the vapour-compression technology, after two centuries of intensive research, development and optimization for refrigeration applications is reaching its efficiency limits [7, 8].

On the whole, the increasing impact of refrigeration on global warming, the ever more stringent commitments to reduce greenhouse gases emissions together with the demands for higher energy efficiencies on refrigeration highlight the urgent need to develop novel, energy-efficient and environmentally-friendly refrigeration technologies [9, 10]. In this regard, the use of materials exhibiting large caloric effects as solid-state refrigerants is a promising technological alternative.

In conventional cooling systems, based on vapour-compression cycles, the temperature change of the refrigerant is induced by fast changes on pressure [11]. In fact, the temperature of every material changes when exposed to a sudden change of an external field (magnetic, electric or mechanical field), and this response is known as the caloric effect [12]. From the thermodynamic point of view, an external field change acts as the driving force that induces changes on the corresponding conjugated generalized displacement, modifying the thermodynamic state of the material, and generating an energy exchange. Depending on the nature of the external field that acts as the driving force, such as a magnetic (H), electric (E) or mechanical (uniaxial stress (σ) or hydrostatic pressure ($-p$)) field, it will induce changes on the magnetization (M), polarization (P), strain (ε) or volume (V) of the material, which are the corresponding conjugated generalized displacements of each external field, and the arising caloric effects can be classified as magnetocaloric

(MCE), electrocaloric (ECE) or mechanocaloric (which encompasses elastocaloric (eCE) and barocaloric (BCE)) effects, respectively. When the external field is adiabatically modified, the material will exhibit a temperature change whereas when the external field is isothermally modified, the material will exhibit an entropy change.

The influence of external fields on materials has been an active research field for centuries. In 1805, John Gough, a blind natural philosopher, observed that India rubber warms up when it is rapidly stretched by slightly touching a piece with his lips [13]. The experience of Gough corresponds to the first description of what we nowadays refer to as elastocaloric effect. In 1859, James P. Joule quantitatively reported temperature changes induced by uniaxial stress in diverse materials such as steel, copper, lead, glass or wood [14], and it was William Thomson (Lord Kelvin) who established a thermodynamic interpretation of such effects [15], later predicting the existence of magnetocaloric and electrocaloric effects [16]. In 1917, P. Weiss and A. Piccard observed a reversible temperature change on nickel at the vicinity of its Curie temperature when applying a magnetic field [17], which corresponds to the first experimental observation and discussion of what they called a *novel magnetocaloric phenomenon*. [5] Similarly, the first experimental observation of an electrocaloric effect was performed in 1930 by P. Kobeko and J. Kurtschatov in Rochelle salt [19].

For many materials, the magnitude of caloric effects is small around room temperature and the field-induced temperature change only becomes relevant at very low temperatures, where the specific heat becomes small [11, 12]. In this regard, the first application based on a caloric effect was theoretically proposed in the midst of 1920s decade, when P. Debye and W. F. Giauque independently recognised the possibility to achieve cryogenic temperatures close to absolute zero based on the adiabatic demagnetization of paramagnetic salts [18]. The idea of this novel technique was to cool down the paramagnetic salt down to cryogenic temperatures with a liquid Helium bath, and isothermally apply a magnetic field. This process leads to a decrease of the magnetic entropy of the salt while keeping the same temperature. In a second step, the magnetized salt is thermally insulated from the Helium bath, and finally the magnetic field is adiabatically removed. This last process leads to an increase of the magnetic entropy of the salt, which is compensated by a decrease of its lattice entropy, resulting in a decrease of the salt temperature [20, 21]. The experimental feasibility of such technique was proved for the first time in 1933 by W. F. Giauque and D. P. MacDougall, reaching temperatures well below 1 K [22, 23], and led W. F. Giauque to the Nobel Prize in Chemistry in 1949. [6] Nevertheless, such cryogenic temperatures below 1 K could not be sustained over time until the first magnetic refrigerators, cyclically exploiting the temperature decrease of paramagnetic salts when adiabatically demagnetized, were developed during the 1950s decade [24, 25].

[5] It is worth to highlight that in 1881, E. Warburg reported an irreversible heating in pure iron at room temperature when cyclically applying and removing a magnetic field. However, he did not consider it to be a new thermal effect and attributed it to the magnetic hysteresis of iron [18].

[6] The Nobel Prize in Chemistry 1949 website: `https://www.nobelprize.org/prizes/chemistry/1949/giauque/facts/`

A breakthrough took place in 1976, when G. V. Brown showed that the magnetocaloric effect could be used for magnetic refrigeration around room temperature. His demonstrator used the element Gd as a refrigerant, and took advantage of its ferromagnetic phase transition (that takes place near room temperature) to induce large reversible temperature changes under a cyclic magnetic field of 7 T [26]. During the following decades, the research on materials exhibiting caloric effects near room temperature started to gain relevance. In this regard, a crucial turning point took place in 1997 with the discovery by V. K. Pecharsky and K. A. Gschneidner of the large magnetocaloric effect exhibited by $Gd_5(Si_2Ge_2)$ [27]. The work on this compound, denoted as a *giant magnetocaloric material*, showed that the occurrence of a first-order phase transition plays a key role in enhancing the magnitude of the caloric effect, as the latent heat of the phase transition makes the major contribution to the field-induced entropy change, and boosted the research on magnetocaloric materials. [7]

Similarly, the research on materials exhibiting electrocaloric effects near room temperature was triggered in 2006 by a seminal work of A. S. Mischenko *et. al.*, where they reported on the giant electrocaloric effect in thin films of $PbZr_{0.95}Ti_{0.05}O_3$ near its ferroelectric transition [29]. With respect to the giant mechanocaloric effects, the work by E. Bonnot *et. al.* in 2008 reporting a giant elastocaloric effect in Cu-Zn-Al [30] [8] and the work by L. Mañosa *et. al.* in 2010 reporting a giant barocaloric effect in Ni-Mn-In [32], both of them emerging in the vicinity of martensitic phase transitions in these materials, strongly motivated the research activity.

Nowadays, the study of materials exhibiting giant caloric effects is one of the leading research fields on material physics, as reflected by the growing number of publications on these topics [33]. During the last decades, an increasingly broad variety of materials exhibiting giant isothermal entropy and adiabatic temperature changes under the application of an external field have been discovered [34–39], and their potential use for solid-state refrigeration has been extensively discussed [12, 33, 40–42], leading to a growing number of solid-state cooling prototypes based on different caloric effects [43, 44]. In fact, as recently stated in a report of the U.S. Department of Energy, solid-state refrigerants based on the giant caloric effects exhibited by diverse materials undergoing a ferroic phase transition are considered to be among the best technological alternatives to conventional refrigeration systems [9, 10, 33], due to their high energy-conversion efficiencies [42, 45, 46] together with the fact that they are environmentally-friendly.

The working principle of a solid-state-based refrigeration cycle is thermodynamically equivalent to that used for conventional systems based on vapour-compression.

[7] In 1990, previously to the work of V. K. Pecharsky and K. A. Gschneidner on $Gd_5(Si_2Ge_2)$, S. A. Nikitin *et. al.* reported on the large magnetocaloric effect exhibited by $Fe_{49}Rh_{51}$ near room temperature [28]. Nevertheless, the later report had a greater influence on sparking the research interest on materials exhibiting giant magnetocaloric effects.

[8] It must be mentioned that in 1980, a giant elastocaloric effect was reported in a Cu-Al-Ni alloy by C. Rodriguez and L. C. Brown [31]. However, this work did not have a significant influence on boosting the research on materials exhibiting giant elastocaloric effects.

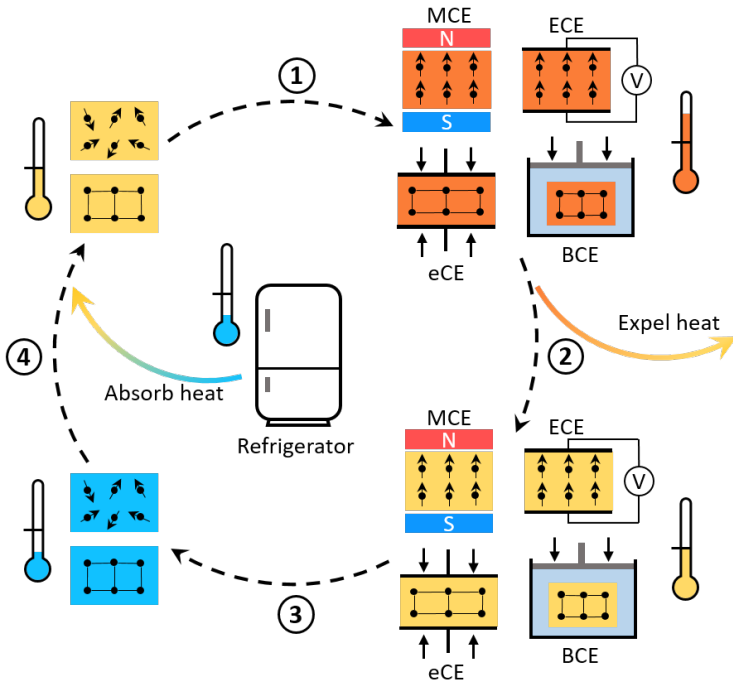

Figure 1.2: *Schematic representation of a four-step cooling cycle based on a solid-state refrigerant that exhibits a conventional giant magnetocaloric (MCE), electrocaloric (ECE), elastocaloric (eCE) or barocaloric (BCE) effect in the vicinity of a first-order phase transition. The atomic structure of the refrigerant material is represented by dots, while the arrows superposed to the dots represent the magnetic or electric dipoles if the material exhibits a magnetocaloric (MCE) or electrocaloric (ECE) effect. The temperature of the refrigerant material in each step of the cooling cycle is indicated by the colour code and the corresponding thermometer.*

Figure 1.2 schematically illustrates a general cooling cycle based on a solid-state refrigerant that exhibits a conventional giant caloric effect in the vicinity of a first-order phase transition under the application of magnetic field (H), electric field (E), uniaxial stress (σ) or hydrostatic pressure ($-p$). Starting with the refrigerant material at a certain temperature in the absence of any applied external field (top left panel illustrated in Figure 1.2), the cooling cycle comprises the following processes:

① Application of an external field (H, E, σ or $-p$) will favour the refrigerant material phase that maximizes the corresponding generalized displacement (M, P, ε or V), acting as the driving force to induce the forward phase transition. As the external field is adiabatically applied, to keep the total entropy constant, the refrigerant material will experience a temperature increase.

② The refrigerant material cools down under a constant external field by transferring heat to the hot reservoir.

③ The external field (H, E, σ or $-p$) is adiabatically removed, which acts as the driving force to induce the reverse phase transition and leads to a further temperature decrease of the refrigerant material.

④ The refrigerant material absorbs heat from the cold reservoir, which corresponds to the refrigerator in Figure 1.2. Therefore, the refrigerator becomes colder while the refrigerant material recovers its initial state.

In spite of all the intensive research devoted during the last decades on the discovery of novel refrigerant materials exhibiting giant caloric effects near room temperature, there are still a series of limitations to overcome that hinder the development of commercial solid-state cooling devices. From a general point of view, many of the promising materials that exhibit giant magnetocaloric, electrocaloric or mechanocaloric effects undergo a first-order phase transition [37, 38, 47]. Consequently, the inherent thermal hysteresis of the phase transition can significantly reduce the material isothermal entropy and adiabatic temperature changes upon cycling the external field, thus compromising the reversibility of the giant caloric effect [48].

So far, most of the research activity has been focused on materials exhibiting a giant magnetocaloric effect, and many solid-state cooling prototypes based on this caloric effect have been developed [33, 44]. However, most of the promising magnetocaloric materials require the application of strong magnetic fields in order to induce large isothermal entropy and adiabatic temperature changes. The vast majority of cooling prototypes use permanent magnets as a magnetic field source, which limits the maximum attainable magnetic fields up to 2 T, leading to moderate values of the reversible field-induced isothermal entropy and adiabatic temperature changes which are currently in the order of $\Delta S_{iso} \sim 10\,\mathrm{JK^{-1}kg^{-1}}$ and $\Delta T_{ad} \sim 5\,\mathrm{K}$, respectively [47]. Furthermore, as the refrigerant materials that are currently used in such prototypes exhibit a significant reversibility of the field-induced magnetocaloric effect, the magnetic field needs to be continuously applied during the heat exchange process and large amounts of permanent magnets (typically made of Nd-Fe-B) are required, which depend on critical materials such as Nd and increase the costs of these prototypes [6, 49].

The use of materials exhibiting a giant electrocaloric effect as a solid-state refrigerant triggers different bottlenecks in order to develop cooling prototypes. Despite the fact that large electrocaloric effects have been theoretically predicted for different materials [37], the maximum experimentally reported values for the isothermal entropy and adiabatic temperature changes are about $\Delta S_{iso} \sim 6\,\mathrm{JK^{-1}kg^{-1}}$ and $\Delta T_{ad} \sim 5\,\mathrm{K}$, respectively [50]. Therefore, large electric fields are needed in order to obtain a significant electrocaloric effect. Secondly, electrocaloric materials need to be thin in order to apply large electric fields and avoid the electrical breakdown, which limits the size of the refrigerant material and thwarts the upscaling of such

electrocaloric-based cooling prototypes.

Finally, although the use of materials exhibiting a giant elastocaloric or barocaloric effect for solid-state refrigeration is still at its dawn [44], [9] diverse mechanocaloric materials have been reported to display isothermal entropy and adiabatic temperature changes which clearly surpass the values reported for the best magnetocaloric and electrocaloric materials [38, 39]. Nevertheless, for the sake of refrigeration prototypes, the fatigue-life of the refrigerant material is a stringent bottleneck as they are prone to breakdown.

Interestingly, most of the materials exhibiting a giant magnetocaloric or electrocaloric effects are also prone to exhibit giant mechanocaloric effects, as the first-order phase transition not only changes the magnetic or polar order of the material but it also modifies its crystal structure [37, 38]. In fact, the strong interplay between the structural and magnetic (polar) degrees of freedom in many of these materials confers the first-order character to the phase transition, which is essential for enhancing the magnitude of the magnetic (electric) field-induced isothermal entropy and adiabatic temperature changes.

The strong coupling between different degrees of freedom confers these materials with a cross-coupled response to different external fields, and their diverse giant caloric effects can be influenced by non-conjugated external fields. For instance, application of uniaxial stress (σ) or hydrostatic pressure ($-p$) can influence the magnetization (M) or polarization (P) of a system, inducing changes on the giant magnetocaloric or electrocaloric effects. Conversely, application of magnetic (H) or electric (E) field can influence the system structure, inducing a strain (ε) or a change in volume (V), which induces changes on the corresponding giant mechanocaloric effects. Such materials, which exhibit a multiferroic phase transition that can be induced by diverse external fields, are denoted as *multicaloric materials* and the caloric effects that arise from simultaneous or sequential change of more than one external field are referred to as *multicaloric effects* [51–53].

The research interest on multicaloric effects has been triggered from the parallel research progress on the diverse caloric effects. Despite the early reports of N. A. Nikitin *et. al.* at the beginning of the 1990s decade on the giant magnetocaloric and elastocaloric effects exhibited by different Fe-Rh samples [28, 54], it was M. P. Annaorazov *et. al* at the mid 1990s who observed both a giant elastocaloric and magnetocaloric effect in the same Fe-Rh specimen [55]. During the 2000s decade, the research was mainly focused on the influence that a constant hydrostatic pressure has on the magnetocaloric effect exhibited by diverse materials [38, 46], but it was not until 2007 when N. A. de Oliveira firstly emphasized the advantages that a simultaneous change on more than one external field can have on inducing a giant caloric effect in a material. In a theoretical study on the magnetocaloric and barocaloric effects exhibited by $ErCo_2$ at cryogenic temperatures [56], he predicted

[9] To our knowledge, there are no working solid-state cooling prototypes based on a refrigerant material exhibiting a giant barocaloric effect, although there are some prototypes under development [33].

that the temperature window where the material exhibits a giant isothermal entropy change can be broadened when simultaneously varying both magnetic field and hydrostatic pressure. Despite of all these early studies, the term *multicaloric effect* was coined in 2010 by L. Mañosa *et. al.* when discussing the possibility to induce the martensitic phase transition of Ni-Mn-In with a combination of magnetic field and hydrostatic pressure [32].

During the last decade the interest on multicaloric materials has significantly grown, and many striking results have already been achieved [57–61], as the possibility to induce large isothermal entropy and adiabatic temperature changes by either a single external field (giant caloric effect) or multiple external fields (giant multicaloric effects) confers them with significant advantages when compared to materials that do not present a strong cross-coupled response to different external fields. For instance, the combination of more than one external field can reduce the field magnitudes required to induce a large caloric effect, and it can as well enlarge the operational temperature window of a given material [62]. Additionally, it has been shown that the combination of diverse external fields provides a strategy to master the hysteresis associated with the first-order phase transition, and thus enhance the reversibility of a given caloric effect [51, 63]. Furthermore, a novel multicaloric cooling cycle based on a suitable combination of magnetic field and uniaxial stress has been recently proposed and tested by T. Gottschall *et. al* [64], demonstrating the possibility to take advantage of the inherent hysteresis of a multicaloric material to increase the reversibility of a given caloric effect while drastically reducing the volume of the magnetic field source needed.

Promising perspectives are envisaged for the use of multicaloric materials for refrigeration applications, as they can help on overcoming some of the previously discussed bottlenecks that hinder the commercial development of solid-state cooling devices [33, 46]. However, the research on multicaloric effects is still germinal, as it requires the development of non-commercial advanced characterization systems [65, 66]. Overall, despite the recent progress, many pages on this story still have to be written.

1.1 Dissertation contents

This dissertation is centred on the study and characterization of the giant caloric and multicaloric effects arising from materials displaying a magnetostructural first-order phase transition near room temperature with a strong coupling between the structural and magnetic degrees of freedom. It is divided into six chapters, which are organized as follows.

After this general motivation and introduction, Chapter 2 provides the theoretical framework used to describe caloric and multicaloric effects arising in a general thermodynamic system. It provides a complete thermodynamic description of such phenomena, and discusses in detail the nature of first-order phase transitions.

Chapter 3 is a keystone of the present work, as therein we introduce the diverse experimental techniques used for the quantitative study of the giant caloric and multicaloric effects. In this regard, special attention is given to calorimetry and adiabatic thermometry under the simultaneous influence of magnetic field and uniaxial compressive stress. Furthermore, detailed descriptions of the bespoke setups we have designed, assembled and calibrated for such purposes are also provided.

Before discussing the experimental results of our research, Chapter 4 renders an overview of the physical properties exhibited by the different families of multicaloric materials under study. Firstly, the Fe-Rh system is introduced, which is nowadays considered a benchmark multicaloric material. Secondly, the family of Ni-Mn-based Heusler alloys is presented in detail, as such compounds are promising candidates for future technological applications due to the strong coupling between the structural and magnetic degrees of freedom that they can exhibit at the martensitic phase transition.

The corresponding results of our research on selected alloys belonging to those families of multicaloric materials are presented in Chapter 5. It is divided into four sections, each one corresponding to a different alloy, which are organized as follows:

- **Section 5.1: Fe-Rh**
  This section is devoted to thoroughly characterize the giant elastocaloric effect of Fe-Rh under the application of uniaxial compressive stress. Furthermore, the effect of a constant magnetic field (uniaxial compressive stress) on the giant elastocaloric (magnetocaloric) effect is also discussed in detail.

- **Section 5.2: Ni-Fe-Co-Mn-Sn**
  In this section, we provide a detailed characterization of the giant magnetocaloric effect exhibited by a novel Ni-Co-Mn-Sn-based Heusler alloy, whose composition has been tailored in order to confer it with outstanding elastocaloric and magnetocaloric effects.

- **Section 5.3: Ni-Mn-In**
  The advantages of the multicaloric effect with respect to the single caloric (magnetocaloric and elastocaloric) effects are analysed in depth on a prototype Ni-Mn-based Heusler alloy exhibiting non-synergic single caloric effects. Furthermore, the feasibility of the novel multicaloric cycle proposed by T. Gottschall *et. al.* is experimentally tested and compared with a conventional magnetic field refrigeration cycle.

- **Section 5.4: Ni-Mn-Ga-Cu**
  For the first time, a thorough characterization of the multicaloric effect and its advantages with respect to the corresponding elastocaloric and magnetocaloric effects is performed on a prototype Ni-Mn-Ga-based Heusler alloy with a tailored composition in order to confer it with synergic single caloric effects. Furthermore, the cross-coupling contribution to the multicaloric effect is computed and discussed.

Finally, Chapter 6 summarizes the main conclusions of this dissertation, and sketches as well some future perspectives.

2 Fundamentals

Throughout the different chapters of this dissertation, concepts such as heat flow, specific heat, temperature and entropy changes, order parameter, external field or phase transition will be extensively used for the interpretation and discussion of the presented results. The aim of this chapter is to provide a theoretical framework to properly describe the experimentally studied caloric and multicaloric effects in solids.

In this regard, a thermodynamic description of a general system under the influence of different external fields is provided as a framework for the derivation of the Maxwell relations, followed by a discussion on the associated caloric and multicaloric effects. By keeping the thermodynamic framework as a keystone, a detailed section centred on the nature of first-order phase transitions is introduced, where the Clausius-Clapeyron equation is derived and the nature of hysteresis is discussed.

2.1 Thermodynamics

Let us consider a closed system under the influence of a certain set of external fields $\{x_i\}$. A generalized displacement X_i can be associated to each applied external field x_i forming a set of pairs of conjugated variables $\{x_i, X_i\}$. For instance, relevant examples of external fields and associated generalized displacements are such as magnetic field $\vec{H}$ and magnetization $\vec{M}$, electric field $\vec{E}$ and polarization $\vec{P}$ or stress $\overline{\overline{\sigma}}$ and strain $\overline{\overline{\varepsilon}}$. [1]

The state of this system can be described by a thermodynamic potential, such as the internal energy, which will be a function of the entropy of the system S and the set of generalized displacements $\{X_i\}$ as $U = U(S, \{X_i\})$. If we now consider a differential change in the internal energy of the system, it can be expressed as:

$$dU(S, \{X_i\}) = \left(\frac{\partial U}{\partial S}\right)_{\{X_i\}} dS + \sum_{i=1}^{n} \left(\frac{\partial U}{\partial X_i}\right)_{S,\{X_{j\neq i}\}} dX_i \tag{2.1}$$

[1] For the sake of simplicity, the notation in the following dissertation will omit the tensorial character of the applied external fields and the generalized displacements. For instance, in the case of the studied caloric and multicaloric effects, the applied external fields are either magnetic field and uniaxial stress. These external fields are applied along a specific direction, and only the parallel component of the generalized displacement will be considered. Therefore, under this specific conditions, these vectors and tensors will take the form of scalars.

where each right hand term of equation 2.1 accounts for the different ways of the system to change its internal energy. If we consider that the system is in equilibrium at both initial and end state involved, and taking into account both first and second laws of thermodynamics [67], we can introduce the temperature of the system T from the first term of equation 2.1 as $\left(\frac{\partial U}{\partial S}\right)_{\{X_i\}} = T$ and the conjugated external fields x_i from the individual terms inside the summation as $\left(\frac{\partial U}{\partial X_i}\right)_{S,\{X_{j\neq i}\}} = x_i$. Therefore, equation 2.1 can be written as:

$$dU(S,\{X_i\}) = TdS + \sum_{i=1}^{n} x_i dX_i \tag{2.2}$$

where TdS accounts for the reversible heat flow and the summation terms $x_i dX_i$ refer to other forms of changing the internal energy of the system under certain applied external fields. Table 2.1 outlines this different energy forms that can be involved in the internal energy change of the system. It is important to point out that the general magnetic and electric energy forms expressed in this table can be separated in two different contributions. As discussed in detail in [11], the magnetic energy form can be expressed as $d'W = \mu_0 HdH + \mu_0 HdM$ and the electric energy as $d'W = \epsilon_0 EdE + EdP$, where M and P correspond to the system magnetization and polarization and μ_0 and ϵ_0 are the vacuum permeability and permittivity, respectively. In these two expressions, the first term corresponds to the energy required to increase the magnetic (electric) field a differential dH (dE), while the second term corresponds to the energy required to increase the system magnetization (polarization) a differential dM (dP), respectively. Therefore, in the case where we only account for the energy forms that act on the system, we solely consider the second terms of the above expressions as they express the differential energy forms for the system to change its magnetization or polarization in a magnetic or electric field, respectively.

Describing the thermodynamic state of the system with the internal energy $U(S,\{X_i\})$ implies that we have to control its natural variables: the entropy S and the set of generalized displacements $\{X_i\}$, which are not easily experimentally controllable. We can define new thermodynamic potentials that depend on different natural variables more suitable to be controlled in the laboratory, such as temperature T and the applied external fields $\{x_i\}$, through the Legendre transforms.

With this purpose, we can introduce two new thermodynamic potentials: the Helmholtz and the Gibbs free energies that are defined as $F(T,\{X_i\}) = U - TS$ and $G(T,\{x_i\}) = F - \sum_{i=1}^{n} x_i X_i$, respectively. A differential change of these free energies can then be expressed as:

$$dF(T,\{X_i\}) = dU - TdS - SdT = -SdT + \sum_{i=1}^{n} x_i dX_i \tag{2.3}$$

Caloric effect	External field (x_i)	Generalized displacement (X_i)	Energy form ($d'W$)
MCE	Magnetic field H	Magnetic induction B	HdB
ECE	Electric field E	Electric displacement D	EdD
eCE	Uniaxial stress σ	Strain ε	$V\sigma d\varepsilon$
BCE	Hydrostatic pressure $-p$	Volume V	$-pdV$

Table 2.1: *Summary of the relevant external fields and generalized displacements for the description of the caloric (magneto-, electro-, elasto- and barocaloric) and multicaloric effects. Each pair of conjugated variables is associated with a different energy form, such as magnetic, electric and mechanic work. See [11] for a detailed description of the different energy forms.*

$$dG(T,\{x_i\}) = dF - \sum_{i=1}^{n} x_i dX_i - \sum_{i=1}^{n} X_i dx_i = -SdT - \sum_{i=1}^{n} X_i dx_i \tag{2.4}$$

Since both Helmholtz and Gibbs free energies are thermodynamic potentials, their second derivatives with respect to its natural variables are independent of the order in which they are performed. For a general function $f(y,z)$ this is expressed as:

$$\frac{\partial^2 f}{\partial y \partial z} = \frac{\partial^2 f}{\partial z \partial y} \tag{2.5}$$

where $f(y,z)$ can either be the Helmholtz $F(T,\{X_i\})$ or the Gibbs $G(T,\{x_i\})$ free energies and y and z account for any pair of natural variables of the considered thermodynamic potential. Therefore, if we take $y = T$ and $z = X_i$ as the variables for the Helmholtz free energy and $y = T$ and $z = x_i$ as the variables for the Gibbs free energy, by applying equation 2.5 and taking into account equations 2.3 and 2.4, we obtain:

$$\left(\frac{\partial S}{\partial X_i}\right)_{T,\{X_{j\neq i}\}} = -\left(\frac{\partial x_i}{\partial T}\right)_{\{X_j\}} \tag{2.6a}$$

$$\left(\frac{\partial S}{\partial x_i}\right)_{T,\{x_{j\neq i}\}} = \left(\frac{\partial X_i}{\partial T}\right)_{\{x_j\}} \tag{2.6b}$$

where equation 2.6a is obtained from the Helmholtz free energy and equation 2.6b from the Gibbs free energy, respectively. These equations are two of the Maxwell relations, and they relate the entropy change with respect to the external field or the generalized displacement with the temperature derivative of the generalized displacement or the external field. Another interesting Maxwell relation to be taken into account is the one obtained when comparing the second derivative of the Gibbs free energy with respect to two different external fields x_i and x_j, which leads to:

$$\left(\frac{\partial X_j}{\partial x_i}\right)_{T,\{x_{k\neq i}\}} = \left(\frac{\partial X_i}{\partial x_j}\right)_{T,\{x_{k\neq j}\}} \tag{2.7}$$

This different Maxwell relation links the response of the generalized displacement X_i with the non-conjugated external fields $x_{j\neq i}$, quantifying the strength of the cross-coupled response of the system. It is important to point out that this Maxwell relation establishes the symmetry of the cross-coupled response, and will be particularly convenient for the description of the multicaloric effect.

2.1.1 Caloric effects

The thermodynamic state changes of the considered system induced under a change of an external field x_i, while keeping the other applied external fields constant $\{x_{j\neq i}\}$, are generally characterized by the field-induced isothermal entropy change ΔS_{iso} and the field-induced adiabatic temperature change ΔT_{ad} [53]. For the determination of these quantities, it is convenient to consider the state function that expresses the entropy of the system S as a function of temperature T and the applied external fields $\{x_i\}$, which are easily controlled variables in an experiment that implies an external field change. This state function, expressed as $S(T,\{x_i\})$, is obtained from the first term of equation 2.4 and by taking into account equation 2.6b and the definition of the specific heat at constant field C as $\frac{C}{T} = \left(\frac{\partial S}{\partial T}\right)_{\{x_i\}}$, a differential change of the entropy $dS(T,\{x_i\})$ can be expressed as:

$$dS(T,\{x_i\}) = \left(\frac{\partial S}{\partial T}\right)_{\{x_i\}} dT + \sum_{i=1}^{n}\left(\frac{\partial S}{\partial x_i}\right)_{T,\{x_{j\neq i}\}} dx_i = \frac{C}{T}dT + \sum_{i=1}^{n}\left(\frac{\partial X_i}{\partial T}\right)_{\{x_j\}} dx_i \tag{2.8}$$

Under isothermal conditions, the temperature T of the system is constant and $dT = 0$. Thus, the isothermal entropy change under a variation of an external field x_i is expressed as:

$$\Delta S(T, x_i^s \rightarrow x_i^f) = \int_{x_i^s}^{x_i^f} \left(\frac{\partial X_i}{\partial T}\right)_{x_i',\{x_{j\neq i}\}} dx_i' \tag{2.9}$$

where x_i^s and x_i^f correspond to the start and end values of the modified external field x_i. Conversely, if the external field is modified adiabatically, the entropy of the system S will be kept constant and $dS = 0$. Consequently, equation 2.8 yields

$$\Delta T(S, x_i^s \rightarrow x_i^f) = -\int_{x_i^s}^{x_i^f} \frac{T}{C}\left(\frac{\partial X_i}{\partial T}\right)_{x_i',\{x_{j\neq i}\}} dx_i' \tag{2.10}$$

Both equations 2.9 and 2.10 describe the caloric response of the system and directly relate the induced isothermal entropy and the adiabatic temperature change to the temperature derivative of the generalized displacement conjugated to the

modified external field. Therefore, the magnitude of $\left(\frac{\partial X_i}{\partial T}\right)_{\{x_i\}}$ will have an important role on tuning the caloric response of a system under the experimental conditions considered in this section. Additionally, as it is deduced from equation 2.7, the generalized displacement X_i has to include a dependency on the other fields that are kept constant during the experiment under consideration $\{x_{j\neq i}\}$. Therefore, for a general description of the caloric response, the generalized displacement can be expressed in the form $X_i = X_i(T, x_i^{'}, \{x_{j\neq i}\})$. Nevertheless, this complete variable dependency has been omitted from equations 2.9 and 2.10 for the sake of simplicity.

Furthermore, equation 2.10 also depends on the isofield specific heat of the system, that is inside the integral. Therefore, the specific heat magnitude will also tune the induced thermal response under a certain external field change $x_i^s \rightarrow x_i^f$. It is also important to take into account that the specific heat includes a dependency on temperature T and all the applied external fields on the system, and it can be expressed in the form $C = C(T, x_i^{'}, \{x_{j\neq i}\})$, but it has been omitted for the sake of clarity.

2.1.2 Multicaloric effects

Multicaloric effects are defined as the induced thermodynamic state change of the considered system under the simultaneous (or sequential) change of more than one of the applied external fields $\{x_i\}$. A detailed theoretical discussion of multicaloric effects can be found in [52, 53].

For the sake of simplicity, and without loss of generality, this section will focus on describing the particular case where the considered system responds to a change of two external fields: x_i and x_j. As the entropy is a state function, the entropy change induced between two states at equilibrium will only depend on the initial and final values. Therefore, the multicaloric entropy change will be given by $\Delta S(T, x_i^s \rightarrow x_i^f, x_j^s \rightarrow x_j^f) = S(T, x_i^f, x_j^f) - S(T, x_i^s, x_j^s)$. Additionally, this field-induced entropy change will be irrespective of the path followed between the start and end equilibrium states and it can be separated into two processes as follows:

$$\Delta S(T, x_i^s \rightarrow x_i^f, x_j^s \rightarrow x_j^f) = \Delta S(T, x_i^s \rightarrow x_i^f, x_j^s) + \Delta S(T, x_i^f, x_j^s \rightarrow x_j^f) \quad (2.11)$$

where both terms on the right hand side correspond to the entropy change of the caloric effect, expressed in equation 2.9, under a constant external field. Thus, the first right-hand term, under a constant external field x_j^s, can be expressed as:

$$\Delta S(T, x_i^s \rightarrow x_i^f, x_j^s) = \int_{x_i^s}^{x_i^f} \left(\frac{\partial X_i}{\partial T}\right)_{x_i^{'}, x_j^s} dx_i^{'} \quad (2.12)$$

and the second right-hand term, under a constant external field x_i^f, can be expressed as:

$$\Delta S(T, x_i^f, x_j^s \rightarrow x_j^f) = \int_{x_j^s}^{x_j^f} \left(\frac{\partial X_j}{\partial T}\right)_{x_j^{'}, x_i^f} dx_j^{'} \tag{2.13}$$

where the dependencies of the generalized displacements can be expressed as $X_i = X_i(T, x_i^{'}, x_j^s)$ and $X_j = X_j(T, x_i^f, x_j^{'})$, respectively, and have been omitted from both equations for the sake of simplicity.

These two caloric contributions given by equations 2.12 and 2.13 can be alternatively described in order to distinguish the effect of the secondary constant external field on the computed caloric effect. A proper identification of the effect of the secondary field will allow us to quantify the relevance of the cross-coupled contribution on the caloric response of the system. To that end, from the definition of a partial derivative, the caloric effect described by equation 2.12 can expressed as:

$$\Delta S(T, x_i^s \rightarrow x_i^f, x_j) - \Delta S(T, x_i^s \rightarrow x_i^f, x_j = 0) = \int_0^{x_j} \frac{\partial}{\partial x_j^{'}} \Delta S(T, x_i^s \rightarrow x_i^f, x_j^{'}) dx_j^{'} \tag{2.14}$$

The left hand side of equation 2.14 accounts for the change induced from the application of a constant secondary external field x_j on the caloric effect induced from a field change $x_i^s \rightarrow x_i^f$, while the right hand side depends on the derivative of the induced caloric effect with respect to the secondary external field. By replacing equation 2.12 into the right hand side integral of equation 2.14, we obtain:

$$\begin{aligned} &\Delta S(T, x_i^s \rightarrow x_i^f, x_j) \\ &\quad = \Delta S(T, x_i^s \rightarrow x_i^f, x_j = 0) + \int_0^{x_j} \frac{\partial}{\partial x_j^{'}} \left[\int_{x_i^s}^{x_i^f} \left(\frac{\partial X_i}{\partial T}\right)_{x_i^{'}, x_j^{'}} dx_i^{'} \right] dx_j^{'} \\ &\quad = \int_{x_i^s}^{x_i^f} \left(\frac{\partial X_i}{\partial T}\right)_{x_i^{'}, x_j = 0} dx_i^{'} + \int_0^{x_j} \int_{x_i^s}^{x_i^f} \left(\frac{\partial^2 X_i}{\partial x_j^{'} \partial T}\right)_{x_i^{'}} dx_i^{'} dx_j^{'} \end{aligned} \tag{2.15}$$

This equation separates the induced caloric effect under a constant secondary external field into two different contributions: the first term corresponds to the caloric effect without any applied secondary field, while the second term depends on the integrand $\left(\frac{\partial^2 X_i}{\partial x_j^{'} \partial T}\right)_{x_i^{'}}$, that can also be expressed as $\frac{\partial}{\partial T}\left(\frac{\partial X_i}{\partial x_j^{'}}\right)_{T, x_i^{'}}$. At this point, it is useful to introduce the cross-susceptibility tensor as:

$$\chi_{ij} = \left(\frac{\partial X_i}{\partial x_j^{'}}\right)_{T, x_i^{'}} \tag{2.16}$$

where its diagonal terms correspond to the standard susceptibilities that measure the response of a generalized displacement with its conjugated external field, whereas the off-diagonal terms, as discussed for equation 2.7, correspond to the coefficients that quantify the strength of the cross-coupled response of the system.

The new term in equation 2.15 evidences that in the presence of interplay between the two generalized displacements of the system and their non conjugated fields (X_i, x_j) and (X_j, x_i), the caloric effect obtained for a certain field change will also depend on the secondary field applied, and the double integral quantifies the cross-coupling magnitude of the two considered conjugated displacements. Moreover, it is important to point out that the cross-coupled contribution is significant if the cross-susceptibility exhibits a notable temperature dependence. A similar derivation and discussion holds true for equation 2.13.

Therefore, taking the above expressions into account we can rewrite the multicaloric entropy change expressed in equation 2.11 as:

$$\begin{aligned}\Delta S(T,&x_i^s \rightarrow x_i^f, x_j^s \rightarrow x_j^f) \\ &= \Delta S(T, x_i^s \rightarrow x_i^f, x_j = 0) + \Delta S(T, x_i = 0, x_j^s \rightarrow x_j^f) \\ &+ \int_0^{x_j^s} \int_{x_i^s}^{x_i^f} \frac{\partial \chi_{ij}}{\partial T} dx_i^{'} dx_j^{'} + \int_0^{x_i^f} \int_{x_j^s}^{x_j^f} \frac{\partial \chi_{ji}}{\partial T} dx_j^{'} dx_i^{'}\end{aligned} \tag{2.17}$$

Equation 2.17 corresponds to the general expression that quantifies the induced entropy change for a multicaloric effect under the sequential (or simultaneous) variation of two external fields. The two first right hand terms correspond to the caloric effects without any applied secondary field and the two last terms account for the cross-coupled response of the system for each individual caloric effect. Figure 2.1 shows a a schematic representation of the isothermal multicaloric entropy change under the variation of two external fields. Two observations must be highlighted from this schematic figure. First of all, as the entropy is a state function, its variation is path independent and the same isothermal entropy change is achieved (A $\rightarrow$ D) irrespectively of the order of application of the external fields. Secondly, due the presence of a cross-coupled response, the magnitude of a caloric effect driven by one external field depends on the magnitude of the secondary constant external field. This effect can be easily observed by comparing each pair of red or blue arrows represented in the figure, which correspond to the two caloric effects under different applied secondary external fields.

So far, we have only considered the field-induced isothermal entropy change of a multicaloric effect, but in order to provide a complete characterization we also have to consider the field-induced adiabatic temperature change [53], generally expressed as $\Delta T(S, x_i^s \rightarrow x_i^f, x_j^s \rightarrow x_j^f)$. For this purpose, a new state function that has the entropy S and the applied external fields $\{x_i\}$ as its natural variables is a suitable function to describe the multicaloric adiabatic temperature change and has to be considered. Such function, expressed as $T(S, \{x_i\})$, can be obtained by performing an inversion to the entropy state function considered in section 2.1.1.

As temperature is also a state function, a temperature change induced between two states at equilibrium will be independent of the path followed between them. Therefore, an equivalent expression to equation 2.11 can be written for the adiabatic temperature change as:

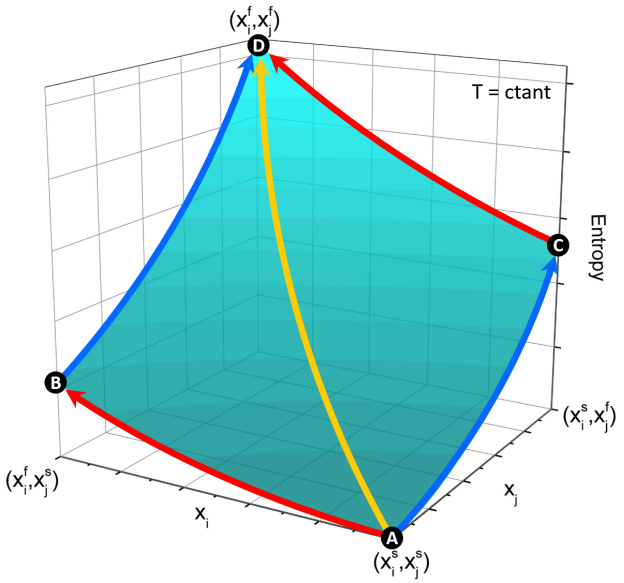

Figure 2.1: *Illustrative representation of the isothermal entropy as a function of both applied external fields x_i and x_j for a system exhibiting a cross-coupled response ($\chi_{ij} \neq 0$). Labels (A-D) indicate the entropy values of the system for selected values the applied external fields, and arrows represent particular paths that correspond to the sequential ($A \rightarrow B \rightarrow D$ or $A \rightarrow C \rightarrow D$) or simultaneous ($A \rightarrow D$) variation of the two external fields.*

$$\Delta T(S, x_i^s \rightarrow x_i^f, x_j^s \rightarrow x_j^f) = \Delta T(S, x_i^s \rightarrow x_i^f, x_j^s) + \Delta T(S, x_i^f, x_j^s \rightarrow x_j^f) \tag{2.18}$$

By following a similar derivation as for the multicaloric entropy change, and additionally taking into account equation 2.10, it is straightforward to obtain an equivalent expression to equation 2.17 giving the temperature change under the sequential (or simultaneous) variation of two external fields, that in its general form is expressed as:

$$\begin{aligned}
&\Delta T(S,x_i^s \rightarrow x_i^f, x_j^s \rightarrow x_j^f) \\
&\quad = \Delta T(S, x_i^s \rightarrow x_i^f, x_j = 0) + \Delta T(S, x_i = 0, x_j^s \rightarrow x_j^f) \\
&\quad - \int_0^{x_j^s} \int_{x_i^s}^{x_i^f} \frac{\partial}{\partial x_j^{'}} \left[\frac{T}{C} \left(\frac{\partial X_i}{\partial T} \right)_{x_i^{'}, x_j^{'}} \right] dx_i^{'} dx_j^{'} \\
&\quad - \int_0^{x_i^f} \int_{x_j^s}^{x_j^f} \frac{\partial}{\partial x_i^{'}} \left[\frac{T}{C} \left(\frac{\partial X_j}{\partial T} \right)_{x_i^{'}, x_j^{'}} \right] dx_j^{'} dx_i^{'}
\end{aligned} \tag{2.19}$$

The general multicaloric equations derived in this section for the isothermal entropy change (equation 2.17) and the adiabatic temperature change (equation 2.19) encompass any possible external field change. Nevertheless, there are two

different relevant situations that have to be considered. For the sake of clarity and simplicity, the following discussion will only focus on the multicaloric entropy change, as the same holds true for the adiabatic temperature change, and we will consider that either the end or the start value of each external field is zero.

1. **Symmetric external field change**
   This particular case corresponds to either the application $(x_i^s = 0, x_j^s = 0) \rightarrow (x_i^f, x_j^f)$ or the removal $(x_i^s, x_j^s) \rightarrow (x_i^f = 0, x_j^f = 0)$ of both external fields. Under these circumstances, and similarly to equation 2.11, the multicaloric entropy change for the application of both fields can be expressed as:

$$\Delta S(T, 0 \rightarrow x_i^f, 0 \rightarrow x_j^f) = \Delta S(T, 0 \rightarrow x_i^f, x_j^s = 0) + \Delta S(T, x_i^f, 0 \rightarrow x_j^f) \tag{2.20}$$

   while the multicaloric entropy change for the removal of both fields can be written as:

$$\Delta S(T, x_i^s \rightarrow 0, x_j^s \rightarrow 0) = \Delta S(T, x_i^s \rightarrow 0, x_j^s) + \Delta S(T, x_i^f = 0, x_j^s \rightarrow 0) \tag{2.21}$$

   In both cases, as it can be deduced from equations 2.20 and 2.21, one of the two terms accounting for the cross-coupled response of the system expressed in equation 2.17 will be zero, while the other term will be different from zero. Therefore, the field-induced multicaloric effect will not be equivalent to the simple sum of the two independent caloric effects in the absence of a secondary external field.

2. **Asymmetric external field change**
   This particular case corresponds to the application of one external field while the other field is removed, and can be expressed as $(x_i^s, x_j^s = 0) \rightarrow (x_i^f = 0, x_j^f)$. For this case of interest, and similarly to equation 2.11, the multicaloric entropy change can be expressed as:

$$\Delta S(T, x_i^s \rightarrow 0, 0 \rightarrow x_j^f) = \Delta S(T, x_i^s \rightarrow 0, x_j^s = 0) + \Delta S(T, x_i^f = 0, 0 \rightarrow x_j^f) \tag{2.22}$$

   As expressed by equation 2.22, the field-induced multicaloric effect can be separated into two independent contributions that correspond to the respective caloric effects in the absence of any secondary external field. Therefore, for this particular situation, the multicaloric effect corresponds to the simple sum of both independent caloric effects as there will be no term that accounts for the cross-coupled response of the system.

2.2 Phase transitions

As shown in the previous section, the temperature derivative of the generalized displacement $\left(\frac{\partial X_i}{\partial T}\right)_{\{x_i\}}$ has an important role on tuning the field-induced thermal response of both the caloric and multicaloric effects. In the present section we will see that significant changes on this term are met in the vicinity of phase transitions, where large changes in conjugate displacements are expected as thermodynamic properties of the system will have a strong temperature dependence.

From the thermodynamics point of view, a phase is a region of matter at a certain thermodynamic state, characterized by a set of homogeneous macroscopic physical properties that take the form of a scalar, a vector or a tensor. Each macroscopic physical property will satisfy certain intrinsic symmetries that will reduce its independent components. Associated with the system structure, certain coordinates transformations (such as translations, rotations, inversions, or combinations of those) leave the system invariant, thus defining a certain symmetry group. In the particular case of crystalline systems, where at the atomic level, its components are arranged in an ordered structure according to a certain crystal lattice, the system symmetries will further condition the independent components of the macroscopic physical properties. The Neumann principle, formulated in the 19th century, expressed this fact as [68]:

> *The symmetry elements of any physical property of a crystal must include all the symmetry elements of the point group of the crystal*, which can be otherwise stated as: *If a crystal is invariant with respect to certain symmetry operations, any of its physical properties must also be invariant with respect to the same symmetry operations.*

Let us consider the same thermodynamic system as in section 2.1. Under the influence of a driving force, such as an applied external field (x_i) or a change on temperature (T), the equilibrium state of the considered system can change, as there may be another thermodynamic state that minimizes the system's free energy under those new conditions. Under these circumstances, the system evolves from one phase to another one, characterized by different values of the macroscopic properties, thus experiencing a phase transition.

Usually, the changes in the macroscopic properties when the considered system undergoes a phase transition are linked to a symmetry breaking, e.g. breaking of spatial inversion, time reversal or rotation symmetry. Although there are also phase transitions which do not involve a symmetry breaking, e.g. a liquid to gas transition. The close relation between symmetry and phase transitions was introduced by L.D. Landau in a work published in 1937 entitled *"On the Theory Phase Transitions"* [69], where he discussed that in a continuous phase transition (those without an associated latent heat, as it will be addressed in section 2.2.1) there must be a symmetry change at the phase transition. Landau introduced the concept of order

parameter (η), which can take the form of a scalar, a vector or a tensor, to study the behaviour of a system near a phase transition. From a general point of view, an order parameter is a characteristic property of the system that measures the degree of order across the boundaries of the phase transition, which vanishes at one side of the phase transition and takes a non-zero value at the other side.

Let us consider a general phase transition taking place at a certain temperature T_C with an associated order parameter η. At the disordered phase, where $\eta = 0$, the set of transformations that leave the system invariant is called the S_0 group. The emergence of the order parameter at the transition temperature induces a symmetry breaking and reduces the symmetry of the system. For instance, let us suppose that $\varrho_0(r)$ defines the density function of the particular high symmetry phase of the system, which is invariant under the S_0 group. At the phase transition, the density starts to change and can be expressed as $\varrho(r) = \varrho_0(r) + \delta\varrho(r)$, where $\delta\varrho(r)$ is small compared to $\varrho_0(r)$ and has a lower symmetry. The set of transformations that leave $\delta\varrho(r)$ invariant constitutes the S group, which is a subgroup of S_0. Then, the density $\varrho(r)$ will also have the same symmetries as $\delta\varrho(r)$. As soon as the transition starts, and the order parameter emerges, the symmetry of the system changes from the S_0 group to the subgroup S.

Specifically, a particular case of interest for this dissertation are the ferroic transitions, which refer to those phase transitions in which a new macroscopic physical property of the system spontaneously emerges at a certain critical temperature T_C, thus breaking a given symmetry. The emerging macroscopic property, referred as the ferroic property of the phase transition, couples to an external field. Therefore, the ferroic property can be switched by the coupled external field, and thus the phase transition can be field-induced [70].

A special case that has to be considered are the systems in which more than one macroscopic property, coupled to different external fields, emerges at distinct phase transitions that can occur at different or at the same temperature [68]. Therefore, these systems exhibit a so called multiferroic transition. A highly relevant feature of multiferroic systems is the possibility of switching a ferroic property by means of a non-conjugated external field, thus exhibiting a cross-coupled response. The interplay between the different ferroic properties and the non-coupled external fields will be enhanced at the vicinity of the lower temperature phase transition, where both ferroic properties will have emerged, thus enhancing the cross-coupled response and allowing the system to exhibit multicaloric effects [53].

Typically, the macroscopic property of a ferroic transition emerges upon cooling from the high-temperature phase (β) at the critical temperature T_C, where the system transforms to the low-temperature phase (α). Therefore, in this case, the order parameter vanishes at the high-temperature phase ($\eta_\beta = 0$), and it takes a non-zero value at the low-temperature phase ($\eta_\alpha \neq 0$). As a consequence, the high-temperature phase is less ordered, and more symmetric, than the low-temperature phase which means that the high-temperature phase has a higher entropy than the low-temperature phase ($S_\beta > S_\alpha$). Nevertheless, in some cases the loss of entropy

associated with the loss of symmetry is compensated by a gain of entropy from another entropic contribution, related to a different degree of freedom associated with a distinct order parameter. A more detailed discussion and examples of these situations will be provided in section 2.2.2.

2.2.1 Classification of phase transitions

The phase transitions considered in this dissertation are induced by a driving field such as an applied external field (x_i) or a change on the system temperature (T). Such driving fields can be easily controlled experimentally, and correspond to the natural variables of the Gibbs free energy, introduced in section 2.1. Therefore, this thermodynamic potential is particularly useful for the description of phase transitions.

Moreover, the behaviour of some relevant parameters of a general thermodynamic system, such as the generalized displacement (X_i), the entropy (S) and the specific heat (C), can be computed from the derivatives of Gibbs free energy with respect to its natural variables. Specifically, from the different terms of equation 2.4 we can write:

$$S = -\left(\frac{\partial G}{\partial T}\right)_{\{x_i\}}, \; X_i = -\left(\frac{\partial G}{\partial x_i}\right)_{T,\{x_{j\neq i}\}} \text{ and } \frac{C}{T} = \left(\frac{\partial S}{\partial T}\right)_{\{x_i\}} = -\left(\frac{\partial^2 G}{\partial T^2}\right)_{\{x_i\}}.$$

For the following discussion, let us consider a general phase transition between two phases, labelled as α and β, where the former corresponds to the equilibrium phase at low temperatures and the latter, to the equilibrium phase at high temperatures. The equilibrium thermodynamic state of the system at a certain external field and temperature will be determined by the phase that minimizes the system Gibbs free energy. For the sake of simplicity, let's consider that we induce the phase transition by changing the temperature as a driving field. Then, there must be a certain point where both phases have the same free energy $G_\alpha(T_t, \{x_i\}) = G_\beta(T_t, \{x_i\})$ at a certain transition temperature T_t.

Paul Ehrenfest introduced in 1933 a classification of phase transitions [71], where the order of the phase transition was defined as the order of the lowest derivative of the Gibbs free energy with respect to its natural variables that shows a discontinuity at the transition temperature T_t between the phases involved. Thus, a phase transition of order n fulfils:

$$\left(\frac{\partial^m G_\alpha}{\partial T^m}\right)_{\{x_i\}} = \left(\frac{\partial^m G_\beta}{\partial T^m}\right)_{\{x_i\}}, \; \left(\frac{\partial^m G_\alpha}{\partial x_i^m}\right)_{T,\{x_{j\neq i}\}} = \left(\frac{\partial^m G_\beta}{\partial x_i^m}\right)_{T,\{x_{j\neq i}\}} \tag{2.23}$$

where $m = 1, 2, ..., n-1$ while:

$$\left(\frac{\partial^n G_\alpha}{\partial T^n}\right)_{\{x_i\}} \neq \left(\frac{\partial^n G_\beta}{\partial T^n}\right)_{\{x_i\}}, \; \left(\frac{\partial^n G_\alpha}{\partial x_i^n}\right)_{T,\{x_{j\neq i}\}} \neq \left(\frac{\partial^n G_\beta}{\partial x_i^n}\right)_{T,\{x_{j\neq i}\}} \tag{2.24}$$

However, the Ehrenfest classification of phase transitions fails on classifying transitions showing a divergence in the derivatives of the Gibbs free energy at the transition temperature. For instance, this is the situation for a ferromagnet near its critical temperature T_C, referred as the Curie temperature, where the system exhibits a transition between a low temperature ferromagnetic phase and a high temperature paramagnetic phase. Near this temperature, the behaviour of the magnetic susceptibility can be expressed as $\chi = \frac{M}{H} \sim \frac{1}{(T - T_C)^{\gamma}}$, where M is the system magnetization and H the applied magnetic field. Therefore, another classification of phase transitions proves necessary in the light of this lack of completeness of the considered classification.

The concept of order parameter, closely related to the symmetries of both phases, emerges as a useful feature that allows us to classify the different phase transitions in a more rigorous way as follows [72]:

1. **First-order phase transitions:**
   They are characterized by a finite discontinuity in one or more of the first derivatives of the corresponding system free energy with respect to its natural variables at the phase transition. For a general system these derivatives correspond to either the entropy (S) or the generalized displacement (X_i), and their discontinuities at the phase transition can be expressed as $\Delta S_t = S^{\beta} - S^{\alpha}$ and $\Delta X_{it} = X_i^{\beta} - X_i^{\alpha}$, respectively. If the system exhibits a discontinuity in the entropy (ΔS_t), it denotes that the phase transition has an associated non-zero latent heat (L).

   It is important to point out that not all first-order phase transitions can be defined by an order parameter, associated with a symmetry change at the phase transition. For instance, there are some first-order phase transitions in which it is not possible to associate an order parameter (e.g. a liquid to gas transition) and the symmetry group of the ordered phase is not strictly a subgroup of the disordered phase.

2. **Continuous phase transitions:**
   They are characterized by a continuous behaviour of the first derivatives of the system free energy with respect to its natural variables, while the second derivatives are discontinuous or show a divergence at the phase transition.

   In contrast to first-order phase transitions, all continuous phase transitions have a properly defined order parameter and exhibit a symmetry change at the phase transition, where the symmetry group of the ordered phase (S) is a subgroup of the disordered phase symmetry group (S_0).

After the formal introduction of the order parameter, it is important to highlight the fact that the generalized displacement (X_i) introduced in section 2.1 corresponds in many cases to an associated order parameter (η) of a system. [2] For

[2] Nevertheless, in some cases the generalized displacement does not vanish at the disordered

instance, the magnetization (M) of a ferromagnet corresponds to the order parameter defining a paramagnetic to ferromagnetic continuous phase transition and it also corresponds to the generalized displacement of the system conjugated to the applied magnetic field ($\mu_0 H$). Therefore, the order parameter will be identified as the generalized displacement for the following parts of this dissertation.

Figure 2.2 shows illustrative examples of the temperature dependence of the generalized displacement (X_i), the entropy (S) and the specific heat (C), together with the Gibbs free energy, in the vicinity of a continuous (left) and a first-order (right) phase transition, respectively. Additionally, for both considered types of phase transitions illustrated in this figure we have added tangent lines to the Gibbs free energy at the transition temperature, representing the first derivative of the free energy. As it can be seen, for a continuous phase transition the derivative is continuous at the transition temperature, while for a first-order phase transition the derivative changes abruptly at the transition temperature, leading to discontinuities in the order parameter X_i and in the entropy S.

When comparing the temperature behaviour of the generalized displacement (X_i) schematically represented in Figure 2.2 for a continuous and a first-order phase transition, it is evident that the former will typically display a lower value for the temperature derivative $\left(\frac{\partial X_i}{\partial T}\right)_{\{x_i\}}$ than the latter at the phase transition. [3] As discussed in sections 2.1.1 and 2.1.2, this derivative has an important role on tuning the field-induced thermal response. Therefore, systems exhibiting first-order phase transitions are of particular interest for field-inducing giant caloric and multicaloric effects, and will be discussed in detail in the following section. Nevertheless, significant caloric effects are also expected in the vicinity of continuous phase transitions, where the associated order parameter changes continuously at the phase transition.

Continuous phase transitions take place around a critical point, where the associated order parameter vanishes (η) $\rightarrow 0$ when approaching the transition temperature $T \rightarrow T_C$. When a system is in the vicinity of a critical point, defined at a temperature T_C, one can observe singularities of measurable physical properties such as the heat capacity, the magnetic susceptibility or the compressibility. Additionally, when the critical point is approached, the fluctuations scale of the associated order parameter gets arbitrarily large, only limited by the size of the system. Despite the fundamental differences between the systems and the completely different physical origin of the symmetry change at the phase transition, the behaviour of the associated order parameters can be described in a similar

phase ($X_i^\beta \neq 0$), where the order parameter must vanish ($\eta_\beta = 0$), and a direct correspondence between both is not possible. Under these circumstances, the order parameter is defined as: $\eta = X_i - X_i^\beta$

[3] For instance, for an ideal first-order phase transition the derivative $\left(\frac{\partial X_i}{\partial T}\right)_{\{x_i\}}$ diverges at the transition temperature. However, for a real system, a first-order phase transition spreads over a certain temperature range and the considered derivative will be properly defined, as it will be discussed latter in this chapter.

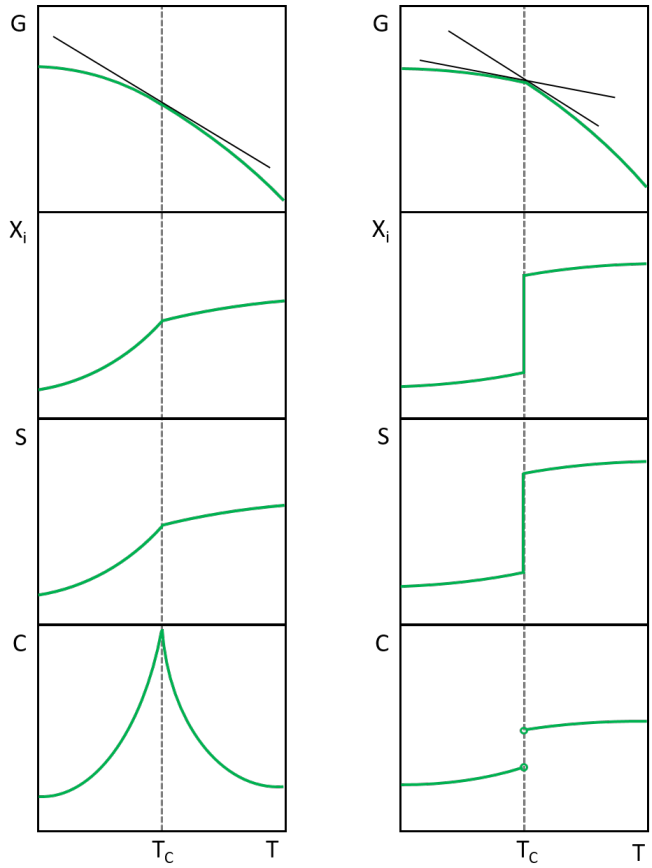

Figure 2.2: *Illustrative representations of the temperature behaviour of the Gibbs free energy (G) and the relevant parameters of the system in the vicinity of a second (left) and a first-order (right) phase transition taking place at a temperature $T = T_C$. For each case, from top to bottom: Gibbs free energy, generalized displacement or order parameter (X_i), entropy (S) and the specific heat (C).*

manner. For instance, a general order parameter around a critical point can be described as $\eta \sim (-\varepsilon)^{\beta}$, where $\varepsilon = \dfrac{T - T_C}{T_C}$ and β represents a certain critical-point exponent. The theory of critical phenomena provides a solid framework to study the behaviour of order parameters in the vicinity of critical points [73].

2.2.2 First-order phase transitions

As discussed in the previous section, there is a large entropy (ΔS_t) and order parameter (ΔX_{it}) change associated with first-order phase transitions. Therefore, with the possibility of inducing this phase transition by an applied external field,

giant caloric and multicaloric effects are expected in its vicinity.

The equations derived in sections 2.1.1 and 2.1.2 for the computation of the field-induced caloric and multicaloric effects, respectively, were derived for a general thermodynamic system and are valid within the framework of thermodynamics. However, as illustrated in Figure 2.2, an ideal first-order phase transition is characterized by a discontinuity of the order parameter at the transition temperature. Therefore, its temperature derivative $\left(\frac{\partial X_i}{\partial T}\right)_{\{x_i\}}$ diverges. Despite this fact, it has been shown that these expressions, which were deduced from the Maxwell relations, can be used to compute the thermal response around a first-order phase transition, but special attention must be paid to the followed measurement protocols [74].

An alternative computation of the caloric effects associated with a first-order phase transition can be performed by considering again the associated Gibbs free energy. Let us reckon a closed system exhibiting a general transition between two phases (α and β). As the system is closed, the total number of particles (N) will be constant and it can be expressed as $N = N^\alpha + N^\beta$, where $\{N^j\}$ corresponds to the number of particles of the system at each phase. Therefore, the Gibbs free energy for such system is written as $G(T, \{x_i\}, \{N^j\})$ and a differential change can be expressed as:

$$dG(T, \{x_i\}, \{N^j\}) = dG_\alpha + dG_\beta = \sum_{j=\alpha}^{\beta} \left(-S^j dT - \sum_{i=1}^{n} X_i^j dx_i + \mu^j dN^j \right) \quad (2.25)$$

where μ^j corresponds to the chemical potential of the phase j, and accounts for the associated free energy change of the system when the particle number at that phase changes.

Let's suppose that the system is in equilibrium at a specific temperature T and under a set of applied external fields $\{x_i\}$ where both phases coexist. At this specific conditions, the Gibbs free energy must be in a minimum. Therefore, all the partial derivatives of the free energy with respect to its natural variables will be zero and thus $dG(T, \{x_i\}, \{N^j\}) = 0$. Additionally, if the given phase equilibrium is kept at constant temperature and applied external fields, $dT = 0$ and $dx_i = 0 \, \forall i \in [1, n]$ and equation 2.25 will lead to:

$$dG(T, \{x_i\}, \{N^j\}) = \mu^\alpha dN^\alpha + \mu^\beta dN^\beta = 0 \quad (2.26)$$

Since the total number of particles is constant, it is straightforward to deduce that $dN^\alpha = -dN^\beta$. Therefore, from equation 2.26 we deduce that $\mu^\alpha = \mu^\beta$ at equilibrium conditions when both phases coexist.

At the transition temperature T_t, under a set of applied external fields $\{x_i\}$, in equilibrium conditions the Gibbs free energy of both phases must coincide $G_\alpha(T_t, \{x_i\}, N^\alpha) = G_\beta(T_t, \{x_i\}, N^\beta)$ as if one phase has a lower free energy than the other one, the system would not be stable and it would evolve to a single phase

to minimize its free energy. It is important to take into account that the applied external fields $\{x_i\}$ can affect the phase stability of the system, and therefore the transition temperature will also depend on the applied external fields $T_t(\{x_i\})$.

If we consider a differential change on one of the applied external fields $x_i + dx_i$, while keeping the others constant $\{x_{j\neq i}\}$, the transition temperature, defining the equilibrium between both phases, will be $T_t + dT_t$. Thus, the system will move along the coexistence line of the transition at the phase diagram. At these new equilibrium conditions, the Gibbs free energies will be $G_\alpha + dG_\alpha$ and $G_\beta + dG_\beta$, respectively. Consequently, as they must coincide in equilibrium conditions, we deduce that $dG_\alpha = dG_\beta$. Therefore, from equation 2.25 we can write:

$$-S^\alpha dT_t - X_i^\alpha dx_i = -S^\beta dT_t - X_i^\beta dx_i \tag{2.27}$$

which can be simplified if we take into account that for a first-order phase transition $\Delta X_{it} = X_i^\beta - X_i^\alpha$ and $\Delta S_t = S^\beta - S^\alpha$, thus leading to the Clausius-Clapeyron equation:

$$\frac{dx_i}{dT_t} = -\frac{\Delta S_t}{\Delta X_{it}} \tag{2.28}$$

The Clausius Clapeyron equation defines the phase coexistence curve in the temperature T versus external field x_i phase diagram, and relates the key parameters for the computation of a caloric effect. On the one hand, to enhance the magnitude of the caloric effect a large transition entropy change ΔS_t is necessary. On the other hand, a large shift of the transition temperature with the applied external field $\frac{dT_t}{dx_i}$ is required to field-induce the phase transition, which is achieved for large changes of the conjugated displacement at the transition ΔX_{it}.

For instance, it has been shown that the Maxwell relations presented in 2.6 reduce to the Clausius-Clapeyron equation for the case of an ideal first-order phase transition [75]. The behaviour of the conjugated displacement for an ideal first-order phase transition around the transition temperature T_t can be written as:

$$X_i(T, \{x_i\}) = X_i^0 + \Delta X_{it}\, H[T - T_t(\{x_i\})] \tag{2.29}$$

where X_i^0 is a function describing its behaviour outside of the transition and $H[T - T_t(\{x_i\})]$ is a Heaviside step function centred at the transition temperature. As discussed in section 2.1.1, equation 2.9 allows us to compute the field-induced entropy change. Thus, by introducing equation 2.29 into 2.9, and assuming X_i^0 to be constant, the following expression is obtained:

$$\Delta S(T, x_i^s \rightarrow x_i^f) = \begin{cases} -\Delta X_{it}\dfrac{dx_i}{dT_t} & T \in [T_t(\{x_i^s\}), T_t(\{x_i^f\})] \\ 0 & T \notin [T_t(\{x_i^s\}), T_t(\{x_i^f\})] \end{cases} \tag{2.30}$$

Therefore, it is clear that equation 2.30 is equivalent to equation 2.28 under the particular conditions considered. Moreover, it is important to point out that, for the above expression, the field-induced entropy change coincides with the transition

entropy change ΔS_t, which sets a maximum boundary to the contribution of the phase transition to the field-induced caloric effect for a system. [4]

From the thermodynamic point of view, two different situations have to be distinguished when considering the effect of an external field on a first-order phase transition. As previously discussed, the order parameter exhibits a discontinuity at the phase transition that can be expressed as $\Delta X_{it} = X_i^{\beta} - X_i^{\alpha}$. When the associated external field (x_i) is applied, the phase that minimizes the Gibbs free energy, which corresponds to the phase that maximizes the order parameter, will be further stabilized. Consequently, depending on the phase at which the order parameter is maximized we can distinguish between a conventional ($X_i^{\beta} < X_i^{\alpha}$) or an inverse ($X_i^{\beta} > X_i^{\alpha}$) caloric effect.

Therefore, as the order parameter change when inducing the transition has a different sign if the system exhibits a conventional ($\Delta X_{it} < 0$) or an inverse ($\Delta X_{it} > 0$) caloric effect, it is straightforward to deduce from equations 2.9, 2.10 and 2.28 that such systems will exhibit opposite features. Figure 2.3 schematically represents the behaviour of the order parameter X_i (left panels) and the corresponding entropy S (right panels) for a system exhibiting a conventional ((a) and (b)) and an inverse ((c) and (d)) caloric effect, respectively. Before discussing in detail both caloric effects, it is important to point out that the order parameters represented in these figures are inspired by the behaviour of the magnetization M under an applied magnetic field $\mu_0 H$ for a system exhibiting an ideal first-order magnetic transition between a high and a low magnetization state at a certain temperature $T_t(\{x_i\})$ [5] together with a ferroic phase transition at a higher temperature T_C, where the associated macroscopic property of the system vanishes, undergoing a continuous phase transition.

For a first-order phase transition exhibiting a conventional caloric effect, as represented in Figure 2.3 (a), the order parameter X_i is maximized at low temperatures. Without any applied external field ($x_i = 0$), the system exhibits a first-order phase transition at a temperature $T_t(0)$ and transforms towards the high-temperature phase (β) with low X_i (red solid line). In principle, the low temperature phase (α) should be stable up to the critical temperature, as illustrated by the red dashed line in the figure, but this behaviour is interrupted by the occurrence of the first-order phase transition.

Under the application of a certain external field ($x_i = x$), the low temperature phase is further stabilized and thus, the transition temperature shifts up to $T_t(x)$ as $\frac{dT_t}{dx_i} > 0$. If the system initially stays at a temperature between $T_t(0)$ and $T_t(x)$, the application of the external field ($0 \rightarrow x$) acts as the driving force of the first-order

[4] It must be mentioned that significant caloric effects can arise from each phase outside the phase transition region, which can enhance the field-induced thermal response of the system, leading to a larger entropy change than that given by the transition entropy change [33].

[5] The fact that the magnetization of a system can exhibit a first-order phase transition is a consequence of the coupling between different degrees of freedom. For instance, this will be the case for magnetostructural transitions, which will be addressed in Chapter 4.

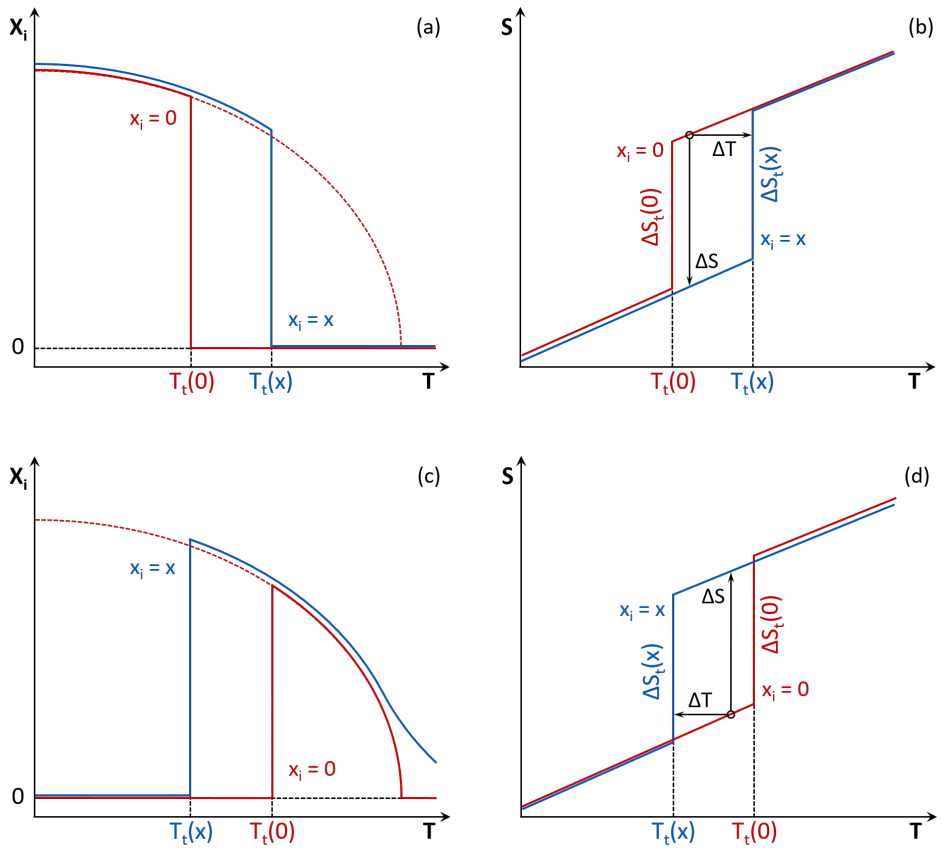

Figure 2.3: *Schematic representations of the order parameter (left) and the corresponding entropy curves (right) for a system exhibiting a conventional caloric effect (panels (a) and (b)) and an inverse caloric effect (panels (c) and (d)) near a first-order phase transition in the absence of an applied external field (red curves) and under an applied field $x_i = x$ (blue curves). At panels (b) and (d), black lines indicate the associated adiabatic temperature ΔT and isothermal entropy changes ΔS induced by an external field change $0 \rightarrow x$.*

phase transition, inducing the transition $\beta \rightarrow \alpha$.

The temperature behaviour of the entropy S that corresponds to such order parameter is represented in Figure 2.3 (*b*). Without any applied external field ($x_i = 0$), the entropy of the system exhibits a discontinuity with an associated transition entropy change $\Delta S_t(0)$ at the transition temperature $T_t(0)$ (red solid line). While under a certain applied external field ($x_i = x$), the entropy curve exhibits a discontinuity with an associated transition entropy change $\Delta S_t(x_i)$ at the transition temperature $T_t(x_i)$ (blue solid line).

Therefore, if the system stays at an initial temperature $T_t(0) < T < T_t(x)$, the isothermal application of the external field leads to a decease of the entropy $\Delta S(T, 0 \rightarrow x) < 0$ and the adiabatic application of the external field leads to an increase of the temperature $\Delta T(S, 0 \rightarrow x) > 0$, as represented by the black lines in Figure 2.3 (b).

For first-order phase transition exhibiting an inverse caloric effect, as represented in Figure 2.3 (c), the order parameter X_i is maximized at high temperatures. Therefore, when compared to a conventional caloric effect (see Figure 2.3 (a)) we observe that it shows an opposite temperature behaviour of the order parameter.

Without any applied external field ($x_i = 0$), the system exhibits a first-order phase transition at a temperature $T_t(0)$ and transforms towards the high temperature phase (β) with high X_i which is stable up to the critical temperature, where the system exhibits a continuous phase transition and the order parameter vanishes. Under the application of an external field ($x_i = x$), the high-temperature phase is further stabilized and the transition temperature shifts down to $T_t(x)$ as $\frac{dT_t}{dx_i} < 0$.

The corresponding entropy S behaviour is represented in Figure 2.3 (d). As for the conventional caloric effect, the entropy curves of the system present a discontinuity associated with the transition entropy change $\Delta S_t(x_i)$ at the transition temperature $T_t(x_i)$. When comparing these curves with the ones presented in Figure 2.3 (b), we notice that the red and blue curves have exchanged their positions. Therefore, if the system stays at an initial temperature $T_t(x) < T < T_t(0)$, the application of the external field ($0 \rightarrow x$) will induce the transition $\alpha \rightarrow \beta$, acting as the driving force of the first-order phase transition. Thus, the isothermal application of the external field leads to an increase of the entropy $\Delta S(T, 0 \rightarrow x) > 0$ and the adiabatic application of the external field leads to an decrease of the temperature $\Delta T(S, 0 \rightarrow x) < 0$.

It is worth pointing out that in the different panels of Figure 2.3, the order parameter X_i and the entropy curves S do not overlap above and below the transition temperature. This effect accounts for an increased order of the system when an external field is applied, as it partially counteracts the disorder due to thermal fluctuations in the system. Consequently, the order parameter is slightly increased and the entropy of the system is slightly reduced under an applied external field. Moreover, the effect of the applied external field is more relevant at the phase where the order parameter is maximized, which corresponds to the low temperature phase for a conventional caloric effect or the high-temperature phase for an inverse caloric effect.

So far, we have considered the total entropy S of the system, but we have not discussed its different contributions. Entropy can be understood as a measure of the disorder in a system, and it can be introduced and modified in many different ways [70]. A special case of interest to consider for this dissertation is a magnetic

system, whose total entropy can be generally separated in the following terms [76, 77]:

$$S(T, x_i) = S_{mag}(T, x_i) + S_{lat}(T, x_i) + S_{el}(T, x_i) \tag{2.31}$$

where S_{mag}, S_{lat} and S_{el} correspond to the magnetic, lattice and electronic contributions, respectively. As the application of a certain external field x_i affects the order of the system, the different terms that contribute to the total entropy of the system can depend on the applied external field. Consequently, the transition entropy change associated with a first-order phase transition, generally expressed as $\Delta S_t = S^{\beta} - S^{\alpha}$, can exhibit an external field dependence. To account for this field-dependence, it can be generally expressed as $\Delta S_t(x_i)$, as represented in Figure 2.3 (b) and (d).

Moreover, the distinction between the different entropy contributions of a system can give us a clue to understand why it can exhibit an inverse caloric effect. As represented in Figure 2.3 (c) and (d), upon heating the system looses entropy of a certain contribution at the phase transition as $X_i^{\beta} > X_i^{\alpha}$, but the total entropy of the system increases with temperature as expected. At the beginning of this section, it was mentioned that a system can loose entropy associated with a particular order parameter if it is compensated by an increase of entropy from another entropic contribution. Inverse caloric effects, described by an adiabatic decrease of temperature ($\Delta T(S, 0 \rightarrow x) < 0$) or an isothermal increase of entropy ($\Delta S(T, 0 \rightarrow x) > 0$) when an external field is applied, have been reported on systems when applying hydrostatic pressure [78], magnetic field [79] or electric field [80], where the lattice, magnetic and dipolar entropy contributions, respectively, decrease when inducing the phase transition.

So far, in this section we have considered the case of an ideal first-order phase transition. A characteristic feature of first-order phase transitions is that they exhibit a certain hysteresis, meaning that the back ($\alpha \rightarrow \beta$) and forth ($\beta \rightarrow \alpha$) phase transitions do not take place at the same transition temperature T_t.

Figure 2.4 illustrates the Gibbs free energy G as a function of temperature T of a system that undergoes a first-order phase transition between two phases, generally named α and β. As previously considered, an ideal first-order phase transition takes place at the transition temperature T_t, where the Gibbs free energies of both phases are equal. However, there will be a certain energy barrier between both initial and final states, and it must be surpassed in order to start the phase transition, where the system will follow a series of metastable states. Therefore, if temperature is the driving field of the phase transition, the system has to be overheated ($T_{th} > T_t$) or undercooled ($T_{tc} < T_t$) in order to start the back ($\alpha \rightarrow \beta$) and forth ($\beta \rightarrow \alpha$) phase transitions, respectively. The system will have an excess of Gibbs free energy at these transition temperatures, represented in Figure 2.4 as $\Delta G_{\alpha\text{-}\beta}$ and $\Delta G_{\beta\text{-}\alpha}$, which describes how much energy can be gained when the phase transition takes place. This decrease in the Gibbs free energy provides the driving force of the temperature driven first-order phase transition, and it increases as the system is further overheated or undercooled [81].

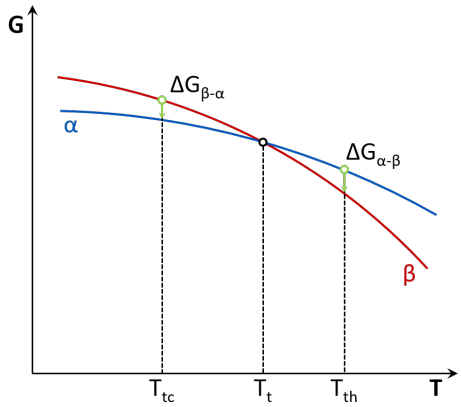

Figure 2.4: *Schematic representation of the Gibbs free energy (G) of a system undergoing a first-order phase transition. The Gibbs free energy of the high-temperature phase (β) is represented by a red line, while the free energy of the low temperature phase (α) is represented by a blue line, respectively. At a temperature T_t both phases have equal Gibbs free energies ($G_\alpha = G_\beta$), but an overheating (undercooling) to T_{th} (T_{tc}) is necessary in order to induce the phase transition. Vertical green arrows indicate the Gibbs free energy difference between both phases at the respective forward and reverse phase transition temperatures.*

For the sake of simplicity we have considered that temperature is the driving field of the phase transition, thus giving place to a certain temperature hysteresis, defined as $\Delta T_{hys} = T_{th} - T_{tc}$. It is important to point out that if the phase transition is induced by an applied external field x_i, the system will also exhibit a certain hysteresis and both back and forth phase transitions will take place at different external fields, generally named x_{th} and x_{tc}, respectively.

The presence of an inherent hysteresis on the systems exhibiting a first-order phase transition will have important consequences on their field-induced caloric response under cyclic operation, which will be discussed in detail along the following chapters.

Furthermore, a real system exhibiting a first-order phase transition will generally show a less abrupt behaviour than the schematically represented phase transitions in Figure 2.3. In a real system, the presence of impurities, composition gradients or lattice defects will affect the Gibbs free energy landscape within the system, thus spreading the first-order phase transition over a certain temperature range.

3 Experimental techniques

This chapter is of fundamental importance to provide robustness to the results presented and discussed along this dissertation. Here we will summarize the fundamentals of the different experimental techniques used for the quantitative determination of the relevant physical properties of a sample around a first-order phase transition, and we will provide as well a detailed description of the bespoke experimental setups designed and used during this thesis (DSC under magnetic fields and uniaxial compressive stress and adiabatic thermometry).

The most relevant physical properties to characterize giant caloric and multicaloric effects near a first-order phase transition when the material is subjected to a change of one or more external fields are the adiabatic temperature change (ΔT_{ad}) and the isothermal entropy change (ΔS_{iso}). The heat exchange (Q) is also a relevant physical parameter to characterize giant caloric and multicaloric effects, and it is related to ΔS_{iso} as $Q = T\Delta S_{iso}$.

The different methods used can be classified into three groups depending on how the thermal response of the sample is measured [41]:

1. **Indirect methods:**
   They rely on the experimental measurement of the phase transition order parameter X_i dependence on temperature and the applied external fields $\{x_i\}$. As discussed in section 2.1, there are two methods to compute the isothermal entropy change from these measurements for a first-order phase transition: The Maxwell relations and the Clausius-Clapeyron relation. Additionally, in order to compute the adiabatic temperature change from the Maxwell relations, one needs accurate measurements of the specific heat dependency with temperature and the applied external fields.

   In our case, for the different caloric effects, the order parameters experimentally measured are the uniaxial strain $\varepsilon(T, \mu_0 H, \sigma)$ and the magnetization $M(T, \mu_0 H)$ for the computation of the elastocaloric and the magnetocaloric effect, respectively. On the one hand, the general Maxwell relation for the computation of the isothermal entropy change when one external field x_i is modified while the others $\{x_{j\neq i}\}$ are kept constant is:

$$\Delta S(x_i^s \rightarrow x_i^f) = \int_{x_i^s}^{x_i^f} \left(\frac{\partial X_i}{\partial T}\right)_{x_i', \{x_{j\neq i}\}} dx_i' \tag{3.1}$$

where x_i^s and x_i^f represent the start and end values of the applied external field. Notice that for this general relation, the order parameter dependencies should be expressed as $X_i(T, x_i^{'}, \{x_{j\neq i}\})$ but it has been omitted from equation 3.1 for the sake of simplicity. On the other hand, the general Clausius-Clapeyron relation can be used to compute the isothermal transition entropy change when the external field x_i is modified as:

$$\Delta S_t = -\Delta X_{it} \frac{dx_i}{dT} \tag{3.2}$$

where ΔX_{it} is the change of the order parameter at the first-order phase transition.

2. **Quasi-direct methods:**
   They rely on the experimental measurement of the heat flux and the heat capacity dependency with temperature under a certain combination of constant external fields.

   As it will be shown in the following section, the measurement of the heat flux as a function of temperature and under constant applied external fields in combination with heat capacity data allows us to construct the isofield entropy curves of the studied material, with the isothermal entropy change to be obtained as: $\Delta S(T, x_s \rightarrow x_f) = S(T, x_f) - S(T, x_s)$. The adiabatic temperature change can also be obtained from the inverted entropy curves as: $\Delta T(S, x_s \rightarrow x_f) = T(S, x_f) - T(S, x_s)$.

3. **Direct methods:**
   They rely on the direct measurement of the thermal response of the material when the external field is scanned either isothermally or adiabatically. These methods are the most reliable if the measurements are carried out under proper adiabatic conditions for the measurement of temperature changes $\Delta T(S, x_s \rightarrow x_f)$ or isothermal conditions for the measurement of the heat flux and the determination of the entropy change $\Delta S(T, x_s \rightarrow x_f)$. These measurements are specially useful to ascertain the values obtained from indirect and quasidirect methods. Additionally, they are highly valuable to prove the reliability of physical models that fit the experimental data obtained from other methods.

   However, performing this kind of measurements is challenging as there are several issues that have to be properly addressed. First of all, they require the use of bespoke setups that have to be designed and properly calibrated. Secondly, the need of keeping proper experimental conditions and minimizing leaks has to be addressed. Specifically, challenges such as heat leaks between the sample and surroundings or keeping a good thermal contact with the sample during the measurement have to be addressed in order to obtain high quality and reliable direct measurements.

3.1 Calorimetry

Calorimetry has been one of the essential techniques to study and characterize the thermal response of the different studied materials in this thesis. The purpose of calorimetry is to measure the heat exchanged between a sample and its surroundings associated with state changes of the sample (such as chemical reactions, physical changes or phase transitions). The use of different calorimetric techniques provides access to diverse physically relevant properties such as the heat flow, latent heat, specific heat, the transition temperature or the kinetic parameters of a chemical reaction which enable a proper characterization of the studied phase transitions and their thermal properties. The book of W. Hemminger and G. Höhne [82] provides an exhaustive report of the diverse calorimetric techniques and details the information that can be accessed by them.

The origins and advances on calorimetry techniques are linked to the progress and development of thermodynamics as a framework for a well established theory of heat. One of the first usable calorimeters was designed by the French scientists Antoine Lavoisier and Pierre-Simon Laplace in 1783 [82]. Figure 3.1 shows a sketch of the design of such calorimeter. The working principle of this device was as follows: The sample chamber was surrounded by a double-walled vessel full of ice, with a small hole at the bottom. This first vessel full of ice is surrounded by a second double-walled vessel filled with a mixture of water and ice, which keeps the entire system in thermal equilibrium at $0°C$. When the sample under study is placed inside the calorimeter, any heat released melts a certain amount of ice in the inner vessel and the obtained water (Δm) is collected below. Thus, if the latent heat of ice (L) is known, the heat involved can be estimated as: $Q = L\Delta m$

The development of such *ice calorimeter* involving a phase transition was possible due to the observations of the Scottish chemist Joseph Black on the nature of heat and temperature. In 1760 Black realized that the delivery of energy to melting ice did not result in an increase of its temperature, and he concluded that the delivered energy must be stored in the water itself in form of a so called *transition latent heat*.

Among many other scientific contributions during the eighteen century, these observations and first attempts on measuring and understanding the nature of heat are fundamental contributions on the dawn of thermodynamics [83]. During the nineteenth century, the development of accurate calorimeters by many different prominent scientists placed the study of heat at the frontier of science. Among many contributions, the work by James Joule has to be highlighted. His work on the determination of the electrical and mechanical equivalents of heat is one of the most important contributions to calorimetry. As the passage of years gave a better understanding of thermodynamics and the theory of heat, calorimetry became a well established scientific technique to accurately measure and determine heat flows.

Originally, the diverse calorimetric techniques operated without the influence of

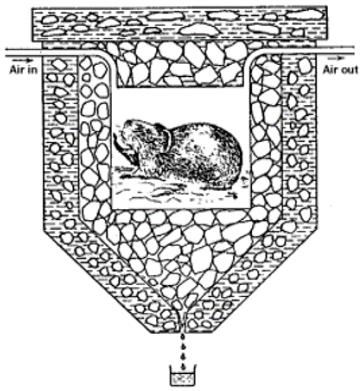

Figure 3.1: *Representation of the calorimeter designed by Lavoisier and Laplace in 1783 (Image taken from: M. Kleiber "Der Energiehaushalt bei Mensch und Tier", Paul Parey, Hamburg)*

any other applied external stimuli and temperature or heat flow were the only driving fields of the sample phase transition. It was not until a few decades ago that special calorimeters have been developed with the particular characteristic of allowing the application of one or more external stimuli during the experiment. Detailed reports can be found describing some of the first bespoke calorimeters allowing the application of different external fields such as: magnetic field [84], mechanical stress [85–88], hydrostatic pressure [89] and electric fields [90–92]. It is specially important to highlight the fundamental role that unconventional bespoke calorimeters had to perform the experiments on the samples studied in this thesis. The design and construction of bespoke calorimeters is a unique tool to study the thermal response of the studied samples when subjected to multiple external fields.

3.1.1 Differential scanning calorimetry

This section presents a general description of the working principles of Differential Scanning Calorimetry, which is the basis beneath the design and construction of the different calorimetric setups presented in this thesis. The ideas discussed in [93] served as inspiration for the following section.

Figure 3.2 shows a sketch of the basic elements of a Differential Scanning Calorimeter (DSC). The main parts of a DSC are a massive calorimetric block with high thermal conductivity, which has two identical thermoelectric sensors on contact with its surface. The sample under study (S) is placed on top of one sensor, and the inert reference (R) [1] is placed on top of the other sensor. Therefore, both sample and reference have an indirect thermal contact with the massive calorimetric block.

[1] A sample that does not undergo any phase transition for the full temperature range under study. In our case, we used a copper piece as an inert reference for all measurements presented in this thesis.

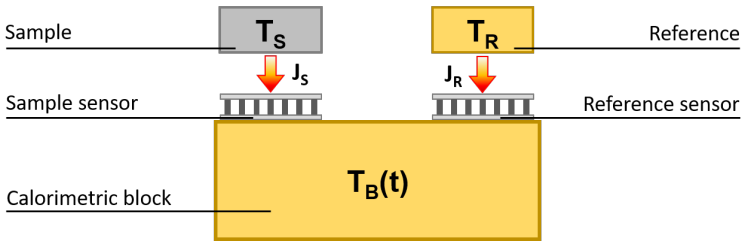

Figure 3.2: *Sketch of a DSC. The calorimetric block is at temperature $T_B(t)$ that will change with time, the sample is at T_S and the reference, at T_R. J_S and J_R represent the corresponding heat fluxes between the sample and the calorimetric block, and between the reference and the calorimetric block, respectively.*

As a differential method, a DSC measures the response difference between the two sensors by subtracting their individual signals. Hence, it is important that both sensors work under similar physical conditions and the design of a DSC has to take into account the symmetry between the different components of the system.

Let's suppose that the calorimetric block temperature is linearly scanned with time as $T_B(t) = T_B(t=0) + \frac{dT_B}{dt}t$, where $\frac{dT_B}{dt} = \dot{T}_B$ is the scanning rate. Then, the measured heat flow can be separated into the following contributions:

$$\frac{dQ}{dt} = \frac{dQ_A}{dt} + \frac{dQ_{Cp}}{dt} + \frac{dH_t}{dt} \tag{3.3}$$

where $\frac{dQ_A}{dt}$ accounts for an asymmetric term of the calorimeter, $\frac{dQ_{Cp}}{dt}$ comes from the specific heat difference between the sample and reference and $\frac{dH_t}{dt}$ is the latent heat contribution when the sample undergoes a first-order phase transition. In this case, the thermal balance equations of the sample and reference can be exposed as:

$$\frac{dH}{dt} = C_S\frac{dT_S}{dt} + J_S \tag{3.4a}$$

$$0 = C_R\frac{dT_R}{dt} + J_R \tag{3.4b}$$

where C_S, C_R, T_S and T_R are the specific heat and the temperature for the studied sample and the reference, respectively, and J_S and J_R correspond to the heat fluxes of each one with the calorimetric block. On the one hand, the first term on the right hand side $\left(C_i\frac{dT_i}{dt}\right)$ corresponds to the energy needed to change the sample or reference temperature, while the second one (J_i) corresponds to the energy that the sample or the reference exchanges with the surroundings due to existing temperature gradients. On the other hand, on the left hand side the term $\left(\frac{dH}{dt}\right)$ accounts for the energy released or absorbed by the sample during a first-order phase transition.

In the quasi-static approximation, the temperature gradients between the sample, reference and the calorimetric block will be small. Therefore, we can assume that the heat fluxes between these components will be proportional to the temperature difference between them, and we use the Fourier law to express them as: $J_i = \frac{T_i - T_B}{R_i}$, where R_i is the thermal resistance (the reciprocal magnitude to thermal conductance) of the medium that separates the sample or the reference and the calorimetric block.

As the DSC is designed to provide similar physical conditions to both the sample and reference environments, we can assume that their thermal resistances will be very close to each other: $R_S \approx R_R \equiv R$. [2] Therefore, if we subtract equations 3.4a and 3.4b we obtain:

$$\frac{dH}{dt} = C_S \frac{dT_S}{dt} - C_R \frac{dT_R}{dt} + \frac{T_S(t) - T_R(t)}{R} \tag{3.5}$$

Additionally, in the quasi-static approximation, where the scanning rate is low enough to allow the sample and reference temperatures to follow the calorimetric block temperature profile, we can further assume that: $\frac{dT_S}{dt} \approx \frac{dT_R}{dt} \approx \frac{dT_B}{dt}$. Therefore, equation 3.5 can be expressed as:

$$\Delta T \equiv T_S(t) - T_R(t) = R \left[\frac{dH}{dt} + (C_R - C_S) \frac{dT_B}{dt} \right] \tag{3.6}$$

The thermoelectric sensors placed between the sample (and the reference) and the calorimetric block provide a voltage that is proportional to the temperature difference between their two faces. As each sensor has one side in contact with the sample or reference and the other one in contact with the calorimetric block, its single voltage output can be expressed as $Y_i = B\,[T_i(t) - T_B(t)]$, where i stands for either the reference ($i = R$) or the sample ($i = S$). Because both sensors are differentially connected, their output will have different sign and the global measured voltage will be:

$$Y = Y_S - Y_R = B\,[T_S(t) - T_R(t)] = B\Delta T \tag{3.7}$$

where B is a proportionality factor that depends on the sensors properties. Therefore, the measured output from a DSC is expressed as:

$$Y(t) = S \left[\frac{dH}{dt} + (C_R - C_S) \frac{dT_B}{dt} \right] \tag{3.8}$$

where $S \equiv BR$ is the calorimeter sensitivity, which calibrates the electric output directly measured from the sensors into heat flow as $\frac{dQ}{dt} = \frac{Y}{S}$. Therefore, equation 3.8 can be rewritten as:

[2] As we use a copper piece as the reference, this approximation is only valid when the sample also has a high thermal conductivity. If it is not the case, the samples geometry (their width, length and height) will add a contribution to the thermal resistance. In our case, as all the studied alloys are metallic compounds, this approximation is valid as the thermal conductivity of the studied samples is high.

$$\frac{dQ}{dt} = \frac{dH}{dt} + (C_R - C_S)\frac{dT_B}{dt} \tag{3.9}$$

Equations 3.8 and 3.9 display the main contributions to the measured signal in a DSC calorimeter, either as a voltage or as heat flow, respectively. The first term, $\frac{dH}{dt}$ corresponds to the latent heat contribution of the sample when it undergoes a first-order phase transition. The second term, $(C_R - C_S)\frac{dT_B}{dt}$ corresponds to the energy difference between the sample and reference needed to change their respective temperatures when scanning the calorimetric block temperature. It is important to point out that this term will always be small, even if the experiment is performed at relatively high temperature scanning rates. As this second term is proportional to the specific heat difference between the sample and reference, it can be minimized by properly selecting a reference with a similar specific heat to the sample. Therefore, the key aspect of a DSC is that, as the sensors are connected differentially, the sample heat flow is subtracted from the reference heat flow and thus the overall measured signal will be small unless the studied sample undergoes a first-order phase transition and $\frac{dH}{dt} \neq 0$. Figure 3.3 shows an illustrative example of a DSC measured signal when the studied sample undergoes a first-order phase transition when sweeping the system temperature at a certain rate. In the absence of any first-order phase transition, the signal measured shows a certain drift from zero that comes from the specific heat difference between the sample and reference and the temperature sweeping rate at which the calorimetric block temperature is scanned (second term of equation 3.8). When the first-order phase transition takes place, the first term of equation 3.8 becomes relevant and we observe a sharp peak in our thermal curve (thermogram).

Changes in the measured signal before and after the first-order phase transition will allow us to gain information on the specific heat of the sample. When a system undergoes a first-order phase transition, it will transform from an initial state α to an end state β with different specific heats: C_S^α and C_S^β, respectively. From equation 3.8, the measured signal before and after the first-order phase transition will only have the contribution of the second term as $\frac{dH}{dt} = 0$. Therefore, DSC becomes a useful technique to measure specific heat changes around a phase transition:

$$\Delta C_S^{\alpha\to\beta} = C_S^\beta - C_S^\alpha = \frac{Y^\beta - Y^\alpha}{S\frac{dT_B}{dt}} \tag{3.10}$$

where Y^α and Y^β correspond to the measured signal when the sample is at the initial or at the end state, respectively. Despite being a useful technique to measure specific heat changes around a phase transition, it is not a suitable technique to accurately measure the absolute value of the sample's specific heat, as the design of a DSC minimizes the specific heat contribution to the measured signal.

To properly compare different heat flow measurements independently of the temperature scanning rate at which they were performed, it is convenient to rescale

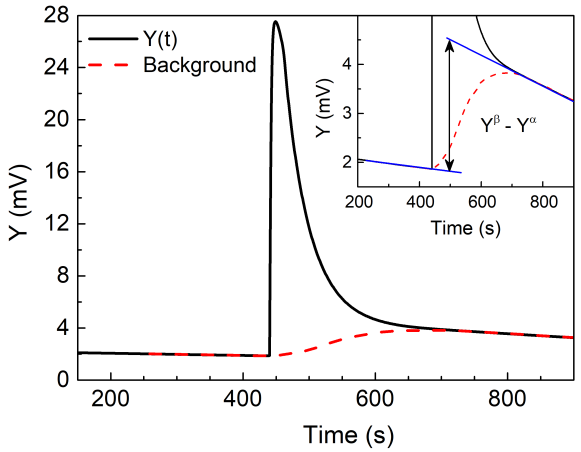

Figure 3.3: *Illustrative example of the DSC measured voltage response when the sample exhibits a first-order phase transition from an initial phase α to an end phase β. The measured voltage output (Y(t)) is displayed as a black continuous line and the baseline is shown as a red dashed line. The insert shows a detail of the background below the calorimetric peak.*

equation 3.9 as a function of temperature rather than time. As $\frac{dQ}{dT} = \frac{\dot{Q}}{\dot{T}_B}$, where $\dot{Q} = \frac{dQ}{dt}$ and $\dot{T}_B = \frac{dT_B}{dt} = \frac{dT}{dt}$, we obtain:

$$\frac{dQ}{dT} = \frac{dH}{dT} + (C_R - C_S) \tag{3.11}$$

From the measured heat flow, we can determine the latent heat or transition enthalpy (ΔH_t) and entropy changes (ΔS_t) associated with a first-order phase transition. For this purpose, a proper integration of equation 3.11 must be done. The challenge here is to properly separate the baseline from the first-order phase transition signal in order to obtain accurate values to characterize the phase transition. The major contribution to the measured baseline is the specific heat difference between the sample and reference $(C_R - C_S)$ together with any asymmetric contribution coming from the calorimeter design.

A good estimate of the baseline is to perform a linear fit above $(C_R - C_S^{\alpha})(T)$ and another one below $(C_R - C_S^{\beta})(T)$ the phase transition, and then extrapolate the baseline behaviour at the phase transition temperature range with a linear combination of the two baselines together with a weight factor. At a certain temperature T within the transition temperature range, an appropriate factor for the linear combination of both background fits is the transformed fraction, which corresponds to the portion of the sample that has transformed from the initial α state to the end β state at that specific temperature: $\chi(T)$. Therefore, the specific heat behaviour of the sample within the transition temperature range can be expressed as:

$$C_S(T) = [1 - \chi(T)]\, C_S^{\alpha}(T) + \chi(T) C_S^{\beta}(T) \tag{3.12}$$

where $\chi(T)$ is the fraction of the sample in the β phase, which is bound by $0 \leqslant \chi \leqslant 1$. Thus, at low temperatures below the phase transition the sample is in the α state and $\chi = 0$ while above the phase transition, the sample has completely transformed to the end state β and $\chi = 1$. Thus, the background can be generally expressed as $\zeta(T) \sim (C_R - C_S)(T)$ and the transition enthalpy and entropy changes will be computed as:

$$\Delta H_t = \int_{T_s}^{T_f} \left(\frac{dQ}{dT'} - \zeta \right) dT' \tag{3.13}$$

$$\Delta S_t = \int_{T_s}^{T_f} \frac{1}{T'} \left(\frac{dQ}{dT'} - \zeta \right) dT' \tag{3.14}$$

where T_s and T_f are the start and end integration temperatures, taken before and after the phase transition and enclosing the temperature range where $\dfrac{dH}{dT} \neq 0$.

It is important to take into account that the transition enthalpy and entropy changes arise from the full transformation of the sample from the initial to the end state. If we now consider an arbitrary end integration temperature T where $T_s \leqslant T \leqslant T_f$, the entropy change can be expressed similarly to the transition entropy change (equation 3.14) as:

$$S(T) - S(T_s) = \int_{T_s}^{T} \frac{1}{T'} \left(\frac{dQ}{dT'} - \zeta \right) dT' \tag{3.15}$$

This partial entropy change from an initial reference value $S(T_s)$ to an end value $S(T)$ arises from the partial transformation of the sample from the initial state to an intermediate state. As the sample fraction that has transformed at this intermediate temperature (T) is expressed by the transformed fraction as $(\chi(T))$, the entropy change of equation 3.15 can be rewritten as $S(T) - S(T_s) = \chi(T)\Delta S_t$. Therefore, the transformed fraction at an arbitrary temperature will be generally expressed as:

$$\chi(T) = \frac{S(T) - S(T_s)}{\Delta S_t} = \frac{\displaystyle\int_{T_s}^{T} \frac{1}{T'} \left(\frac{dQ}{dT'} - \zeta \right) dT'}{\Delta S_t} \tag{3.16}$$

3.1.1.1 Isothermal DSC calorimetry

Commercial DSC calorimeters are designed to work under temperature scans. However, when we want to characterize the caloric and multicaloric effects near a first-order phase transition that is sensitive to different applied external fields, it is necessary to develop bespoke setups that allow us to perform calorimetric measurements under the influence of other external fields $\{x_i\}$. These unique setups give us the possibility to perform calorimetric measurements at constant temperature while scanning other external fields.

In this kind of measurements, the external field is linearly scanned with a rate $\frac{dx_i}{dt}$ while the calorimetric block temperature is kept constant at a certain temperature T_B. In this scenario, the thermal balance equations 3.4a and 3.4b still hold true, and if we assume again that the thermal resistances are very close to each other ($R_S \approx R_R \equiv R$), we can rewrite equation 3.6 as:

$$\Delta T \equiv T_S(t) - T_R(t) = R\left[\frac{dH}{dt} + C_R\frac{dT_R}{dt} - C_S\frac{dT_S}{dt}\right] \tag{3.17}$$

As before, the electric output measured from both thermoelectric sensors can be converted to heat flow using the calorimeter sensitivity as $\frac{dQ}{dt} = \frac{Y}{S(T,x_i)}$. It is important to notice that under the new experimental conditions, we must know the external field dependency of the sensitivity to convert the measured electric output to heat flow. Under these assumptions, equation 3.17 becomes:

$$\frac{dQ}{dt} = \frac{dH}{dt} + C_R\frac{dT_R}{dt} - C_S\frac{dT_S}{dt} \tag{3.18}$$

This equation displays the main contributions to the heat flow measured with a DSC calorimeter working under isothermal conditions while scanning the external field x_i. In the absence of a first-order phase transition, the first term of the equation vanishes and the measured signal corresponds to a combination from a certain marginal field-induced signal of the sensors together with any asymmetric contribution coming from the calorimeter design. As now the calorimetric block temperature is kept constant, the signal coming from the last two terms of this equation is rather small when compared to this same term when scanning the temperature (equation 3.9).

To properly compare different heat flow measurements independently of the external field scanning rate used, it is convenient to rescale equation 3.18 as $\frac{dQ}{dx_i} = \frac{\dot{Q}}{\dot{x}_i}$, where $\dot{Q} = \frac{dQ}{dt}$ and $\dot{x}_i = \frac{dx_i}{dt}$. Therefore:

$$\frac{dQ}{dx_i} = \frac{dH}{dx_i} + C_R\frac{dT_R}{dx_i} - C_S\frac{dT_S}{dx_i} \tag{3.19}$$

From this measured heat flow, a proper integration must be done to determine the field-induced enthalpy or entropy changes. For this purpose, a suitable baseline has to be chosen. Analogously to the previous case, the background can be generally expressed as $\zeta(x_i) \sim C_R\frac{dT_R}{dx_i} - C_S\frac{dT_S}{dx_i}$ and the induced enthalpy and entropy change will be computed as:

$$H(x) - H(x_i^s) = \int_{x_i^s}^{x}\left(\frac{dQ}{dx_i'} - \zeta\right)dx_i' \tag{3.20}$$

$$S(x) - S(x_i^s) = \int_{x_i^s}^{x}\frac{1}{T}\left(\frac{dQ}{dx_i'} - \zeta\right)dx_i' \tag{3.21}$$

where x_i^s and x are the start and end integration external fields. It is important to point out that in this case, x_i^s corresponds to the external field at which the phase transition starts, while the end integration external field x is rather limited to the available external field range of our setups. When performing a measurement under specific conditions $\{T, x_i(t)\}$), the available external field range may be enough to fully induce the phase transition of the studied sample, or it may be able to induce only a partial transformation of the sample. In the former case, equations 3.20 and 3.21 correspond to the transition enthalpy (ΔH_t) and entropy (ΔS_t) change respectively, whereas in the latter case they correspond to the partial enthalpy $\Delta H(x_i^s \rightarrow x)$ and entropy change $\Delta S(x_i^s \rightarrow x)$.

3.1.1.2 Entropy curves

The diverse calorimetric thermograms measured under isofield conditions while scanning the temperature can be used to create accurate entropy curves of the studied samples. For this purpose, we have to take under consideration the calorimetric data $\frac{dQ(T,x_i)}{dT}$ together with measurements of the specific heat dependency with temperature and the external field before and after the phase transition, expressed as $C_S^{\alpha}(T,x_i)$ and $C_S^{\beta}(T,x_i)$ respectively. By taking under consideration equations 3.15 and 3.16, from each calorimetric thermogram a corresponding entropy curve can be computed by the following expression:

$$S(T,x)-S(T_0,x) = \begin{cases} \displaystyle\int_{T_0}^{T} \frac{C_S^{\alpha}(T',x)}{T'} dT' & T \leq T_s \\ \displaystyle S(T_s,x) + \int_{T_s}^{T} \frac{1}{T'} \left[C_S(T',x) + \frac{dH(T',x)}{dT'} \right] dT' & T_s < T \leq T_f \\ \displaystyle S(T_f,x) + \int_{T_f}^{T} \frac{C_S^{\beta}(T',x)}{T'} dT' & T > T_f \end{cases} \tag{3.22}$$

where $S(T_0,x)$ is the sample entropy at a temperature $T = T_0$ under an applied external field $x_i = x$, taken as the reference entropy for the particular entropy curve, and the specific heat $C_S(T,x)$ can be expressed as $C_S = (1-\chi)\, C_S^{\alpha} + \chi C_S^{\beta}$, where the transformed fraction and the different single-phase specific heats depend on both the temperature and applied external field.

Equation 3.22 divides into three different temperature regions an entropy curve. On the one hand, for the two regions below and above the phase transition temperature range $[T_s, T_f]$, the entropy curve is computed from the single phase specific heat behaviour with temperature and the applied external field by integrating the expression $dS = \frac{C_S^i}{T} dT$. On the other hand, within the phase transition temperature range we have two contributions: the specific heat contribution when the sample is in a combination of both phases and the latent heat from the phase transition, as expressed in equation 3.15.

From a set of different isofield entropy curves characterizing the studied material under the influence of a certain applied external field, it is possible to compute its thermal response, either as an isothermal entropy change or an adiabatic temperature change, associated with the caloric effect when the material is subjected to a change on the applied external field from $x_i = x_s$ to $x_i = x_f$. For this purpose, the isothermal entropy change arising from an external field change is obtained by subtracting entropy curves at the initial and end external field values, and it is expressed as:

$$\Delta S(T, x_s \rightarrow x_f) = S(T, x_f) - S(T, x_s) \tag{3.23}$$

Conversely, to compute the adiabatic temperature change arising from this external field change we have to perform an inversion of both entropy curves involved $T(S, x)$, and it will be expressed as:

$$\Delta T(S, x_s \rightarrow x_f) = T(S, x_f) - T(S, x_s) \tag{3.24}$$

Equation 3.23 provides the isothermal entropy change as a function temperature, while equation 3.24 provides the adiabatic temperature change as a function of entropy. For the latter, it is customary to plot temperature changes as a function of temperature. Such temperature dependence is obtained by plotting each $\Delta T(S, x_s \rightarrow x_f)$ data at the temperature given by the initial entropy curve prior to the change on the external field $S(T, x_s)$.

3.1.2 Measurement protocols for DSC calorimetry

So far, this section has focused on discussing the general methods to compute the relevant physical parameters that characterize the caloric and multicaloric effects (such as the transition latent heat ΔH_t, the transition entropy change ΔS_t and the isothermal entropy and adiabatic temperature changes) near a first-order phase transition, obtained from calorimetric measurements performed under either isothermal $\{T, x_i(t)\}$ or isofield $\{T(t), x_i\}$ conditions.

As discussed in section 2.2.2, inherent to the first-order character of the phase transition, a certain temperature and external field hysteresis will take place in all the studied materials. Therefore, the back and forth transitions between the low-temperature (α) and the high-temperature (β) phases will not take place at the same temperature and external field. This fact has far-reaching consequences on the thermal response of the studied materials when subjected to cyclic external field changes. Therefore, the thermal history of the sample has to be taken into account and proper thermodynamic paths have to be designed in order to precisely control the initial thermodynamic state of the sample before performing any calorimetric experiment.

3.1.2.1 Isothermal measurements

As illustrated in Figure 3.4, isothermal measurements are performed under a cyclic external field profile which allows us to properly determine the irreversible and reversible contributions of the caloric effects at a certain constant temperature.

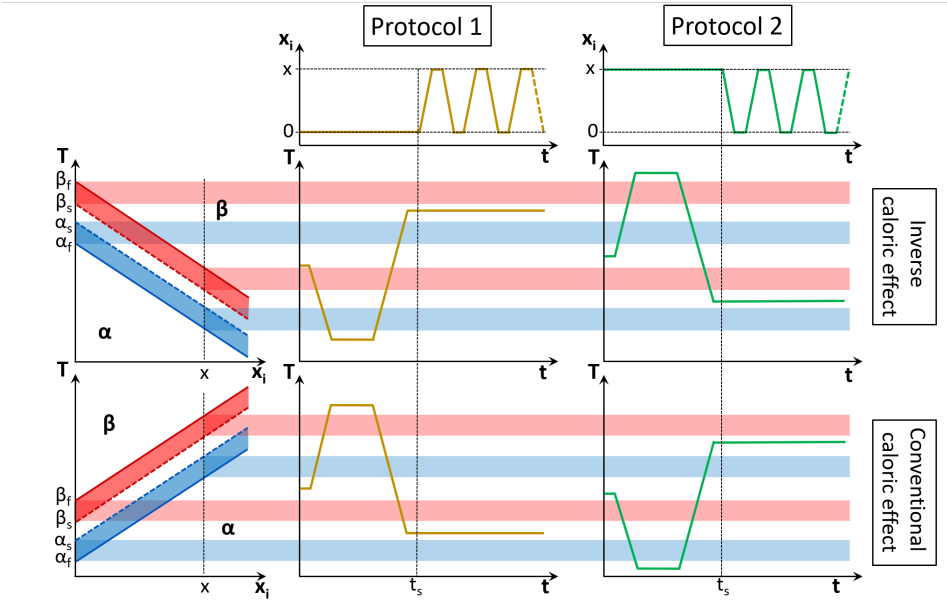

Figure 3.4: *Scheme of the measurement protocols followed for calorimetric runs under isothermal conditions for a material displaying an inverse caloric effect (second row) and a conventional caloric effect (third row). On the left side, the transition temperature behaviour under an applied external field is plotted for a material exhibiting either an inverse (top) or a conventional (bottom) caloric effect. The temperature regions at which the forward ($\beta \rightarrow \alpha$) and reverse ($\alpha \rightarrow \beta$) transitions take place are bounded by $[\alpha_s(x), \alpha_f(x)]$ and $[\beta_s(x), \beta_f(x)]$, respectively. The temperature width of both transitions are indicated as blue (forward transition) and red (reverse transition) shaded areas for both the lowest $x_i = 0$ and highest $x_i = x$ external field applied, and act as guides to the eye for the temperature profiles for each measurement protocol. The top panels display the time dependence of the applied field during both experiment protocols, and the start time (t_s) of the first field ramp is indicated by a vertical dashed line.*

For this purpose, the measurement protocols have to take into account the thermal history of the sample and different temperature paths have to be performed in order to control the sample's initial state before the measurement start, indicated by t_s in the figure.

As discussed in detail in section 2.2.2, we can distinguish two different situations when considering the behaviour of a first-order phase transition under an applied external field. On the one hand, a system where the order parameter is maximized at the low temperature phase ($X_i^\beta < X_i^\alpha$) will show a conventional caloric effect, and under the application of an external field the transition temperature will shift to higher temperatures as $\dfrac{dT_t}{dx_i} > 0$. On the other hand, a system where the order

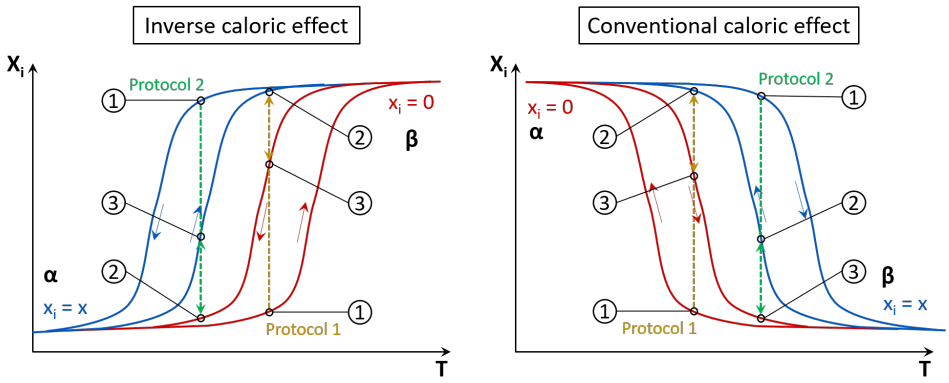

Figure 3.5: *Scheme of the temperature dependence of the order parameter X_i upon heating and cooling at zero field $x_i = 0$ (red) and under an applied external field $x_i = x$ (blue) for a material displaying an inverse (left) or a conventional (right) caloric effect. In each figure, the dotted vertical lines represent the change in X_i as a consequence of the external field ramps of protocol 1 (yellow) or protocol 2 (green). Numbers point out the start and end order parameter value of the first field ramp ① → ② and successive ramps ② ↔ ③ for each measurement protocol at a certain constant temperature.*

parameter is maximized at the high-temperature phase ($X_i^\beta > X_i^\alpha$) will show an inverse caloric effect, and under the application of an external field the transition temperature will shift to lower temperatures as $\dfrac{dT_t}{dx_i} < 0$.

In light of this clear distinction of the phase transition behaviour under an applied external field, the temperature paths needed for each measurement protocol will depend on whether the sample exhibits a conventional or an inverse caloric effect. Figure 3.5 shows the temperature dependence of the order parameter for both caloric effects at zero field $x_i = 0$ and under an applied external field $x_i = x$. As it can be seen, the order parameter change strongly depends on the measurement temperature and will also significantly differ between the first and subsequent field ramps. Therefore, the measurement protocols are designed as follows:

1. **Protocol 1:**
   Before the measurement start at t_s, the sample is brought to a state at which the order parameter X_i is minimized at zero external field $x_i = 0$.

   For a material exhibiting an inverse (conventional) caloric effect, the application of the external field $0 \rightarrow x$ induces the reverse ($\alpha \rightarrow \beta$) (forward ($\beta \rightarrow \alpha$)) phase transition. Therefore, before the experiment start the material is completely transformed to the α (β) phase and then it is heated (cooled) to the desired measurement temperature.

2. **Protocol 2:**
   Before the measurement start at t_s, the sample is brought to a state at which the order parameter X_i is maximized under an applied external field $x_i = x$.

   For a material exhibiting an inverse (conventional) caloric effect, the removal of the external field $x \rightarrow 0$ induces the forward ($\beta \rightarrow \alpha$) (reverse ($\alpha \rightarrow \beta$)) phase transition. Therefore, before the experiment start the material is completely transformed to the β (α) phase and then it is cooled (heated) to the desired measurement temperature.

3.1.2.2 Isofield measurements

Figure 3.6 shows a scheme of the applied external field and temperature profiles during an isofield calorimetric measurement. As the temperature profile depicted in the figure can be applied cyclically, a reasonable temperature margin below $\alpha_s(x)$ and above $\beta_s(x)$ has to be allowed in order to ensure that the forward and reverse transitions are completed. Consequently, after a proper determination of the calorimetric baseline these measurements will provide accurate values of the transition entropy and enthalpy change.

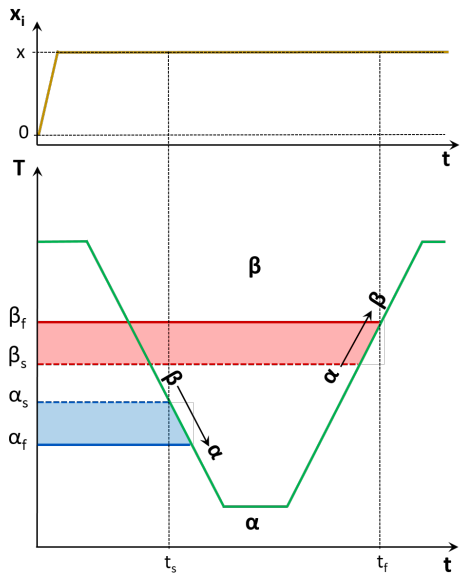

Figure 3.6: *Scheme of the measurement protocol followed for calorimetric runs under isofield conditions. The top panel shows the applied external field during all the experiment at $x_i = x$. The temperature regions at which the forward ($\beta \rightarrow \alpha$) and reverse ($\alpha \rightarrow \beta$) transitions take place are bounded by $[\alpha_s(x), \alpha_f(x)]$ and $[\beta_s(x), \beta_f(x)]$, respectively. Two vertical dashed lines mark the start time (t_s) and end time (t_f) of the forward and reverse transitions.*

3.1.3 DSC under magnetic fields

The DSC measurements under magnetic field have been performed with a bespoke calorimeter previously designed and built by our research group described in [94]. Figure 3.7 shows a scheme of the experimental setup used to perform the measurements with this device.

The calorimeter is placed on top of a copper container that is connected to a $RP-890C$ Lauda® GmbH Proline thermal bath. The thermal bath uses silicon oil that flows through the cooper container, and controls its temperature and flow within this closed circuit (see panel (a) in Figure 3.7). The calorimeter and copper container are placed into the bore of a 6T Cryogen-Free Magnet from *Cryogenic Ltd.*®. Nitrile rubber pipe insulation is placed around the container and calorimeter to isolate the system from the surrounding and guarantee a proper temperature working range for the experiments. The height and centring of the calorimeter is adjusted in order to place the sample in the region where the applied magnetic field is homogeneous (see panel (b) in Figure 3.7). Two Peltier modules connected differentially, made of a battery of P-N junctions, are used as thermoelectric sensors. One side of each Peltier module is placed in contact with the calorimeter copper block. On the free side of the Peltier module that lays next to the centre of the calorimeter we place the sample under study, and on the other module, a copper reference. A thin layer of silicone heat transfer compound (HTS) from *Electrolube*® is placed on both surfaces of the Peltier modules to ensure a proper thermal contact between the sensors and the calorimeter copper block, the sample and reference. Additionally, sample, reference and the Peltier modules are tightly wrapped with Teflon tape to keep them in place (see panel (c) in Figure 3.7). To increase the thermal homogeneity of the calorimeter and minimize air convection, a copper cover is placed on top of the calorimeter block. The temperature of the calorimeter is measured with a Pt-100 platinum resistance that is embedded inside the calorimeter copper block. Two *Keithley*® 2000 multimeters are used to measure the signal of both the Pt-100 platinum resistance and the differentially connected thermoelectric sensors. The whole system is controlled by a personal computer using Labview software. Readings of the time, temperature and calorimetric output are performed at typical rates of 0.5 Hz.

3.1.3.1 Setup calibration

As previously stated, it is necessary to determine the sensitivity (S) of a calorimeter to be able to convert the directly measured voltage output of the thermoelectric sensors (Y) to the exchanged heat ($\dot{Q}$). As the properties of the thermoelectric sensors depend on the temperature, the sensitivity of the calorimeter will also depend on the temperature. Therefore, to calibrate a calorimeter we have to measure the sensitivity at different temperatures ranging within the working temperature range of the particular setup.

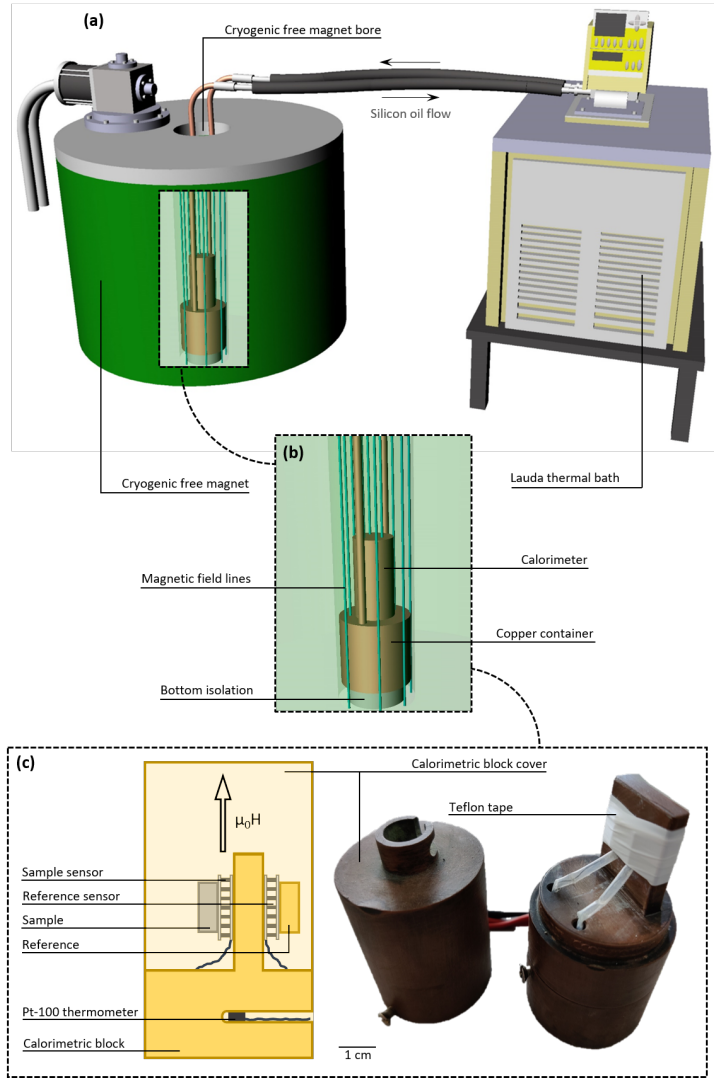

Figure 3.7: *Different views of the differential scanning calorimeter under magnetic fields. Panel (a) shows a representation of the 6T Cryogen-Free Magnet from Cryogenic Ltd.® in which the purpose-built device is placed inside its bore. A RP − 890C Lauda® GmbH Proline thermal bath is used to control the temperature of a copper container placed below the calorimeter. Panel (b) illustrates the ensemble of the differential scanning calorimeter and the copper container which are placed inside the magnet bore and panel (c) shows a sketch of the calorimeter and the corresponding picture, where the sample and reference are covered by Teflon tape.*

To perform a calibration at a specific temperature, we have to dissipate a known amount of energy (P) onto the sample thermoelectric sensor and measure the electrical output of the calorimeter (Y) at the stationary state [93]. Figure 3.8 shows a sketch of the electrical circuit used to determine the sensitivity of a calorimeter. The sample is replaced by a resistor R_S and when the circuit is closed, a current of intensity I_S circulates through it. The power dissipated by Joule effect onto the thermoelectric sensor will be $P = I_S \Delta V_S$. The current intensity I_S is determined by measuring the voltage drop ΔV_R at a standard resistor $R_R = 100\,\Omega$ connected in series to the sample resistor as $I_S = \dfrac{\Delta V_R}{R_R}$. Therefore, if we measure the voltage drop at the sample and standard resistors we can determine the sensitivity as $S = \dfrac{Y - Y_0}{P}$, where Y corresponds to the electrical output of the calorimeter at the stationary state and Y_0 to the output when no energy is being dissipated at the sample sensor, which is subtracted as a base line. The voltage drops at the sample and standard resistors (ΔV_S and ΔV_R, respectively) are measured by *Keithley*® 2000 multimeters, and the same copper reference is used for the calibration measurements and the experiments carried out afterwards.

To calibrate the DSC under magnetic fields, we applied a voltage of 3 V with the power supply and used a strain gauge ($R_S \approx 120\,\Omega$) as the sample resistor, and a copper block as the reference. The circuit was closed for a period of $\backsim 100\,s$ at each temperature until the stationary state was reached. Figure 3.9 (a) shows the electrical output of the calorimeter as a function of time for calibration measurements performed at different constant temperatures. Before the energy dissipation on the sample sensor takes place, the calorimetric signal exhibits a certain constant drift from zero. When the electric circuit is closed, the dissipation

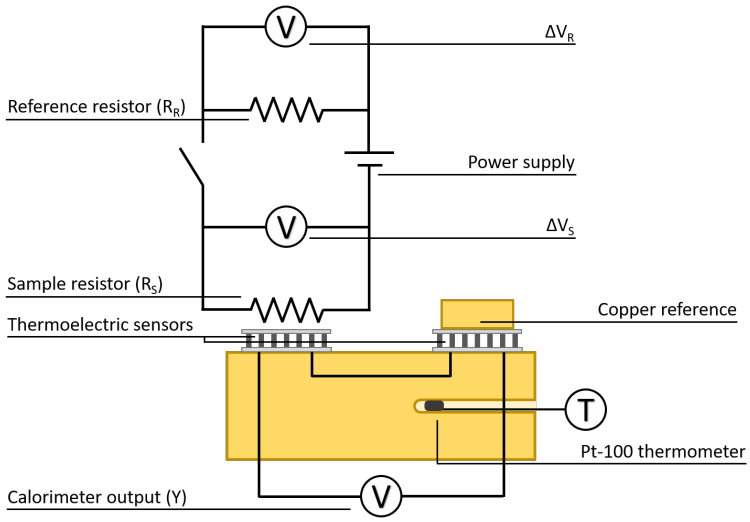

Figure 3.8: *Sketch of the experimental setup mounted to perform the calibration of a DSC.*

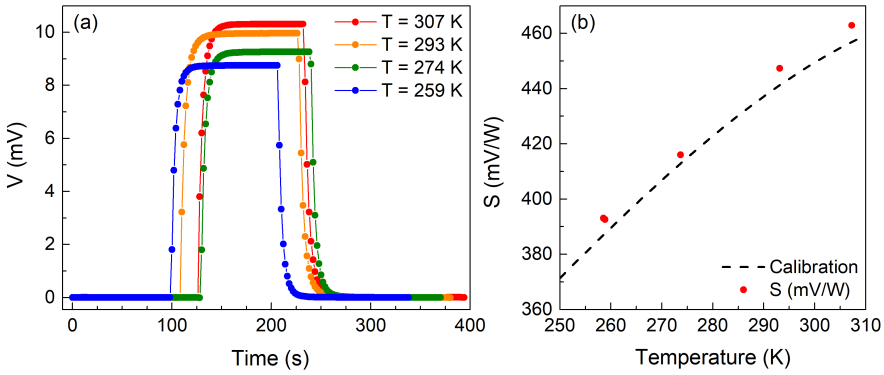

Figure 3.9: *Illustrative examples of calibration measurements for the DSC under magnetic field calorimeter.* (*a*) : *Voltage output* (Y) *as a function of time measured at different constant temperatures for the calorimeter calibration.* (*b*) : *Comparative plot of the calorimeter sensitivity as a function of temperature. Red dots correspond to the sensitivities obtained from the measurements shown in panel* (*a*) *and the dashed line corresponds to the sixth order polynomial fit of the previous calibration (January of 2014):* $S(T) = 412(0.4) + 1.625(8)T - 0.007(0.1)T^2 - 5.9(0.1)10^{-5}T^3 - 9.4(0.9)10^{-8}T^4 + 7.6(0.5)10^{-10}T^5 + 2.9(0.3)10^{-12}T^6$ *for* $T \in [-200, 150]\,^{\circ}C$.

process starts and we detect a sharp onset of the calorimetric signal that saturates to a plateau. Once the circuit is opened again, the signal relaxes back to its baseline. The obtained sensitivity values from these measurements compare well with the previous calibration of the setup, as it can be seen in Figure 3.9 (*b*). The new sensitivity measurements show a relative discrepancy within the range $[0.8, 1.4]\%$ with the polynomial fit of the previous calibration (January of 2014) [92].

As the discrepancies obtained between the new sensitivity measurements and the previous calibration polynomial fit are small, we conclude that the calibration polynomial function (January of 2014) correctly describes the actual temperature dependence of the DSC sensitivity in the temperature range $T \in [260, 310]\,\mathrm{K}$. Therefore, the same polynomial function will be used to compute the sensitivity of the DSC under magnetic fields to analyse the measurements performed with this setup.

Besides, the dependence of the thermoelectric sensors voltage output with the applied magnetic field was studied by means of measurements on a known diamagnetic Cu-Zn-Al sample under different applied magnetic fields [84]. It was found that the thermoelectric sensors voltage output is not affected by the applied magnetic field. Therefore, the calorimeter sensitivity was verified to be independent of the applied magnetic field [94].

3.1.4 DSC under magnetic fields and uniaxial compressive stress

The study of materials exhibiting a cross-coupled response under different external fields requires the development of bespoke experimental setups that allow the simultaneous application of multiple external fields. For this purpose, a bespoke differential scanning calorimeter allowing the application of uniaxial compressive stress together with magnetic field has been designed and built. This unique setup aims for the analysis of the caloric and multicaloric effects arising from materials displaying a magnetostructural transition with a strong coupling between the structural and magnetic degrees of freedom, as these materials are prone to show a cross-coupled response.

This device is an improved and upgraded version of a previous setup designed and built by our research group, and presented in [92]. There was a twofold motivation for the development of this unique experimental setup: First of all, there was an absence of calorimetric techniques capable of measuring under applied uniaxial stress. Secondly, there is scarce reported experimental data for multicaloric effects among the different families of multicaloric materials. The development of this new setup is a step forward on addressing this lack of experimental data.

3.1.4.1 Calorimeter design

Figure 3.10 shows a scheme of the experimental system. The calorimeter core is made of a 15 mm diameter and 45 mm length copper cylinder (1) with two Peltier modules (2, 3) glued on the top and bottom surfaces by a thin layer of *GE Varnish*. These Peltier modules are used as the thermoelectric sensors and are connected differentially. The temperature of the calorimeter is measured with a Pt-100 platinum resistance (4) that is embedded inside the calorimeter copper block. The free side of the bottom module is in thermal contact with the reference (5). For all experiments performed on this device, a copper sample of mass $m = 601.195$ mg has been used as reference. The free side of the top Peltier module is in thermal contact with a 10 mm diameter and 3 mm thickness high-strength aluminium disk (6) and the studied sample (7) is placed on top of this disk. A thin layer of silicone heat transfer compound (HTS) from *Electrolube*® is placed on the surfaces of each Peltier module to ensure a proper thermal contact. To protect the top Peltier module of any damage from the applied uniaxial load to the studied sample, the high-strength aluminium disk is placed into a Polyether ether ketone (PEEK) holder (8) that leans on the inner wall of the high-strength aluminium container (9) that surrounds the calorimeter copper block. This aluminium container is connected to a $RP - 890C$ Lauda® GmbH Proline thermal bath (not shown in Figure 3.10 for the sake of simplicity) through two copper pipes (10). The thermal bath uses silicon oil that flows through the aluminium container, and controls its temperature and flow around this closed circuit.

The ensemble of the calorimeter copper core and the surrounding aluminium container is placed inside the bore of a 6T Cryogen-free Magnet from *Cryogenic*

Ltd.® (11). Uniaxial load is applied to the sample through a high-strength aluminium rod (12) whose upper end is in contact with a free mobile platform (13) outside of the cryogen-free magnet bore (see panel (*a*) in Figure 3.10). To minimize the shear components of the stress applied to the studied sample, a cylindrical plastic centring platform (14) that fits to the diameter of the magnet bore is attached to the high-strength aluminium rod. A second centring platform is placed at the top of the magnet bore (15) that additionally improves the thermal insulation of the calorimetric ensemble placed inside the magnet bore. At the bottom end of the high-strength aluminium rod, a 10 mm thickness PEEK disk (16) is attached to the aluminium rod in order to minimize the thermal coupling between the sample and the rod. To increase the thermal homogeneity of the calorimeter and minimize both the air convection around the sample and the thermal loses from the aluminium container to the surrounding, a plastic cover is added around the container that goes up to the plastic centring platform (not shown in Figure 3.10 for the sake of simplicity). In addition to the calorimetric signal of the Peltier modules, the setup is also designed to measure the length changes of the studied samples during the experiments. A linear variable differential transformer (LVDT) sensor (17) from *Solartron Metrology*® in contact with the mobile platform that measures its relative position is used with this purpose. The LVDT sensor is mounted onto a mobile holder, whose position can be adjusted with a micrometer. The mobile holder has a certain margin of movement along the side of a fix platform placed on top of the Cryogen-free magnet. The uniaxial load is applied by adding the desired dead weight from pre-weighted lead ingots (18) on top of the mobile platform.

The setup allows the performance of simultaneous calorimetric and dilatometric measurements within the temperature range $T \in [210, 360]\,\mathrm{K}$, under applied compressive forces up to $F = 1200\,\mathrm{N}$ and magnetic fields up to 6T. The LVDT sensor is excited by applying 10 V with an AC voltage source. The electric signals from the differentially connected Peltier modules, the Pt-100 platinum resistance and the LVDT sensor are read by two Two *Keithley*® 2000 and one *Agilent*® 34401A multimeters, respectively. The whole system is controlled by a personal computer using Labview software. Readings of time, temperature, calorimetric output and length changes are performed at typical rates of 1 Hz.

This new version of the calorimeter implied an in-depth redesign of the device, incorporating several modifications with respect to the previous setup described in [92]. When performing calorimetric measurements while scanning the temperature, the previous device showed a poor behaviour of the measured baselines, thus hindering the calorimetric signal of the sample and reducing the information that could be accessed. This major issue was addressed in the new version by including a massive calorimeter copper block (1) that is embedded inside the high-strength aluminium container, where the silicon oil flows through. This massive calorimeter centre, that is in direct contact with both thermoelectric sensors, gives more thermal inertia to the setup. As copper has a high thermal conductivity, it helps to minimize temperature gradients of the system and reduces the effect of thermal fluctuations from temperature changes of the silicon oil on both sample and reference thermoelectric sensors when measuring.

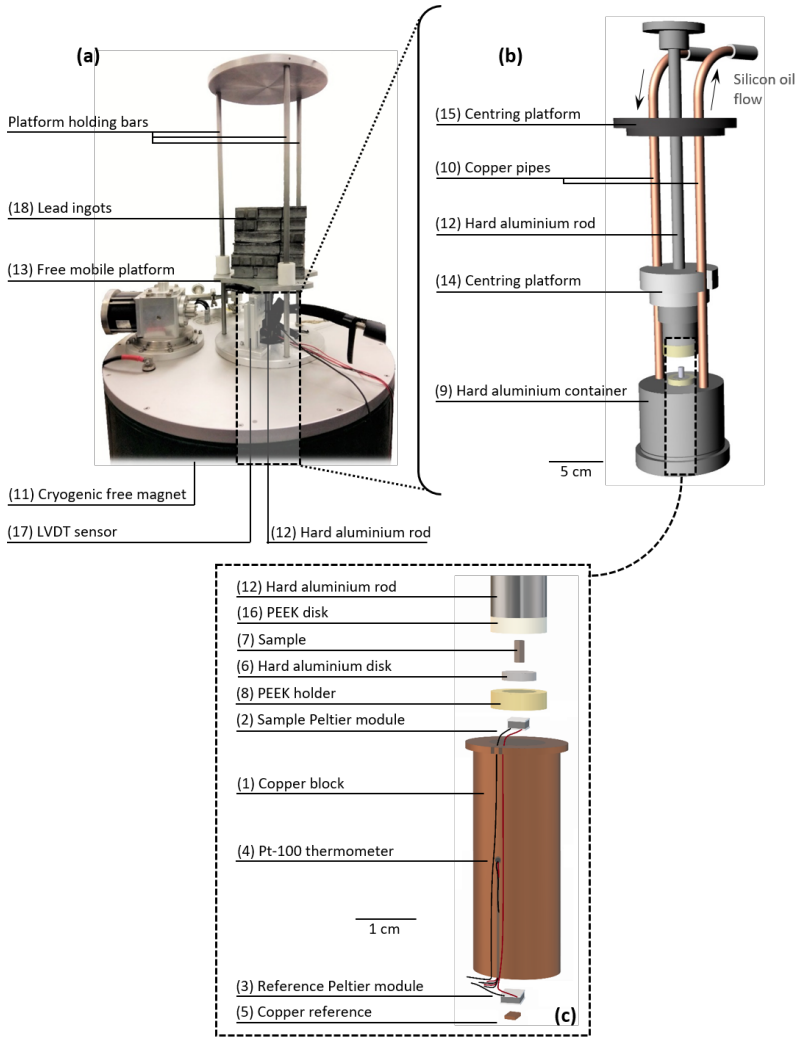

Figure 3.10: *Different views of the differential scanning calorimeter under magnetic fields and uniaxial compressive stress. Panel (a) shows a picture of the 6T Cryogen-Free Magnet from Cryogenic Ltd.® in which the purpose-built device is coupled to its bore. Panel (b) illustrates the ensemble of the differential scanning calorimeter and the aluminium container which are placed inside the magnet bore and panel (c) shows the details of the calorimeter which is embedded in the aluminium container.*

Moreover, the sensitivity of the device is of crucial importance for the clear measurement of the sample heat flow during the experiments. In our device, a high-strength aluminium disk (6) is placed between the sample and its thermoelectric sensor, and its size has a critical effect on the sensibility of the calorimeter. Nevertheless, the disk is of fundamental importance to ensure the protection of the sample thermoelectric sensor when applying uniaxial compressive load. This issue

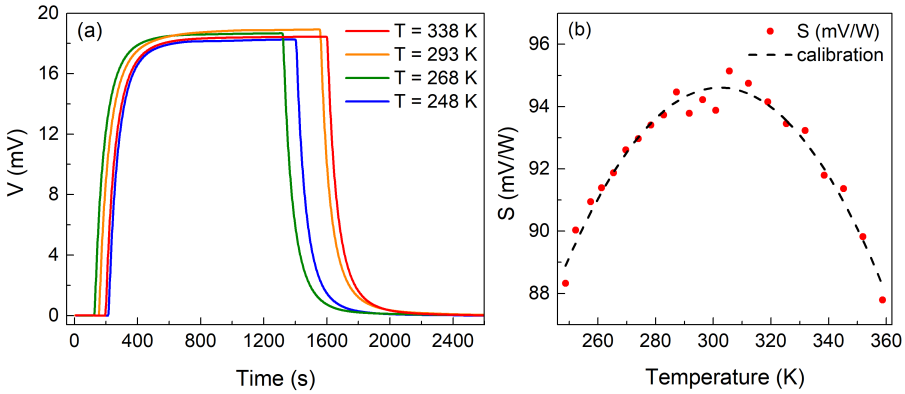

Figure 3.11: *Illustrative examples of calibration measurements for the DSC under magnetic field and uniaxial compressive stress calorimeter.* (a) *: Voltage output* (Y) *as a function of time measured at different constant temperatures for the calorimeter calibration.* (b) *: Plot of the sensitivity of the calorimeter as a function of temperature. Red dots correspond to the sensitivities obtained from the experimental measurements and the dashed line corresponds to the second order polynomial fit:* $S(T) = -88(8) + 1.21(5)T - 2(0.08)10^{-3}T^2$ *for* $T \in [250, 360]\,K$.

was addressed in the design of the device by modifying the diameter and thickness of the high-strength aluminium disk in order to reduce its total mass and at the same time guarantee the protection of the thermoelectric sensor. In the previous version of the setup, the disk had a diameter of 15 mm and a thickness of 2 mm. Therefore, the size of the high-strength aluminium disk has been reduced by one third. Additionally, as the thickness of the disk has been increased, it is expected that a negligible deformation of the disk will take place when applying uniaxial compressive loads.

3.1.4.2 Setup calibration

The calibration of this calorimeter is performed by following the same general procedure as previously described in section 3.1.3.1. An electric circuit similar to the one schematically presented in Figure 3.8 is mounted onto the sample thermoelectric sensor of the calorimeter.

For this setup, we use a copper block with dimensions $8.3 \times 7.8 \times 3.9\,\mathrm{mm}^3$ that has a resistance embedded inside ($R_S = 120\,\Omega$) as the sample resistor of the calibration circuit. To perform each measurement, the circuit is closed for a period of $\backsim 1200 - 1400\,\mathrm{s}$ at each temperature until the stationary state is reached, and the applied voltage with the power supply is 9 V for all the measurements. Figure 3.11 (a) shows the electrical output of the calorimeter as a function of time for calibration measurements performed at different constant temperatures. The start of each measurement has been slightly shifted in time in order to facilitate the comparison between the different measurements and their corresponding plateaus.

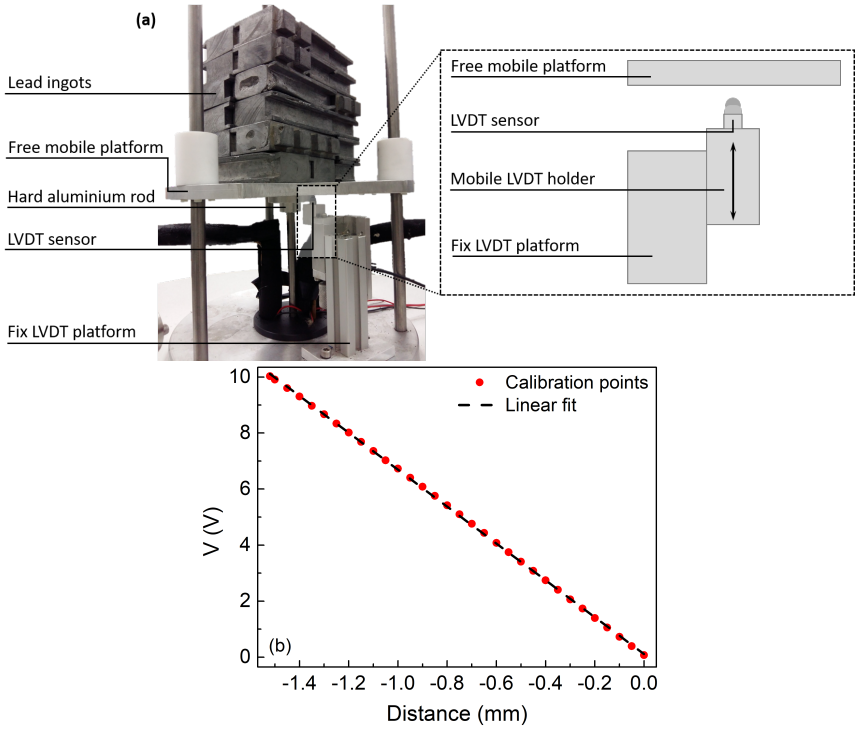

Figure 3.12: (*a*): *Picture of the DSC structure on top of the cryogenic free magnet with the LVDT sensor from Solartron Metrology® (left) together with a sketch of the LVDT sensor and its relative position with respect to the free mobile platform (right).* (*b*): *Voltage output of the LVDT sensor with respect to the distance from the free mobile platform. Red dots correspond to the calibration measurements and the dashed line corresponds to the linear fit:* $X(mm) = (-0.1519 \pm 0.0003)V + (0.017 \pm 0.002)$

The values for the sensitivity obtained from each measurement are plotted as red dots in Figure 3.11 (*b*), and the black dashed line is a second order polynomial fit to the data.

If we compare the values obtained from this measurements with the calibration of the previous setup presented in [92], we observe an increase of the sensitivity of around 20% for our improved design in the full temperature range. This increase of the sensibility is in accordance with the reduction of the size of the high-strength aluminium disk.

The calibration of the linear variable differential transformer (LVDT) sensor is performed by measuring the voltage output for different fixed displacements, measured by means of a digital Varnier caliper, with respect to the free mobile platform. Figure 3.12 shows a picture and a sketch of the LVDT sensor (*a*) and its voltage

output measured for different relative positions with respect to the platform (b). In this configuration, a zero distance corresponds to the contact position between the tip of the sensor and the platform, and negative distances correspond to the compression of the sensor against the platform. As expected, its voltage output shows a great linearity with displacement within an operational range of 1.5 mm.

3.2 Adiabatic thermometry

For the work presented in this dissertation, the performance of adiabatic thermometry measurements has been an important complement to calorimetric techniques in order to thoroughly characterize the induced thermal response on materials near a first-order phase transition that is sensitive to different applied external fields. The purpose of adiabatic thermometry is to directly measure the adiabatic temperature change associated with state changes of the sample induced by a change on the applied external field ($x_i^s \rightarrow x_i^f$).

Direct measurements of the field-induced adiabatic temperature change are generally performed under the influence of a single external field, such as magnetic field [35, 95–98], mechanical stress [31, 54, 99–101], hydrostatic pressure [78, 102, 103] or electric field [104]. However, the study of materials exhibiting a cross-coupled response under different external fields requires the development of bespoke setups that allow the simultaneous or sequential application of multiple external fields. The design and assembly of such purpose-built setups had an important role on the work presented in this thesis, and they lay the first stone on the direct measurement of field-induced multicaloric adiabatic temperature changes.

This section will focus on the description of two bespoke setups that were designed and built during this thesis and allow us to perform direct contact thermometry measurements under the influence of uniaxial load and magnetic field. A fundamental difference between these setups is the magnetic field source used in each case. The first described setup uses an electromagnet allowing us to apply or remove the magnetic field in a few seconds, while the second setup is placed inside a solenoid that allows us to apply magnetic field pulses that last few milliseconds. The different time scales involved in both measurements, together with the different available magnetic field intensities, allow us to access information on both the thermal response and the dynamics of the field-induced phase transition [97].

3.2.1 Measurement protocols for adiabatic thermometry

Adiabatic temperature change measurements induced by an external field change can be performed either under isothermal conditions at the desired starting measurement temperatures T or under a continuously changing temperature $T(t)$. As previously discussed in section 2.2, the first-order character of the studied phase transitions implies a certain temperature and external field hysteresis. Therefore, the thermal history of the sample has to be taken into account to perform adia-

batic thermometry measurements and the followed protocols have to be properly designed in order to follow the desired thermodynamic paths. Taking all this into account, we can define the discontinuous and continuous measurement protocols, respectively, as follows:

1. **Discontinuous protocol:**
   The thermodynamic path followed for this protocol corresponds to the isothermal protocol discussed in section 3.1.2.1 for DSC calorimetry. After following a certain temperature path in order to control the initial thermodynamic state of the sample, the system is brought to the desired measurement temperature where a cyclic external field profile is applied. It is important to point out that under the influence of multiple external fields, we only apply a cyclic pattern on one of the external fields while keeping the others constant during the experiment.

   As the sample initial state is not affected by the previous measurements performed, the application of a cyclic external field pattern allows us to directly determine the reversible and irreversible induced adiabatic temperature changes of the sample under study.

2. **Continuous protocol:**
   Under this measurement protocol, the sample is either continuously heated or cooled at a certain rate, while single external field pulses are applied at certain temperatures. It is important to point out that under the influence of multiple external fields, the successive applied single field pulses can be of different external fields.

   Under this measurement pattern, the thermodynamic state of the sample is directly influenced by the previously applied external field pulses. Therefore, the induced thermal response for a certain external field pulse not only depends on the instantaneous measurement temperature, but also on the previous thermodynamic end state after the last external field pulse applied.

3.2.2 Direct thermometry with a bench-top electromagnet

A bespoke setup to perform direct thermometry measurements under the simultaneous or sequential change of magnetic field and uniaxial compressive stress has been designed and built. The aim of this setup is to complement the measurements performed with the DSC that allows the application of magnetic field together with uniaxial compressive stress presented in section 3.1.4. The combined measurements of both setups allows us to perform in-depth analysis of the caloric and multicaloric effects arising from materials displaying a magnetostructural transition with a strong coupling between the structural and magnetic degrees of freedom, as these materials are prone to show a cross-coupled response.

The setup described in this section is an upgraded version of a previous setup presented in [65].

3.2.2.1 Setup design

Figure 3.13 shows a detailed scheme of the experimental system: panel (*a*) shows a 3D representation of the whole system, while panel (*b*) shows a vertical section of the bespoke direct thermometry setup. The sample (1) is glued on top of a 1.5 mm thickness polyether ether ketone (PEEK) disk (2) by a thin layer of *GE Varnish*. The PEEK disk sits on top of a high-strength aluminium container (3), which is connected to a $RP-890C$ Lauda® GmbH Proline thermal bath (not shown in Figure 3.13 for the sake of simplicity) through two copper pipes (4). The high-strength aluminium container sits on top of a 2 mm thickness PEEK disk (5) in order to thermally isolate the aluminium container base from the surroundings. The thermal bath uses silicon oil that flows through the aluminium container, and controls its temperature and flow around this closed circuit. The temperature of the sample is directly measured with a fine gauge K-thermocouple (0.075 mm diameter) (6) that is attached to a free surface of the specimen under study. A small drop of silicone heat transfer compound (HTS) from *Electrolube*® is placed on the sample surface to ensure a proper thermal contact between the specimen and the thermocouple. Additionally, the sample and the thermocouple are tightly wrapped with Teflon tape to keep them in place.

Uniaxial load is applied to the sample by means of a screw (7) that compresses a spring (8) and pushes a free-mobile high-strength aluminium rod (9) that is in direct contact with the sample. The bottom end of the high-strength aluminium rod is protected with a 10 mm PEEK disk (2) to thermally isolate the sample from the aluminium rod. To minimize any shear or torsion components from the screw to the compression spring, a high-strength aluminium holding platform (10) is placed between them. A second two-piece holding platform (11) is placed between the spring and the high-strength aluminium rod that protects and keeps in place the load cell (12) from *Omega*® that measures the applied force. Two high-strength aluminium guides (13), isolated at the bottom side from the aluminium container by two PEEK pieces (5), go through both holding platforms (10 and 11) and improve the stability of the system under compression. A high-strength aluminium frame (14) holds the guides, the screw and the aluminium container together. Two PEEK pieces (not shown in Figure 3.13 for the sake of simplicity) are placed between the aluminium frame and the aluminium container in order to reduce the heat leaks between these two elements. The setup is placed between the bores of a bench-top electromagnet (15) (see panel (*a*) in Figure 3.13) from *GMW Magnet Systems*®. The direct thermometry setup has been designed in order to keep the sample position in the centre of the region where the applied magnetic field is homogeneous, which is measured by a Hall probe (16) that is placed next to the sample. To isolate the system from the surrounding and improve the adiabaticity of the experiments, plates of expanded polystyrene are placed around the direct thermometry setup.

The setup allows the direct measurement of the sample's temperature change under applied compressive forces up to $F = 1000\,\mathrm{N}$ and magnetic fields up to 2 T

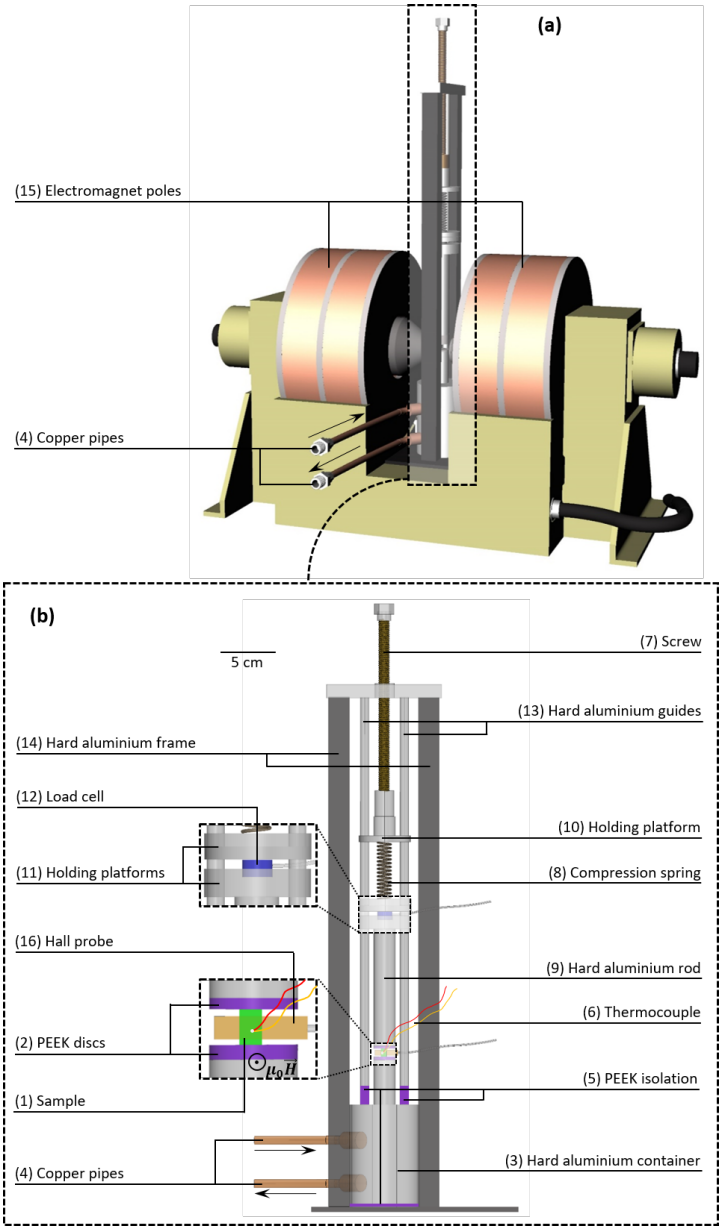

Figure 3.13: *Different views of the direct thermometry with a bench-top electromagnet setup. Panel (a) illustrates the bench-top electromagnet from GMW Magnet Systems® in which the purpose-built device is placed between its bores. Panel (b) shows a sketch of the direct thermometry setup and its components. The electromagnet has been omitted from this view for the sake of clarity.*

within a temperature range $T \in [260, 350]$ K. The electromagnet is controlled by a specific personal computer using a Labview software, and application and removal

of the magnetic field is performed at a rate of $\backsim 1.5\,\mathrm{Ts}^{-1}$. The load cell is excited by applying 5 V with a DC voltage source. The electric signals from the thermocouple, the load cell and the Hall probe are reecorded by three *Keithley*® 2000 multimeters. The whole system is controlled by a second personal computer using Labview software. Readings of time, temperature, applied force and magnetic field are performed at typical rates of 2 Hz.

The setup described in this section incorporates several modifications in order to improve its performance with respect to the previous version described in [65]. There is a threefold motivation for the introduced modifications: First of all, the availability of higher magnetic fields for the experiments. Secondly, an improvement of the applied force control during the experiments. Thirdly, an improvement of the thermal insulation to increase the working temperature range.

For these purposes, the diameter of the high-strength aluminium rod (9) has been reduced, thus allowing to bring closer the electromagnet bores and achieve higher magnetic fields up to 2 T. Additionally, the length of the high-strength aluminium rod has been increased by 10 cm in order to separate the load cell from the electromagnet and minimize the effect of magnetic field pulses on the recorded force. In order to increase the applied force control, the described system incorporates a compression spring (8) between the screw (7) and the load cell (12). The purpose of the spring is to minimize the applied force change measured at the load cell when the sample under study experiences a length change due to the field-induced magnetostructural transition. Last but not least, the thermal loses of the high-strength aluminium container (3) to its surroundings have been minimized by adding PEEK pieces at the different contact surfaces with other elements, such as the hard-aluminium guides (13) and frame (14). Moreover, the thickness of the PEEK disk below the sample has been optimized in order to increase the working temperature range of the setup.

3.2.2.2 Setup calibration

The calibration of this setup consisted on the measurement of the load cell linearity, the calibration of the fine-gauge K thermocouple and the assessment of the adiabaticity during the measurements.

Firstly, the load cell response is calibrated by measuring the voltage output for different applied forces, which are controlled by hanging different calibrated weights to the sensor. Figure 3.14 (*a*) shows the load cell voltage output for different applied forces. As expected, the sensor shows a great linearity within the full force range.

Secondly, the reference junction temperature of the fine-gauge K thermocouple has to be adjusted. In our case, it is simulated by a *Keithley*® 2000 multimeter, which is the thermocouple measuring unit. This multimeter allows us to modify the reference junction temperature, which is adjusted in order to measure zero degrees Celcius when the thermocouple is immersed into a mixture of distilled water and ice in equilibrium.

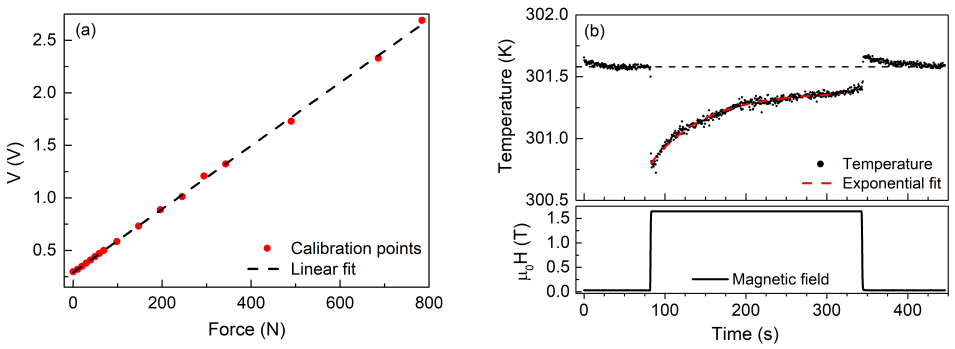

Figure 3.14: *(a): Voltage output of the load cell with respect to the applied force. Red dots correspond to the calibration measurements and the dashed line corresponds to the linear fit:* $F(N) = (332 \pm 2)V - (97 \pm 2)$. *(b): Measured temperature versus time profile for a Ni-Mn-In sample upon the application of a* $\mu_0 H = 1.6\,T$ *constant magnetic field, together with an exponential fit (red dashed curve) to the relaxation process (top). Time profile of the applied magnetic field (bottom).*

Thirdly, as the measured field-induced temperature change greatly depends on the quality of the adiabatic conditions during the experiments, the adiabaticity of the setup has to be addressed. As the sample is in thermal contact with its surroundings, the adiabatic conditions depend on the fast application or removal of the magnetic field in comparison to the time needed by the sample to exchange heat. Therefore, if τ_m corresponds to the magnetic field application or removal time constant and τ_s is the sample time constant characterizing its heat exchange with the surroundings, the value of the ratio $\dfrac{\tau_m}{\tau_s}$ will quantify how close the experiment is from adiabatic conditions. For instance, the smaller the ratio is, the closer the experiment will be from adiabatic conditions [105]. Figure 3.14 (b) shows a relaxation measurement performed with this setup on a Ni-Mn-In sample under the application and removal of 1.6 T magnetic field. The details of the sample and its caloric and multicaloric effects are thoroughly discussed in section 5.3, here the measurement is used as an example to study the adiabaticity of the system. The field-induced adiabatic temperature change is computed as the temperature change before and after the magnetic field application as $\Delta T(0 \rightarrow 1.6\,\mathrm{T}) = T(1.6\,\mathrm{T}) - T(0\,\mathrm{T}) \approx -0.8\,\mathrm{K}$. If we keep the magnetic field applied, a relaxation towards the initial temperature can be seen. When the applied magnetic field is removed, we observe that the sample's temperature relaxes back to the initial temperature of the experiment. The characteristic time constant magnitude of the relaxation process after the field application (τ_s) can be determined by performing an exponential fit. The magnitude of the sample's time constant is directly related to the capacity of the sample to exchange heat with its surroundings, as a bigger time constant implies that the sample exchanges less heat per unit time.

Therefore, on the one hand, the electromagnet allows a fast application or removal

of magnetic fields up to 2 T with a time constant of $\tau_m \simeq 1$ s. On the other hand, the time constant of the relaxation process associated with the heat exchange with the surroundings is found to be $\tau_s \simeq 70$ s. Accordingly, as $\tau_m \ll \tau_s$, the application and removal of magnetic field are performed with a negligible heat exchange between the sample and its surroundings, and the measurements can be considered close to adiabatic conditions.

Furthermore, the measured adiabatic temperature changes with this bespoke setup on this Ni-Mn-In sample under an external field change of 1.6 T (see section 5.3) show a good agreement with the adiabatic temperature changes reported in the supplementary information of [64] for the same specimen, which were performed under proper adiabatic conditions. The concordance found between these two sets of measurements provides a solid proof on the close to adiabatic conditions of the measurements performed on our bespoke setup.

3.2.3 Pulsed magnetic fields

A bespoke setup to perform direct thermometry and strain measurements under the influence of pulsed magnetic fields and uniaxial compressive stress has been designed and built during my stay at Helmholtz Zentrum Dresden-Rossendorf (HZDR), in close collaboration with Dr. Tino Gottschall and Eduard Bykov.

The pulsed-field facility at the HZDR research institute *Dresden High Magnetic Field Laboratory* (Hochfeld-Magnetlabor Dresden, HLD-EMFL [3]) has different types of available solenoids, allowing the application of magnetic field pulses up to 95 T. This facility provides excellent conditions to perform direct measurements of the field-induced multicaloric adiabatic temperature change under high-strength magnetic field pulses and uniaxial compressive stress. The bespoke setup has been specifically designed to be embedded inside the type E solenoids, [4] allowing the application of magnetic field pulses up to 50 T that last 75 ms.

3.2.3.1 Setup design

Figure 3.15 shows a detailed scheme of the designed insert (panels (*a*) and (*b*)) and the experimental system (panel (*c*)). The sample (1) is cut in two pieces and their surfaces are polished in order to be parallel. The sample temperature is directly measured by a T-type differential thermocouple (not shown in Figure 3.15), made of copper and constantan wires with a thickness of 0.025 mm. The differential thermocouple has a fork-like structure, where one end is glued between the two sample pieces with silver epoxy in order to provide a good thermal contact, and the reference end is placed near a Pt-100 platinum resistance (2), which is embedded inside the surrounding Cu-Be cell (3), that monitors the absolute temperature of the setup. The heater (4), made of two manganese wire coils placed above and below the sample position on the Cu-Be cell surface, is controlled by a *Lakeshore cryotronics*® 350 temperature controller that uses the reading from

[3] HDL-HZDR web site: `https://www.hzdr.de/db/Cms?pNid=580`
[4] Magnets specifications: `https://www.hzdr.de/db/Cms?pNid=2686`

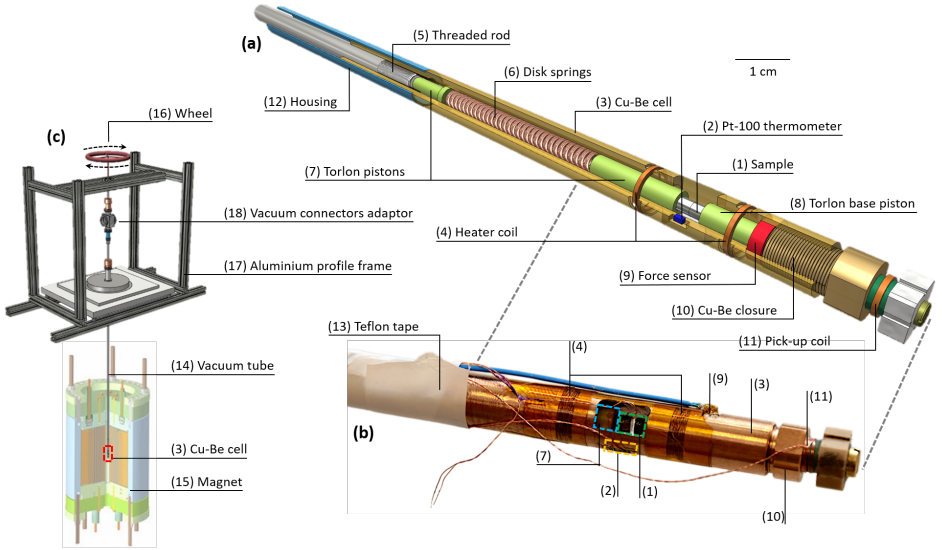

Figure 3.15: *Different views of the pulsed thermometry setup. Panel (a) illustrates a 3D representation of the insert with all the main components. Panel (b) shows a picture of the designed insert, with lines pointing at the visible components. Two grey dashed lines from panel (a) to (b) show the equivalence of the encompassed insert section between them. Panel (c) shows a simplified sketch of the configuration of the complete experimental setup: the insert, the magnet solenoid and the outside aluminium frame.*

the Pt-100 platinum resistance, and it is meant to control the temperature of the insert. Changes in the sample length are measured with a strain gauge (not shown in Figure 3.15) that is attached to the lateral surface of one sample piece. The grid size of the strain gauge used is $0.78 \times 1.57\,\mathrm{mm}^2$, and its output is measured by means of a Wheatstone bridge circuit.

Uniaxial load is applied to the sample by means of a stainless steel threaded rod (5) that compresses a set of disk springs (6), encompassed by two high-performance polymer Torlon® pistons (7). The sample is in direct contact with the second Torlon® piston, which directly transmits the applied force. The sample lays on top of a third Torlon® piston (8), and the applied force is measured with a piezoelectric force sensor (9) model $CLP/3\mathrm{kN}$ from *HBM*® which is monitored by a *Keithley*® 6517B electrometer. The back pressure to hold the applied uniaxial load is generated by a Cu-Be threaded closure (10), that holds the force sensor. At the end of the insert, a pick-up coil (11) is placed in order to measure the applied magnetic field pulse close to the sample position. The insert is fixed with stycast two-component glue to the housing (12), which is then tightly wrapped with Teflon tape (13) in order to protect the wires of all the sensors and components (differential thermocouple, strain gauge, force sensor, Pt-100 platinum resistance, heater coils and the pick-up coil). To ensure adiabatic conditions during the measurements, both insert and housing are placed inside a stainless steel high-vacuum tube (14). The vacuum

achieved during the experiments is typically of $\sim 1 \cdot 10^{-6}$ mbar.

The magnet solenoid (15) is kept at cryogenic temperatures inside a cryostat (not shown in Figure 3.15 for the sake of simplicity) surrounded by liquid Nitrogen, and filled with Helium. The high-vacuum tube is introduced into the bore of this cryostat, and the Helium inside acts as an exchange medium to cool down the insert via thermal radiation. The length of the housing was chosen in order to keep the sample position in the centre of the region where the applied magnetic field is maximum and homogeneous. The force applied on the sample is tuned from the outside with a wheel (16) that is connected to the threaded rod (5). To give mechanical stability to the experimental system, an aluminium profile frame (17) is placed onto the solenoid cryostat that fixes the wheel and the high-vacuum tube. A vacuum connector adaptor (18) is placed at the top end of the high-vacuum tube in order to connect the different wires of the all sensors and components of the insert to the different measuring and controlling units, while allowing to keep a proper vacuum level for the experiments.

Preliminary experiments have been conducted on a Ni-Mn-Ti-Co Heusler alloy to test the performance of the system. Figure 3.16 shows the time dependence of a 10 T magnetic field pulse, together with the induced strain and adiabatic temperature changes as a function of time for different initial sample temperatures and applied uniaxial stresses.

As shown in the magnetic field dependence (panel (a) of Figure 3.16), the maximum magnetic field intensity is reached after 13 ms, and the maximum field sweep rate is 1400 Ts^{-1}. As it can be seen in panel (b), at an initial temperature of 265 K, the sample cools down by 17.7 K. It is important to point out that the reaction of the thermocouple is almost instantaneous despite this rapid field sweep rates. Therefore, a proper thermal coupling between the sample and the thermocouple has been achieved. Additionally, after 100 ms the applied magnetic field has practically returned to zero, but the temperature does not return to the initial value. This effect is also observed for the measurements shown in panels (c) and (d), and is related to the thermal hysteresis of the studied sample, which results on a partial irreversibility of the field-induced phase transition. Moreover, as the sample temperature remains constant after the magnetic field returns to zero, we conclude that at the considered time scales of the experiments there is no significant heat exchange between the sample and the pistons. Therefore, adiabatic conditions are achieved during the experiments to a very good extent.

When the initial starting temperature is increased to 270 K, a reduction of the maximum adiabatic temperature change is observed and a plateau appears, which indicates that the phase transition is completed. Under the application of a uniaxial load of 40 MPa, a further reduction of the maximum adiabatic temperature change is observed, together with a reduction of the plateau. On the other hand, a peculiar behaviour of the strain measurements is observed. At panel (b), for an initial temperature of 265 K, we measured a length change of the sample 16 ms after the pulse start, which means that the length change started 3 ms after the applied

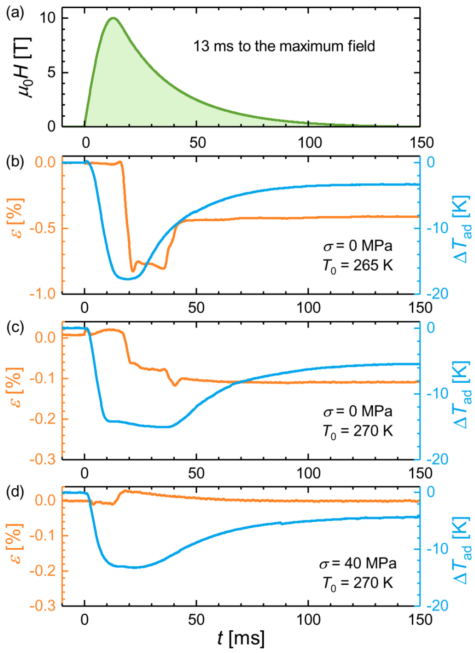

Figure 3.16: *(a): Time dependence of the applied magnetic field pulse with the solenoid. (b) – (d): Direct measurements of the sample strain $\varepsilon(\%)$ (left) and adiabatic temperature change $\Delta T_{ad}(K)$ (right). The figure has been taken from [66].*

magnetic field reached its maximum. After a small plateau, the initially measured length change of 0.8 % is reduced to 0.4 %. Conversely, at an initial temperature of 270 K, the measured length change is much smaller, around 0.1 %, and there is no recovery afterwards. When we apply uniaxial load, as presented in panel (*d*), the observed length change reverses its sign with respect to the previous measurements, and relaxes back to zero slowly. The reason for the observed time-delay on the strain gauge response with respect to the magnetic field pulse is not clear, and further measurements are required in order to clarify the observed behaviour.

A detailed discussion on the multicaloric effects induced on this alloy under pulsed magnetic fields and uniaxial load can be found in [66].

As shown and discussed, promising results have already been obtained with this bespoke setup on the direct measurement of pulsed-field induced multicaloric effects. It is anticipated that this setup will have an important role on further future research, as it is a suitable and unique tool to gain insight on the dynamics of the field-induced phase transition under the influence of multiple external fields.

3.3 CuZnAl: a calibration sample for the DSC under magnetic fields and uniaxial compressive stress

Before using the bespoke DSC setup described in section 3.1.4 for the characterization of the caloric and multicaloric effects arising from materials exhibiting a cross-coupled response under the simultaneous application of magnetic field and uniaxial compressive stress, a reference sample was studied in order to validate the agreement between the measured data and the reported data in the literature. For this purpose, we selected a Cu-Zn-Al shape-memory alloy as a calibration sample, for which the elastocaloric properties are well established.

Cu-Zn-Al is a diamagnetic alloy that exhibits a structural (martensitic) transition between a high-temperature bcc (body centered cubic) phase and a low-temperature martensitic phase (see section 4.2 for a discussion on structural transitions and Heusler alloys), and the associated transition entropy change has been properly determined over a broad composition range [106, 107]. Associated with the structural transition, these alloys exhibit a significant length change at the phase transition under the application of stress, thus leading to prominent elastocaloric effects. An exhaustive discussion on the crystallographic characteristics and the physical properties of these alloys is reported elsewhere [108].

3.3.1 Sample details

The calibration experiments have been performed on a single-crystalline $Cu_{68.3}Zn_{14.2}Al_{17.5}$ shape-memory alloy with dimensions $5.4 \times 5.3 \times 6.4\,\mathrm{mm}^3$ and a mass of 1.383 g. The same specimen was previously used in reference [109], where a detailed discussion on the applicability of exploiting the associated elastocaloric effect for an active regenerator-based cooling device is presented.

3.3.2 Experimental details

Simultaneous dilatometric and DSC measurements have been performed with the bespoke DSC setup at typical temperature scanning rates of $\pm 0.5\,\mathrm{K\,min}^{-1}$ within a temperature range $T \in [270, 330]\,\mathrm{K}$ under constant values of uniaxial compressive stress $\{\sigma_i\} = \{1.7, 6.8, 13.6, 20.3, 27.1, 33.9\}\,\mathrm{MPa}$. [5]

[5] Along this dissertation, the uniaxial compressive stresses are computed as $\sigma_i = \frac{F_i}{A_s}$, where F_i corresponds to the applied compressive force and A_s to the sample surface measured in the absence of applied external fields.

3.3.3 Indirect derivation of the elastocaloric effect

For the indirect derivation of the elastocaloric effect, we will use the dilatometric measurements performed with the LVDT sensor. The strain of the sample is computed as:

$$\varepsilon(T,\sigma) = \frac{l(T,\sigma) - l_{ref}}{l_{ref}} \tag{3.25}$$

where $l(t,\sigma)$ is the length of the sample parallel to the direction of the applied force, and l_{ref} is the reference length measured beyond the phase transition region. Therefore, for heating measurements the reference length is taken at the low temperature (martensitic) phase at 270 K, i.e. $l^M_{ref} = 6.0\,\text{mm}$, while for cooling measurements it is taken at the high-temperature β phase at 330 K, i.e. $l^A_{ref} = 6.4\,\text{mm}$.

Figure 3.17 displays the raw measured ε–T curves for cooling and heating runs, respectively. It must be mentioned that the origin of the ε–T cooling runs has been shifted to $T = 270\,\text{K}$ i order to simplify their comparison with the heating curves.

The first-order phase transition is seen as a sharp change in strain, which spreads over a larger temperature range for cooling than for heating runs. Overlying the first-order phase transition signal we identify a linear background, which exhibits a similar behaviour for all the applied uniaxial stresses. The first-order phase transition shifts to higher temperatures when increasing the applied uniaxial compressive stress, together with a decrease on the associated transition strain for both heating and cooling runs.

The linear background mainly arises from the thermal expansion of the setup components when scanning the temperature, as the LVDT sensor sits far away from the sample (see Figure 3.10). To exclude this constant contribution from the

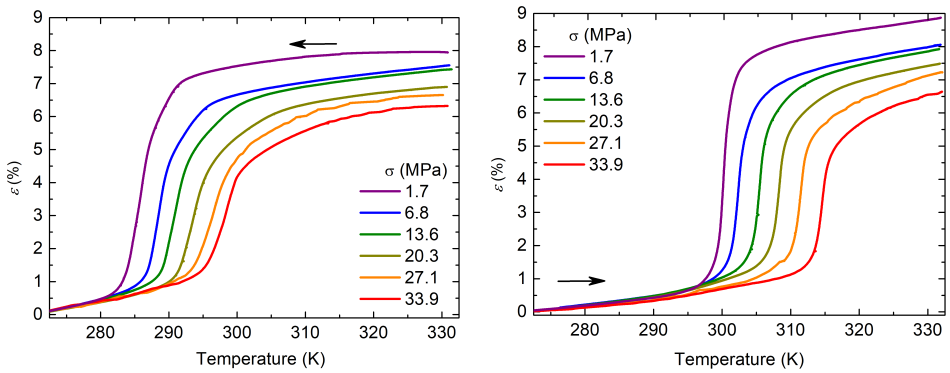

Figure 3.17: *Strain as a function of temperature at selected values of uniaxial compressive stress measured with the LVDT sensor for cooling (left) and heating (right) runs.*

raw dilatometric signal, we measured an INCONEL sample with low thermal expansion during temperature scans at typical rates of $\pm 0.5\,\mathrm{K\,min^{-1}}$ under different applied uniaxial compressive stresses, and then we subtracted this signal from our measurements. Figure 3.18 (a) and (b) display the background corrected ε-T curves obtained for cooling and heating runs, respectively.

To validate the observed decrease of the transition strain with applied uniaxial stress, a second set of dilatometric measurements was performed using a more ac-

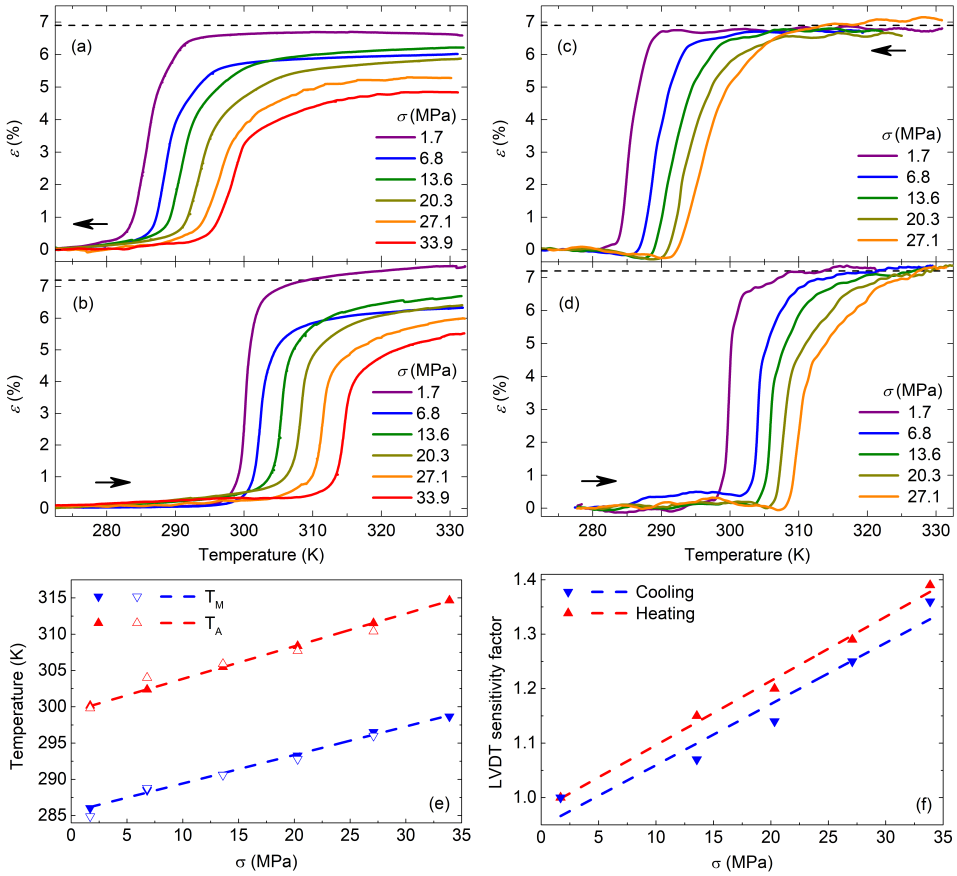

Figure 3.18: *Strain as a function of temperature at selected values of uniaxial compressive stress measured with the LVDT sensor (left) and a dynamic extensometer (right) for cooling (panels (a) and (c)) and heating (panels (b) and (d)) runs. (e) Transition temperature as a function of stress for the forward (T_M) and reverse (T_A) transitions obtained from the inflection points of the cooling and heating ε-T curves, respectively. Solid symbols correspond to the transition temperatures obtained from the LVDT curves and open symbols to the values from the dynamic extensometer. (f) LVDT sensitivity factor as a function of stress for both heating (red) and cooling (blue) runs. Dashed lines in panels (e) and (f) correspond to linear fits to the solid symbols.*

curate experimental setup, described in [110], where a dynamic extensometer from *Instron*® model 2620-601 was used as a dilatometric sensor. The described setup is mounted inside an environmental chamber from *Instron*® and a K-type thermocouple (0.075 mm diameter), attached to a free surface of the sample, was used as a temperature sensor. The experiments were performed at typical scanning rates of $\pm 1\,\mathrm{K min}^{-1}$ within a temperature range $T \in [270,\ 335]\,\mathrm{K}$ under constant values of uniaxial compressive stress $\{\sigma_i\} = \{1.7,\ 6.8,\ 13.6,\ 20.3,\ 27.1\}\,\mathrm{MPa}$. The strain of the sample is computed as before, and the associated ε-T curves are represented in Figure 3.18 (c) and (d) for cooling and heating runs, respectively.

In contrast to the LVDT dilatometric measurements, the first-order phase transition strain does not show a dependency on the applied uniaxial compressive stress. The strain change of the forward (cooling) and reverse (heating) martensitic transition are found to be $\Delta\varepsilon_t^M = (6.9 \pm 0.2)\,\%$ and $\Delta\varepsilon_t^A = (7.2 \pm 0.2)\,\%$, respectively, and are represented as dashed black lines in panels (a) - (d) in Figure 3.18. As both transition strains are compatible and within the errors, they are taken as constant for the forward and reverse martensitic transitions at $\Delta\varepsilon_t^{M,A} = (7.0 \pm 0.3)\,\%$.

When comparing the ε-T curves obtained from both experimental setups for cooling (panels (a) and (c)) and heating (panels (b) and (d)) runs, respectively, two observations must be emphasised. Firstly, it is important to point out that at low compressive stresses the measured transition strains are comparable, while for higher stresses the behaviour observed with the LVDT sensor deviates from the dynamic extensometer measurements. Secondly, the transition temperature values of the forward (T_t^M) and the reverse (T_t^A) transitions, identified as the inflection point of the ε-T curves, show a good agreement between both data sets.

Figure 3.18 (e) illustrates the behaviour of the transition temperature as a function of the applied uniaxial compressive stress. As represented in this figure, the transition has an associated hysteresis of $T_t^A - T_t^M = 14\,\mathrm{K}$ and takes place about room temperature for low values of the applied compressive stress. Under the application of higher stresses, the first-order phase transition shifts to higher temperatures at rates $\dfrac{dT_t^M}{d\sigma} = (0.40 \pm 0.02)\,\mathrm{KMPa}^{-1}$ and $\dfrac{dT_t^A}{d\sigma} = (0.45 \pm 0.02)\,\mathrm{KMPa}^{-1}$. These rates agree with typical reported values for composition-related Cu-Zn-Al shape-memory alloys [30, 111].

The origin of the transition strain decrease when increasing the applied compressive stress measured with the LVDT sensor has not been clearly identified, and a systematic study with different reference samples would be necessary. Still, it is reasonable to partially attribute its origin to the fact that, according to the design of our bespoke DSC, the dilatometric sensor is placed far away from the sample. These measurements can be corrected by introducing an LVDT sensitivity factor in order to correct their deviation from the more precise measurements performed with the dynamic extensometer. This LVDT sensitivity factor is defined as:

$$X_{LVDT} = \frac{\Delta l_t(\sigma = 1.7\,\mathrm{MPa})}{\Delta l_t(\sigma)} \tag{3.26}$$

where $\Delta l_t(\sigma) = l^{A,M}(\sigma) - l^{M,A}_{ref}$ corresponds to the transition length change of the sample measured by the LVDT sensor under a certain applied uniaxial compressive stress. Figure 3.18 (f) illustrates the sensitivity factor directly obtained from the LVDT measurements as a function of stress. The ε-T curves represented in Figure 3.18 (a) and (b) are rescaled according to the linear fits on the LVDT sensitivity factor, and the corrected curves are represented in Figure 3.19 (a) and (b) as solid lines.

As discussed in section 2.1.1, and taking into account Table 2.1, the elastocaloric entropy change can be obtained indirectly from the Maxwell relations as:

$$\Delta S(T, \sigma_s \rightarrow \sigma_f) = \upsilon_0 \int_{\sigma_s}^{\sigma_f} \left(\frac{\partial \varepsilon(T,\sigma)}{\partial T} \right)_{\sigma} d\sigma \tag{3.27}$$

where υ_0 corresponds to the specific volume, which is $\upsilon_0 = 1.318 \cdot 10^{-4}\,\mathrm{m^3 kg^{-1}}$ for the studied sample.

A proper determination of the isothermal entropy change $\Delta S(T, \sigma_s \rightarrow \sigma_f)$ using equation 3.27 requires knowledge of ε-T curves at close enough values of applied uniaxial compressive stress in order to reduce the errors associated with the numerical computation of the derivatives involved in the previous equation. If the transition temperature shift with the applied uniaxial compressive stress $\left(\frac{dT_t^{A,M}}{d\sigma} \right)$ is significant and there are not enough dilatometric measurements in the studied stress range, an analytical function of the strain $\varepsilon(T, \sigma)$ can be determined in order to phenomenologically reproduce its experimental behaviour, for either heating or cooling processes, over the entire phase space $\varepsilon(T, \sigma)$ under study.

In our case, the mathematical expression of the analytical function is defined in order to reproduce the behaviour of the strain curves represented in Figure 3.19 (a) and (b). Several observations have to be stated in order to define a suitable analytical function.

First of all, to capture the sharp change in strain taking place at the first-order phase transition, we have used an hyperbolic tangent centred at the transition temperature. Secondly, it can be observed that the temperature range where the phase transition takes place tends to spread over larger temperature spans when increasing the applied uniaxial compressive stress, specially at the high temperature side, for both cooling (panel (a)) and heating (panel (b)) runs. This asymmetric behaviour of the strain curves suggests that more than one hyperbolic tangent is necessary in order to properly reproduce the experimental measurements. Thirdly, a linear background has to be included, with different slope at both sides of the phase transition, in order to incorporate the ε-T curves behaviour far away from the transition temperature.

Therefore, the analytical function we used is composed of two hyperbolic tangents, that may be centred at different transition temperatures $T_{t,1}$ and $T_{t,2}$, which

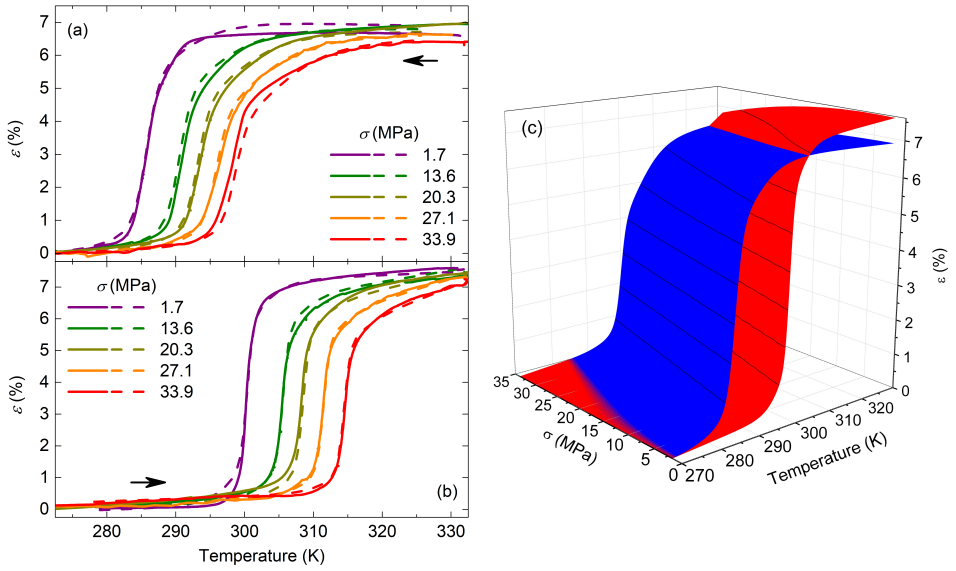

Figure 3.19: *Strain as a function of temperature at selected values of uniaxial compressive stress for cooling (a) and heating (b) runs. Solid lines refer to the corrected experimental curves obtained with the LVDT sensor and dashed lines are the corresponding analytical fits. (c) Strain as a function of temperature and the applied uniaxial compressive stress for heating (red surface) and cooling (blue surface) processes, obtained from both analytical fits.*

are superposed to a linear background with different slopes at each side of the phase transition. Equation 3.28 represents the general form of this analytical function:

$$l(T,\sigma) = \Delta l_1 \tanh(a_1(T-T_{t,1}))+\Delta l_2 \tanh(a_2(T-T_{t,2}))+b+\begin{cases} m\cdot(T-T_t) & T<T_t \\ n\cdot(T-T_t) & T\geq T_t \end{cases} \tag{3.28}$$

where $T_t = \dfrac{T_{t,1}+T_{t,2}}{2}$ and the free parameters $\{\Delta l_1, \Delta l_2, a_1, a_2, T_{t,1}, T_{t,2}, b, m, n\}$ are allowed to depend only on the applied uniaxial compressive stress (σ).

For a better approach to the experimental behaviour, where the ε-T curves show a different shape for heating and cooling runs, the fitting procedure of the analytical function is performed independently for heating and cooling processes.

For each experimental data set, consisting of either the heating or cooling strain curves measured under different stresses, an initial fit to all the single strain curves is performed without applying any constrain to the free parameters. Each independent fit provides different values for all the free parameters of the analytical function. Then, the stress dependence of each free parameter is evaluated by fitting its different values obtained from the fits as a function of stress. It is important

to point out that the free parameters are allowed to either be independent of stress, thus constant, or to show a linear dependence with the stress. The purpose of this constrain is to avoid an over fitting of the behaviour of the different free parameters, and obtain an as simple as possible analytical function able to reproduce the experimental measurements. Additionally, it must be mentioned that the free parameters are fixed individually. Once a free parameter is constrained, new fits to all the single strain curves are performed, as the values of the remaining free parameters may be affected by the previous constrains on other fixed parameters. This process is sequentially repeated until all the free parameters have been properly fixed, thus leading to an analytical function that depends on temperature and stress, and reproduces the experimental results over the phase space under study.

By following this fitting procedure, the parameters that define the analytical function to reproduce the experimental heating curves are:

$$\Delta l_1(\sigma) = -4(0.5)\cdot 10^{-4}\sigma + 0.14(2)\ (\text{mm}) \tag{3.29a}$$
$$\Delta l_2(\sigma) = -1.4(1)\cdot 10^{-3}\sigma + 0.091(3)\ (\text{mm}) \tag{3.29b}$$
$$T_{t,1}(\sigma) = T_{t,2}(\sigma) = 0.438(5)\sigma + 299.6(1)\ (\text{K}) \tag{3.29c}$$
$$a_1 = 1.15(3)\ (\text{K}^{-1}) \tag{3.29d}$$
$$a_2 = 0.21(4)\ (\text{K}^{-1}) \tag{3.29e}$$
$$b(\sigma) = -1.1(2)\cdot 10^{-3}\sigma + 0.236(4)\ (\text{mm}) \tag{3.29f}$$
$$m = 5(1)\cdot 10^{-4}\ (\text{mmK}^{-1}) \tag{3.29g}$$
$$n(\sigma) = 1.4(6)\cdot 10^{-4}\sigma + 4(2)\cdot 10^{-4}\ (\text{mmK}^{-1}) \tag{3.29h}$$

while for the experimental cooling curves, the parameters that define the analytical function are:

$$\Delta l_1(\sigma) = -1.3(8)\cdot 10^{-3}\sigma + 0.14(2)\ (\text{mm}) \tag{3.30a}$$
$$\Delta l_2(\sigma) = 3(1)\cdot 10^{-4}\sigma + 0.085(4)\ (\text{mm}) \tag{3.30b}$$
$$T_{t,1}(\sigma) = 0.40(2)\sigma + 285.1(4)\ (\text{K}) \tag{3.30c}$$
$$T_{t,2}(\sigma) = 0.47(4)\sigma + 287.5(9)\ (\text{K}) \tag{3.30d}$$
$$a_1 = 0.55(7)\ (\text{K}^{-1}) \tag{3.30e}$$
$$a_2 = 0.12(3)\ (\text{K}^{-1}) \tag{3.30f}$$
$$b(\sigma) = 6(4)\cdot 10^{-4}\sigma - 0.22(1)\ (\text{mm}) \tag{3.30g}$$
$$m = 4(1)\cdot 10^{-4}\ (\text{mmK}^{-1}) \tag{3.30h}$$
$$n(\sigma) = 3(2)\cdot 10^{-5}\sigma - 4(3)\cdot 10^{-4}\ (\text{mmK}^{-1}) \tag{3.30i}$$

The dashed lines represented in Figure 3.19 (a) and (b) correspond to the results obtained from the cooling and heating analytical functions, respectively. An excellent agreement between both experimental and simulated ε–T curves is found, thus proving that the general mathematical expression of the analytical functions

correctly captures the strain behaviour around a first-order phase transition. A tree-dimensional map of $\varepsilon(T, \sigma)$ in the complete phase space studied is represented in panel (c) of the same figure. The overlap observed between the heating (red surface) and cooling (blue surface) does not yield significant consequences on the indirect computation of the elastocaloric effect, and it is attributed to a certain background influence magnified by the application of the LVDT sensitivity factor.

As discussed in detail is section 2.2.2, it is worth mentioning that the application of uniaxial compressive stress favours the low temperature phase (the martensitic phase), in agreement with the positive transition temperature shift observed. Accordingly, the application of stress ($\Delta\sigma > 0$) will promote the forward phase transition (from austenite to martensite), while the removal of stress ($\Delta\sigma < 0$) will promote the reverse phase transition (from martensite to austenite). In light of this clear distinction, a thermodynamic process in which stress is applied can be identified with a cooling process, as both induce the forward phase transition, whereas a process in which stress is removed can be identified with a heating process, as both induce the reverse phase transition. Therefore, the caloric response of a thermodynamic process in which stress is applied ($\Delta\sigma > 0$) will be computed from the cooling analytical function (blue surface in Figure 3.19 (c)), whereas in those processes in which stress is removed ($\Delta\sigma < 0$) it will be computed from the heating analytical function (red surface in Figure 3.19 (c)).

Figure 3.20 displays the elastocaloric entropy change computed from the ε-T curves obtained from both analytical functions, as expressed in equation 3.27. Panel (a) displays the elastocaloric entropy curves $\Delta S(T, 1.7\,\mathrm{MPa} \leftrightarrow \sigma')$, for the discrete experimental values of the applied stress, where $\{\sigma'\} = \{6.8, 13.6, 20.3, 27.1, 33.9\}$ MPa. The shaded area of each curve accounts for a $\pm 10\,\%$ estimated error. As the analytical functions allow us to calculate any ε-T curve within the phase space under study, the corresponding elastocaloric entropy change for the removal ($\sigma' \rightarrow 1.7\,\mathrm{MPa}$) and application ($1.7\,\mathrm{MPa} \rightarrow \sigma'$) of stress, where $\sigma' \in [1.7, 33.9]\,\mathrm{MPa}$, are represented in panels (b) and (c) of the same figure, respectively.

The magnitude of the induced elastocaloric entropy change increases with the stress change $|\Delta\sigma|$, and the caloric effect expands towards higher temperatures, as expected from the positive shift of the transition temperature. Moreover, at high values of the applied uniaxial compressive stress, the maxima of the induced elastocaloric entropy change tends to saturate at a constant value, indicating that we are able to fully induce the phase transition with the applied stresses. For instance, the saturation value for the forward and reverse transition are $\Delta S = (-18 \pm 2)\,\mathrm{JK^{-1}kg^{-1}}$ and $\Delta S = (19 \pm 2)\,\mathrm{JK^{-1}kg^{-1}}$, respectively.

Additionally, when comparing panels (b) and (c) of Figure 3.20, it can be easily seen that the temperature span associated with the reverse ($\Delta\sigma < 0$) transition is narrower in comparison to the forward ($\Delta\sigma > 0$) transition. For a certain stress change $|\Delta\sigma|$, the sharpness of the field-driven reverse transition gives rise to an en-

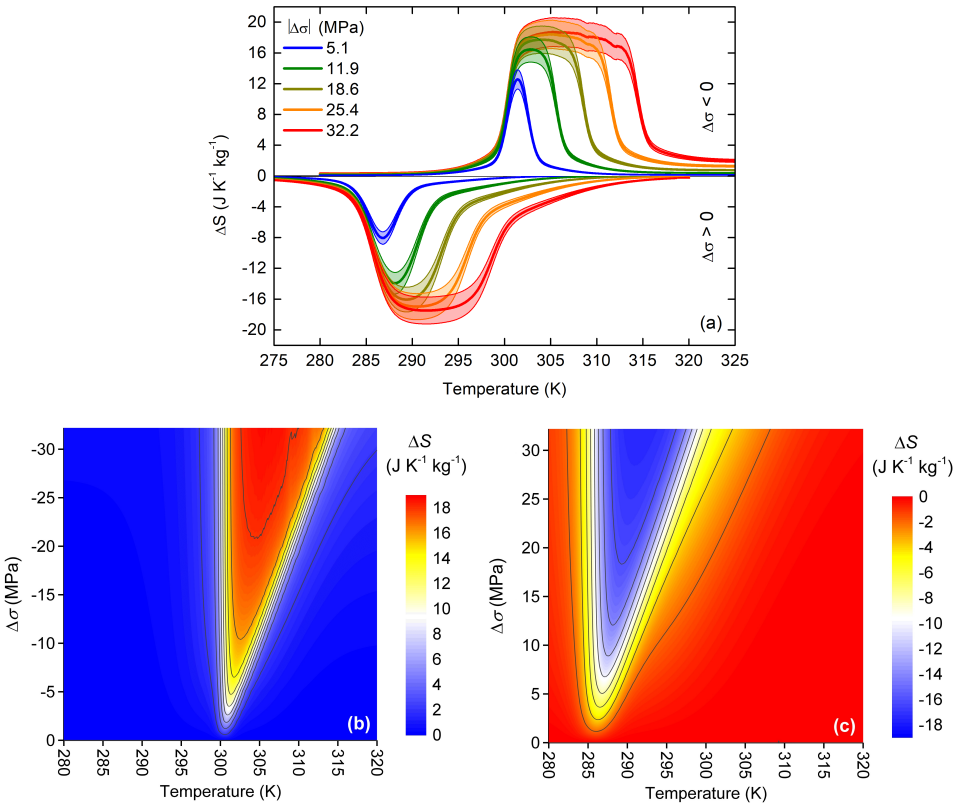

Figure 3.20: *(a) Indirect estimates of the elastocaloric entropy change computed for the selected values of the stress change $\Delta S(\sigma' \rightarrow 1.7\,MPa)$ (positive values) and $\Delta S(1.7\,MPa \rightarrow \sigma')$ (negative values) obtained from the set of ε-T analytical fits for heating and cooling processes, respectively. Coloured shaded regions indicate an estimated error of $\pm 10\,\%$. Panels (b) and (c) display contour colour maps of ΔS values as a function of temperature and the continuous spectra of field changes $\Delta\sigma = \sigma' \rightarrow 1.7\,MPa < 0$ and $\Delta\sigma = 1.7\,MPa \rightarrow \sigma' > 0$, respectively.*

largement of the elastocaloric effect when compared to the forward transition, as indicated by the closer level lines in panel (b). Consequently, the saturation of the thermal response is achieved for lower values of the applied compression for the reverse transition.

3.3.4 Quasidirect derivation of the elastocaloric effect

The raw DSC thermograms measured at selected values of applied uniaxial compressive stress are shown in Figure 3.21 for heating (a) and cooling (b) runs, respectively.

The latent heat associated with the martensitic transition gives rise to an exother-

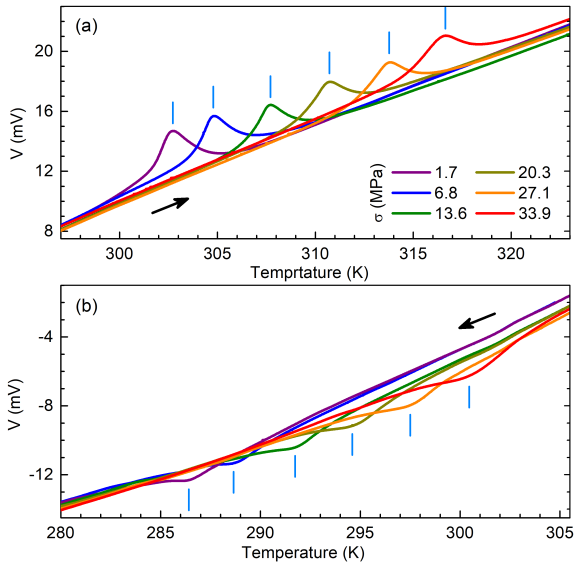

Figure 3.21: *Calorimetric signal as a function of temperature at selected values of uniaxial compressive stress. Panel (a) corresponds to heating runs and panel (b) to cooling runs, respectively. Vertical blue lines indicate the position of the calorimetric peak.*

mal (negative) peak when inducing the forward transition (cooling) and to an endothermal (positive) peak when inducing the reverse transition (heating). In accordance with the strain measurements, an increase of the applied uniaxial compressive stress shifts the calorimetric peaks to higher temperatures, which is in agreement with a further stabilization of the martensitic phase upon compression.

As discussed in section 3.1.1, the measured thermograms at selected values of uniaxial compressive stress must be properly corrected in order to compute the transition entropy change associated with the induced first-order martensitic transition, which can be expressed as:

$$\Delta S_t(\sigma) = \int_{T_s}^{T_f} \frac{1}{T'} \left(\frac{dQ(T',\sigma)}{dT'} - \zeta(T',\sigma) \right) dT' \tag{3.31}$$

where T_s and T_f are the start and finish integration temperatures, taken before and after the phase transition calorimetric peak, $\zeta(T,\sigma)$ corresponds to the baseline signal and $\frac{dQ(T,\sigma)}{dT} = \frac{\dot{Q}(T,\sigma)}{\dot{T}} = \frac{Y(T,\sigma)dt}{S(T)dT}$, to the calorimetric signal where $Y(T,\sigma)$ corresponds to the raw calorimetric signal and $S(T)$ corresponds to the DSC sensitivity.

To analyse calorimetric curves, a custom Python program has been developed (see Appendix A for a detailed discussion), and the obtained corrected thermograms after baseline subtraction are presented in Figure 3.22 (a). It is significant to point

out that the shape of the heating and cooling calorimetric peaks is clearly different. The reverse transition is sharp and spreads over 5 K while the forward transition is broader and spreads over 15 K. Additionally, a decrease of the height of the calorimetric peaks recorded upon heating is observed when increasing the applied uniaxial compressive stress, whereas the shape of the calorimetric peaks recorded upon cooling is not significantly affected by stress.

The corresponding transition entropy changes ($\Delta S_t(\sigma)$) are computed using equation 3.31, and the results are displayed in Figure 3.22 (b). Different smoothing processes (see Appendix A) are applied to the analysis of each thermogram. This leads to small differences in the determination of the baseline, and provides a good estimation of the error in determining the transition entropy change. For Cu-Zn-Al, we have obtained an estimated error of $\pm 1\,\mathrm{JK^{-1}kg^{-1}}$.

The computed transition entropy change decreases when increasing the applied uniaxial compressive stress for both heating and cooling runs. At the lowest compressive stress, corresponding to an applied force of 50 N, the transition entropy change is found to be $\Delta S_t^{M,A}(1.7\,\mathrm{MPa}) = (20 \pm 1)\,\mathrm{JK^{-1}kg^{-1}}$ for both forward and reverse martensitic transitions, respectively.

To validate the transition entropy change measured with our bespoke DSC at low compressive stresses, a high sensitivity DSC was used to measure the same sample without any applied uniaxial compressive stress. The corresponding corrected thermograms, together with the computed transition entropy change, for both heating and cooling runs are displayed at panels (a) and (b) of Figure 3.22 as grey lines and solid grey triangles, respectively. The associated transition entropy change for the forward and reverse martensitic transition are found to be $\Delta S_t^M(0\,\mathrm{MPa}) = (-22.1 \pm 0.5)\,\mathrm{JK^{-1}kg^{-1}}$ and $\Delta S_t^A(0\,\mathrm{MPa}) = (22.4 \pm 0.5)\,\mathrm{JK^{-1}kg^{-1}}$.

When comparing the results obtained for both setups, we notice that there is approximately a 10 % difference on the measured transition entropy change at low stresses. In order to shed light on this issue, these values can be compared with the transition entropy change deduced from the application of the Clausius-Clapeyron equation on the dilatometric measurements performed with the dynamic extensometer. For this purpose, taking into account Table 2.1 and equation 2.28, the Clausius-Clapeyron equation for the elastocaloric effect can be expressed as:

$$\frac{d\sigma}{dT_t} = -\frac{\Delta S_t}{v_0 \Delta \varepsilon_t} \tag{3.32}$$

where v_0 corresponds to the specific volume of the sample.

Therefore, from the transition strain ($\Delta\varepsilon_t$) and the average transition temperature shift $\left(\frac{dT_t}{d\sigma}\right)$ obtained from the ε-T curves, we obtain a transition entropy change of $|\Delta S_t| \sim 22\,\mathrm{JK^{-1}kg^{-1}}$, which is in excellent agreement with the transition entropy changes obtained from the high sensitivity DSC thermograms.

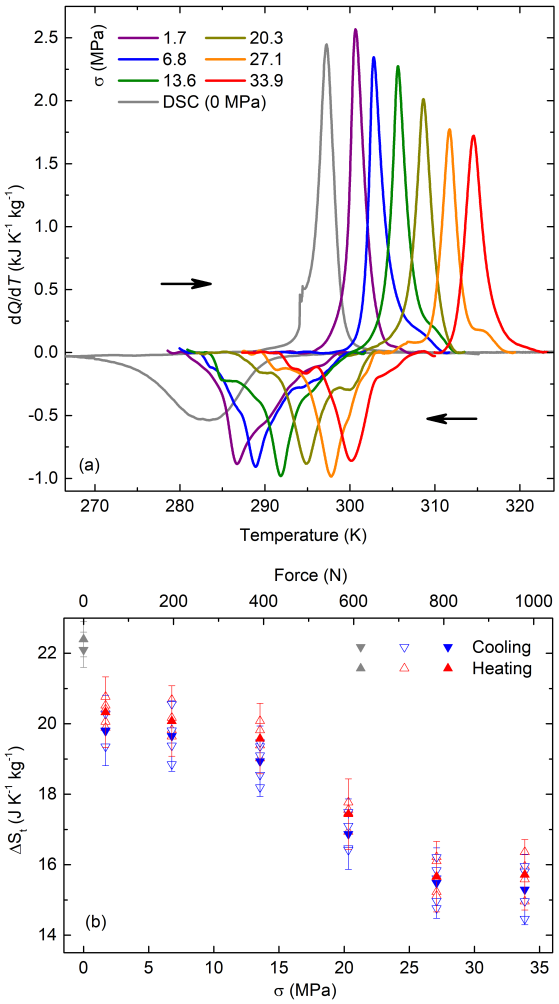

Figure 3.22: *(a) Calorimetric curves at selected values of uniaxial compressive stress as a function of temperature recorded upon heating (positive peaks) and cooling (negative peaks) after baseline subtraction. (b) Transition entropy change as a function of uniaxial compressive stress (bottom axis) and the applied force (top axis) for both heating (top triangles) and cooling (bottom triangles) runs. For both data sets, open symbols correspond to different background subtractions of the thermograms and solid symbols correspond to the averaged transition entropy change. The grey calorimetric curves, and the corresponding transition entropy change values, were measured without any applied uniaxial compressive stress by means of a high sensitivity bespoke DSC.*

It is not straightforward to identify the origin of the lower transition entropy change computed from our bespoke DSC setup at low applied compressive stresses when compared to more accurate measurements performed in the absence of compressive stress. Even so, two considerations must be taken into account in order to gain some insight into this issue.

First of all, it is significant to point out that the martensite structure of the sample will depend on the applied stress. For instance, as it will be discussed in section 4.2.1, in the absence of applied stress a multivariant martensite is formed whereas application of stress favours the growth of a specific martensite variant, and under high stresses even a single variant martensite is formed. Previous tensile experiments on a composition related Cu-Zn-Al shape-memory alloy reported an enhancement of the transition entropy change when a multivariant martensite is induced compared to the transition entropy change deduced from stress-strain curves, where a single variant martensite was formed. The enhancement on the transition entropy change was attributed to kinetic constraints occurring during the phase transition that favour extra dissipative effects [30]. However, it must also be considered that the applied compressive stress is much smaller in our case and even if a particular variant is favoured, a single variant martensite is not expected for these stress levels.

Secondly, the specific design of our bespoke calorimeter (see section 3.1.4) may also contribute to this difference. As it can be seen from its design, the studied sample is not directly in contact with the corresponding thermoelectric sensor, as a 3 mm thickness high-strength aluminium disk sits between both (see Figure 3.10). Therefore, when performing the calibration measurements, where a known amount of energy is dissipated on top of the disk and the sensitivity as a function of temperature is determined, a certain part of this energy will be dissipated to the surroundings and consequently, it will not be detected by the thermoelectric sensor. This possible energy loss mechanism is already captured by the sensitivity of the calorimeter, and thus it is properly considered when measuring a real sample.

Nevertheless, the fact that a certain deviation between both measured transition entropy changes on the same specimen is observed suggests that a certain energy loss mechanism is enhanced with respect to the calibration measurements, and thus it is not correctly captured by the sensitivity. In fact, this deviation can be attributed to a bigger part of the energy exchanged by the sample when undergoing the martensitic phase transition that is being dissipated to the surroundings, and thus it is not being detected by the corresponding thermoelectric sensor.

The origin of this possible enhancement of the energy loss mechanism when measuring this alloy can not be clearly identified. Still, it is reasonable to partially attribute its origin to the particular shape of the specimen. Specifically, to the fact that this sample is significantly higher than the calibration copper block. Therefore, when performing a measurement the signal detected by the thermoelectric sensor may be influenced by the part of the sample that is transforming at a specific time. If a fragment that is far away from the thermoelectric sensor is undergoing the phase transition, a bigger part of its exchanged energy can be dissipated to the surroundings when compared to another sample fragment that sits closer to the high-strength aluminium disk.

A this point, it is useful to compare the behaviour observed from the ε–T curves presented in Figure 3.19 (a) with the corrected thermograms of Figure 3.22 (a).

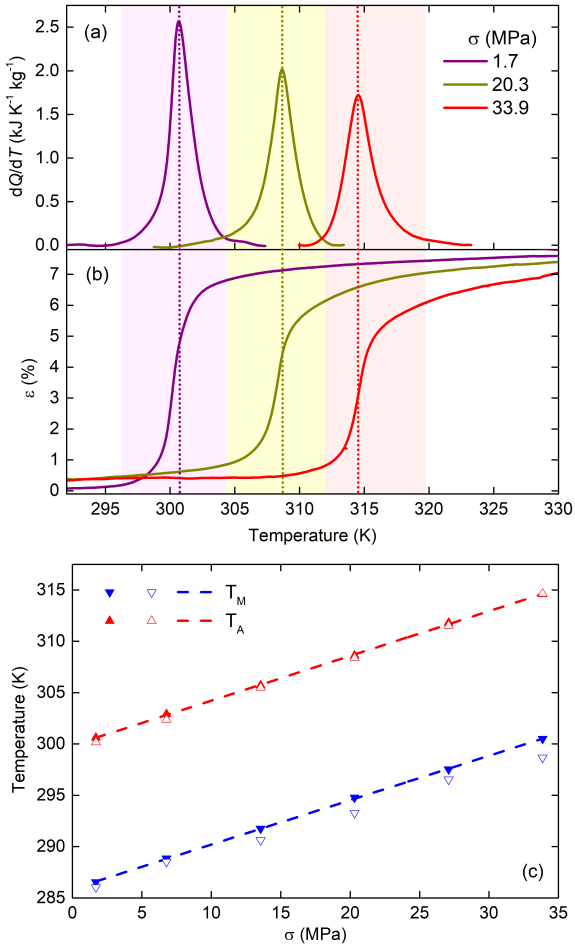

Figure 3.23: *Calorimetric curves after baseline subtraction (a) and the corresponding corrected strain measured with the LVDT sensor (b) as a function of temperature recorded upon heating at selected values of uniaxial compressive stress. (c) Transition temperatures of the forward (T_M) and reverse (T_A) transitions as a function of the applied stress. Solid symbols correspond to the transition temperatures obtained from the calorimetric peaks and open symbols to the values obtained from the LVDT curves, represented in Figure 3.18 (e).*

Both data sets are plotted together in Figure 3.23 (a) for heating runs at selected values of applied uniaxial compressive stress. As illustrated by the shaded areas and the corresponding vertical lines centred at the calorimetric peaks, both simultaneous measurements reveal the occurrence of the transition strain change and the heat exchange associated with the transition latent heat centred at the same temperature range, as a consequence of the fact that both phenomena arise from the structural first-order phase transition. Additionally, both data sets also show an agreement on the temperature span where the transition occurs, which is broader for cooling runs than for heating runs.

The transition temperatures of the forward (T_t^M) and reverse (T_t^A) transitions can be identified with the peak position of both heating and cooling corrected thermograms, respectively. Figure 3.23 (b) illustrates the behaviour of the transition temperature as a function of the applied uniaxial compressive stress, where solid symbols correspond to the transition temperatures obtained from the thermograms, whereas open symbols correspond to the transition temperatures obtained from the ε-T curves.

Both data sets show a good agreement for both forward and reverse transitions, exhibiting a thermal hysteresis of $T_t^M - T_t^A = 14\,\mathrm{K}$ which remains approximately constant with applied compressive stress. From the calorimetric peak transition temperatures, the first-order phase transition shifts to higher temperatures under the application of higher stresses at rates $\frac{dT_t^M}{d\sigma} = (0.43 \pm 0.02)\,\mathrm{KMPa}^{-1}$ and $\frac{dT_t^A}{d\sigma} = (0.44 \pm 0.02)\,\mathrm{KMPa}^{-1}$, which are in good agreement with the results obtained from the ε-T curves and previous reported values for composition-related Cu-Zn-Al shape-memory alloys [30, 111].

As discussed in section 3.1.1.2, the quasidirect determination of the elastocaloric effect relies on the construction of the corresponding accurate entropy curves. On account of the small deviation observed between the transition entropy change measured with our bespoke DSC setup and the accurate measurements performed with the high sensitivity DSC, a constant calibration factor has been introduced:

$$\gamma^{A,M} = \frac{\Delta S_t^{A,M}(0\,\mathrm{MPa})}{\Delta S_t(1.7\,\mathrm{MPa})} \tag{3.33}$$

and the transition entropy changes will be computed as $\Delta S_t^{cal}(\sigma) = \gamma^{A,M}\Delta S_t(\sigma)$. For the forward transition, the calibration factor is found to be $\gamma^M = 1.12$ while for the reverse transition it is $\gamma^A = 1.1$. The transition entropy changes represented in Figure 3.22 (b) are rescaled according to these factors, and the calibrated results are represented in Figure 3.24 (a) together with two horizontal lines corresponding to the transition entropy change values determined with the high sensitivity DSC for the forward (blue dashed line) and reverse (red dashed line) martensitic transition.

After the application of these calibration factors, it is significant to stress that for applied forces up to $F = 200\,\mathrm{N}$ there is no significant decrease on the measured transition entropy change. When the applied force increases to $F = 400\,\mathrm{N}$, a small decrease on the transition entropy change can be observed, but still the deviation is small and falls within the experimental error for both forward and reverse transitions. On the other hand, for higher applied compressive stresses, a significant decrease is observed.

This behaviour under high applied stresses is not consistent with the transition strain observed from the ε-T curves measured with the dynamic extensometer (see Figure 3.18 (c) and (d)). From these curves, where a constant transition strain was found for all the measurements, the application of the Clausius-Clapeyron

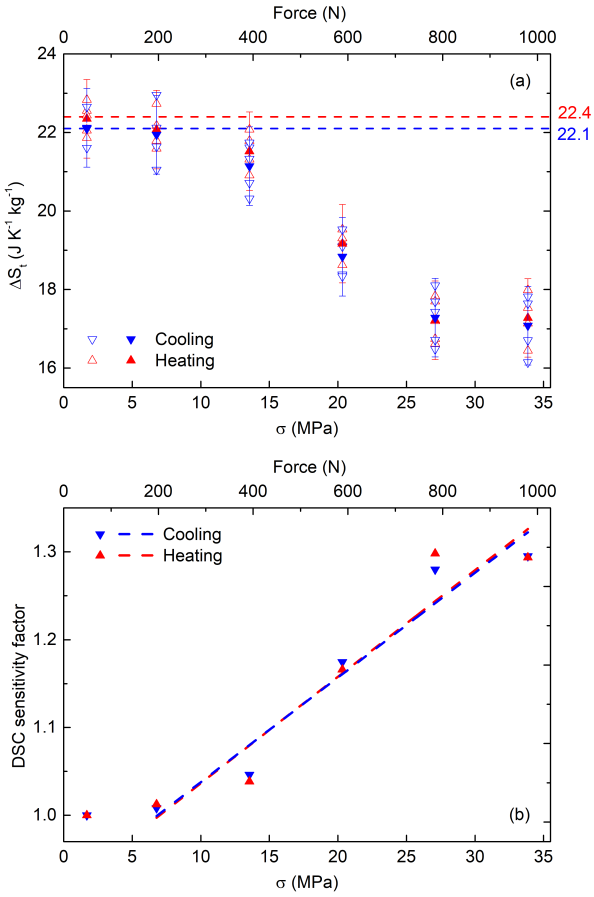

Figure 3.24: *(a) Calibrated transition entropy change as a function of uniaxial compressive stress (bottom axis) and the applied force (top axis) for both heating (red) and cooling (blue) runs. For both data sets, open symbols correspond to different background subtractions of the thermograms and solid symbols correspond to the averaged transition entropy change. Red and blue dashed lines represent the transition entropy change measured in the absence of applied uniaxial compressive stress with the high sensitivity DSC for both heating and cooling runs, respectively. (b) DSC sensitivity factor as a function of stress for both heating (red) and cooling (blue) runs. Dashed lines correspond to linear fits to the solid symbols.*

equation leads to a constant transition entropy change as a function of the applied uniaxial compressive stress. In the same line, previous tensile experiments on a composition-related Cu-Zn-Al shape-memory alloy already reported that the total transition entropy change is independent of the applied stress [30]. Moreover, a good agreement was also observed between the transition entropy change measured from calorimetric runs in the absence of stress and the value determined from strain-stress measurements for a Cu-Zn-Al single crystal [112].

The origin of the transition entropy change decrease at high applied uniaxial compressive stresses has not been systematically studied with different reference samples. Still, it is reasonable to partially attribute its origin to a change on the thermal contact between the sample and its corresponding thermoelectric sensor. When a significant dead load is placed on top of the free mobile platform to apply a high compressive force on the studied sample (see Figure 3.10), the different system components may experience a certain elastic deformation or bending. In particular, the high-strength aluminium disk and its PEEK holder will hold all the applied force in order to protect the thermoelectric sensor, and any deformation of these components may affect the thermal contact between the sample and its sensor, thus affecting the sensitivity of the calorimeter. These measurements at high applied compressive stress can be corrected by introducing a DSC sensitivity factor, which is defined as:

$$X_{DSC} = \frac{\Delta S_t(0\,\mathrm{MPa})}{\Delta S_t(\sigma)} \tag{3.34}$$

where $\Delta S_t(0\,\mathrm{MPa})$ corresponds to the transition entropy change measured with the high sensitivity DSC and $\Delta S_t(\sigma)$ to the averaged transition entropy change computed from the measurements performed with our bespoke DSC. Figure 3.24 (b) illustrates the sensitivity factor obtained, and the corresponding transition entropy changes under applied forces $F \geq 400\,\mathrm{N}$ are rescaled according to the linear fits on the DSC sensitivity factor.

At this point, the corresponding entropy curves can be constructed. As discussed in section 3.1.1.2, from the integration of the corrected thermograms, which provide both the transformed fraction curves ($\chi(T,\sigma)$) and the corresponding transition entropy changes ($\Delta S_t(\sigma)$), and the reported specific heat data of the martensite $C_M(T)$ and austenite $C_A(T)$ phases obtained from [113], yields the construction of the entropy curves referenced to a certain temperature well below the martensitic transition [114]:

$$S(T,\sigma) - S_{ref} = \int_{T_{ref}}^{T} \frac{1}{T'} \left(C(T',\sigma) + \frac{dQ(T',\sigma)}{dT'} \right) dT' \tag{3.35}$$

where $S_{ref} = S(T = 270\,\mathrm{K})$ and the specific heat of the sample $C(T',\sigma)$ can be expressed as $C = (1-\chi)C_M + \chi C_A$, where χ corresponds to the transformed fraction ($\chi = 1$ when the sample is completely in the austenitic phase). Figure 3.25 displays the computed entropy curves at selected values of applied uniaxial compressive stress. It is significant to point out that the computation of these curves has assumed that the specific heat of both the martensite and austenite phases does not exhibit any stress dependency.

Additionally, it is worth noting that the heating and cooling entropy curves have distinct shapes around the phase transition region, where the former exhibit a sharper transition than the latter. This difference is in accordance with the different shape of heating and cooling calorimetric peaks, where the former are sharper and spread over a narrower temperature span than the latter, which leads to a similar

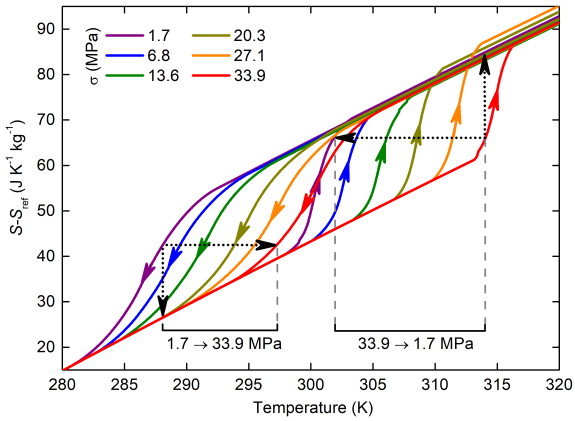

Figure 3.25: *Entropy curves referenced to $S_{ref} = S(T = 270\,K)$ at selected values of applied uniaxial compressive stresses for heating and cooling runs. Dotted black arrows illustrate the resulting adiabatic temperature change ΔT (horizontal arrows) and the isothermal entropy change ΔS (vertical arrows) for the removal ($33.9\,MPa \rightarrow 1.7\,MPa$) and application ($1.7\,MPa \rightarrow 33.9\,MPa$) of stress.*

behaviour on the computed transformed fraction curves and significantly affecting the corresponding entropy curves.

Reverting to section 3.1.1.2, the corresponding isothermal elastocaloric entropy changes are computed by subtracting the entropy curves at the start and finish external field values:

$$\Delta S(T, \sigma_s \rightarrow \sigma_f) = S(T, \sigma_f) - S(T, \sigma_s) \tag{3.36}$$

As for the indirect computation of the elastocaloric effect, presented in the previous section, a process in which stress is applied is associated with the cooling entropy curves (as both promote the forward phase transition) and its isothermal entropy change is computed as $\Delta S(T, 1.7\,\text{MPa} \rightarrow \sigma')$, whereas a process in which stress is removed is associated with the heating entropy curves (as both promote the reverse phase transition) and its isothermal entropy change is computed as $\Delta S(T, \sigma' \rightarrow 1.7\,\text{MPa})$. These two processes are illustrated as vertical dotted arrows in Figure 3.25, and the corresponding results are presented in Figure 3.26 (a) as a function of temperature.

Conversely, adiabatic temperature changes are computed after inverting the corresponding entropy curves:

$$\Delta T(S, \sigma_s \rightarrow \sigma_f) = T(S, \sigma_f) - T(S, \sigma_s) \tag{3.37}$$

As for the elastocaloric entropy changes, from the cooling entropy curves the adiabatic temperature change is computed as $\Delta T(S, 1.7\,\text{MPa} \rightarrow \sigma')$, whereas from the heating entropy curves it is computed as $\Delta T(S, \sigma' \rightarrow 1.7\,\text{MPa})$. These two processes are illustrated as horizontal dotted arrows in Figure 3.25. Application of

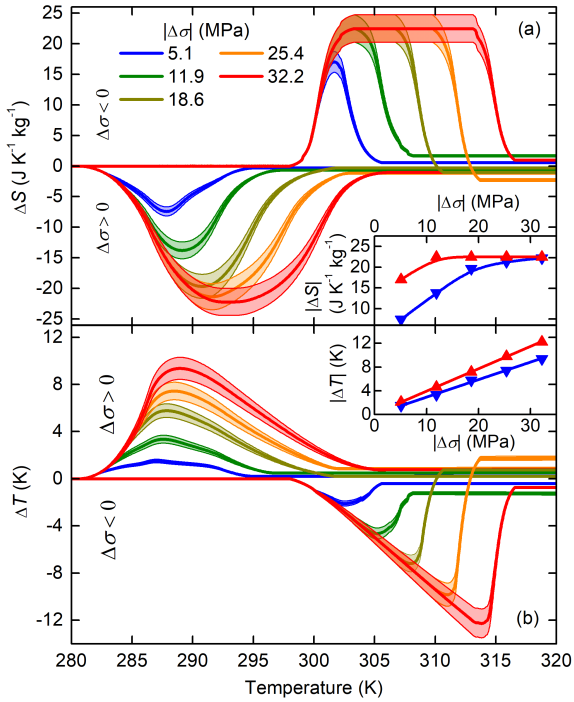

Figure 3.26: *(a) Quasidirect estimates of the isothermal entropy change for selected values of the stress change $\Delta S(T, \sigma' \rightarrow 1.7\,MPa)$ (positive values) and $\Delta S(T, 1.7\,MPa \rightarrow \sigma')$ (negative values) obtained from the heating and cooling entropy curves, respectively. (b) Quasidirect estimates of the adiabatic temperature change corresponding to selected processes of application ($\Delta\sigma > 0$) (negative values) and removal ($\Delta\sigma < 0$) (positive values) of uniaxial compressive stress. Coloured shaded regions indicate an estimated error of $\pm 10\,\%$. Inserts in both panels display the maxima of the field-driven $|\Delta S|$ and $|\Delta T|$ values as a function of the applied uniaxial compressive stress. Blue down triangles correspond to $1.7\,MPa \rightarrow \sigma'$ processes and red up triangles to $\sigma' \rightarrow 1.7\,MPa$.*

equation 3.37 provides the adiabatic temperature change as a function of entropy, but it is customary to represent it as a function of the temperature of the initial state at which the stress is adiabatically applied or removed. The corresponding results are presented in Figure 3.26 (b) as a function of temperature.

Additionally, the maxima of the stress-driven $|\Delta S|$ and $|\Delta T|$ are shown in the inserts of panels (a) and (b), respectively, in Figure 3.26 as a function of the stress change $|\Delta\sigma|$ for both application (blue symbols) and removal (red symbols) of stress.

As it can be seen from the quasidirect estimates of both the elastocaloric entropy and temperature changes, the magnitude of the caloric response increases with the stress change $|\Delta\sigma|$, and expands towards higher temperatures, in accordance

with the positive shift of the transition temperature with stress. When considering the elastocaloric entropy change, represented in Figure 3.26 (a), the field-induced entropy change tends to saturate at a constant value, indicating that we are able to fully transform the sample. For instance, the saturation value for the forward and reverse transition is $|\Delta S| = (22 \pm 2)\,\mathrm{JK^{-1}kg^{-1}}$. Conversely, when looking at the behaviour of the elastocaloric temperature change, represented in Figure 3.26 (b), we observe that it linearly increases with the stress change.

In this case, the maximum field-induced value for the forward and reverse transitions are $|\Delta T(1.7\,\mathrm{MPa} \rightarrow 33.9\,\mathrm{MPa})| = (9.4 \pm 1)\,\mathrm{K}$ and $|\Delta T(33.9\,\mathrm{MPa} \rightarrow 1.7\,\mathrm{MPa})| = (12.3 \pm 1)\,\mathrm{K}$, respectively. The associated elastocaloric strengths can be determined from the linear fits fitted to the maxima of the stress-driven $|\Delta T|$ represented in the insert of panel (b) and they are found to be $\frac{|\Delta T|}{|\Delta \sigma|} = (0.29 \pm 0.01)\,\mathrm{KMPa^{-1}}$ and $\frac{|\Delta T|}{|\Delta \sigma|} = (0.38 \pm 0.01)\,\mathrm{KMPa^{-1}}$ for the forward and reverse transitions, respectively.

The differences between the forward and reverse stress-driven maxima thermal response as a function of the stress change represented in both inserts emphasises the effect of the distinct shape of the cooling and heating entropy curves. In this regard, the sharpness of the heating entropy curves is responsible of an enlargement of the elastocaloric strength when field inducing the reverse phase transition ($\sigma' \rightarrow 1.7\,\mathrm{MPa}$), bringing its thermal response to saturation for lower values of the stress change. Specifically, when looking at the maxima of the stress-driven entropy change, it can be seen that a stress change of $|\Delta\sigma| = 25.4\,\mathrm{MPa}$ is necessary to reach the saturation value for the forward transition, whereas a stress change of just $|\Delta\sigma| = 11.9\,\mathrm{MPa}$ is required for the reverse transition.

The maxima of the stress-driven adiabatic temperature change will also reach a saturation value, despite not being observed in the insert of panel (b). According to the transition entropy change determined for this Cu-Zn-Al alloy, the maximum expected adiabatic temperature change is given by $|\Delta T| = \frac{T|\Delta S|}{C} \sim 15\,\mathrm{K}$, which is close to recent direct ΔT measurements on a Cu-Zn-Al single crystal [115]. Thus, according to the determined elastocaloric strengths, the saturation value would be achieved by a stress change of $|\Delta\sigma| = 51\,\mathrm{MPa}$ for the forward transition, whereas a stress change of $|\Delta\sigma| = 40\,\mathrm{MPa}$ would be necessary for the reverse transition.

Moreover, the quasidirect estimates of both the stress-induced isothermal entropy and adiabatic temperature changes allow us to compute the associated refrigerant capacity (RC) of this alloy. This quantity provides an estimate of the transferred heat from the cold end (T_{cold}) to the hot end (T_{hot}) of a refrigerator during a thermodynamic cycle [116] and it is usually estimated as $RC = \Delta S_{MAX} \Delta T_{FWHM}$, where ΔS_{MAX} corresponds to the maxima of the elastocaloric entropy change and ΔT_{FWHM} to its temperature span, computed as the full width at half maximum of the corresponding isothermal entropy change curves [34].

In this regard, the temperature span of the elastocaloric entropy change curves represented in Figure 3.26 (a), computed as ΔT_{FWHM}, increases proportionally to the martensitic phase transition temperature shift with the applied compressive stress $\left(\frac{dT_t^{A,M}}{d\sigma}\right)$ and the stress change, and it can be expressed as $\Delta T_{FWHM} = \frac{dT_t^{A,M}}{d\sigma}\Delta\sigma$. For instance, the full width at half maximum for the stress-induced elastocaloric entropy change goes up to $\Delta T_{FWHM}(33.9\,\mathrm{MPa} \rightarrow 1.7\,\mathrm{MPa}) = 14.5\,\mathrm{K}$ for the reverse transition. Therefore, taking into account that the elastocaloric entropy change saturates at a constant value ($|\Delta S| = (22 \pm 2)\,\mathrm{JK^{-1}kg^{-1}}$) and considering the previous expression for ΔT_{FWHM}, the refrigerant capacity will also scale linearly with the stress change and the transition temperature shift with applied stress up to a maximum refrigerant capacity of $RC(33.9\,\mathrm{MPa} \rightarrow 1.7\,\mathrm{MPa}) = (330 \pm 30)\,\mathrm{Jkg^{-1}}$ for the reverse transition, in agreement with previously reported results [109, 111]. The strong sensitivity of the transition temperature with the applied compressive stress enhances ΔT_{FWHM} and allows this alloy to exhibit a large refrigerant capacity. In fact, it is predicted to increase linearly for larger values of stress change and overcome the values for the best magnetocaloric materials, summarized in [117], for $|\Delta\sigma| > 50\,\mathrm{MPa}$.

It is important to point out that the stress-induced thermal response can significantly differ upon field cycling, as the irreversible processes associated with the thermal hysteresis of the alloy contribute as an additional energy cost for cyclically driving the phase transition. Therefore, a significant drop on the field-induced thermal response may take place after the first application or removal of the compressive stress if the values of the driving field are not large enough.

For the particular case under study, the sample exhibits a thermal hysteresis of $T_t^M - T_t^A = 14\,\mathrm{K}$ which remains approximately constant within the applied compressive stress range. Taking into account the transition temperature shift with the applied stress, it is possible to compute the stress needed in order to overcome the thermal hysteresis, and it can be estimated as $(T_t^M - T_t^A)\frac{d\sigma}{dT_t^{A,M}} \sim 32\,\mathrm{MPa}$. This estimation of the effective hysteresis on stress is in accordance with the entropy curves represented in Figure 3.25, where the heating and cooling entropy curves measured under applied uniaxial stresses of 1.7 MPa and 33.9 MPa, respectively, are overlapped.

In this regard, the stress-induced thermal response of this alloy will persist upon cyclic loading and unloading operation for values of the stress change $|\Delta\sigma| > 32\,\mathrm{MPa}$, where the driving field will be large enough to overcome the effective hysteresis and the forward and reverse transitions will be at least partially driven during the successive cycles. Consequently, by taking into account that a stress change of $|\Delta\sigma| > 25.4\,\mathrm{MPa}$ is necessary in order to reach the isothermal entropy change saturation value, indicating that we are fully inducing the phase transition, it is predicted that a stress change of $|\Delta\sigma| > 57\,\mathrm{MPa}$ will be needed in order to cyclically induce the complete phase transition on this alloy.

3.3.5 Comparison between the indirect and quasidirect derivations of the elastocaloric effect

When comparing both indirect and quasidirect computations of the elastocaloric effect associated with the martensitic transition exhibited by the Cu-Zn-Al alloy under study, respectively illustrated in Figures 3.20 and 3.26, we observe that they provide a set of concordant results.

Nevertheless, it is important to stress that elastocaloric entropy changes computed in each case show slightly different saturation values. The major contribution to the exchanged heat, which gives rise to the entropy change, is the latent heat associated with the first-order martensitic transition. Therefore, the elastocaloric entropy change saturation value is expected to coincide with the transition entropy change, which was determined to be $|\Delta S_t| = (22 \pm 1)\mathrm{JK}^{-1}\mathrm{kg}^{-1}$ from the corrected thermograms.

While this is the case for the quasidirect saturation value, which is in agreement with previously reported indirect data at larger stresses [109], the indirect saturation value falls a little bit short. This difference is attributed to the minor accuracy of the corrected strain measurements, which might lead to an underestimation of the transition strain change. In particular, it is important to highlight that the dilatometric sensor is placed far away from the sample. Hence, its output data is expected to carry a larger error. Additionally, the use of an INCONEL sample to exclude the background signal from the raw dilatometric measurements may have introduced a further deviation on the corrected strain curves, as it may have not completely removed the background signal from some measurements, thus hindering the determination of the transition strain change.

3.3.6 Summary and conclusions

We have studied the giant elastocaloric effect in a Cu-Zn-Al shape-memory alloy, which was used as a calibration sample for our novel experimental setup that provides simultaneous DSC and dilatometric data. Both measurements report a martensitic phase transition, occurring around room temperature, that is highly sensitive to the applied compressive stress on account of the large transition strain. The output data allows the indirect estimate of the elastocaloric effect together with a unique quasidirect approach of the stress-induced thermal response.

On the one hand, the dilatometric data allows us to construct the ε-T curves. These measurements showed a decrease of the transition strain when increasing the applied compressive stress, while more accurate dilatometric measurements found a constant transition strain of $\Delta\varepsilon_t^{M,A} = (7.0 \pm 0.3)\,\%$. Even though both measurement sets were concordant at low compressive stresses, a sensitivity factor for the LVDT sensor had to be introduced in order to correct the dilatometric measurements performed with our bespoke setup. The indirect computation of the elastocaloric effect relies on the use of the Maxwell relations on the ε-T curves obtained

from two analytical functions that fit the experimental behaviour of the measured strain curves. These analytical functions allow us to compute the elastocaloric effect over the continuous (T, σ) phase space. The isothermal stress-driven entropy changes saturate at $\Delta S = (-18 \pm 2)\,\mathrm{JK^{-1}kg^{-1}}$ and $\Delta S = (19 \pm 2)\,\mathrm{JK^{-1}kg^{-1}}$ for the forward and reverse transitions, respectively.

On the other hand, the DSC measurements allow us to determine the transition entropy change of the martensitic phase transition. At low compressive stresses, the ΔS_t obtained with our bespoke setup was found to be a little bit smaller when compared to more accurate DSC measurements from which a value of $\Delta S_t^M(0\,\mathrm{MPa}) = (22.1 \pm 0.5)\,\mathrm{JK^{-1}kg^{-1}}$ and $\Delta S_t^A(0\,\mathrm{MPa}) = (22.4 \pm 0.5)\,\mathrm{JK^{-1}kg^{-1}}$ was found for the forward and reverse transitions, respectively. This difference suggested that a constant calibration factor had to be introduced in order to analyse the thermograms measured with our bespoke setup, and a similar calibration factor will have to be determined and introduced for further experiments performed with this unique setup.

Additionally, the transition entropy change determined from the measured thermograms decreases when increasing the applied compressive stress, while a constant behaviour can be anticipated from the application of the Clausius-Clapeyron relation on the ε-T curves determined from the accurate dilatometric measurements. Even though the deviation is small and falls within the experimental error for applied compressive forces up to $F = 400\,\mathrm{N}$, a sensitivity factor for the DSC measurements had to be introduced in order to correct the decrease observed for higher stresses. The quasidirect derivation of the elastocaloric effect relies on the computation of the entropy curves at selected applied uniaxial compressive stresses, which are constructed from the corrected thermograms and the specific heat of the studied alloy.

While the isothermal stress-driven entropy changes saturate at $|\Delta S_t| = (22 \pm 1)\mathrm{JK^{-1}kg^{-1}}$ for a stress change of $|\Delta\sigma| > 25.4\,\mathrm{MPa}$, the stress-driven adiabatic temperature changes increase linearly with the applied stress and are expected to saturate at $|\Delta T| \sim 15\,\mathrm{K}$ for a stress change of $|\Delta\sigma| > 51\,\mathrm{MPa}$. The material exhibits a giant elastocaloric effect within a broad temperature window together with high refrigerant capacity (RC) values, which are predicted to be comparable with the values for the best magnetocaloric materials for stress changes of $|\Delta\sigma| > 50\,\mathrm{MPa}$. The potential use of the Cu-Zn-Al alloy under study for refrigeration applications would require large and reversible values of the elastocaloric thermal response under field cycling. In our Cu–Zn–Al alloy, an additional stress change of $|\Delta\sigma| = 32\,\mathrm{MPa}$ is needed in order to overcome the effective hysteresis and yield reversible values of the stress-driven thermal response. To cyclically field-induce the complete martensitic phase transition, it has been predicted that a stress change of $|\Delta\sigma| > 57\,\mathrm{MPa}$ is necessary.

When comparing both indirect and quasidirect estimates of the thermal response of this alloy, they provide concordant results. Nevertheless, the dilatometric measurements carry a minor accuracy and the computed indirect elastocaloric effect

is slightly underestimated. Therefore, for further experiments performed with this setup the dilatometric data will be taken as complementary to the DSC measurements but they will not be analysed in detail.

Overall, it has been shown that the development and implementation of calorimetric techniques that allow the application of uniaxial compressive stresses can yield an accurate characterization of the elastocaloric effect. Moreover, under the simultaneous application of magnetic field and uniaxial compressive stress, this bespoke setup proves as a unique and useful tool for the study and characterization of the thermal response arising from materials exhibiting a cross-coupled response.

4 Materials physical properties

4.1 The Fe-Rh system: an overview

The first studies on the magnetic properties of the Fe-Rh alloy system were performed on the late 1930s [118, 119], reporting that close to 1:1 stoichiometry this alloy system exhibited a sudden increase on the magnetization upon heating. During the following decades, intensive research was devoted at characterizing the equilibrium phases of the Fe-Rh alloy system and their physical properties. A detailed phase diagram of Fe-Rh over a broad composition range can be found in [120, 121].

Nevertheless, for the purposes of the present work, a narrow region of interest is defined near equiatomic compositions. For a Rhodium content between $\sim 48\%$ and $\sim 55\%$, the Fe-Rh system exhibits a first-order metamagnetic phase transition, taking place at a transition temperature that rapidly falls when decreasing the Rhodium content within the range $300\,\mathrm{K} \leq T_t \leq 370\,\mathrm{K}$.

Within this composition range, this alloy system solidifies in a CsCl structure (space group $Pm\bar{3}m$), which orders ferromagnetically below its Curie temperature ($T_C \sim 680\,\mathrm{K}$). Upon further cooling, it exhibits a first-order phase transition from a high-temperature ferromagnetic (FM) (α' phase) to a low-temperature antiferromagnetic (AFM) phase (α'' phase). There is no crystal symmetry change associated with the phase transition, as both phases have a CsCl-type crystal structure. At the high-temperature ferromagnetic phase, the Fe atoms present a magnetic moment of $\sim 3\mu_B$ while the Rh atoms exhibit a magnetic moment of $\sim 1\mu_B$. At the low-temperature antiferromagnetic phase, the Rh atoms do not exhibit a significant magnetic moment whereas the Fe atoms present a moment of $\sim 3\mu_B$ with opposite sign on successive layers of (111) planes [122]. Moreover, due to the strong coupling between magnetic and structural degrees of freedom, the volume of the FM phase is $\sim 1\,\%$ larger than that of the AFM phase. [1] Figure 4.1 illustrates a sketch of the AFM and FM atomic structures.

Despite the fact that the magnetic properties of Fe-Rh are an object of study since the late 1930s [118, 119], the physical origin of the mechanisms that give rise

[1] A detailed summary on the main contributions characterizing the diverse crystal structures of the Fe-Rh alloy system, together with the magnetic moment values of the Fe and Rh atoms at the different phases, can be found in [120, 121].

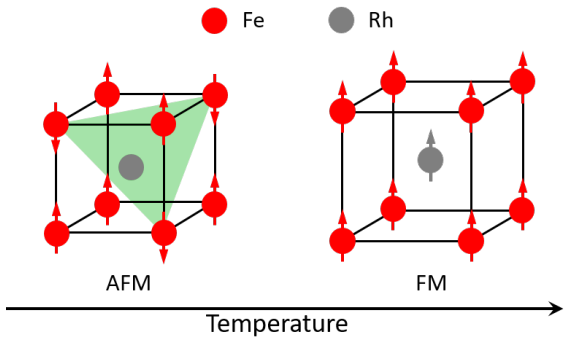

Figure 4.1: *Schematic illustration of the AFM (left) and FM (right) atomic structures for near equiatomic Fe-Rh. Red dots correspond to the Fe atoms, whereas grey dots to the Rh atoms. The corresponding magnetic spin configurations of each phase are indicated by the arrows. The green triangle at the AFM atomic structure indicates the (111) plane that contains Fe atoms with parallel magnetic spin configuration.*

to the first-order metamagnetic phase transition are still an active research field [123–128].

Furthermore, due to the volume and magnetization change exhibited at the first-order metamagnetic phase transition, it can be induced by the application (or removal) of both magnetic and mechanical fields. Therefore, as discussed in Chapter 2, giant caloric and multicaloric effects are expected in its vicinity. In the early decade of 1990s, S. Nikitin *et. al.* reported that Fe-Rh exhibits giant magnetocaloric [28] and elastocaloric [54] effects. Despite these early reports, studies on Fe-Rh were very scarce as it was considered to be of no practical use because it was believed that its caloric effects were not reproducible upon external field cycling [55, 129, 130]. Later reports showed that Fe-Rh exhibited a reproducible caloric effect upon field cycling by following a suitable thermodynamic path in the phase space [131], but it was not until the last decade that this alloy received considerable attention, after its potential interest for a wide range of technological applications was suggested [121].

Recently, giant and reproducible magnetocaloric and barocaloric effects have been reported on Fe-Rh [114, 132, 133], and its multicaloric response under the combined action of magnetic field and hydrostatic pressure has also been thoroughly studied [59]. Fe-Rh is nowadays considered one of the benchmark materials exhibiting giant caloric and multicaloric effects [134].

4.2 Heusler alloys

This material class is named after Friedrich Heusler, who discovered in 1903 that when alloying Cu-Mn bronze with different elements such as Sn, Al, Sb, Bi or B, the resulting compounds were ferromagnetic even though that the different base elements are non magnetic by themselves [135]. [2] It was not until 1934, with the studies carried by Bradley and Rodgers on the Cu-Mn-Al compound, that a relation between the stoichiometry X_2YZ, the alloy crystal structure and its magnetic properties was established [138].

Since these early studies, intensive research has been carried out on this alloy family, and nowadays more than 1000 Heusler compounds are known [139]. The strong interest on this material class comes from the prominent magnetic, structural and electronic properties that many of them exhibit, which leads to functional and multifunctional properties such as giant magnetocaloric and mechanocaloric effects [32, 38, 79], magneto-optical properties [140], spin polarization of the conduction electrons [141], tunability of the band gap and topological insulator behaviour [142], superconductivity [143], thermoelectrical applications [144, 145], magnetoresistance, magnetic shape-memory properties and magnetic superelasticity [75]. Moreover, it is significant to highlight that Heusler alloys have also drawn a lot of attention during the last decades due to their suitability for spintronic applications [146, 147].

Heusler alloys are intermetallic compounds, conformed by three distinct elements generally named as X, Y and Z. In general, one has to distinguish between two distinct families [139]:

1. **Full-Heusler compounds:**
   They correspond to the X_2YZ stoichiometry and present a characteristic cubic crystal structure $L2_1$ (space group $Fm\bar{3}m$). The structure $L2_1$, represented in Figure 4.2 (a), can be interpreted as four interpenetrated fcc (face centered cubic) sublattices. The X atoms are positioned on both the I and II sublattices, whereas Y and Z atoms occupy the III and IV sublattices, respectively.

2. **Half-Heusler compounds:**
   They correspond to the XYZ stoichiometry and present a cubic crystal structure $C1_b$ (space group $F\bar{4}3m$). This structure can be interpreted as an $L2_1$ structure (see Figure 4.2 (a)) where one of the sublattices which is occupied by the X element for the case of Full-Heusler compounds (sublattices I or II) is substituted by vacant lattice sites.

Figure 4.3 shows an overview of the main X, Y and Z elements that contribute to the crystallization of a Heusler phase. Usually, 3d and 4d transition metals are

[2] At the time when F. Heusler did his discoveries, it was not known that Mn atoms are magnetic. Nowadays, it is known that the Mn element presents a complex magnetic behaviour due to the variety of crystalline structures that it can exhibit [136, 137].

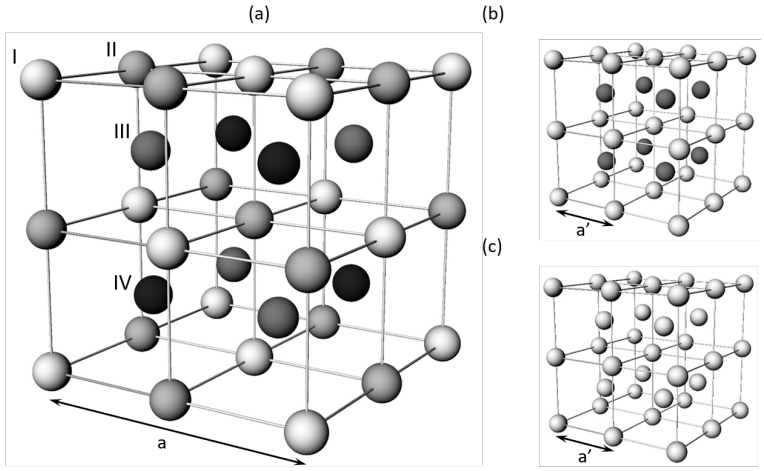

Figure 4.2: *Schematic illustration of the $L2_1$ (a), B2 (b) and A2 (c) crystal structures, characteristic of Full-Heusler alloys (X_2YZ). For the case of $L2_1$ phase in (a), each of the four fcc sublattices (labelled from I to IV) is occupied by a defined element (X, Y or Z). The atomic positions of each sublattice are indicated as spheres with different tones of grey. The lattice parameter is a. For the case of the B2 phase in (b), only two sublattices are distinguished, as indicated by the spheres with two different tones of grey, whereas for the A2 phase (c) all the sublattices atomic positions are randomly occupied. The lattice parameter for the A2 and B2 structures is a' = a/2.*

used as X and Y elements, but sometimes rare earths can be used as the Y element, whereas the Z element is usually taken from the main group block. [3] Nevertheless, these conditions do not guarantee the formation of a stable Heusler phase.

The physical properties of Heusler alloys, such as the electronic structure and its magnetic properties, are strongly dependent on the degree of atomic order of their constituents in the crystal structure [139]. For the case of Half-Heusler compounds, it has been reported that their crystal structure retains its atomic order up to the decomposition temperature [151]. Conversely, Full-Heusler compounds frequently display considerable atomic disorder as they do not directly crystallize on the ordered $L2_1$ crystal structure [139]. These compounds solidify in a fully disordered bcc (body centered cubic) phase (A2 phase), and on cooling they exhibit an order-disorder transition to a partially ordered intermediate B2 phase, which consists on a CsCl-type structure where the Y and Z atoms are mixed and randomly occupy both III and IV sublattices while the X atoms already occupy both sublattices I and II. On further cooling, another order-disorder transition takes place and the $L2_1$ structure emerges [152, 153]. Both B2 and A2 structures are represented in Figure 4.2 (b) and (c), respectively.

[3] Recently, Heusler alloys composed of only 3d transition metals have been reported (such as Ni-Mn-Ti or Ni-Mn-Ti-Co), where Ti replaces the Z element [148, 149].

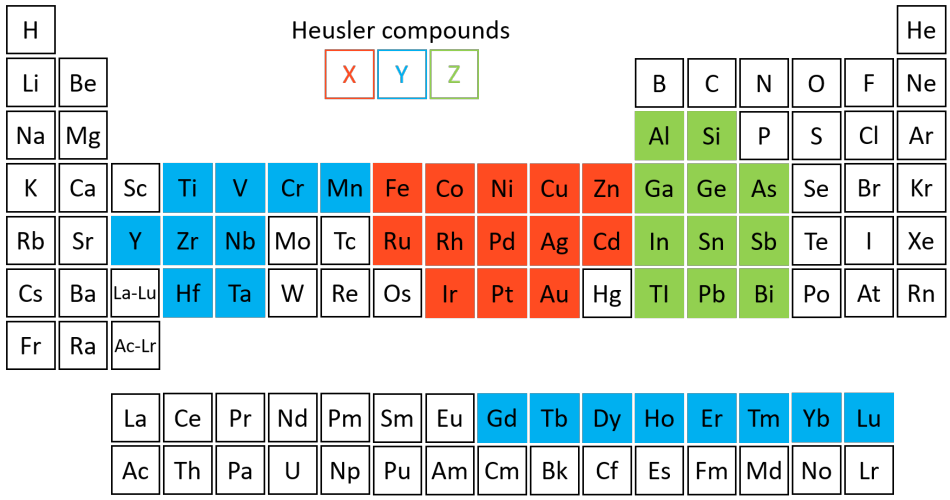

Figure 4.3: *Periodic table of the elements. The highlighted regions are indicative of the typical X (red), Y (blue) and Z (green) elements used for Heusler compounds. The figure has been modified from [150].*

Typically, the degree of atomic order can be tuned by heat treatments [154] and therefore the physical properties of Heusler alloys can be strongly influenced by the annealing temperature [155]. Despite this fact, some Heusler alloys (such as Ni-Mn based alloys) have difficulties to order completely at the $L2_1$ crystal structure, and they display traces of retained B2 phase [152].

So far, we have only considered Heusler alloys with a stoichiometric composition. Nevertheless, it is important to highlight that there is a rich variety of Heusler alloys that have an off-stoichiometric composition. Interestingly, small deviations from the stoichiometric composition can be regarded as an intrinsic disorder of the alloys, which can have a great influence on the material physical properties. In this regard, a particular case of interest for the present work are quaternary Heusler compounds, which are composed by two different X and X' elements and their composition can be generally expressed as (XX')YZ [139].

On cooling, the cubic crystal structure of some Heusler alloys becomes unstable and they can exhibit a martensitic transition.

4.2.1 The martensitic phase transition

In recognition of the early studies of Adolf Martens on the structure of steels, M. F. Osmond proposed in 1895 the term *martensite* to describe the microstructure found in quenched steels [156]. Over time, the term *martensitic transition* has been generalized to encompass the structural transformations that occur in other materials and alloys by similar mechanisms than those observed in steel.

Nowadays, a martensitic phase transition refers to a solid-to-solid first-order structural transformation that is driven by the nucleation and growth of the new phase, which takes place by a displacive and diffusionless rearrangement of atoms from the parent phase and is dominated by shear-like displacements [157]. As the phase transition is displacive, the chemical bonds between the diverse atoms are not broken during their rearrangement to the new crystal structure. There is no long-range movement of the atoms. Despite the structure and symmetry changes, the individual atomic movements are smaller than the interatomic distances and their local neighbourhood is maintained through the martensitic phase transition.

On the one hand, the high-temperature phase, with a cubic crystal structure, is referred as the *parent phase*. Alternatively, this phase is commonly referred as *austenite*, where this term was coined after William Chandler Roberts-Austen in recognition of his early works on the physical properties of metals and alloys. On the other hand, the low-temperature phase, which is induced at the martensitic phase transition is usually referred as the *product phase* or *martensite*. On cooling, the martensitic phase is induced from the high-temperature austenite, and this process is referred as the forward martensitic phase transition. Conversely, on heating, the austenitic phase is induced from the low-temperature martensite, and this process is referred as the reverse martensitic phase transition.

For the purpose of the present work, the following discussion is centered on the phenomenology exhibited at the martensitic phase transition by shape-memory alloys. [4] When the martensitic transition starts, the nuclei of the new martensite phase start to grow and they define a phase boundary with the remaining austenite phase, which is called the habit plane. As both phases have a crystal structure with different lattice parameters, there is a certain lattice mismatch at the habit plane that generates stress on the crystal structure of both phases, and the phase boundary has an energetic cost. The habit plane defines an energy barrier that has to be overcome in order to start the nucleation and growth process of the martensitic transformation. Therefore, as already discussed in section 2.2.2, the martensitic transition will exhibit a certain thermal hysteresis. However, local defects of the crystal structure or an improvement of the geometrical compatibility between both martensitic and austenitic phases can reduce the energy barrier and enhance the nucleation process, having a significant impact on the thermal hysteresis of the phase transition [158–161].

As the martensitic crystal structure has a lower symmetry than the cubic austenitic phase, from a single austenite crystal the martensitic phase can be formed in a set of different equivalent orientations, which are called martensite variants. On cooling, when the martensitic transition starts, none of the different martensite variants is favoured and all of them can nucleate and grow on the austenite matrix. However, the cubic crystal structure of the austenitic phase at one side of the habit plane constrains the martensitic variants that can be formed at the other side. In fact, the nucleation of a single martensite variant can induce a strong elastic and plas-

[4] Other systems that present martensitic phase transitions, such as steels or ceramic materials, do not necessarily exhibit the same phenomenology that is presented in this section.

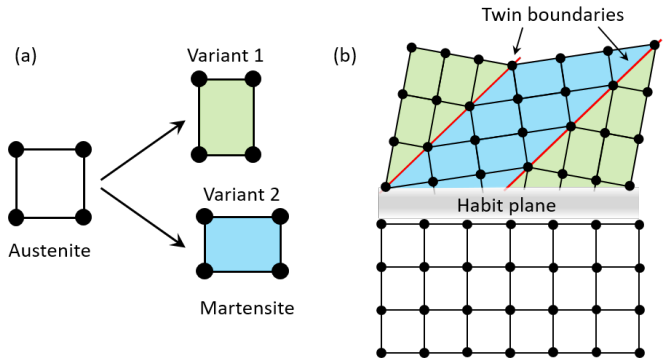

Figure 4.4: *(a) Schematic representation of the change in crystal structure under a martensitic transformation based on a tetragonal lattice distortion in a 2D system. Two equivalent martensite variants can be formed from an austenite cubic unit cell. (b) Schematic illustration of the habit plane (grey shaded region) defined between both martensite and austenite phases. The martensite phase develops twin boundaries between both variants (red lines) to minimize the elastic and plastic deformations of the crystal.*

tic deformation of the crystal. This energy can be reduced by alternating different martensite variants along the habit plane, defining twin boundaries between them. Therefore, the martensitic phase of a macroscopic sample is constituted by a complex microstructure of martensite variants which are separated by hierarchically distributed twin boundaries on many length scales [162]. Importantly, it must be mentioned that a twin boundary between the different martensite variants can be moved by applying a certain mechanical stress, as it breaks the energetic equivalence between the different variants and favours the growth of some of them. This process results in a macroscopic deformation of the material with strains as large as 10 %. Furthermore, this deformation can be reverted when heating the material back to the high-temperature austenitic phase, where the system recovers its original shape, which gives rise to the so-called shape-memory effect [163].

Figure 4.4 schematically illustrates the martensite growth and twinning at the nanoscale. For the sake of simplicity, a 2D system is considered for this example. In comparison to the cubic austenite, the martensite is deformed tetragonally and it can be formed in two different equivalent orientations, thus defining two martensite variants (illustrated in green and blue in Figure 4.4 (a)). On cooling, when the martensitic phase transition starts, the new martensite phase nucleates and grows, defining an habit plane between both austenite and martensite phases. The cubic structure of the austenite constrains the growing martensite phase, which combines the two variants (Figure 4.4 (b)). There is a certain lattice mismatch at the twin boundaries, which has an energetic cost, but this scenario is more energetically favourable than the transformation to a single martensite variant, as the elastic and plastic deformation of the crystal are reduced.

When the martensitic transition starts, each nucleus of the new phase grows until

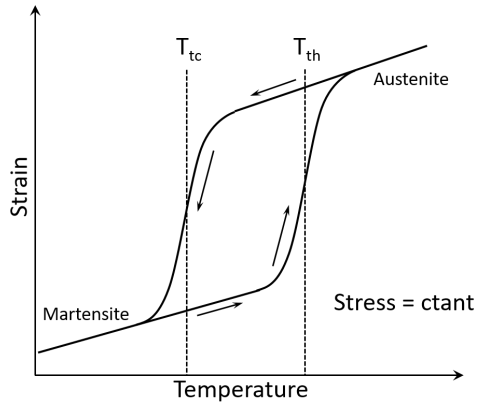

Figure 4.5: *Schematic representation of the strain of a system exhibiting a martensitic phase transition as a function of temperature under a constant stress. Vertical dashed lines indicate the temperature at the mid point of the forward (T_{tc}) and reverse (T_{th}) martensitic phase transitions.*

it encounters another nucleus or hits a high angle boundary [81]. As the diverse nucleus start to present obstacles between them for their further growth, the driving force of the phase transition has to increase in order to complete the martensitic phase transformation. Therefore, the system has to be further undercooled (see section 2.2.2) and consequently, the martensitic phase transition will spread over a certain temperature range. Taking into account the thermal hysteresis and the transition width inherent to a martensitic phase transition, Figure 4.5 illustrates the temperature dependence of the strain of a system around a martensitic phase transition. Under a certain applied mechanical stress, the growth of some martensite variants will be favoured and the system will exhibit a strain change across the martensitic transition ($\Delta\varepsilon_t$). Black arrows illustrate the different transformation paths followed for the forward (cooling) and reverse (heating) transitions, which occur at a different transition temperature as illustrated by vertical dashed lines.

So far, we have considered that temperature is the driving field of the martensitic phase transitions. Nevertheless, as the system exhibits a strain change ($\Delta\varepsilon_t$), it can also be induced by a mechanical stress. At temperatures above the austenite finish temperature, [5] application of stress will induce the forward phase transition, favouring the formation of a single-variant martensitic phase. When the stress is removed, the reverse phase transition will be induced with a certain hysteresis, and the system will recover its initial shape. This process, which results in a reversible macroscopic deformation of the sample, gives rise to the so-called superelastic effect.

Martensitic phase transitions are observed in a rich variety of materials, such as metallic alloys, ceramics, polymers or superconductors [163]. Their study is of

[5] The austenite finish temperature (A_f) corresponds to the temperature at which the reverse phase transition is completed, which will be higher than the reverse transition temperature (T_{th}).

fundamental and technological interest, as martensitic transitions not only play an important role on the hardening of steel [164], but they are also important for the development of sensors and actuators, as martensitic phase transitions confer some alloys shape-memory and superelastic properties. For the sake of many technological applications, the cyclability of the martensitic phase transition is of utmost importance. In this regard, it is important to highlight that the lattice mismatch between both martensitic and austenitic phases has a significant impact on the stresses generated at the habit plane, which leads to a gradual degradation of the samples that is observed by the promotion of dislocations and microcracks at the microstructure [161].

A detailed discussion on the martensitic phase transition, their crystallographic and thermodynamic characteristics, the nucleation and growth mechanisms as well as their properties can be found in [108, 163, 165, 166].

4.2.2 Ni-Mn-based Heusler alloys

For the purpose of the present work, our interest is focused on the Ni-Mn-Z (Z = Ga, In, Sn, Sb, Al) Heusler alloys, as they exhibit a martensitic phase transition near room temperature that involves a change in both structural and magnetic order [63, 75, 167–169]. These Heusler alloys have drawn a great deal of attention over the last decades as they exhibit a strong coupling between the structural and magnetic degrees of freedom at the martensitic phase transition, giving rise to a cross-response to different external stimuli and exhibiting a strong multicaloric character that anticipates promising perspectives for future technological applications [51, 62–64, 170, 171].

4.2.2.1 Structural properties and phase diagrams

In the austenitic phase, as discussed in section 4.2, Heusler alloys exhibit a $L2_1$ crystal structure, illustrated in Figure 4.2, which is generally created after a series of order-disorder transitions. At the stoichiometric composition, the Ni atoms occupy both sublattices I and II, whereas Mn and Z occupy the III and IV sublattices, respectively. On cooling, these alloys can exhibit a martensitic phase transition. At low concentrations of the Z element, Ni-Mn-based Heusler alloys transform to a martensitic phase with a $L1_0$ tetragonal crystal structure (space group $P4/mmm$), since it also corresponds to the ground-state crystal structure of the parent compound $Ni_{50}Mn_{50}$ [75, 172]. Figure 4.6 schematically illustrates the $L2_1$ crystal structure and its relationship with the $L1_0$ tetragonal structure. Nevertheless, it has been reported that Ni-Mn-based Heusler alloys can exhibit other related structures at the martensitic phase, specially for higher concentrations of the Z element. In particular, monoclinic structures, which can be described as modulated variations of the $L1_0$ tetragonal structure stacked in a specific order, with a five-layered (5M) or seven-layered (7M) periodicity have been observed [75]. [6] These modulated martensitic structures have been interpreted as an adaptative phase constituted by

[6] Depending on how the periodicity of the modulated structure is defined, these structures are labelled 5M and 7M or 10M and 14M, respectively, in the literature.

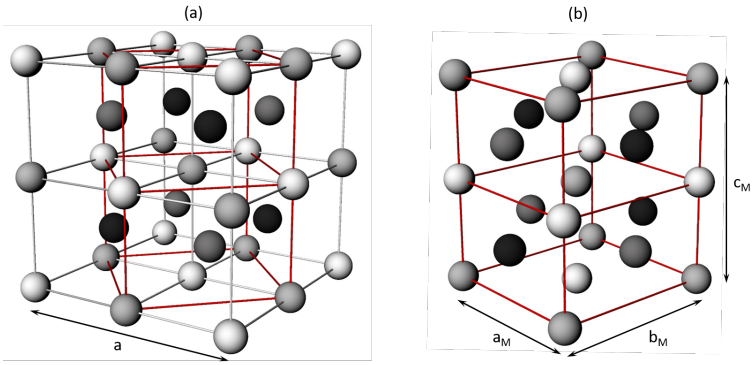

Figure 4.6: *(a) Schematic illustration of the $L2_1$ crystal structure, characteristic of Full-Heusler alloys, and its relation to the tetragonal $L1_0$ crystal structure, which is also illustrated separately in (b). As for Figure 4.2, the atomic positions of each sublattice are indicated as spheres with different tones of grey.*

a nanoscale microstructure of the $L1_0$ tetragonal martensite variants stacked with a certain order [173]. As discussed in section 4.2.1 and schematically illustrated in Figure 4.4 (b) for a 2D system, the formation of these microstructures enables a drastic reduction of the elastic and plastic deformation of the crystal at the habit plane, which favours the nucleation process. Furthermore, some Heusler alloys can exhibit a series of first-order phase transitions, which involve the presence of inter-martensitic or premartensitic phases, before reaching the martensitic ground state [174, 175].

Interestingly, Ni-Mn-Ga is the only Ni-Mn-based Heusler alloy that exhibits a martensitic phase transition at the stoichiometric composition Ni_2MnGa [170, 176], exhibiting almost no volume change at the phase transition. For this particular case, the atoms of each element occupy the positions of specific sublattices and its crystal structures can be visualized as those illustrated in Figure 4.6. Conversely, for the cases in which ($Z \neq Ga$), the martensitic transition takes place only for off-stoichiometric compositions, exhibiting a certain volume change at the phase transition [177]. Despite this fact, similar crystal structures are observed on these alloys at the martensitic phase [178, 179].

As previously discussed in section 4.2, the material physical properties such as the magnetic order, the martensitic transition temperature or its crystal structures will depend on the chemical composition of a Heusler alloy. Interestingly, some of the physical properties of many Heusler compounds, including the Ni-Mn-based ones, can be predicted from the average number of valence electrons per atom (e/a) [139, 180]. Therefore, it is possible to represent a complete structural and magnetic phase diagram for Ni-Mn-Z compounds with different chemical compositions as a function of the average valence electron concentration per atom (e/a), which are illustrated in Figure 4.7 for Ni-Mn-Sn (a), Ni-Mn-In (b) and Ni-Mn-Ga (c).

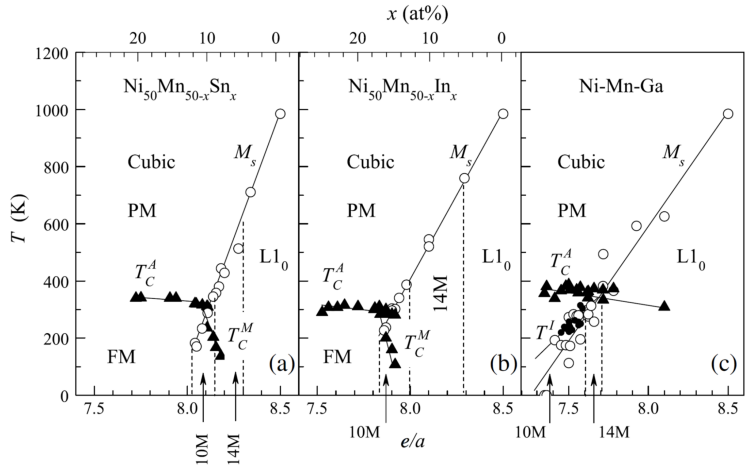

Figure 4.7: *Magnetic and structural transition temperatures as a function of the average valence electron concentration per atom (e/a) for Ni-Mn-Z Heusler alloys, with Z as Sn (a), In (b) and Ga (c). The triangles and circles correspond to the magnetic and martensitic transformation temperatures, respectively. The regions corresponding to different crystal structures are separated by dashed lines. Small solid circles in (c) correspond to premartensitic transition temperatures. This figure has been taken from [75].*

Each individual phase diagram starts from the parent compound $Ni_{50}Mn_{50}$, which has an average number of valence electrons per atom of $e/a = 8.5$ and is in the $L1_0$ tetragonal crystal structure even at high temperatures. When progressively increasing the concentration of the Z element, as these atoms provide less valence electrons than Ni and Mn, it leads to a decrease of the average number of valence electrons per atom (e/a) for the three different families of Ni-Mn-Z Heusler compounds under consideration.

On the one hand, when considering the structural phases of these compounds, it has been reported that a decrease of the average number of valence electrons per atom (e/a) leads to a shift of the martensitic start temperature (M_s) [7] to lower temperatures with a good linearity. For the three different families of Ni-Mn-Z Heusler compounds illustrated in Figure 4.7, the ground state crystal structure evolves as cubic $\rightarrow$ 10M $\rightarrow$ 14M $\rightarrow$ $L1_0$ when decreasing the concentration of the Z element, which corresponds to an increase on e/a.

On the other hand, when considering the magnetic phases of these compounds, it is shown that the austenitic Curie temperature (T_C^A) does not significantly change when altering the chemical composition within each Heusler compound family, although it shows a tendency to decrease when increasing e/a. Further-

[7] The martensitic start temperature (M_s) corresponds to the temperature at which the forward phase transition is initiated, which will be higher than the forward transition temperature (T_{tc}) considered in section 4.2.1.

more, these families display comparable austenitic Curie temperatures in the range $T_C^A \in [300, 400]$ K, despite the fact that their magnetic interactions giving rise to the ferromagnetic behaviour strongly differ between them [181]. Interestingly, except for Z = Ga, the martensitic Curie temperature (T_C^M) exhibits a significant dependence on the chemical composition of the alloy, as it rapidly decreases when increasing e/a. [8]

Intensive research has been carried during the last decades on Ni-Mn-based Heusler alloys owing to the strong coupling exhibited between the structural and magnetic degrees of freedom. This unique interplay makes Ni-Mn-based Heusler alloys suitable candidates to exhibit magnetic shape-memory effects, which corresponds to the possibility of inducing large recoverable strains by the application of magnetic field and represented a major breakthrough for the development of a new generation of sensors and actuators [75]. Special attention has been given to Ni-Mn-Ga-based Heusler compounds, as they can display strains within 10-12 % [183, 184].

The magnetic anisotropy energy, which corresponds to the energy necessary to rotate the magnetic moment of a single crystal from the easy to the hard direction, as well as the mobility of twin boundaries play an important role on the magnetostructural properties of these alloys. While the cubic austenitic phase has a low magnetocrystalline anisotropy, the low-temperature martensitic variants can exhibit a significant anisotropy, which is specially important for the case of Ni-Mn-Ga alloys. At low temperatures, below the Curie point without any applied magnetic field, the magnetization of the magnetic domains within the different martensite variants point along the easy axis and are oriented in a way to minimize the magnetoelastic energy [185–187]. When a magnetic field is applied, the magnetic moments within the twin variants tend align with the magnetic field direction. At this point, if the magnetic anisotropy is weak, the magnetic moments will rotate within each martensite variant, resulting in a small change of the sample dimensions. Nevertheless, if the magnetic anisotropy is high, the rotation of the magnetic moments within each variant is less energetically favourable than the movement of the twin boundaries in order to generate a single-variant martensitic structure with the easy axis aligned with the magnetic field. In this process, magnetic field plays the same role that stress in shape-memory alloys, as both promote the formation of single-variant martensite structures.

4.2.2.2 Magnetic properties

The magnetic behaviour of Ni-Mn-based Heusler alloys is strongly linked to their crystal structure and the role of Mn atoms. From neutron scattering experiments, it was found that the magnetic moment for most of the X_2MnZ Heusler alloys is mainly confined at the Mn atoms with a value in the range of $4\mu_B$ [188, 189]

[8] The decrease on the austenitic and martensitic Curie temperatures when increasing e/a is related to the weakening of the ferromagnetic coupling when increasing the Mn content. As discussed in section 4.2.2.2, decreasing the interatomic distance between neighbouring Mn atoms strongly enhances the antiferromagnetic exchange [75, 182].

independently of the X and Z elements. [9] In 1983, Kübler *et al.* showed that the electron density of states plays a major role on the origin of localized magnetic moments at the Mn atoms. Based on the first density functional theory calculations on a series of full-Heusler alloys with composition X_2MnZ, they established that Mn atoms give rise to confined magnetic moments due to the exclusion of the minority-spin electrons [190].

For the particular case of Ni-Mn-based Heusler alloys in the austenitic phase, where these alloys exhibit an $L2_1$ crystal structure, each Mn atom has eight Ni atoms as nearest neighbours. In this case, theoretical studies have shown that there is a hybridization between the 3d orbitals of Mn and Ni atoms [181, 190–193]. Consequently, whereas the majority spin-up states are almost completely occupied as they lay below the Fermi energy, the minority spin-down states of the d-electrons are partially empty as they are pushed up above the Fermi energy. The difference between spin-up and spin-down occupied states gives rise to a net magnetic moment localized at the Mn atoms which is composed of itinerant electrons that form a common d band [191].

In these Heusler alloys, the interatomic distance between neighbouring Mn atoms is large, preventing a significant direct interaction between them. Therefore, indirect coupling mechanisms play a major role in defining the magnetic ordering. The interaction between Mn atoms can be described in terms of the model proposed by Ruderman, Kittel, Kasuya and Yosida, known as RKKY model [194–196], which supposes that the indirect coupling mechanism between localized magnetic moments is mediated by the conduction electrons, which belong to the s and p energy levels. In this model, a localized magnetic moment spin-polarizes the conduction electron gas, which in turn couples to another localized magnetic moment at a distance r. The corresponding exchange energy given by this model depends on the distance between the magnetic moments and has as oscillatory character, which can give rise to either ferromagnetic or antiferromagnetic order depending on the distance between the localized magnetic moments.

Whereas elementary Mn exhibits a variety of crystal structures with antiferromagnetic coupling [136, 137], an increase on the distance between neighbouring Mn atoms can lead to a ferromagnetic coupling. This behaviour can be described in terms of the Bethe-Slater curve, which is schematically illustrated in Figure 4.8. As it can be seen, the elements with positive exchange energy order ferromagnetically, such as Fe, Co or Ni. Elementary Mn has a negative exchange energy, but an increase on the distance between neighbouring Mn atoms can lead to a positive exchange energy thus giving rise to a ferromagnetic coupling.

Even if the Mn atoms exhibit a similar magnetic moment for most of the X_2MnZ Heusler alloys, the fact that the interaction between them is indirect and mediated by the conduction electrons gives rise to diverse magnetic behaviours depending

[9] However, when the X element presents a significant magnetic moment such as for Co, there is nearest neighbours interaction between magnetic atoms and the system will present a tendency to itinerant magnetism.

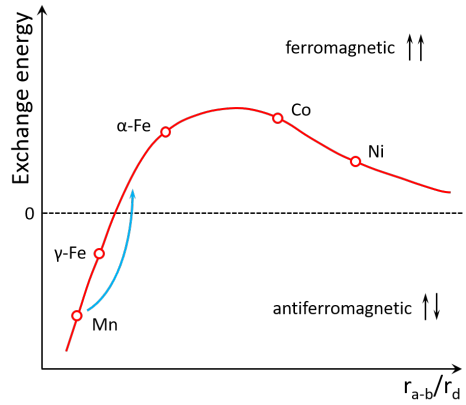

Figure 4.8: *Schematic representation of the Bethe-Slater curve, which illustrates the exchange energy as a function of the ratio between the interatomic distance (r_{a-b}) and the radius of the 3d orbital (r_d) for different elements [197]. The blue arrow illustrates the change from an antiferromagnetic to a ferromagnetic ordering for Mn atoms when increasing their interatomic distance.*

on the X and Z elements. While the X element plays an important role in defining the lattice parameter of the alloy, [10] the Z element has a strong influence on the concentration of sp-conduction electrons, which mediate the exchange interaction between Mn atoms [181, 190, 200]. These factors highlight the strong influence of the crystal structure, which directly tunes the distance between Mn atoms, on the magnetic behaviour of Ni-Mn-based Heusler alloys [181, 201].

Moreover, as previously discussed in section 4.2, the magnetic behaviour of a Heusler alloy will depend on its specific chemical composition. Specifically, alloys that have an off-stoichiometric composition will have a certain disorder in their crystal structure. In this regard, the excess Mn atoms will decrease the distance between neighbouring Mn atoms and will affect their exchange interaction, thus modifying the magnetic behaviour of the alloy [75, 202].

Furthermore, the magnetic moment per atom will also depend on the chemical composition of a Heusler alloy, which determines the number of valence electrons per atom (e/a) [139]. This dependency follows the Slater-Pauling behaviour [20, 203], which is illustrated in Figure 4.9 for diverse 3d metals and alloys, together with some Ni-Mn-based Heusler alloys. For each compound, the number of valence electrons per atom (e/a) is given by a number of majority spin-up ($N_\uparrow$) and minority spin-down ($N_\downarrow$) electrons, and can be generally expressed as $e/a = N_\uparrow + N_\downarrow$. Accordingly, the average magnetic moment per atom is given by the difference between both electrons populations, and can be expressed as $\mu = (N_\uparrow - N_\downarrow)\mu_B = (e/a - 2N_\downarrow)\mu_B$. Therefore, for a fixed number of minority

[10] Nevertheless, the X element can also influence on other aspects. For instance, for the particular case of Ni-Mn-based Heusler alloys, the Ni atoms also exhibit a certain magnetic moment [198, 199], which is significantly smaller than that associated with Mn atoms.

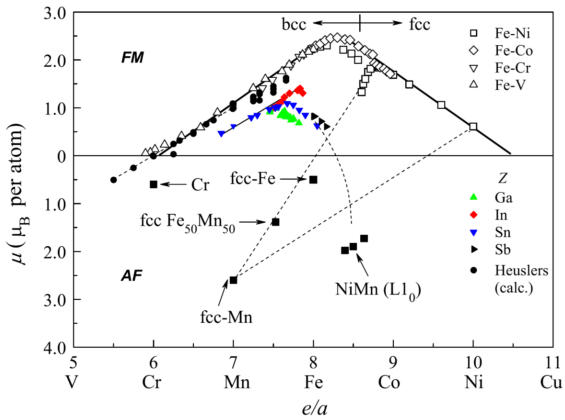

Figure 4.9: *Magnetic moment as a function of the valence electron concentration per atom (e/a) for diverse 3d metals and alloys (open symbols), Ni-Mn-Z Heusler alloys (solid triangles), calculated full-Heuslers and half-Heuslers (solid circles) and some antiferromagnets (solid squares). The alloys that lay above the zero magnetic moment line exhibit a ferromagnetic (FM) order, whereas those that lay below exhibit an antiferromagnetic (AF) order. The figure has been taken from [75].*

spin-down electrons per atom, there is a direct proportionality between the average magnetic moment per atom (μ) and the number of valence electrons per atom (e/a) [193, 204].

When changing the composition for diverse 3d alloys in order to modify the number of valence electrons per atom (e/a), represented in Figure 4.9 as open symbols, their associated magnetic moments follow the increasing (e/a $<$ 8.5) and decreasing (e/a $>$ 8.5) branches of the Slater-Pauling curve. Typically, materials with e/a $>$ 8.5 display an fcc structure, whereas they display a bcc structure for e/a $<$ 8.5. For the sake of completeness, the magnetic moment of some antiferromagnets is also included in Figure 4.9, illustrated as solid squares. Interestingly, deviations from the Slater-Pauling curve can occur, as it can be seen for certain Fe-Ni alloys, which is indicative of changes on the magnetic behaviour for those particular compositions.

When considering the case of Heusler alloys, the calculated magnetic moments for full-Heusler and half-Heusler alloys (solid circles in Figure 4.9) perfectly fit on the increasing branch of the Slater-Pauling curve. Furthermore, the experimental values for diverse Ni-Mn-Z Heusler alloys are represented as solid triangles. As it can be seen, these experimental values nearly follow the Slater-Pauling curve with the same slope but they deviate from it at high e/a values, which corresponds to off-stoichiometric compositions with an excess of Mn atoms. As previously discussed, an excess of Mn atoms decreases the distance to neighbouring Mn atoms and affects the magnetic behaviour of the alloy. Eventually, for a high excess of Mn atoms, their magnetic behaviour would approach to that of the parent compound $Ni_{50}Mn_{50}$, as

indicated by the black dashed line in Figure 4.9, which is antiferromagnetic.

4.2.2.3 Challenges and future perspectives for technological applications

During the last years many efforts have been devoted at developing high-performance Ni-Mn-based magnetic shape-memory alloys, characterized by exhibiting giant mechanocaloric [205, 206] and magnetocaloric [207] effects as well as an enhanced cyclability of their thermal response [208, 209], which is of utmost importance for any technological application. In spite of the significance of such achievements, there are a series of bottlenecks mostly related to the first-order character of the martensitic phase transitions that need to be further addressed. On the one hand, the required external fields in order to achieve a giant caloric effect are still too large. On the other hand, the inherent hysteresis associated with the first-order character of the martensitic phase transition reduces the reversibility of the field-induced caloric effects and compromises the possible technological applications [48].

Different strategies have been recently proposed in order to overcome some of these limitations by taking advantage of the magnetostructural character of the martensitic phase transition exhibited by these alloys, and its sensitivity to diverse external fields. For instance, a suitable combination of more than one external field can help in increasing the reversibility of the field-induced thermal response [51, 210]. To address this issue, different approaches have already been taken into practice, and it has been shown that a suitable combination of magnetic field and hydrostatic pressure or uniaxial stress drastically reduces the magnetic-field-effective hysteresis [59, 61, 63, 65]. Furthermore, a novel multicaloric cycle that takes advantage of the inherent thermal hysteresis of these alloys and operates under the sequential application of magnetic field and uniaxial compressive stress has very recently been proposed and successfully tested [64].

5 Results and discussion

5.1 Fe-Rh

Regardless of the early studies performed by S. Nikitin *et. al.* on the giant elastocaloric effects exhibited by this alloy [54], where a giant adiabatic temperature change was reported when applying tensile stresses, no further studies were performed on this line and a complete characterization of the elastocaloric effect was lacking until a few years ago. [1]

The present work on this alloy has a twofold objective. First of all, it is aimed at providing a thorough characterization of the giant elastocaloric effect of Fe-Rh when subjected to a uniaxial compressive stress. Secondly, it is intended to provide a detailed discussion on the effect of the combined action of magnetic field and uniaxial compressive stress on the caloric properties of Fe-Rh.

5.1.1 Sample details

The experiments were performed on a polycrystalline $Fe_{49}Rh_{51}$ sample prepared by arc melting with dimensions $3.3 \times 3.0 \times 5.6\,\mathrm{mm}^3$, shaped as a parallelepiped. This sample was fabricated at the Indian Association for the Cultivation of Science (IACS), Kolkata (India), and details of the sample preparation and heat treatment are given in [59, 114, 132].

5.1.2 Experimental details

Direct measurements of the adiabatic temperature change induced under a cyclic external field in the range $0 \rightleftarrows 1.7\,\mathrm{T}$ and a constant compressive stress of $\sigma = 100\,\mathrm{MPa}$ have been performed with the bespoke setup described in section 3.2.2. Following the discontinuous measurement protocol, discussed in section 3.2.1, suitable thermal excursions were performed prior to each measurement to control the initial thermodynamic state of the sample. Afterwards, the sample was brought to the desired measurement temperature, which was within the range $T \in [295, 330]\,\mathrm{K}$ for all measurements.

[1] The results of these studies are published in reference [65].

5.1.3 Adiabatic thermometry of the magnetocaloric temperature change under a constant uniaxial stress

As discussed in section 2.2.2, the first-order character of the metamagnetic phase transition exhibited by Fe-Rh implies that it will present a certain temperature and external field hysteresis. Therefore, as described in section 3.2, the thermal history of the sample has to be taken into account in order to properly measure the reversible and irreversible field-induced adiabatic temperature change under a cyclic external field.

The design of suitable thermodynamic paths before the measurement start has to take into account the phase transition behaviour under the application of the different considered external fields. As stated before in section 2.2.1, a system exhibiting a first-order phase transition is characterized by a discontinuity on the corresponding order parameter and under the application of a certain external field, as discussed in section 2.2.2, the phase that maximizes the conjugated order parameter will be favoured.

For the particular case of the first-order metamagnetic phase transition in Fe-Rh, a discontinuity on both the magnetic order and the lattice parameter of the unit cell occur at the phase transition. Therefore, application of magnetic field will favour the phase that maximizes the magnetization, which corresponds to the high-temperature FM phase, and the transition temperature will shift to lower values as the material will exhibit an inverse magnetocaloric effect. Conversely, application of hydrostatic pressure will favour the phase where the crystal structure is more compact, which corresponds to the low-temperature AFM phase, and the transition temperature will shift to higher values as the material will exhibit a conventional barocaloric effect. The inverse character of the magnetocaloric effect and the conventional character of the barocaloric effect have been thoroughly studied in previous studies such as [59, 114, 132, 133].

When considering the effect of uniaxial stress on the metamagnetic phase transition, a distinct behaviour has been observed between the application of a tensile stress [54] and a compressive stress [65]. For instance, the transition temperature increases when applying a compressive stress, which corresponds to the stabilization of the low-volume AFM phase, while it decreases when applying a tensile stress, reflecting a stabilization of the high-volume FM phase.

The volume change experienced at the phase transition gives rise to a uniaxial strain component $\Delta\varepsilon_t \approx \frac{1}{3}\frac{\Delta v}{v}$, where $\frac{\Delta v}{v}$ corresponds to the relative volume change at the FM to AFM phase transition. Some insight on the relative phase stability between the FM and AFM phases under the application of uniaxial stress can be gained from the the Clausius-Clapeyron equation for the elastocaloric effect (see Table 2.1 and equation 2.28), which can be written as:

$$\frac{dT_t}{d\sigma} = -v_0\frac{\Delta\varepsilon_t}{\Delta S_t} \approx -\frac{v_0}{3}\frac{\Delta v/v}{\Delta S_t} \tag{5.1}$$

Consequently, for a compressive stress ($\sigma < 0$) the transition temperature shift is positive $\left(\frac{dT_t}{d|\sigma|} > 0\right)$ and the low-volume AFM phase is stabilized, whereas for a tensile stress ($\sigma > 0$) the transition temperature shift is negative $\left(\frac{dT_t}{d|\sigma|} < 0\right)$ and the large-volume FM phase is stabilized. Furthermore, it is important to highlight that as uniaxial stress is not the conjugated field for a volume change, a much smaller sensitivity of the transition temperature is expected when applying a uniaxial stress when compared to hydrostatic pressure [92].

Taking into account that the application of magnetic field stabilizes the high-temperature FM phase, promoting the AFM to FM phase transition (as a heating process does), while the removal of magnetic field stabilizes the low-temperature AFM phase and promotes the FM to AFM phase transition (as a cooling process does), which gives rise to an inverse magnetocaloric effect, the protocols described in section 3.1.2.1 that correspond to an inverse caloric effect were followed to carry out the direct measurements of the adiabatic temperature change under a cyclic magnetic field. In this regard, to characterize the thermal response when inducing the AFM to FM phase transition (heating protocol), the sample is initially fully transformed to the AFM phase in the absence of magnetic field, and then it is heated up to the initial measurement temperature. Once the sample is at isothermal equilibrium, the magnetic field is cycled, starting with a $0 \rightarrow 1.7\,\mathrm{T}$ scan. By contrast, to characterize the thermal response when inducing the FM to AFM phase transition (cooling protocol), the sample is initially fully transformed to the FM phase under a constant magnetic field, and then it is cooled down to the initial measurement temperature. Once the sample is at isothermal equilibrium, the magnetic field is cycled, starting with a $1.7\,\mathrm{T} \rightarrow 0$ scan.

Figure 5.1 illustrates examples of the temperature (top) and magnetic field (bottom) measurements recorded upon cycling the magnetic field in the range $0 \rightleftarrows 1.7\,\mathrm{T}$ under a constant compressive stress of $\sigma = 100\,\mathrm{MPa}$ for both heating (left) and cooling (right) protocols. Consistently with the inverse nature of the magnetocaloric effect in Fe-Rh, we measured a temperature decrease upon application of an external magnetic field and a temperature increase upon removal of the magnetic field. As it can be seen in both panels (a) and (b), the temperature changes measured for the first magnetic field scan (n = 1) are larger than the temperature changes measured for the subsequent magnetic field scans (n > 1). The reduction of the field-induced adiabatic temperature change between the first and subsequent magnetic field scans is due to the hysteresis inherent to the first-order character of the metamagnetic phase transition.

The adiabatic temperature change for a certain magnetic field scan ($\mu_0 H^s \rightarrow \mu_0 H^f$) is determined as $\Delta T_{ad}(\mu_0 H^s \rightarrow \mu_0 H^f) = T(\mu_0 H^f) - T(\mu_0 H^s)$, where $T(\mu_0 H^s)$ and $T(\mu_0 H^f)$ correspond to the sample temperature before and after the magnetic field scan, respectively. The whole set of measurements is compiled in Figure 5.2, where the adiabatic temperature changes are plotted as a function of the initial temperature of the sample.

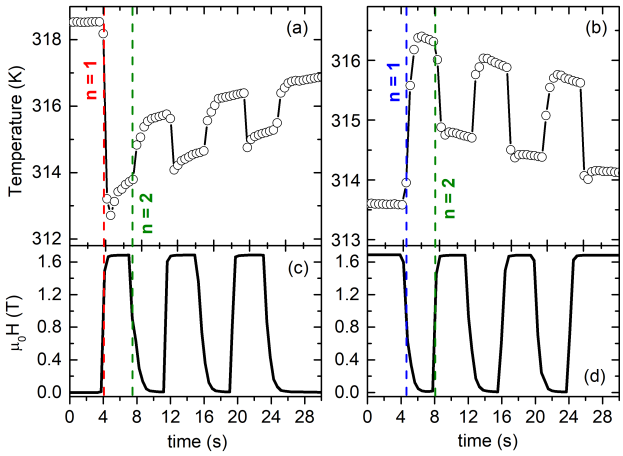

Figure 5.1: *Illustrative examples of the recorded temperature ((a) and (b)) and magnetic field ((c) and (d)) for heating (left) and cooling (right) protocols under a constant applied compressive stress of* 100 *MPa. Red and blue dashed vertical lines (n = 1) indicate the first application and removal of magnetic field, respectively, while green dashed vertical lines (n = 2) indicate the second removal and application of magnetic field.*

The maximum adiabatic temperature change values measured for the first application and removal of the magnetic field are around $|\Delta T| \approx 5\,\mathrm{K}$, while it decreases to $|\Delta T| \approx 2\,\mathrm{K}$ upon successive magnetic field scans. These values are smaller than previous measurements in the absence of applied uniaxial compressive stress [114]. This difference between both measurement sets can be mainly attributed to the fact that the current adiabatic temperature measurements were performed with the thermocouple attached to the sample surface, while for previous measurements the thermocouple was embedded into the sample, which worsens the thermal contact between the sample and the thermocouple. Additionally, for the present measurements the sample is in direct contact with two PEEK discs (see the scheme of the setup in Figure 3.13) which reduces the adiabaticity of the measurements.

The effect of the uniaxial compressive stress on the adiabatic temperature change can be noticed when comparing the present results with previously reported data in the absence of compressive stress [114]. When comparing the temperature at which the measured adiabatic temperature change is maximum (or minimum), we observe that the present measurements are shifted to higher temperatures as $\delta T = (3.1 \pm 0.3)\,\mathrm{K}$. Taking into account that the present measurements were performed under a constant uniaxial compressive stress of $\sigma = 100\,\mathrm{MPa}$, the corresponding transition temperature shift with uniaxial compressive stress will be $\frac{dT_t}{d|\sigma|} = (0.031 \pm 0.003)\,\mathrm{KMPa}^{-1}$, which is in agreement with previous results obtained from calorimetric measurements [65, 92].

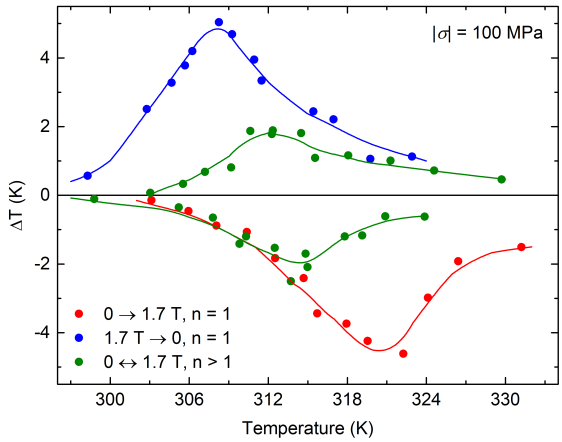

Figure 5.2: *Adiabatic temperature change corresponding to the application and removal of a 1.7 T magnetic field under a constant applied compressive stress of 100 MPa. Red and blue symbols correspond to the first application and removal ($n = 1$) of the magnetic field for the heating and cooling protocols, respectively. Green symbols correspond to the subsequent field cycles ($n > 1$), and lines are guides to the eye.*

5.1.4 Magnetocaloric effect under a constant uniaxial stress

Previous studies on the caloric and multicaloric effects exhibited by Fe-Rh under the influence of magnetic field and hydrostatic pressure showed an excellent agreement between indirect [59], quasidirect [132] and direct [114, 132] estimates of the field-induced thermal response.

In order to complement the direct measurements of the adiabatic temperature change presented in the previous section, and those reported in reference [65], the computation of the corresponding quasidirect estimates of the field-induced thermal response under a magnetic field change ($0 \rightleftarrows \mu_0 H$) and a constant uniaxial compressive stress of $\sigma = 100\,\mathrm{MPa}$ proves as a good approach to further characterize the effect of the combined action of magnetic field and uniaxial compressive stress on the caloric properties of Fe-Rh.

As discussed along Chapter 3 and exemplified for the elastocaloric effect of Cu-Zn-Al, the quasidirect computation of the field-induced thermal response is based on the construction of the corresponding isofield entropy curves from calorimetric measurements and heat capacity data. For the case of Fe-Rh, high-quality isofield calorimetric measurements under the influence of magnetic field without any applied uniaxial compressive stress were previously performed [132], whereas isofield calorimetric measurements under the combined influence of magnetic field and uniaxial compressive stress performed with a previous version of the bespoke setup described in section 3.1.4 showed a poor baseline and could not be properly integrated for the construction of the corresponding entropy curves [92]. Nevertheless, a good

approach to construct the isofield-isostress entropy curves, generally expressed as $(S(T, \mu_0 H, \sigma))$, is to use the isofield entropy curves computed from the high-quality calorimetric measurements in the absence of stress $(S(T, \mu_0 H, \sigma = 0\,\mathrm{MPa}))$ [114] and assume that the effect of uniaxial compressive stress on the entropy curves is a pure shift of the transition temperature without any significant change in its shape [38]. Under this assumption, the isofield-isostress entropy curves will be computed as:

$$S(T, \mu_0 H, \sigma) = S(T, \mu_0 H, \sigma = 0\,\mathrm{MPa}) \frac{dT_t}{d\sigma} \sigma \tag{5.2}$$

From these curves, as described in section 3.1.1.2, we have computed the quasidirect estimates of the adiabatic temperature $(\Delta T(S, 0 \rightleftarrows \mu_0 H, \sigma = 100\,\mathrm{MPa}))$ and isothermal entropy $(\Delta S(T, 0 \rightleftarrows \mu_0 H, \sigma = 100\,\mathrm{MPa}))$ changes. In accordance with the inverse nature of the magnetocaloric effect, application of magnetic field is associated with a heating process, as both promote the AFM to FM phase transition, and the corresponding adiabatic temperature and isothermal entropy changes are computed as $\Delta T(S, 0 \rightarrow \mu_0 H, \sigma = 100\,\mathrm{MPa})$ and $\Delta S(T, 0 \rightarrow \mu_0 H, \sigma = 100\,\mathrm{MPa})$, respectively, whereas removal of magnetic field is associated with a cooling process, as both promote the FM to AFM phase transition, and the corresponding adiabatic temperature and isothermal entropy changes are computed as $\Delta T(S, \mu_0 H \rightarrow 0, \sigma = 100\,\mathrm{MPa})$ and $\Delta S(T, \mu_0 H \rightarrow 0, \sigma = 100\,\mathrm{MPa})$, respectively. Results corresponding to magnetic fields of 1.7 and 6 T under a constant compressive stress of $\sigma = 100\,\mathrm{MPa}$ are shown as lines in Figure 5.3. The corresponding shaded green areas account for the reversible regions for each magnetic field.

The results for the direct adiabatic temperature measurements presented in the previous section are shown as solid symbols in Figure 5.3 (a). Red and blue symbols correspond to the first application and removal (n=1) of the magnetic field, respectively, while green symbols correspond to the measured adiabatic temperature changes under successively cycling the magnetic field (n>1). As it can be seen, there is a good coincidence between direct and quasidirect measurements, but directly measured ΔT values are lower than quasidirect ones. As mentioned before, this difference is mainly attributed to the fact that the thermocouple was attached to the sample surface, which worsens the thermal contact between the sample and sensor, an to a reduced adiabaticity.

In order to provide further reliability to the quasidirect estimates of the thermal response of Fe-Rh, it proves useful to compare them with previous direct isothermal entropy change measurements. Under isothermal conditions, calorimetric thermal curves recorded upon increasing and decreasing the magnetic field in the range $0 \rightleftarrows 6\,\mathrm{T}$ under a constant applied compressive stress of $\sigma = 100\,\mathrm{MPa}$ showed a good baseline and could be integrated, as discussed in section 3.1.2.1. These direct isothermal entropy change measurements were taken from reference [92].

The results for the direct isothermal entropy change measurements are shown as solid symbols in Figure 5.3 (b). Red and blue symbols correspond to the first application and removal of the magnetic field, respectively, while green symbols cor-

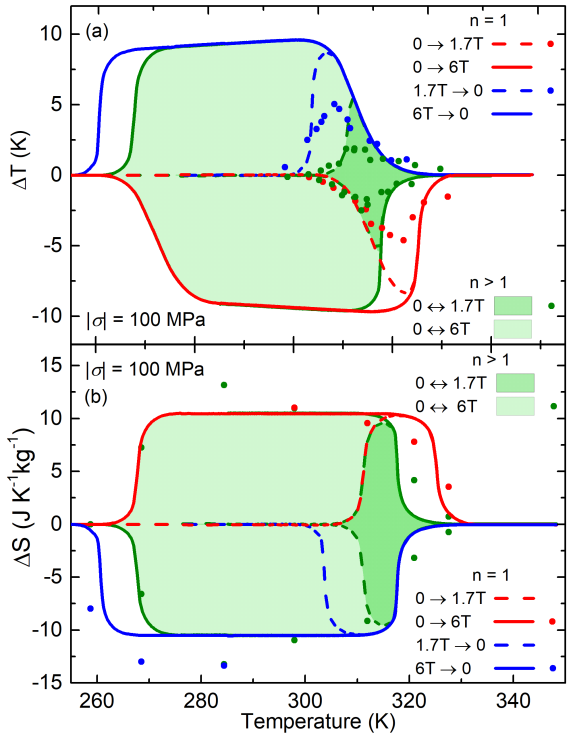

Figure 5.3: *Adiabatic temperature (a) and isothermal entropy (b) changes corresponding to the magnetocaloric effect under an applied uniaxial compressive stress of* 100 *MPa. Lines correspond to the quasidirect estimates computed from the entropy curves* $S(T, \mu_0 H, \sigma)$*, where dashed curves correspond to a magnetic field of* 1.7 *T and solid curves to a magnetic field of* 6 *T. Symbols stand for directly measured values, where isothermal entropy change data were taken from [92]. Red lines and symbols indicate the thermal response for the first (n=1) magnetic field application, blue lines and symbols correspond to the first (n=1) magnetic field removal, and green lines and symbols correspond to the successive field cycling. The green shaded areas represent the reversible regions for each magnetic field.*

respond to the measured isothermal entropy changes for successive cycles. Within experimental uncertainity, there is a good coincidence between both quasidirect estimates and direct measurements.

Furthermore, by comparing the directly measured data under a constant uniaxial compressive stress (represented in Figure 5.3) to data recorded in the absence of stress [114, 132], it is observed that application of uniaxial compressive stress shifts the thermal response of the sample without increasing its maximum values. This behaviour is similar, but of lower magnitude, to the effect of applying hydrostatic pressure [59], which is consistent with the pure dilation that takes place at the phase transition.

5.1.5 Elastocaloric effect in the absence of magnetic field

Given that the reliability of the quasidirect computation of the thermal response has been corroborated in the previous section, where direct measurements and quasidirect estimates of the magnetocaloric effect under a constant uniaxial compressive stress showed a good agreement, we have proceeded with the computation of the elastocaloric effect of Fe-Rh using the same procedure.

Even though previous isofield-isostress calorimetric measurements can not be properly integrated, a good approach to construct the corresponding isostress entropy curves in the absence of magnetic field, generally expressed as ($S(T, \mu_0 H = 0\,\mathrm{T}, \sigma)$), is to use a high-quality calorimetric measurement in the absence of stress and magnetic field [114] and assume, as in the previous section, that the effect of uniaxial compressive stress is a pure shift of the transition temperature without any significant change in its shape [38].

The isostress entropy curves, computed from the previous high-quality calorimetric measurement and the specific heat data from [126], in the absence of stress and under an applied compressive stress of 100 MPa are plotted in Figure 5.4 (a). It is important to highlight that the computation of these curves has assumed that the specific heat of both the AFM and FM phases does not exhibit any stress dependency.

From these curves, the quasidirect estimates of the adiabatic temperature ($\Delta T(S, \mu_0 H = 0\,\mathrm{T}, 0 \rightleftarrows 100\,\mathrm{MPa})$) and isothermal entropy ($\Delta S(T, \mu_0 H = 0\,\mathrm{T}, 0 \rightleftarrows 100\,\mathrm{MPa})$) changes are computed as described in section 3.1.1.2. The corresponding results are shown in Figures 5.4 (b) and (c), respectively. As illustrated by the red arrows in Figure 5.4 (a), the adiabatic application of compressive stress leads to a temperature increase whereas if it is isothermally applied, it leads to a decrease of the entropy. Therefore, as described in section 2.2.2, uniaxial compressive stress induces a conventional elastocaloric effect. In this regard, application of compressive stress shifts the transition temperature upwards, further stabilizing the AFM phase, and induces the FM to AFM phase transition (as a cooling process does), whereas removal of compressive stress shifts the transition temperature downwards, further stabilizing the FM phase, and induces the AFM to FM phase transition (as a heating process does). These two processes are illustrated as red and blue arrows in Figure 5.4 (a), respectively, where horizontal arrows stand for stress-induced adiabatic temperature changes and vertical ones stand for stress-induced isothermal entropy changes.

As previously mentioned, this result is in contrast with earlier adiabatic temperature change measurements under a tensile stress [54]. Such a different elastocaloric behaviour is in concordance with the promotion of the FM to AFM phase transition upon application of compressive stress and the promotion of the AFM to FM phase transition upon application of tensile stress.

The maximum stress-induced isothermal entropy change is $|\Delta S| = 7.9\,\mathrm{JK^{-1}kg^{-1}}$,

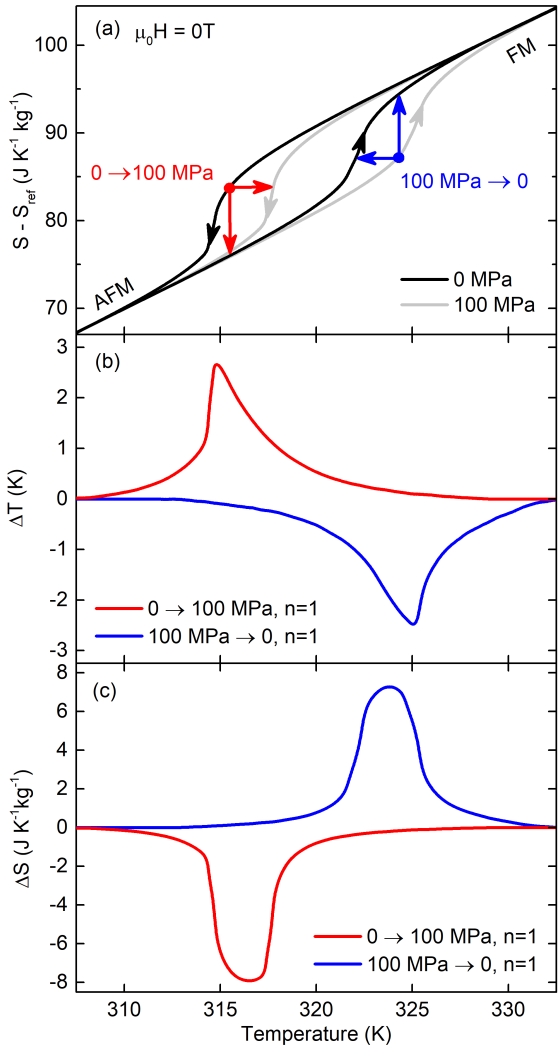

Figure 5.4: *(a) Entropy curves referenced to $S_{ref} = S(T = 250\,K)$ at zero (black curves) and at 100 MPa (grey curves) applied uniaxial compressive stress in the absence of magnetic field. Vertical and horizontal arrows indicate respectively the isothermal entropy and adiabatic temperature changes corresponding to the first (n=1) application and removal of a 100 MPa stress. The resulting adiabatic temperature and isothermal entropy changes are represented in panels (b) and (c), respectively. Red arrows and lines indicate the thermal response for the application of stress, whereas blue arrows and lines correspond to the removal of stress.*

which is lower than the transition entropy change determined from previous calorimetric measurements $|\Delta S_t| = 11\,\mathrm{JK^{-1}kg^{-1}}$ [92]. This difference indicates that a stress of 100 MPa is not enough to fully drive the phase transition. When consider-

ing the stress-induced adiabatic temperature change, a maximum of $|\Delta T| = 2.6\,\mathrm{K}$ is obtained. This value is similar to the adiabatic temperature change directly measured under a tensile stress of 150 MPa [54], but it is worth mentioning that direct measurements tend to be smaller than quasidirect estimates due to the difficulty of performing the measurements under adiabatic conditions [38].

Moreover, it is important to point out that the stress-induced thermal response is not expected to be reversible under stress cycling for the low-stress considered here. As it can be clearly seen in Figure 5.4 (a), a stress of 100 MPa is not enough to overcome the thermal hysteresis inherent to the first-order metamagnetic phase transition, which was found to be of $T_t^{AFM} - T_t^{FM} \sim 13\,\mathrm{K}$ from isofield-isostress calorimetric measurements [92]. For instance, we can compute the stress needed to overcome the thermal hysteresis by taking into account the transition temperature shift with uniaxial stress previously determined, and it can be estimated as $(T_t^{AFM} - T_t^{FM})\dfrac{d\sigma}{dT_t} \sim 430\,\mathrm{MPa}$.

5.1.6 Elastocaloric effect under a constant magnetic field

For the sake of completeness on the discussion of the combined effect of magnetic field and uniaxial compressive stress on the caloric properties of Fe-Rh, in the present section we discuss the effect of a constant magnetic field on the elastocaloric effect.

The corresponding isofield-isostress entropy curves, generally expressed as $S(T, \mu_0 H, \sigma)$, are constructed by following the same procedure described in section 5.1.4. Form these curves, we have computed the quasidirect estimates of the adiabatic temperature ($\Delta T(S, \mu_0 H, 0 \rightleftarrows 100\,\mathrm{MPa})$) and isothermal entropy ($\Delta S(T, \mu_0 H, 0 \rightleftarrows 100\,\mathrm{MPa})$) changes for applied magnetic fields of 0, 1.7 and 6 T. The corresponding results are shown in Figures 5.5 (a) and (b), respectively.

From these results, we observe that application of magnetic field shifts the stress-induced elastocaloric effect towards lower temperatures without modifying its overall magnitude. It is relevant to emphasize that application of moderate magnetic fields ($< 2\,\mathrm{T}$) enables to tune the elastocaloric effect within a temperature window of $\sim 20\,\mathrm{K}$. Although the elastocaloric effect is not expected to be reversible under compressive stress cycling for stresses below $\sim 430\,\mathrm{MPa}$, which corresponds the previously estimated effective hysteresis in stress, application of a secondary field can help us to obtain a reversible elastocaloric effect under stress cycling with lower stresses, as it has been proven that a secondary field can drastically reduce the effective hysteresis in the given external field [51, 63].

The reproducibility of a caloric effect under field cycling is an important feature for potential technological applications. A suitable combination of low stresses and low magnetic field can enhance the reversibility of the elastocaloric effect, and some estimates on its reproducibility and the required external fields can be made when considering the previously determined thermal hysteresis of $\sim 13\,\mathrm{K}$,

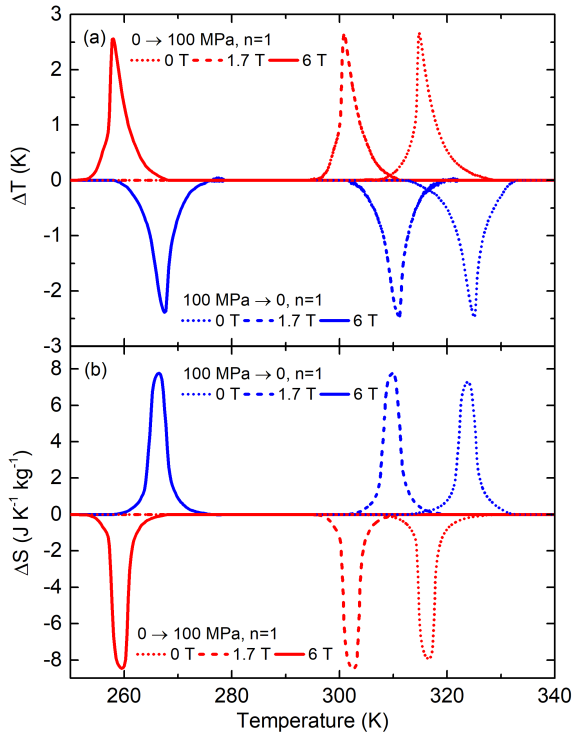

Figure 5.5: *Quasidirect estimates computed from the entropy curves $S(T, \mu_0 H, \sigma)$ of the adiabatic temperature (a) and isothermal entropy (b) changes corresponding to the elastocaloric effect without any applied magnetic field (dotted lines) and under a magnetic field of 1.7 T (dashed lines) and 6 T (solid lines). Red lines correspond to the thermal response for the first (n=1) stress application whereas blue lines correspond to the thermal response for the first (n=1) stress removal.*

together with representative values of the reported transition temperature shifts with magnetic field and stress, determined from the isofield-isostress calorimetric measurements reported in [92], which were found to be $\frac{dT_t}{d\mu_0 H} \sim -10\,\mathrm{KT}^{-1}$ and $\frac{dT_t}{d\sigma} \sim 0.03\,\mathrm{KMPa}^{-1}$, respectively. According to these results, Fe-Rh exhibits an effective hysteresis on magnetic field of $\sim 1.3\,\mathrm{T}$, and the magnetocaloric effect is expected to be reproducible for higher fields, whereas it exhibits an effective hysteresis on uniaxial compressive stress of $\sim 430\,\mathrm{MPa}$.

Application of a moderate magnetic field is enough to overcome the effective hysteresis, and the elastocaloric effect is expected to be reproducible under the sequence represented in Figure 5.6. In order to illustrate the sample fraction that can be reversibly driven across the phase transition, each panel of the sketched multicaloric cycle shows the corresponding sample fraction at the high-temperature FM phase as a function of temperature at the initial (dashed lines) and final (solid

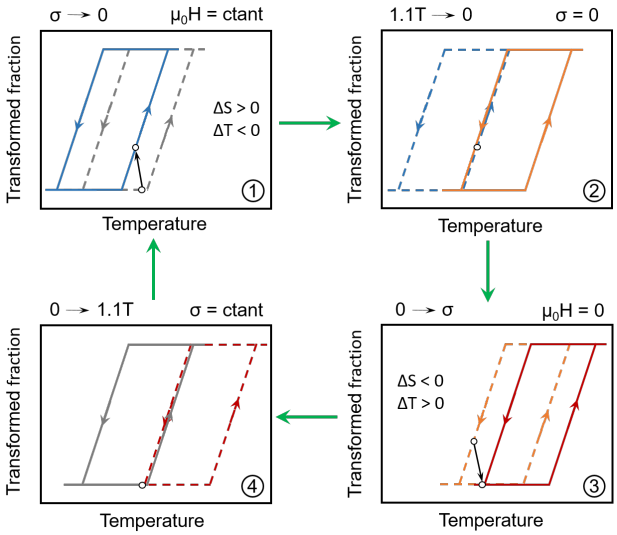

Figure 5.6: *Sketch of a multicaloric reversible cycle showing the fraction of the sample at the high-temperature FM phase as a function of temperature, for selected values of magnetic field and uniaxial stress. Panel 1: Removal of stress under an applied (constant) magnetic field. Panel 2: Removal of magnetic field in the absence of stress. Panel 3: Application of stress in the absence of magnetic field. Panel 4: Application of magnetic field under an applied (constant) stress.*

lines) configuration of applied compressive stress and magnetic field. Before the discussion of each cycle step, it is important to point out that partial hysteresis loops have not been considered for the sake of simplicity.

1. **Panel 1:**
   While keeping the magnetic field constant, removal of the compressive stress shifts the phase transition to lower temperatures (blue curves) and the sample, initially in the low-temperature AFM phase, partially transforms to the high-temperature FM phase, as indicated by the black arrow.

2. **Panel 2:**
   Removal of the 1.1 T applied magnetic field [2] shifts the phase transition to higher temperatures (orange curves) in a way that the state of the sample (in the absence of magnetic field and stress) lies on the cooling branch of the inherent hysteresis of the phase transition.

3. **Panel 3:**
   Application of the compressive stress shifts the phase transitions to higher

[2] The selected magnitude of the applied magnetic field is smaller than the field necessary to overcome the effective hysteresis, which would induce the back transformation to the low-temperature AFM phase.

temperatures (red curves) and the sample transforms back to the low-temperature AFM phase, as indicated by the black arrow.

4. **Panel 4:**
   Application of the magnetic field of 1.1 T shifts the phase transition to lower temperatures (grey curves) in a way that the state of the sample (under magnetic field and compressive stress) lies on the heating branch of the hysteresis loop, thus recovering the initial state of the first panel.

Furthermore, it is significant to highlight that T. Gottschall *et. al.* recently proposed a novel multicaloric cycle that takes advantage of the inherent hysteresis of materials exhibiting a first-order magnetostructural phase transition [64], termed as exploiting-hysteresis cycle. The behaviour observed for $Fe_{49}Rh_{51}$ under magnetic field and uniaxial compressive stress make it a suitable candidate to study its performance under this exploiting-hysteresis cycle, which will be discussed in greater detail in section 5.3.7.1.

5.1.7 Comparison of the elastocaloric properties of Fe-Rh with other caloric materials

Shape-memory alloys are prototype elastocaloric materials, and a thorough comparison of their properties with Fe-Rh will be provided in this section.

As discussed in detail in section 4.2, shape-memory alloys undergo a martensitic phase transition from a high-temperature cubic phase (austenite) towards a low-temperature phase with lower symmetry (martensite). The major contribution to the exchanged heat when inducing the first-order martensitic phase transition, which gives rise to the elastocaloric entropy change, comes from its associated latent heat [38, 39]. The category of shape-memory alloys is broad and includes non-magnetic materials, where the transition is purely structural, as well as magnetic materials, where the transition involves both a structural and magnetic order change. In the latter case, due to the sensitivity of the martensitic transition to diverse external fields, they are also prone to exhibit giant magnetocaloric [75] and barocaloric [32] effects. It is significant to point out that non-magnetic shape-memory alloys exhibit excellent mechanical properties, whereas most magnetic shape-memory alloys are brittle, which limits the supported stresses and decimates their mechanocaloric performance [38]. Nevertheless, recent reports have shown that colossal elastocaloric [206] and barocaloric [211] effects can be achieved for alloys composed of all-d-metal elements, which have superior mechanical properties.

There are a number of differences between the elastocaloric effect in Fe-Rh and the reported typical values of shape-memory alloys. First of all, the sensitivity of the transition temperature with stress is significantly lower for Fe-Rh, where we reported $\frac{dT_t}{d\sigma} \sim 0.03\,\mathrm{KMPa^{-1}}$, than for shape-memory alloys, for which typically $\frac{dT_t}{d\sigma} \sim 0.1 - 1\,\mathrm{KMPa^{-1}}$. This difference is a consequence of the lower uniaxial

strain exhibited by Fe-Rh at the phase transition, which can be estimated as $\Delta\varepsilon_t \approx \frac{1}{3}\frac{\Delta v}{v} \sim 0.33\,\%$, when compared to typical values for shape-memory alloys, around $\Delta\varepsilon_t \sim 3 - 10\,\%$ [38].

Secondly, it has been shown that the transition temperature of Fe-Rh increases when applying compressive stress, while it decreases when applying a tensile stress. Conversely, for shape-memory alloys the transition temperature increases for both tensile and compressive stresses. The different behaviour of the phase stability of Fe-Rh when applying compressive or tensile stresses gives rise to a conventional [65] or an inverse [54] elastocaloric behaviour, respectively, whereas for shape-memory alloys a conventional elastocaloric effect is observed for both compressive and tensile stresses.

The origin of this distinct behaviour between both materials arises from a different nature of the structural distortion that takes place at the phase transition. For instance, as discussed in section 4.1, the magnetostructural phase transition of Fe-Rh from the high-temperature FM phase to the low-temperature AFM phase does not involve a crystal symmetry breaking, as the lattice distortion corresponds to a pure dilation, which results in $\Delta\varepsilon_t < 0$ for both compressive and tensile stress. Conversely, the structural change that takes place at the martensitic phase transition of shape-memory alloys between the high-temperature cubic and the low-temperature lower symmetry phase involves a crystal symmetry breaking, and the lattice distortion can be described by a combination of shear and dilation strains. As discussed in section 4.2.1, symmetry enables a number of different deformations at the low-temperature martensite phase, which are called martensite variants, and under the application of an external field the formation of the specific variant that is energetically favoured is promoted. Accordingly, application of a compressive stress will lead to $\Delta\varepsilon_t < 0$ whereas application of a tensile stress will lead to $\Delta\varepsilon_t > 0$, as different martensite variants will be energetically favoured in each case [212].

Lastly, the quasidirect estimate of the maximum stress-induced isothermal entropy ($|\Delta S| = 7.9\,\mathrm{JK^{-1}kg^{-1}}$) and adiabatic temperature ($|\Delta T| = 2.6\,\mathrm{K}$) changes for Fe-Rh under a stress change of 100 MPa are lower than typical reported values for shape-memory alloys under similar stresses, where standard values of isothermal entropy and adiabatic temperature changes are in the ranges of $|\Delta S| = 10 - 20\,\mathrm{JK^{-1}kg^{-1}}$ and $|\Delta T| = 5 - 10\,\mathrm{K}$ respectively [38].

The similarities and differences in the stress-induced mechanocaloric properties of Fe-Rh, non-magnetic and magnetic shape-memory alloys are summarized in Table 5.1, and they provide a guide to anticipate the mechanocaloric effects of other caloric materials. Specifically, we will consider the case of La-Fe-Si, which undergoes a magnetostructural transition from a high-temperature paramagnetic (PM) phase to a low-temperature ferromagnetic (FM) phase. There is no symmetry change associated with the phase transition, as both phases have a cubic crystal structure ($Fm\bar{3}c$ space group), but a volume increase of $\sim 1\,\%$ takes place when the sample transforms from the high-temperature to the low-temperature phase. Due

Caloric effect	$Fe_{49}Rh_{51}$	SMA (non-magnetic)	SMA (magnetic)
BCE	C $\left(\frac{dT_t}{dp} > 0\right)$	$\left(\frac{dT_t}{dp} \sim 0\right)$	C $\left(\frac{dT_t}{dp} > 0\right)$
eCE (compressive, $\sigma < 0$)	C $\left(\frac{dT_t}{d\lvert\sigma\rvert} > 0\right)$	C $\left(\frac{dT_t}{d\lvert\sigma\rvert} > 0\right)$	C $\left(\frac{dT_t}{d\lvert\sigma\rvert} > 0\right)$
eCE (tensile, $\sigma > 0$)	I $\left(\frac{dT_t}{d\lvert\sigma\rvert} < 0\right)$	C $\left(\frac{dT_t}{d\lvert\sigma\rvert} > 0\right)$	C $\left(\frac{dT_t}{d\lvert\sigma\rvert} > 0\right)$

Table 5.1: *Mechanocaloric properties of selected materials. C and I refer to a conventional or an inverse caloric effect, respectively.*

to the volume and magnetization change exhibited, magnetic and mechanical fields can induce the magnetostructural transition. In this regard, giant magnetocaloric and barocaloric effects have been reported.

As a consequence of the larger volume of the low-temperature FM phase, application of hydrostatic pressure will further stabilize the high-temperature PM phase, leading to an inverse barocaloric effect [78], whereas application of magnetic field will further stabilize low-temperature FM phase, leading to a conventional magnetocaloric effect [213].

Accordingly, it can be anticipated that application of a compressive stress will further stabilize the high-temperature low-volume PM phase, leading to an inverse elastocaloric effect, whereas application of a tensile stress will further stabilize the low-temperature high-volume FM phase, leading to a conventional elastocaloric effect. Moreover, as uniaxial stress is not the conjugated field for a volume change, it is also reasonable to expect a lower sensitivity of the phase transition to uniaxial stress than to hydrostatic pressure.

5.1.8 Summary and conclusions

We have used a bespoke setup to directly measure the adiabatic temperature change of $Fe_{49}Rh_{51}$ induced under the simultaneous application of cyclic magnetic field and constant uniaxial compressive stress. Consistently with previous measurements, the field-induced magnetocaloric effect shows an inverse nature. When comparing these results with previously reported data in the absence of stress, we observe that the application of uniaxial compressive stress shifts the magnetocaloric thermal response to higher temperatures. This effect is consistent with a further stabilization of the low-temperature AFM phase for compressive stresses.

Despite the lack of high-quality isofield-isostress calorimetric measurements, the corresponding entropy curves were computed from previous isofield entropy curves in the absence of stress, where the effect of compressive stress was taken as a pure shift of the transition temperature. A good concordance between direct mea-

surements and the quasidirect estimates, obtained from the constructed isofield-isostress entropy curves, of the magnetocaloric effect under a constant uniaxial stress was found, providing reliability to the quasidirect computation of the thermal response and to the construction method of the entropy curves.

A similar procedure was followed to construct the isostress entropy curves from previous high-quality calorimetric measurements in the absence of stress and magnetic field together with previously reported specific heat measurements. The quasidirect estimates of the elastocaloric effect showed a maximum stress-driven isothermal entropy change of $|\Delta S| = 7.9\,\mathrm{JK^{-1}kg^{-1}}$ under a stress change of 100 MPa, which is lower than the transition entropy change and indicates that higher compressive stresses are needed in order to fully drive the phase transition. Furthermore, a maximum stress-driven adiabatic temperature change of $|\Delta T| = 2.6\,\mathrm{K}$ was computed. However, it is important to point out that the elastocaloric effect is not expected to be reversible for stresses below $\sim 430\,\mathrm{MPa}$.

The present results show that $Fe_{49}Rh_{51}$ exhibits a conventional elastocaloric effect under compressive stresses, whereas an inverse elastocaloric effect was previously reported under tensile stresses. This difference arises from a distinct behaviour of the magnetostructural phase transition under compressive or tensile stresses. For instance, compressive stress stabilizes the low-temperature AFM phase, increasing the transition temperature, whereas tensile stress stabilizes the high-temperature FM phase, decreasing the transition temperature.

For the sake of completeness, a thorough characterization of the thermal response of $Fe_{49}Rh_{51}$ when subjected to the combined action of uniaxial compressive stresses and magnetic field has been provided. No significant increase of the maximum field-induced thermal response corresponding to the magnetocaloric and elastocaloric effects has been observed when applying a secondary non-conjugated external field. Nevertheless, it is important to highlight that application of a secondary field shifts the temperature window where the giant elastocaloric and magnetocaloric effect occur.

It has been shown that the sensitivity of the phase transition to a secondary field enables tuning the inherent hysteresis of the metamagnetic phase transition, and the combined action of two fields opens up the possibility of further boosting the potential interest of Fe-Rh for diverse technological applications. In particular, an enhancement of the reversibility of the field-induced thermal response of $Fe_{49}Rh_{51}$, together with a decrease of the needed external fields for such purposes, can be achieved by a suitable combination of magnetic field and uniaxial compressive stress.

5.2 Ni-Fe-Co-Mn-Sn

Many of the reported Ni-Mn-based magnetic shape-memory alloys exhibiting a strong metamagnetic transition and a large elastocaloric effect still require the application of large driving fields to induce giant caloric effects. Moreover, they display an inadequate cyclic stability of the elastocaloric effect for technological applications [208, 209, 214]. Therefore, it is imperative to develop Ni-Mn-based shape-memory alloys simultaneously exhibiting a strong metamagnetic transition that requires low driving magnetic fields, accessible by permanent magnets, together with a cyclically stable giant elastocaloric effect. Ni-Co-Mn-Sn-based alloys are suitable candidates for these purposes, as they exhibit relatively good mechanical properties together with a large transition entropy change arising from a first-order metamagnetic phase transition taking place between a high-temperature ferromagnetic austenitic phase and a low-temperature low-magnetization martensitic phase [215, 216], anticipating a good mechanical stability upon cyclic operation together with a large field-induced caloric effect. Moreover, the low cost of the different raw materials that conform this alloy, together with the fact that there are no toxic constituents, make it an appealing candidate for diverse technological applications.

Nevertheless, the martensitic phase transition of Ni-Co-Mn-Sn-based alloys occurs above room temperature [216], and for the sake of multifunctional applications it is highly convenient to develop Heusler alloys where the phase transition takes place near room temperature. In this regard, it has been shown that the substitution of Ni by Fe rapidly decreases the martensitic transition temperature together with its associated transition entropy change, without significantly affecting the austenitic Curie temperature [61]. For Fe concentrations up to 1 at%, the martensitic transition temperature can be tuned within a broad temperature window of $\sim 100\,\mathrm{K}$ while keeping a relatively large transition entropy change. Furthermore, for these low Fe concentrations, the associated thermal hysteresis of the martensitic phase transition, as well as its temperature width, are not significantly modified while the alloy keeps exhibiting a strong metamagnetic phase transition that requires low driving magnetic fields. Therefore, we have selected a Ni-Fe-Co-Mn-Sn alloy with low Fe concentration as a suitable candidate for multifunctional applications.

The present work on this alloy has a twofold objective. On the one hand, it is aimed at providing a detailed characterization of the giant magnetocaloric effect. On the other hand, it is intended to confer reliability on the different methods used to compute the field-induced magnetocaloric and multicaloric effects. Specifically, a comparison between direct measurements and two different indirect estimates of the field-induced magnetocaloric effect is provided, where the first indirect method consists on the application of the Maxwell relation to isothermal $M(H)$ curves reported in [61] and the second one is based on a phenomenological model described in detail in [63] to simulate the austenite transformed fraction and compute the corresponding caloric or multicaloric effects.

5.2.1 Sample details

The experiments were performed on a polycrystalline $Ni_{42.5}Fe_{1.0}Co_{6.5}Mn_{39.5}Sn_{10.5}$ sample prepared by arc melting with dimensions $2.1 \times 1.9 \times 0.5\,mm^3$ and a mass of 11.7 mg, shaped as a parallelepiped. This sample was fabricated at the University of Science and Technology, Beijing (China), and details of the sample preparation and heat treatment are given in [61].

5.2.2 Experimental details

1. A previous calorimetric characterization of the first-order martensitic phase transition in the absence of any applied external field was performed by means of a DSC Q2000 setup from *TA Instruments*®, at a scanning rate of $\pm 5\,K min^{-1}$.

2. Isothermal calorimetric measurements have been performed with the bespoke DSC setup described in section 3.1.3 under a cyclic external magnetic field in the range $0 \rightleftarrows 6\,T$, with typical scanning rates of $\frac{d\mu_0 H}{dt} \sim 0.32\,T min^{-1}$. From these measurements, as discussed in section 3.1.1.1, the field-induced entropy change can be directly computed.

   Following the measurement protocols described in section 3.1.2.1, suitable thermal excursions were performed prior to each measurement to control the initial thermodynamic state of the sample. Afterwards, the sample was brought to the desired measurement temperature, which was selected within the range $T \in [250, 295]\,K$ for all measurements.

5.2.3 Calorimetric characterization of the phase transition in the absence of external fields

Before characterizing the first-order martensitic phase transition of Ni-Fe-Co-Mn-Sn under the application of an external magnetic field with a bespoke DSC setup, it is useful to perform a previous measurement in the absence of any applied external field with a commercial DSC setup. The corresponding recorded thermograms for heating and cooling runs are illustrated in Figure 5.7.

The latent heat associated with the martensitic phase transition gives rise to an exothermal (negative) peak when inducing the forward transition (cooling), and to an endothermal (positive) peak when inducing the reverse transition (heating). Interestingly, the recorded calorimetric peaks look very different between both thermograms. While a smooth peak is recorded upon heating, a spiky calorimetric peak is observed upon cooling. As discussed in section 4.2.1, the forward martensitic phase transition is driven by the formation of martensite nuclei in the austenite matrix, and the spikes observed in calorimetry are due to their avalanche-like growth [217].

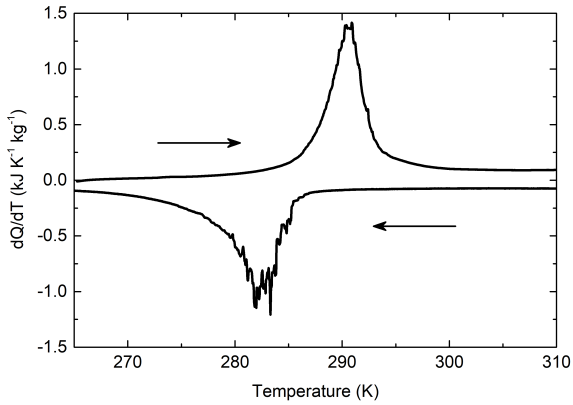

Figure 5.7: *Calorimetric signal as a function of temperature recorded upon heating (positive peak) and cooling (negative peak), measured at a scanning rate of* $\pm 5\,Kmin^{-1}$ *with a DSC Q2000 from TA Instruments®*

As discussed in section 3.1.1, the corresponding transition entropy changes (ΔS_t) can be computed after a proper baseline correction. For these thermograms, the baseline signal can be accurately approximated by a straight line, fitted before and after the temperature range where the calorimetric peak spreads $[T_s, T_f]$. This straight line defines the baseline signal of the complete thermogram, and the corresponding transition entropy changes for the forward and reverse martensitic transition are found to be $\Delta S_t^M = (-19.5 \pm 0.5)\,\mathrm{JK^{-1}kg^{-1}}$ and $\Delta S_t^A = (20.3 \pm 0.5)\,\mathrm{JK^{-1}kg^{-1}}$. Moreover, the calorimetric peak position of each thermogram defines its transition temperature, which are found to be $T_t^M = 282.5\,\mathrm{K}$ and $T_t^A = 290.7\,\mathrm{K}$ respectively, defining a thermal hysteresis of $T_t^M - T_t^A = 8\,\mathrm{K}$ in the absence of external fields.

5.2.4 Isothermal calorimetric measurements

As discussed in section 3.1.1.1, isothermal DSC calorimetry is a unique tool to directly measure the field-induced isothermal entropy change of a sample when scanning the external field. Moreover, these measurements allow us to determine the reversible and irreversible field-induced caloric effect under a cyclic external field profile, and the reproducibility of the caloric effect can be studied.

In the present case, we performed isothermal DSC measurements under a cyclic magnetic field. As previously discussed in section 3.1.2.1, in order to properly measure the reversible and irreversible contributions, suitable temperature paths have to be performed before the measurement start in order to control the sample's initial state. Previous magnetization measurements in Ni-Co-Mn-Sn-based shape-memory alloys showed that the transition temperature shifts to lower values when an external magnetic field is applied $\left(\dfrac{dT_t}{d\mu_0 H} < 0\right)$ [207, 216], leading to an inverse magnetocaloric effect. Therefore, the measurement protocols described in section

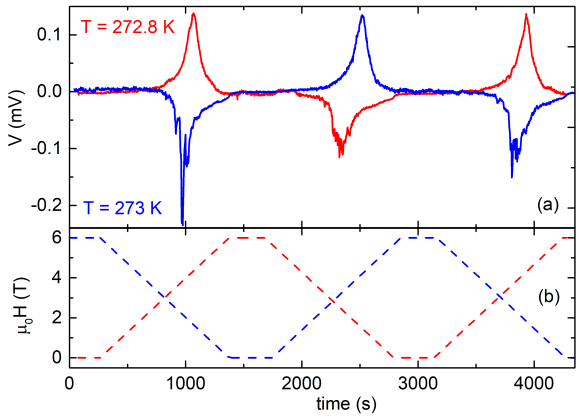

Figure 5.8: *Isothermal calorimetric signal at selected temperatures (a) and the corresponding cyclic magnetic field (b) for the heating (red lines) and cooling (blue lines) protocols as a function of time.*

3.1.2.1 that correspond to an inverse caloric effect were followed. In this regard, to characterize the thermal response when inducing the martensite to austenite (reverse) phase transition (heating protocol), the sample is initially fully transformed to the the low-temperature martensitic phase in the absence of magnetic field, and then it is heated up to the desired measurement temperature. Once it is at isothermal equilibrium, the magnetic field is cycled starting with a $0 \rightarrow 6\,\mathrm{T}$ scan. By contrast, to characterize the austenite to martensite (forward) phase transition (cooling protocol), the sample is initially fully transformed to the high-temperature austenitic phase and then it is cooled down, under a constant applied magnetic field, to the desired measurement temperature. Once the isothermal equilibrium is reached, the magnetic field is cycled starting with a $6\,\mathrm{T} \rightarrow 0$ scan. Figure 5.8 illustrates examples of the raw isothermal DSC thermograms (top) and magnetic field (bottom) measurements recorded upon cycling the magnetic field in the range $0 \rightleftarrows 6\,\mathrm{T}$ for the heating (red lines) and cooling (blue lines) protocols.

Both measurements show a good reversibility of the isothermal calorimetric signal under successive magnetic field scans. When cyclically field-inducing the martensitic phase transition, the associated latent heat gives rise to an exothermal (negative) peak when the forward transition is induced (decreasing the magnetic field) and to an endothermal (positive) peak when the reverse transition is induced (increasing the magnetic field). This is in accordance with the stabilization of the austenitic phase under the application of magnetic field, which is in accordance with the expected behaviour for a material exhibiting an inverse magnetocaloric effect.

As discussed in section 3.1.1.1, the measured isothermal DSC thermograms must be properly corrected in order to compute the reversible and irreversible field-induced isothermal entropy changes. For such purpose, the measured raw calorimetric signal is analysed separately for each magnetic field scan, and the corrected

calorimetric signal is computed as:

$$\frac{dQ}{d\mu_0 H} = \frac{\dot{Q}(T, \mu_0 H)}{\mu_0 \dot{H}} = \frac{Y(T, \mu_0 H) dt}{S(T) d\mu_0 H} \tag{5.3}$$

where $Y(T, \mu_0 H)$ corresponds to the raw calorimetric signal and $S(T)$ to the DSC sensitivity previously determined.

Figure 5.9 displays the complete set of corrected isothermal DSC thermograms at selected temperatures for the cooling (left) and heating (right) measurement protocols. Panels (a) and (c) display the recorded thermograms during the first magnetic field scan (n=1), whereas panels (b) and (d) display the corresponding thermograms during the second magnetic field scan (n=2).

When comparing the measured isothermal calorimetric signal between the first and second magnetic field scans for each measurement protocol, we observe that there is a good reversibility of the field-induced martensitic transition for a broad temperature range. The calorimetric peak of the different thermograms defines the magnetic field necessary to drive the martensitic phase transition at each temperature. As it can be seen, a higher magnetic field is necessary when decreasing the measurement temperature, which is consistent with the inverse nature of the magnetocaloric effect.

It is possible to determine the equilibrium lines of the forward (T_t^M) and reverse (T_t^M) phase transitions from each measurement temperature and the magnetic field at the calorimetric peak, deduced from the first magnetic field scan of the cooling and heating protocols, respectively. These results are illustrated in Figure 5.9 (e) as solid symbols. Additionally, the transition temperatures deduced from isofield magnetization measurements $M(T)$ reported in [207] are represented as open symbols.

Both data sets show a good agreement for both forward and reverse transitions, exhibiting a thermal hysteresis of $T_t^M - T_t^A = 9\,\mathrm{K}$ at low magnetic fields of $\mu_0 H = 1\,\mathrm{T}$ that increases up to $T_t^M - T_t^A = 11\,\mathrm{K}$ at $\mu_0 H = 5\,\mathrm{T}$. From the linear fits fitted to the solid symbols, the rates at which the first-order martensitic phase transition shifts under the application of magnetic field are determined to be $\frac{dT_t^M}{d\mu_0 H} = (-4.99 \pm 0.06)\,\mathrm{KT}^{-1}$ and $\frac{dT_t^A}{d\mu_0 H} = (-4.58 \pm 0.08)\,\mathrm{KT}^{-1}$, which are in good agreement with previous reported values for composition-related Ni-Mn-Co-Sn-based alloys [207, 218].

5.2.5 Direct computation of the magnetocaloric effect

As discussed in section 3.1.1.1, from each isothermal DSC thermogram measured at a certain temperature T, the corresponding magnetic field-induced isothermal entropy change is computed as:

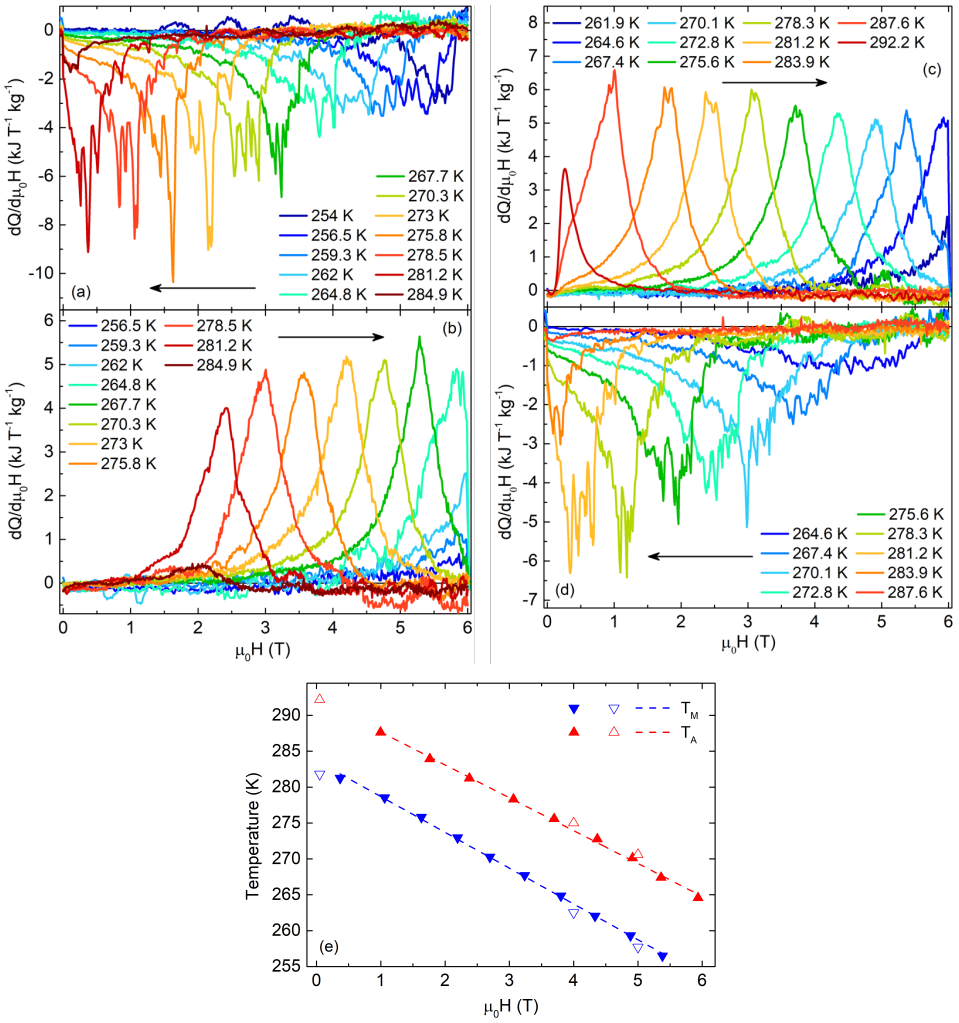

Figure 5.9: *Isothermal calorimetric curves obtained by scanning the magnetic field in the range* $0 \rightleftarrows 6$ *T for the cooling (left) and heating (right) protocols at selected temperatures. Panels (a) and (c) correspond to the calorimetric curves recorded under the first magnetic field scan (n=1), whereas panels (b) and (d) correspond to the calorimetric curves recorded under the second magnetic field scan (n=2). Arrows in each panel indicate whether the magnetic field is applied or removed. (e) Transition temperature as a function of magnetic field for the forward* (T_M) *and reverse* (T_A) *transitions. Solid symbols correspond to the temperatures obtained from the isothermal calorimetric peaks and open symbols correspond to the values obtained from the isofield magnetization curves* ($M(T)$) *reported in [61]. Dashed lines correspond to linear fits to the solid symbols.*

$$\Delta S(T, \mu_0 H_s \rightarrow \mu_0 H_f) = \int_{\mu_0 H_s}^{\mu_0 H_f} \frac{1}{T} \left(\frac{dQ(T, \mu_0 H')}{d\mu_0 H'} - \zeta(T, \mu_0 H') \right) d\mu_0 H' \quad (5.4)$$

where $\mu_0 H_s$ and $\mu_0 H_f$ correspond to the start and finish integration magnetic fields, taken before and after the phase transition calorimetric peak, $\zeta(T, \mu_0 H)$ corresponds to the baseline signal and $\frac{dQ(T, \mu_0 H)}{d\mu_0 H}$ to the corrected calorimetric signal.

As it can be seen for the complete set of isothermal DSC thermograms illustrated in Figure 5.9 (a)-(d), the baseline has much lower values than the magnitude of the respective calorimetric peaks. The behaviour observed for these measurements is in contrast to that observed for previous isofield DSC measurements, where the baseline signals were significant. As discussed in section 3.1.1.1, the fact that the temperature of the calorimeter is kept constant during isothermal measurements reduces the magnitude of the heat flux coming from the specific heat difference between the sample and reference, and improves the signal-to-baseline ratio.

For these measurements, the baseline signal is approximated by a straight line, fitted before and after the magnetic field range where the calorimetric peak spreads $[\mu_0 H_s, \mu_0 H_f]$. This straight line defines the baseline signal of the complete thermogram, and the corresponding field-induced isothermal entropy changes are computed after subtracting the respective baseline from each thermogram.

Figure 5.10 illustrates the isothermal entropy changes induced under three consecutive magnetic field scans in the range $0 \rightleftarrows 6\,\mathrm{T}$ as a function of the measurement temperature for the heating (red symbols) and cooling (blue symbols) measurement protocols.

When looking at the field-induced magnetocaloric isothermal entropy change obtained for the first magnetic field scan (n=1), we observe that it saturates at a constant value, indicating that we are able to fully induce the phase transition with the applied or removed magnetic field within a temperature range of $\sim 20\,\mathrm{K}$. For instance, the saturation value for the forward and reverse martensitic transition are $\Delta S = (-18 \pm 1)\,\mathrm{JK^{-1}kg^{-1}}$ and $\Delta S = (19 \pm 1)\,\mathrm{JK^{-1}kg^{-1}}$, respectively, which are in good agreement with the forward and reverse transition entropy changes determined with the commercial DSC in the absence of magnetic field. Furthermore, the fact that the field-induced isothermal entropy change shows a constant saturation value within a broad temperature range indicates that, within the error, the transition entropy change of this alloy does not show a significant dependence on the applied magnetic field. This behaviour is in agreement with that observed for isofield magnetization measurements $M(T)$ reported in [207], where the magnetization change across the phase transition does not show a significant dependence on the applied magnetic field.

When considering the entropy change induced under successive magnetic field scans (n>1), we observe that the magnetocaloric effect displays an excellent reproducibility, and the martensitic phase transition can be reversibly driven within a temperature range of $\sim 15\,\mathrm{K}$.

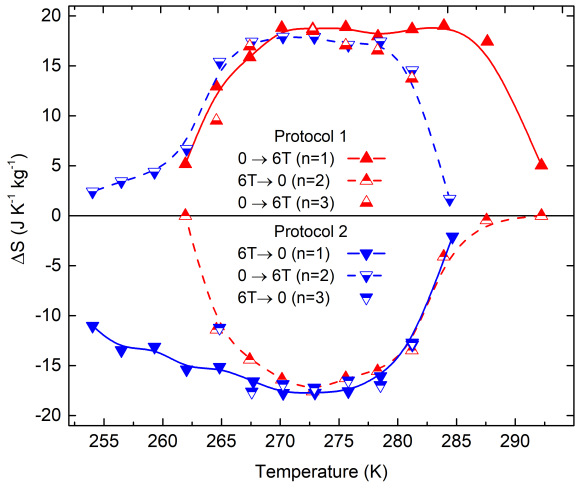

Figure 5.10: *Isothermal entropy change corresponding to the application and removal of a 6 T magnetic field as a function of temperature. Symbols correspond to the computed results from the isothermal calorimetric curves for the heating (red) and cooling (blue) protocols and lines are guides to the eye. Solid symbols correspond to the first magnetic field scan (n=1), while half-solid symbols correspond to successive field scans (n>1) for each protocol.*

In order to study the potential of Ni-Mn-Co-Sn-based alloys for future technological applications, it is interesting to characterize its magnetocaloric effect exhibited under the cyclic application and removal of a low magnetic field in the range $0 \rightleftarrows 2\,\mathrm{T}$. For this purpose, the corrected isothermal DSC thermograms presented in Figure 5.9 (a) and (c) can be analysed within this reduced magnetic field range (omitting the thermal response recorded for higher magnetic fields). The corresponding field-induced isothermal entropy changes are computed applying equation 5.4, and the same procedure is applied in order to correct the background signal.

Figure 5.11 illustrates the isothermal entropy changes induced under the first magnetic field scan (n=1) in the range $0 \rightleftarrows 2\,\mathrm{T}$ as a function of the measurement temperature for the heating (red solid symbols) and cooling (blue solid symbols) measurement protocols. Due to the reduction of the considered magnetic field range, it is important to point out that the isothermal entropy changes induced under successive magnetic field scans (n>1) have not been computed from the thermograms illustrated in Figure 5.9 (b) and (d), as the end state after the first reduced magnetic field scan may be different than the end state after the complete magnetic field scan, inducing some partial hysteresis loops that can affect the initial state of the sample before the second reduced magnetic field scan.

The maximum field-induced isothermal entropy change for the forward and reverse martensitic transition are $\Delta S = (-17 \pm 1)\,\mathrm{JK^{-1}kg^{-1}}$ and $\Delta S = (17 \pm 1)\,\mathrm{JK^{-1}kg^{-1}}$, respectively, which are slightly lower than previously determined values when considering the complete magnetic field scanning range. The lack of sat-

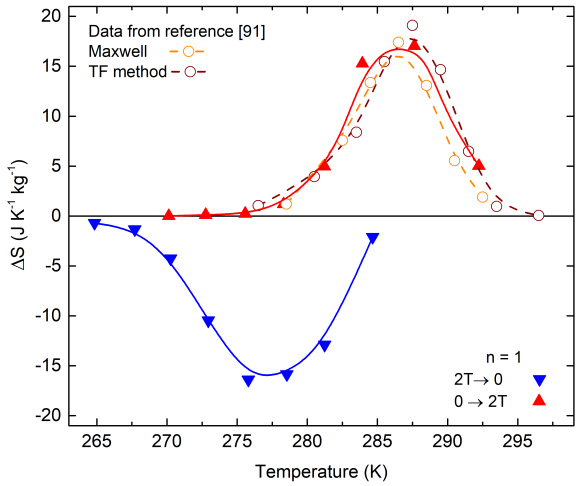

Figure 5.11: *Isothermal entropy change corresponding to the application and removal of a 2 T magnetic field as a function of temperature. Solid symbols correspond to the computed results from the isothermal calorimetric curves for the heating (red) and cooling (blue) protocols, whereas open symbols correspond to the computed results from the Maxwell relation (orange) and the transformed fraction method (wine) based on $M(H)$ data reported in reference [61]. The different represented lines are guides to the eye for each data series.*

uration indicates that a magnetic field change of $|\mu_0 \Delta H| = 2\,\mathrm{T}$ falls a little bit short to fully drive the martensitic phase transition. For the sake of completeness, two different indirect methods have been used to estimate the field-induced isothermal entropy change. On the one hand, isothermal magnetization curves ($M(H)$) reported in [61] have been used to compute the field-induced isothermal entropy change based on the Maxwell relation for the magnetocaloric effect. The corresponding results have been added to Figure 5.11 as orange open symbols. On the other hand, a phenomenological model described in detail in [63] to simulate the austenite transformed fraction has been used to compute the corresponding field-induced isothermal entropy change, and the results obtained have been added to Figure 5.11 as wine open symbols.

As it can be seen, within experimental errors, there is a good coincidence between the directly measured field-induced isothermal entropy change and the computed estimates from both indirect methods.

5.2.6 Summary and conclusions

We have used a bespoke setup to directly measure the isothermal DSC thermograms of $Ni_{42.5}Fe_{1.0}Co_{6.5}Mn_{39.5}Sn_{10.5}$ under a cyclic magnetic field in the range $0 \rightleftarrows 6\,\mathrm{T}$. From the calorimetric peaks of these thermograms, we built the corresponding phase diagram of the transition temperatures under an applied magnetic field, verifying that this alloy exhibits an inverse magnetocaloric effect, in agreement

with the behaviour observed for previous isofield magnetization measurements.

After a proper baseline correction of the recorded field-induced isothermal DSC thermograms, integration of the corresponding calorimetric peaks allows us to directly compute the reproducible field-induced isothermal entropy changes. When the magnetic field is cycled within the range $0 \rightleftarrows 6\,\mathrm{T}$, the field-induced isothermal entropy change saturates at $\Delta S = (-18 \pm 1)\,\mathrm{JK^{-1}kg^{-1}}$ and $\Delta S = (19 \pm 1)\,\mathrm{JK^{-1}kg^{-1}}$ for the forward and reverse transitions, respectively. Such saturation indicates that we are able to fully induce the martensitic phase transition within a temperature range of $\sim 20\,\mathrm{K}$. Furthermore, the field-induced isothermal entropy change shows an excellent reproducibility for subsequent magnetic field scans within a temperature window of $\sim 15\,\mathrm{K}$, indicating that the complete martensitic phase transition can be reversibly driven within that temperature range.

Furthermore, when considering future technological applications, it is interesting to characterize the field-induced magnetocaloric effect under the application and removal of a low magnetic field, which can be provided by permanent magnets, in the range $0 \rightleftarrows 2\,\mathrm{T}$. To address this issue, we analysed the measured isothermal DSC thermograms within the reduced magnetic field range, and the maximum field-induced isothermal entropy change for the forward and reverse martensitic transition are $\Delta S = (-17 \pm 1)\,\mathrm{JK^{-1}kg^{-1}}$ and $\Delta S = (17 \pm 1)\,\mathrm{JK^{-1}kg^{-1}}$, respectively. These values are slightly smaller than the saturation field-induced isothermal entropy change values previously determined, indicating that the considered low magnetic field is not enough to fully induce the martensitic phase transition. Significantly, these direct measurements show an excellent agreement with the indirect estimates computed from two different methods currently used in the analysis of magnetocaloric materials, where the first one consists on the application of the corresponding Maxwell relation on isothermal magnetization measurements and the second one consists on the simulation of the austenite transformed fraction based on a phenomenological model.

The good agreement between these three data sets provides reliability to the indirect estimates of the field-induced magnetocaloric effect, allowing to compute further indirect estimates of the field-induced multicaloric thermal response from the phenomenological model.

5.3 Ni-Mn-In

As discussed in Chapters 2 and 4, materials with a strong coupling between different degrees of freedom are prone to exhibit a cross-response to different external stimuli. In those materials, entropy and temperature changes can be driven by either a single stimulus (single caloric effect) or by multiple stimuli (multicaloric effect), which can be applied/removed either simultaneously or sequentially [51, 53]. The study of multicaloric materials and effects is a quite novel research field and very interesting and significant results have already been achieved [57–61, 63–65].

However, the study of multicaloric effects is still challenging. Although the theoretical thermodynamic framework is well established [52, 53], [3] experimental studies are scarce as the obtention of the physical properties quantifying these multicaloric effects requires the development of non-commercial advanced characterization systems [65, 66, 88].

Taking advantage of the experience gained from the analysis of the Cu-Zn-Al calibration sample presented in section 3.3, we have used the same purpose-built DSC setup described in section 3.1.4 to study the caloric and multicaloric response in terms of the isothermal entropy and adiabatic temperature changes of a prototype Ni-Mn-based magnetic shape-memory alloy subjected to the combined effect of magnetic field and uniaxial compressive stress. Specifically, we have selected a Ni-Mn-In alloy with a martensitic transition temperature close to the austenitic Curie temperature. The proximity between both phase transitions in this alloy anticipates a pronounced coupling between the structural and magnetic degrees of freedom, so that application of magnetic field has a strong influence on the martensitic transition.

The present work on this alloy has a twofold objective. On the one hand, it is aimed at thoroughly characterizing the advantages of the multicaloric effect with respect to the single caloric (magnetocaloric and elastocaloric) effects. On the other hand, the present work is intended to test the technical feasibility of a novel multicaloric cycle proposed by T.Gottschall *et. al.* in [64], and compare its performance with respect to the results obtained under a conventional magnetic field refrigeration cycle.

5.3.1 Sample details

The experiments were performed on a sample with nominal composition $Ni_{50}Mn_{35.5}In_{14.5}$ prepared by arc melting, and further treated using the suction-casting option of the arc melter. This sample was fabricated at the Technical University of Darmstadt, Darmstadt (Germany), and details of the sample preparation and heat treatment are given in [64].

[3] See section 2.1.2 for a detailed discussion on the thermodynamic framework of multicaloric effects.

A sample, shaped as a rod, with 3 mm diameter and 5.5 mm length that had a mass of 301.7 mg was cut from the ingot prepared by arc melting. A small piece was cut from the sample (12.62 mg) to perform a previous characterization with a commercial DSC in the absence of any applied external field. The remaining part of the sample, with 3 mm diameter and 4.9 mm length (268.8 mg), was polished and used to perform both differential scanning calorimetry and adiabatic temperature change measurements under the influence of magnetic field and uniaxial stress. Thermomagnetization and specific heat measurements were performed on smaller pieces cut from the initial ingot.

5.3.2 Experimental details

1. A previous calorimetric characterization of the first-order martensitic phase transition in the absence of any applied external field was performed by means of a DSC Q2000 setup from *TA Instruments*®, at a scanning rate of $\pm 5\,\mathrm{K min^{-1}}$.

2. The magnetic measurements were made on a commercial PPMS from *Quantum Design*®, using the vibrating sample magnetometer mode, in the absence of any applied uniaxial compressive stress at a temperature scanning rate of $\pm 2\,\mathrm{K min^{-1}}$.

3. Simultaneous dilatometric and DSC measurements have been performed with the bespoke DSC setup described in section 3.1.4 at typical temperature scanning rates of $\pm 0.5\,\mathrm{K min^{-1}}$ within a temperature range $T \in [260,\ 315]\,\mathrm{K}$ under constant values of uniaxial compressive stress $\{\sigma_i\} = \{0,\ 10,\ 20,\ 30,\ 40,\ 50\}\,\mathrm{MPa}$ and magnetic field $\{\mu_0 H_j\} = \{0,\ 1,\ 2,\ 3,\ 4,\ 5,\ 6\}\,\mathrm{T}$.

   The applied compressive stresses required the application of forces $\{F_i\} = \{0,\ 68,\ 137,\ 205,\ 273,\ 342\}\,\mathrm{N}$ to the sample. Therefore, as discussed in detail for Cu-Zn-Al in section 3.3, as $F_i < 400\,\mathrm{N}$ it is not necessary to introduce a stress sensitivity factor to correct the DSC thermograms and compute the corresponding transition entropy changes, as any possible deviation on the calorimetric signal from the effect of the applied stress on the bespoke setup would fall within the experimental error.

4. Direct measurements of the adiabatic temperature change have been performed with the bespoke setup described in section 3.2.2. Two different sets of measurements were performed by following the continuous and discontinuous measurement protocols, [4] respectively.

   In the former case, the sample was continuously heated in the background with a rate of $0.25\,\mathrm{K min^{-1}}$ while single alternate pulses of of magnetic field $0 \rightleftarrows 1.8\,\mathrm{T}$ and uniaxial stress $0 \rightleftarrows 80\,\mathrm{MPa}$ were applied. In the latter

[4] See section 3.2.1 for detailed descriptions of both measurement protocols

case, measurements following the discontinuous measurement protocol were performed under a cyclic magnetic field in the range $0 \rightleftarrows 1.64\,\mathrm{T}$ in the absence of stress and under a constant compressive stress of $\sigma = 40\,\mathrm{MPa}$.

5. Specific heat measurements of the martensitic and austenitic phases were performed using two different systems. On the one hand, a bespoke AC calorimeter [219] was used to perform measurements at temperatures up to 310 K under constant applied magnetic fields $\{\mu_0 H_j\} = \{0, 1, 2\}\,\mathrm{T}$. On the other hand, a commercial relaxation calorimeter implemented in a PPMS from *Quantum Design*® was used to measure at temperatures up to $T = 380\,\mathrm{K}$ under constant applied magnetic fields $\{\mu_0 H_j\} = \{0, 1, 2, 3, 4\}\,\mathrm{T}$.

5.3.3 Characterization of the martensitic phase transition with commercial devices

Before characterizing the first-order martensitic phase transition of Ni-Mn-In with our bespoke setups under the influence of uniaxial compressive stress and magnetic field, we performed a previous characterization with two commercial devices: a DSC and a vibrating sample magnetometer.

5.3.3.1 Calorimetric characterization of the phase transition in the absence of external fields

A commercial DSC (model Q2000) was used to perform a DSC measurement in the absence of any applied external field. The corresponding thermograms for heating and cooling runs are illustrated in Figure 5.12.

The martensitic phase transition gives rise to an exothermal (negative) peak when cooling and to an endothermal (positive) peak when heating, arising from

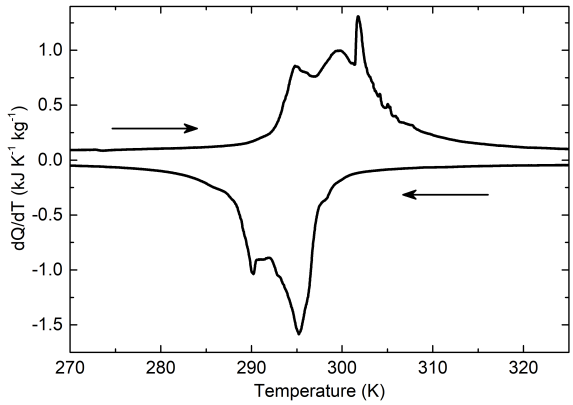

Figure 5.12: *Calorimetric signal as a function of temperature recorded upon heating (positive peak) and cooling (negative peak), measured at a scanning rate of* $\pm 5\,\mathrm{K\,min^{-1}}$ *with a DSC Q2000 from TA Instruments*®

the associated latent heat of the phase transition.

The base line signal of both thermograms can be accurately approximated by a straight line, fitted before and after the temperature range where the calorimetric peak spreads $[T_s, T_f]$. This straight line defines the baseline for the complete thermogram, and after performing the corresponding baseline correction as discussed in section 3.1.1, the transition entropy changes for the forward and reverse martensitic transitions are found to be $\Delta S_t^M = (-37.3 \pm 0.5)\,\mathrm{JK^{-1}kg^{-1}}$ and $\Delta S_t^A = (37.7 \pm 0.5)\,\mathrm{JK^{-1}kg^{-1}}$, respectively, which are in excellent agreement with previously reported values for composition-related Ni-Mn-In shape-memory alloys [178, 220, 221]. Moreover, the transition temperature is defined by the calorimetric peak position of each thermogram, which are found to be $T_t^M = 295\,\mathrm{K}$ and $T_t^A = 302\,\mathrm{K}$ respectively, defining a thermal hysteresis of $T_t^M - T_t^A = 7\,\mathrm{K}$ in the absence of external fields.

5.3.3.2 Thermomagnetic characterization of the phase transition

A commercial vibrating sample magnetometer was used to record thermomagnetization curves as a function of temperature at selected values of applied constant magnetic field in the absence of applied uniaxial compressive stress. The corresponding curves are illustrated in Figure 5.13.

The sample under study exhibits a first-order magnetostructural phase transition, together with a ferromagnetic phase transition at a higher temperature ($T_C \sim 303\,\mathrm{K}$). This behaviour is in accordance with previously reported measurements on composition-related metamagnetic Ni-Mn-In Heusler alloys [75, 178].

On cooling, the magnetization increases due to the onset of the ferromagnetic order in the austenitic phase at the Curie temperature (T_C), and upon further cooling the sample undergoes a first-order magnetostructural phase transition and

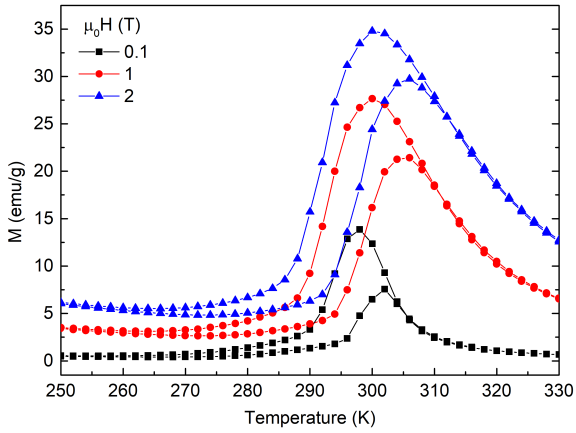

Figure 5.13: *Thermomagnetization curves at selected values of applied magnetic field in the absence of applied uniaxial stress.*

transforms to the low-temperature martensitic phase. As a consequence of the short range antiferromagnetic correlations in the martensitic phase of Ni-Mn-In alloys [222], the first-order martensitic phase transition leads to a sharp decrease on the magnetization.

Under the application of a magnetic field, the martensitic phase transition shifts to lower temperatures, which is in agreement with a further stabilization of the high-magnetization austenitic phase. Therefore, as discussed in section 2.2.2, application of a magnetic field will lead to an inverse magnetocaloric effect on this metamagnetic alloy.

The transition temperatures of the forward and reverse martensitic transitions can be identified as the inflection point of the corresponding thermomagnetization curves. Under an applied magnetic field of $\mu_0 H = 0.1\,\mathrm{T}$, they are found to be $T_t^M = 293\,\mathrm{K}$ and $T_t^A = 299\,\mathrm{K}$ respectively, defining a thermal hysteresis of $T_t^M - T_t^A = 5\,\mathrm{K}$. These values are in accordance with the previously determined values from the calorimetric measurements in the absence of any applied external field. Moreover, it is important to highlight that the heating and cooling branch of the thermomagnetization curves measured under a magnetic field of $\mu_0 H = 2\,\mathrm{T}$ and $\mu_0 H = 0.1\,\mathrm{T}$, respectively, are almost superposed. Therefore, an applied magnetic field of $\mu_0 H \sim 2\,\mathrm{T}$ is approximately enough to overcome the thermal hysteresis. The rate at which the first-order martensitic phase transition shifts under the application of magnetic field is $\dfrac{dT_t}{d\mu_0 H} \sim -2.5\,\mathrm{K T^{-1}}$.

5.3.4 Calorimetry under constant magnetic field and uniaxial stress

The raw DSC thermograms measured with our bespoke setup at selected constant values of applied uniaxial compressive stress and magnetic field are shown in Figure 5.14. Panels (a), (c), (e), (g), (i) and (k) illustrate the recorded thermograms for the heating runs, whereas panels (b), (d), (f), (h), (j) and (l) illustrate those corresponding to the cooling runs. The first-order martensitic phase transition gives rise to an exothermal calorimetric peak on cooling and to an endothermal calorimetric peak on heating.

Under a certain constant uniaxial compressive stress, an increase of the applied magnetic field shifts the calorimetric peaks to lower temperatures, which is in accordance with the behaviour observed for the thermomagnetization measurements and corresponds to a stabilization of the austenitic phase. Conversely, under a certain constant magnetic field, an increase of the applied compressive stress shifts the calorimetric peaks to higher temperatures, which is in accordance with a stabilization of the martensitic phase.

Consequently, as discussed in detail in section 2.2.2, as the application of magnetic field stabilizes the high-temperature austenitic phase (shifting the transition temperature to lower values), the studied material will exhibit an inverse magneto-

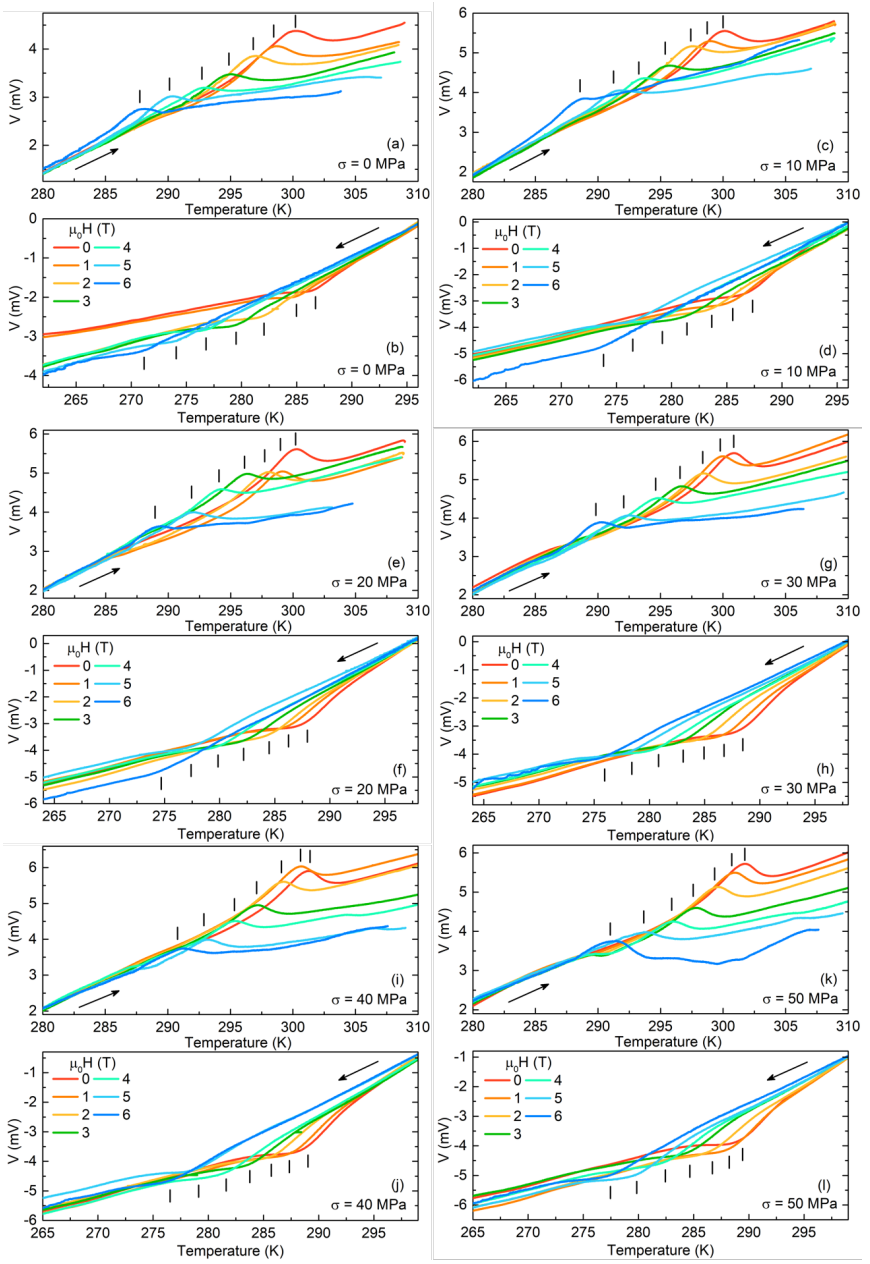

Figure 5.14: *Calorimetric signal as a function of temperature at selected values of uniaxial compressive stress and magnetic field. Panels (a), (c), (e), (g), (i) and (k) correspond to heating runs and panels (b), (d), (f), (h), (j) and (l) to cooling runs, respectively. Vertical black lines indicate the position of the calorimetric peaks. A vertical shift has been applied to selected curves for the sake of clarity.*

caloric effect. Conversely, as the application of stress stabilizes the low-temperature

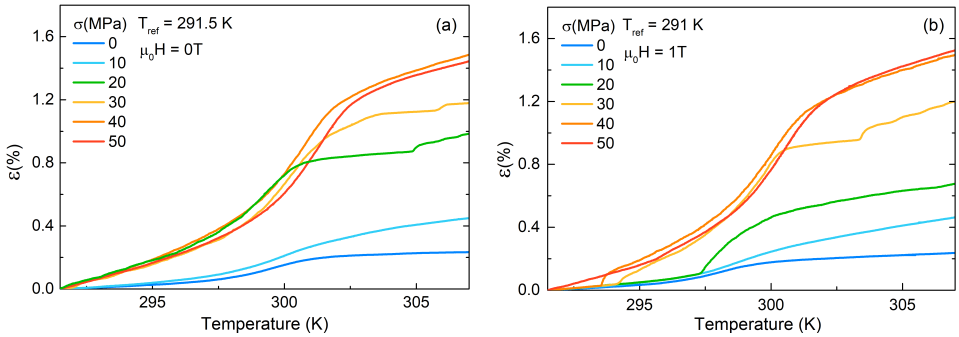

Figure 5.15: *Strain as a function of temperature at selected values of uniaxial compressive stress in the absence of magnetic field (a) and under an applied magnetic field of $\mu_0 H = 1$ T (b).*

martensitic phase (shifting the transition temperature to higher values), this material will exhibit a conventional elastocaloric effect.

To complement the DSC measurements, it is interesting to compare them with the specimen's strain, which is computed from the dilatometric measurements as:

$$\varepsilon(T, \mu_0 H, \sigma) = \frac{l(T, \mu_0 H, \sigma) - l_{ref}}{l_{ref}} \tag{5.5}$$

where $l(T, \mu_0 H, \sigma)$ is the length of the sample parallel to the direction of the applied force, and l_{ref} is the reference length, measured in the absence of stress and magnetic field at a temperature $T_{ref} = 291\,\mathrm{KT}$.

As previously discussed for Cu-Zn-Al in section 3.3, the dilatometric measurements performed with our bespoke setup will not be analysed in detail. Therefore, for the sake of simplicity, Figure 5.15 only illustrates selected examples of the computed strain for the heating runs at selected values of stress and magnetic field.

The first-order phase transition is seen as a sharp change in strain, which increases with increasing the applied uniaxial stress as a result of the increase of the percentage of favourably oriented martensitic variants [223]. Moreover, it is worth noticing the good correlation of the transition temperature region between both sets of measurements (DSC and dilatometric), which indicates that both phenomena arise from the first-order magnetostructural phase transition.

5.3.4.1 Transition temperature phase diagram

The transition temperatures of the forward (T_t^M) and reverse (T_t^A) martensitic transitions can be identified with the calorimetric peak position of the heating and cooling runs, respectively. Figure 5.16 (a) illustrates the phase diagram of the transition temperatures in the magnetic field and compressive stress coordinate space. The experimental values are plotted as blue and red solid symbols for the

forward and reverse martensitic transitions, respectively, and their behaviour is parametrized by two non-linear surface fits with equations:

$$\begin{aligned} T_t^M(\mu_0 H, \sigma) &= 286.0(2) - 1.6(1)\mu_0 H + 0.10(1)\sigma - 0.15(2)\mu_0 H^2 \\ &\quad - 8(3)\cdot 10^{-4}\sigma^2 + 0.010(2)\mu_0 H\sigma \text{ (K)} \end{aligned} \tag{5.6a}$$

$$\begin{aligned} T_t^A(\mu_0 H, \sigma) &= 299.8(1) - 1.17(7)\mu_0 H + 0.038(8)\sigma - 0.13(1)\mu_0 H^2 \\ &\quad + 6(14)\cdot 10^{-5}\sigma^2 + 0.005(1)\mu_0 H\sigma \text{ (K)} \end{aligned} \tag{5.6b}$$

On the one hand, the red surface corresponds to the reverse martensitic transition, which can be induced by either increasing the temperature, increasing the magnetic field or decreasing the stress. On the other hand, the blue surface corresponds to the forward martensitic transition, which can be induced by either decreasing the temperature, decreasing the magnetic field or increasing the stress. All these different possibilities to induce both forward and reverse transitions are indicated by black arrows in the figure.

It is important to highlight that the martensitic phase transition spreads over a certain temperature range. Therefore, each forward and reverse transition surfaces have a certain thickness, which has been omitted from the figure for the sake of clarity. Thus, well above the red surface the sample will completely be in the austenitic phase, whereas well below the blue surface the sample will be in the martensitic phase. Furthermore, the temperature region between both surfaces accounts for the hysteresis of the martensitic phase transition, and within that range the sample's thermodynamic state will depend on its thermal history.

From the tree dimensional representation of the transition temperature phase diagram as a function of magnetic field and stress, the corresponding projections on the T-$\mu_0 H$ and T-σ planes are shown in Figures 5.16 (b) and (c), respectively.

For all values of applied stress, both forward and reverse martensitic transition temperatures linearly decrease when increasing the applied magnetic field, with slopes in the range $\frac{dT_t}{d\mu_0 H} \in [-2.6, -1.7]\,\mathrm{KT}^{-1}$ that compare well with typical data for Ni-Mn-based magnetic shape-memory alloys with similar compositions [75]. Likewise, for all values of applied magnetic field, both forward and reverse martensitic transition temperatures linearly increase when increasing the applied stress, with slopes in the range $\frac{dT_t}{d\sigma} \in [0.03, 0.13]\,\mathrm{KMPa}^{-1}$. In this case, the slope determined in the absence of magnetic field is lower but comparable to the values reported for Ni-Mn-based magnetic shape-memory alloys with similar compositions [223].

The slopes determined from the linear fits to the forward and reverse martensitic transition temperatures as a function of magnetic field (Figure 5.16 (b)) and as a function of compressive stress (Figure 5.16 (c)) have been found to depend on the secondary applied field. These dependencies are illustrated in Figure 5.16 (d),

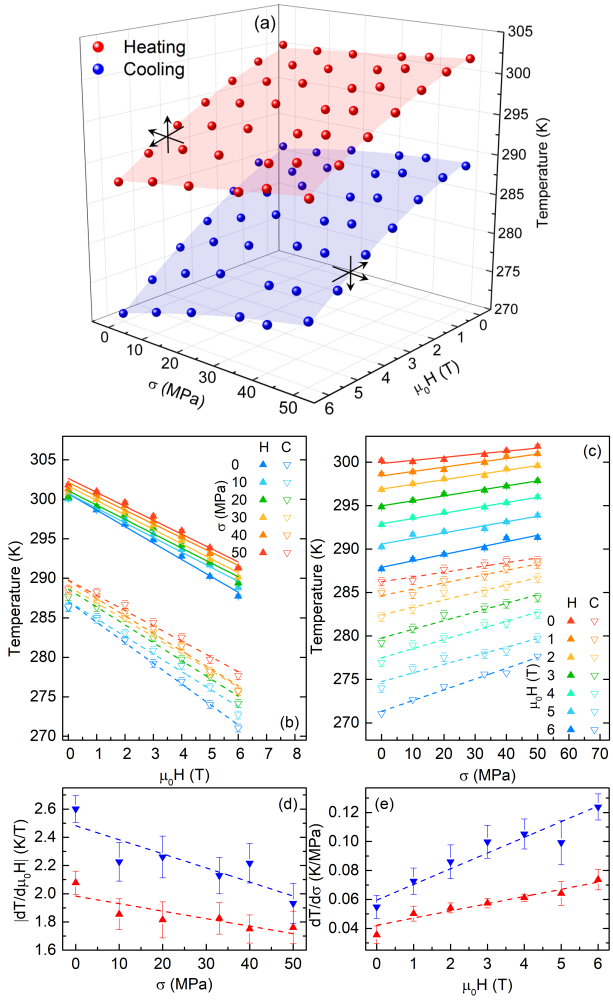

Figure 5.16: *(a) Transition temperature as a function of magnetic field and uniaxial stress. Solid symbols correspond to the transition temperatures obtained from the calorimetric peaks, and surfaces to the best fits to these values. Upper red surface corresponds to the reverse (T_A) martensitic transition, whereas the lower blue surface to the forward (T_M) martensitic transition. The arrows in each surface indicate the changes in temperature, magnetic field and uniaxial stress to cross each surface and induce the forward or reverse martensitic phase transition, respectively. (b) Transition temperatures as a function of magnetic field at constant uniaxial stress, and as a function of stress at constant magnetic fields (c). For both panels, solid symbols stand for the reverse transition and open symbols stand for the forward transition. (d) Stress dependence of the slope of the fitted transition temperature as a function of magnetic field. (e) Magnetic field dependence of the slope of the fitted transition temperature as a function of stress. Lines are linear fits to the data.*

which shows a decrease in $\left|\frac{dT_t}{d\mu_0 H}\right|$ when increasing the applied compressive stress, and in Figure 5.16 (e), which shows an increase in $\frac{dT_t}{d\sigma}$ when increasing the applied magnetic field. There are very few studies characterizing the thermal response of materials when subjected to the combined action of more than one external field, where most of them were performed under the combined action of hydrostatic pressure and magnetic field [59, 60, 224]. The combined effect of uniaxial stress and magnetic field has been previously studied for the first-order metamagnetic phase transition in Fe-Rh (see section 5.1), where no effect of the secondary field was found on the values of the transition temperatures shift rates with magnetic field $\left(\frac{dT_t}{d\mu_0 H}\right)$ and uniaxial stress $\left(\frac{dT_t}{d\sigma}\right)$ [65].

5.3.4.2 Computation of the transition entropy change

Due to the complexity of our bespoke DSC setup, the recorded thermograms illustrated in Figure 5.14 (a)-(l) under the simultaneous application of magnetic field and uniaxial compressive stress exhibit a poorer baseline when compared to the recorded thermograms with a commercial DSC. In particular, the calorimetric peaks recorded on cooling runs are less pronounced than those recorded on heating runs, and they spread over a wider temperature range. Additionally, under the application of high magnetic fields ($\mu_0 H > 4\,\mathrm{T}$), the signal-to-baseline ratio worsens for both heating and cooling runs, increasing the difficulty to properly analyse those thermograms.

As a consequence of the poor signal-to-baseline ratio, a reliable analysis could not be performed for the thermograms recorded for cooling runs and under high magnetic fields. For this reason, the analysis in the following sections has been restricted to the thermograms recorded for heating runs under applied magnetic fields of $\mu_0 H \leq 4\,\mathrm{T}$.

As discussed in section 3.1.1, the measured thermograms at selected values of applied magnetic field and uniaxial compressive stress have to be properly corrected in order to compute the transition entropy change associated with the induced first-order martensitic phase transition, which can be expressed as:

$$\Delta S_t(\mu_0 H, \sigma) = \int_{T_s}^{T_f} \frac{1}{T'} \left(\frac{dQ(T', \mu_0 H, \sigma)}{dT'} - \zeta(T', \mu_0 H, \sigma) \right) dT' \tag{5.7}$$

where T_s and T_f are the start and finish integration temperatures, taken before and after the phase transition calorimetric peak, $\zeta(T, \sigma)$ corresponds to the baseline signal and $\frac{dQ(T, \mu_0 H, \sigma)}{dT} = \frac{\dot{Q}(T, \mu_0 H, \sigma)}{\dot{T}} = \frac{Y(T, \mu_0 H, \sigma) dt}{S(T) dT}$, to the calorimetric signal where $Y(T, \mu_0 H, \sigma)$ corresponds to the raw calorimetric signal and $S(T)$ corresponds to the DSC sensitivity.

The measured thermograms were analysed with a custom Python program (discussed in detail in Appendix A) and the corrected thermograms after baseline

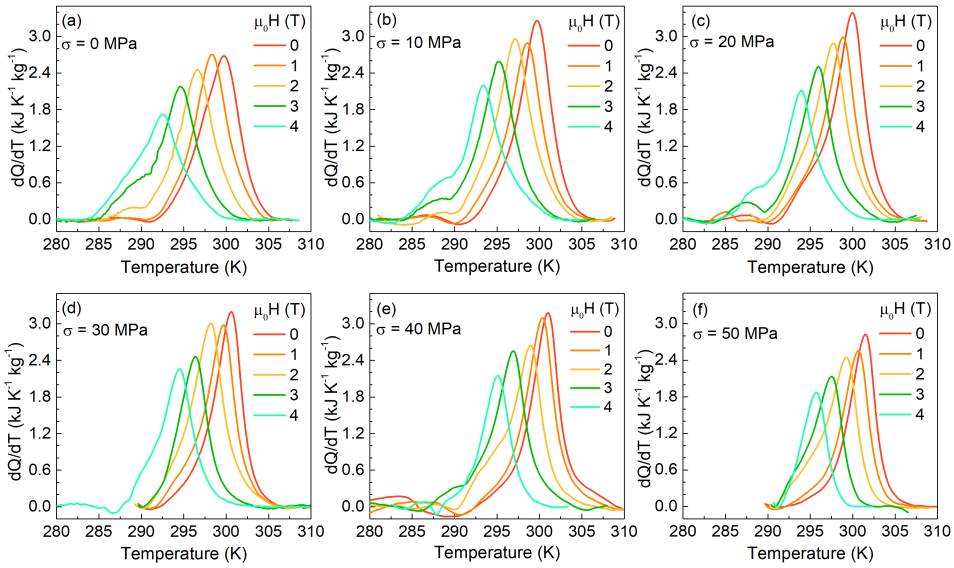

Figure 5.17: *Calorimetric curves after baseline subtraction as a function of temperature recorded upon heating at selected values of magnetic field* $\{\mu_0 H_j\} = \{0, 1, 2, 3, 4\}$ *T under different constant uniaxial compressive stresses, indicated by the labels in each panel.*

subtraction are presented in Figure 5.17 (a)-(f). It is significant to point out that under the application of magnetic field, the calorimetric peaks tend to be broader and spread over a wider temperature range. Moreover, the corrected thermograms recorded under an applied compressive stress of $\sigma = 50\,\mathrm{MPa}$, which corresponds to a compressive force of $F = 342\,\mathrm{N}$, are systematically smaller than the thermograms recorded for lower values of applied compressive stress. Although this deviation is not expected to arise from a systematic effect of our bespoke setup, as the applied compressive forces are small, it is not possible to anticipate if it corresponds to a real effect of the sample due to the lack of measurements at higher applied compressive stresses.

Therefore, the measured thermograms under an applied compressive stress of $\sigma = 50\,\mathrm{MPa}$ will not be considered for the following analysis of the transition entropy change.

The corresponding transition entropy changes ($\Delta S_t(\mu_0 H, \sigma)$) are computed using equation 5.7. As discussed in detail for Cu-Zn-Al along section 3.3, a constant calibration factor has to be introduced in order to analyse the thermograms measured with our bespoke setup. For the sample under study, the constant calibration factor is defined as:

$$\gamma^A = \frac{\Delta S_t^A(0\,\mathrm{T}, 0\,\mathrm{MPa})}{\Delta S_t(0\,\mathrm{T}, \sigma)} \tag{5.8}$$

where $\Delta S_t^A(0\,\mathrm{T}, 0\,\mathrm{MPa})$ corresponds to the transition entropy change computed from the heating thermogram measured with the commercial DSC, and $\overline{\Delta S_t(0\,\mathrm{T}, \sigma)}$ corresponds to the average of the computed transition entropy changes from the corrected thermograms represented in Figure 5.17 (a)-(e) under different compressive stresses up to $\sigma = 40\,\mathrm{MPa}$ in the absence of magnetic field. The corresponding transition entropy changes are computed as $\Delta S_t^{cal}(\mu_0 H, \sigma) = \gamma^A \Delta S_t(\mu_0 H, \sigma)$, and they are illustrated in Figure 5.18 as a function of the applied magnetic field for all the analysed thermograms. As for Cu-Zn-Al, different smoothing processes (see Appendix A) are applied to analyse each thermogram, leading to small differences in the determination of the baseline. These differences provide a good estimation of the error in determining the transition entropy change, which are found to be of ± 1-$2\,\mathrm{JK^{-1}kg^{-1}}$ for the studied sample.

For applied compressive stresses up to $\sigma = 40\,\mathrm{MPa}$, we have not found any systematic dependence of the transition entropy change with applied stress. By contrast, under an applied compressive stress of $\sigma = 50\,\mathrm{MPa}$, as anticipated from the smaller calorimetric peaks of the corrected thermograms illustrated in Figure 5.17 (f), the computed transition entropy changes are systematically smaller than the values obtained from the other measurement series.

Conversely, the computed transition entropy changes decrease when increasing the applied magnetic field for all applied compressive stresses. An average transition entropy change at each magnetic field was computed taking into account the measurements performed under a compressive stress up to $\sigma = 40\,\mathrm{MPa}$, and by fitting a linear regression the transition entropy change behaviour can be parametrized as:

$$\Delta S_t(\mu_0 H) = 38(1) - 1.9(5)\mu_0 H \ (\mathrm{JK^{-1}kg^{-1}}) \tag{5.9}$$

defining a transition entropy change decrease rate when increasing the applied magnetic field of $\dfrac{d\Delta S_t(\mu_0 H)}{d\mu_0 H} = (-1.9 \pm 0.5)\,\mathrm{JK^{-1}kg^{-1}T^{-1}}$.

To gain some light onto the origin of this dependency under the application of magnetic fields, one has to take into account that, as discussed in section 2.2.2, the transition entropy change can be generally separated into the following contributions [220]:

$$\Delta S_t = \Delta S_{lat} + \Delta S_{mag} + \Delta S_{el} \tag{5.10}$$

where the distinct terms correspond to the entropy change of the lattice (ΔS_{lat}), of the magnetic ordering (ΔS_{mag}) and of the electronic system (ΔS_{el}), respectively. As discussed in section 2.2.2, the distinct transition entropy contributions may depend on the applied external fields, but this notation has been omitted from equation 5.10 for the sake of simplicity.

T. Kihara *et. al* experimentally demonstrated that the electronic contribution is negligibly small for Ni-Mn based Heusler alloys [225]. Therefore, the transition entropy change associated with a magnetostructural phase transition of these Heusler

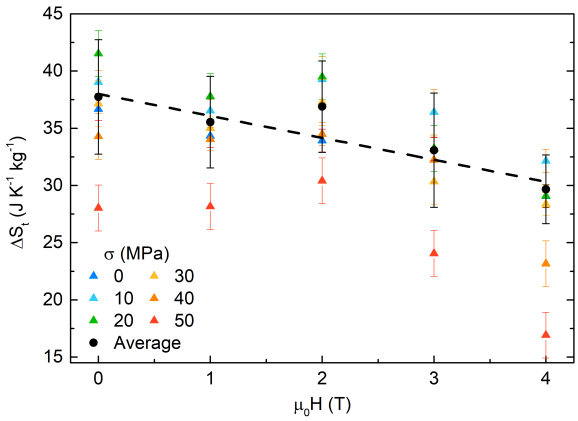

Figure 5.18: *Transition entropy change as a function of magnetic field at constant uniaxial stress computed from the heating runs. Solid triangles correspond to the averaged transition entropy change from different background subtractions of each thermogram, whereas solid circles correspond to the average of the computed transition entropy changes under different uniaxial compressive stresses up to $\sigma = 40\,MPa$. Black dashed line corresponds to a linear fit to the solid circles.*

alloys can be mainly attributed to changes on the lattice vibrations (phonons) of the alloy and to changes on the magnetic ordering between both high and low temperature phases.

With respect to the lattice entropy change, it has been reported that the vibrational entropy contribution is lower in the martensitic phase than in the austenitic phase ($S^M_{lat} < S^A_{lat}$) in magnetic shape-memory alloys [226]. The higher lattice entropy in the high-temperature phase is closely associated with the phonon modes in the transverse TA_2 branch. In fact, these phonon modes represent the major contribution to the vibrational entropy change, as they have significantly lower energies than phonons in other branches and are more likely to be excited [107]. For the particular case of Ni-Mn-In alloys, the energy of the phonons lying on the TA_2 branch linearly decreases when decreasing the temperature but does not exhibit a significant softening at the Curie temperature, where the high-temperature austenitic phase orders ferromagnetically [182]. Therefore, it is a reasonable approximation to assume that the vibrational entropy contribution does not significantly depend on magnetic field.

When considering the magnetic entropy contribution, it is important to take into account that the studied Ni-Mn-In Heusler alloy exhibits an inverse magnetocaloric effect. As illustrated from the thermomagnetization curves (Figure 5.13), the austenitic phase is more magnetically ordered than the martensitic phase. Therefore, the martensitic phase will have a larger magnetic entropy contribution than the austenitic phase ($S^M_{mag} > S^A_{mag}$).

Therefore, for a shape-memory alloy exhibiting an inverse magnetocaloric effect,

the vibrational and magnetic entropy contributions will have opposite signs. When increasing the temperature, while the vibrational entropy change is found to be positive, constituting the dominant contribution that drives the martensitic phase transition [107], the magnetic entropy change is negative and competes with the vibrational contribution [220]. Under these circumstances, the transition entropy change expressed in equation 5.10 can be rewritten as:

$$\Delta S_t(\mu_0 H) = \Delta S_{lat} - |\Delta S_{mag}(\mu_0 H)| \tag{5.11}$$

Under the application of an external magnetic field, the martensitic transition temperature decreases as the high-magnetization austenitic phase is further stabilized. The decrease on the transition temperature leads to an increase of the saturation magnetization of the austenitic phase, as the transition temperature is further separated from the Curie temperature. Therefore, the magnetization change across the phase transition increases when increasing the applied magnetic field, and the magnetic entropy contribution is enhanced as well. As a consequence, we observe a decrease of the transition entropy change when increasing the applied magnetic field.

At this point, it is interesting to compare our estimate of the transition entropy change decrease under the application of magnetic fields, with the detailed study on the transition entropy change dependency with the transition temperature for a set of Ni-Mn-In Heusler alloys reported in [220]. In that work, T. Gottschall *et. al.* reported a decrease of the transition entropy change below the austenitic Curie temperature as the transition temperature was lowered by small changes on the alloys composition. Below the austenitic Curie temperature, the magnetic entropy contribution gained importance when the transition temperature was taking place at lower temperatures, and therefore it was compensating a larger fraction of the vibrational entropy change, which was approximated as constant for the diverse samples as the composition changes were small.

Around room temperature, they found a transition entropy change decrease of $\frac{d\Delta S_t}{dT_t} \sim -0.6\,\mathrm{JK^{-2}kg^{-1}}$. In our case, from the transition temperature shift under the application of a magnetic field, we can approximate the transition entropy decrease as a function of the transition temperature as $\frac{d\Delta S_t(\mu_0 H)}{dT_t} = \frac{d\Delta S_t(\mu_0 H)}{d\mu_0 H}\frac{d\mu_0 H}{dT_t}$ $\sim (-0.9 \pm 0.3)\,\mathrm{JK^{-2}kg^{-1}}$. Despite the complexity of our calorimetric measurements, both estimates show a good agreement.

5.3.4.3 Construction of the isofield-isostress entropy curves

As discussed in section 3.1.1.2, the corresponding isofield-isostress entropy curves ($S(T, \mu_0 H, \sigma)$) can be constructed from the integration of the corrected thermograms, which provide both the transformed fraction curves ($\chi(T, \mu_0 H, \sigma)$) and the corresponding transition entropy changes ($\Delta S_t(\mu_0 H)$), and from specific heat data of both martensitic (C_M) and austenitic (C_A) phases [38]. Combining all these elements, the entropy curves referenced to a certain temperature (T_{ref}) well below

the martensitic transition can be generally expressed as [114]:

$$S(T,\mu_0 H,\sigma) - S_{ref} = \int_{T_{ref}}^{T} \frac{1}{T'}\left(C(T',\mu_0 H,\sigma) + \frac{dQ(T',\mu_0 H,\sigma)}{dT'}\right) dT' \quad (5.12)$$

where $S_{ref} = S(T_{ref})$ corresponds to the entropy at the reference temperature in the absence of any applied external field and the specific heat of the sample $C(T',\mu_0 H,\sigma)$ can be expressed as $C = (1-\chi)C_M + \chi C_A$, where χ corresponds to the transformed fraction ($\chi = 1$ when the sample is completely in the austenitic phase).

In these computations, as previously considered for Cu-Zn-Al in section 3.3.4, it is common to assume that the specific heat does not depend on the applied external fields. While the assumption that the specific heat is independent of stress is still a good approximation in our case, the proximity between the first-order martensitic phase transition and the ferromagnetic phase transition (see Figure 5.13) in this sample implies that the specific heat will depend on the applied magnetic field. Therefore, we have measured the temperature dependence of the martensitic and austenitic specific heats at selected values of applied magnetic fields. Figure 5.19 (a) illustrates the specific heat measurements for the sample under study ($Ni_{50}Mn_{35.5}In_{14.5}$) in the absence of magnetic field and under an applied magnetic field of $\mu_0 H = 2\,\mathrm{T}$.

From the C–T curves illustrated in this figure, three distinct regions can be identified. At temperatures below the first-order martensitic phase transition, there is no dependence of the specific heat of the martensite (C_M) with the applied magnetic field. As illustrated in the insert of panel (a) with a black line, its temperature dependence can be parametrized with a linear regression expressed as:

$$C_M(T) = 132(16) + 1.16(6)T \ (\mathrm{JK^{-1}kg^{-1}}) \quad (5.13)$$

Around room temperature, within the transition region, the latent heat associated with the first-order martensitic phase transition gives rise to an apparent peak in the specific heat. Under the application of magnetic field, this peak shifts to lower temperatures at an approximate rate of $\frac{dT_t}{d\mu_0 H} \sim -2\,\mathrm{KT^{-1}}$, which is in excellent agreement with the shift observed from the DSC thermograms recorded upon heating (see Figures 5.14 and 5.16).

Above the martensitic transition, a small peak (centred at a temperature $T = 303\,\mathrm{K}$) associated with the Curie point of the austenitic phase is clearly visible for the measurement performed in the absence of magnetic field. Under an applied magnetic field of $\mu_0 H = 2\,\mathrm{T}$, this peak is smoothed and spreads over a wider temperature range.

At this point, when comparing the specific heat measurements (see Figure 5.19) with the calorimetric measurements performed with the commercial (see Figure 5.12) and the bespoke (see Figure 5.14) DSC setups on the sample under study, it

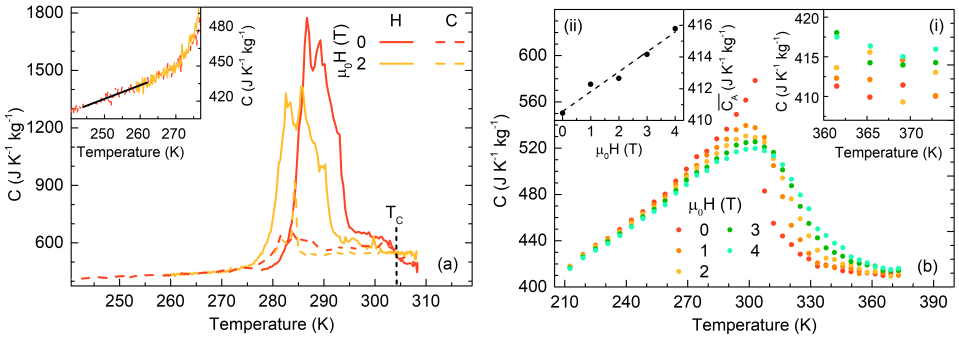

Figure 5.19: *(a) Specific heat of $Ni_{50}Mn_{35.5}In_{14.5}$ as a function of temperature in the absence of magnetic field (red lines) and under an applied field of $\mu_0 H = 2\,T$ (yellow lines) for both heating (solid lines) and cooling (dashed lines) runs, measured with a bespoke AC calorimeter [219]. The inset shows an enlarged view of the specific heat below the first-order martensitic phase transition. The black line is a linear fit to the data. (b) Specific heat of $Ni_{50}Mn_{34}In_{16}$ as a function of temperature under applied magnetic fields $\{\mu_0 H_j\} = \{0, 1, 2, 3, 4\}\,T$ for heating runs, measured using a commercial relaxation calorimeter (PPMS from Quantum Design®). Insets: (i) Enlarged view of the specific heat above the austenitic Curie temperature. (ii) Average specific heat of the paramagnetic austenite as a function of magnetic field. The black dashed line is a linear fit to the data.*

is worth noting that in the absence of applied external fields the heat flow related to the second-order transition around the austenitic Curie temperature can not be distinguished from the first-order calorimetric peak for both DSC setups, as both contributions are overlapped. This overlap is attributed to the much faster scanning temperature rates used for both DSC devices when compared to the scanning rate used for the AC calorimeter, which was around $0.05\,\mathrm{K min^{-1}}$.

Furthermore, it is significant to highlight that after a proper baseline correction, the transition entropy change of this sample can also be computed from the specific heat measurements as:

$$\Delta S_t = \int_{T_s}^{T_f} \left(\frac{C(T')}{T'} - \zeta \right) dT' \tag{5.14}$$

where T_s and T_f are the start and finish integration temperatures, taken below and above the apparent peak associated with the phase transition, and ζ corresponds to the baseline signal.

For the measurement performed the absence of applied magnetic field, when integrating both the apparent peak of the first-order martensitic phase transition and the small peak of the austenitic Curie temperature, the baseline can be accurately approximated as a straight line, fitted below the martensitic phase transition and above the austenitic Curie peak. After performing the corresponding baseline correction, the transition entropy change for the reverse martensitic transition is found to be $\Delta S_t^A(\mu_0 H = 0\,\mathrm{T}) = (37.6 \pm 0.5)\,\mathrm{JK^{-1}kg^{-1}}$, which is in excellent agreement

with the transition entropy change determined with the commercial DSC in the absence of applied external fields (see section 5.3.3).

As the bespoke AC calorimeter is limited at high temperatures, it is not possible to accurately determine the specific heat of the paramagnetic austenite (C_A) under different applied magnetic fields. For this reason, we have used a second (commercial) relaxation calorimeter to measure the specific heat under different applied magnetic fields over a broader temperature range. In order to separate the contributions from the first-order martensitic phase transition and the Curie point of the austenitic phase, a second sample ($Ni_{50}Mn_{34}In_{16}$) for which its martensitic phase transition takes place at a temperature well below its Curie point was used. It has been previously reported that small composition differences do not have a significant influence on the Curie temperature in Ni-Mn-In Heusler alloys [155, 178], and it is not expected that such changes affect the specific heat of the paramagnetic austenitic phase (C_A). Figure 5.19 (b) illustrates the corresponding specific heat measurements around the Curie point under different applied magnetic fields.

As for the C–T curves illustrated in Figure 5.19 (a), the peak associated with the austenitic Curie temperature smooths and spreads over a wider temperature range under the application of magnetic field. The specific heat behaviour above the Curie temperature, where the austenitic phase is paramagnetic, is illustrated in the insert (i) of Figure 5.19 (b). Within this temperature range, the specific heat is almost independent of temperature, but it shows a small dependence on the applied magnetic field. The average specific heat of the paramagnetic austenite ($\overline{C_A}$) under each applied magnetic field can be computed, and its dependence with the applied magnetic field is illustrated in the insert (ii) of Figure 5.19 (b), and by fitting a linear regression its behaviour can be parametrized as:

$$C_A(\mu_0 H) = 410.6(3) + 1.3(1)\mu_0 H \ (\mathrm{JK^{-1}kg^{-1}}) \tag{5.15}$$

Therefore, from the parametrized dependencies of the transition entropy change (see equation 5.9), and the martensitic (see equation 5.13) and austenitic (see equation 5.15) specific heats, together with the transformed fraction curves obtained from the base-line corrected thermograms (see Figure 5.17), we have computed the isofield-isostress entropy curves ($S(T, \mu_0 H, \sigma)$) referenced to $S_{ref} = S(T = 256\,\mathrm{K})$ in the absence of stress and magnetic field. Figure 5.20 (a)-(e) displays the computed entropy curves at selected values of uniaxial stress $\{\sigma_i\} = \{0, 10, 20, 30, 40\}$ MPa under different constant applied magnetic fields, whereas Figure 5.21 (a)-(e) displays the computed entropy curves at selected values of magnetic field $\{\mu_0 H_j\} = \{0, 1, 2, 3, 4\}$ T under different constant applied compressive stresses.

As illustrated in Figure 5.20 (a)-(e), for each constant magnetic field the computed entropy curves shift towards higher temperatures when increasing the applied stress. It is important to notice that in the high-temperature region, all the entropy curves merge, indicating a stress-independent entropy in the austenitic phase. On the other hand, as illustrated in Figure 5.21 (a)-(e), for each constant compressive stress, the computed entropy curves shift towards lower temperatures

when increasing the applied magnetic field. Significantly, in the high-temperature region, the entropy curves exhibit a crossover, indicating a decrease of the entropy at the austenitic phase when increasing the applied magnetic field. Such decrease reflects the reduction of the transition entropy change when increasing the applied magnetic field, as illustrated in Figure 5.18.

As previously discussed in section 3.1.1.2, from the set of isofield-isostress entropy curves we can compute the corresponding elastocaloric and magnetocaloric isothermal entropy (ΔS) and adiabatic temperature (ΔT) changes. As these entropy curves were computed from the thermograms recorded for heating runs, they correspond to the reverse phase transition (from martensite to austenite). Therefore, the elastocaloric and magnetocaloric thermal responses presented in the following section will correspond as well with the field-induced reverse phase transition (application of magnetic field and removal of stress), which corresponds to trajectories from below to above the red surface in Figure 5.16 (a).

5.3.4.4 Elastocaloric and magnetocaloric effects under the influence of a secondary field

On the one hand, to compute the elastocaloric thermal response under the influence of a constant magnetic field, it is important to highlight that the application of uniaxial stress favours the low-temperature martensitic phase, which is in agreement with the positive transition temperature shift when increasing the applied stress reported in section 5.3.4.1.

Accordingly, the removal of stress ($\Delta\sigma < 0$) will promote the reverse phase transition (from martensite to austenite), and consequently a thermodynamic process in which stress is removed is associated with the heating entropy curves. Specifically, the elastocaloric isothermal entropy change under a certain constant magnetic field will be computed as:

$$\Delta S(T, \mu_0 H, \sigma \to 0) = S(T, \mu_0 H, 0) - S(T, \mu_0 H, \sigma) \tag{5.16}$$

and the corresponding results are illustrated in Figure 5.20 (f)-(j) under different constant applied magnetic fields. Conversely, adiabatic temperature changes are computed after inverting the corresponding entropy curves ($T(S, \mu_0 H, \sigma)$) as:

$$\Delta T(S, \mu_0 H, \sigma \to 0) = T(S, \mu_0 H, 0) - T(S, \mu_0 H, \sigma) \tag{5.17}$$

While this expression provides the adiabatic temperature change as a function of entropy, it is customary to represent it as a function of temperature. Such temperature dependence is obtained by plotting each $\Delta T(S, \mu_0 H, \sigma \to 0)$ data at the temperature given by the initial entropy curve prior to the removal of the uniaxial stress. Figure 5.20 (k)-(o) illustrates the corresponding adiabatic temperature changes under different constant applied magnetic fields.

In light of all the results illustrated in Figure 5.20, the computed elastocaloric effect has been found to be conventional. At this point, it is important to highlight

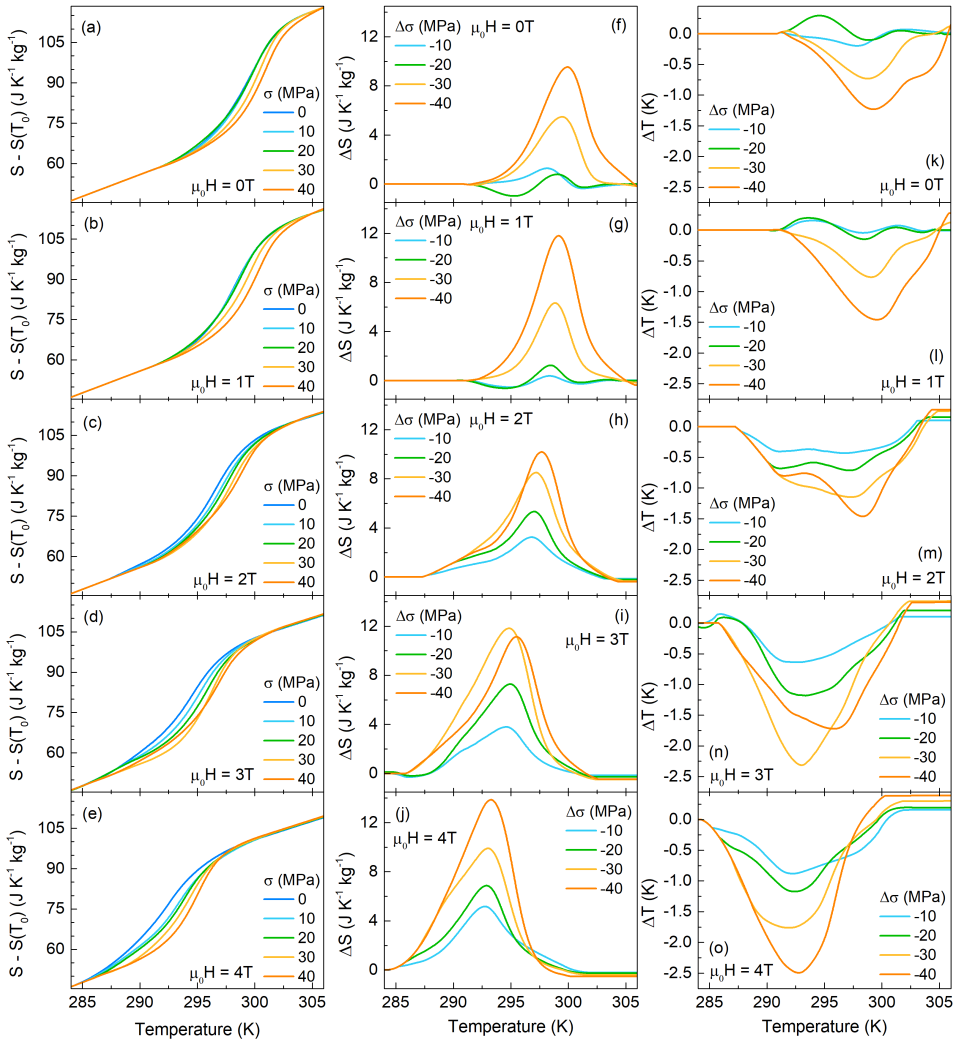

Figure 5.20: *(a)-(e) Entropy curves (referenced to $S_{ref} = S(T = 256\,K)$ in the absence of stress and magnetic field) as a function of temperature at selected values of uniaxial stress $\{\sigma_i\} = \{0, 10, 20, 30, 40\}$ MPa under different constant magnetic fields. Elastocaloric isothermal entropy changes ((f)-(j)), and adiabatic temperature changes ((k)-(o)) corresponding to the removal of uniaxial stress ($\sigma \rightarrow 0$). Each row corresponds to a different constant applied magnetic field $\{\mu_0 H_j\} = \{0, 1, 2, 3, 4\}$ T, and the value of the uniaxial stress is indicated by the colour code.*

that under low applied magnetic fields ($\{\mu_0 H_j\} = \{0, 1\}$ T), the transition temperature shift with stress is very small (see Figure 5.16 (e)), and the field-induced elastocaloric effect at low stresses shows small fluctuations for both isothermal entropy and adiabatic temperature changes around zero. These fluctuations can not be considered physically meaningful within experimental errors.

On the other hand, to compute the magnetocaloric thermal response under the influence of a constant stress, it is important to highlight that the application of magnetic field favours the high-temperature austenitic phase, which is in agreement with the negative transition temperature shift when increasing the applied magnetic field reported in section 5.3.4.1.

Accordingly, the application of magnetic field ($\Delta\mu_0 H > 0$) will promote the reverse phase transition (from martensite to austenite), and consequently a process in which magnetic field is applied is as well associated with the heating entropy curves. Therefore, similarly to the elastocaloric effect, the magnetocaloric isothermal entropy change under a certain constant stress will be computed as:

$$\Delta S(T, 0 \rightarrow \mu_0 H, \sigma) = S(T, \mu_0 H, \sigma) - S(T, 0, \sigma) \tag{5.18}$$

and the corresponding results are illustrated in Figure 5.21 (f)-(j) under different constant applied stresses. Conversely, the magnetocaloric adiabatic temperature changes are computed as:

$$\Delta T(S, 0 \rightarrow \mu_0 H, \sigma) = T(S, \mu_0 H, \sigma) - T(S, 0, \sigma) \tag{5.19}$$

and the corresponding results, represented as a function of the temperature given by the initial entropy curve prior to the application of the magnetic field, are illustrated in Figure 5.21 (k)-(o) under different constant applied stresses.

Interestingly, the computed magnetocaloric thermal response has been found to exhibit a crossover from inverse (at low temperatures) to conventional (at high temperatures). The inverse magnetocaloric effect arises from the field-induced martensitic phase transition, whereas the arising conventional magnetocaloric effect is associated with changes in the ferromagnetic order in the vicinity of the Curie point of the austenite phase.

Additionally, it is important to notice that for both elastocaloric and magnetocaloric thermal responses under the influence of a secondary field, an increase in the external field change that drives the martensitic phase transition (stress for the elastocaloric effect, represented in Figure 5.20, and magnetic field for the magnetocaloric effect, represented in Figure 5.21) enlarges the temperature window of the corresponding caloric effect.

Furthermore, it is particularly interesting to examine the behaviour of the extreme values of the isothermal entropy (ΔS_{max}) and the adiabatic temperature (ΔT_{max}) changes as a function of the driving field that induces the martensitic phase transition for both caloric effects. Figure 5.22 illustrates the isothermal entropy (a) and the adiabatic temperature (b) changes for the magnetocaloric effect as a function of the applied magnetic field ($\Delta\mu_0 H$) (under different constant applied stresses), whereas the isothermal entropy and the adiabatic temperature changes for the elastocaloric effect as a function of the absolute value of the released stress ($|\Delta\sigma|$) (under different constant magnetic fields) are shown in panels (c) and (d), respectively.

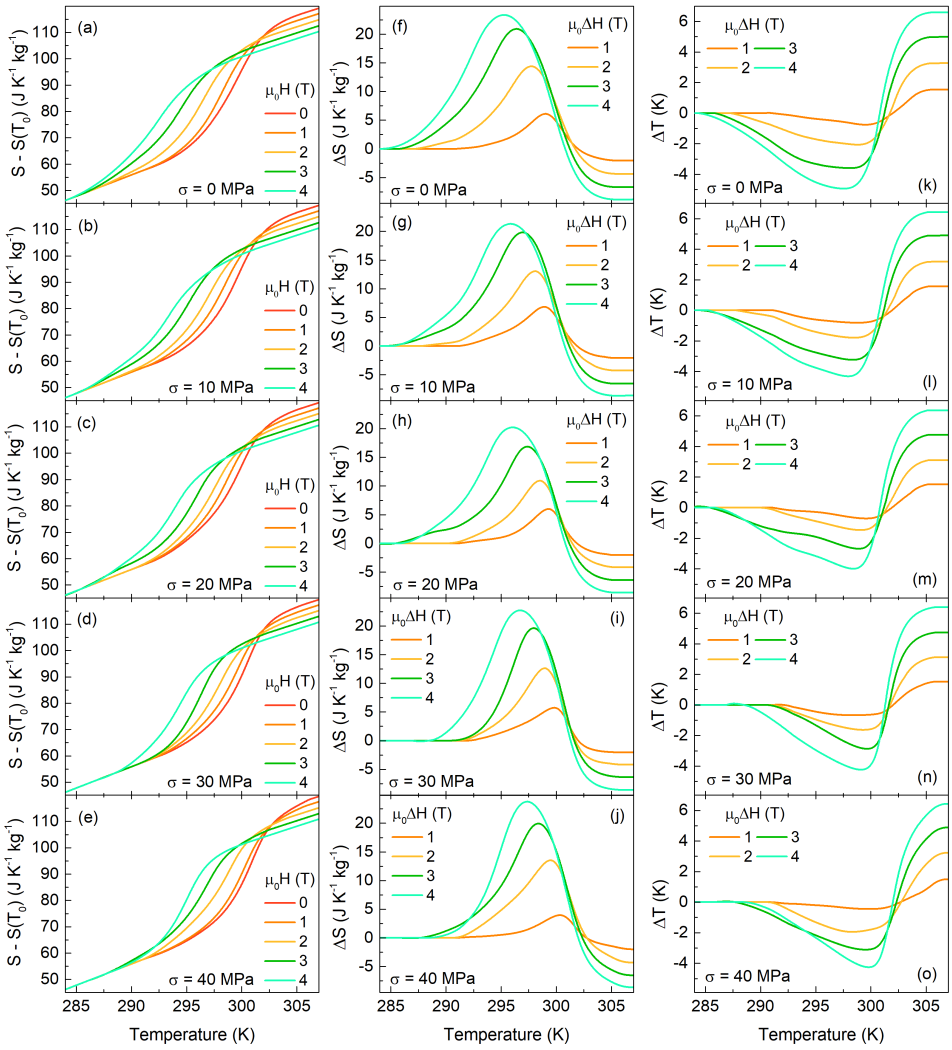

Figure 5.21: *(a)-(e) Entropy curves (referenced to $S_{ref} = S(T = 256\,K)$ in the absence of stress and magnetic field) as a function of temperature at selected values of magnetic field $\{\mu_0 H_j\} = \{0, 1, 2, 3, 4\}$ T under different constant uniaxial stresses. Magnetocaloric isothermal entropy changes ((f)-(j)), and adiabatic temperature changes ((k)-(o)) corresponding to the application of magnetic field $(0 \rightarrow \mu_0 H)$. Each row corresponds to a different constant applied uniaxial stress $\{\sigma_i\} = \{0, 10, 20, 30, 40\}$ MPa, and the value of the magnetic field is indicated by the colour code.*

As it can be seen from the quasidirect estimates of both the magnetocaloric isothermal entropy (ΔS_{max}) and adiabatic temperature (ΔT_{max}) changes, the magnitude of the field-induced thermal response increases for higher magnetic fields for all applied stresses. While the increase in ΔT_{max} is found to be linear, the increase in ΔS_{max} shows a tendency to saturate at high fields. The fact that ΔS_{max}

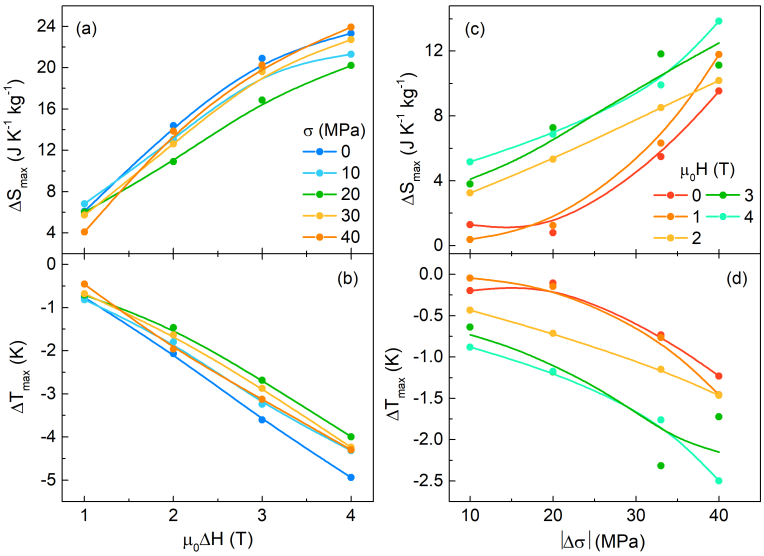

Figure 5.22: *Left: Magnetic field dependence of the maximum values for the field-driven magnetocaloric isothermal entropy (a) and adiabatic temperature (b) changes under different constant values of applied stress. Right: Stress dependence of the maximum values for the field-driven elastocaloric isothermal entropy (c) and adiabatic temperature (d) changes under different constant values of applied magnetic field. Solid symbols correspond to the experimental values whereas lines are guides to the eye for each data series.*

values are lower than the transition entropy changes ($\Delta S_t(\mu_0 H)$, illustrated in Figure 5.18), together with the fact that we do not observe a complete saturation of the magnetocaloric isothermal entropy change, indicate that the sample does not completely transform for the studied range of applied magnetic fields.

On the other hand, for the quasidirect estimates of both elastocaloric ΔS_{max} and ΔT_{max}, they exhibit a significant scattering but the magnitude of the field-induced thermal response also increases for higher stress changes ($|\Delta\sigma|$) for all applied magnetic fields. As for the magnetocaloric effect, ΔS_{max} values are lower than the transition entropy changes ($\Delta S_t(\mu_0 H)$), indicating that larger stresses are required in order to completely drive the martensitic phase transition.

When considering the effect of the secondary constant field on ΔS_{max} and ΔT_{max}, we could not observe a systematic dependence of the magnetocaloric effect on the applied stress within the studied range. Conversely, the elastocaloric thermal response clearly depends on the secondary constant external field, increasing both ΔS_{max} and ΔT_{max} values for higher applied magnetic fields. Although this behaviour seems to be in contrast with the transition entropy change decrease when increasing the applied magnetic field, it is important to take into account that the transition temperature shift with the applied stress $\left(\frac{dT_t}{d\sigma}\right)$, illustrated in Figure

5.16 (e), increases with the applied magnetic field. Therefore, for the same stress removal, the transition temperature will shift more when a higher magnetic field is applied, thus leading to an increase of the sample fraction in the martensitic phase that transforms to the austenitic phase upon stress removal, and leading to a larger elastocaloric thermal response.

5.3.5 Simulation of the isofield-isostress entropy curves: an analytical model

The experimental isofield-isostress entropy curves ($S(T, \mu_0 H, \sigma)$), constructed in section 5.3.4.3 and illustrated in Figure 5.20 (a)-(e) and Figure 5.21 (a)-(e), are only known for given values of uniaxial stress $\{\sigma_i\} = \{0, 10, 20, 30, 40\}$ MPa and magnetic field $\{\mu_0 H_j\} = \{0, 1, 2, 3, 4\}$ T. Therefore, the corresponding caloric effects can only be computed at certain points of the entire $(T, \mu_0 H, \sigma)$ coordinate space under study. Moreover, there are not enough available experimental entropy curves to accurately compute the corresponding multicaloric effect. [5]

In order to overcome these issues, it is necessary to define a numerical function ($S(T, \mu_0 H, \sigma)$) and fit it to the experimental entropy curves in order to phenomenologically reproduce their behaviour. The purpose of such numerical function is to simulate the entropy curves for any combination of magnetic field and uniaxial stress within the entire thermodynamic coordinate space under study, allowing us to accurately compute the corresponding caloric and multicaloric effects.

At this point, it is useful to rewrite the expression that defines the isofield-isostress experimental entropy curves (see equation 5.12) by taking into account the definition of the transformed fraction (see equation 3.16). For the particular case of the sample under study ($Ni_{50}Mn_{35.5}In_{14.5}$), taking into account the parametrized behaviour of the transition entropy change ($(\Delta S_t(\mu_0 H))$, see Figure 5.18 and equation 5.9) together with the dependencies of both martensitic ($C_M(T)$) and austenitic ($C_A(\mu_0 H)$) specific heats (see Figure 5.19 and equations 5.13 and 5.15, respectively), the equation that defines the isofield-isostress entropy curves can be expressed as:

$$S(T, \mu_0 H, \sigma) - S_{ref} = \int_{T_{ref}}^{T} \frac{C(T', \mu_0 H, \sigma)}{T'} dT' + \Delta S_t(\mu_0 H)\chi(T, \mu_0 H, \sigma) \quad (5.20)$$

where $S_{ref} = S(T = 256\,\mathrm{K})$ and $C(T, \mu_0 H, \sigma) = [1 - \chi(T, \mu_0 H, \sigma)]\, C_M(T) + \chi(T, \mu_0 H, \sigma) C_A(\mu_0 H)$.

It is important to highlight that all the different elements that constitute equation 5.20, except the austenitic transformed fraction ($\chi(T, \mu_0 H, \sigma)$), have already been accurately parametrized within the complete $(T, \mu_0 H, \sigma)$ coordinate space along the previous sections. Therefore, it necessary to define an analytical function to reproduce the experimental behaviour of the transformed fraction over the complete

[5] See section 2.1.2 for a detailed discussion on the multicaloric effects

thermodynamic phase space under study in order to define a suitable numerical function ($S(T, \mu_0 H, \sigma)$) that reproduces the complete set of isofield-isostress experimental entropy curves.

For such purpose, two observations have to be stated in order to define a suitable analytical function. On the one hand, as previously discussed in section 3.1.1, it is important to take into account that the transformed fraction at a certain temperature is computed from the partial integration of the corrected thermograms with respect to the integration over the complete transition temperature range, which provides the transition entropy change (see equation 3.16). Therefore, it is a normalized function that defines the portion of the sample that has transformed to the high-temperature austenitic phase. As a consequence, it will vanish ($\chi = 0$) at the low-temperature martensitic phase and at the high-temperature austenitic phase it takes the value $\chi = 1$.

On the other hand, as it can be seen from the corrected thermograms illustrated in Figure 5.17 (a)-(f), the calorimetric signal is mainly given by a single peak spreading over a certain transition temperature range that depends on the applied external fields. Therefore, the transformed fraction obtained from the integration of these peaks will provide a single S-shaped curve, which will sharply change over the transition temperature range from $\chi = 0$ to $\chi = 1$.

Therefore, the analytical function we used includes a sigmoid function, centred at the transition temperature, expressed as:

$$\chi(T, \mu_0 H, \sigma) = 1 - \frac{1}{e^{B(T-T_t)} + 1} \tag{5.21}$$

where the free parameters $\{B, T_t\}$ are allowed to depend only on the applied magnetic field and the uniaxial compressive stress.

Similarly to the fitting procedure described for Cu-Zn-Al in section 3.3.3, an initial fit to all the single transformed fraction curves is performed without applying any constrain to the free parameters. Each independent fit provides different values for both free parameters of the analytical function. Then, the magnetic field and stress dependence of each free parameter is evaluated by fitting its different values obtained from the individual fits with a non-linear surface fit. It is important to point out that, as for Cu-Zn-Al, the free parameters are fixed individually. Once the first free parameter is constrained, new fits to all the single transformed fraction curves are performed, as the values of the remaining free parameter may be affected by the previous constrains. This process is sequentially repeated, until all the free parameters have been properly fixed, thus leading to an analytical function that depends on temperature, magnetic field ans stress, and reproduces the experimental results over the phase space under study.

By following this fitting procedure, the parameters that define the analytical function to reproduce the experimental transformed fraction curves are:

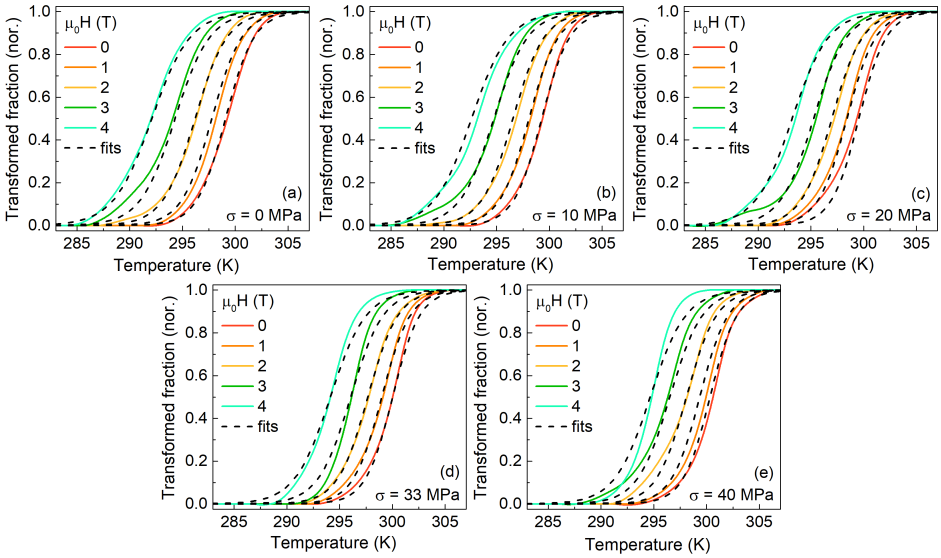

Figure 5.23: *(a)-(e) Austenitic transformed fraction as a function of temperature at selected values of magnetic field* $\{\mu_0 H_j\} = \{0, 1, 2, 3, 4\}$ *T under different constant uniaxial stresses, indicated by the labels in each panel. Solid lines correspond to the experimental data obtained from the corrected thermograms, and dashed lines, to the fitted analytical function* $\chi(T\mu_0 H, \sigma)$ *expressed in equation 5.21.*

$$T_t(\mu_0 H, \sigma) = 299.1(2) - 1.14(14)\mu_0 H + 0.016(15)\sigma - 0.15(3)\mu_0 H^2 + 4(3)\cdot 10^{-4}\sigma^2 + 0.008(3)\mu_0 H\sigma \text{ (K)} \quad (5.22a)$$

$$B(\mu_0 H, \sigma) = 0.74(2) - 0.032(18)\mu_0 H + 0.0019(17)\sigma - 0.004(4)\mu_0 H^2 - 2(4)\cdot 10^{-5}\sigma^2 - 0.2(4)\cdot 10^{-4}\mu_0 H\sigma \text{ (K}^{-1}) \quad (5.22b)$$

Figure 5.23 (a)-(e) illustrates the agreement between the simulated (dashed lines) and experimental (solid lines) transformed fraction curves at selected values of magnetic field and uniaxial stress. As it can be seen, the deviation between both data sets is small, proving that the analytical function correctly captures the transformed fraction behaviour around the martensitic phase transition.

Consequently, taking into account that all the distinct elements that define the isofield-isostress entropy curves, expressed in equation 5.20, have been successfully parametrized within the complete $(T, \mu_0 H, \sigma)$ coordinate space, we have all the necessary ingredients to phenomenologically reproduce their behaviour. For the particular case of the sample under study, taking into account that equation 5.13 can be generally expressed as $C_M(T) = \alpha_M T + \beta_M$, introducing equation 5.21 into equation 5.20 leads to:

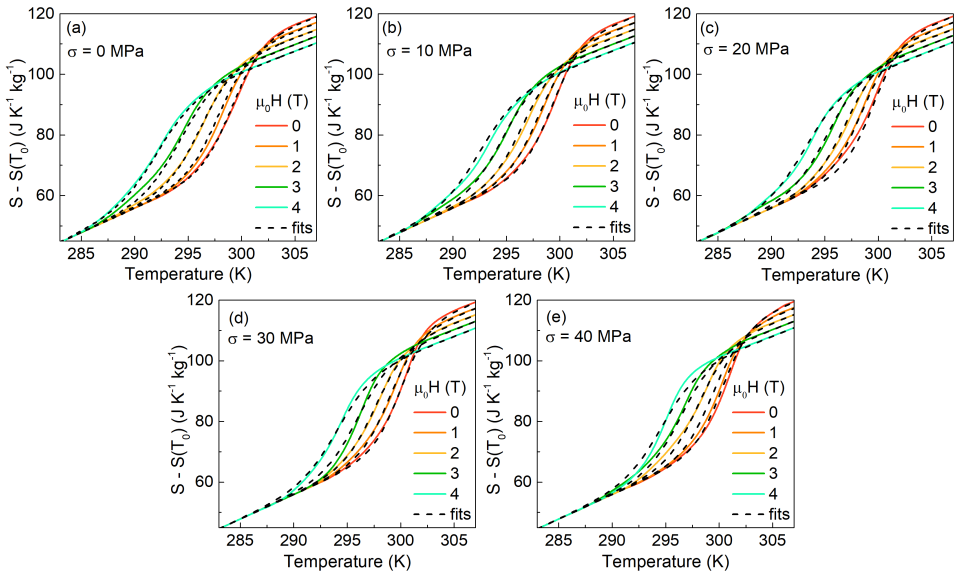

Figure 5.24: *(a)-(e) Entropy curves (referenced to $S_{ref} = S(T = 256\,K)$ in the absence of stress and magnetic field) as a function of temperature at selected values of magnetic field $\{\mu_0 H_j\} = \{0,\ 1,\ 2,\ 3,\ 4\}$ T under different constant uniaxial stresses, indicated by the labels in each panel. Solid lines correspond to the experimental data, and dashed lines, to the fitted analytical function.*

$$
\begin{aligned}
S(T, \mu_0 H, \sigma) - S_{ref} = \\
\alpha_M (T - T_{ref}) + \beta_M \ln\left(\frac{T}{T_{ref}}\right) - \frac{\alpha_M}{B} \ln\left[\frac{e^{B(T-T_t)} + 1}{e^{B(T_{ref}-T_t)} + 1}\right] \\
+ [C_A(\mu_0 H) - \beta_M] \int_{T_{ref}}^{T} \frac{\chi(T', \mu_0 H, \sigma)}{T'} dT' + \Delta S_t(\mu_0 H) \chi(T, \mu_0 H, \sigma)
\end{aligned}
\tag{5.23}
$$

where the parameters $\{B, T_t\}$ depend on both the applied magnetic field and stress according to equations 5.22b and 5.22a, respectively, and the integral over temperature of $\dfrac{\chi(T', \mu_0 H, \sigma)}{T'}$ was computed numerically by a cumulative trapezoidal integration for any point of the $(T, \mu_0 H, \sigma)$ coordinate space under study.

Figure 5.24 (a)-(e) illustrates the good agreement between the numerically computed (dashed lines) and experimental (solid lines) isofield-isostress entropy curves at selected values of magnetic field and stress. Therefore, from the numerical $S(T, \mu_0 H, \sigma)$ function, the corresponding caloric and multicaloric effects can be computed for any combination of temperature, magnetic field and stress within the entire phase space under study.

It is worthwhile to remember that the experimental isofield-isostress entropy curves were computed from the thermograms recorded for heating runs and thus,

they correspond to the reverse phase transition. As a result, the analysis of the caloric effects (see section 5.3.4.4) was restricted to the application of magnetic field and the removal of stress, as they both induce the reverse phase transition, and correspond to trajectories from below to above the red surface illustrated in Figure 5.16 (a). Furthermore, when considering trajectories that involve a simultaneous or sequential change on both external fields, both of them have to promote the phase transition in the same direction. Otherwise, due to the hysteresis of the phase transition, they would drive the sample through a minor hysteresis loop within the two-phase coexistence region (which corresponds to the temperature range between both surfaces illustrated in Figure 5.16 (a)), for which no experimental data are available.

Consequently, the numerically simulated entropy curves are only representative for the reverse phase transition, and the computation of the corresponding caloric and multicaloric effects will be restricted to the diverse trajectories in the phase space from below to above the red surface.

Figures 5.25 (a) and (b) illustrate respectively the numerically simulated isofield and isostress entropy surfaces as a function of temperature and stress (a), and as a function of temperature and magnetic field (b). The crossover behaviour for the isofield entropy surfaces (see Figure 5.25 (a)) is evident within all the range of temperatures and stresses under study. Furthermore, the isostress entropy surfaces also evidence the transition entropy change decrease when increasing the applied magnetic field (see Figure 5.25 (b)), together with the weak dependence in stress.

Moreover, equation 5.23 allows us to compute the corresponding isothermal entropy surfaces as a function of stress and magnetic field, illustrated in Figure 5.25 (c)-(f) at selected values of temperature. For temperatures at the onset of the reverse phase transition, the entropy increase when removing the stress is more pronounced. Accordingly, for temperatures above the phase transition, the entropy increase when removing the stress in drastically reduced. On the other hand, the entropy increases when applying the magnetic field up to a maximum, and then decreases for larger fields. The value of the magnetic field where the maximum occurs depends on the temperature. For temperatures above the reverse phase transition, the entropy decreases when increasing the applied magnetic field, which reflects the decrease of the entropy at the austenitic phase when increasing the magnetic field, in accordance with its ferromagnetic nature.

5.3.5.1 Elastocaloric and magnetocaloric effects under the influence of a secondary field

Similarly to the results presented in section 5.3.4.4, we can compute the elastocaloric effect under a certain constant applied magnetic field and the magnetocaloric effect under a certain constant applied stress from the numerical $S(T, \mu_0 H, \sigma)$ function. The corresponding results are illustrated in Figures 5.26 and 5.27, respectively, as colour contour plot maps. Additionally, the corresponding three-dimensional representations of both caloric effects are shown in Appendix B.

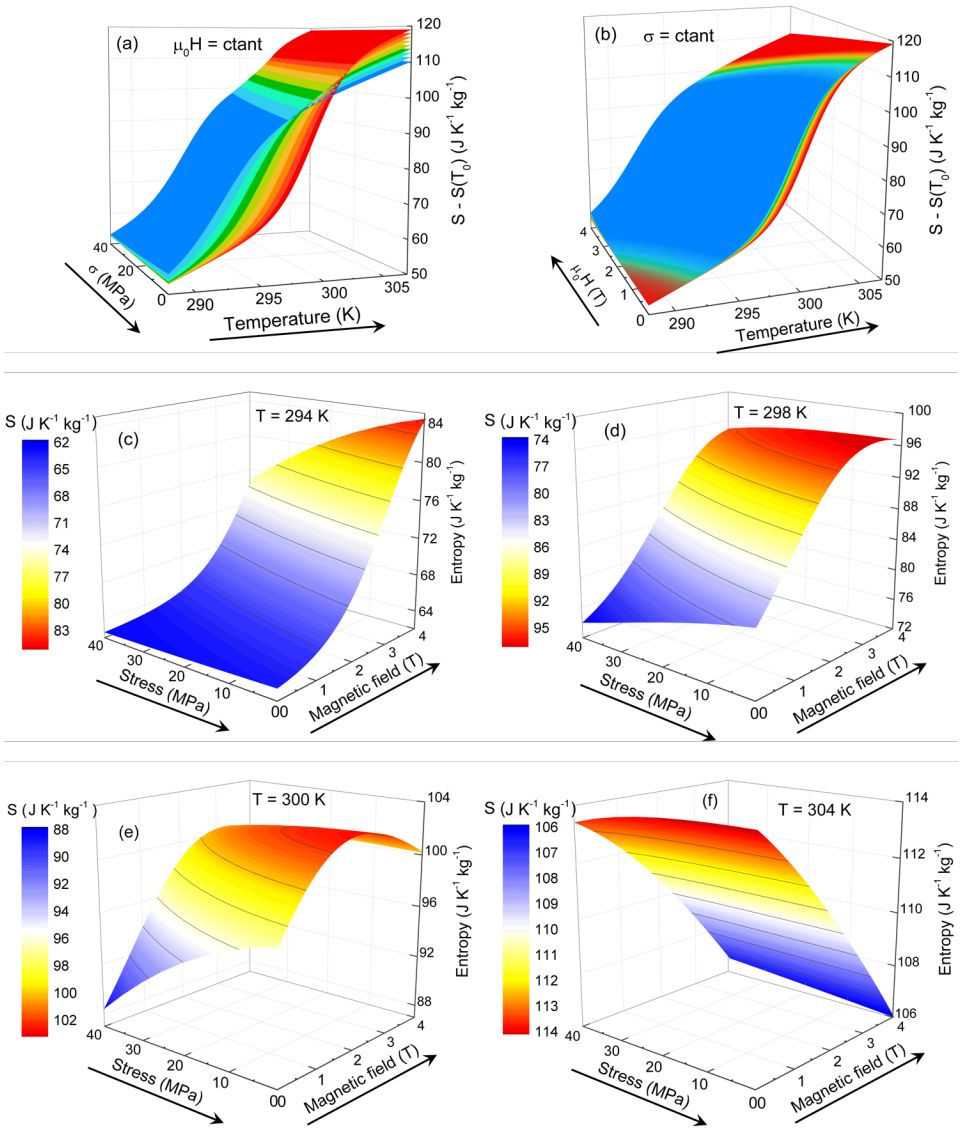

Figure 5.25: *(a) Isofield entropy surfaces as a function of stress and temperature at selected values of magnetic field in the range* $\{\mu_0 H_j\} \in \{0, 4\}$ *T. (b) Isostress entropy surfaces as a function of magnetic field and temperature at selected values of stress in the range* $\{\sigma_i\} \in \{0, 40\}$ *MPa. (c)-(d) Isothermal entropy surfaces as a function of magnetic field and stress. In all cases, the entropy is referenced to* $S_{ref} = S(T = 256\,K)$ *in the absence of stress and magnetic field. Arrows indicate the direction of the temperature, magnetic field and uniaxial stress change.*

Overall, there is an excellent agreement between both numerically simulated and experimentally computed elastocaloric (Figures 5.20 and 5.26) and magnetocaloric (Figures 5.21 and 5.27) thermal responses, respectively. Such an agreement confirms

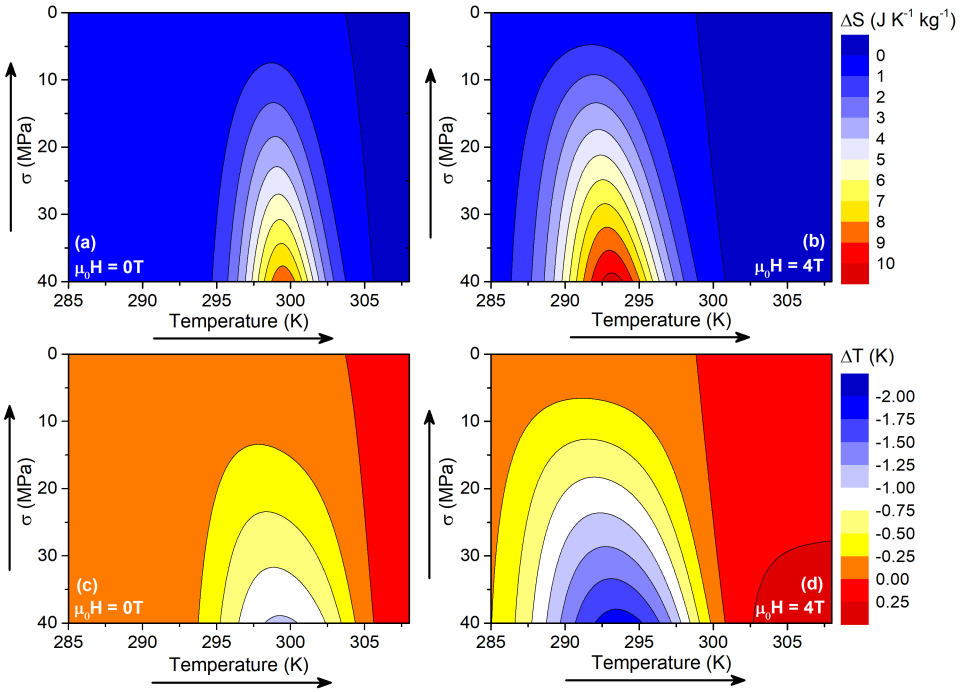

Figure 5.26: *Contour plots of the elastocaloric isothermal entropy (panels (a) and (b)) and adiabatic temperature (panels (c) and (d)) changes resulting from the removal of uniaxial stress ($\sigma \rightarrow 0$) as a function of temperature. Left side panels ((a) and (c)) correspond to the elastocaloric thermal response in the absence of magnetic field, whereas right side panels ((b) and (d)) to data under an applied magnetic field of $\mu_0 H = 4$ T. Arrows along the axis indicate the direction of the temperature and uniaxial stress changes.*

the robustness of our analytical model in order to phenomenologically reproduce the experimentally computed entropy curves, thus providing confidence in the computation of the multicaloric effect, which will be discussed in detail in the following section.

Let us first discuss the elastocaloric effect, illustrated in Figure 5.26. As it can be clearly seen when comparing panel (a) with panel (b), and panel (c) with panel (d), application of magnetic field shifts the stress-induced elastocaloric effect towards lower temperatures. In addition, application of magnetic field enlarges the temperature window where the elastocaloric effect occurs, and it also enhances the magnitude of its thermal response, which is in agreement with the fact that the transition temperature shift with stress in strongly enhanced when applying magnetic field (see Figure 5.16 (e)). In particular, for the maximum stress removal (40 MPa $\rightarrow$ 0 MPa), in the absence of magnetic field the elastocaloric thermal response renders $\Delta S = 8.7\,\mathrm{JK^{-1}kg^{-1}}$ and $\Delta T = -1.0\,\mathrm{K}$, whereas under an applied magnetic field of $\mu_0 H = 4\,\mathrm{T}$ these values increase to $\Delta S = 10.4\,\mathrm{JK^{-1}kg^{-1}}$ and

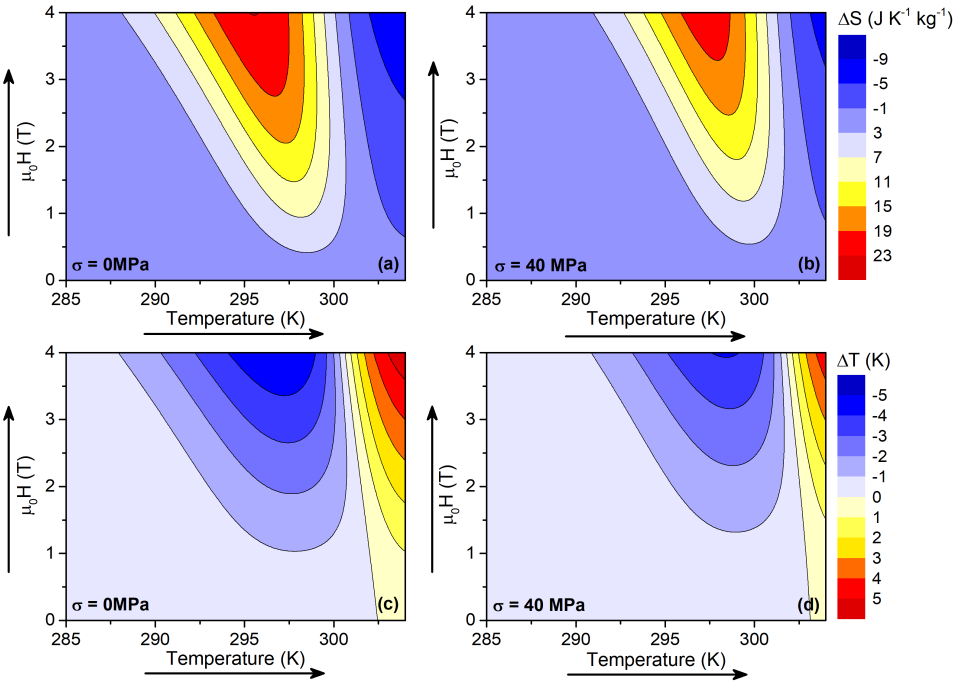

Figure 5.27: *Contour plots of the magnetocaloric isothermal entropy (panels (a) and (b)) and adiabatic temperature (panels (c) and (d)) changes resulting from the application of magnetic field ($0 \rightarrow \mu_0 H$) as a function of temperature. Left side panels ((a) and (c)) correspond to the magnetocaloric thermal response in the absence of stress, whereas right side panels ((b) and (d)) to data under an applied stress of $\sigma = 40$ MPa. Arrows along the axis indicate the direction of the temperature and magnetic field changes.*

$\Delta T = -1.9\,\mathrm{K}$.

In relation to the magnetocaloric effect, illustrated in Figure 5.27, when comparing panel (a) with panel (b), and panel (c) with panel (d), we observe a slight shift of the field-induced magnetocaloric effect towards higher temperatures when applying stress. Due to the restricted range of applied stresses, the influence of uniaxial stress on the magnetocaloric effect is weaker than the influence that magnetic field has on the elastocaloric effect. Furthermore, we observe a small shift of the thermal response to higher magnetic fields when applying uniaxial stress. For instance, if we focus on the contour line corresponding to $\Delta S = 19\,\mathrm{JK^{-1}kg^{-1}}$ illustrated in both panels (a) and (b), we observe that a magnetic field of $\mu_0 H = 2.7\,\mathrm{T}$ is necessary to field-induce such entropy change in the absence of stress, whereas a magnetic field of $\mu_0 H = 3.3\,\mathrm{T}$ is necessary to induce the same entropy change under an applied stress of $\sigma = 40\,\mathrm{MPa}$. This shift of the magnetocaloric thermal response towards higher magnetic field values is due to the fact that application of uniaxial stress further stabilizes the martensitic phase. For the maximum applied magnetic field ($0\,\mathrm{T} \rightarrow 4\,\mathrm{T}$), in the absence of stress the magnetocaloric thermal response

renders $\Delta S = 23.1\,\mathrm{JK^{-1}kg^{-1}}$ and $\Delta T = -5.0\,\mathrm{K}$, whereas under an applied stress of $\sigma = 40\,\mathrm{MPa}$ these values decrease to $\Delta S = 21.4\,\mathrm{JK^{-1}kg^{-1}}$ and $\Delta T = -4.1\,\mathrm{K}$.

5.3.5.2 Multicaloric effect

As discussed in section 2.1.2, the multicaloric effect refers to the field-induced isothermal entropy and adiabatic temperature changes under the simultaneous or sequential change of more than one external fields. As the numerically simulated entropy curves are only representative for the reverse phase transition, we are restricted to processes in which stress is removed and magnetic field is applied. Therefore, the multicaloric isothermal entropy change at a certain temperature will be computed as:

$$\Delta S(T, 0 \rightarrow \mu_0 H, \sigma \rightarrow 0) = S(T, \mu_0 H, 0) - S(T, 0, \sigma) \tag{5.24}$$

and the corresponding results are illustrated in Figure 5.28 (a)-(f) as contour colour maps at selected temperatures. Conversely, the multicaloric adiabatic temperature change is computed after inverting and interpolating the numerically simulated entropy curves as:

$$\Delta T(S, 0 \rightarrow \mu_0 H, \sigma \rightarrow 0) = T(S, \mu_0 H, 0) - T(S, 0, \sigma) \tag{5.25}$$

As for the single caloric effects, the corresponding multicaloric adiabatic temperature changes are plotted as a function of the temperature given by the initial entropy curve ($S(T, 0, \sigma)$) prior the simultaneous or sequential external field change. Figure 5.29 (a)-(f) illustrates the corresponding adiabatic temperature changes as contour colour maps at selected initial temperatures.

As a result of the combined effect of the two external stimuli, the multicaloric field-induced thermal response, illustrated in both Figures 5.28 and 5.29, shows a clear improvement with respect to the single caloric thermal response (illustrated in Figures 5.26 and 5.27 for the elastocaloric and magnetocaloric effects, respectively) for the studied alloy.

Let us first focus on the isothermal entropy change. On the one hand, the maximum values achieved for the multicaloric effect are $\Delta S_{max} = 25.2\,\mathrm{JK^{-1}kg^{-1}}$ at $T = 296\,\mathrm{K}$ and $\Delta S_{max} = 24.9\,\mathrm{JK^{-1}kg^{-1}}$ at $T = 297\,\mathrm{K}$, which clearly exceed the values obtained for the single elastocaloric and magnetocaloric effects. Furthermore, values exceeding the single caloric effect maxima can be obtained within a range of stress and magnetic field. In particular, at $T = 297\,\mathrm{K}$ (see Figure 5.28 (d)), if we focus on the contour line corresponding to $\Delta S = 24\,\mathrm{JK^{-1}kg^{-1}}$, we can obtain equal or larger entropy changes for the combination of magnetic field and stress changes ranging in a window limited by the following values: $((0\,\mathrm{T}, 30\,\mathrm{MPa}) \rightarrow (4\,\mathrm{T}, 0\,\mathrm{MPa}))$ and $((0\,\mathrm{T}, 40\,\mathrm{MPa}) \rightarrow (3\,\mathrm{T}, 0\,\mathrm{MPa}))$. On the other hand, it is possible to induce large entropy changes for relatively low values of applied magnetic field. In particular, if we focus on an applied magnetic field of $\mu_0 H = 1\,\mathrm{T}$, which is readily accessible by permanent magnets, the field-induced magnetocaloric entropy changes are in the range $\Delta S(T, 0 \rightarrow 1\,\mathrm{T}, \sigma) = 4\text{-}7\,\mathrm{JK^{-1}kg^{-1}}$ (see Figures 5.22 (a) and 5.27 (a)-(b)). Interestingly, this values can be doubled when combining the application

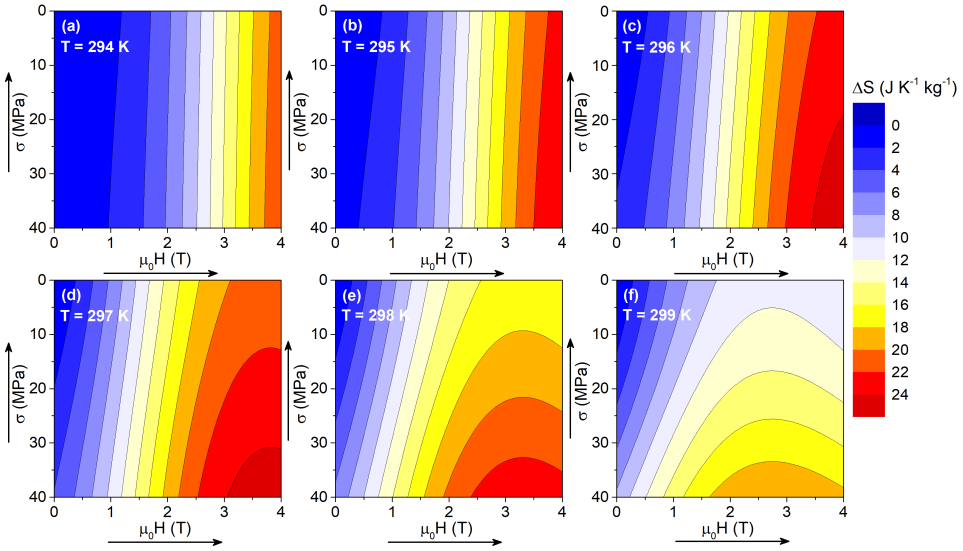

Figure 5.28: *Contour plots of the multicaloric isothermal entropy changes resulting from the application of magnetic field and the removal of uniaxial stress* $((0, \sigma) \rightarrow (\mu_0 H, 0))$ *at selected temperatures. Arrows along the axis indicate the direction of the magnetic field and uniaxial stress changes.*

of magnetic field ($\mu_0 H : 0 \rightarrow 1\,\mathrm{T}$) with the removal of stress ($\sigma : 40 \rightarrow 0\,\mathrm{MPa}$). Specifically, the achieved multicaloric entropy changes are $\Delta S = 10.5\,\mathrm{JK^{-1}kg^{-1}}$ at $T = 297\,\mathrm{K}$, $\Delta S = 13.9\,\mathrm{JK^{-1}kg^{-1}}$ at $T = 298\,\mathrm{K}$ and $\Delta S = 15.1\,\mathrm{JK^{-1}kg^{-1}}$ at $T = 299\,\mathrm{K}$.

When considering the adiabatic temperature change, similar trends are also observed when comparing the multicaloric effect with the single caloric effects. On the one hand, the maximum values achieved for the multicaloric effect are $\Delta T_{max} = -5.7\,\mathrm{K}$ at $T = 297\,\mathrm{K}$, $\Delta T_{max} = -5.9\,\mathrm{K}$ at $T = 298\,\mathrm{K}$ and $\Delta T_{max} = -5.8\,\mathrm{K}$ at $T = 299\,\mathrm{K}$, which clearly exceed the values obtained for the single elastocaloric and magnetocaloric effects. As for the isothermal entropy change, such larger values can be obtained within a range of stress and magnetic field. In particular, at $T = 298\,\mathrm{K}$ (see Figure 5.29 (e)), if we focus on the contour line corresponding to $\Delta T = -5\,\mathrm{K}$, we can obtain equal or larger temperature changes for the combination of magnetic field and stress changes ranging in a window limited by the following values: $((0\,\mathrm{T}, 10\,\mathrm{MPa}) \rightarrow (4\,\mathrm{T}, 0\,\mathrm{MPa}))$ and $((0\,\mathrm{T}, 40\,\mathrm{MPa}) \rightarrow (3.4\,\mathrm{T}, 0\,\mathrm{MPa}))$. On the other hand, at low applied magnetic fields accessible by permanent magnets, the field-induced magnetocaloric temperature changes are in the range $|\Delta T(S, 0 \rightarrow 1\,\mathrm{T}, \sigma)| = 0.5\text{-}1\,\mathrm{K}$ (see Figures 5.22 (b) and 5.27 (c)-(d)). Interestingly, when combining the application of magnetic field ($\mu_0 H : 0 \rightarrow 1\,\mathrm{T}$) together with the removal of stress($\sigma : 40 \rightarrow 0\,\mathrm{MPa}$) , the multicaloric temperature change increases up to $\Delta T_{max} = -2\,\mathrm{K}$ at $T = 299\,\mathrm{K}$.

At this point, it is important to highlight that in general, as discussed in section

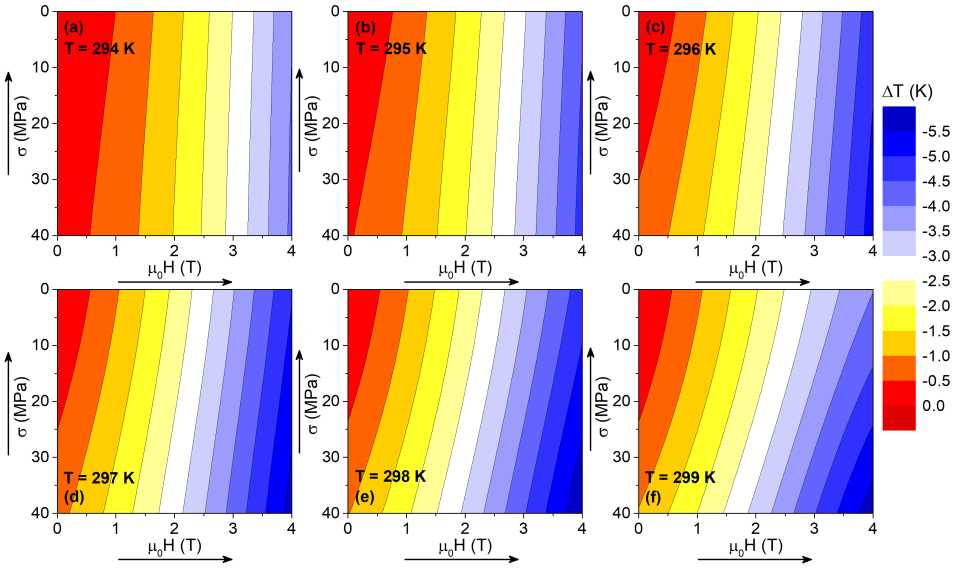

Figure 5.29: *Contour plots of the multicaloric adiabatic temperature changes resulting from the application of magnetic field and the removal of uniaxial stress* $((0, \sigma) \rightarrow (\mu_0 H, 0))$ *at selected temperatures. Arrows along the axis indicate the direction of the magnetic field and uniaxial stress changes.*

2.1.2, the field-induced multicaloric thermal response is not given by the sum of the single caloric effects [51, 53], as there is also a contribution from the cross-coupled response of the material to the application of non-conjugated external fields. Nevertheless, in the present case under study there is no contribution from the cross-coupled response of the material as we are performing an asymmetric external field change [6] and the multicaloric isofield entropy change can be separated into the following contributions:

$$\begin{aligned} &\Delta S(T, 0 \rightarrow \mu_0 H, \sigma \rightarrow 0) = \\ &\qquad \Delta S(T, \mu_0 H = 0\,\mathrm{T}, \sigma \rightarrow 0) + \Delta S(T, 0 \rightarrow \mu_0 H, \sigma = 0\,\mathrm{MPa}) \end{aligned} \tag{5.26}$$

As expressed by equation 5.26, the field-induced multicaloric effect corresponds to the direct sum of each respective single caloric effects in the absence of any applied secondary field.

5.3.6 Adiabatic thermometry of the magnetocaloric temperature change under a constant uniaxial stress

With the aim of corroborating the magnetocaloric thermal response crossover from inverse (at low temperatures) to the conventional (at high temperatures), illustrated in Figures 5.21 and 5.27, and to confirm the temperature region where the

[6] As discussed in section 2.1.2, it refers to the particular case where one external field is applied while the other one is removed.

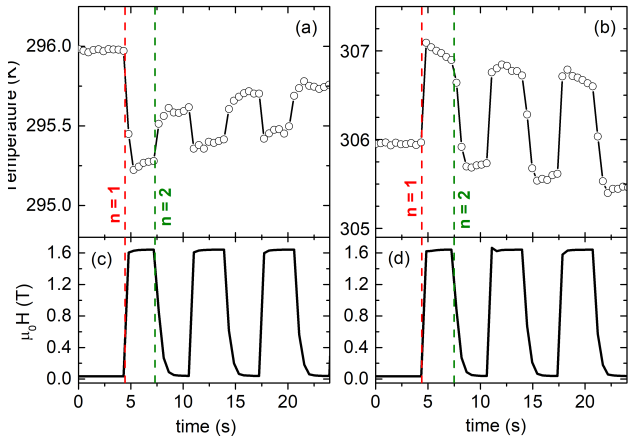

Figure 5.30: *Illustrative examples of the recorded temperature ((a) and (b)) and magnetic field ((c) and (d)) for the heating protocol in the absence of applied stress. Red dashed vertical lines (n = 1) indicate the first magnetic field ramp, while green dashed lines (n = 2) indicate the second magnetic field ramp.*

inverse magnetocaloric effect takes place, we have performed direct measurements of the adiabatic temperature change under a cyclic magnetic field in the absence of stress and under an applied compressive stress of $\sigma = 40\,\mathrm{MPa}$.

Taking into account that application of magnetic field promotes the reverse phase transition, leading to an inverse magnetocaloric effect, the protocols described in section 3.1.2.1 that correspond to an inverse caloric effect were followed. In this regard, as our study has been restricted to the reverse phase transition, to characterize its thermal response (heating protocol), the sample is initially fully transformed to the low-temperature martensitic phase in the absence of magnetic field, and then it is heated up to the initial measurement temperature. Once the sample is at isothermal equilibrium, the magnetic field is cycled, starting with a $0 \rightarrow 1.64\,\mathrm{T}$ scan.

Figure 5.30 illustrates selected examples of the temperature (top) and magnetic field (bottom) measurements recorded upon cycling the magnetic field in the range $0 \rightleftarrows 1.64\,\mathrm{T}$ in the absence of stress for the heating protocol at different initial temperatures.

At low temperatures, consistently with the inverse nature of the magnetocaloric effect, we measured a temperature decrease upon application of an external magnetic field and a temperature increase upon removal. Conversely, at higher temperatures, we measured a temperature increase upon application of an external magnetic field and a temperature decrease upon removal, which is consistent with a conventional magnetocaloric effect. Interestingly, at low temperatures (see panel (a)), the temperature change measured for the first magnetic field scan (n = 1) is larger than the temperature changes measured for the subsequent magnetic field

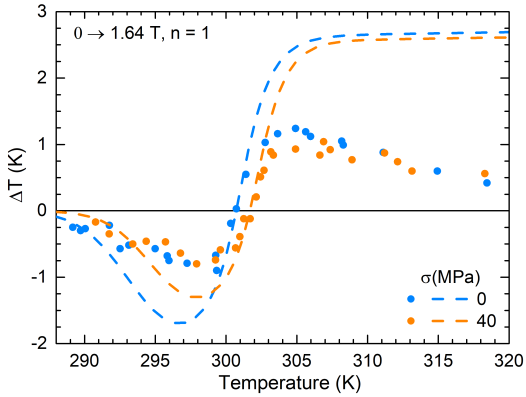

Figure 5.31: *Adiabatic temperature changes resulting from the first application (n = 1) of a 1.64 T magnetic field in the absence of applied stress (cyan symbols and line), and under an applied compressive stress of $\sigma = 40$ MPa (red symbols and line). Symbols correspond to directly measured values and lines, to the magnetocaloric adiabatic temperature change computed from the numerically simulated isofield-isostress entropy curves ($S(T, \mu_0 H, \sigma)$).*

scans (n > 1). This behaviour is in agreement with the thermal hysteresis inherent to the first-order martensitic phase transition. Oppositely, at high temperatures (see panel (b)), the measured temperature change is almost constant between the first (n = 1) and subsequent (n > 1) magnetic field scans. This behaviour is in agreement with the fact that the conventional magnetocaloric effect at high temperatures is associated with changes in the ferromagnetic order in the vicinity of the Curie point of the austenite, which exhibits a negligible thermal hysteresis as illustrated in Figures 5.13 and 5.19 (a). A similar behaviour was observed for the measurements performed under an applied compressive stress of $\sigma = 40$ MPa.

As for the direct thermometry measurements presented in section 5.1.3, the adiabatic temperature change for a certain magnetic field scan ($\mu_0 H^s \rightarrow \mu_0 H^f$) is determined as $\Delta T_{ad}(\mu_0 H^s \rightarrow \mu_0 H^f) = T(\mu_0 H^f) - T(\mu_0 H^s)$, where $T(\mu_0 H^s)$ and $T(\mu_0 H^f)$ correspond to the sample temperature before and after the magnetic field scan, respectively. The whole set of measurements for the first magnetic field scan (n = 1) is compiled in Figure 5.31, where the adiabatic temperature change measurements are plotted as a function of the initial temperature of the sample in the absence of stress (cyan symbols) and under an applied compressive stress of $\sigma = 40$ MPa (red symbols). Furthermore, the direct measurements can be compared with the corresponding values of the magnetocaloric effect computed from the numerical isofield-isostress entropy curves ($S(T, \mu_0 H, \sigma)$), which are illustrated as dashed lines in Figure 5.31.

At low temperatures, where the magnetocaloric effect is inverse, the maximum adiabatic temperature change values directly measured are $|\Delta T| \approx 0.9$ K, whereas at high temperatures, where the effect is conventional, the maximum values are found to be $\Delta T \approx 1.2$ K. Significantly, it is important to highlight that the com-

parison between direct and numerically simulated data provides a confirmation of the temperature region where the inverse magnetocaloric effect occurs, including the crossover temperature from an inverse to a conventional magnetocaloric effect. Furthermore, it also confirms the temperature shift of magnetocaloric effect with the application of uniaxial compressive stress.

Nevertheless, as it can be clearly seen in Figure 5.31, it is noteworthy that the directly measured values are systematically smaller than the numerically simulated ones. At the inverse magnetocaloric temperature region, the differences between both data sets are $\sim 0.7\,\mathrm{K}$ and can be mainly attributed to the lack of absolute adiabaticity of our bespoke setup (see section 3.2.2), together with the fact that the thermocouple is attached to the sample surface, which worsens the thermal contact between the sensor and the sample under study. In contrast, larger differences are found for the conventional magnetocaloric effect temperature region. In this case, the discrepancy between both data series must be ascribed to the fact that our method based on the construction of isofield-isostress entropy curves, and their numerical simulation, provides accurate data for the caloric and multicaloric entropy and temperature changes arising from first-order phase transitions, but it is less suited to study the arising caloric effects around continuous phase transitions. For that reason, although our numerically simulated data correctly captures the crossover of the magnetocaloric effect from inverse to conventional, actual data for the entropy and temperature changes associated with the conventional magnetocaloric effect around the Curie temperature (T_C) might be inaccurate.

5.3.7 Reproducibility of the caloric effects under field cycling

The characterization of the reproducibility of a caloric effect under field cycling is a relevant feature for potential technological applications. Nevertheless, a thorough analysis of the reproducibility of the caloric and multicaloric effects in the Ni-Mn-In alloy under study has not been possible as our analysis has been restricted to the thermograms recorded for heating runs.

Despite this fact, some estimates on the reproducibility and the required external fields can be made when considering the previously determined thermal hysteresis of the martensitic transition, together with representative values of the reported dependences of the transition temperature with stress and magnetic field. By considering a thermal hysteresis of $\sim 12\,\mathrm{K}$, and taking representative values (see Figure 5.16 (d) and (e)) for the shift of the martensitic transition with magnetic field and stress of $\frac{dT_t}{d\mu_0 H} \sim -2\,\mathrm{KT}^{-1}$ and $\frac{dT_t}{d\sigma} \sim 0.08\,\mathrm{KMPa}^{-1}$, respectively, the Ni-Mn-In alloy under study exhibits an estimated effective hysteresis on magnetic field of $\sim 6\,\mathrm{T}$, and the magnetocaloric effect is expected to be reproducible for higher field changes, [7] whereas it exhibits an effective hysteresis on uniaxial compressive stress

[7] Nevertheless, as illustrated in Figure 5.30 (a), a certain reversible adiabatic temperature change can be induced upon cycling a lower magnetic field. This behaviour is in accordance with the fact that minor hysteresis loops have a smaller thermal hysteresis than the complete phase transition, leading to an enhancement of the reversibility upon cycling the external field [227].

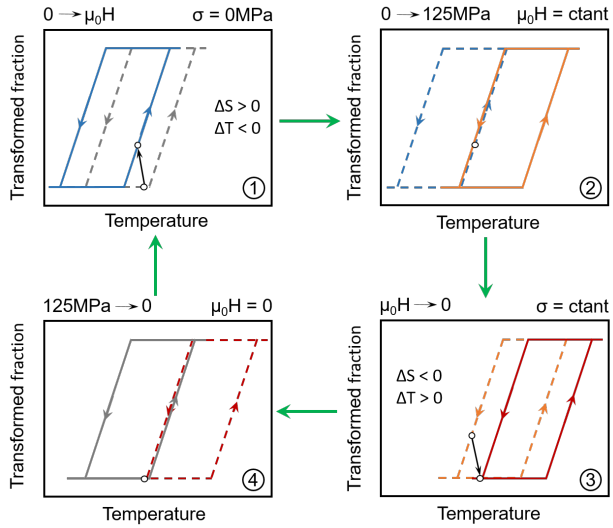

Figure 5.32: *Sketch of a multicaloric reversible cycle showing the fraction of the sample at the high-temperature austenitic phase as a function of temperature, for selected values of magnetic field and uniaxial stress. Panel 1: Application of magnetic field in the absence of stress. Panel 2: Application of stress under an applied (constant) magnetic field. Panel 3: Removal of magnetic field under an applied (constant) stress. Panel 4: Removal of stress in the absence of magnetic field.*

of $\sim 150\,\mathrm{MPa}$.

While application of magnetic fields in the order of $\sim 6\,\mathrm{T}$ are unfeasible for practical technological applications, it is important to take into account that application of a secondary external field can drastically reduce the effective hysteresis in a given external field [51, 63]. For the case under study, taking advantage of the magnetostructural character of the martensitic phase transition, application of stress can enhance the reproducibility of the magnetocaloric effect.

Considering the cyclic application and removal of a moderate magnetic field in the range of $|\mu_0 \Delta H| \sim 1\,\mathrm{T}$, the magnetocaloric effect is expected to be reproducible under the sequence represented in Figure 5.32. Each panel of the sketched multicaloric cycle shows the corresponding sample fraction at the high-temperature austenitic phase as a function of temperature at the initial (dashed lines) and final (solid lines) configuration of magnetic field and applied stress. Before the discussion of each cycle step, it is important to point out that partial hysteresis loops have not been considered for the sake of simplicity.

1. **Panel 1:**
   Application of magnetic field shifts the phase transition to lower temperatures (blue curves) and the sample, initially in the low-temperature martensitic phase, partially transforms to the high-temperature austenitic phase, as

indicated by the black arrow.

2. **Panel 2:**
   Application of a 125 MPa compressive stress [8] shifts the phase transition to higher temperatures (orange curves) in a way that the state of the sample (under magnetic field and compressive stress) lies on the cooling branch of the inherent hysteresis of the phase transition.

3. **Panel 3:**
   While keeping the stress constant, removal of magnetic field shifts the phase transitions to higher temperatures (red curves) and the sample transforms back to the low-temperature martensitic phase, as indicated by the black arrow.

4. **Panel 4:**
   Removal of the 125 MPa applied stress shifts the phase transition to lower temperatures (grey curves) in a way that the state of the sample (in the absence of magnetic field and compressive stress) lies on the heating branch of the hysteresis loop, thus recovering the initial state of the first panel.

Hence, it is seen that application of a moderate stress turns Ni-Mn-In into a suitable material for refrigeration devices using permanent magnets.

5.3.7.1 Exploiting-hysteresis cycle: a novel multicaloric approach

Recently, T. Gottschall *et. al.* proposed a novel multicaloric cycle that exploits the inherent thermal hysteresis of magnetostructural first-order phase transitions, rejecting the conventional idea that it must be minimized in order to enhance the reversibility of a given caloric effect under a cyclic application and removal of external fields [64].

From a general point of view, as discussed along sections 2.2.1 and 2.2.2, let us consider a thermodynamic system exhibiting a discontinuity of the corresponding order parameter ($\Delta X_{it} = X_i^{\beta} - X_i^{\alpha}$) at a first-order phase transition taking place at a certain temperature between two phases (α and β). As previously discussed, application of an external field drives the phase transition towards the phase that maximizes the corresponding order parameter. When the external field is removed, due to the inherent hysteresis of the phase transition, the system is locked and remains at the same phase. However, a second external field is required in order to drive the reverse phase transition and return the system to its initial thermodynamic state. Therefore, a system exhibiting a first-order phase transition that is sensitive to multiple external fields is a prerequisite to take advantage of the inherent hysteresis.

[8] The selected magnitude of the applied stress is smaller than the field necessary to overcome the effective hysteresis, which would induce the back transformation to the low-temperature martensitic phase.

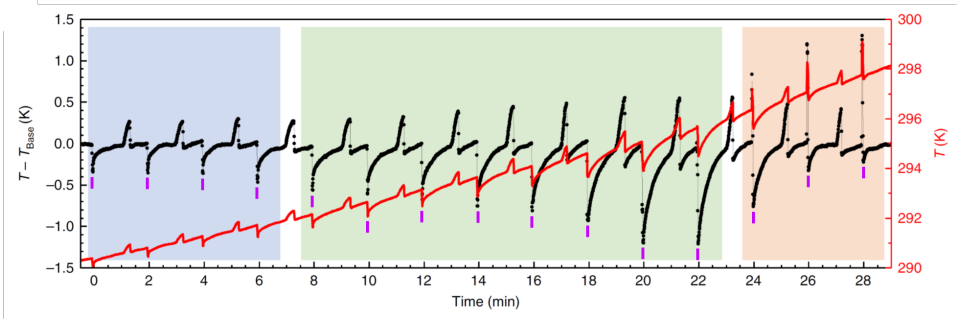

Figure 5.33: *Recorded adiabatic temperature change of the sample under study as a function of time when it is alternatively exposed to uniaxial stress pulses of* 80 *MPa (odd minutes) and magnetic field pulses of* 1.8 *T (even minutes, indicated by vertical purple lines), while it is continuously heated at a sweeping rate of* 0.25 $Kmin^{-1}$. *The absolute temperature of the sample along the experiment is shown on the right-hand side axis, and illustrated as a red line, whereas the baseline-subtracted temperature profile of the sample is shown on the left-hand side axis, illustrated as black solid symbols. The background colour of the figure separates the measured thermal response in three regions, corresponding to different behaviours of the magnetocaloric effect (MCE) exhibited by the alloy under study within the measured temperature window* $T \in [290, 298]$ *K. Blue: The sample exhibits an inverse MCE that is reversible. Green: The sample exhibits an inverse MCE that is irreversible. Red: The sample exhibits a conventional MCE that is reversible. The figure has been taken from [64].*

Such exploiting-hysteresis cycle has been proposed to take advantage of magnetostructural first-order phase transitions, as they can be driven by both magnetic field and stress. A detailed discussion of the corresponding cycle and its advantages with respect to other refrigeration cycles can be found in [64].

As a proof of concept, we have applied the corresponding exploiting-hysteresis cycle to the same Ni-Mn-In alloy under study, as it exhibits a martensitic phase transition and application of magnetic field favours the high-temperature austenitic phase whereas application of stress favours the low-temperature martensitic phase, allowing us to recover the initial state of the sample. We have performed direct measurements of the adiabatic temperature change using the bespoke setup described in section 3.2.2 and following the continuous measurement protocol. According to the different steps of the exploiting-hysteresis cycle, alternate pulses of magnetic field ($0 \rightleftarrows 1.8$ T) and stress ($0 \rightleftarrows 80$ MPa) were applied to the sample at minute intervals, while the system was continuously heated on the background at a sweeping rate of 0.25 $Kmin^{-1}$ within the temperature range $T \in [290, 298]$ K in order to test the response of the alloy at different regions of the martensitic phase transition. The corresponding results are illustrated in Figure 5.33.

The diagonal red line of the figure represents the absolute temperature of the sample during the complete experiment, referenced at the right-hand side axis. Additionally, in order to enhance the clarity of the temperature profile of the sample,

allowing us to easily identify the field-induced adiabatic temperature changes, the heating baseline was subtracted and the corrected temperature of the sample is illustrated as solid black dots, referenced at the left-hand side axis.

Three different regions can be identified from the magnetic field-induced thermal response of the sample. At low temperatures, below approximately $T \approx 292\,\mathrm{K}$ (minutes 0-7, blue shaded region), the sample is predominantly at the low-temperature martensitic phase. Upon application of an external magnetic field, we measure a small temperature decrease, consistently with the inverse nature of the magnetocaloric effect. Interestingly, when the magnetic field is removed, the temperature of the sample immediately increases and almost reverts to its initial value before the magnetic field pulse, meaning that the magnetocaloric effect is predominantly reversible at this temperature range. This behaviour is in agreement with the fact that only a small fraction of the sample can be transformed and locked to the austenitic phase when the magnetic field is applied. Consequently, we also measure a small temperature increase upon application of stress, consistently with the conventional nature of the elastocaloric effect. When the stress is removed, the temperature of the sample almost reverts to its initial value before the stress pulse, meaning that the elastocaloric effect is also predominantly reversible at this temperature range. Therefore, only a small fraction of the sample that was at the austenitic phase is transformed back to the low-temperature martensite. In consequence, at this temperature range, the sample is mainly at the martensitic phase along the different steps of the exploiting-hysteresis cycle.

At intermediate temperatures, above $T \approx 292\,\mathrm{K}$ (minutes 7-23, green shaded region), an increasing amount of martensite is transformed to austenite when the magnetic field is applied, leading to an increase of the inverse magnetocaloric effect thermal response. Furthermore, when the magnetic field is removed, the temperature of the sample is not reverting immediately to its initial value before the magnetic field pulse. Interestingly, it rather takes a certain time ($t \sim 60\,\mathrm{s}$) until the initial temperature is recovered. This behaviour is further enhanced for higher absolute temperatures of the sample within the green shaded region. The measurement of an irreversible field-induced adiabatic temperature change indicates that increasing amounts of austenite are locked by the thermal hysteresis of the sample after the magnetic field removal, which prevents it to transform back to the martensitic phase. As a bigger fraction of the sample is retained at the austenitic phase, when we apply the uniaxial stress pulse we also observe an enhancement of the conventional elastocaloric effect, meaning that a larger fraction of austenite is transformed back to martensite. Interestingly, when the stress is removed, we measure an immediate temperature decrease followed by a small irreversible stress-induced adiabatic temperature change. Therefore, even if a certain part of the recovered martensite immediately transforms back to the high-temperature austenitic phase, the irreversible temperature change indicates that a certain amount of martensite is locked by the thermal hysteresis of the sample after the stress removal. Overall, despite the fact that a certain part of the sample is not locked by the thermal hysteresis along the different steps, the exploiting-hysteresis cycle provides an irreversible field-induced adiabatic temperature change of $|\Delta T| \approx 1.2\,\mathrm{K}$ around $T \approx 296\,\mathrm{K}$.

In contrast, at temperatures above $T \approx 296\,\mathrm{K}$ (minutes 23-29, red shaded region), the sample is predominantly at the high-temperature austenitic phase. Upon application of an external magnetic field, as the absolute temperature of the sample is close to the austenitic Curie temperature ($T_C \sim 303\,\mathrm{K}$), an arising conventional magnetocaloric effect associated with changes in the ferromagnetic order in the vicinity of the Curie point of the austenite starts to gain importance with respect to the inverse magnetocaloric effect associated with the sample fraction that transforms from the martensitic to the austenitic phase. When the magnetic field is removed, consistently with the negligible thermal hysteresis of the Curie point of the austenite, we observe that the field-induced conventional magnetocaloric effect is reversible. Interestingly, the remaining inverse magnetocaloric effect is irreversible, indicating that still a certain amount of austenite is locked by the thermal hysteresis. This behaviour is further enhanced for higher absolute temperatures of the sample within the red shaded region. When the uniaxial stress pulse is applied, only a small fraction of the austenite can be transformed back to the martensitic phase, leading to a reduction of the corresponding conventional elastocaloric effect. When the stress is removed, we still observe a small irreversible stress-induced adiabatic temperature change, meaning that a shrinking part of the recovered martensite is still locked by the thermal hysteresis after the stress removal. For higher absolute temperatures of the sample, the effect of the stress pulse is further reduced and the amount of locked martensite keeps fading away. In consequence, at this temperature range, the sample is mainly at the austenitic phase along the different steps of the exploiting-hysteresis cycle.

When comparing these results with the previously measured temperature profile of the sample under a cyclic magnetic field (see Figure 5.30 (a)), we clearly see the significant advantage that this new approach provides on enhancing the reversibility of the field-induced magnetocaloric effect. For instance, a significant decrease of the field-induced adiabatic temperature change between the first (n = 1, $|\Delta T| \approx 0.8\,\mathrm{K}$) and successive (n > 1, $|\Delta T| \approx 0.3\,\mathrm{K}$) magnetic field scans was previously reported around the first-order martensitic phase transition. Conversely, an adiabatic temperature change of $|\Delta T| \approx 1.2\,\mathrm{K}$ can be cyclically obtained (within a certain working temperature range) when following the recently proposed exploiting-hysteresis cycle.

Furthermore, it is particularly important to highlight that this novel multicaloric cycle only requires the application of magnetic field over a small region to induce the irreversible phase transition, as the inherent hysteresis of the phase transition locks-in the high-temperature austenitic phase when the magnetic field is removed. Therefore, this recently proposed multicaloric approach drastically reduces the required amount of permanent magnets (typically made of Nd-Fe-B) when compared to conventional magnetic refrigerators [43, 44, 228], where the magnetic field has to be applied continuously while the heat-exchange process of the refrigerant material takes place, as the field-induced phase transition is mostly reversible.

5.3.8 Summary and conclusions

Taking advantage of the experience gained during the analysis of the Cu-Zn-Al calibration sample, we have used our unique DSC that allows the simultaneous application of compressive stress and magnetic field to study the giant elastocaloric, magnetocaloric and multicaloric effects in a Ni-Mn-In alloy. A previous characterization of the sample was performed with two commercial devices (a DSC and a vibrating sample magnetometer), reporting a martensitic phase transition that takes place around room temperature, which is close to the austenitic Curie point. The proximity between both martensitic and ferromagnetic phase transitions confer this alloy a significant interplay between the structural and magnetic degrees of freedom. The associated martensitic transition entropy change in the absence of applied external fields was determined to be $\Delta S_t^M = (-37.3 \pm 0.5)\,\mathrm{JK^{-1}kg^{-1}}$ and $\Delta S_t^A = (37.7 \pm 0.5)\,\mathrm{JK^{-1}kg^{-1}}$ for the forward and reverse martensitic transitions, respectively.

The calorimetric measurements performed with our bespoke setup allowed us to determine both the transition temperature phase diagram and the transition entropy change behaviour within the magnetic field and compressive stress coordinate space under study.

The transition temperature of the forward and reverse martensitic transitions was identified by the calorimetric peak position of the DSC measurements. For all values of applied compressive stress, both forward and reverse martensitic transition temperatures linearly decreased when increasing the applied magnetic field with slopes in the range $\frac{dT_t}{d\mu_0 H} \in [-2.6, -1.7]\,\mathrm{KT^{-1}}$, thus giving rise to an inverse magnetocaloric effect. Conversely, for all values of applied magnetic field, both forward and reverse martensitic transition temperatures linearly increased when increasing the applied compressive stress with slopes in the range $\frac{dT_t}{d\sigma} \in [0.03, 0.13]\,\mathrm{KMPa^{-1}}$, leading to a conventional elastocaloric effect. Interestingly, as anticipated by the proximity between the martensitic phase transition and the austenitic Curie point, we found that a secondary applied external field has an important effect on the transition temperatures shift rates with either magnetic field and uniaxial stress. Therefore, the sample exhibits a significant cross-coupled response.

The DSC measurements allowed us to determine the transition entropy change of the martensitic phase transition. Due to the complexity of our bespoke DSC setup, some of the recorded thermograms exhibit a poor signal-to-baseline ratio. Therefore, we restricted our analysis to the thermograms recorded for the heating runs under applied magnetic fields of $\mu_0 H \leq 4\,\mathrm{T}$. As for the Cu-Zn-Al calibration sample, a constant calibration factor had to be introduced to the baseline corrected thermograms in order to properly determine the corresponding transition entropy changes. For all values of applied compressive stress, the transition entropy change decreases when increasing the applied magnetic field. This behaviour is a consequence of the increase in the magnetic entropy change contribution when increasing the applied magnetic field, which opposes the vibrational entropy change, associated with the

phonon modes of the alloy crystal lattice, which is larger than the magnetic contribution in absolute value. Interestingly, we could not observe any systematic dependence of the transition entropy change for applied stresses up to $\sigma = 40\,\mathrm{MPa}$ and the corresponding average transition entropy change behaviour (for stresses up to $\sigma = 40\,\mathrm{MPa}$) was parametrized as $\Delta S_t(\mu_0 H) = 38(1) - 1.9(5)\mu_0 H$ ($\mathrm{JK^{-1}kg^{-1}}$).

The quasidirect derivation of the elastocaloric and magnetocaloric effects relies on the computation of the corresponding experimental isofield-isostress entropy curves, which are constructed from the integration of the corrected thermograms together with the specific heat data at the martensitic and austenitic phases. While it is common to assume that the specific heat does not depend on the applied external field, due to the proximity between the martensitic and ferromagnetic phase transitions for the alloy under study, its specific heat will exhibit a certain dependence on the applied magnetic field. On the one hand, the specific heat of the martensitic phase, measured with a bespoke AC calorimeter, was found to increase linearly with temperature but it was independent of the applied magnetic field. On the other hand, the specific heat of the austenitic phase for a Ni-Mn-In alloy with a similar composition, measured with a commercial relaxation calorimeter (that allowed us to reach higher temperatures), was found to be constant in temperature but it linearly increased when increasing the applied magnetic field.

The field-induced isothermal entropy and adiabatic temperature changes for the elastocaloric and magnetocaloric effects were computed by subtracting the corresponding experimental isofield-isostress entropy curves. As expected, the computed elastocaloric effect has been found to be conventional. Interestingly, the magnetocaloric thermal response has been found to exhibit a crossover from inverse (at low temperatures) to conventional (at high temperatures). While the inverse magnetocaloric effect is associated with the field-induced martensitic phase transition, the arising conventional magnetocaloric effect is associated with changes in the ferromagnetic order of the austenitic phase in the vicinity of its Curie point.

For both caloric effects, an increase of the martensitic phase transition driving field (stress for the elastocaloric effect and magnetic field for the magnetocaloric effect) enlarges the field-induced thermal responses for all values of the applied secondary external field. Moreover, application of a secondary external field shifts the temperature window where the giant elastocaloric and magnetocaloric effects occur. The maximum field-induced entropy changes are $\Delta S_{max} = 24\,\mathrm{JK^{-1}kg^{-1}}$ and $\Delta S_{max} = 14\,\mathrm{JK^{-1}kg^{-1}}$ for the magnetocaloric and elastocaloric effects, respectively. The fact that these values are smaller than the transition entropy change of this alloy indicate that we are not able to fully induce the martensitic phase transition for the studied range of external fields.

In order to compute the corresponding caloric and multicaloric effects for any combination of magnetic field and compressive stress changes, we have defined an analytical function to phenomenologically reproduce the behaviour of the isofield-isostress entropy curves. The numerical treatment of our calorimetric data enabled us to accurately reproduce the entropy of the alloy over the whole temperature,

magnetic field and uniaxial compressive stress phase space under study. We found a good agreement between the numerically simulated and the quasidirectly computed elastocaloric and magnetocaloric field-induced thermal responses, confirming the robustness of our analytical model in order to phenomenologically reproduce the experimentally computed entropy curves.

Furthermore, with the aim of providing reliability to both the quasidirect and the numerically simulated thermal responses, we have used a bespoke setup to directly measure the magnetocaloric adiabatic temperature change induced under the application of a cyclic magnetic field and different applied constant stresses. Significantly, the comparison between the directly measured and the numerically simulated data confirmed the temperature region where the inverse magnetocaloric effect takes place, including the crossover temperature from an inverse to a conventional magnetocaloric effect. Moreover, it also confirmed the temperature shift of the magnetocaloric effect with the application of uniaxial stress. Nevertheless, both data series exhibit a significant difference at the conventional magnetocaloric effect temperature region, which is ascribed to the fact that our method based on isofield-isostress calorimetric measurements is less suited to study the arising caloric effects around continuous phase transitions. Even so, it is important to emphasize that both data series compare well at the temperature region where the field-induced caloric effect arises from the first-order martensitic phase transition, and around this temperature range both quasidirect and numeric methods provide accurate values for the field-induced caloric and multicaloric thermal responses.

Concerning the numerically simulated multicaloric effect, our results show that a suitable combination of magnetic field and stress give rise to isothermal entropy and adiabatic temperature changes larger than those achievable when only a single external field is swept. Specifically, the maximum isothermal entropy changes that can be obtained are $\Delta S_{max} = 25.2\,\mathrm{JK^{-1}kg^{-1}}$ at $T = 296\,\mathrm{K}$ and $\Delta S_{max} = 24.9\,\mathrm{JK^{-1}kg^{-1}}$ at $T = 297\,\mathrm{K}$. Furthermore, the combination of two external fields enlarges the temperature window where the alloy exhibits a giant field-induced thermal response.

When considering the relevance of multicaloric effects to future technological applications, it is particularly important to highlight that the application of a moderate magnetic field of $\mu_0 H = 1\,\mathrm{T}$, which is readily accessible by permanent magnets, together with a stress removal of $\sigma = 40\,\mathrm{MPa}$ yields an isothermal entropy change of $\Delta S_{max} = 13.9\,\mathrm{JK^{-1}kg^{-1}}$ at $T = 298\,\mathrm{K}$ and $\Delta S_{max} = 15.1\,\mathrm{JK^{-1}kg^{-1}}$ at $T = 299\,\mathrm{K}$, which are more than double the maximum single caloric isothermal entropy changes achievable by the same moderate external fields. Similar trends are observed when considering the field-induced adiabatic temperature changes of both single caloric and multicaloric effects.

The reversibility of the field-induced thermal response is of utmost importance when considering the applicability of multicaloric materials for diverse technological applications. In this regard, two different approaches have been discussed for the alloy under study.

On the one hand, taking advantage of the magnetostructural character of the martensitic phase transition, it has been shown that its sensitivity to a secondary field enables tuning the inherent hysteresis of the martensitic phase transition. In particular, an enhancement of the reversibility of the field-induced thermal response, together with a decrease of the needed external fields for such purposes, can be achieved by a suitable combination of magnetic field and uniaxial compressive stress.

On the other hand, the Ni-Mn-In alloy under study has been used to test the feasibility of a novel multicaloric cycle, proposed by T. Gottschall *et. al.* in [64], that instead of trying to minimize the inherent hysteresis of first-order phase transitions, takes advantage of it to lock-in the sample at a certain phase and prevent the back transformation when removing the phase transition driving field. As a proof of concept, we have performed direct measurements of the adiabatic temperature change with a bespoke setup when the sample is subjected to alternate pulses of magnetic field and compressive stress. The results showed that the exploiting-hysteresis cycle provides an adiabatic temperature change of $|\Delta T| \approx 1.2\,\mathrm{K}$ that can be cyclically obtained around $T = 296\,\mathrm{K}$, which clearly outperforms the reversible adiabatic temperature change measured under a cyclic magnetic field for the same sample.

5.4 Ni-Mn-Ga-Cu

So far, experimental studies on multicaloric materials subjected to the combined effect of magnetic field and uniaxial stress have only been conducted on alloys exhibiting an inverse magnetocaloric effect and a conventional mechanocaloric effect, such as Fe-Rh [65] or several Ni-Mn-based Heusler alloys [61, 62, 66]. In the latter case, as discussed in section 5.3.4.2, the magnetic entropy contribution competes against the vibrational one, which plays a dominant role on driving the phase transition between the low-temperature low-magnetization martensitic phase and the high-temperature ferromagnetic austenitic phase. [9] Furthermore, due to the different nature of both caloric effects, these materials require an asymmetric external field change [10] in order to field-induce the first-order phase transition via the simultaneous or sequential change of both magnetic field and uniaxial compressive stress. Therefore, as discussed in section 2.1.2, their multicaloric thermal response corresponds to the simple sum of both single caloric effects in the absence of a secondary field.

In light of these facts, multicaloric materials exhibiting a first-order magnetostructural phase transition between a high-temperature low-magnetization phase and a low-temperature ferromagnetic phase, where both magnetocaloric and mechanocaloric effects are conventional, can present significant advantages. On the one hand, their vibrational and magnetic contributions to the transition entropy change will not compete against each other as they will have the same sign. On the other hand, as both caloric effects will have the same nature, the first order phase transition can be field-induced via a symmetric external field change [11] of both magnetic field and uniaxial compressive stress. Therefore, as discussed in section 2.1.2, their multicaloric thermal response will not correspond to the simple sum of both single caloric effects in the absence of a secondary field, as the cross-coupled response of the system will play a role. These multicaloric materials, which will exhibit synergic single caloric effects, are very appealing for technological applications based on multicaloric effects.

Specifically, we have selected a Ni-Mn-Ga-Cu alloy as a prototype material. The substitution of Mn by Cu in Ni_2MnGa Heusler alloy shifts the martensitic phase transition to higher temperatures while decreasing the austenitic Curie temperature, and both transitions join at a triple point close to 6 at% of Cu [229]. Therefore, the proximity between both phase transitions increases when increasing the Cu content, which anticipates a pronounced coupling between the structural and magnetic degrees of freedom. Specifically, a martensitic phase transition between

[9] Conversely, the magnetostructural phase transition of Fe-Rh is driven by electronic and magnetic entropy contributions, while the vibrational competes against them. Furthermore, it must be mentioned that there is still some controversy on whether the electronic or magnetic entropy contribution is the dominant one [132].

[10] As discussed in section 2.1.2, it refers to the particular case where one external field is applied while the other one is removed.

[11] As discussed in section 2.1.2, it refers to the particular case where both external fields are either applied or removed.

a high-temperature paramagnetic phase to a low-temperature ferromagnetic phase will take place for Cu concentrations above 6 at%.

Taking advantage of the experience gained from the analysis of both the Cu-Zn-Al calibration sample, presented in section 3.3, and the metamagnetic Ni-Mn-In shape-memory alloy, presented in section 5.3, we have used the same purpose-built DSC setup described in section 3.1.4 to study the caloric and multicaloric response in terms of the isothermal entropy and adiabatic temperature changes of a prototype Ni-Mn-Ga-Cu magnetic shape-memory alloy when subjected to the combined effect of magnetic field and uniaxial compressive stress. The present work on this alloy is aimed at thoroughly characterizing the advantages of the multicaloric effect with respect to the single caloric (magnetocaloric and elastocaloric) effects in alloys exhibiting synergic single caloric effects.

5.4.1 Sample details

The experiments were performed on a sample with nominal composition $Ni_{50}Mn_{18.5}Ga_{25}Cu_{6.5}$ prepared by arc melting, and further treated using the suction-casting option of the arc melter. This sample was fabricated at the Ningbo Institute of Materials Technology and Engineering, Ningbo (China), and details of the sample preparation and heat treatment are given in [229].

A sample, shaped as a rod, with 3.2 mm diameter and 6.7 mm length that had a mass of 419.06 mg was cut from the ingot prepared by arc melting. A small piece was cut from the sample (19.74 mg) to perform a previous characterization with a commercial DSC in the absence of any applied external field. The remaining part of the sample, with 3.2 mm diameter and 6.1 mm length (380.23 mg), was polished and used to perform the differential scanning calorimetry measurements under the influence of magnetic field and uniaxial stress. Specific heat measurements were performed on a smaller piece cut from the initial ingot.

5.4.2 Experimental details

1. A previous calorimetric characterization of the first-order martensitic phase transition in the absence of any applied external field was performed by means of a DSC Q2000 setup from *TA Instruments*®, at a scanning rate of $\pm 5\,\mathrm{K min^{-1}}$.

2. Simultaneous dilatometric and DSC measurements have been performed with the bespoke DSC setup described in section 3.1.4 at typical temperature scanning rates of $\pm 0.5\,\mathrm{K min^{-1}}$ within a temperature range $T \in [280,\ 340]\,\mathrm{K}$ under constant values of uniaxial compressive stress $\{\sigma_i\} = \{0,\ 5,\ 10,\ 20,\ 30\}\,\mathrm{MPa}$ and magnetic field $\{\mu_0 H_j\} = \{0,\ 1,\ 2,\ 3,\ 4,\ 5,\ 6\}\,\mathrm{T}$.

   The applied compressive stresses required the application of forces $\{F_i\} = \{0,\ 40,\ 80,\ 160,\ 240\}\,\mathrm{N}$ to the sample. Therefore, as discussed in detail for

Cu-Zn-Al in section 3.3, as $F_i < 400\,\mathrm{N}$ it is not necessary to introduce a stress sensitivity factor to correct the DSC thermograms and compute the corresponding transition entropy changes, as any possible deviation on the calorimetric signal from the effect of the applied stress on the bespoke setup would fall within the experimental error.

3. Specific heat measurements of the martensitic and austenitic phases were performed using two different systems. On the one hand, a bespoke Peltier cell calorimeter [230, 231] was used to perform measurements within a temperature range $T \in [50,\ 350]\,\mathrm{K}$ under constant applied magnetic fields $\{\mu_0 H_j\} = \{0,\ 1,\ 2\,3\}\,\mathrm{T}$. On the other hand, a commercial relaxation calorimeter implemented in a PPMS from *Quantum Design*® was used to measure the specific heat within a temperature range $T \in [330,\ 400]\,\mathrm{K}$ under constant applied magnetic fields $\{\mu_0 H_j\} = \{0,\ 1,\ 2,\ 3,\ 4,\ 5,\ 6\}\,\mathrm{T}$.

5.4.3 Calorimetric characterization of the martensitic phase transition in the absence of external fields

Before characterizing the first-order martensitic phase transition of Ni-Mn-Ga-Cu with our bespoke DSC setup under the influence of uniaxial compressive stress and magnetic field, it is useful to perform a previous measurement in the absence of any applied external field with a commercial DSC. The corresponding recorded thermograms for heating and cooling runs are illustrated in Figure 5.34.

The latent heat associated with the martensitic phase transition gives rise to an exothermal (negative) peak when inducing the forward transition (cooling), and to an endothermal (positive) peak when inducing the reverse transition (heating).

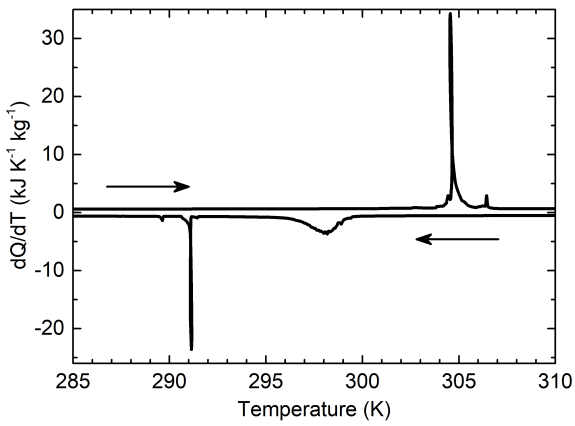

Figure 5.34: *Calorimetric signal as a function of temperature recorded upon heating (upper curve) and cooling (lower curve), measured at a scanning rate of* $\pm 5\,K min^{-1}$ *with a DSC Q2000 from TA Instruments*®

The base line signal of both thermograms can be accurately approximated by a straight line, fitted before and after the temperature range where the calorimetric peak spreads $[T_s, T_f]$. This straight line defines the baseline for the complete thermogram, and after performing the corresponding baseline correction as discussed in section 3.1.1, the transition entropy changes for the forward and reverse martensitic transitions are found to be $\Delta S_t^M = (-27.9 \pm 0.5)\,\mathrm{JK^{-1}kg^{-1}}$ and $\Delta S_t^A = (27.2 \pm 0.5)\,\mathrm{JK^{-1}kg^{-1}}$, respectively, which are in agreement with previously reported values for composition-related Ni-Mn-Ga-Cu shape-memory alloys [229, 232]. Interestingly, the forward phase transition displays two clearly distinct contributions to its calorimetric signal, centred at different temperatures, and the whole phase transition spreads over a significantly broader temperature range than that of the reverse phase transition. Nevertheless, the transition temperature can still be defined by the main calorimetric peak position of each thermogram, which are found to be $T_t^M = 298\,\mathrm{K}$ and $T_t^A = 305\,\mathrm{K}$ respectively, defining a thermal hysteresis of $T_t^M - T_t^A = 7\,\mathrm{K}$ in the absence of external fields.

5.4.4 Calorimetry under constant magnetic field and uniaxial stress

The raw DSC thermograms measured with our bespoke setup at selected constant values of applied uniaxial compressive stress and magnetic field are shown in Figure 5.35. Panels (a), (c), (e), (g) and (i) illustrate the recorded thermograms for the heating runs, whereas panels (b), (d), (f), (h) and (j) illustrate those corresponding to the cooling runs. The first-order martensitic phase transition gives rise to an exothermal calorimetric peak on cooling and to an endothermal calorimetric peak on heating.

Under a certain constant uniaxial compressive stress, an increase of the applied magnetic field shifts the calorimetric peaks to higher temperatures, which corresponds to a stabilization of the martensitic phase. In the same way, under a certain constant magnetic field, an increase of the applied compressive stress also shifts the calorimetric peaks to higher temperatures, indicating that the martensitic phase is also stabilized by magnetic field.

Consequently, as discussed in detail in section 2.2.2, as the application of magnetic field and stress stabilizes the low-temperature martensitic phase (shifting the transition temperature to higher values), the material under study will exhibit conventional magnetocaloric and elastocaloric effects.

Furthermore, it is interesting to compare the DSC measurements with the specimen's strain, which is computed from the dilatometric measurements as:

$$\varepsilon(T, \mu_0 H, \sigma) = \frac{l(T, \mu_0 H, \sigma) - l_{ref}}{l_{ref}} \tag{5.27}$$

where $l(T, \mu_0 H, \sigma)$ is the length of the sample parallel to the direction of the applied force, and l_{ref} is the sample length measured at a reference temperature (T_{ref}).

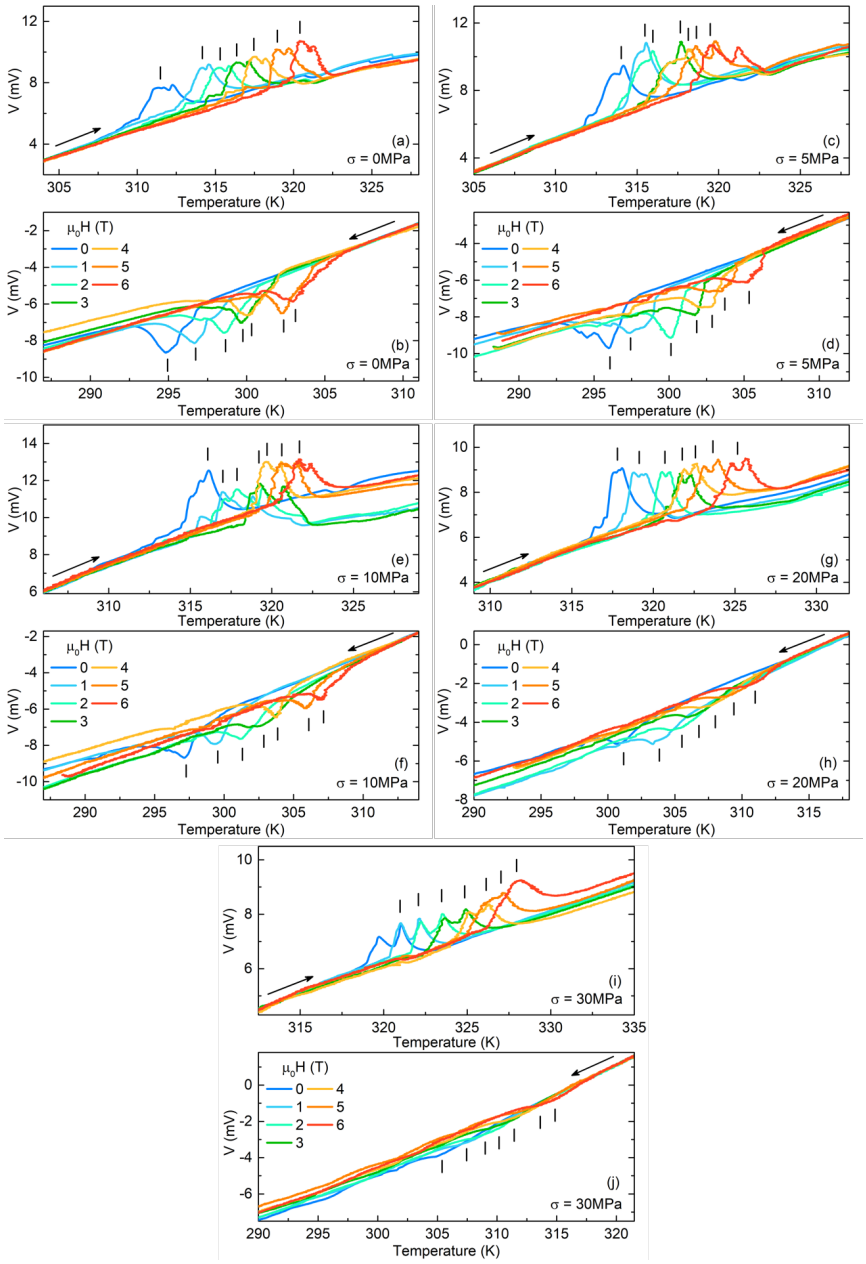

Figure 5.35: *Calorimetric signal as a function of temperature at selected values of uniaxial compressive stress and magnetic field. Panels (a), (c), (e), (g) and (i) correspond to heating runs and panels (b), (d), (f), (h) and (j) to cooling runs, respectively. Vertical black lines indicate the position of the calorimetric peaks. A vertical shift has been applied to selected curves for the sake of clarity.*

For the cooling runs, l_{ref} is taken as the sample length at the high-temperature

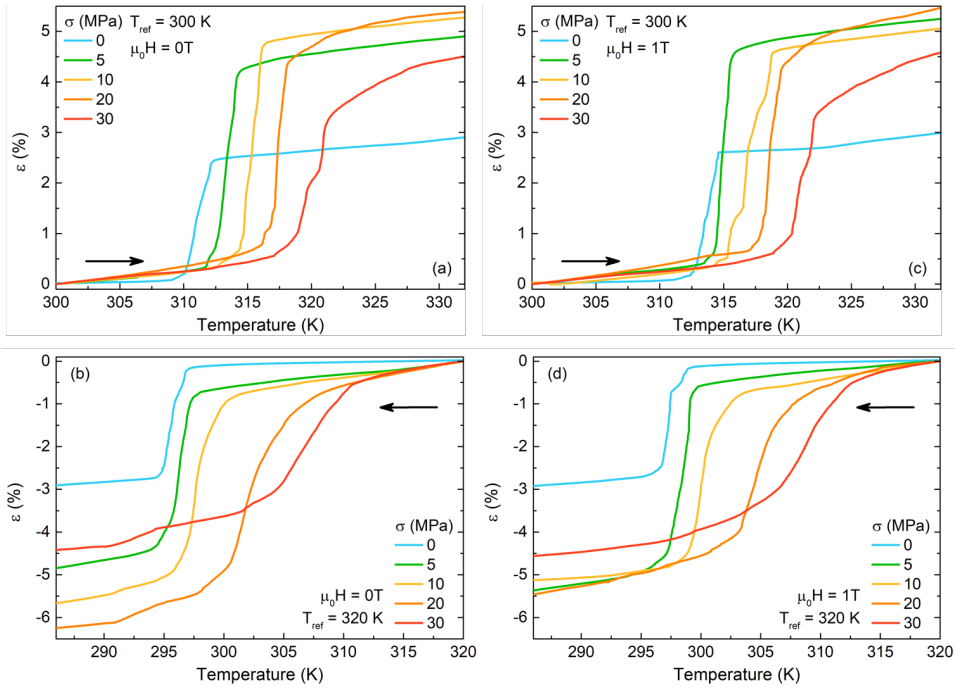

Figure 5.36: *Strain as a function of temperature at selected values of uniaxial compressive stress in the absence of magnetic field (left) and under an applied magnetic field of $\mu_0 H = 1\,T$ (right) for both heating ((a) and (c)) and cooling ((b) and (d)) runs.*

austenitic phase. As the material under study is paramagnetic at the austenitic phase, and the applied compressive stresses are small, it is assumed that the sample length at the austenitic phase shows a negligible dependence on the applied external fields. Therefore, it is taken as $l_{ref} = l_A = 6.22\,\text{mm}$ for all cooling runs, which corresponds to the sample length measured in the absence of external fields.

Conversely, for heating runs, l_{ref} is taken as the sample length at the low-temperature martensitic phase. As the application of external fields can increase the percentage of favourably oriented martensite variants [223], the sample length at the martensitic phase can depend on the specific combination of applied external fields. Therefore, l_{ref} for each heating run is computed from the corresponding transition strain associated with the forward martensitic phase transition under each specific combination of applied external fields as: $l_{ref}(T, \mu_0 H, \sigma) = (1 - \Delta\varepsilon_t(\mu_0 H, \sigma))l_A$.

As previously discussed for Cu-Zn-Al in section 3.3, the dilatometric measurements performed with our bespoke setup will not be analysed in detail. Therefore, for the sake of simplicity, Figure 5.36 only illustrates selected examples of the computed strain for the heating ((a) and (c)) and cooling ((b) and (d)) runs at selected values of stress and magnetic field.

The first-order phase transition is seen as a sharp change in strain, which spreads over a broader temperature range when inducing the forward phase transition than the reverse phase transition. In this regard, it is worth noticing the good correlation of the transition temperature region between both sets of measurements (DSC and dilatometric) for both heating and cooling runs, which indicates that both phenomena arise from the first-order magnetostructural phase transition. Furthermore, the sharp change in strain increases when increasing the applied uniaxial stress as a result of the increase of the percentage of favourably oriented martensitic variants [223]. Nevertheless, the measured transition strains under an applied compressive stress of $\sigma = 30\,\mathrm{MPa}$ are systematically lower than the strains measured under $\sigma = 20\,\mathrm{MPa}$. In this regard, it must be mentioned that the specimen under study exhibited visible cracks after completing the measurement series under an applied compressive stress of $\sigma = 30\,\mathrm{MPa}$. Therefore, it is reasonable to ascribe this decrease to the sample degradation.

5.4.4.1 Transition temperature phase diagram

The transition temperatures of the forward (T_t^M) and reverse (T_t^A) martensitic transitions can be identified with the calorimetric peak position of the heating and cooling runs, respectively. Figure 5.37 (a) illustrates the phase diagram of the transition temperatures in the magnetic field and compressive stress coordinate space. The experimental values are plotted as blue and red solid symbols for the forward and reverse martensitic transitions, respectively, and their behaviour is parametrized by two non-linear surface fits with equations:

$$\begin{aligned} T_t^M(\mu_0 H, \sigma) &= 294.4(2) + 1.97(14)\mu_0 H + 0.28(3)\sigma \\ &\quad - 0.08(2)\mu_0 H^2 + 2.9(0.8)\cdot 10^{-3}\sigma^2 \ \text{(K)} \end{aligned} \tag{5.28a}$$

$$\begin{aligned} T_t^A(\mu_0 H, \sigma) &= 312.7(2) + 1.21(13)\mu_0 H + 0.26(2)\sigma \\ &\quad - 8(20)\cdot 10^{-3}\mu_0 H^2 + 7(8)\cdot 10^{-4}\sigma^2 \ \text{(K)} \end{aligned} \tag{5.28b}$$

On the one hand, the red surface corresponds to the reverse martensitic transition, which can be induced by either increasing the temperature or decreasing the applied external fields (magnetic field and/or stress). On the other hand, the blue surface corresponds to the forward martensitic transition, which can be induced by either decreasing the temperature or increasing the applied external fields. All these different possibilities to induce both forward and reverse transitions are indicated by black arrows in the figure.

It is important to highlight that the martensitic phase transition spreads over a certain temperature range. Therefore, each forward and reverse transition surfaces have a certain thickness, which has been omitted from the figure for the sake of clarity. Thus, well above the red surface the sample will completely be in the austenitic phase, whereas well below the blue surface the sample will be in the martensitic phase. Furthermore, the temperature region between both surfaces accounts for the hysteresis of the martensitic phase transition, which slightly decreases when

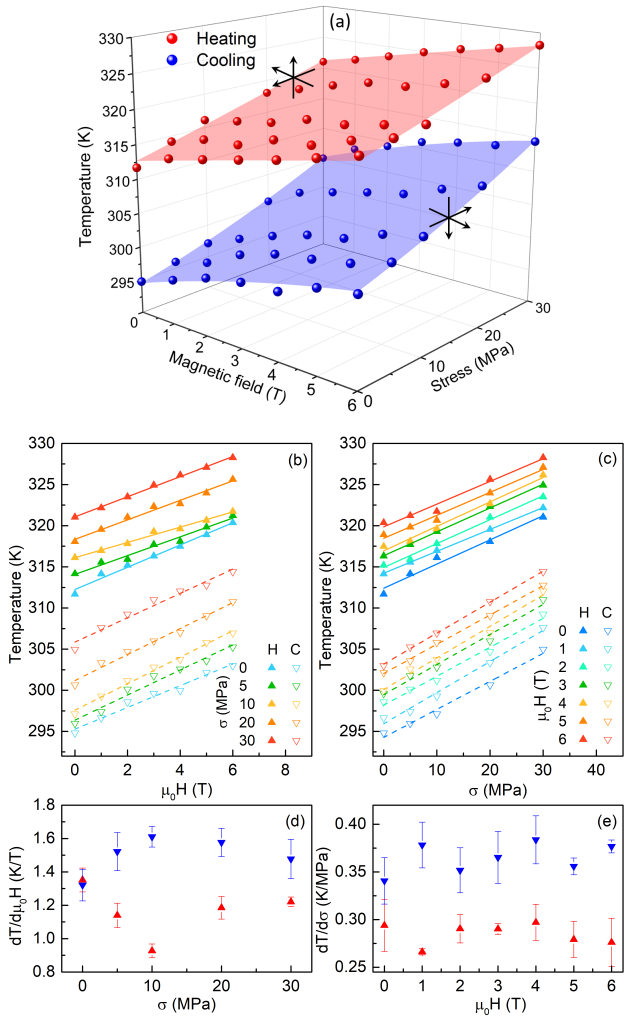

Figure 5.37: *(a) Transition temperature as a function of magnetic field and uniaxial stress. Solid symbols correspond to the transition temperatures obtained from the calorimetric peaks, and surfaces to the best fits to these values. Upper red surface corresponds to the reverse (T_A) martensitic transition, whereas the lower blue surface to the forward (T_M) martensitic transition. The arrows in each surface indicate the changes in temperature, magnetic field and uniaxial stress to cross each surface and induce the forward or reverse martensitic phase transition, respectively. (b) Transition temperatures as a function of magnetic field at constant uniaxial stress, and as a function of stress at constant magnetic fields (c). For both panels, solid symbols stand for the reverse transition and open symbols stand for the forward transition. (d) Stress dependence of the slope of the fitted transition temperature as a function of magnetic field. (e) Magnetic field dependence of the slope of the fitted transition temperature as a function of stress. Lines are linear fits to the data.*

increasing the applied external fields. Within this temperature range, the sample's thermodynamic state will depend on its thermal history.

From the tree dimensional representation of the transition temperature phase diagram as a function of magnetic field and stress, the corresponding projections on the T–$\mu_0 H$ and T–σ planes are shown in Figures 5.37 (b) and (c), respectively.

For all values of applied stress, both forward and reverse martensitic transition temperatures linearly increase when increasing the applied magnetic field, with slopes in the range $\frac{dT_t}{d\mu_0 H} \in [0.9, 1.6]\,\mathrm{KT}^{-1}$ that compare well with previously reported values for Ni-Mn-Ga-Cu magnetic shape-memory alloys with similar compositions in the absence of applied stress [229, 233]. Likewise, for all values of applied magnetic field, both forward and reverse martensitic transition temperatures linearly increase when increasing the applied stress, with slopes in the range $\frac{dT_t}{d\sigma} \in [0.27, 0.38]\,\mathrm{KMPa}^{-1}$. In this case, the slope determined in the absence of magnetic field is larger but comparable to the values reported for Ni-Mn-Ga-Cu magnetic shape-memory alloys with similar compositions [233].

Interestingly, as illustrated in Figure 5.37 (d) and (e), no effect of the secondary field has been found on the slopes determined from the linear fits to the forward and reverse martensitic transition temperatures as a function of magnetic field $\left(\frac{dT_t}{d\mu_0 H}\right)$ and compressive stress $\left(\frac{dT_t}{d\sigma}\right)$.

5.4.4.2 Computation of the transition entropy change

Due to the complexity of our bespoke DSC setup, the recorded thermograms illustrated in Figure 5.35 (a)-(j) under the simultaneous application of magnetic field and stress exhibit a poorer baseline when compared to the recorded thermograms with a commercial DSC. In particular, the measurements performed under an applied compressive stress of $\sigma = 30\,\mathrm{MPa}$ (illustrated in Figure 5.35 (i) and (j)) exhibit a poorer signal-to-baseline ratio, particularly significant for the cooling runs, and a proper analysis of these curves is not possible.

As a consequence, and taking into account that the sample exhibited a visible degradation after completing this measurement series, we decided to restrict the analysis in the following sections on the thermograms recorded for heating and cooling runs under applied compressive stresses up to $\sigma = 20\,\mathrm{MPa}$.

As discussed in section 3.1.1, the measured thermograms at selected values of applied magnetic field and uniaxial compressive stress have to be properly corrected in order to compute the transition entropy change associated with the first-order martensitic phase transition. The baseline subtraction is performed following the same procedure as for the previously studied Ni-Mn-In magnetic shape-memory alloy (see section 5.3.4.2), and the corresponding corrected thermograms are illustrated in Figure 5.38 for both heating (top panels) and cooling (bottom panels)

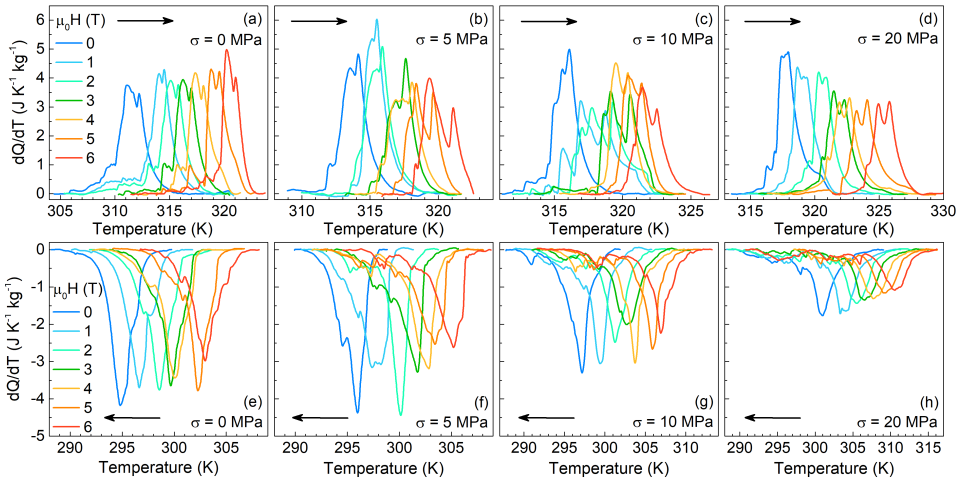

Figure 5.38: *Calorimetric curves after baseline subtraction as a function of temperature recorded upon heating (panels (a)-(d)) and cooling (panels (e)-(h)) at selected values of magnetic field* $\{\mu_0 H_j\} = \{0, 1, 2, 3, 4, 5, 6\}$ *T under different constant uniaxial compressive stresses, indicated by the labels in each panel.*

runs. It is important to highlight that the application of magnetic field or uniaxial compressive stress has a clear influence on the shape of the calorimetric peak of the corrected thermograms.

When either increasing the applied magnetic field or the compressive stress while keeping the secondary field constant, the calorimetric peaks tend to decrease. This effect is particularly significant for the cooling runs when increasing the applied compressive stress. Furthermore, the calorimetric peaks also tend to be broader and spread over a wider temperature range. Interestingly, a similar broadening effect was also observed for the baseline corrected thermograms of the previously studied Ni-Mn-In alloy (see Figure 5.17) when increasing the applied magnetic field.

The corresponding transition entropy changes ($\Delta S_t(\mu_0 H, \sigma)$) are computed using equation 5.7. As discussed in detail for Cu-Zn-Al along section 3.3, a constant calibration factor has to be introduced in order to analyse the thermograms measured with our bespoke setup. For the sample under study, the constant calibration factors for the forward (M) and reverse (A) martensitic transitions are defined as:

$$\gamma^{A,M} = \frac{\Delta S_t^{A,M}(0\,\mathrm{T}, 0\,\mathrm{MPa})}{\Delta S_t(0\,\mathrm{T}, 0\,\mathrm{MPa})} \tag{5.29}$$

where $\Delta S_t^{A,M}(0\,\mathrm{T}, 0\,\mathrm{MPa})$ corresponds to the transition entropy change for the forward (M) and reverse (A) martensitic transition computed from the thermograms measured with the commercial DSC, and $\Delta S_t(0\,\mathrm{T}, 0\,\mathrm{MPa})$ corresponds to the transition entropy change computed from the corrected thermograms measured in the absence of any applied external field represented in Figure 5.38 (a) and (e) upon

heating and cooling, respectively. The corresponding transition entropy changes are computed as $\Delta S_t^{cal}(\mu_0 H, \sigma) = \gamma^{A,M} \Delta S_t(\mu_0 H, \sigma)$, and they are illustrated in Figure 5.39 as a function of magnetic field under constant stress (panels (a) and (b)) and as a function of stress under constant magnetic field (panels (c) and (d)) for both heating and cooling runs, respectively. As for Cu-Zn-Al, different smoothing processes (see Appendix A) are applied to analyse each thermogram, leading to small differences in the determination of the baseline. These differences provide a good estimation of the error in determining the transition entropy change, which are found to be of ± 1-$2\,\mathrm{JK^{-1}kg^{-1}}$ for the studied sample.

For all values of applied stress, both forward and reverse transition entropy changes linearly decrease when increasing the applied magnetic field, with slopes in the range $\frac{d\Delta S_t}{d\mu_0 H} \in [-1.1, -0.7]\,\mathrm{JK^{-1}kg^{-1}T^{-1}}$. Interestingly, the transition entropy change linearly decreases when increasing the applied stress with slopes in the range $\frac{d\Delta S_t}{d\sigma} \in [-0.5, -0.2]\,\mathrm{JK^{-1}kg^{-1}MPa^{-1}}$ for all values of applied magnetic field. In this regard, it must be highlighted that the highest applied stress is $\sigma = 20\,\mathrm{MPa}$, which corresponds to a compressive force of $F = 160\,\mathrm{N}$. Taking into account that for the previously studied Ni-Mn-In alloy, as discussed in section 5.3.4.2, we could not observe any systematic dependence of the transition entropy change with applied stress when applying compressive forces up to $F = 273\,\mathrm{N}$, we consider that the behaviour observed for the Ni-Mn-Ga-Cu alloy corresponds to a real effect of the sample.

Furthermore, as illustrated in Figure 5.39 (e) and (f), no systematic effect of the secondary field has been found of the slopes determined from the linear fits to the forward and reverse transition entropy changes as a function of magnetic field and stress.

Figure 5.39 (g) illustrates the behaviour of the transition entropy change within the complete magnetic field and compressive stress coordinate space under study. The experimental values are plotted as blue and red solid symbols for the forward and reverse martensitic transitions, respectively, and their behaviour is parametrized by two planes with equations:

$$\Delta S_t^M(\mu_0 H, \sigma) = 27.9(5) - 0.8(3)\mu_0 H - 0.35(2)\sigma \ (\mathrm{JK^{-1}kg^{-1}}) \tag{5.30a}$$

$$\Delta S_t^A(\mu_0 H, \sigma) = 27.2(5) - 0.8(3)\mu_0 H - 0.31(2)\sigma \ (\mathrm{JK^{-1}kg^{-1}}) \tag{5.30b}$$

Firstly, let us focus on the origin of the transition entropy change decrease when increasing the applied magnetic field. Even though this behaviour is not straightforward to understand, some insight into this issue can be gained when considering the different contributions to the transition entropy change.

As discussed in section 5.3.4.2, the transition entropy change associated with the magnetostructural phase transition in Ni-Mn-based Heusler alloys can be mainly

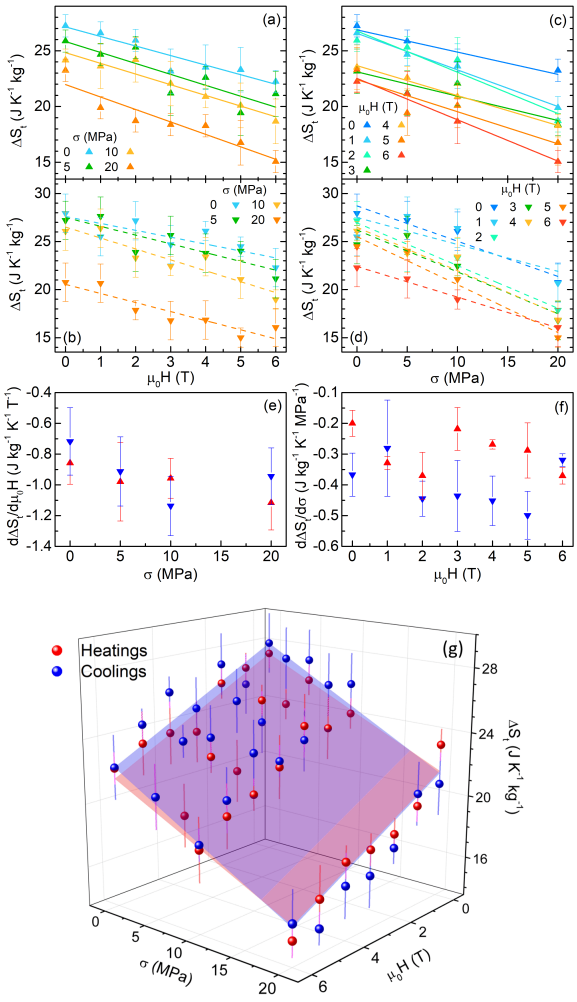

Figure 5.39: *Averaged transition entropy change as a function of magnetic field at constant uniaxial stress computed for both heating (a) and cooling (b) runs. Averaged transition entropy change as a function of stress at constant magnetic fields computed for both heating (c) and cooling (d) runs. Solid and dashed lines correspond to linear fits to heating and cooling data, respectively. (e) Stress dependence of the slope of the fitted transition entropy change as a function of magnetic field. (f) Magnetic field dependence of the slope of the fitted transition entropy change as a function of stress. (g) Transition entropy change as a function of magnetic field and uniaxial stress. Solid symbols correspond to the averaged transition entropy changes from different background subtractions of each thermogram, and planes to the best fits to these values. Red symbols and plane correspond to the reverse martensitic phase transition (ΔS_t^A) whereas blue symbols and plane to the forward martensitic phase transition (ΔS_t^M).*

attributed to the lattice entropy change (ΔS_{lat}), associated with changes on the lattice vibrations (phonons) of the alloy, and to the magnetic entropy change (ΔS_{mag}),

associated with changes on the magnetic ordering, as the electronic contribution is negligibly small [225].

On the one hand, as for the previously studied Ni-Mn-In alloy, the phonon modes in the transverse TA_2 branch provide the major contribution to the vibrational entropy change, as they have significantly lower energies than phonons in other branches and are more likely to be excited [107].

On the other hand, when considering the magnetic entropy contribution, it is important to take into account that the studied Ni-Mn-Ga-Cu Heusler alloy exhibits a conventional magnetocaloric effect. Therefore, in contrast to the previously studied Ni-Mn-In alloy, the martensite phase is more magnetically ordered than the austenite phase. [12] Therefore, the austenite phase will have a larger magnetic entropy contribution than the martensite phase ($S^A_{mag} > S^M_{mag}$). Consequently, the vibrational and magnetic entropy contributions will have the same sign and they synergically contribute to the transition entropy change. Under these circumstances, the transition entropy change expressed in equation 5.10 can be rewritten as:

$$\Delta S_t(\mu_0 H) = \Delta S_{lat} + \Delta S_{mag}(\mu_0 H) \tag{5.31}$$

Under the application of an external magnetic field, the magnetization change across the martensitic phase transition slightly increases, and the magnetic entropy contribution should be enhanced as well. However, the analysis of our thermograms indicates a transition entropy change decrease when increasing the applied magnetic field.

This apparent contradicting behaviour may point to a certain interplay between vibrational entropy contribution and the applied magnetic field ($\Delta S_{lat}(\mu_0 H)$), in such a way that it decreases when increasing the magnetic field.

While it is usually assumed that the vibrational entropy contribution does not significantly depend on the magnetic field [220], it may not hold true for Ni-Mn-Ga alloys. In fact, the vibrational entropy change is expected to be different in Ni-Mn-Ga Heusler alloys with respect to that of Ni-Mn-In or Ni-Mn-Sn. This is suggested when comparing the transition entropy change of all these Ni-Mn-based Heusler alloys for compositions where the martensitic phase transition takes place above the austenitic Curie temperature, where the alloy is paramagnetic and the magnetic entropy contribution does not play a role in the transition entropy change in the absence of magnetic field. Under these conditions, the transition entropy change of Ni-Mn-Ga alloys is in the order of $\Delta S_t \sim 20 - 30\,\mathrm{JK^{-1}kg^{-1}}$ [182, 233], whereas for Ni-Mn-In and Ni-Mn-Sn it is around $\Delta S_t \sim 40 - 50\,\mathrm{JK^{-1}kg^{-1}}$ [220, 221].

Furthermore, for the particular case of Ni-Mn-Ga alloys, the energy of the phonons lying on the TA_2 branch exhibit an enhanced softening at the Curie temperature,

[12] The thermomagnetization curves at selected values of applied magnetic field for the Ni-Mn-Ga-Cu alloy under study can be found in [229].

where the sample orders ferromagnetically [182], indicating a significant coupling between the magnetic and structural degrees of freedom.

Secondly, with respect to the origin of the transition entropy change decrease when increasing the applied stress, it must be taken into account that the martensitic structure of the sample can be influenced by the applied stress. As discussed in section 4.2.1, the application of stress breaks the energetic equivalence between the different martensite variants, favouring the growth of some of them. In this regard, a previous study on a Cu-Zn-Al shape-memory alloy has reported a lower transition entropy change when inducing a single variant martensite structure with respect to the transition entropy change measured when inducing a multivariant martensite [30]. Consequently, the behaviour observed for the sample under study may point to a rearrangement of the martensite variants when inducing the martensitic phase transition under a certain applied stress.

Overall, despite the experimental observation of the transition entropy change decrease when increasing either the applied magnetic field or the compressive stress, further studies are required in order to clarify this issue and gain some light onto this aspect.

5.4.4.3 Construction of the isofield-isostress entropy curves

As discussed in section 3.1.1.2, the corresponding isofield-isostress entropy curves ($S(T, \mu_0 H, \sigma)$) can be constructed from the integration of the corrected thermograms, which provide both the transformed fraction curves ($\chi(T, \mu_0 H, \sigma)$) and the corresponding transition entropy changes ($\Delta S_t(\mu_0 H, \sigma)$), and from specific heat data of both martensitic (C_M) and austenitic (C_A) phases [38].

In these computations, as previously considered for Cu-Zn-Al in section 3.3.4, it is common to assume that the specific heat does not depend on the applied external fields. However, as previously discussed for Ni-Mn-In (see section 5.3.4.3), this assumption does not apply for alloys exhibiting a strong coupling between the structural and magnetic degrees of freedom. While the assumption that the specific heat is independent of stress is still a good approximation, the phonons of the sample under study are sensitive to the applied magnetic field. Therefore, we have measured the temperature dependence of the martensitic and austenitic specific heats at selected values of applied magnetic fields.

Figure 5.40 (a) illustrates the specific heat measurements at selected values of magnetic field performed with a bespoke Peltier cell calorimeter. Within the transition region, the latent heat associated with the first-order martensitic phase transition gives rise to an apparent peak in the specific heat. Under the application of magnetic field, this peak sharpens and shifts to higher temperatures at an approximate rate of $\frac{dT_t}{d\mu_0 H} \sim 1.4\,\mathrm{KT}^{-1}$, which is in excellent agreement with the shift observed from the DSC measurements performed with our bespoke setup (see Figures 5.35 and 5.37).

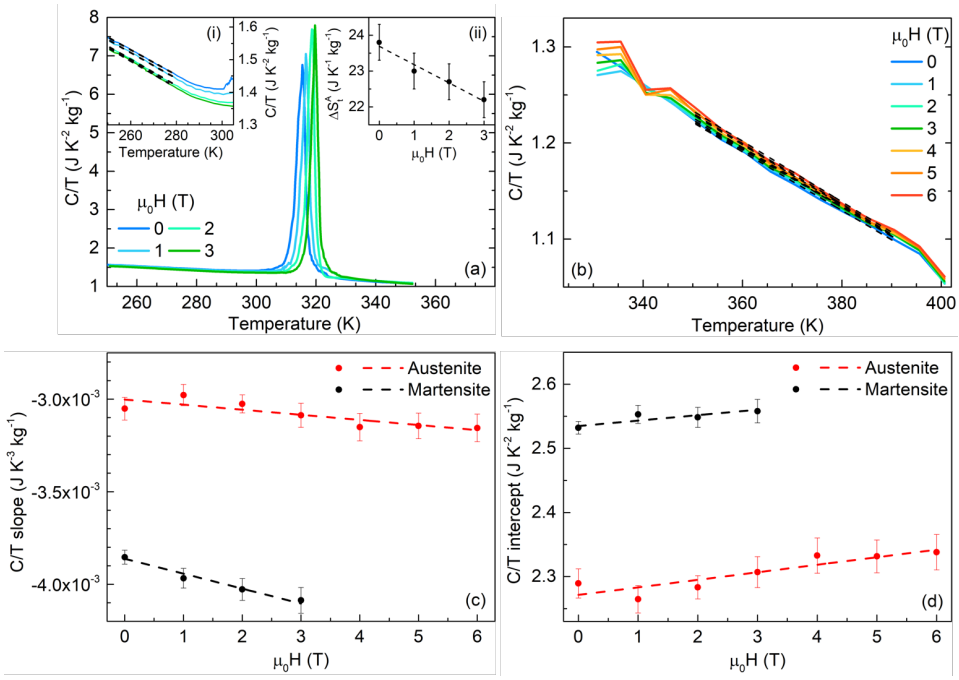

Figure 5.40: *(a) Temperature dependence of C/T under applied magnetic fields $\{\mu_0 H_j\} = \{0, 1, 2, 3\}$ T, measured with a bespoke Peltier cell calorimeter [230, 231]. Insets: (i) Enlarged view of C/T below the first-order martensitic phase transition. (ii) Average transition entropy change as a function of magnetic field computed from the C/T measurements. (b) Temperature dependence of C/T under applied magnetic fields $\{\mu_0 H_j\} = \{0, 1, 2, 3, 4, 5, 6\}$ T above the first-order martensitic phase transition, measured using a commercial relaxation calorimeter (PPMS from Quantum Design®). (c) Slope of the linear fits on the C/T curves at the martensitic (black) and austenitic (red) phases as a function magnetic field. (d) Intercept of the linear fits on the C/T curves at the martensitic (black) and austenitic (red) phases as a function magnetic field. Dashed lines in the different panels and inserts are linear fits to the data.*

At temperatures below the martensitic transition, the specific heat of the ferromagnetic martensite phase (C_M) shows a dependence on both the temperature and the applied magnetic field. As illustrated in the insert (i) of Figure 5.40 (a), for each applied magnetic field, its temperature dependence can be parametrized with a linear regression expressed as:

$$\frac{C_M(T, \mu_0 H)}{T} = m_M(\mu_0 H) T + b_M(\mu_0 H) \ (\mathrm{JK^{-2}kg^{-1}}) \tag{5.32}$$

where the slope ($m_M(\mu_0 H)$) and the intercept ($b_M(\mu_0 H)$) depend on the applied magnetic field.

Furthermore, as for the previously studied Ni-Mn-In alloy, the transition entropy change can be computed from the specific heat measurements after a proper

baseline correction, as expressed by equation 5.14. For the diverse isofield measurements illustrated in Figure 5.40 (a), the baselines can be accurately approximated as a straight line, fitted above and below the apparent peak of the specific heat. The corresponding transition entropy changes for the reverse martensitic transition (ΔS_t^A) are illustrated in the insert (ii) of Figure 5.40 (a) as a function of the applied magnetic field.

In the absence of magnetic field, the transition entropy change is found to be $\Delta S_t^A(\mu_0 H = 0\,\mathrm{T}) = (23.8 \pm 0.5)\,\mathrm{JK^{-1}kg^{-1}}$, which is slightly smaller that the transition entropy change determined with the commercial DSC in the absence of applied external fields (see section 5.4.3). The difference between both values may arise from small composition differences within the initial Ni-Mn-Ga-Cu ingot from which both samples were cut. Nevertheless, it is particularly important to highlight that the transition entropy change computed from the specific heat measurements linearly decreases when increasing the applied magnetic field with a slope of $\dfrac{d\Delta S_t^A}{d\mu_0 H} = (-0.5 \pm 0.1)\,\mathrm{JK^{-1}kg^{-1}T^{-1}}$, which is consistent with the decrease computed from our calorimetric measurements discussed in section 5.4.4.2.

In order to accurately determine the temperature and magnetic field dependence of the specific heat of the paramagnetic austenite (C_A), we have used a commercial relaxation calorimeter that allows us to perform measurements under different applied magnetic fields up to higher temperatures.

The corresponding results are illustrated in Figure 5.40 (b). As for the martensitic phase, the specific heat of the paramagnetic austenite depends on both the temperature and the applied magnetic field. For each applied magnetic field its temperature dependence can be parametrized with a linear regression expressed as:

$$\frac{C_A(T, \mu_0 H)}{T} = m_A(\mu_0 H) T + b_A(\mu_0 H)\ (\mathrm{JK^{-2}kg^{-1}}) \tag{5.33}$$

where the slope ($m_A(\mu_0 H)$) and the intercept ($b_A(\mu_0 H)$) depend on the applied magnetic field.

The magnetic field dependence of the slopes and intercepts of the linear regressions for both the ferromagnetic martensite and paramagnetic austenite specific heats are illustrated in panels (c) and (d) of Figure 5.40, respectively. On the one hand, for both austenite and martensite phases, an increase on the applied magnetic field linearly increases the absolute value of the specific heat slope. Their behaviour can be respectively parametrized as:

$$m_M(\mu_0 H) = -8(1) \cdot 10^{-5} \mu_0 H - 3.86(2) \cdot 10^{-3}\ (\mathrm{JK^{-3}kg^{-1}}) \tag{5.34a}$$

$$m_A(\mu_0 H) = -2.8(8) \cdot 10^{-5} \mu_0 H - 3.00(3) \cdot 10^{-3}\ (\mathrm{JK^{-3}kg^{-1}}) \tag{5.34b}$$

On the other hand, for both austenite and martensite phases, an increase on the applied magnetic field linearly increases the intercept of the specific heat, and their

behaviour can be parametrized as:

$$b_M(\mu_0 H) = 8(3) \cdot 10^{-3} \mu_0 H + 2.535(5) \ (\mathrm{JK^{-2}kg^{-1}}) \tag{5.35a}$$

$$b_A(\mu_0 H) = 12(3) \cdot 10^{-3} \mu_0 H + 2.27(1) \ (\mathrm{JK^{-2}kg^{-1}}) \tag{5.35b}$$

Therefore, as for the previously studied Ni-Mn-In alloy, from the parametrized dependencies of the transition entropy change for both forward and reverse martensitic transitions (see equation 5.30), and the martensitic and austenitic specific heats (see equations (5.32) to (5.35)), together with the transformed fraction curves obtained from the base-line corrected thermograms for both forward and reverse transitions (see Figure 5.38), we can compute the isofield-isostress entropy curves ($S(T, \mu_0 H, \sigma)$) upon heating and cooling.

For the sample under study, we have referenced all the entropy curves at $S_{ref} = S(T = 426\,\mathrm{K})$ in the absence of any applied external field. This reference temperature has been selected as it corresponds to the point where the specific heat of the paramagnetic austenite, extrapolated from equation 5.33, is expected to become independent of the applied magnetic field. Even though the reference temperature has been taken well above the martensitic transition, the isofield-isostress entropy curves can still be generally expressed by equation 5.12, but the specific heat of the sample $C(T, \mu_0 H, \sigma)$ is expressed as $C = \chi C_M + (1 - \chi) C_A$, where χ corresponds to the martensitic transformed fraction ($\chi = 1$ when the sample is completely in the martensitic phase). Figure 5.41 (a)-(g) displays the computed entropy curves at selected values of uniaxial stress $\{\sigma_i\} = \{0, 5, 10, 20\}$ MPa under different constant magnetic fields, whereas Figure 5.42 (a)-(d) displays the computed entropy curves at selected values of magnetic field $\{\mu_0 H_j\} = \{0, 1, 2, 3, 4, 5, 6\}$ T under different constant compressive stresses.

As illustrated in Figure 5.41 (a)-(g), for each constant magnetic field the computed entropy curves shift towards higher temperatures when increasing the applied stress. Similarly, as illustrated in Figure 5.42 (a)-(d), for each constant compressive stress, the computed entropy curves also shift towards higher temperatures when increasing the applied magnetic field. It is important to notice that at the low-temperature region, the heating and cooling entropy curves illustrated in both figures exhibit a crossover, which reflects the decrease of the transition entropy change when increasing either the applied magnetic field or the compressive stress, as illustrated in Figure 5.39 (g).

As previously discussed in section 3.1.1.2, from the set of isofield-isostress entropy curves we can compute the corresponding elastocaloric and magnetocaloric isothermal entropy (ΔS) and adiabatic temperature (ΔT) changes. As these entropy curves were computed from the thermograms recorded for both heating and cooling runs, they correspond to the reverse (from martensite to austenite) and forward (from austenite to martensite) phase transitions, respectively. Therefore, in the following section we will be able to compute the field-induced elastocaloric and magnetocaloric thermal responses for both the reverse and forward phase transitions. In accordance to the transition temperature phase diagram illustrated in

Figure 5.37 (a), the reverse phase transition corresponds to trajectories from below to above the red surface, whereas the forward phase transition to trajectories from above to below the blue surface.

5.4.4.4 Elastocaloric and magnetocaloric effects under the influence of a secondary field

To compute the elastocaloric (magnetocaloric) thermal response under the influence of a constant magnetic field (stress), it is important to highlight that the application of stress (magnetic field) favours the low-temperature martensitic phase, which is in agreement with the positive transition temperature shift when increasing the applied stress (magnetic field) reported in section 5.4.4.1. Accordingly, the removal of stress (magnetic field) favours the high-temperature austenitic phase.

Consequently, the application of stress (magnetic field) will promote the forward phase transition, whereas the removal of stress (magnetic field) will promote the reverse phase transition. Therefore, a thermodynamic process in which stress (magnetic field) is applied is associated with the entropy curves for the cooling runs, whereas a thermodynamic process in which stress (magnetic field) is removed is associated with the entropy curves for the heating runs.

On the one hand, for the elastocaloric effect, the corresponding isothermal entropy change induced by the application of stress under a certain constant magnetic field is computed from the entropy curves for the cooling runs as:

$$\Delta S(T, \mu_0 H, 0 \rightarrow \sigma) = S(T, \mu_0 H, \sigma) - S(T, \mu_0 H, 0) \tag{5.36}$$

whereas the isothermal entropy change induced by the removal of stress is computed from the entropy curves for the heating runs as:

$$\Delta S(T, \mu_0 H, \sigma \rightarrow 0) = S(T, \mu_0 H, 0) - S(T, \mu_0 H, \sigma) \tag{5.37}$$

The corresponding results are illustrated in Figure 5.41 (h)-(n) under different applied magnetic fields. Conversely, the adiabatic temperature changes are computed after inverting the corresponding isofield-isostress entropy curves ($T(S, \mu_0 H, \sigma)$). Thus, the adiabatic temperature change induced by the application of stress under a certain constant magnetic field is computed from the inverted entropy curves for the cooling runs as:

$$\Delta T(S, \mu_0 H, 0 \rightarrow \sigma) = T(S, \mu_0 H, \sigma) - T(S, \mu_0 H, 0) \tag{5.38}$$

whereas the adiabatic temperature change induced by the removal of stress is computed from the inverted entropy curves for the heating runs as:

$$\Delta T(S, \mu_0 H, \sigma \rightarrow 0) = T(S, \mu_0 H, 0) - T(S, \mu_0 H, \sigma) \tag{5.39}$$

As for the previously studied Ni-Mn-In alloy (see section 5.3.4.4), the adiabatic temperature changes are represented as a function of the temperature given by the initial entropy curve prior to the external field change. The corresponding results are illustrated in Figure 5.41 (o)-(u) under different applied magnetic fields.

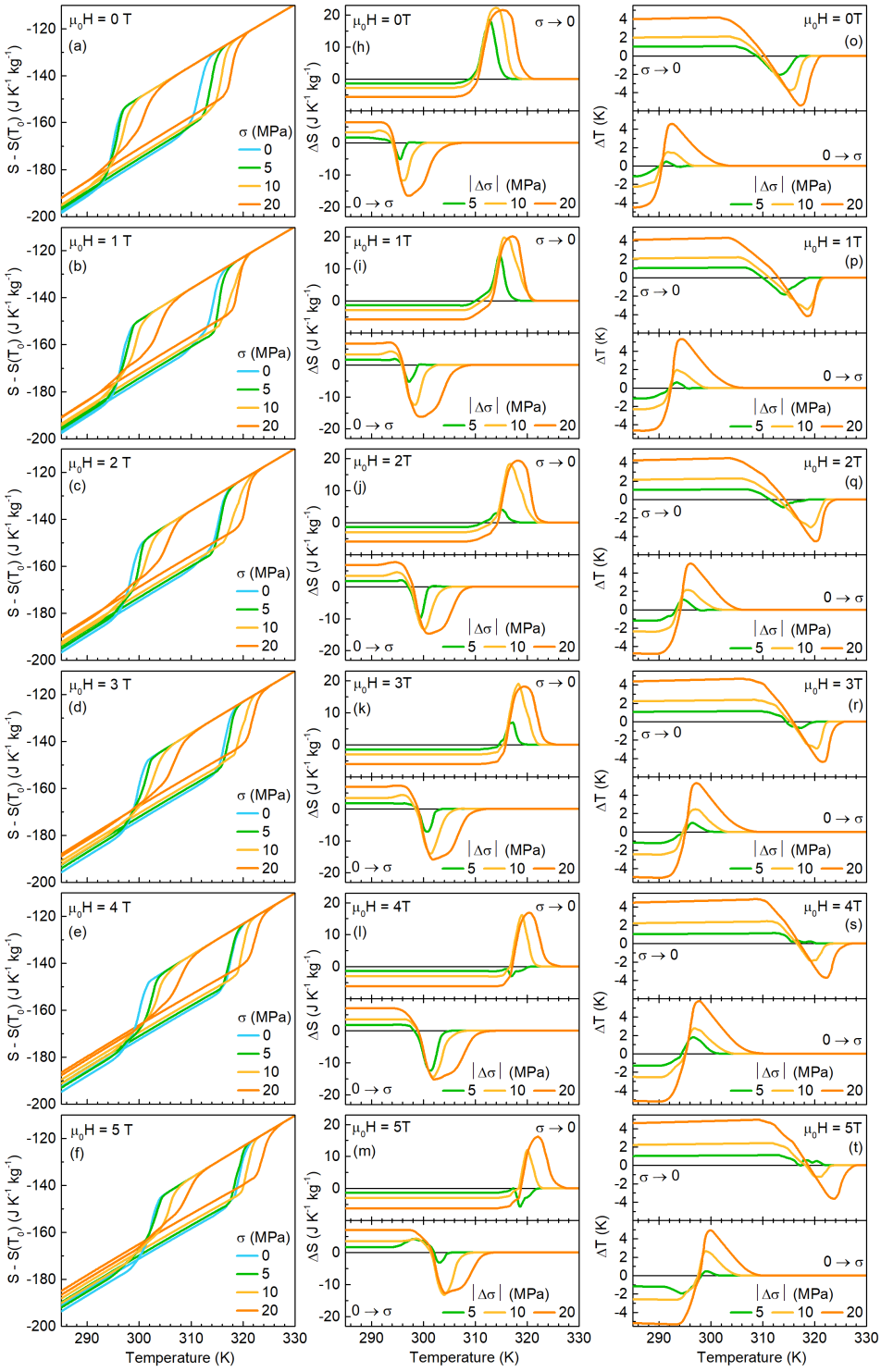
μ0H = 0 T
(a)
μ0H = 1 T
(b)
μ0H = 2 T
(c)
μ0H = 3 T
(d)
μ0H = 4 T
(e)
μ0H = 5 T
(f)
S - S(T0) (J K-1 kg-1)
σ (MPa)
0
5
10
20
μ0H = 0T
(h)
μ0H = 1T
(i)
μ0H = 2T
(j)
μ0H = 3T
(k)
μ0H = 4T
(l)
μ0H = 5T
(m)
ΔS (J K-1 kg-1)
σ → 0
0 → σ
|Δσ| (MPa)
5
10
20
μ0H = 0T
(o)
μ0H = 1T
(p)
μ0H = 2T
(q)
μ0H = 3T
(r)
μ0H = 4T
(s)
μ0H = 5T
(t)
ΔT (K)
Temperature (K)

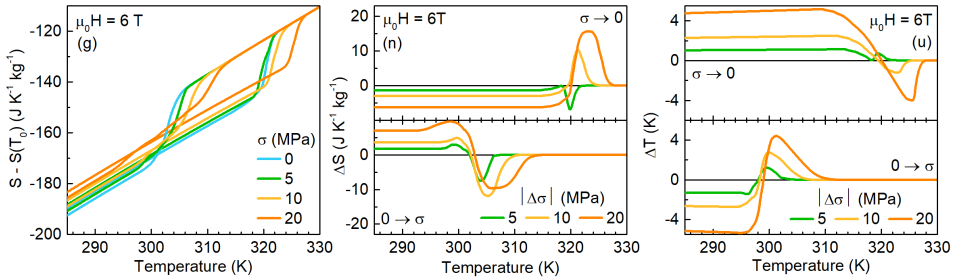

Figure 5.41: *(a)-(g) Entropy curves (referenced to $S_{ref} = S(T = 426\,K)$ in the absence of stress and magnetic field) as a function of temperature at selected values of uniaxial stress $\{\sigma_i\} = \{0, 5, 10, 20\}$ MPa under different constant magnetic fields for heating and cooling runs. Elastocaloric isothermal entropy changes ((h)-(n)), and adiabatic temperature changes ((o)-(u)), corresponding to the removal (top, $\sigma \to 0$) and application (bottom, $0 \to \sigma$) of uniaxial stress. Each row corresponds to a different constant applied magnetic field $\{\mu_0 H_j\} = \{0, 1, 2, 3, 4, 5, 6\}$ T, and the value of the uniaxial stress is indicated by the colour code.*

At this point, it is important to highlight that under certain constant magnetic fields, as the transition temperature shift with stress for the reverse phase transition is small (see Figure 5.37), the temperature shift at low stresses falls within experimental errors. Therefore, some entropy curves at low stresses are overlapped or partially transposed, and the corresponding field-induced elastocaloric thermal response at low stress changes shows an opposite behaviour when compared to the thermal response induced at higher stress changes. These isothermal entropy and adiabatic temperature change curves showing an opposite behaviour can not be considered physically meaningful.

On the other hand, for the magnetocaloric effect, the corresponding isothermal entropy change induced by the application of magnetic field under a certain constant stress is computed from the entropy curves for the cooling runs as:

$$\Delta S(T, 0 \to \mu_0 H, \sigma) = S(T, \mu_0 H, \sigma) - S(T, 0, \sigma) \tag{5.40}$$

whereas the isothermal entropy change induced by the removal of magnetic filed is computed from the entropy curves for the heating runs as:

$$\Delta S(T, \mu_0 H \to 0, \sigma) = S(T, 0, \sigma) - S(T, \mu_0 H, \sigma) \tag{5.41}$$

The corresponding results are illustrated in Figure 5.42 (e)-(h) under different applied stresses. Conversely, as for the elastocaloric effect, the magnetocaloric adiabatic temperature change induced by the application of magnetic field under a certain constant stress is computed from the inverted entropy curves for the cooling runs as:

$$\Delta T(S, 0 \to \mu_0 H, \sigma) = T(S, \mu_0 H, \sigma) - T(S, 0, \sigma) \tag{5.42}$$

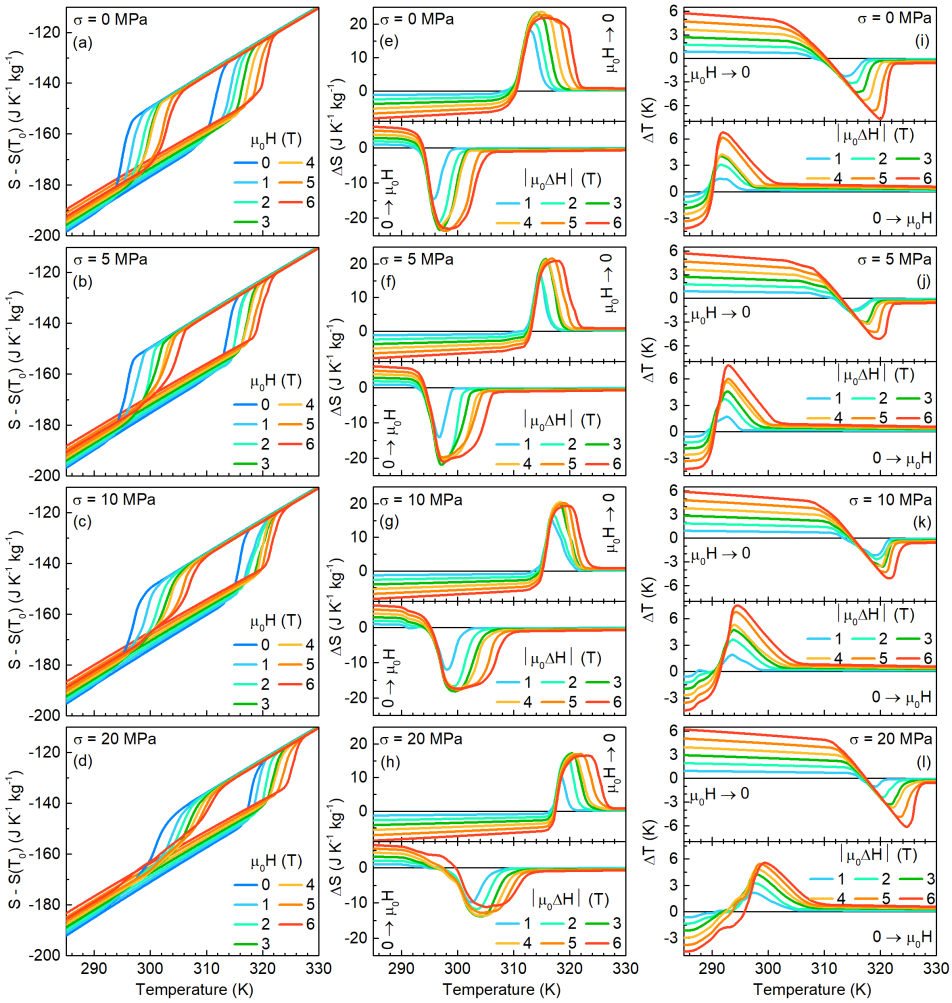

Figure 5.42: *(a)-(d) Entropy curves (referenced to $S_{ref} = S(T = 426\,K)$ in the absence of stress and magnetic field) as a function of temperature at selected values of magnetic field $\{\mu_0 H_j\} = \{0, 1, 2, 3, 4, 5, 6\}$ T under different constant uniaxial stresses for heating and cooling runs. Magnetocaloric isothermal entropy changes ((e)-(h)), and adiabatic temperature changes ((i)-(l)), corresponding to the removal (top, $\mu_0 H \rightarrow 0$) and application (bottom, $0 \rightarrow \mu_0 H$) of magnetic field. Each row corresponds to a different constant applied uniaxial stress $\{\sigma_i\} = \{0, 5, 10, 20\}$ MPa, and the value of the uniaxial stress is indicated by the colour code.*

whereas the adiabatic temperature change induced by the removal of magnetic field is computed from the inverted entropy curves for the heating runs as:

$$\Delta T(S, \mu_0 H \rightarrow 0, \sigma) = T(S, 0, \sigma) - T(S, \mu_0 H, \sigma) \tag{5.43}$$

The corresponding results, represented as a function of the temperature given by

the initial entropy curve prior to the external field change, are illustrated in Figure 5.42 (i)-(l) under different applied stresses.

In light of all the results illustrated in Figures 5.41 and 5.42, the computed elastocaloric and magnetocaloric effects have been found to be conventional.

Interestingly, the thermal response computed for both caloric effects exhibits a crossover from inverse (at low temperatures) to conventional (at high temperatures). While the conventional caloric effects arise from the field-induced martensitic phase transition, the inverse caloric effects observed below the martensitic phase transition are associated with the transition entropy change decrease when increasing either the applied magnetic field or the compressive stress.

Additionally, it is important to notice that for both elastocaloric and magnetocaloric thermal responses under the influence of a secondary field, an increase in the external field change that drives the martensitic phase transition (stress for the elastocaloric effect, represented in Figure 5.41, and magnetic field for the magnetocaloric effect, represented in Figure 5.42) enlarges the temperature window of the corresponding caloric effect.

Furthermore, as for the previously studied Ni-Mn-In alloy, it is particularly interesting to examine the behaviour of the maximum isothermal entropy and the adiabatic temperature changes as a function of the driving field that induces the martensitic phase transition for both caloric effects. Figure 5.43 illustrates the absolute values of the maximum isothermal entropy ($|\Delta S_{max}|$, (a)) and the adiabatic temperature ($|\Delta T_{max}|$, (b)) changes for the magnetocaloric effect as a function of the absolute value of the magnetic field change ($|\Delta \mu_0 H|$) (under different constant applied stresses), whereas the absolute values of the maximum isothermal entropy and the adiabatic temperature changes for the elastocaloric effect as a function of the absolute value of the stress change ($|\Delta \sigma|$) (under different constant magnetic fields) are shown in panels (c) and (d), respectively.

On the one hand, for the magnetocaloric effect, the magnitude of the field-induced isothermal entropy ($|\Delta S_{max}|$) and adiabatic temperature ($|\Delta T_{max}|$) changes increase when increasing the magnetic field change for all applied stresses. While the increase in $|\Delta T_{max}|$ is found to be linear, $|\Delta S_{max}|$ initially increases but it saturates for magnetic field changes in the range $|\mu_0 \Delta H| \sim 3 - 4\,\mathrm{T}$, which indicates that we are able to fully drive the martensitic phase transition. Interestingly, for higher magnetic field changes $|\Delta S_{max}|$ slightly decreases, which arises from the transition entropy change decrease when increasing the applied magnetic field (see Figure 5.39).

In addition, it is particularly important to highlight that under a low magnetic field change of $|\mu_0 \Delta H| = 1\,\mathrm{T}$, the current alloy under study exhibits a field-induced isothermal entropy change of $|\Delta S_{max}| \sim 15\,\mathrm{JK^{-1}kg}$, which surpasses the values reported for most of the Heusler alloys under the same magnetic field change [234–236].

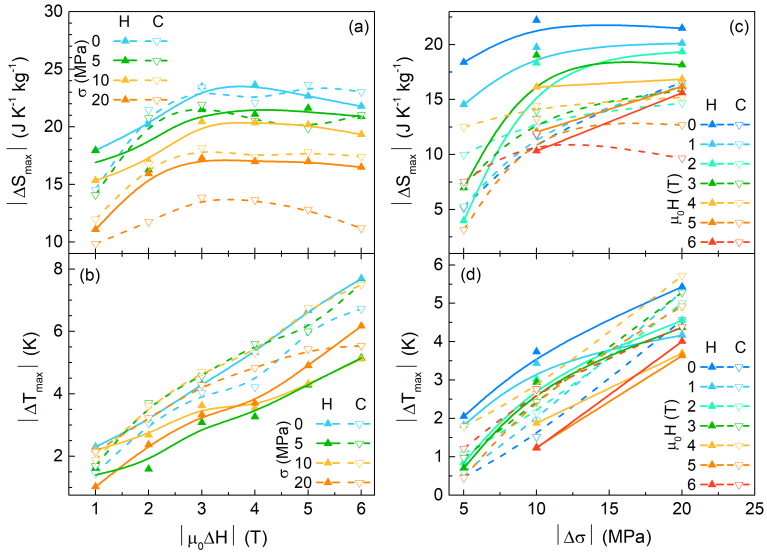

Figure 5.43: *Left: Magnetic field dependence of the maximum values for the field-driven magnetocaloric isothermal entropy (a) and adiabatic temperature (b) changes under different constant values of applied stress. Right: Stress dependence of the maximum values for the field-driven elastocaloric isothermal entropy (c) and adiabatic temperature (d) changes under different constant values of applied magnetic field. Solid symbols stand for the experimental values obtained from the heating entropy curves whereas open symbols stand for the values obtained from the cooling entropy curves. Lines are guides to the eye for each data series.*

On the other hand, for the elastocaloric effect, the field-induced isothermal entropy ($|\Delta S_{max}|$) and adiabatic temperature ($|\Delta T_{max}|$) changes exhibit a larger scattering but their magnitude also increases for higher stress changes for all applied magnetic fields. While the increase in $|\Delta T_{max}|$ is found to be linear, $|\Delta S_{max}|$ shows a tendency to saturate for high stress changes. The fact that a complete saturation is not reached under all the applied constant magnetic fields indicates that we can not fully drive the martensitic phase transition for the considered stress changes within the complete coordinate space under study. Interestingly, for the data series that exhibit a complete saturation of the elastocaloric isothermal entropy change, we also observe a slight decrease of the isothermal entropy change for higher stress changes, which arises from the transition entropy change decrease when increasing the applied stress (see Figure 5.39).

When considering the effect of the secondary constant field on the field-induced thermal responses, we have to distinguish between the isothermal entropy and the adiabatic temperature changes. In the former case, we observe that $|\Delta S_{max}|$ decreases when increasing the secondary field for both caloric effects. This behaviour is in agreement with the transition entropy change decrease when increasing either the applied magnetic field or the compressive stress. In the latter case, no

systematic dependence of $|\Delta T_{max}|$ on the secondary field can be observed. In this regard, it is important to take into account that the transition temperature shift with either the applied magnetic field $\left(\frac{dT_t}{d\mu_0 H}\right)$ or the compressive stress $\left(\frac{dT_t}{d\sigma}\right)$, respectively illustrated in Figure 5.37 (d) and (e), do not significantly change when increasing the secondary field. Therefore, the transition temperature will shift approximately the same independently of the applied secondary field, leading to a similar field-induced adiabatic temperature change.

5.4.5 Simulation of the isofield-isostress entropy curves: an analytical model

As previously discussed for Ni-Mn-In in section 5.3.5, to compute the corresponding caloric and multicaloric effects for any combination of magnetic field and uniaxial stress changes within the entire $(T, \mu_0 H, \sigma)$ thermodynamic coordinate space under study it is necessary to define a numerical function $(S(T, \mu_0 H, \sigma))$ and fit it to the experimental isofield-isostress entropy curves in order to phenomenologically reproduce their behaviour.

For the particular case under study ($Ni_{50}Mn_{18.5}Ga_{25}Cu_{6.5}$), taking into account the parametrized behaviour of the transition entropy change for both forward and reverse martensitic phase transition ($(\Delta S_t^{M,A}(\mu_0 H), \sigma)$, see Figure 5.39 and equation 5.30) together with the dependencies of both martensitic ($C_M(T, \mu_0 H)$) and austenitic ($C_A(T, \mu_0 H)$) specific heats (see Figure 5.40 and equations (5.32) to (5.35)), the general expression that defines the isofield-isostress entropy curves (see equation 5.12) can be rewritten by taking into account the definition of the transformed fraction (see equation 3.16) as:

$$S(T, \mu_0 H, \sigma) - S_{ref} = \int_{T_{ref}}^{T} \frac{C(T', \mu_0 H, \sigma)}{T'} dT' - \Delta S_t^{A,M}(\mu_0 H, \sigma)\chi(T, \mu_0 H, \sigma) \tag{5.44}$$

where $S_{ref} = S(T = 426\,\mathrm{K})$ and, as the reference temperature has been taken above the martensitic transition, the specific heat of the sample is expressed as $C(T, \mu_0 H, \sigma) = \chi(T, \mu_0 H, \sigma) C_M(T, \mu_0 H) + [1 - \chi(T, \mu_0 H, \sigma)]\, C_A(T, \mu_0 H)$. It is important to highlight that all the different elements that constitute equation 5.44, except the martensitic transformed fraction $(\chi(T, \mu_0 H, \sigma))$, have already been accurately parametrized within the complete $(T, \mu_0 H, \sigma)$ coordinate space along the previous sections.

Therefore, as for the previously studied Ni-Mn-In alloy, it is necessary to define an analytical function to reproduce the experimental behaviour of the transformed fraction over the complete phase space under study in order to define a suitable numerical function $(S(T, \mu_0 H, \sigma))$.

For such purpose, it is noteworthy that the corrected calorimetric curves, illustrated in Figure 5.38 for both heating (panels (a)-(d)) and cooling (panels (e)-(h))

runs, exhibit irregular shapes and can not be simply approximated by a single peak spreading over a certain temperature range. Furthermore, the shape of the calorimetric peaks for both forward and reverse transitions changes differently when increasing the applied external fields, which is particularly noticeable for the applied compressive stress. Accordingly, the martensitic transformed fraction obtained from the integration of these calorimetric peaks will provide an S-shaped curve, which can exhibit significant tails and will change over the transition temperature range from $\chi = 1$ (at the martensitic phase) to $\chi = 0$ (at the austenitic phase).

Therefore, we have defined two distinct analytical functions, one for the forward and another one for the reverse phase transition, that are composed of two sigmoid functions with different widths, centred at slightly different transition temperatures, that can be generally expressed as:

$$\chi(T, \mu_0 H, \sigma) = \frac{1 - D}{e^{B_1(T - T_{t1})} + 1} - \frac{D}{e^{B_2(T - T_{t2})} + 1} \tag{5.45}$$

where the free parameters $\{D, B_1, B_2, T_{t1}, T_{t2}\}$ are allowed to depend only on the applied magnetic field and the uniaxial compressive stress.

By following the same fitting procedure as for the transformed fraction analytical function of the previously studied Ni-Mn-In magnetic shape-memory alloy (see section 5.3.5), the parameters that define the analytical function to reproduce the experimental transformed fraction curves upon heating are:

$$\begin{aligned} T_{t1}(\mu_0 H, \sigma) &= 313.1(3) + 1(0.2)\mu_0 H + 0.21(5)\sigma + 0.04(3)\mu_0 H^2 \\ &\quad + 0.03(2)\sigma^2 \text{ (K)} && \text{(5.46a)} \\ T_{t2}(\mu_0 H, \sigma) &= 312.3(6) + 1.6(3)\mu_0 H + 0.3(1)\sigma - 0.10(6)\mu_0 H^2 \\ &\quad - 3(4) \cdot 10^{-3}\sigma^2 \text{ (K)} && \text{(5.46b)} \\ B_1 &= 1.5(4) \text{ (K}^{-1}\text{)} && \text{(5.46c)} \\ B_2(\mu_0 H, \sigma) &= 5.5(8) - 4(2)\mu_0 H + 1(0.7)\sigma + 0.7(4)\mu_0 H^2 \\ &\quad - 0.03(3)\sigma^2 - 0.11(9)\mu_0 H\sigma \text{ (K}^{-1}\text{)} && \text{(5.46d)} \\ D(\mu_0 H, \sigma) &= 0.96(7) - 3(2) \cdot 10^{-3}\mu_0 H\sigma \text{ (1)} && \text{(5.46e)} \end{aligned}$$

whereas for the experimental transformed fraction curves upon cooling, the parameters that define the analytical function are:

$$\begin{aligned} T_{t1}(\mu_0 H, \sigma) &= 294.7(2)) + 2.1(1)\mu_0 H + 0.22(3)\sigma - 0.10(2)\mu_0 H^2 \\ &\quad + 6(2) \cdot 10^{-3}\sigma^2 \text{ (K)} && \text{(5.47a)} \\ T_{t2}(\mu_0 H, \sigma) &= 294.9(8) + 0.7(5)\mu_0 H - 0.2(1)\sigma + 0.07(7)\mu_0 H^2 \\ &\quad + 0.017(5)\sigma^2 \text{ (K)} && \text{(5.47b)} \\ B_1(\mu_0 H, \sigma) &= 2.1(1) - 0.09(2)\mu_0 H - 0.041(6)\sigma \text{ (K}^{-1}\text{)} && \text{(5.47c)} \end{aligned}$$

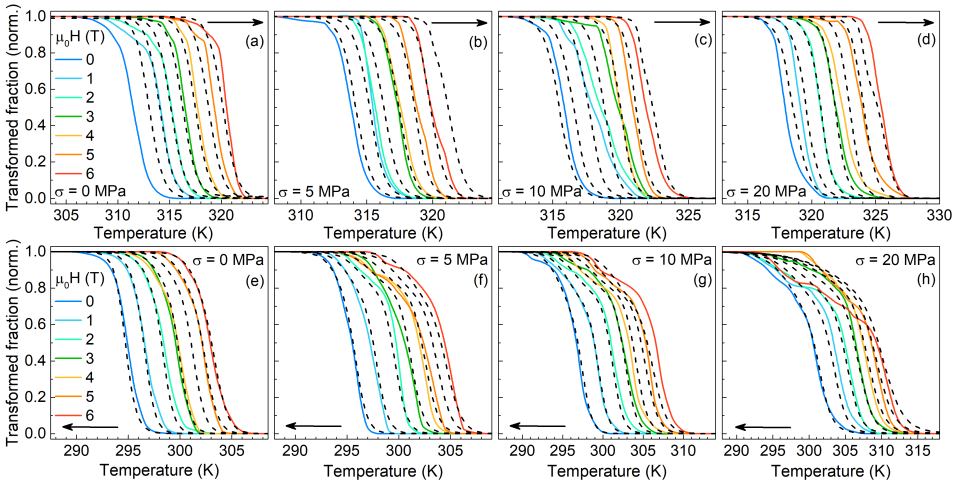

Figure 5.44: *Martensitic transformed fraction as a function of temperature upon heating (panels (a)-(d)) and cooling (panels (e)-(h)) at selected values of magnetic field* $\{\mu_0 H_j\} = \{0, 1, 2, 3, 4, 5, 6\}$ *T under different constant uniaxial stresses, indicated by the labels in each panel. Solid lines correspond to the experimental data obtained from the corrected thermograms, and dashed lines, to the fitted analytical function* $\chi(T\mu_0 H, \sigma)$ *expressed in equation 5.45.*

$$B_2(\mu_0 H, \sigma) = 1.4(2) - 0.04(4)\mu_0 H - 0.04(1)\sigma \ (\mathrm{K}^{-1}) \tag{5.47d}$$

$$D(\mu_0 H) = 0.71(7) + 0.08(3)\mu_0 H - 0.013(5)\mu_0 H^2 \ (1) \tag{5.47e}$$

Figure 5.44 illustrates the agreement between the simulated (dashed lines) and experimental (solid lines) transformed fraction curves at selected values of magnetic field under different constant uniaxial stresses upon heating (panels (a)-(d)) and cooling (panels (e)-(h)). On the whole, both data sets show a good agreement over the complete phase space under study, proving that the analytical functions correctly capture the transformed fraction behaviour around the forward and reverse martensitic phase transition.

Consequently, taking into account that all the distinct elements that define the isofield-isostress entropy curves, expressed in equation 5.44, have been successfully parametrized within the complete $(T, \mu_0 H, \sigma)$ coordinate space, we have all the necessary ingredients to phenomenologically reproduce their behaviour. For the particular case under study, introducing equation 5.33 into equation 5.44 leads to:

$$\begin{aligned} S(T, \mu_0 H, \sigma) - S_{ref} = & \\ & \int_{T_{ref}}^{T} \left[\frac{C_M(T', \mu_0 H)}{T'} - \frac{C_A(T', \mu_0 H)}{T'} \right] \chi(T', \mu_0 H, \sigma) dT' \\ & + \frac{1}{2} m_A(\mu_0 H) \left[T^2 - T_{ref}^2 \right] + b_A(\mu_0 H) \left[T - T_{ref} \right] \\ & - \Delta S_t^{A,M}(\mu_0 H, \sigma) \chi(T, \mu_0 H, \sigma) \end{aligned} \tag{5.48}$$

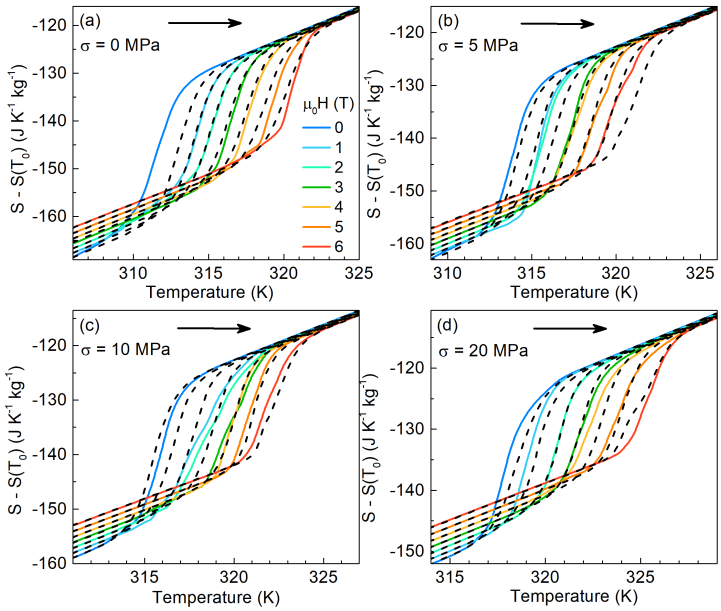

Figure 5.45: *Entropy curves (referenced to $S_{ref} = S(T = 426\,K)$ in the absence of stress and magnetic field) as a function of temperature upon heating at selected values of magnetic field $\{\mu_0 H_j\} = \{0,\ 1,\ 2,\ 3,\ 4,\ 5,\ 6\}$ T under different constant uniaxial stresses, indicated by the labels in each panel. Solid lines correspond to the experimental data, and dashed lines, to the fitted analytical function for the heating runs.*

where the integral over temperature was computed numerically by a cumulative trapezoidal integration for any point of the $(T, \mu_0 H, \sigma)$ coordinate space under study.

Figures 5.45 and 5.46 illustrate the agreement between the numerically computed (dashed lines) and experimental (solid lines) isofield-isostress entropy curves at selected values of magnetic field under different constant uniaxial stresses upon heating and cooling, respectively. Therefore, from the numerical $S(T, \mu_0 H, \sigma)$ entropy curves, the corresponding caloric and multicaloric effects can be computed for any combination of magnetic field and uniaxial stress changes within the entire $(T, \mu_0 H, \sigma)$ thermodynamic coordinate space under study.

At this point, it is important to emphasize that from the experimental isofield-isostress entropy curves upon heating (cooling), we were able to compute the elastocaloric and magnetocaloric effects that correspond to the induction of the reverse (forward) phase transition (see section 5.4.4.4). These processes, in accordance to the transition temperature phase diagram illustrated in Figure 5.37 (a), correspond to trajectories from below to above the red surface and to trajectories from above to below the blue surface, respectively. When considering trajectories that involve a simultaneous or sequential change on both external fields, both of them have to

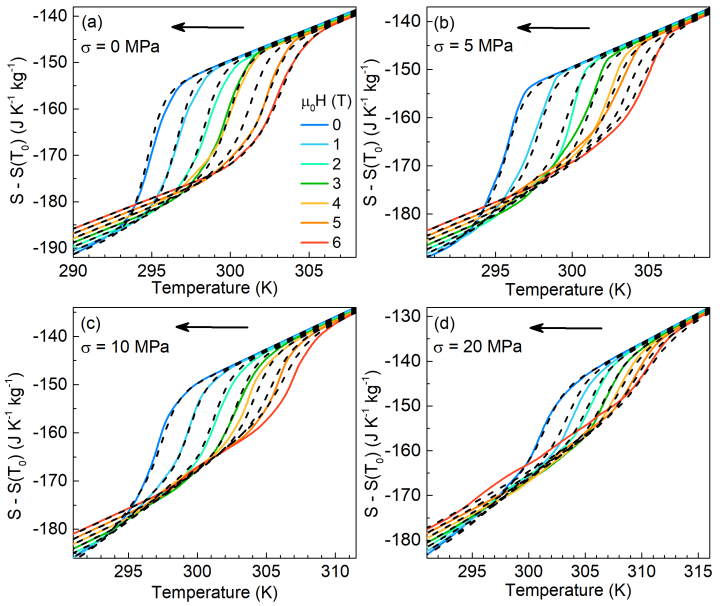

Figure 5.46: *Entropy curves (referenced to $S_{ref} = S(T = 426\,K)$ in the absence of stress and magnetic field) as a function of temperature upon cooling at selected values of magnetic field $\{\mu_0 H_j\} = \{0, 1, 2, 3, 4, 5, 6\}$ T under different constant uniaxial stresses, indicated by the labels in each panel. Solid lines correspond to the experimental data, and dashed lines, to the fitted analytical function for the cooling runs.*

promote the phase transition in the same direction. Otherwise, due to the hysteresis of the phase transition, they would drive the sample through a minor hysteresis loop within the two-phase coexistence region (which corresponds to the temperature range between the upper and lower surfaces illustrated in Figure 5.37 (a)), for which no experimental data are available.

Consequently, the numerically simulated entropy curves upon heating are only representative for the reverse phase transition, allowing us to compute the caloric and multicaloric effects that are associated with trajectories in the phase space from below to above the red surface, whereas the numerically simulated entropy curves upon cooling are only representative for the forward phase transition, allowing us to compute the caloric and multicaloric effects that are associated with trajectories in the phase space from above to below the blue surface.

The numerically simulated isofield entropy surfaces as a function of temperature and stress, and the isostress entropy surfaces as a function of temperature and magnetic field, are illustrated in panels (a) and (b) of Figures 5.47 (upon heating) and 5.48 (upon cooling), respectively. All these entropy surfaces evidence the transition temperature shift towards higher temperatures when increasing either the applied stress or the magnetic field. Additionally, the isofield and isostress entropy surfaces

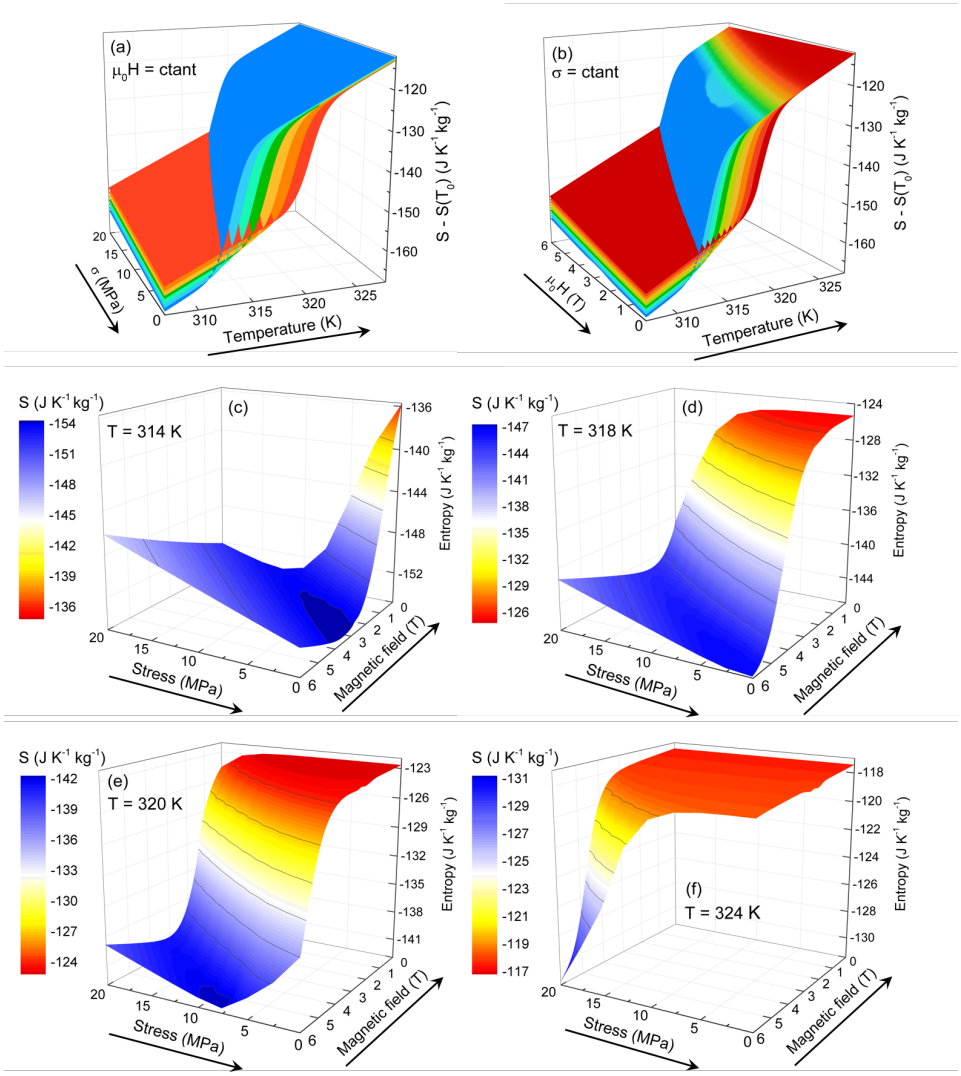

Figure 5.47: *Entropy surfaces obtained from the analytical function upon heating. (a) Isofield entropy surfaces as a function of stress and temperature at selected values of magnetic field in the range* $\{\mu_0 H_j\} \in \{0, 6\}$ *T. (b) Isostress entropy surfaces as a function of magnetic field and temperature at selected values of stress in the range* $\{\sigma_i\} \in \{0, 20\}$ *MPa. (c)-(d) Isothermal entropy surfaces as a function of magnetic field and stress. In all cases, the entropy is referenced to* $S_{ref} = S(T = 426\,K)$ *in the absence of stress and magnetic field. Arrows indicate the direction of the temperature, magnetic field and uniaxial stress change.*

also evidence the transition entropy change decrease when increasing either the applied stress or the magnetic field, respectively. Furthermore, it is particularly important to highlight that the crossover behaviour at the low-temperature region

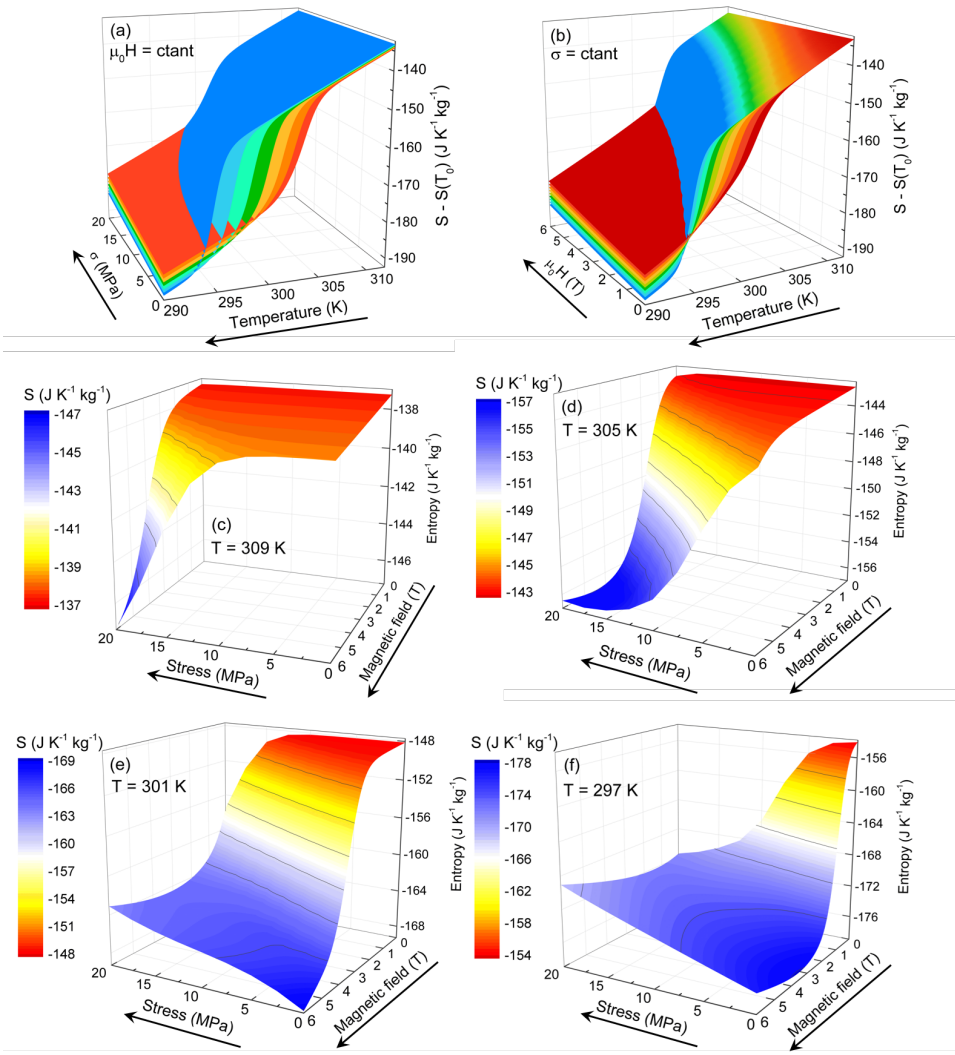

Figure 5.48: *Entropy surfaces obtained from the analytical function upon cooling. (a) Isofield entropy surfaces as a function of stress and temperature at selected values of magnetic field in the range* $\{\mu_0 H_j\} \in \{0, 6\}$ *T. (b) Isostress entropy surfaces as a function of magnetic field and temperature at selected values of stress in the range* $\{\sigma_i\} \in \{0, 20\}$ *MPa. (c)-(d) Isothermal entropy surfaces as a function of magnetic field and stress. In all cases, the entropy is referenced to* $S_{ref} = S(T = 426\,K)$ *in the absence of stress and magnetic field. Arrows indicate the direction of the temperature, magnetic field and uniaxial stress change.*

can be clearly observed for both isofield and isostress entropy surfaces upon heating and cooling within the complete temperature, magnetic field and stress coordinate space under study.

Moreover, the numerically simulated isofield-isostress entropy curves, generally expressed by equation 5.48, also allow us to compute the corresponding isothermal entropy surfaces as a function of stress and magnetic field. The corresponding entropy surfaces at selected values of temperature are illustrated in panels (c)-(f) of Figures 5.47 and 5.48 upon heating and cooling, respectively. For temperatures before the onset of the field-induced martensitic phase transition ($T = 314\,\mathrm{K}$ upon heating and $T = 309\,\mathrm{K}$ upon cooling), the removal (application) of large external fields leads to an increase (decrease) of the entropy, as the reverse (forward) phase transition is induced. Interestingly, at $T = 314\,\mathrm{K}$ upon heating, we observe an initial entropy decrease before inducing the reverse phase transition, which arises from the crossover behaviour at the low-temperature region and reflects the decrease of the transition entropy change when increasing either the applied magnetic field or the compressive stress. At temperatures within the transition region ($\{T\} = \{318, 320\}\,\mathrm{K}$ upon heating and $\{T\} = \{301, 305\}\,\mathrm{K}$ upon cooling), we observe that the increase (decrease) of the entropy is more pronounced when removing (applying) the external fields. Furthermore, it is worth pointing out that smaller external field changes are required to induce the phase transition. At temperatures after the onset of the field-induced martensitic phase transition ($T = 324\,\mathrm{K}$ upon heating and $T = 297\,\mathrm{K}$ upon cooling), the removal (application) of the external fields leads to a smaller increase (decrease) of the entropy. Interestingly, at $T = 297\,\mathrm{K}$ upon cooling, we observe an entropy increase after inducing the forward phase transition. As previously mentioned, this feature arises from the crossover behaviour at the low-temperature region.

5.4.5.1 Elastocaloric and magnetocaloric effects under the influence of a secondary field

Similarly to the results presented in section 5.4.4.4, we can compute the single caloric effects under the influence of a constant secondary external field from the numerically simulated $S(T, \mu_0 H, \sigma)$ entropy curves. Figure 5.49 illustrates the elastocaloric effect under selected constant magnetic fields upon heating (panels (a)-(f)) and cooling (panels (g)-(l)), whereas Figure 5.50 illustrates the magnetocaloric effect under selected constant stresses upon heating (panels (a)-(f)) and cooling (panels (g)-(l)). These figures show both the isothermal entropy and adiabatic temperature changes for each single caloric effect as colour contour plot maps. The corresponding three dimensional representations of both caloric effects are shown in Appendix C.

Overall, there is a good agreement between both numerically simulated and experimentally computed elastocaloric (Figures 5.41 and 5.49) and magnetocaloric (Figures 5.42 and 5.50) thermal responses, respectively. As for the previously studied Ni-Mn-In alloy, such an agreement confirms the robustness of our analytical model to phenomenologically reproduce the isofield-isostress experimental entropy curves upon heating and cooling, and provides confidence in the computation of the multicaloric thermal response of the alloy under study.

Let us first discuss the elastocaloric effect, illustrated in Figure 5.49. The max-

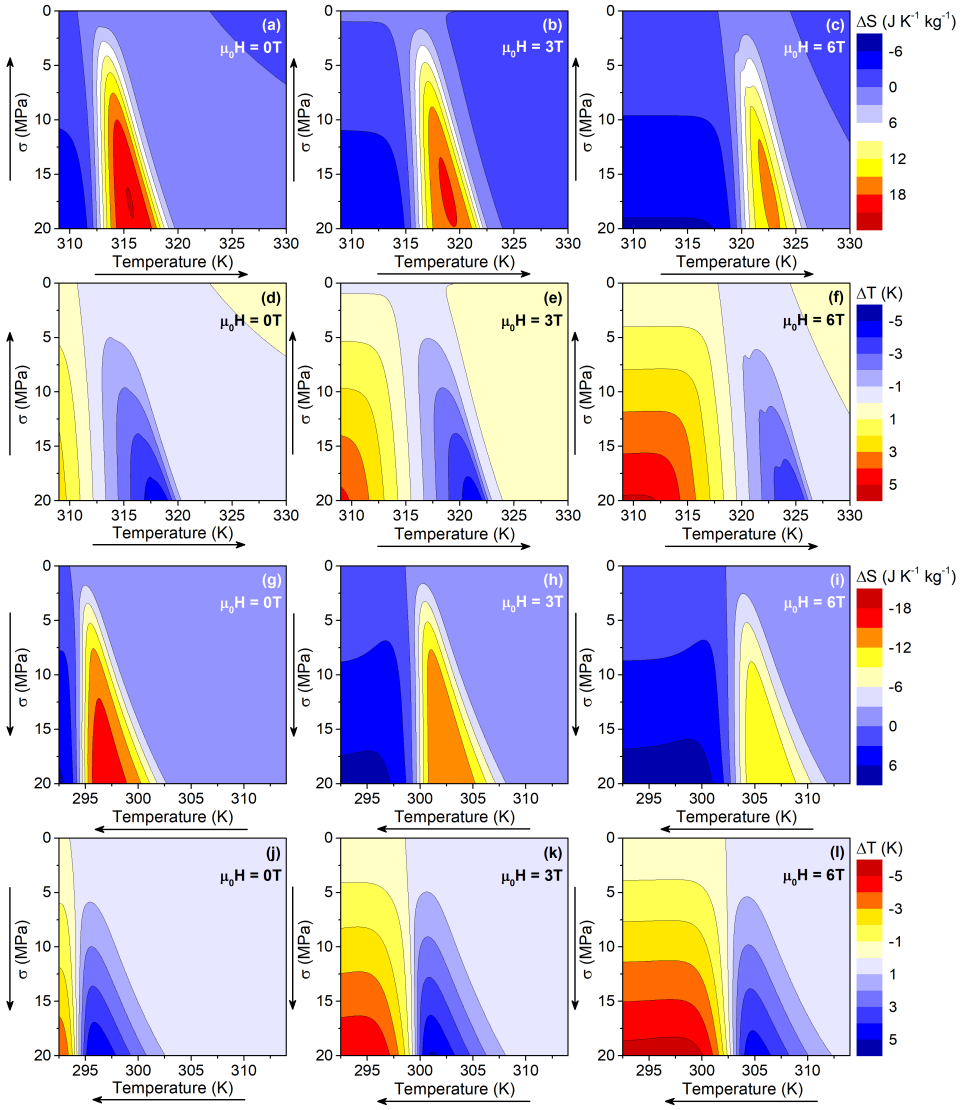

Figure 5.49: *Contour plots of the elastocaloric isothermal entropy (panels (a)-(c) and (g)-(i)) and adiabatic temperature (panels (d)-(f) and (j)-(l)) changes computed from the entropy curves upon heating (panels (a)-(f)) and cooling (panels (g)-(l)) as a function of temperature at selected values of magnetic field* $\{\mu_0 H_j\} = \{0, 3, 6\}$ *T. Arrows along the axis indicate the direction of the temperature and uniaxial stress changes.*

imum stress-induced elastocaloric thermal response is obtained in the absence of magnetic field. Upon the removal of stress, it accounts for $\Delta S_{max} = 21.1\,\mathrm{JK^{-1}kg^{-1}}$ and $\Delta T_{max} = -4.5\,\mathrm{K}$, whereas upon the application of stress it accounts for $\Delta S_{max} = -17.4\,\mathrm{JK^{-1}kg^{-1}}$ and $\Delta T_{max} = 5.0\,\mathrm{K}$. Furthermore, as it can be clearly

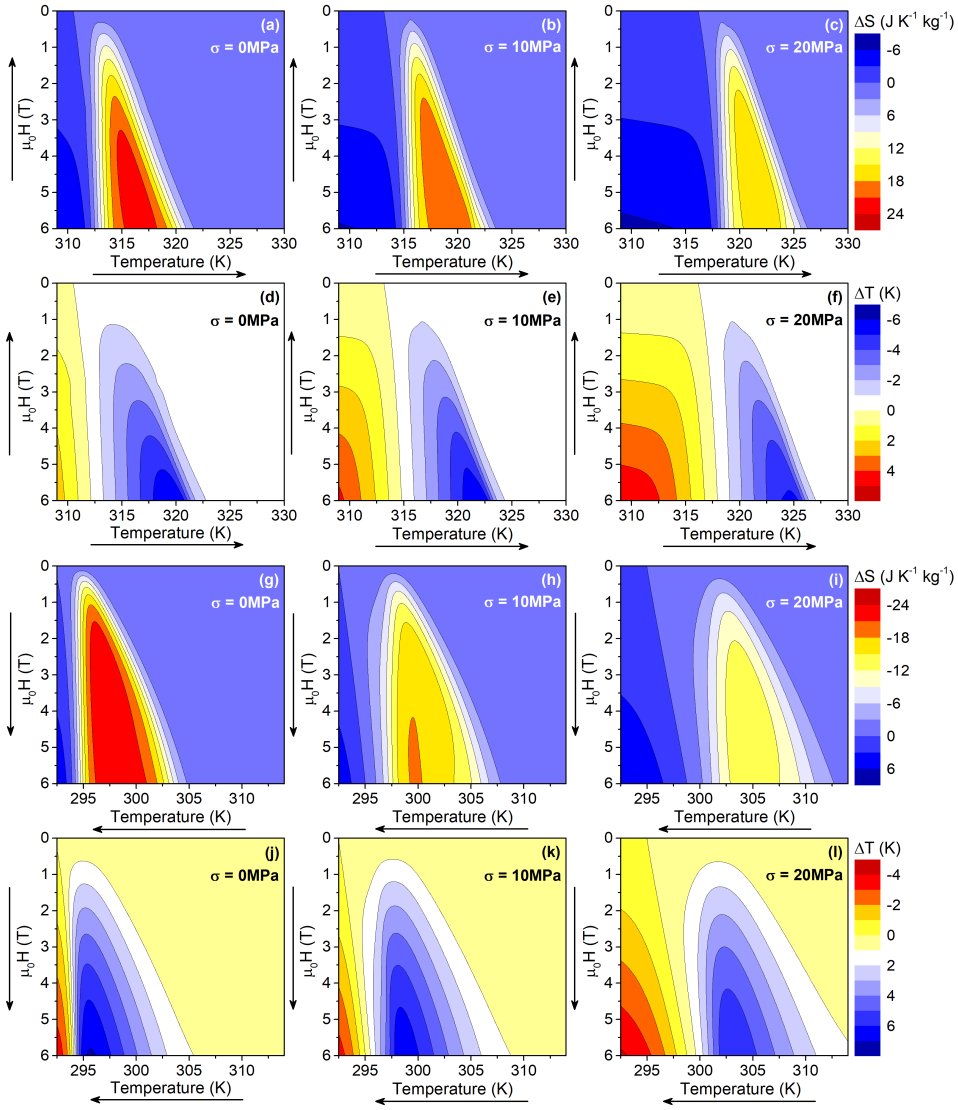

Figure 5.50: *Contour plots of the magnetocaloric isothermal entropy (panels (a)-(c) and (g)-(i)) and adiabatic temperature (panels (d)-(f) and (j)-(l)) changes computed from the entropy curves upon heating (panels (a)-(f)) and cooling (panels (g)-(l)) as a function of temperature at selected values of applied stress* $\{\sigma_i\} = \{0, 10, 20\}$ *MPa. Arrows along the axis indicate the direction of the temperature and uniaxial stress changes.*

seen when comparing the different panels in each row of the figure, when increasing the applied magnetic field the stress-induced elastocaloric effect shifts towards higher temperatures upon heating and cooling but, in addition, it decreases the elastocaloric thermal response. Interestingly, this decrease can be clearly seen for

the isothermal entropy change, whereas it is less pronounced for the adiabatic temperature change. In particular, the elastocaloric thermal response upon heating for the maximum stress removal (20 MPa $\rightarrow$ 0 MPa) renders $\Delta S = 20.9\,\mathrm{JK^{-1}kg^{-1}}$ and $\Delta T = -4.5\,\mathrm{K}$ in the absence of magnetic field, whereas these values decrease to $\Delta S = 15.3\,\mathrm{JK^{-1}kg^{-1}}$ and $\Delta T = -3.8\,\mathrm{K}$ under an applied magnetic field of $\mu_0 H = 6\,\mathrm{T}$. Similarly, the elastocaloric thermal response upon cooling for the maximum stress application (0 MPa $\rightarrow$ 20 MPa) renders $\Delta S = -17.4\,\mathrm{JK^{-1}kg^{-1}}$ and $\Delta T = 5.0\,\mathrm{K}$ in the absence of magnetic field, whereas these values decrease to $\Delta S = -11.8\,\mathrm{JK^{-1}kg^{-1}}$ and $\Delta T = 4.6\,\mathrm{K}$ under an applied magnetic field of $\mu_0 H = 6\,\mathrm{T}$. The significant decrease of the elastocaloric isothermal entropy change is in agreement with the transition entropy change decrease when increasing the applied magnetic field upon heating and cooling (see Figure 5.39 (e)), whereas the smaller influence on the adiabatic temperature change is in agreement with the fact that the transition temperature shift with stress is not significantly influenced by the applied magnetic field (see Figure 5.37 (e)).

In relation to the field-induced magnetocaloric effect, illustrated in Figure 5.49, the maximum thermal response is also obtained in the absence of applied stress. Upon the removal of magnetic field, it accounts for $\Delta S_{max} = 22.4\,\mathrm{JK^{-1}kg^{-1}}$ and $\Delta T_{max} = -6.0\,\mathrm{K}$, whereas upon the application of magnetic field it accounts for $\Delta S_{max} = -24\,\mathrm{JK^{-1}kg^{-1}}$ and $\Delta T_{max} = 7.1\,\mathrm{K}$. When comparing the different panels in each row of the figure, similar trends can be observed when increasing the applied stress with respect to the elastocaloric effect when increasing the applied magnetic field. In particular, the magnetocaloric thermal response upon heating for the maximum magnetic field removal (6 T $\rightarrow$ 0 T) renders $\Delta S = 21.9\,\mathrm{JK^{-1}kg^{-1}}$ and $\Delta T = -6.0\,\mathrm{K}$ in the absence of applied stress, whereas these values decrease to $\Delta S = 16.5\,\mathrm{JK^{-1}kg^{-1}}$ and $\Delta T = -5.2\,\mathrm{K}$ under an applied stress of $\sigma = 20\,\mathrm{MPa}$. Similarly, the magnetocaloric thermal response upon cooling for the maximum magnetic field application (0 MPa $\rightarrow$ 6 T) renders $\Delta S = -23\,\mathrm{JK^{-1}kg^{-1}}$ and $\Delta T = 7.1\,\mathrm{K}$ in the absence of applied stress, whereas these values decrease to $\Delta S = -13.4\,\mathrm{JK^{-1}kg^{-1}}$ and $\Delta T = 5.9\,\mathrm{K}$ under an applied stress of $\sigma = 20\,\mathrm{MPa}$. The significant decrease of the isothermal entropy change when increasing the applied stress upon heating and cooling is in agreement with the transition entropy change decrease when increasing the applied stress (see Figure 5.39 (f)), whereas the smaller influence on the adiabatic temperature change is in agreement with the fact that the transition temperature shift with magnetic field is not significantly influenced by the applied stress (see Figure 5.37 (d)).

5.4.5.2 Multicaloric effect

As discussed in section 2.1.2, the multicaloric effect refers to the field-induced isothermal entropy and adiabatic temperature changes under the simultaneous or sequential change of more than one external field. As the numerically simulated $S(T, \mu_0 H, \sigma)$ entropy curves upon cooling and heating are representative of the forward and reverse phase transitions, respectively, we will be able to completely characterize the multicaloric thermal response for any trajectory in the phase space (see Figure 5.37 (a) for the complete transition temperature phase diagram) from

below to above the red surface and from above to below the blue surface. Specifically, as the removal of either magnetic field or uniaxial stress favours the high-temperature austenitic phase, the entropy curves upon heating will allow us to compute the multicaloric thermal response under the simultaneous or sequential removal of magnetic field and stress. Accordingly, as the application of either magnetic field or uniaxial stress favours the low-temperature martensitic phase, the entropy curves upon cooling will allow us to compute the multicaloric thermal response under the simultaneous or sequential application of magnetic field and stress.

Therefore, at a certain constant temperature, the multicaloric isothermal entropy change induced by the removal of stress and magnetic field is computed from the entropy curves upon heating as:

$$\Delta S(T, \mu_0 H \rightarrow 0, \sigma \rightarrow 0) = S(T, 0, 0) - S(T, \mu_0 H, \sigma) \tag{5.49}$$

whereas the multicaloric isothermal entropy change induced by the application of stress and magnetic field is computed from the entropy curves upon cooling as:

$$\Delta S(T, 0 \rightarrow \mu_0 H, 0 \rightarrow \sigma) = S(T, \mu_0 H, \sigma) - S(T, 0, 0) \tag{5.50}$$

The corresponding results are illustrated in Figures 5.51 (a)-(h) and 5.52 (a)-(h), respectively, as contour colour plot maps at selected temperatures. Conversely, the multicaloric adiabatic temperature changes are computed after inverting and interpolating the corresponding numerically simulated entropy curves. Thus, the multicaloric adiabatic temperature change induced by the removal of stress and magnetic field is computed from the inverted entropy curves upon heating as:

$$\Delta T(S, \mu_0 H \rightarrow 0, \sigma \rightarrow 0) = T(S, 0, 0) - T(S, \mu_0 H, \sigma) \tag{5.51}$$

whereas the multicaloric adiabatic temperature change induced by the application of stress and magnetic field is computed from the inverted entropy curves upon cooling as:

$$\Delta T(S, 0 \rightarrow \mu_0 H, 0 \rightarrow \sigma) = T(S, \mu_0 H, \sigma) - T(S, 0, 0) \tag{5.52}$$

As for the single caloric effects, the multicaloric adiabatic temperature changes are represented as a function of the temperature given by the initial entropy curve prior to the external field change, and the corresponding results are illustrated in Figures 5.53 (a)-(h) and 5.54 (a)-(h), respectively, as contour colour plot maps at selected temperatures.

As for the previously studied Ni-Mn-In alloy, the combined effect of both external fields leads to a clear improvement of the multicaloric field-induced thermal response with respect to the single caloric effects, illustrated in Figures 5.41 and 5.21 respectively.

Let us first focus on the isothermal entropy change, illustrated in Figures 5.51 and 5.52. The maximum values induced by the removal of the applied external fields

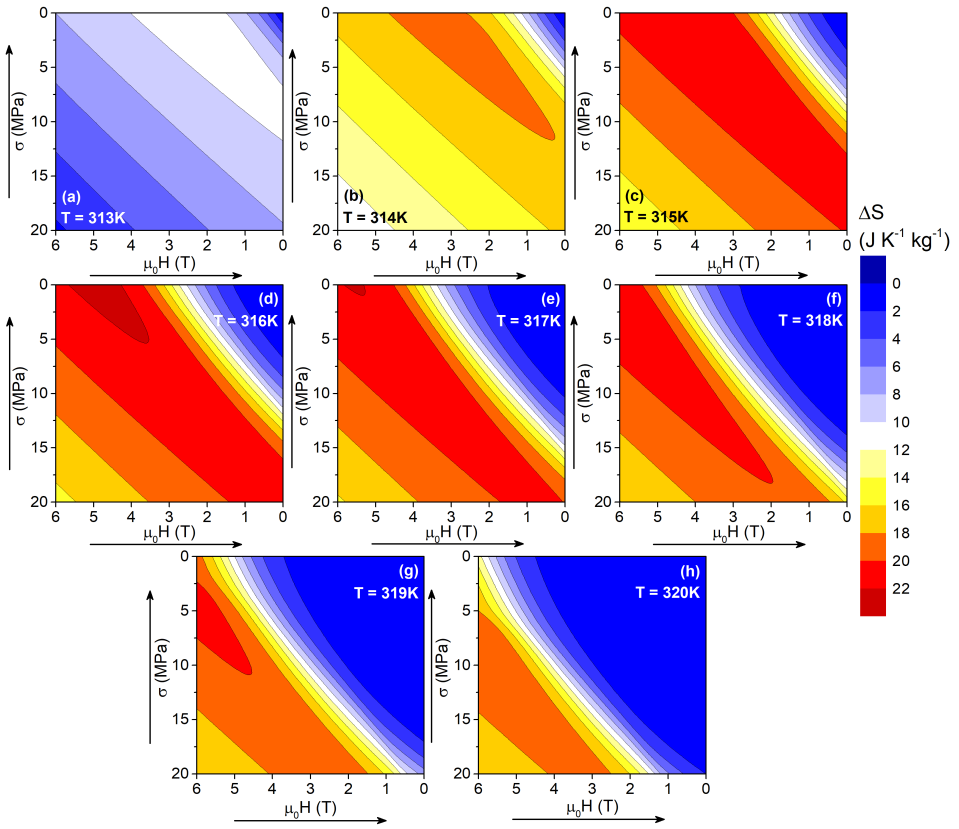

Figure 5.51: *Contour plots of the multicaloric isothermal entropy changes computed from the entropy curves upon heating resulting from the removal of uniaxial stress and magnetic field* $((\mu_0 H, \sigma) \rightarrow (0,0))$ *at selected temperatures. Arrows along the axis indicate the direction of the magnetic field and uniaxial stress changes.*

are $\Delta S_{max} = 22\,\mathrm{JK^{-1}kg^{-1}}$ at $T = 315\,\mathrm{K}$, $\Delta S_{max} = 22.4\,\mathrm{JK^{-1}kg^{-1}}$ at $T = 316\,\mathrm{K}$ and $\Delta S_{max} = 22.1\,\mathrm{JK^{-1}kg^{-1}}$ at $T = 317\,\mathrm{K}$, whereas upon the application of the external fields the maximum values induced are $\Delta S_{max} = -23.7\,\mathrm{JK^{-1}kg^{-1}}$ at $T = 298\,\mathrm{K}$, $\Delta S_{max} = -24\,\mathrm{JK^{-1}kg^{-1}}$ at $T = 297\,\mathrm{K}$ and $\Delta S_{max} = -22.7\,\mathrm{JK^{-1}kg^{-1}}$ at $T = 296\,\mathrm{K}$. It is relevant to highlight that these values clearly exceed the maximum stress-induced elastocaloric effect in the absence of magnetic field, whereas they match the maximum field-induced magnetocaloric effect in the absence of stress. This behaviour is indicative that we are able to fully drive the forward and reverse martensitic phase transitions when simultaneously changing both external fields. Furthermore, the combined effect of both external fields allows us to drastically reduce the magnitude of the fields needed to yield the same thermal response when compared to the single caloric effects. For example, at $T = 316\,\mathrm{K}$ (see Figure 5.51 (d)), if we focus on the contour line corresponding to $\Delta S = 20\,\mathrm{JK^{-1}kg^{-1}}$, to obtain such thermal response in the absence of stress we need to remove a magnetic field of

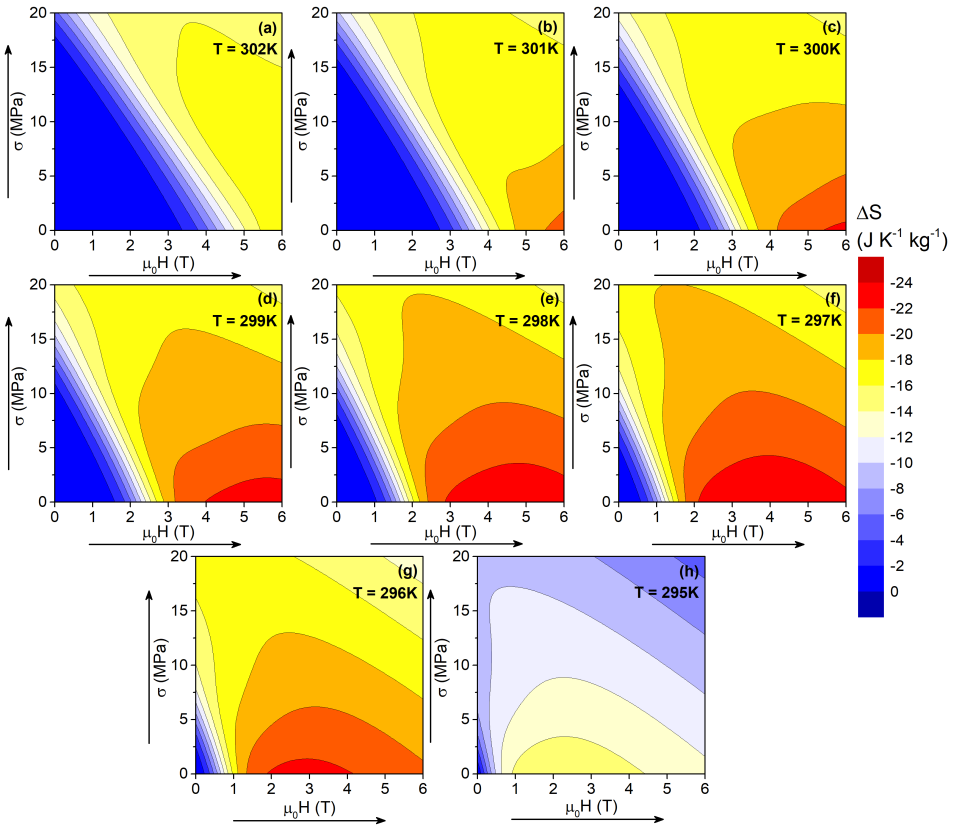

Figure 5.52: *Contour plots of the multicaloric isothermal entropy changes computed from the entropy curves upon cooling resulting from the application of uniaxial stress and magnetic field* $((0,0) \rightarrow (\mu_0 H, \sigma))$ *at selected temperatures. Arrows along the axis indicate the direction of the magnetic field and uniaxial stress changes.*

$\mu_0 H = 3.7\,\mathrm{T}$. However, if we also remove a stress of $\sigma = 12\,\mathrm{MPa}$ the magnetic field needed to obtain the same thermal response decreases to $\mu_0 H = 1\,\mathrm{T}$. Similar trends are observed as well at other selected temperatures illustrated in Figure 5.51 and for the thermal response induced upon the application of the external fields at selected temperatures, represented in Figure 5.52. Likewise, when considering the potential of multicaloric effects for future technological applications, it is particularly important to compare their thermal response under moderate magnetic field changes of $|\mu_0 \Delta H| = 1\,\mathrm{T}$, which can be readily provided by permanent magnets, with that of single caloric effects. Under these conditions, the field-induced magnetocaloric isothermal entropy changes are in the range $\Delta S(T, 1 \rightarrow 0\,\mathrm{T}, \sigma) = 8.5\text{-}9.3\,\mathrm{JK^{-1}kg^{-1}}$ and $|\Delta S(T, 0 \rightarrow 1\,\mathrm{T}, \sigma)| = 7.6\text{-}17.3\,\mathrm{JK^{-1}kg^{-1}}$ for both reverse and forward phase transitions (see Figure 5.21), respectively. Interestingly, when combining the magnetic field change with a moderate stress change of $|\Delta\sigma| = 20\,\mathrm{MPa}$, these values increase up to $\Delta S_{max} = 19.3\,\mathrm{JK^{-1}kg^{-1}}$ at $T = 315\,\mathrm{K}$, $\Delta S_{max} = 20.3\,\mathrm{JK^{-1}kg^{-1}}$ at

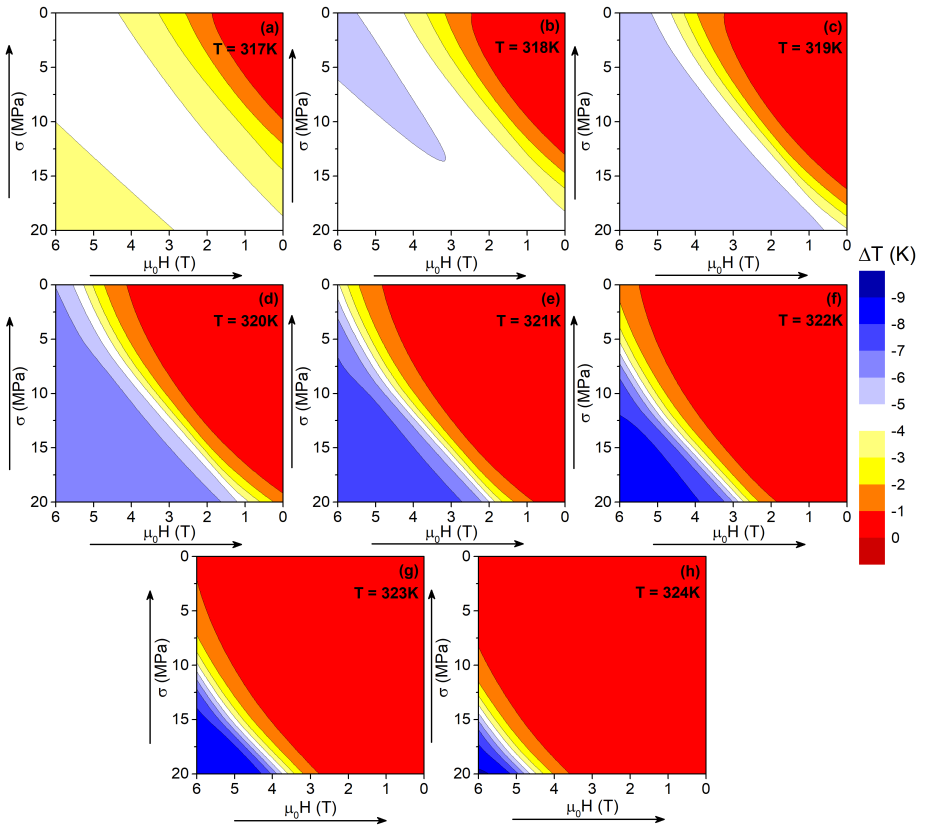

Figure 5.53: *Contour plots of the multicaloric adiabatic temperature changes computed from the entropy curves upon heating resulting from the removal of uniaxial stress and magnetic field* $((\mu_0 H, \sigma) \rightarrow (0,0))$ *at selected temperatures. Arrows along the axis indicate the direction of the magnetic field and uniaxial stress changes.*

$T = 316\,\mathrm{K}$ and $\Delta S_{max} = 20.4\,\mathrm{JK^{-1}kg^{-1}}$ at $T = 317\,\mathrm{K}$ for the reverse phase transition, and up to $\Delta S_{max} = -17.5\,\mathrm{JK^{-1}kg^{-1}}$ at $T = 298\,\mathrm{K}$, $\Delta S_{max} = -18\,\mathrm{JK^{-1}kg^{-1}}$ at $T = 297\,\mathrm{K}$ and $\Delta S_{max} = -16.6\,\mathrm{JK^{-1}kg^{-1}}$ at $T = 296\,\mathrm{K}$ for the forward phase transition. Furthermore, it is particularly important to highlight that the multicaloric effect not only provides a larger thermal response, but it also spreads over a significantly wider temperature window with respect to single caloric effects.

When considering the adiabatic temperature change, illustrated in Figures 5.53 and 5.54, the maximum values induced by the removal of the applied external fields are $\Delta T_{max} = -8.3\,\mathrm{K}$ at $T = 322\,\mathrm{K}$, $\Delta T_{max} = -9.0\,\mathrm{K}$ at $T = 323\,\mathrm{K}$ and $\Delta T_{max} = -9.2\,\mathrm{K}$ at $T = 324\,\mathrm{K}$, whereas upon the application of the external fields the maximum values induced are $\Delta T_{max} = 8.7\,\mathrm{K}$ at $T = 299\,\mathrm{K}$, $\Delta T_{max} = 9.1\,\mathrm{K}$ at $T = 298\,\mathrm{K}$ and $\Delta T_{max} = 9.3\,\mathrm{K}$ at $T = 297\,\mathrm{K}$. It is relevant to highlight that these values clearly exceed the maximum values obtained for the single elastocaloric

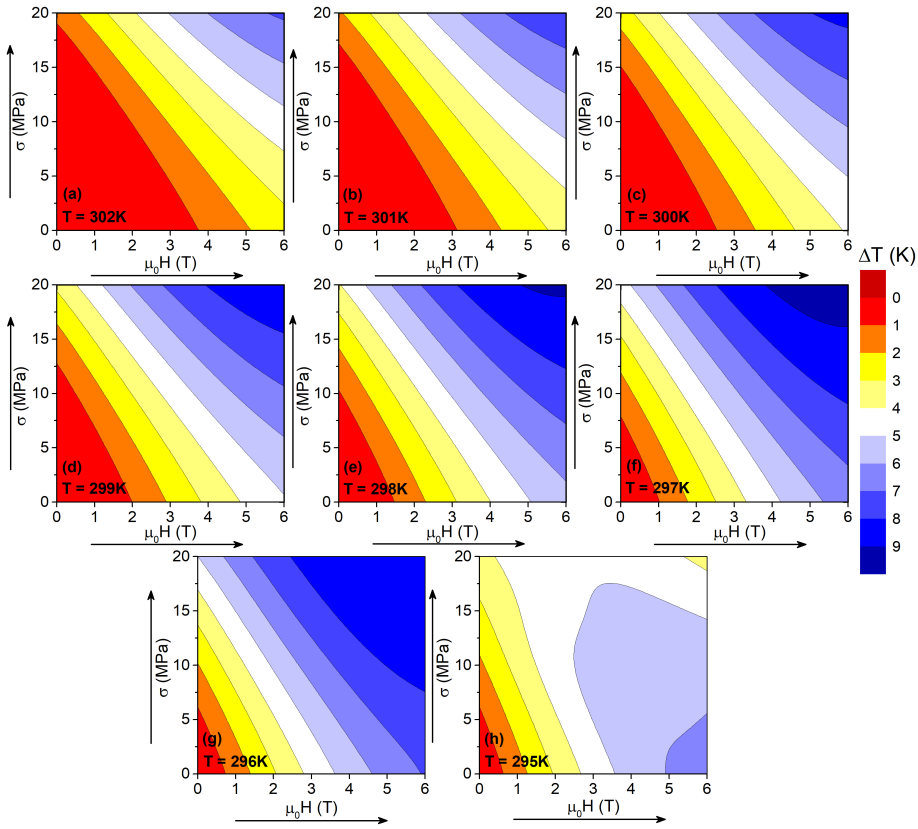

Figure 5.54: *Contour plots of the multicaloric adiabatic temperature changes computed from the entropy curves upon cooling resulting from the application of uniaxial stress and magnetic field* $((0,0) \rightarrow (\mu_0 H, \sigma))$ *at selected temperatures. Arrows along the axis indicate the direction of the magnetic field and uniaxial stress changes.*

and magnetocaloric effects. Furthermore, similar trends are also observed when considering the advantages that combining changes on both external fields provide with respect to the single caloric effects. Specifically, it is particularly relevant to compare their thermal response under moderate magnetic field changes of $|\mu_0 \Delta H| = 1\,\mathrm{T}$. While the field-induced magnetocaloric adiabatic temperature changes are in the range $|\Delta T(S, 1 \rightarrow 0\,\mathrm{T}, \sigma)| = 0.9$-$1.7\,\mathrm{K}$ for both forward and reverse transitions, when combining the magnetic field change with a moderate stress change of $|\Delta\sigma| = 20\,\mathrm{MPa}$, these values increase up to $\Delta T = -4.9\,\mathrm{K}$ at $T = 318\,\mathrm{K}$ or $\Delta T = -5.4\,\mathrm{K}$ at $T = 319\,\mathrm{K}$ for the reverse phase transition, and up to $\Delta T = 6.5\,\mathrm{K}$ at $T = 296\,\mathrm{K}$ or $\Delta T = 6.2\,\mathrm{K}$ at $T = 297\,\mathrm{K}$ for the forward phase transition.

5.4.5.3 Cross-coupling contribution to the multicaloric effect

As discussed in section 2.1.2, the field-induced multicaloric thermal response is not generally given by the direct sum of the two single caloric effects [51, 53], as there can be a contribution from the cross-coupled response of the material to the application of non-conjugated external fields. Certainly, as for the sample under study we are performing a symmetric external field change [13] to field-induce the multicaloric effect, the cross-coupled response of the system will play a role.

In particular, for a thermodynamic process in which stress and magnetic field are applied, the general equation for the multicaloric isofield entropy change (see equation 2.17) can be split into the following contributions:

$$\begin{aligned}\Delta S(T, 0 \rightarrow \mu_0 H, 0 \rightarrow \sigma) = \\ \Delta S(T, 0 \rightarrow \mu_0 H, \sigma = 0\,\mathrm{MPa}) + \Delta S(T, \mu_0 H = 0\,\mathrm{T}, 0 \rightarrow \sigma) \\ + \int_0^{\mu_0 H} \int_0^{\sigma} \frac{\partial \chi_{21}}{\partial T} d\sigma' d\mu_0 H'\end{aligned} \tag{5.53}$$

Similarly, for a thermodynamic processes in which stress and magnetic field are removed, the general equation for the multicaloric isofield entropy change can be written as:

$$\begin{aligned}\Delta S(T, \mu_0 H \rightarrow 0, \sigma \rightarrow 0) = \\ \Delta S(T, \mu_0 H = 0\,\mathrm{T}, \sigma \rightarrow 0) + \Delta S(T, \mu_0 H \rightarrow 0, \sigma = 0\,\mathrm{MPa}) \\ - \int_0^{\sigma} \int_0^{\mu_0 H} \frac{\partial \chi_{12}}{\partial T} d\mu_0 H' d\sigma'\end{aligned} \tag{5.54}$$

where the two first right hand terms of both equations correspond to the single caloric effects in the absence of a secondary field, whereas the last terms depend on $\chi_{21} = \left(\frac{\partial \varepsilon}{\partial \mu_0 H}\right)_{T,\sigma}$ and $\chi_{12} = \left(\frac{\partial M}{\partial \sigma}\right)_{T,\mu_0 H}$, which are off-diagonal coefficients of the cross-susceptibility tensor (see equations 2.7 and 2.16) that quantify the strength of the cross-coupled response of the system to the application of non-conjugated external fields. Along the following discussion, we will refer to the last right hand terms of equations 5.53 and 5.54 as $\Delta S^{coupling}$ for the sake of simplicity, as they quantify the cross-coupling magnitude between magnetization *(M)* and the applied stress (σ) and strain (ε) and the applied magnetic field ($\mu_0 H$) for the system under study.

As the numerically simulated $S(T, \mu_0 H, \sigma)$ entropy curves allowed us to compute both single caloric effects in the absence of a secondary field (see section 5.4.5.1) together with the multicaloric effect induced by either the application or removal of the external fields (see section 5.4.5.2), the corresponding cross-coupling magnitude to the multicaloric isothermal entropy changes can be computed as:

[13] As discussed in section 2.1.2, it refers to the particular case where both external fields are either applied or removed.

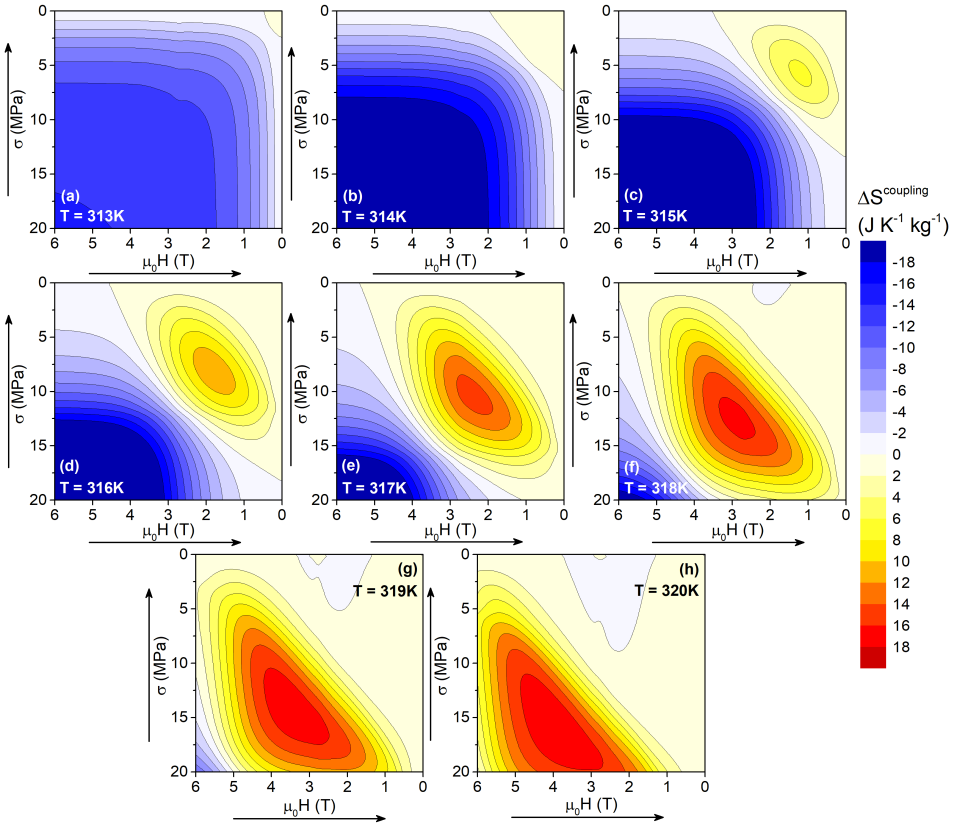

Figure 5.55: *Contour plots of the cross-coupling contribution to the multicaloric isothermal entropy changes computed from the entropy curves upon heating resulting from the removal of uniaxial stress and magnetic field* $((\mu_0 H, \sigma) \rightarrow (0,0))$ *at selected temperatures. Arrows along the axis indicate the direction of the magnetic field and uniaxial stress changes.*

$$\Delta S^{coupling}(T, 0 \rightleftarrows \mu_0 H, 0 \rightleftarrows \sigma) = \Delta S(T, 0 \rightleftarrows \mu_0 H, 0 \rightleftarrows \sigma) - \Delta S(T, \mu_0 H = 0\,\mathrm{T}, 0 \rightleftarrows \sigma) - \Delta S(T, 0 \rightleftarrows \mu_0 H, \sigma = 0\,\mathrm{MPa}) \tag{5.55}$$

where the double arrows indicate that either the external fields are removed or applied, which corresponds to the thermodynamic processes that field-induce either the reverse or forward phase transition. The corresponding results are illustrated in Figures 5.55 (a)-(h) and 5.56 (a)-(h), respectively, as contour colour plot maps at selected temperatures.

At low temperatures, when field-inducing the reverse (forward) phase transition upon the removal (application) of large external fields (see Figure 5.55 (a)-(b) and Figure 5.56 (g)-(h), respectively), the cross-coupling contribution to the multicaloric isothermal entropy change is negative (positive) and opposes the corre-

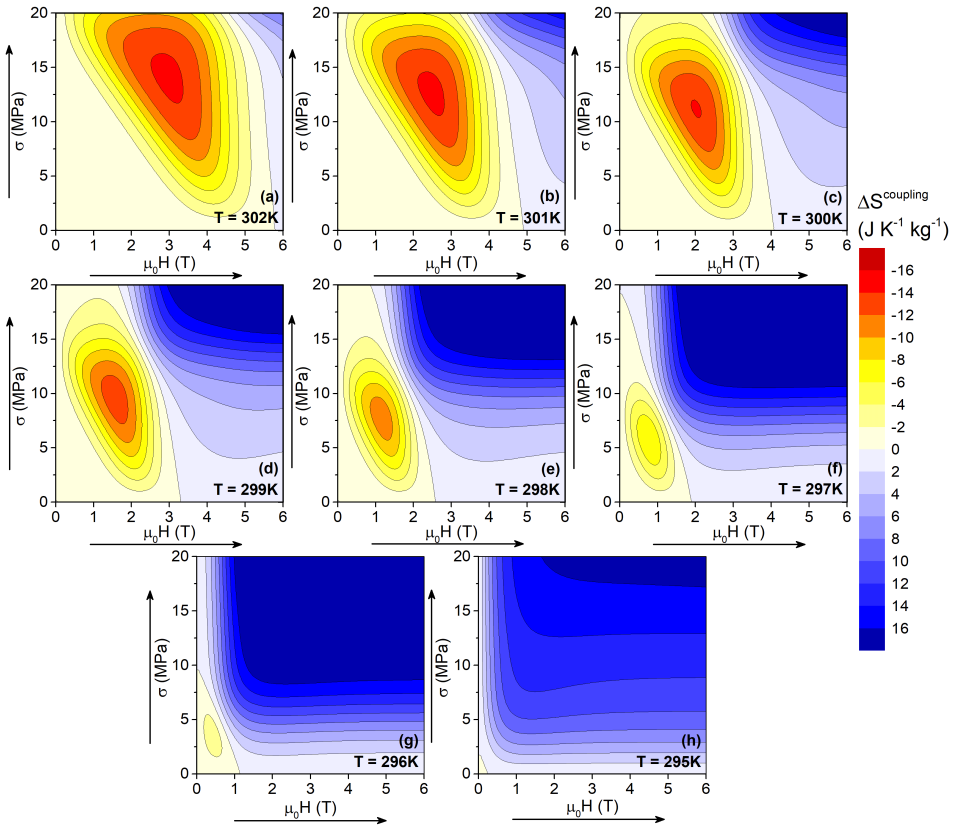

Figure 5.56: *Contour plots of the cross-coupling contribution to the multicaloric isothermal entropy changes computed from the entropy curves upon cooling resulting from the application of uniaxial stress and magnetic field* $((0,0) \rightarrow (\mu_0 H, \sigma))$ *at selected temperatures. Arrows along the axis indicate the direction of the magnetic field and uniaxial stress changes.*

sponding field-induced multicaloric isothermal entropy changes, illustrated in Figures 5.51 (a)-(b) and 5.52 (g)-(h). Despite this opposing behaviour, when decreasing the change on one of the removed (applied) external fields the cross-coupling contribution tends to increase (decrease), and it vanishes at the single caloric effect limit, where only one external field is changed in the absence of a secondary field.

To gain some insight into the origin of the cross-coupling contributions that oppose the corresponding field-induced multicaloric effects, it is particularly instructive to consider a particular combination of applied or removed external fields at a certain temperature. For instance, let us consider the application of $\mu_0 H = 3\,\mathrm{T}$ and $\sigma = 10\,\mathrm{MPa}$ at $T = 296\,\mathrm{K}$. Under these conditions, on the one hand, the elastocaloric effect in the absence of magnetic field (see Figure 5.49 (g)) renders $\Delta S(T, \mu_0 H = 0\,\mathrm{T}, 0 \rightarrow 10\,\mathrm{MPa}) = -13.9\,\mathrm{JK^{-1}kg^{-1}}$ whereas the magnetocaloric effect in the absence of stress (see Figure 5.50 (g)) renders $\Delta S(T, 0 \rightarrow 3\,\mathrm{T}, \sigma =$

$0\,\mathrm{MPa}) = -22.6\,\mathrm{JK^{-1}kg^{-1}}$. On the other hand, the field-induced multicaloric effect (see Figure 5.52 (g)) renders $\Delta S(T, 0 \rightarrow 3\,\mathrm{T}, 0 \rightarrow 10\,\mathrm{MPa}) = -18.8\,\mathrm{JK^{-1}kg^{-1}}$. Consequently, in accordance to equation 5.55, the cross-coupling contribution to the multicaloric isothermal entropy change is $\Delta S^{coupling}(T, 0 \rightarrow 3\,\mathrm{T}, 0 \rightarrow 10\,\mathrm{MPa}) = 17.7\,\mathrm{JK^{-1}kg^{-1}}$. Similarly, when considering the removal of $\mu_0 H = 5\,\mathrm{T}$ and $\sigma = 20\,\mathrm{MPa}$ at $T = 313\,\mathrm{K}$, the elastocaloric and magnetocaloric effects in the absence of a secondary field, illustrated in Figures 5.49 (a) and 5.50 (a), respectively render $\Delta S(T, \mu_0 H = 0\,\mathrm{T}, 20 \rightarrow 0\,\mathrm{MPa}) = 7.8\,\mathrm{JK^{-1}kg^{-1}}$ and $\Delta S(T, 5 \rightarrow 0\,\mathrm{T}, \sigma = 0\,\mathrm{MPa}) = 9.1\,\mathrm{JK^{-1}kg^{-1}}$, while the field-induced multicaloric effect (see Figure 5.51 (a)) renders $\Delta S(T, 5 \rightarrow 0\,\mathrm{T}, 20 \rightarrow 0\,\mathrm{MPa}) = 2.8\,\mathrm{JK^{-1}kg^{-1}}$. Consequently, in accordance to equation 5.55, the cross-coupling contribution to the multicaloric isothermal entropy change is $\Delta S^{coupling}(T, 5 \rightarrow 0\,\mathrm{T}, 20 \rightarrow 0\,\mathrm{MPa}) = -14.1\,\mathrm{JK^{-1}kg^{-1}}$.

At this point, as previously discussed in section 2.1.2, it is important to highlight that the field-induced multicaloric entropy change is irrespective of the thermodynamic path followed between the initial and final states. Therefore, taking into account the general equation 2.11, we can alternatively separate the multicaloric isothermal entropy change induced upon the application of stress and magnetic field (see equation 5.53) as:

$$\begin{aligned}\Delta S(T, 0 \rightarrow \mu_0 H, 0 \rightarrow \sigma) = \\ \Delta S(T, 0 \rightarrow \mu_0 H, \sigma = 0\,\mathrm{MPa}) + \Delta S(T, \mu_0 H, 0 \rightarrow \sigma)\end{aligned} \tag{5.56}$$

Similarly, for a thermodynamic processes in which stress and magnetic field are removed (see equation 5.54), the multicaloric isofield entropy change can be alternatively written as:

$$\begin{aligned}\Delta S(T, \mu_0 H \rightarrow 0, \sigma \rightarrow 0) = \\ \Delta S(T, \mu_0 H \rightarrow 0, \sigma) + \Delta S(T, \mu_0 H = 0\,\mathrm{T}, \sigma \rightarrow 0)\end{aligned} \tag{5.57}$$

where in the former case, the magnetocaloric effect is induced in the absence of a secondary field while the elastocaloric effect is induced under a constant applied magnetic field. Conversely, in the latter case, we have the opposite situation. The single caloric effects under a constant secondary field can also be computed from the numerically simulated $S(T, \mu_0 H, \sigma)$ entropy curves (see section 5.4.5.1) and evidently, the sum of both single caloric effects in these expressions yields the same values of the field-induced multicaloric isothermal entropy change when compared to the values computed in section 5.4.5.2. When considering the same particular combinations of applied or removed external fields that were previously discussed, the stress-induced elastocaloric effect when applying $\sigma = 10\,\mathrm{MPa}$ under a constant magnetic field of $\mu_0 H = 3\,\mathrm{T}$ at $T = 296\,\mathrm{K}$ (see Figure 5.49 (h)) renders $\Delta S(T, \mu_0 H = 3\,\mathrm{T}, 0 \rightarrow 10\,\mathrm{MPa}) = 3.8\,\mathrm{JK^{-1}kg^{-1}}$, whereas the field-induced magnetocaloric effect when removing $\mu_0 H = 5\,\mathrm{T}$ under a constant stress of $\sigma = 20\,\mathrm{MPa}$ at $T = 313\,\mathrm{K}$ (see Figure 5.50 (c)) renders $\Delta S(T, 5 \rightarrow 0\,\mathrm{T}, \sigma = 20\,\mathrm{MPa}) = -5.0\,\mathrm{JK^{-1}kg^{-1}}$.

In accordance to the discussion presented in section 5.4.5.1, an increase of the secondary constant field shifts the single caloric effects towards higher temperatures and drastically reduces its magnitude. Furthermore, as illustrated in Figures 5.49 and 5.50, the single caloric effects exhibit a crossover from inverse (at low temperatures) to conventional (at high temperatures) below the martensitic phase transition, which is associated with the transition entropy change decrease when increasing the applied external fields. Consequently, at a certain constant temperature around the martensitic phase transition, an increase of the secondary constant field can lead to an inversion (from conventional to inverse) of the field-induced single caloric effects, which in fact corresponds to the situation for both particular examples under consideration.

Overall, these factors highlight the fact that, at temperatures where the forward (reverse) martensitic phase transition can be partially or completely induced by the application (removal) of each external field in the absence of a secondary field, the additional application (removal) of a secondary field can lead to a significant decrease of field-induced multicaloric effect when compared to the individual single caloric effects in the absence of a secondary field. Therefore, as defined by equation 5.55, these scenarios lead to a cross-coupling contribution that opposes to the corresponding multicaloric isothermal entropy change. In consequence, at a certain temperature, a positive (negative) cross-coupling contribution to the field-induced multicaloric isothermal entropy change upon the application (removal) of a certain combination of external fields indicates that the multicaloric effect does not represent a gain with respect to the simple sum of both single caloric effects in the absence of a secondary field.

Interestingly, when further increasing the temperature, a positive (negative) cross-coupling contribution appears when field-inducing the reverse (forward) phase transition upon the removal (application) of small external fields, as illustrated in Figure 5.55 (c)-(d) and Figure 5.56 (e)-(f), respectively. In this regard, it must be highlighted that the emergence of a positive (negative) cross-coupling contribution indicates that the multicaloric effect induced upon the removal (application) of the external fields represents a gain with respect to the simple sum of both single caloric effects in the absence of a secondary field. For example, the field-induced multicaloric isothermal entropy change when applying $\mu_0 H = 1\,\mathrm{T}$ and $\sigma = 10\,\mathrm{MPa}$ at $T = 298\,\mathrm{K}$ (see Figure 5.52 (e)) renders $\Delta S(T, 0 \rightarrow 1\,\mathrm{T}, 0 \rightarrow 10\,\mathrm{MPa}) = -16.1\,\mathrm{JK^{-1}kg^{-1}}$, from which the cross-coupling contribution accounts for $\Delta S^{coupling}(T, 0 \rightarrow 1\,\mathrm{T}, 0 \rightarrow 10\,\mathrm{MPa}) = -9.6\,\mathrm{JK^{-1}kg^{-1}}$. Similarly, the field-induced multicaloric isothermal entropy change when removing $\mu_0 H = 1\,\mathrm{T}$ and $\sigma = 10\,\mathrm{MPa}$ at $T = 316\,\mathrm{K}$ (see Figure 5.51 (d)) renders $\Delta S(T, 1 \rightarrow 0\,\mathrm{T}, 10 \rightarrow 0\,\mathrm{MPa}) = 16.8\,\mathrm{JK^{-1}kg^{-1}}$, from which the cross-coupling contribution accounts for $\Delta S^{coupling}(T, 1 \rightarrow 0\,\mathrm{T}, 10 \rightarrow 0\,\mathrm{MPa}) = 8.8\,\mathrm{JK^{-1}kg^{-1}}$. Consequently, the cross-coupling contribution plays an important role in increasing the entropy change at low external field changes. Furthermore, it is also important to notice that these positive (negative) cross-coupling contributions at the low external field regions positively contribute at the edge of the corresponding field-induced multicaloric isothermal entropy changes (where the contour lines are close to each other), il-

lustrated in Figures 5.51 (c)-(d) and 5.52 (e)-(f). Therefore, the cross-coupling contribution also helps on enlarging the window of external field changes where giant multicaloric isothermal entropy changes can be induced. Nevertheless, at these temperatures, a negative (positive) cross-coupling contribution persists when field-inducing the reverse (forward) phase transition upon the removal (application) of large external fields.

At even higher temperatures, as illustrated in Figure 5.55 (e)-(h) and 5.56 (a)-(d), the window of external field changes where a positive (negative) cross-coupling contribution that favours the corresponding multicaloric isothermal entropy changes when field-inducing the reverse (forward) phase transition is enlarged. Furthermore, the cross-coupling contribution is gradually intensified and moves towards the region of large external field changes. Eventually, at the highest temperatures represented in both figures, the cross-coupling term becomes the main contribution of the multicaloric isothermal entropy change when inducing the reverse (forward) phase transition over a broad window of external field changes, as it can be seen when comparing Figure 5.55 (h) with Figure 5.51 (h) and Figure 5.56 (a) with Figure 5.52 (a), respectively.

So far, we have only considered the cross-coupling contribution to the field-induced multicaloric isothermal entropy change, but in order to provide a complete discussion we also have to consider its effect on the field-induced multicaloric adiabatic temperature change. By following a similar derivation procedure as for the isothermal entropy change, and taking into account that the general expression for the multicaloric adiabatic temperature change is given by equation 2.19, we can also compute the corresponding cross-coupling magnitude to the multicaloric adiabatic temperature change as:

$$\begin{aligned}\Delta T^{coupling}(S, 0 \rightleftarrows \mu_0 H, 0 \rightleftarrows \sigma) = \Delta T(S, 0 \rightleftarrows \mu_0 H, 0 \rightleftarrows \sigma) \\ - \Delta T(S, \mu_0 H = 0\,\mathrm{T}, 0 \rightleftarrows \sigma) - \Delta T(S, 0 \rightleftarrows \mu_0 H, \sigma = 0\,\mathrm{MPa})\end{aligned} \tag{5.58}$$

In this regard, it is important to highlight that the numerically simulated entropy curves were inverted and interpolated ($T(S, \mu_0 H, \sigma)$) in order to compute both the single caloric adiabatic temperature changes in the absence of a secondary field (see section 5.4.5.1) and the multicaloric adiabatic temperature changes induced by either the application or removal of the external fields (see section 5.4.5.2). The corresponding results are illustrated in Figures 5.57 (a)-(h) and 5.58 (a)-(h), which respectively correspond to thermodynamic processes that field-induce either the reverse or forward phase transition, as contour colour plot maps at selected temperatures.

Overall, the cross-coupling contribution to the multicaloric adiabatic temperature change shows similar trends than those observed for the cross-coupling contribution to the multicaloric isothermal entropy change. At low temperatures, when field-inducing the phase transition with large external fields (see Figures 5.57 (a) and 5.58 (g)-(h)), the cross-coupling contribution opposes the corresponding mul-

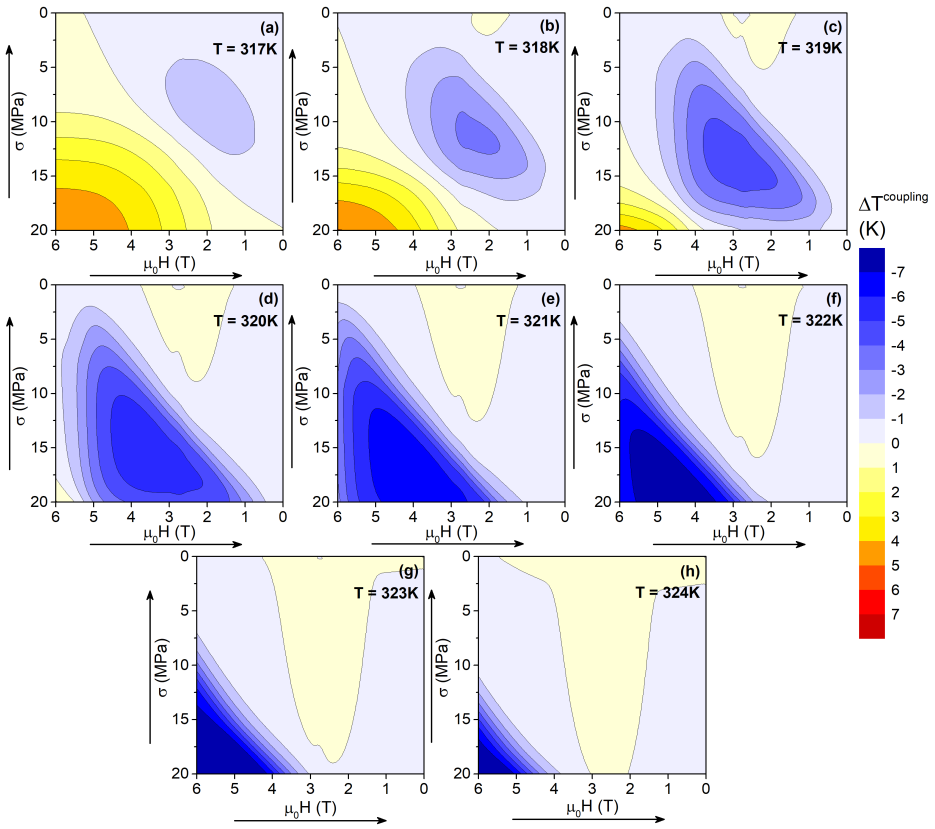

Figure 5.57: *Contour plots of the cross-coupling contribution to the multicaloric adiabatic temperature changes computed from the entropy curves upon heating resulting from the removal of uniaxial stress and magnetic field* $((\mu_0 H, \sigma) \rightarrow (0,0))$ *at selected temperatures. Arrows along the axis indicate the direction of the magnetic field and uniaxial stress changes.*

ticaloric adiabatic temperature change. Interestingly, as it can be clearly seen when comparing Figures 5.56 and 5.58, this behaviour is only observed within a smaller window of external field changes. In this regard, as discussed in section 5.4.5.1, it must be mentioned that the application of a secondary field had a smaller influence on the magnitude of the single caloric adiabatic temperature changes. Consequently, the additional application (removal) of a secondary field will lead to smaller changes on the field-induced multicaloric adiabatic temperature change which in turn, as defined by equation 5.58, lessens the window of external field changes where the cross-coupling contribution opposes the multicaloric effect.

When increasing the temperature (see Figures 5.57 (b)-(c) and 5.58 (e)-(f)), a region where the cross-coupling contribution favours the corresponding multicaloric adiabatic temperature change emerges when field-inducing the phase transition with small external fields. Specifically, when considering the potential of mul-

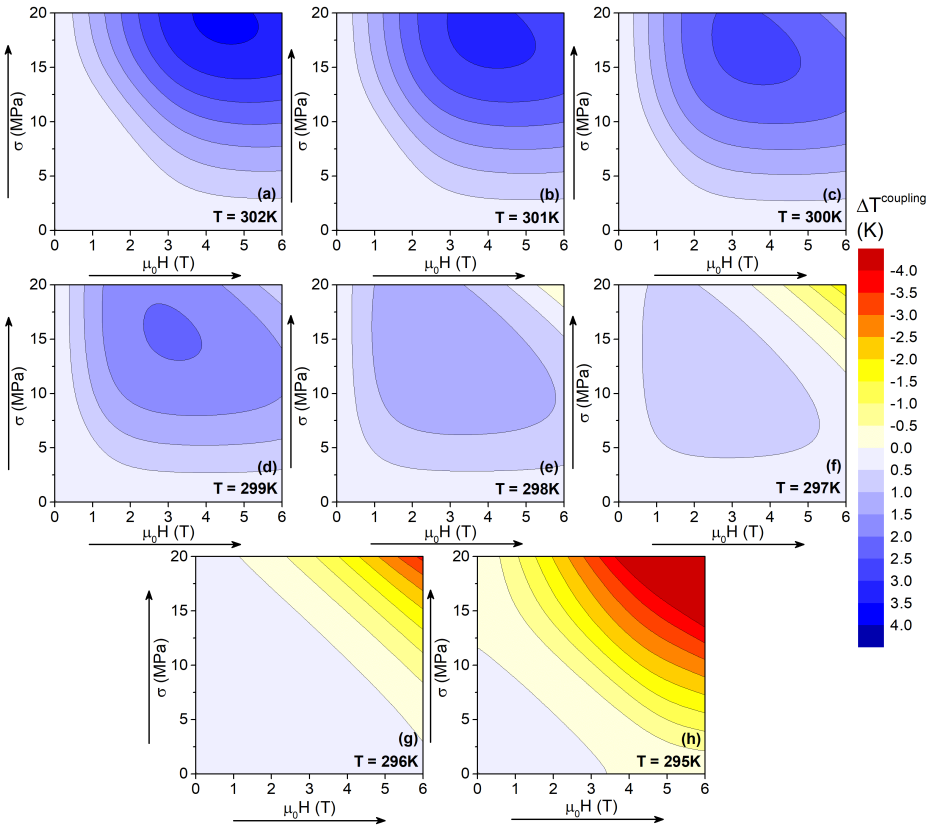

Figure 5.58: *Contour plots of the cross-coupling contribution to the multicaloric adiabatic temperature changes computed from the entropy curves upon cooling resulting from the application of uniaxial stress and magnetic field* $((0,0) \rightarrow (\mu_0 H, \sigma))$ *at selected temperatures. Arrows along the axis indicate the direction of the magnetic field and uniaxial stress changes.*

ticaloric effects for future technological applications, it is particularly relevant to compute the cross-coupling contribution to the multicaloric adiabatic temperature change under moderate magnetic field changes of $|\mu_0 \Delta H| = 1\,\mathrm{T}$, which can be readily provided by permanent magnets. For example, the field-induced multicaloric adiabatic temperature change when applying $\mu_0 H = 1\,\mathrm{T}$ and $\sigma = 20\,\mathrm{MPa}$ at $T = 298\,\mathrm{K}$ (see Figure 5.54 (e)) renders $\Delta T(S, 0 \rightarrow 1\,\mathrm{T}, 0 \rightarrow 20\,\mathrm{MPa}) = 5.5\,\mathrm{K}$, from which the cross-coupling contribution accounts for $\Delta T^{coupling}(S, 0 \rightarrow 1\,\mathrm{T}, 0 \rightarrow 20\,\mathrm{MPa}) = 1.1\,\mathrm{K}$. Similarly, the field-induced multicaloric adiabatic temperature change when removing $\mu_0 H = 1\,\mathrm{T}$ and $\sigma = 20\,\mathrm{MPa}$ at $T = 319\,\mathrm{K}$ (see Figure 5.53 (c)) renders $\Delta T(S, 1 \rightarrow 0\,\mathrm{T}, 20 \rightarrow 0\,\mathrm{MPa}) = -5.4\,\mathrm{K}$, from which the cross-coupling contribution accounts for $\Delta T^{coupling}(S, 1 \rightarrow 0\,\mathrm{T}, 20 \rightarrow 0\,\mathrm{MPa}) = -1.2\,\mathrm{K}$. Therefore, the cross-coupling contribution to the multicaloric adiabatic temperature change also plays an important role on increasing the multicaloric thermal response at low external field changes. Furthermore, as the cross-coupling contribu-

tion is relevant at the edge of the multicaloric adiabatic temperature change (where the contour lines are close to each other) induced by low external field changes, it is important to highlight that it additionally helps on expanding the window of external field changes were a giant multicaloric thermal response can be induced.

At even higher temperatures (see Figures 5.57 (d)-(h) and 5.58 (a)-(d)), the cross-coupling contribution that favours the corresponding multicaloric adiabatic temperature change is gradually intensified, and moves towards the region of large external field changes.

5.4.6 Reproducibility of the caloric effects under field cycling

The characterization of the reproducibility of a caloric effect under field cycling is a relevant feature for potential technological applications. Nevertheless, as illustrated in Figures 5.41 and 5.42, the sample under study exhibits a poor reversibility of the single caloric effects for the magnetic field and stress changes considered along this chapter to field-induce the phase transition. For instance, if we consider that the Ni-Mn-Ga-Cu alloy under study exhibits a thermal hysteresis of $\sim 16\,\mathrm{K}$ (see Figure 5.37 (d) and (e)), and taking representative values for the shifts of the transition temperature with magnetic field and stress (see Figure 5.37 (d) and (e)) of $\frac{dT_t}{d\mu_0 H} \sim 1.3\,\mathrm{KT}^{-1}$ and $\frac{dT_t}{d\sigma} \sim 0.3\,\mathrm{KMPa}^{-1}$, respectively, the alloy under study exhibits an estimated effective hysteresis on magnetic field of $\sim 12\,\mathrm{T}$, and of $\sim 54\,\mathrm{MPa}$ on stress. Therefore, the single caloric effects are only expected to be reproducible for higher external field changes than the corresponding effective hysteresis.

While the application of such magnetic fields is unfeasible for practical technological applications, the combined action of magnetic field and stress can enhance the reproducibility of the magnetocaloric effect under field cycling by taking advantage of the magnetostructural character of the martensitic phase transition. In particular, considering the cyclic application and removal of a moderate magnetic field of $|\mu_0 \Delta H| \sim 1\,\mathrm{T}$, the magnetocaloric effect is expected to be reproducible under the sequence presented in Figure 5.59. Each panel of the sketched multicaloric cycle shows the corresponding sample fraction at the high-temperature austenitic phase as a function of temperature at the initial (dashed lines) and final (solid lines) configuration of magnetic field and applied stress. Before the discussion of each cycle step, it is important to point out that partial hysteresis loops have not been considered for the sake of simplicity.

1. **Panel 1:**
   Removal of magnetic field shifts the phase transition to lower temperatures (blue curves) and the sample, initially in the low-temperature martensitic phase, partially transforms to the high-temperature austenitic phase, as indicated by the black arrow.

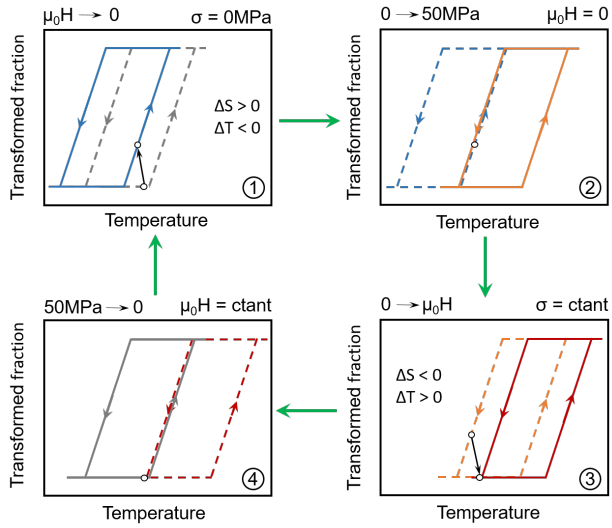

Figure 5.59: *Sketch of a multicaloric reversible cycle showing the fraction of the sample at the high-temperature austenitic phase as a function of temperature, for selected values of magnetic field and uniaxial stress. Panel 1: Removal of magnetic field in the absence of stress. Panel 2: Application of stress in the absence of magnetic field. Panel 3: Application of magnetic field under an applied (constant) stress. Panel 4: Removal of stress under an applied (constant) magnetic field.*

2. **Panel 2:**
   Application of a 50 MPa compressive stress [14] shifts the phase transition to higher temperatures (orange curves) in a way that the state of the sample (in the absence of magnetic field and under compressive stress) lies on the cooling branch of the inherent hysteresis of the phase transition.

3. **Panel 3:**
   While keeping the stress constant, application of magnetic field shifts the phase transitions to higher temperatures (red curves) and the sample transforms back to the low-temperature martensitic phase, as indicated by the black arrow.

4. **Panel 4:**
   Removal of the 50 MPa applied stress shifts the phase transition to lower temperatures (grey curves) in a way that the state of the sample (under magnetic field and in the absence of compressive stress) lies on the heating branch of the hysteresis loop, thus recovering the initial state of the first panel.

[14] The selected magnitude of the applied stress is smaller than the field necessary to overcome the effective hysteresis, which would induce the back transformation to the low-temperature martensitic phase.

Hence, application of a moderate stress turns Ni-Mn-Ga-Cu into a suitable material for refrigeration devices using permanent magnets.

Furthermore, it is also worth mentioning that the novel multicaloric cycle proposed by T. Gottschall *et. al* in [64], which consists on the "hysteresis-positive" approach discussed in section 5.3.7.1, can be adapted for materials exhibiting conventional elastocaloric and magnetocaloric effects.

In such cases, application of magnetic field favours the low-temperature martensitic phase, as does the application of uniaxial compressive stress. Therefore, to induce the reverse phase transition, we can remove a previously applied uniaxial compressive stress. Keeping the same working idea that the inherent hysteresis of the magnetostructural first-order phase transition locks the sample phase after the external field pulses, thus preventing the back transformation, the magnetic field has to be applied under a constant compressive stress, favouring the low-temperature martensitic phase, whereas the removal of the previously applied compressive stress is used to favour the high-temperature phase and return the system to the initial thermodynamic state.

5.4.7 Summary and conclusions

Employing our unique DSC that works under the simultaneous application of magnetic field and compressive stress, we have been able to study the giant elastocaloric, magnetocaloric and multicaloic effects in a Ni-Mn-Ga-Cu alloy. The composition of the studied sample, and in particular its Cu content, has been selected in order to overlap the martensitic transition temperature and the austenitic Curie temperature, which confers this alloy a pronounced coupling between the structural and magnetic degrees of freedom and leads to the exhibition of synergic single caloric effects. A previous characterization of the sample was performed with a commercial DSC, reporting a martensitic phase transition near room temperature. The associated martensitic transition entropy change in the absence of applied external fields was determined to be $\Delta S_t^M = (-27.9 \pm 0.5)\,\mathrm{JK^{-1}kg^{-1}}$ and $\Delta S_t^A = (27.2 \pm 0.5)\,\mathrm{JK^{-1}kg^{-1}}$ for the forward and reverse martensitic transitions, respectively.

The calorimetric measurements performed with our bespoke setup allowed us to determine both the transition temperature phase diagram and the transition entropy change behaviour within the magnetic field and compressive stress coordinate space under study.

On the one hand, the transition temperature of the forward and reverse martensitic transitions was identified by the calorimetric peak position of the DSC measurements. For all values of applied compressive stress, both forward and reverse martensitic transition temperatures linearly increased when increasing the applied magnetic field with slopes in the range $\frac{dT_t}{d\mu_0 H} \in [0.9, 1.6]\,\mathrm{KT^{-1}}$, thus giving rise to a conventional magnetocaloric effect. Likewise, for all values of applied mag-

netic field, both forward and reverse martensitic transition temperatures linearly increased when increasing the applied compressive stress with slopes in the range $\frac{dT_t}{d\sigma} \in [0.27, 0.38]\,\mathrm{KMPa}^{-1}$, leading to a conventional elastocaloric effect. Interestingly, no effect of the secondary field has been found on the transition temperatures shift rates with either magnetic field and uniaxial stress.

On the other hand, the DSC measurements allowed us to determine the transition entropy change of the forward and reverse martensitic phase transitions. Due to the complexity of our bespoke DSC setup, some of the recorded thermograms exhibit a poor signal-to-baseline ratio and a proper analysis of these curves is not possible. Therefore, we have restricted our analysis to the thermograms recorded for heating and cooling runs under applied compressive stresses up to $\sigma = 20\,\mathrm{MPa}$. As for the Cu-Zn-Al calibration sample, a constant calibration factor had to be introduced to the baseline corrected thermograms in order to properly determine the corresponding transition entropy changes. Interestingly, for all values of applied stress, both forward and reverse transition entropy changes linearly decrease when increasing the applied magnetic field with slopes in the range $\frac{d\Delta S_t}{d\mu_0 H} \in [-1.1, -0.7]\,\mathrm{JK}^{-1}\mathrm{kg}^{-1}\mathrm{T}^{-1}$. Furthermore, for all values of applied magnetic field, both forward and reverse transition entropy changes linearly decrease when increasing the applied stress with slopes in the range $\frac{d\Delta S_t}{d\sigma} \in [-0.5, -0.2]\,\mathrm{JK}^{-1}\mathrm{kg}^{-1}\mathrm{MPa}^{-1}$. These external field dependencies are not straightforward to understand, as they are in apparent contradiction with the fact that, for the alloy under study, both vibrational and magnetic entropy contributions have the same sign and synergically contribute to the transition entropy change. On the one hand, the transition entropy change decrease when increasing the applied magnetic field may point to a certain interplay between the vibrational entropy contribution and the applied magnetic field, in a way that it decreases when increasing the applied magnetic field. On the other hand, the transition entropy change decrease when increasing the applied stress may arise from a rearrangement of the martensite variants when inducing the phase transition under a certain applied stress. Overall, despite the experimental observation of these dependencies, further studies are required in order to gain some insight into their origin.

The quasidirect derivation of the elastocaloric and magnetocaloric effects relies on the computation of the corresponding experimental isofield-isostress entropy curves, which are constructed from the integration of the corrected thermograms together with the specific heat data at the martensitic and austenitic phases. As for the previously studied Ni-Mn-In alloy, due to the strong coupling between the structural and magnetic degrees of freedom, its specific heat will exhibit a certain dependence on the applied magnetic field. Whereas a bespoke Peltier cell calorimeter was used to measure the specific heat of the martensitic phase, a commercial relaxation calorimeter (that allows us to reach higher temperatures) was used to measure the specific heat of the austenitic phase. For both phases, the specific heat showed a dependency on both the temperature and the applied magnetic field. Furthermore, the specific heat measurements performed with the bespoke Peltier cell calorimeter

allowed us also to compute the transition entropy change for the reverse martensitic phase transition, which was found to linearly decrease when increasing the applied magnetic field at a rate of $\frac{d\Delta S_t^A}{d\mu_0 H} = (-0.5 \pm 0.1)\,\mathrm{JK^{-1}kg^{-1}T^{-1}}$. The fact that we have observed the same behaviour for the transition entropy change when increasing the applied magnetic field with two distinct experimental setups provides reliability to the performance of our bespoke DSC.

The field-induced isothermal entropy and adiabatic temperature changes for the elastocaloric and magnetocaloric effects were computed by subtracting the corresponding experimental isofield-isostress entropy curves. As expected, both elastocaloric and magnetocaloric effects have been found to be conventional. Interestingly, both caloric effects show a crossover from inverse (at low temperatures) to conventional (at high temperatures). While the conventional caloric effects are associated with the field-induced martensitic phase transition, the inverse effects that arise below the martensitic phase transition are associated with the transition entropy change decrease when increasing either the applied magnetic field or the compressive stress.

For both caloric effects, an increase of the external field change that drives the martensitic phase transition (stress for the elastocaloric effect and magnetic field for the magnetocaloric effect) enlarges the temperature window of the giant thermal response for all values of the applied secondary field. Additionally, an increase of the secondary field shifts towards higher temperatures the temperature window where the giant caloric effects occur. While the maximum field-induced adiabatic temperature change is found to increase linearly when increasing the driving field for both caloric effects, the maximum field-induced isothermal entropy change initially increases but then it shows a tendency to saturate. The saturation is completely reached for the magnetocaloric effect under all applied stresses, whereas it is only reached for the elastocaloric effect under certain applied magnetic fields. This different behaviour indicates that we are able to fully drive the martensitic phase transition with magnetic field, while we are close to fully drive the phase transition with compressive stress. Upon the removal of the external field, the maximum isothermal entropy changes for the magnetocaloric and elastocaloric effects are $\Delta S_{max} = 24\,\mathrm{JK^{-1}kg^{-1}}$ and $\Delta S_{max} = 22\,\mathrm{JK^{-1}kg^{-1}}$, whereas upon the application of the external field the maximum values are $\Delta S_{max} = -24\,\mathrm{JK^{-1}kg^{-1}}$ and $\Delta S_{max} = -16.5\,\mathrm{JK^{-1}kg^{-1}}$, respectively. Interestingly, after reaching saturation, the maximum isothermal entropy change exhibits a certain decrease when further increasing the driving field. This behaviour is in accordance with the transition entropy change decrease when either increasing the applied magnetic field or the compressive stress.

Additionally, it is significant to highlight that under a moderate magnetic field change of $|\mu_0 \Delta H| = 1\,\mathrm{T}$, the alloy under study exhibits a field-induced isothermal entropy change of $|\Delta S_{max}| \sim 15\,\mathrm{JK^{-1}kg}$, which surpasses the values reported for most of the Heusler alloys under the same magnetic field change [234–236].

In order to compute the corresponding caloric and multicaloric effects for any combination of magnetic field and uniaxial stress changes, we have defined two different analytical functions (one for the forward and the other one for the reverse phase transition) to phenomenologically reproduce the behaviour of the isofield-isostress entropy curves. The numerical treatment of our calorimetric data enabled us to correctly reproduce the entropy of the alloy over the complete temperature, magnetic field and compressive stress coordinate space under study. Based on the numerically simulated isofield-isostress entropy curves, we computed the field-induced elastocaloric and magnetocaloric thermal responses. Upon the removal of the external field, the maximum isothermal entropy changes for the simulated magnetocaloric and elastocaloric effects are $\Delta S_{max} = 22.4\,\mathrm{JK^{-1}kg^{-1}}$ and $\Delta S_{max} = 21.1\,\mathrm{JK^{-1}kg^{-1}}$, whereas upon the application of the external field the maximum values are $\Delta S_{max} = -24\,\mathrm{JK^{-1}kg^{-1}}$ and $\Delta S_{max} = -17.4\,\mathrm{JK^{-1}kg^{-1}}$, respectively. Overall, there is a good agreement between the numerically simulated and the quasidirectly computed single caloric thermal responses, confirming the robustness of our analytical functions in order to phenomenologically reproduce the experimental entropy curves.

As the analytical functions have been shown to be reliable over the complete coordinate space under study, we have been able to completely characterize the multicaloric thermal response for any external field change that field-induces either the forward or reverse phase transition.

On the one hand, with respect to the multicaloric isothermal entropy changes, the maximum values induced upon the removal of the applied external fields are $\Delta S_{max} = 22.4\,\mathrm{JK^{-1}kg^{-1}}$ at $T = 316\,\mathrm{K}$ and $\Delta S_{max} = 22.1\,\mathrm{JK^{-1}kg^{-1}}$ at $T = 317\,\mathrm{K}$, whereas upon the application of the external fields the maximum values induced are $\Delta S_{max} = -23.7\,\mathrm{JK^{-1}kg^{-1}}$ at $T = 298\,\mathrm{K}$ and $\Delta S_{max} = -24\,\mathrm{JK^{-1}kg^{-1}}$ at $T = 297\,\mathrm{K}$. These values clearly exceed the maximum isothermal entropy change of the simulated elastocaloric effect, whereas they match the maximum values for the simulated magnetocaloric effect, meaning that we are able to fully drive the forward and reverse phase transitions. When considering the potential of multicaloric effects for technological applications, it is important to highlight that a moderate magnetic field change of $|\mu_0 \Delta H| = 1\,\mathrm{T}$, which can be readily provided by permanent magnets, combined with a moderate stress change of $|\Delta\sigma| = 20\,\mathrm{MPa}$ yields an isothermal entropy change of $\Delta S_{max} = 20.3\,\mathrm{JK^{-1}kg^{-1}}$ at $T = 316\,\mathrm{K}$ and $\Delta S_{max} = 20.4\,\mathrm{JK^{-1}kg^{-1}}$ at $T = 317\,\mathrm{K}$ when field-inducing the reverse phase transition, and of $\Delta S_{max} = -17.5\,\mathrm{JK^{-1}kg^{-1}}$ at $T = 298\,\mathrm{K}$ and $\Delta S_{max} = -18\,\mathrm{JK^{-1}kg^{-1}}$ at $T = 297\,\mathrm{K}$ when field-inducing the forward phase transition. These values clearly exceed the isothermal entropy changes obtained from the single caloric effects under the same moderate external field changes.

On the other hand, with respect to the adiabatic temperature changes, the maximum values induced are found to clearly exceed the maximum adiabatic temperature changes obtained for both single caloric effects. In addition, under the same moderate external field changes previously considered, similar trends are observed with respect to the isothermal entropy change when comparing the multicaloric

effect with the single caloric effects.

On the whole, it is noteworthy that the combined change of two external fields, even if they are of moderate magnitude, significantly enlarges the temperature window where the alloy exhibits a giant field-induced thermal response.

In contrast to the previously studied Ni-Mn-In alloy, the multicaloric thermal response of the alloy under study does not simply correspond to the sum of both single caloric effects in the absence of a secondary field, as the cross-coupling contribution between the structural and magnetic degrees of freedom will also play a role. The numerically simulated entropy curves allowed us to compute the cross-coupling contributions for both isothermal entropy and adiabatic temperature changes when field-inducing either the forward or reverse phase transition. Interestingly, it has been found that the cross-coupling contribution plays an important role on increasing the multicaloric thermal response induced by low external field changes. Furthermore, it is important to highlight that the cross-coupling contributions are relevant at the edge of the multicaloric thermal response, where the contour lines are close to each other, and they contribute on expanding the window of temperatures and external field changes where giant multicaloric effects can be induced.

The reversibility of the field-induced thermal response is of utmost importance when considering the applicability of multicaloric materials for diverse technological applications. In this regard, by taking advantage of the magnetostructural character of the martensitic phase transition, a secondary field allows us to tune the effective hysteresis of the phase transition. In particular, it has been shown that under a suitable sequence of moderate magnetic field and compressive stress changes, the reversibility of the field-induced thermal response can be improved. Furthermore, it has been suggested that a modified version of the multicaloric cycle proposed by T. Gottschall *et. al* in [64] can be employed on materials exhibiting a conventional magnetocaloric and elastocaloric effect, which also takes advantage of the inherent hysteresis of first-order phase transitions to lock-in the sample at a certain phase.

6 Conclusions and outlook

In this work, we have extensively investigated the giant caloric and multicaloric effects arising from multiferroic materials displaying a magnetostructural first-order phase transition with a strong coupling between the structural and magnetic degrees of freedom, which gives rise to a cross-coupled response to the application of non-conjugated external fields. The quantitative characterization of the caloric and multicaloric thermal responses is based on the indirect, quasidirect or direct determination of the adiabatic temperature and isothermal entropy changes induced when the materials are subjected to a certain external field change.

The study of multiferroic materials exhibiting a cross-coupled response requires the development of non-commercial advanced characterization systems that allow the simultaneous application of diverse external fields. The process of design, assembly and calibration of such bespoke systems has been a keystone of this work.

Firstly, a bespoke differential scanning calorimeter allowing the application of uniaxial compressive forces up to $F = 1000\,\mathrm{N}$ together with magnetic fields up to $\mu_0 H = 6\,\mathrm{T}$ has been designed and built (see section 3.1.4). This setup is an improved and upgraded version of a previous purpose-built DSC of our research group, described in [92], that can simultaneously perform dilatometric measurements and allows us to characterize the caloric and multicaloric thermal response of multiferroic materials via the quasidirect and indirect methods. The performance of this setup was initially tested with a Cu-Zn-Al shape-memory alloy, for which a constant transition strain of $\Delta\varepsilon_t^{M,A} = (7.0 \pm 0.3)\,\%$ and transition entropy change of $\Delta S_t^{M,A} = (22.3 \pm 0.5)\,\mathrm{JK^{-1}kg^{-1}}$ have been reported with accurate experimental setups. On the one hand, a constant calibration factor had to be introduced in order to compute the transition entropy change from the thermograms measured with our bespoke setup. While a constant behaviour within experimental errors was reported for applied compressive forces up to $F = 400\,\mathrm{N}$, a decrease was observed under higher loads and a sensitivity factor had to be introduced in order to correct those measurements. On the other hand, the dilatometric measurements showed a decreasing tendency when increasing the applied stress and had to be corrected with a sensitivity factor. After the correction of both measurement series, the thermal response computed from both indirect and quasidirect methods showed a concordant behaviour, but the minor accuracy of the dilatometric measurements lead to a slight underestimation of the computed elastocaloric effect via the indirect method. It is predicted that the complete martensitic phase transition of this alloy can be cyclically induced under stress changes of $|\Delta\sigma| > 57\,\mathrm{MPa}$, leading to a large

refrigerant capacity comparable to the best magnetocaloric materials [117]. These results, which are presented in section 3.3 and published in [88], envisage promising perspectives for the development of refrigeration devices based on the elastocaloric effect. Overall, these experiments have demonstrated that using a constant calibration factor, the performance of our bespoke differential scanning calorimeter allows an accurate characterization of the thermal response under applied compressive forces up to $F = 400\,\mathrm{N}$ via the quasidirect method, proving it as a unique tool for the characterization of multiferroic materials.

Secondly, two distinct setups to perform direct adiabatic thermometry measurements under the influence of uniaxial compressive stress and magnetic field have been designed and built. On the one hand, the first setup uses an electromagnet as the magnetic field source, and allows the application of uniaxial compressive forces up to $F = 1000\,\mathrm{N}$ together with magnetic fields up to $\mu_0 H = 2\,\mathrm{T}$. This setup, which is described in section 3.2.2, is complementary to the bespoke DSC, allowing us to compare direct measurements with quasidirect or indirect results of the field-induced thermal response. On the other hand, the second setup is embedded inside a solenoid, which allows us to apply high-strength magnetic field pulses up to $\mu_0 H = 50\,\mathrm{T}$ that last few milliseconds, and can simultaneously perform strain measurements of the sample. This setup, described in section 3.2.3, was designed and built during my stay at the *Dresden High Magnetic Field Laboratory* (HLD-EMFL) in close collaboration with Dr. Tino Gottschall and Eduard Bykov. Preliminary experiments were conducted on a Ni-Mn-Ti-Co Heusler alloy, which was selected due to its enhanced mechanical properties together with the giant elastocaloric and magnetocaloric effects that it displays around the first-order martensitic phase transition. Despite the complexity of this bespoke setup, our device allows to directly measure the multicaloric thermal response under uniaxial load and pulsed magnetic fields with high quality, as discussed in [66].

Due to the different time scales involved on the magnetic field sweeping rates in both setups, they also allow us to gain insight into the dynamics of the field-induced phase transition, and lay the first stone on the direct thermometry of field-induced multicaloric effects.

Our research has focused on two distinct families of multiferroic materials, Fe-Rh and Ni-Mn-based Heusler alloys, when inducing their magnetostructural first-order phase transition with magnetic field, uniaxial compressive stress or a combination of both, which gives rise to magnetocaloric, elastocaloric or multicaloric effects, respectively.

Nowadays, Fe-Rh is considered one of the benchmark materials exhibiting giant caloric and multicaloric effects [134]. Nevertheless, despite the early studies performed by S. Nikitin *et. al.* on the giant elastocaloric effect exhibited by this alloy [54], no further studies were performed and a complete characterization of the elastocaloric effect was lacking. We have used the setup described in section 3.2.2 to perform direct thermometry measurements of the magnetocaloric effect under a constant compressive stress. Interestingly, application of compressive stress

shifts the thermal response to higher temperatures, which is consistent with a conventional elastocaloric effect, and is in contrast with the inverse effect previously reported under tensile stresses [54]. A detailed justification for this apparent discrepancy has been provided. The good concordance between direct measurements and quasidirect estimates, computed from isofield entropy curves where the effect of stress was taken as a pure shift to the transition temperature, provided reliability to the quasidirect computation of the thermal response of this alloy and allowed us to completely characterize the elastocaloric thermal response under different constant magnetic fields. The application of a constant secondary field drastically tunes the temperature widow where the giant elastocaloric effect occurs without significantly increasing the maximum thermal response. Despite the fact that the elastocaloric effect is only expected to be reversible for stress changes of $|\Delta\sigma| > 430\,\mathrm{MPa}$, it has been shown that a suitable combination of a moderate magnetic field and compressive stress can tune the effective hysteresis of the alloy and enhance the reversibility of the elastocaloric effect. These results are presented in section 5.1 and published in [65].

The development of new multiferroic Ni-Mn-based Heusler alloys exhibiting a strong metamagnetic phase transition that requires low driving magnetic fields together with a good cyclical stability of the elastocaloric effect is of utmost importance for the sake of technological applications. In this regard, a Ni-Fe-Co-Mn-Sn Heusler alloy with a tailored composition has been selected as a suitable candidate. We have performed isothermal DSC measurements with a bespoke setup previously designed and built by our research group, described in section 3.1.3. These measurements reported a strong increase of the magnetic field necessary to drive the metamagnetic phase transition when decreasing the temperature, which is consistent with an inverse magnetocaloric effect, and allowed us to perform a direct characterization of the magnetocaloric isothermal entropy change within a broad temperature range. Under a moderate magnetic field change of $|\mu_0\Delta H| = 2\,\mathrm{T}$, the alloy under study yields $|\Delta S| = (17 \pm 1)\mathrm{JK}^{-1}\mathrm{kg}^{-1}$. The direct characterization of field-induced caloric effects is crucial, as these measurements are highly reliable but scarce in the literature. Furthermore, the excellent agreement reported between the direct measurements and the indirect estimates computed by two different methods, which are described in [61], has been essential for providing reliability to the computation of the corresponding multicaloric effects. These results are discussed in section 5.2 and published in [61].

The potential of our bespoke DSC to thoroughly characterize the caloric and multicaloric thermal response of a multiferroic material was investigated on a prototype Ni-Mn-In alloy with a martensitic transition temperature close to the austenitic Curie temperature, which conferred it a pronounced coupling between the structural and magnetic degrees of freedom.

The calorimetric measurements allowed us to characterize the transition temperature phase diagram within the complete coordinate space under study, reporting an inverse magnetocaloric effect and a conventional elastocaloric effect. Nevertheless, some thermograms show a poor signal-to baseline ratio due to the complexity

of our setup, and the transition entropy change could only be computed for the thermograms recorded upon heating within a region of the coordinate space. The transition entropy change was found to decrease when increasing the applied magnetic field, and was parametrized as $\Delta S_t(\mu_0 H) = 38(1) - 1.9(5)\mu_0 H$ ($\mathrm{JK^{-1}kg^{-1}}$). The reported decrease rate with magnetic field is in accordance with previous studies on the transition entropy change dependency with the transition temperature for a set of Ni-Mn-In alloys [220], and it arises from the competition between the vibrational and magnetic entropy contributions to the transition entropy change in alloys exhibiting an inverse magnetocaloric effect. The quasidirect estimates of the giant elastocaloric and magnetocaloric effects could only be computed for the thermodynamic processes that field-induce the reverse phase transition (which corresponds to a heating process). Interestingly, while application of a constant compressive stress did not significantly influence the magnitude of the magnetocaloric effect, application of a constant magnetic field significantly enhanced the corresponding elastocaloric effect.

The computation of the multicaloric thermal response for any external field change within the coordinate space under study requires the definition of a numerical function to phenomenologically reproduce the experimental isofield-isostress entropy curves. The robustness of this numerical analysis is confirmed by the good agreement between the numerically simulated and quasidirectly computed elastocaloric and magnetocaloric effects. With respect to the multicaloric effect, our results show that the combined change of magnetic field and compressive stress not only increases the field-induced thermal response with respect to single caloric effects, but also enlarges the temperature window where the alloy exhibits a giant thermal response. Furthermore, when combining a moderate magnetic field change of $|\mu_0 \Delta H| = 1\,\mathrm{T}$ with a stress change of $|\Delta\sigma| = 40\,\mathrm{MPa}$, the multicaloric thermal response yields $\Delta S_{max} = 15.1\,\mathrm{JK^{-1}kg^{-1}}$ at $T = 299\,\mathrm{K}$, which is more than double the maximum magnetocaloric isothermal entropy change that can be obtained from the same moderate magnetic field change. Similar trends are also observed when considering the adiabatic temperature change, and it is expected that they may be also valid for other multiferroic materials.

The reversibility of the field-induced thermal response is of utmost importance for the sake of technological applications. Taking advantage of the magnetostructural character of the martensitic phase transition, two different approaches have been discussed. As previously considered for Fe-Rh, it has been shown that a suitable combination of a moderate magnetic field and compressive stress can tune the effective hysteresis of the alloy and enhance the reversibility of the magnetocaloric effect. In contrast, the feasibility of a novel multicaloric cycle proposed by T. Gottschall *et. al.* in [64] has been tested in this alloy, where instead of minimizing the inherent hysteresis of first-order phase transitions, we take advantage of it to lock-in the sample at a certain phase. Direct thermometry measurements were performed with the bespoke setup presented in 3.2.2, showing that under this novel exploiting-hysteresis cycle an adiabatic temperature change of $|\Delta T| \approx 1.2\,\mathrm{K}$ at $T = 296\,\mathrm{K}$ can be cyclically obtained, which clearly outperforms the reversible adiabatic temperature change under a cyclic magnetic field for the same sample.

Furthermore, it is important to highlight that this novel multicaloric cycle only requires the application of magnetic field over a small region to induce the irreversible phase transition, as the inherent hysteresis locks-in the sample phase when the magnetic field is removed. All these results are discussed along section 5.3 and published in [62, 64].

So far, the combined effect of magnetic field and compressive stress has only been studied on multiferroic alloys with non-synergic caloric effects, exhibiting an inverse magnetocaloric effect together with a conventional elastocaloric effect. For those alloys, due to the different nature of both caloric effects, an asymmetric external field change is necessary in order to field-induce the multicaloric thermal response and as a consequence, it corresponds to the simple sum of the single caloric effects in the absence of a secondary field. Conversely, for multiferroic materials with synergic caloric effects, where both magnetocaloric and elastocaloric effects are conventional, the multicaloric thermal response does not correspond to the simple sum of both single caloric effects in the absence of a secondary field, as the cross-coupled response of the material will also play a role. Such multiferroic materials are particularly appealing with respect to their potential for technological applications based on multicaloric effects.

In this regard, a Ni-Mn-Ga-Cu Heusler alloy with a tailored composition in order to overlap the martensitic transition temperature and the austenitic Curie temperature, conferring it a pronounced coupling between the structural and magnetic degrees of freedom, has been selected as a prototype multiferroic material exhibiting synergic caloric effects. A thorough characterization of the caloric and multicaloric thermal response, including the computation of the cross-coupled contribution to the multicaloric effect, has been performed with our bespoke DSC.

The calorimetric measurements allowed us to characterize the transition temperature phase diagram within the complete coordinate space under study, reporting both a conventional magnetocaloric and elastocaloric effects. Nevertheless, the transition entropy change could only be computed for the thermograms recorded upon heating and cooling within a portion of the coordinate space under study. Interestingly, for all values of applied compressive stress, both forward and reverse transition entropy changes were found to linearly decrease when increasing the applied magnetic field with rates in the range $\frac{d\Delta S_t}{d\mu_0 H} \in [-1.1, -0.7]\,\mathrm{JK^{-1}kg^{-1}T^{-1}}$. Furthermore, for all values of applied magnetic field, both forward and reverse transition entropy changes were also found to linearly decrease when increasing the applied stress with rates in the range $\frac{d\Delta S_t}{d\sigma} \in [-0.5, -0.2]\,\mathrm{JK^{-1}kg^{-1}MPa^{-1}}$. Although further studies are required in order to gain some light into the origin of such behaviour, it must be mentioned that a decrease with a similar rate when increasing the applied magnetic field has also been observed from specific heat measurements. The quasidirect estimates of the field-induced elastocaloric and magnetocaloric effects were computed for both the forward and reverse phase transitions, providing a complete characterization of the thermal response. Under a moderate magnetic field change of $|\mu_0 \Delta H| = 1\,\mathrm{T}$, the alloy under study yields an

isothermal entropy change around $|\Delta S_{max}| \sim 15\,\mathrm{JK^{-1}kg}$, which outperforms most of the reported Heusler alloys [234–236]. Interestingly, while application of a constant secondary field decreased the magnitude of the isothermal entropy change, no systematic dependence was observed for the adiabatic temperature change.

In a similar way to that followed for Ni-Mn-In, two numerical functions are defined in order to phenomenologically reproduce the experimental isofield-isostress entropy curves upon heating and cooling. The good agreement between the numerically simulated and quasidirectly computed elastocaloric and magnetocaloric effects confirms the robustness of our numerical analysis and allows us to completely characterize the multicaloric thermal response for any external field change under study. When combining a moderate magnetic field change of $|\mu_0 \Delta H| = 1\,\mathrm{T}$ with a stress change of $|\Delta\sigma| = 20\,\mathrm{MPa}$, the multicaloric thermal response increases to $\Delta S_{max} = 20.4\,\mathrm{JK^{-1}kg^{-1}}$ at $T = 317\,\mathrm{K}$ when inducing the reverse phase transition, and up to $\Delta S_{max} = -18\,\mathrm{JK^{-1}kg^{-1}}$ at $T = 297\,\mathrm{K}$ when inducing the forward phase transition. These values clearly exceed the isothermal entropy changes that can be obtained from the single caloric effects under the same moderate external field changes, and similar trends are also observed for the adiabatic temperature change. Furthermore, the combined change of magnetic field and stress, even if they are of moderate magnitude, enlarges the temperature window where the alloy exhibits a giant field-induced thermal response.

To complete the analysis of the multicaloric thermal response, we have computed the cross-coupled contribution between the structural and magnetic degrees of freedom to the isothermal entropy and adiabatic temperature changes. Interestingly, we found that the cross-coupled contribution not only plays an important role on increasing the multicaloric thermal response induced by moderate external field changes, but also contributes on expanding the window of temperature and external field changes where the alloy exhibits a giant multicaloric effect. All these results are discussed along section 5.4.

Overall, this work has shown that the development of advanced characterization devices that allow the simultaneous application of magnetic field and uniaxial compressive stress is a unique strategy to accurately characterize the thermal response of multiferroic materials with a strong coupling between the structural and magnetic degrees of freedom. For the purpose of the present work, we have focused on Ni-Mn-based Heusler alloys, thoroughly characterizing the advantages of the multicaloric effect with respect to the single caloric (elastocaloric and magnetocaloric) effects in alloys exhibiting either synergic or non-synergic single caloric effects. It is expected that many of the trends found along sections 5.3 and 5.4 may also be valid for other multiferroic materials with a strong coupling between different degrees of freedom when subjected to the combined effect of diverse external fields.

Moreover, while many efforts are being devoted on the development of refrigeration devices based on single caloric effects [44], the prominent results found along this thesis should inspire the development of novel refrigeration devices that take advantage of the multicaloric thermal response exhibited by multiferroic materials.

Bibliography

[1] Intergovernmental Panel on Climate Change. "Sixth Assessment Report, Summary for Policymakers". (2021), [Online]. Available: https://www.ipcc.ch/report/ar6/wg1/#SPM.

[2] United Nations. "Paris Agreement". (2015), [Online]. Available: https://unfccc.int/process-and-meetings/the-paris-agreement/the-paris-agreement.

[3] J. L. Dupont, P. Domanski, P. Lebrun, and F. Ziegler. "38$^{\text{th}}$ Note on Refrigeration Technologies: The Role of Refrigeration in the Global Economy", International Institute of Refrigeration. (2019), [Online]. Available: https://iifiir.org/en/fridoc/the-role-of-refrigeration-in-the-global-economy-2019-142028.

[4] N. Shah *et al.* "Opportunities for simultaneous efficiency improvement and refrigerant transition in air conditioning", International Energy Analysis Department, Lawrence Berkeley National Laboratory. (2017), [Online]. Available: https://international.lbl.gov/publications/opportunities-simultaneous-efficiency.

[5] International Energy Agency. "The Future of Cooling". (2018), [Online]. Available: https://www.iea.org/reports/the-future-of-cooling.

[6] R. Gauß, G. Homm, and O. Gutfleisch, "The resource basis of magnetic refrigeration", *Journal of Industrial Ecology*, vol. 21, pp. 1291–1300, 2017.

[7] O. Sari and M. Balli, "From conventional to magnetic refrigerator technology", *International Journal of Refrigeration*, vol. 37, pp. 8–15, 2014.

[8] O. Gutfleisch, M. A. Willard, E. Brück, C. H. Chen, S. G. Sankar, and J. Pin Liu, "Magnetic materials and devices for the 21st century: Stronger, lighter and more energy efficient", *Advanced Materials*, vol. 23, pp. 821–842, 2011.

[9] W. Goetzler, R. Zogg, J. Young, and C. Johnson. "Energy savings potential and RD&D opportunities for non-vapor-compression HVAC technologies", US Department of Energy. (2014), [Online]. Available: https://www.energy.gov/eere/buildings/downloads/non-vapor-compression-hvac-technologies-report.

[10] W. Goetzler, R. Shandross, J. Young, O. Petritchenko, D. Ringo, and S. McClive. "Energy savings potential and RD&D opportunities for commercial building HVAC systems", US Department of Energy. (2017), [Online]. Available: https://www.energy.gov/sites/prod/files/2017/12/f46/bto-DOE-Comm-HVAC-Report-12-21-17.pdf.

[11] M. W. Zemansky and R. H. Dittman, *Heat and Thermodynamics*. US: McGraw-Hill Inc., 1981.

[12] L. Mañosa, A. Planes, and M. Acet, "Advanced materials for solid state refrigeration", *Journal of Materials Chemisty A*, vol. 1, pp. 4925–4936, 2013.

[13] J. A. Gough, "A description of a property of caoutchouc, or Indian rubber; with some reflections on the cause of the elasticity of this substance", *Memoirs of the Literacy and Philosophical Society of Manchester*, vol. 1, pp. 288–295, 1805.

[14] J. P. Joule, "On some thermo-dynamic properties of solids", *Philosophical Transactions of the Royal Society*, vol. 149, pp. 91–131, 1859.

[15] W. Thomson, "On the thermoelastic and thermomagnetic properties of matter", *The Quarterly Journal of Pure and Applied Mathematics*, vol. 1, pp. 57–77, 1855.

[16] W. Thomson, "On the thermoelastic, thermomagnetic, and pyroelectric properties of matter", *The London, Edinburgh, and Dublin Philosophical Magazine and Journal of Science*, vol. 5, pp. 4–27, 1878.

[17] P. Weiss and A. Piccard, "Le phénomène magnétocalorique", *Journal de Physique Théorique et Appliquée*, vol. 7, pp. 103–109, 1917.

[18] A. Smith, "Who discovered the magnetocaloric effect?", *The European Physical Journal H*, vol. 38, pp. 507–517, 2013.

[19] P. Kobeko and J. Kurtschatov, "Dielektrische eigenschaften der seignettesalzkristalle", *Zeitschrift für Physik*, vol. 66, pp. 192–205, 1930.

[20] K. H. J. Buschow and F. R. de Boer, *Physics of Magnetism and Magnetic Materials*. New York: Kluwer Academic Publishers, 2003.

[21] C. Kittel, *Introduction to Solid State Physics*. US: John Wiley & Sons, Inc., 2004.

[22] W. F. Giauque and D. P. MacDougall, "Attainment of temperatures below 1° absolute by demagnetization of $Gd_2(SO_4)_3 \cdot 8H_2O$", *Physical Review*, vol. 43, p. 768, 1933.

[23] W. F. Giauque and D. P. MacDougall, "The production of temperatures below one degree absolute by adiabatic demagnetization of Gadolinium Sulfanate", *Journal of the American Chemical Society*, vol. 57, pp. 1175–1185, 1935.

[24] S. C. Collins and F. J. Zimmerman, "Cyclic adiabatic demagnetization", *Physical Review*, vol. 90, pp. 991–992, 1953.

[25] C. V. Heer, C. B. Barnes, and J. G. Daunt, "The design and operation of a magnetic refrigerator for maintaining temperatures below 1°K", *Review of Scientific Instruments*, vol. 25, pp. 1088–1098, 1954.

[26] G. V. Brown, "Magnetic heat pumping near room temperature", *Journal of Applied Physics*, vol. 47, pp. 3673–3680, 1976.

[27] V. K. Pecharsky and K. A. Gschneidner Jr., "Giant magnetocaloric effect in $Gd_5(Si_2Ge_2)$", *Physical Review Letters*, vol. 78, pp. 4494–4497, 1997.

[28] S. A. Nikitin, G. Myalikgulyev, A. M. Tishin, M. P. Annaorazov, K. A. Asatryan, and A. L. Tyurin, "The magnetocaloric effect in $Fe_{49}Rh_{51}$ compound", *Physics Letters A*, vol. 148, pp. 363–366, 1990.

[29] A. S. Mischenko, Q. Zhang, J. F. Scott, R. W. Whatmore, and N. D. Mathur, "Giant electrocaloric effect in thin-film $PbZr_{0.95}Ti_{0.05}O_3$", *Science*, vol. 311, pp. 1270–1271, 2006.

[30] E. Bonnot, R. Romero, L. Mañosa, E. Vives, and A. Planes, "Elastocaloric effect associated with the martensitic transition in shape-memory alloys", *Physical Review Letters*, vol. 100, 125901-1–125901-4, 2008.

[31] C. Rodriguez and L. C. Brown, "The thermal effect due to stress-induced martensite formation in β-CuAlNi single crystals", *Metallurgical Transactions A*, vol. 11A, pp. 147–150, 1980.

[32] L. Mañosa *et al.*, "Giant solid-state barocaloric effect in the Ni-Mn-In magnetic shape memory alloy", *Nature Materials*, vol. 9, pp. 478–481, 2010.

[33] X. Moya and N. D. Mathur, "Caloric materials for cooling and heating", *Science*, vol. 370, pp. 797–803, 2020.

[34] K. A. Gschneidner Jr., V. K. Pecharsky, and A. O. Tsokol, "Recent developments in magnetocaloric materials", *Reports on Progress in Physics*, vol. 68, pp. 1479–1539, 2005.

[35] A. Smith, C. R. H. Bahl, R. Bjørk, K. Engelbrecht, K. K. Nielsen, and N. Pryds, "Materials challenges for high performance magnetocaloric refrigeration devices", *Advanced Energy Materials*, vol. 2, pp. 1288–1318, 2012.

[36] V. Franco, J. S. Blázquez, J. J. Ipus, J. Y. Law, L. M. Moreno-Ramírez, and A. Conde, "Magnetocaloric effect: From materials research to refrigeration devices", *Progress in Materials Science*, vol. 93, pp. 112–232, 2018.

[37] M. Valant, "Electrocaloric materials for future solid-state refrigeration technologies", *Progress in Materials Science*, vol. 57, pp. 980–1009, 2012.

[38] L. Mañosa and A. Planes, "Materials with giant mechanocaloric effects: Cooling by strength", *Advanced Materials*, vol. 29, 1603607-1–1603607-25, 2017.

[39] L. Mañosa and A. Planes, "Solid-state cooling by stress: A perspective", *Applied Physics Letters*, vol. 116, 050501-1–050501-5, 2020.

[40] S. Fähler *et al.*, "Caloric effects in ferroic materials: New concepts for cooling", *Advanced Engineering Materials*, vol. 14, pp. 10–19, 2012.

[41] X. Moya, S. Kar-Narayan, and N. D. Mathur, "Caloric materials near ferroic phase transitions", *Nature Materials*, vol. 13, pp. 439–450, 2014.

[42] I. Takeuchi and K. Sandeman, "Solid-state cooling with caloric materials", *Physics Today*, vol. 68, pp. 48–54, 2015.

[43] F. Scarpa, G. Tagliafico, and L. A. Tagliafico, "A classification methodology applied to existing room temperature magnetic refrigerators up to the year 2014", *Renewable and Sustainable Energy Reviews*, vol. 50, pp. 497–503, 2015.

[44] A. Greco, C. Aprea, A. Maiorino, and C. Masselli, "A review of the state of the art of solid-state caloric cooling processes at room-temperature before 2019", *International Journal of Refrigeration*, vol. 106, pp. 66–88, 2019.

[45] X. Moya, E. Defay, V. Heine, and N. D. Mathur, "Too cool to work", *Nature Physics*, vol. 11, pp. 202–205, 2015.

[46] H. Hou, S. Qian, and I. Takeuchi, *Materials, physics, and systems for multicaloric cooling*, 2021. arXiv: 2111.12180 [cond-mat.mtrl-sci].

[47] T. Gottschall *et al.*, "Making a cool choice: The materials library of magnetic refrigeration", *Advanced Energy Materials*, vol. 9, 1901322-1–1901322-13, 2019.

[48] O. Gutfleisch *et al.*, "Mastering hysteresis in magnetocaloric materials", *Philosophical Transactions of the Royal Society A*, vol. 374, p. 20 150 308, 2016.

[49] B. Monfared, R. Furberg, and B. Palm, "Magnetic vs. vapor-compression household refrigerators: A preliminary comparative life cycle assessment", *International Journal of Refrigeration*, vol. 42, pp. 69–76, 2014.

[50] B. Nair *et al.*, "Large electrocaloric effects in oxide multilayer capacitors over a wide temperature range", *Nature*, vol. 575, pp. 468–472, 2019.

[51] E. Stern-Taulats, T. Castán, L. Mañosa, A. Planes, N. D. Mathur, and X. Moya, "Multicaloric materials and effects", *MRS bulletin*, vol. 43, pp. 295–299, 2018.

[52] M. M. Vopson, "The multicaloric effect in multiferroic materials", *Solid State Communications*, vol. 152, pp. 2067–2070, 2012.

[53] A. Planes, T. Castán, and A. Saxena, "Thermodynamics of multicaloric effects in multiferroics", *Philosophical Magazine*, vol. 94(17), pp. 1893–1908, 2014.

[54] S. A. Nikitin, G. Myalikgulyev, M. P. Annaorazov, A. L. Tyurin, R. W. Myndyev, and S. A. Akopyan, "Giant elastocaloric effect in FeRh alloy", *Physics Letters A*, vol. 171, pp. 234–236, 1992.

[55] M. P. Annaorazov, S. A. Nikitin, A. L. Tyurin, K. A. Asatryan, and A. K. Dovletov, "Anomalously high entropy change in FeRh alloy", *Journal of Applied Physics*, vol. 79(3), pp. 1689–1695, 1996.

[56] N. A. de Oliveira, "Entropy change upon magnetic field and pressure variations", *Applied Physics Letters*, vol. 90, 052501-1–052501-3, 2007.

[57] Y. Y. Gong *et al.*, "Electric field control of the magnetocaloric effect", *Advanced Materials*, vol. 27, pp. 801–805, 2015.

[58] Y. Liu, L. C. Phillips, R. Mattana, M. Bibes, A. Barthélémy, and B. Dkhil, "Large reversible caloric effect in FeRh thin films via a dual-stimulus multicaloric cycle", *Nature Communications*, vol. 7, 11614-1–11614-6, 2016.

[59] E. Stern-Taulats *et al.*, "Giant multicaloric response of bulk $Fe_{49}Rh_{51}$", *Physical Review B*, vol. 95, 104424-1–104424-11, 2017.

[60] F. X. Liang *et al.*, "Experimental study on coupled caloric effect driven by dual fields in metamagnetic Heusler alloy $Ni_{50}Mn_{35}In_{15}$", *Applied Physics Letters Materials*, vol. 7, 051102-1–051102-8, 2019.

[61] Y. Qu *et al.*, "Outstanding caloric performances for energy-efficient multicaloric cooling in a Ni-Mn-based multifunctional alloy", *Acta Materialia*, vol. 177, pp. 46–55, 2019.

[62] A. Gràcia-Condal, T. Gottschall, L. Pfeuffer, O. Gutfleisch, A. Planes, and L. Mañosa, "Multicaloric effects in metamagnetic Heusler Ni-Mn-In under uniaxial stress and magnetic field", *Applied Physics Reviews*, vol. 7, 041406-1–041406-14, 2020.

[63] J. Liu, T. Gottschall, K. P. Skokov, J. D. Moore, and O. Gutfleisch, "Giant magnetocaloric effect driven by structural transitions", *Nature Materials*, vol. 11, pp. 620–626, 2012.

[64] T. Gottschall *et al.*, "A multicaloric cooling cycle that exploits thermal hysteresis", *Nature Materials*, vol. 17, pp. 929–934, 2018.

[65] A. Gràcia-Condal, E. Stern-Taulats, A. Planes, and L. Mañosa, "Caloric response of $Fe_{49}Rh_{51}$ subjected to uniaxial load and magnetic field", *Physical Review Materials*, vol. 2, 084413-1–084413-8, 2018.

[66] T. Gottschall *et al.*, "Advanced characterization of muticaloric materials in pulsed magnetic fields", *Journal of Applied Physics*, vol. 127, 185107-1–185107-7, 2020.

[67] F. W. Sears and G. L. Salinger, *Thermodynamics, Kinetic theory and Statistical Thermodynamics*. Massachusetts: Addison-Weisley Pub. Co., 1975.

[68] V. Wadhawan, *Introduction to Ferroic Materials*. US: CRC Press, 2000.

[69] L. D. Landau, "On the theory of phase transitions", in *Collected Papers of L.D. Landau*, D. Ter Haar, Ed., London: Pergamon press, 1965, pp. 193–216.

[70] R. E. Newnham, *Properties of Materials*. New York: Oxford University Press, 2005.

[71] G. Jaeger, "The Ehrenfest classification of phase transitions: Introduction and evolution", *Archive for History of Exact Sciences*, vol. 53, pp. 51–81, 1998.

[72] J. M. Yeomans, *Statistical Mechanics of Phase Transitions*. New York: Oxford University Press, 1992.

[73] J. J. Binney, N. J. Dowrick, A. J. Fisher, and M. Newman, *The Theory of Critical Phenomena: an Introduction to the Renormalization Group*. New York: Oxford University Press, 1992.

[74] L. Caron, Z. Q. Ou, T. T. Nguyen, D. T. Cam Thanh, O. Tegus, and E. Brück, "On the determination of the magnetic entropy change in materials with first-order transitions", *Journal of Magnetism and Magnetic Materials*, vol. 321, pp. 3559–3566, 2009.

[75] A. Planes, L. Mañosa, and M. Acet, "Magnetocaloric effect and its relation to shape-memory properties in ferromagnetic Heusler alloys", *Journal of Physics: Condensed Matter*, vol. 21(23), p. 233 201, 2009.

[76] A. M. Tishin and Y. I. Spichkin, *The Magnetocaloric Effect and its Applications*. US: CRC Press, 2003.

[77] A. M. Tishin, "Magnetocaloric effect in strong magnetic fields", *Cryogenics*, vol. 30(2), pp. 127–136, 1990.

[78] L. Mañosa *et al.*, "Inverse barocaloric effect in the giant magnetocaloric La-Fe-Si-Co compound", *Nature Communications*, vol. 2:595, pp. 1–5, 2011.

[79] T. Krenke *et al.*, "Inverse magnetocaloric effect in ferromagnetic Ni-Mn-Sn alloys", *Nature Materials*, vol. 4, pp. 450–454, 2005.

[80] J. Peräntie, J. Hagberg, A. Uusimäki, and H. Jantunen, "Electric-field-induced dielectric and temperature changes in a <011>-oriented $Pb(Mg_{1/3}Nb_{2/3})O_3PbTiO_3$ single crystal", *Physical Review B*, vol. 82, 134119-1–134119-8, 2010.

[81] D. A. Porter, K. E. Easterling, and M. Y. Sherif, *Phase Transformations in Metals and Alloys*. US: CRC Press, 2009, pp. 383–435.

[82] W. Hemminger and G. Höhne, *Calorimetry. Fundamentals and Practice*. Weinheim: Verlag Chemie GmbH, 1984.

[83] G. T. Armstrong, "The calorimeter and its influence on the development of Chemistry", *Journal of Chemical Education*, vol. 41(6), pp. 297–307, 1964.

[84] J. Marcos, F. Casanova, X. Batlle, A. Labarta, A. Planes, and L. Mañosa, "A high-sensitivity differential scanning calorimeter with magnetic field for magnetostructural transitions", *Review of Scientific Instruments*, vol. 74(11), pp. 4768–4771, 2003.

[85] M. M. Gilbert Sinicki and J.-L. Macqueron, "Calorimétrie", *Comptes Rendus de l'Académie des Sciences de Paris - Série B*, vol. 264, pp. 1697–1699, 1967.

[86] J. Ortin, L. Mañosa, C. M. Friend, A. Planes, and M. Yoshikawa, "Calorimetric measurements on the $\beta \rightleftharpoons \gamma'$ and $\beta \rightleftharpoons \beta'$ martensitic transformations in a Cu-Al-Ni single crystal subjected to uniaxial tensile stress", *Philosophical Magazine A*, vol. 65(2), pp. 461–475, 1992.

[87] M. C. Gallardo, J. Jiménez, and J. del Cerro, "Experimental device for measuring the influence of a uniaxial stress on specific heat: Application to the strontium titanate ferroelastic crystal", *Review of Scientific Instruments*, vol. 66(11), pp. 5288–5291, 1995.

[88] A. Gràcia-Condal, E. Stern-Taulats, A. Planes, E. Vives, and L. Mañosa, "The giant elastocaloric effect in a Cu-Zn-Al shape-memory alloy: A calorimetric study", *Physica Status Solidi B*, vol. 255, 1700422-1–1700422-7, 2018.

[89] J. D. Baloga and C. W. Garland, "AC calorimetry at high pressure", *Review of Scientific Instruments*, vol. 48(2), pp. 105–110, 1977.

[90] G. C. Lin, X. M. Xiong, J. X. Zhang, and Q. Wei, "Latent heat study of phase transition in $Ba_{0.73}Sr_{0.27}TiO_3$ induced by electric field", *Journal of Thermal Analysis and Calorimetry*, vol. 81, pp. 41–44, 2005.

[91] S. G. Lu *et al.*, "Organic and inorganic relaxor ferroelectrics with giant electrocaloric effect", *Applied Physics Letters*, vol. 97, 162904-1–162904-3, 2010.

[92] E. Stern-Taulats, "Giant caloric effects in the vicinity of first-order phase transitions", Ph.D. dissertation, Universitat de Barcelona, 2017.

[93] L. Mañosa, M. Bou, C. Calles, and A. Cirera, "Low-cost differential scanning calorimeter", *American Journal of Physics*, vol. 64(3), pp. 283–287, 1996.

[94] B. Emre *et al.*, "Large reversible entropy change at the inverse magnetocaloric effect in Ni-Co-Mn-Ga-In magnetic shape memory alloys", *Journal of Applied Physics*, vol. 113(21), 213905-1–213905-8, 2013.

[95] J. Kamarád, J. Kaštil, and Z. Arnold, "Practical system for the direct measurement of magneto-caloric effect by micro-thermocouples", *Review of Scientific Instruments*, vol. 83, 083902-1–083902-7, 2012.

[96] F. Cugini *et al.*, "Millisecond direct measurement of the magnetocaloric effect of a Fe_2P-based compound by the mirage effect", *Applied Physics Letters*, vol. 108, 012407-1–012407-4, 2016.

[97] T. Gottschall *et al.*, "Dynamical effects of the martensitic transition in magnetocaloric Heusler alloys from direct ΔT_{ad} measurements under different magnetic-field-sweep rates", *Physical Review Applied*, vol. 5, 024013-1–024013-8, 2016.

[98] J. Lyubina, "Magnetocaloric materials for energy efficient cooling", *Journal of Physics D: Applied Physics*, vol. 50, 053002-1–053002-28, 2017.

[99] E. Vives *et al.*, "Temperature contour maps at the strain-induced martensitic transition of a Cu-Zn-Al shape-memory single crystal", *Applied Physics Letters*, vol. 98, 011902-1–011902-3, 2011.

[100] G. J. Pataky, E. Ertekin, and H. Sehitoglu, "Elastocaloric cooling potential of NiTi, Ni_2FeGa and CoNiAl", *Acta Materialia*, vol. 96, pp. 420–427, 2015.

[101] L. Ianniciello, M. Romanini, L. Mañosa, A. Planes, K. Engelbrecht, and E. Vives, "Tracking the dynamics of power sources and sinks during the martensitic transformation of a Cu-Al-Ni single crystal", *Applied Physics Letters*, vol. 116, 183901-1–183901-5, 2020.

[102] E. L. Rodriguez and F. E. Filiski, "Thermoelastic temperature changes in poly(methyl methacrylate) at high hydrostatic pressure: Experimental", *Journal of Applied Physics*, vol. 53(10), pp. 6536–6540, 1982.

[103] D. Matsunami, A. Fujita, K. Takenaka, and M. Kano, "Giant barocaloric effect enhanced by the frustration of the antiferromagnetic phase in Mn_3GaN", *Nature Materials*, vol. 14, pp. 73–78, 2014.

[104] Y. Liu, J. F. Scott, and B. Dkhil, "Direct and indirect measurements on electrocaloric effect: Recent developments and perspectives", *Applied Physics Reviews*, vol. 3, 031102-1–031102-18, 2016.

[105] A. M. Tishin *et al.*, "Magnetocaloric effect near a second-order magnetic phase transition", *Journal of Magnetism and Magnetic Materials*, vol. 310, pp. 2800–2804, 2007.

[106] R. Romero and J. L. Pelegrina, "Entropy change between the β phase and the martensite in Cu-based shape-memory alloys", *Physical Review B*, vol. 50, pp. 9046–9052, 1994.

[107] A. Planes and L. Mañosa, "Vibrational properties of shape-memory alloys", *Solid State Physics*, vol. 55, pp. 159–267, 2001.

[108] M. Ahlers, "Martensite and equilibrium phases in Cu-Zn and Cu-Zn-Al alloys", *Progress in Materials Science*, vol. 30, pp. 135–186, 1986.

[109] J. Tušek *et al.*, "The elastocaloric effect: A way to cool efficiently", *Advanced Energy Materials*, vol. 5, 1500361-1–1500361-5, 2015.

[110] E. K. H. Salje, D. E. Soto-Parra, A. Planes, E. Vives, M. Reinecker, and W. Schranz, "Failure mechanism in porous materials under compression: Crackling noise in mesoporous SiO_2", *Philosophical Magazine Letters*, vol. 91(8), pp. 554–560, 2011.

[111] L. Mañosa, S. Jarque-Farnos, E. Vives, and A. Planes, "Large temperature span and giant refrigerant capacity in elastocaloric Cu-Zn-Al shape memory alloys", *Applied Physics Letters*, vol. 103, 211904-1–211904-4, 2013.

[112] A. Planes, R. Romero, and M. Ahlers, "Thermal properties of the martensitic transformation of Cu-Zn and Cu-Zn-Al shape memory alloys", *Scripta Metallurgica*, vol. 23, pp. 989–994, 1989.

[113] J. C. Lashley *et al.*, "Contribution of low-frequency modes to the specific heat of Cu-Zn-Al shape-memory alloys", *Physical Review B*, vol. 75, 064304-1–064304-7, 2007.

[114] E. Stern-Taulats *et al.*, "Reversible adiabatic temperature changes at the magnetocaloric and barocaloric effects in $Fe_{49}Rh_{51}$", *Applied Physics Letters*, vol. 107, 152409-1–152409-4, 2015.

[115] Y. Wu, E. Ertekin, and H. Sehitoglu, "Elastocaloric cooling capacity of shape memory alloys - Role of deformation temperatures, mechanical cycling, stress hysteresis and inhomogeneity of transformation", *Acta Materialia*, vol. 135, pp. 158–176, 2017.

[116] M. E. Wood and W. H. Potter, "General analysis of magnetic refrigeration and its optimization using a new concept: Maximization of refrigerant capacity", *Cryogenics*, vol. 25(12), pp. 667–683, 1985.

[117] L. Huang, D. Y. Cong, H. L. Suo, and Y. D. Wang, "Giant magnetic refrigeration capacity near room temperature in $Ni_{40}Co_{10}Mn_{40}Sn_{10}$ multifunctional alloy", *Applied Physics Letters*, vol. 104, 132407-1–132407-5, 2014.

[118] M. Fallot, "The alloys of Iron with metals of the Platinum family", *Annales de Physique*, vol. 10, pp. 291–332, 1938.

[119] M. Fallot and R. Hocart, "On the appearance of ferromagnetism upon elevation of temperature of Iron and Rhodium", *Revue Scientifique*, vol. 77, pp. 498–501, 1939.

[120] L. J. Swartzendruber, "The Fe-Rh (Iron - Rhrodium) System", *Bulletin of Alloy Phase Diagrams*, vol. 5(5), pp. 456–462, 1984.

[121] L. H. Lewis, C. H. Marrows, and S. Langridge, "Coupled magnetic, structural and electronic phase transitions in FeRh", *Journal of Physics D: Applied Physics*, vol. 49, 323002-1–323002-18, 2016.

[122] G. Shirane, R. Nathans, and C. W. Chen, "Magnetic moments and unpaired spin densities in the Fe-Rh alloys", *Physical Review*, vol. 134(6A), A1547–A1553, 1964.

[123] S. O. Mariagner *et al.*, "Structural and magnetic dynamics of a laser induced phase transition in FeRh", *Physical Review Letters*, vol. 108, 087201-1–087201-5, 2012.

[124] A. X. Gray *et al.*, "Electronic structure changes across the metamagnetic transition in FeRh via hard X-ray photoemission", *Physical Review Letters*, vol. 108, 257208-1–257208-5, 2012.

[125] P. M. Derlet, "Landau-Heisenberg hamiltonian model for FeRh", *Physical Review B*, vol. 85, 174431-1–174431-15, 2012.

[126] D. W. Cooke, F. Hellman, C. Baldasseroni, C. Bordel, S. Moyerman, and E. E. Fullerton, "Thermodynamic measurements of Fe-Rh alloys", *Physical Review Letters*, vol. 109, 255901-1–255901-5, 2012.

[127] M. A. de Vries, M. Loving, A. P. Mihai, L. H. Lewis, D. Heiman, and C. H. Marrows, "Hall-effect characterization of the metamagnetic transition in FeRh", *New Journal of Physics*, vol. 15, 013008-1–013008-12, 2013.

[128] J. B. Staunton, R. Banerjee, M. dos Santos Dias, A. Deak, and L. Szunyogh, "Fluctuating local moments, itinerant electrons, and the magnetocaloric effect: Compositional hypersensitivity of FeRh", *Physical Review B*, vol. 89, 054427-–054427-7, 2014.

[129] V. Franco, J. S. Blázquez, B. Ingale, and A. Conde, "The magnetocaloric effect and magnetic refrigeration near room temperature: Materials and models", *Annual Review of Materials Research*, vol. 42(1), pp. 305–342, 2012.

[130] V. K. Pecharsky and K. A. Gschneidner Jr., "Tunable magnetic regenerator alloys with giant magnetocaloric effect for magnetic refrigeration from ~ 20 to $\sim 290\,\mathrm{K}$", *Applied Physics Letters*, vol. 70(24), pp. 3299–3301, 1997.

[131] M. Manekar and S. B. Roy, "Reproducible room temperature giant magnetocaloric effect in Fe-Rh", *Journal of Physics D: Applied Physics*, vol. 41, 192004-1–192004-4, 2008.

[132] E. Stern-Taulats *et al.*, "Barocaloric and magnetocaloric effects in $Fe_{49}Rh_{51}$", *Physical Review B*, vol. 89, 214105-1–214105-8, 2014.

[133] A. Chirkova, K. P. Skokov, L. Schultz, N. V. Baranov, O. Gutfleisch, and T. G. Woodcock, "Giant adiabatic temperature change in FeRh alloys evidenced by direct measurements under cyclic conditions", *Acta Materialia*, vol. 106, pp. 15–21, 2016.

[134] K. G. Sandeman, "Magnetocaloric materials: The search for new systems", *Scripta Materialia*, vol. 67(6), pp. 566–571, 2012.

[135] F. Heusler, *Über magnetische Manganlegierungen*. Braunschweig: Verhandlungen der Deutsche Physikalischen Gesellschaft, 1903, pp. 219–223.

[136] D. Hobbs, J. Hafner, and D. Spišák, "Understanding the complex metallic element Mn. I. Crystalline and noncollinear magnetic structure of α-Mn", *Physical Review B*, vol. 68, 014407-1–014407-18, 2003.

[137] J. Hafner and D. Hobbs, "Understanding the complex metallic element Mn. II. Geometric frustration in β-Mn, phase stability, and phase transitions", *Physical Review B*, vol. 68, 014408-1–014408-15, 2003.

[138] A. J. Bradley and J. W. Rodgers, "The crystal structure of the Heusler alloys", *Proceedings of the Royal Society of London A*, vol. 144, pp. 340–359, 1934.

[139] T. Graf, C. Felser, and S. S. P. Parkin, "Simple rules for the understanding of Heusler compounds", *Progress in Solid State Chemistry*, vol. 39, pp. 1–50, 2011.

[140] P. G. van Engen, K. H. J. Buschow, R. Jongebreur, and M. Erman, "PtMnSb, a material with very high magneto-optical Kerr effect", *Applied Physics Letters*, vol. 42, pp. 202–204, 1983.

[141] T. Graf, C. Felser, and S. S. P. Parkin, "Heusler compounds: Applications in spintronics", in *Handbook of Spintronics*, Y. Xu, D. D. Awschalom, and J. Nitta, Eds., Dordrecht: Springler, 2016, pp. 335–364.

[142] S. Chadov, X. Qi, J. Kübler, G. H. Fecher, C. Felser, and S. C. Zhang, "Tunable multifunctional topological insulators in ternary Heusler compounds", *Nature Materials*, vol. 9, pp. 541–545, 2010.

[143] T. Klimczuk *et al.*, "Superconductivity in the Heusler family of intermetallics", *Physical Review B*, vol. 85, 174505-1–174505-8, 2012.

[144] S. Sakurada and N. Shutoh, "Effect of Ti substitution on the thermoelectric properties of (Zr,Hf)NiSn half-Heusler compounds", *Applied Physics Letters*, vol. 86, 082105-1–082105-3, 2005.

[145] J. Krez and B. Balke, "Thermoelectric Heusler compounds", in *Heusler alloys: Properties, Growth, Applications*, C. Felser and A. Hirohata, Eds., Cham.: Springler, 2016, pp. 249–267.

[146] W. E. Pickett and J. S. Moodera, "Half metallic magnets", *Physics Today*, vol. 54, pp. 39–44, 2001.

[147] G. A. Prinz, "Magnetoelectronics", *Science*, vol. 282, pp. 1660–1663, 1998.

[148] Z. Y. Wei *et al.*, "Realization of multifunctional shape-memory ferromagnets in all-d-metal Heusler phases", *Applied Physics Letters*, vol. 107, 022406-1–022406-5, 2015.

[149] Z. Y. Wei *et al.*, "Magnetostructural martensitic transformations with large volume changes and magneto-strains in all-d-metal Heusler alloys", *Applied Physics Letters*, vol. 109, 071904-1–071904-5, 2016.

[150] A. Hirohata *et al.*, "Heusler alloy/semiconductor hybrid structures", *Current opinion in Solid State and Materials Science*, vol. 10, pp. 93–107, 2006.

[151] I. Skovsen *et al.*, "Multi-temperature synchrotron PXRD and physical properties study of half-Heusler TiCoSb", *Dalton Transactions*, vol. 39, pp. 10 154–10 159, 2010.

[152] X. Moya, "Comportament vibracional i magnètic d'aliatges funcionals tipus Heusler", Ph.D. dissertation, Universitat de Barcelona, 2008.

[153] S. Aksoy, "Magnetic interactions in martensitic Ni-Mn-based Heusler systems", Ph.D. dissertation, Universität Duisburg-Essen, 2010.

[154] T. Miyamoto, W. Ito, R. Y. Umetsu, T. Kanomata, K. Ishida, and R. Kainuma, "Influence of annealing conditions on magnetic properties of $Ni_{50}Mn_{50-x}In_x$ Heusler-type alloys", *Materials Transactions*, vol. 52, pp. 1836–1839, 2011.

[155] W. Ito, M. Nagasako, R. Y. Umetsu, R. Kainuma, T. Kanomata, and K. Ishida, "Atomic ordering and magnetic properties in the $Ni_{45}Co_5Mn_{36.7}In_{13.3}$ metamagnetic shape memory alloy", *Applied Physics Letters*, vol. 93, 232503-1–232503-3, 2008.

[156] M. F. Osmond, "Méthode générale pour l'analyse micrographique des aciers au carbone", *Arts Chemiques*, vol. 94, pp. 480–518, 1895.

[157] J. W. Christian, G. B. Olson, and M. Cohen, "Classification of displacive transformations: What is a Martensitic transformation?", *Journal de Physique IV*, vol. 5, C8-3–C8-10, 1995.

[158] R. Niemann *et al.*, "Reducing the nucleation barrier in magnetocaloric Heusler alloys by nanoindentation", *APL Materials*, vol. 4, 064101-1–064101-7, 2016.

[159] Z. Zhang, R. D. James, and S. Müller, "Energy barriers and hysteresis in martensitic phase transformations", *Acta Materialia*, vol. 57, pp. 4332–4352, 2009.

[160] V. Srivastava, X. Chen, and R. D. James, "Hysteresis and unusual magnetic properties in the singular Heusler alloy $Ni_{45}Co_5Mn_{40}Sn_{10}$", *Applied Physics Letters*, vol. 97, 014101-1–014101-3, 2010.

[161] Y. Song, X. Chen, V. Dabade, T. W. Shield, and R. D. James, "Enhanced reversibility and unusual microstructure of a phase-transforming material", *Nature*, vol. 502, pp. 85–88, 2013.

[162] S. Kaufmann *et al.*, "Modulated martensite: Why it forms and why it deforms easily", *New Journal of Physics*, vol. 13, 053029-1–053029-24, 2011.

[163] K. Otsuka and C. M. Wayman, *Shape Memory Materials*. Cambridge: Cambridge University Press, 1998.

[164] H. K. D. K. Bhadeshia, "21 - Physical Metallurgy of Steels", in *Physical Metallurgy (Fifth Edition)*, D. E. Laughlin and K. Hono, Eds., Oxford: Elsevier, 2014, pp. 2157–2214.

[165] C. M. Wayman, *Introduction to the crystallography of martensitic transformations*. New York: Macmillan, 1964.

[166] J. Ortin and A. Planes, "Thermodynamic analysis of thermal measurements in thermoelastic martensitic transformations", *Acta Metallurgica*, vol. 36, pp. 1873–1889, 1988.

[167] Y. Sutou *et al.*, "Magnetic and martensitic transformations of NiMnX (X = In, Sn, Sb) ferromagnetic shape memory alloys", *Applied Physics Letters*, vol. 85, pp. 4358–4360, 2004.

[168] I. Dubenko, M. Khan, A. K. Pathak, B. R. Gautam, S. Stadler, and N. Ali, "Magnetocaloric effects in Ni-Mn-X based heusler alloys with X=Ga, Sb, In", *Journal of Magnetism and Magnetic Materials*, vol. 321, pp. 754–757, 2009.

[169] R. Kainuma, W. Ito, R. Y. Umetsu, K. Oikawa, and K. Ishida, "Magnetic field-induced reverse transformation in B2-type NiCoMnAl shape memory alloys", *Applied Physics Letters*, vol. 93, 091906-1–091906-3, 2008.

[170] K. Ullakko, J. K. Huang, C. Kantner, R. C. O'Handley, and V. V. Korokin, "Large magnetic-field-induced strains in Ni_2MnGa single crystals", *Applied Physics Letters*, vol. 69, p. 1966, 1996.

[171] R. Kainuma *et al.*, "Magnetic-field-induced shape recovery by reverse phase transformation", *Nature*, vol. 439, pp. 957–960, 2006.

[172] N. A. Gokcen, "The Mn-Ni (Manganese - Nickel) System", *Journal of Phase Equilibria*, vol. 12, pp. 313–321, 1991.

[173] S. Kaufmann *et al.*, "Adaptative modulations of martensites", *Physical Review Letters*, vol. 104, 145702-1–145702-4, 2010.

[174] A. Çakır, L. Rigi, F. Albertini, M. Acet, M. Farele, and S. Aktürk, "Extended investigation of intermartensitic transitions in Ni-Mn-Ga magnetic shape memory alloys: A detailed phase diagram determination", *Journal of Applied Physics*, vol. 114, 183912-1–183912-9, 2013.

[175] V. A. Chernenko, J. Pons, C. Seguí, and E. Cesari, "Premartensitic phenomena and other phase transformations in Ni-Mn-Ga alloys studied by dynamical mechanical analysis and electron diffraction", *Acta Materialia*, vol. 50, pp. 53–60, 2002.

[176] R. Ranjan, S. Banik, S. R. Barman, U. Kumar, P. K. Mukhopadhyay, and D. Pandey, "Powder X-ray diffraction study of the thermoelastic martensitic transition in $Ni_2Mn_{1.05}Ga_{0.95}$", *Physical Review B*, vol. 74, 224443-1–224443-8, 2006.

[177] A. Aksoy *et al.*, "Magnetization easy axis in martensitic Heusler alloys estimated by strain measurements under magnetic field", *Applied Physics Letters*, vol. 91, 251915-1–251915-3, 2007.

[178] T. Krenke, M. Acet, E. F. Wassermann, X. Moya, L. Mañosa, and A. Planes, "Ferromagnetism in the austenitic and martensitic states of Ni-Mn-In alloys", *Physical Review B*, vol. 73, 174413-1–174413-10, 2006.

[179] T. Krenke, M. Acet, E. F. Wassermann, X. Moya, L. Mañosa, and A. Planes, "Martensitic transitions and the nature of ferromagnetism in the austenitic and martensitic states of Ni-Mn-Sn alloys", *Physical Review B*, vol. 72, 014412-1–014412-9, 2005.

[180] P. Entel *et al.*, "Modelling the phase diagram of magnetic shape memory Heusler alloys", *Journal of Physics D: Applied Physics*, vol. 39, pp. 865–889, 2006.

[181] E. Şaşıoğlu, L. M. Sandratskii, and P. Bruno, "First-principles calculation of the intersublattice exchange interactions and Curie temperatures of the full Heusler alloys Ni_2MnX (X = Ga, In, Sn, Sb)", *Physical Review B*, vol. 70, 024427-1–024427-5, 2004.

[182] M. Acet, L. Mañosa, and A. Planes, "Magnetic-field-induced effects in martensitic Heusler-based magnetic shape memory alloys", in *Handbook of Magnetic Materials*, K. H. J. Buschow, Ed., New Holland: Elsevier Science & Technology, 2011, pp. 231–289.

[183] A. Sozinov, A. A. Likhachev, N. Lanska, and K. Ullakko, "Giant magnetic-field-induced strain in NiMnGa seven-layered martensite phase", *Applied Physics Letters*, vol. 80, pp. 1746–1748, 2002.

[184] A. Sozinov, N. Lanska, A. Soroka, and W. Zou, "12 % Magnetic field-induced strain in Ni-Mn-Ga-based non-modulated martensite", *Applied Physics Letters*, vol. 102, 021902-1–021902-5, 2013.

[185] R. Tickle, R. D. James, T. Shield, M. Wuttig, and V. V. Kokorin, "Ferromagnetic shape memory in the NiMnGa system", *IEEE Transactions on Magnetics*, vol. 35, pp. 4301–4310, 1999.

[186] Q. Pan and R. D. James, "Micromagnetic study of Ni_2MnGa under applied field (invited)", *Journal of Applied Physics*, vol. 87, pp. 4702–4706, 2000.

[187] Y. W. Lai *et al.*, "Absence of magnetic domain wall motion during magnetic field induced twin boundary motion in bulk magnetic shape memory alloys", *Applied Physics Letters*, vol. 90, 192504-1–192504-3, 2007.

[188] Y. Ishikawa, "Different degrees of itineracy in 3d alloys revealed by measurements of neutron spin wave scattering", *Physica B & C*, vol. 91B, pp. 130–137, 1977.

[189] P. J. Webster and R. S. Trebble, "The magnetic and chemical ordering of the Heusler alloys Pd_2MnIn, Pd_2MnSn and Pd_2MnSb", *Philosophical Magazine*, vol. 16, pp. 347–361, 1967.

[190] J. Kübler, A. R. Williams, and C. B. Sommers, "Formation and coupling of magnetic moments in Heusler alloys", *Physical Review B*, vol. 28, pp. 1745–1755, 1983.

[191] E. Şaşıoğlu, "First-principles study of the exchange interactions and curie temperature in Heusler alloys", Ph.D. dissertation, Martin-Luther-Universität, 1975.

[192] P. Borogohain and M. B. Sahariah, "Effect of compositional and antisite disorder on the electronic and magnetic properties of Ni-Mn-In Heusler alloy", *Journal of Physics: Condensed Matter*, vol. 27, p. 175 502, 2015.

[193] I. Galanakis, "Theory of Heusler and full-Heusler compounds", in *Heusler alloys: Properties, Growth, Applications*, C. Felser and A. Hirohata, Eds., Cham.: Springler, 2016, pp. 3–36.

[194] M. A. Ruderman and C. Kittel, "Indirect exchange coupling of nuclear magnetic moments by conduction electrons", *Physical Review*, vol. 96, pp. 99–102, 1954.

[195] T. Kasuya, "A theory of metallic ferro- and antiferromagnetism on Zener's model", *Progress of Theoretical Physics*, vol. 16, pp. 45–57, 1956.

[196] K. Yosida, "Magnetic properties of Cu-Mn alloys", *Physical Review*, vol. 106, pp. 893–898, 1957.

[197] J. C. Slater, "Cohesion in monovalent metals", *Physical Review*, vol. 35, pp. 509–529, 1930.

[198] P. J. Brown, A. Y. Bargawi, J. Crangle, K. U. Neumann, and K. R. A. Ziebeck, "Direct observation of a band Jahn-Teller effect in the martensitic phase transition of Ni_2MnGa", *Journal of Physics: Condensed Matter*, vol. 11, pp. 4715–4722, 1999.

[199] Z. Islam *et al.*, "An X-ray study of non-zero nickel moment in a ferromagnetic shape-memory alloy", *Journal of Magnetism and Magnetic Materials*, vol. 303, pp. 20–25, 2006.

[200] E. Şaşıoğlu, L. M. Sandratskii, and P. Bruno, "Role of conduction electrons in mediating exchange interactions in Mn-based Heusler alloys", *Physical Review B*, vol. 77, 064417-1–064417-15, 2008.

[201] V. D. Buchelnikov *et al.*, "First-principles and Monte Carlo study of magnetostructural transition and magnetocaloric properties of $Ni_{2+x}Mn_{1-x}Ga$", *Physical Review B*, vol. 81, 094411-1–094411-19, 2010.

[202] A. Planes, "Viewpoint: Controlling the martensitic transition in Heusler shape-memory materials", *Physics*, vol. 3,36, 2010.

[203] J. M. D. Coey, *Magnetism and Magnetic Materials*. Cambridge: Cambridge University Press, 2010.

[204] I. Galanakis, P. H. Dederichs, and N. Papanikolaou, "Slater-Pauling behaviour and origin of the half-metallicity of the full-Heuslers alloys", *Physical Review B*, vol. 66, 174429-1–174429-9, 2002.

[205] Z. Yang, D. Y. Cong, X. M. Sun, Z. H. Nie, and Y. D. Wang, "Enhanced cyclabillity of the elastocaloric effect in boron-microalloyed Ni-Mn-In magnetic shape memory alloys", *Acta Materialia*, vol. 127, pp. 33–42, 2017.

[206] D. Y. Cong *et al.*, "Colossal elastocaloric effect in ferroelastic Ni-Mn-Ti alloys", *Pysical Review Letters*, vol. 122, 255703-1–255703-7, 2019.

[207] Y. Qu *et al.*, "Giant and reversible room-temperature magnetocaloric effect in Ti-doped Ni-Co-Mn-Sn magnetic shape memory alloys", *Acta Materialia*, vol. 134, pp. 236–248, 2017.

[208] D. W. Zhao *et al.*, "Giant caloric effect of low-hysteresis metamagnetic shape memory alloys with exceptional cyclic functionallity", *Acta Materialia*, vol. 133, pp. 217–223, 2017.

[209] Z. Yang *et al.*, "Ultrahigh cyclability of a large elastocaloric effect in multiferroic phase-transforming materials", *Materials Research Letters*, vol. 7(4), pp. 137–144, 2019.

[210] A. Czernuszewicz, J. Kaleta, and D. Lewandowski, "Multicaloric effect: Toward a breakthrough in cooling technology", *Energy Conversion and Management*, vol. 178, pp. 335–342, 2018.

[211] A. Aznar *et al.*, "Giant barocaloric effect in all-d-metal Heusler shape memory alloys", *Physical Review Materials*, vol. 3, 044406-1–044406-7, 2019.

[212] V. Novák and P. Šittner, "Micromechanics modelling of NiTi pollycrystalline aggregates transforming under tension and compression stress", *Materials Science and Engineering A*, vol. 378, pp. 490–498, 2004.

[213] A. Fujita, S. Fujieda, Y. Hasegawa, and K. Fukamichi, "Itinerant-electron metamagnetic transition and large magnetocaloric effects in $La(Fe_xSi_{1-x})_{13}$ compounds and their hydrides", *Physical Review B*, vol. 67, 104416-1–104416-12, 2003.

[214] Y. Shen, W. Sun, Z. Y. Wei, Q. Shen, Y. F. Zhang, and J. Liu, "Orientation dependent elastocaloric effect in directionally solidified Ni-Mn-Sn alloys", *Scripta Materialia*, vol. 163, pp. 14–18, 2019.

[215] D. M. Liu *et al.*, "Low-hysteresis tensile superelasticity in a Ni-Co-Mn-Sn magnetic shape memory microwire", *Journal of Alloys and Compounds*, vol. 728, pp. 655–658, 2017.

[216] L. Huang *et al.*, "Large magnetic entropy change and magnetoresistance in a $Ni_{41}Co_9Mn_{40}Sn_{10}$ magnetic shape memory alloy", *Journal of Alloys and Compounds*, vol. 647, pp. 1081–1085, 2015.

[217] F. J. Pérez-Reche, M. Stipcich, E. Vives, L. Mañosa, A. Planes, and M. Morin, "Kinetics of martensitic transitions in Cu-Al-Mn under thermal cycling: Analysis at multiple length scales", *Physical Review B*, vol. 69, 064101-1–064101-7, 2004.

[218] N. M. Bruno *et al.*, "The effect of heat treatments on $Ni_{43}Mn_{42}Co_4Sn_{11}$ meta-magnetic shape memory alloys for magnetic refrigeration", *Acta Materialia*, vol. 74, pp. 66–84, 2014.

[219] T. Stöter *et al.*, "Tuning the interactions in the spin-ice materials $Dy_2Ge_{2-x}Si_xO_7$ by silicon substitution", *Physical Review B*, vol. 100, 054403-1–054403-8, 2019.

[220] T. Gottschall, K. P. Skokov, D. Benke, M. E. Gruner, and O. Gutfleisch, "Contradictory role of the magnetic contribution in inverse magnetocaloric Heusler materials", *Physical Review B*, vol. 93, 184431-1–184431-6, 2016.

[221] W. Ito, Y. Imano, R. Kainuma, Y. Sutou, K. Oikawa, and K. Ishida, "Martensitic and magnetic transformation behaviors in Heusler-type NiMnIn and NiCoMnIn metamagnetic shape memory alloys", *Metallurgical and Materials Transactions A*, vol. 38, pp. 759–766, 2007.

[222] A. Aksoy, M. Acet, P. P. Deen, L. Mañosa, and A. Planes, "Magnetic correlations in martensitic Ni-Mn-based Heusler shape-memory alloys: Neutron polarization analysis", *Physical Review B*, vol. 79, 212401-1–212401-4, 2009.

[223] H. E. Karaca, I. Karaman, B. Basaran, Y. Ren, Y. I. Chumlyakov, and H. J. Maier, "Magnetic field-induced phase transformation in Ni-Mn-Co-In magnetic shape-memory alloys - A new actuation mechanism with large work output", *Advanced Functional Materials*, vol. 19, pp. 983–998, 2009.

[224] J. Z. Hao *et al.*, "Multicaloric and coupled-caloric effects", *Chinese Physics B*, vol. 29(4), 047504-1–047504-10, 2020.

[225] T. Kihara, X. Xu, W. Ito, R. Kainuma, and M. Tokunaga, "Direct measurements of inverse magnetocaloric effects in metamagnetic shape-memory alloy NiCoMnIn", *Physical Review B*, vol. 90, 214409-1–214409-6, 2014.

[226] V. Recarte, J. I. Pérez-Landázabal, V. Sánchez-Alarcos, V. Zablotskii, E. Cesari, and S. Kustov, "Entropy change linked to the martensitic transformation in metamagnetic shape memory alloys", *Acta Materialia*, vol. 60, pp. 3168–3175, 2012.

[227] T. Gottschall, K. P. Skokov, B. Frincu, and O. Gutfleisch, "Large reversible magnetocaloric effect in Ni-Mn-In-Co", *Applied Physics Letters*, vol. 106, 021901-1–021901-4, 2015.

[228] J. Romero Gómez, R. Ferreiro Garcia, A. De Miguel Catoira, and M. Romero Gómez, "Magnetocaloric effect: A review of the thermodynamic cycles in magnetic refrigeration", *Renewable and Sustainable Energy Reviews*, vol. 17, pp. 74–82, 2013.

[229] D. Zhao, T. Castán, A. Planes, Z. Li, W. Sun, and J. Liu, "Enhanced caloric effect induced by magnetoelastic coupling in NiMnGaCu Heusler alloys: Experimental study and theoretical analysis", *Physical Review B*, vol. 96, 224105-1–224105-7, 2017.

[230] G. Porcari and ohers, "Convergence of direct and indirect methods in the magnetocaloric study of first order transformations: The case of Ni-Co-Mn-Ga Heusler alloys", *Physical Review B*, vol. 86, 104432-1–104432-5, 2012.

[231] F. Guillou, G. Porcari, H. Yibole, N. van Dijk, and E. Brück, "Taming the first-order transition in giant magnetocaloric materials", *Advanced Materials*, vol. 26, pp. 2671–2675, 2014.

[232] S. K. Sarkar, Sarita, P. D. Babu, A. Biswas, V. Siruguri, and M. Krishnan, "Giant magnetocaloric effect from reverse martensitic transformation in Ni-Mn-Ga-Co ferromagnetic shape memory alloys", *Journal of Alloys and Compounds*, vol. 670, pp. 281–288, 2016.

[233] C. Seguí, J. Torrens-Serra, E. Cesari, and P. Lázpita, "Optimizing the caloric properties of Cu-doped Ni-Mn-Ga alloys", *Materials*, vol. 13, pp. 1–14, 2020.

[234] T. Gottschall, K. P. Skokov, R. Burriel, and O. Gutfleisch, "On the S(T) diagram of magnetocaloric materials with first-order transition: Kinetic and cyclic effects of Heusler alloys", *Acta Materialia*, vol. 107, pp. 1–8, 2016.

[235] R. Wroblewski, K. Sielicki, and M. Leonowicz, "Magnetocaloric properties of $Ni_{49.9}Mn_{19.6}Cu_{5.7}Ga_{24.8}$ single crystal processed by Bridgman method with stationary crucible", *Materials Letters*, vol. 218, pp. 83–85, 2018.

[236] P. Czaja, M. Kowalczyk, and W. Maziarz, "On the magnetic contribution to the inverse magnetocaloric effect in Ni-Co-Cu-Mn-Sn metamagnetic shape memory alloys", *Journal of Magnetism and Magnetic Materials*, vol. 474, pp. 381–392, 2019.

[237] J. Ortin, "Thermally induced martensitic transformations: Theoretical analysis of a complete calorimetric run", *Thermochimica Acta*, vol. 121, pp. 397–412, 1987.

Appendix A

Python program for the treatment of calorimetric curves

A custom Python program has been developed to perform the signal treatment and the corresponding thermodynamic calculations on DSC thermograms that correspond to thermally-induced martensitic phase transitions. It is important to emphasize that the custom Python program can be easily adapted to analyse DSC thermograms corresponding to field-induced martensitic phase transitions.

The program presented in this appendix is based on a previous script from 2001 written in QBasic, where improvements on the signal smoothing filters and the baseline correction have been implemented. The working procedure of both data treatment programs is based on the discussion reported in reference [237].

The general working procedure of the custom Python program can be summarized in the following steps:

1. **Reading the measurement data file**
   The Python program reads the file recorded from the experimental device, which consists of a two column data file with the raw calorimetric signal ($Y(T)$) and the temperature (T), expressed in units of Volt and Kelvin, respectively. After introducing the sampling period of the measurement, it creates the time axis (t) and plots the calorimetric signal and the temperature as a function of time.

2. **Smoothing on the raw data file**
   It gives the possibility to apply a smoothing filter on the calorimetric signal and the temperature before performing the corresponding thermodynamic calculations. The applied filters can be different for each data column, and the current version of the program provides five different smoothing options: no smoothing, Moving average, [1] Savitzky-Golay filter, [2] Butterworth filter,

[1] Average:
https://pandas.pydata.org/pandas-docs/stable/reference/api/pandas.DataFrame.mean.html
[2] Savitzky-Golay documentation:
https://docs.scipy.org/doc/scipy/reference/generated/scipy.signal.savgol_filter.html#scipy.signal.savgol_filter

[3] and Percentile filter. [4]

After the smoothing process, it displays a comparative figure for the raw and smoothed data as a function of time for both the calorimetric signal and the temperature. At this point, the user can decide to repeat the smoothing procedure.

3. **Correction of the calorimetric signal**

The gradient function [5] is used to compute the time derivative of the temperature $\left(\frac{dT}{dt}\right)$, and the program gives the possibility of applying two consecutive smoothing filters from the ones mentioned before. After the smoothing process, a comparative figure of the raw time derivative of the temperature together with the results of the smoothing processes as a function of time is displayed. At this point, the user can decide to repeat the smoothing procedure.

After a successful smoothing of the temperature derivative, the user selects the sensitivity function of the calorimeter used in the experiments ($S(T)$). Then, as discussed in section 3.1.1, the raw calorimetric signal is corrected as:

$$\frac{dQ(T)}{dT} = \frac{\dot{Q(T)}}{\dot{T}} = \frac{Y(T)dt}{S(T)dT} \tag{A.1}$$

4. **Baseline selection**

The corrected calorimetric signal $\left(\frac{dQ(T)}{dT}\right)$ is plotted as a function of temperature, where the first-order phase transition is seen as a peak spreading within a certain temperature range $[T_s, T_f]$. In order to separate the baseline from the first-order phase transition signal, the user has to select four data points (T_i^{bg}, where $i \in [1,4]$) on the displayed plot, two below ($T_i^{bg} < T_s$, where $i = 1,2$) and two above ($T_i^{bg} > T_f$, where $i = 3,4$) the first-order phase transition temperature range. The selected data points define two data ranges where the measured signal only comes from the baseline contribution, one below $[T_1^{bg}, T_2^{bg}]$ and the other one above $[T_3^{bg}, T_4^{bg}]$ the phase transition temperature range.

After the selection of these data points, two different functions can be

[3] Butterworth filter documentation:
https://docs.scipy.org/doc/scipy/reference/generated/scipy.signal.butter.html#scipy.signal.butter

[4] Percentile moving filter:
https://pandas.pydata.org/pandas-docs/stable/reference/api/pandas.core.window.rolling.Rolling.quantile.html

[5] Gradient documentation:
https://numpy.org/doc/stable/reference/generated/numpy.gradient.html

selected in order to define the baseline behaviour of the corrected calorimetric signal.

On the one hand, two different linear functions are fitted to identify the baseline behaviour, one below ($\zeta_1(T)$) and the other one above ($\zeta_2(T)$) the phase transition temperature range. Each linear fit is fitted to each data range selected by the user.

On the other hand, a third order polynomial function can be fitted to identify the baseline behaviour ($\zeta_{poly}(T)$). It is important to point out that the third order polynomial function is fitted to both data ranges, and a single function defines the baseline of the corrected calorimetric signal.

5. **Baseline correction and integration**

The baseline correction process is different depending on the function that has been chosen to define the baseline behaviour.

If two linear functions have been selected to define the baseline of the corrected calorimetric signal, the user has to identify the peak position of the first-order phase transition signal (T^{peak}). Then, each linear fit is extrapolated within the phase transition temperature range, defining the first approximation of the complete baseline:

$$\zeta(T) = \begin{cases} \zeta_1(T) & T < T^{peak} \\ \\ \zeta_2(T) & T \geq T^{peak} \end{cases} \tag{A.2}$$

The first approximation of the baseline allows us to compute a first estimate of both the transition entropy change (ΔS_t) and the transformed fraction ($\chi(T)$), which were defined in section 3.1.1 as:

$$\Delta S_t = \int_{T_s}^{T_f} \frac{1}{T'} \left(\frac{dQ(T')}{dT'} - \zeta(T') \right) dT' \tag{A.3}$$

$$\chi(T) = \frac{S(T) - S(T_s)}{\Delta S_t} = \frac{\displaystyle\int_{T_s}^{T} \frac{1}{T'} \left(\frac{dQ(T')}{dT'} - \zeta(T') \right) dT'}{\Delta S_t} \tag{A.4}$$

At this point, it is important to point out that the integrals expressed in these equations are computed numerically by a cumulative trapezoidal integration. [6]

In order to improve the baseline to subtract from the corrected calorimetric signal, defined by equation A.2, the transformed fraction is used as a weight factor to define a linear combination of the two baseline functions fitted at

[6] Cumulative trapezoidal integration documentation:
https://docs.scipy.org/doc/scipy-0.18.1/reference/generated/scipy.integrate.cumtrapz.html

each side of the phase transition temperature range. Therefore, the complete baseline can be defined as:

$$\zeta(T) = [1 - \chi(T)]\zeta_1(T) + \chi(T)\zeta_2(T) \tag{A.5}$$

This new baseline is used to compute again the transition entropy change and the transformed fraction, expressed in both equations A.3 and A.4, respectively, which allows us to compute again a new baseline, as expressed in equation A.5. The redefinition of the baseline to be subtracted and the computation of both the transition entropy change and the transformed fraction is done iteratively, seeking a convergence of the computed transition entropy change with respect to the previous integration performed, within a certain defined tolerance margin.

Conversely, if a third order polynomial function has been selected to define the baseline of the corrected calorimetric signal, the transition entropy change and the transformed fraction are computed as expressed in equations A.3 and A.4, respectively, but they are not further corrected in an iterative process.

6. **Computed results and storage**

After the integration process, the corrected calorimetric signal $\left(\frac{dQ(T)}{dT}\right)$ and the final baseline ($\zeta(T)$) are plotted together as a function of temperature. Moreover, for the sake of clarity the resulting transformed fraction ($\chi(T)$) as a function of temperature is also displayed. At this point, the user can decide to repeat the integration procedure and the program resumes from the fourth step, allowing to select a new baseline for the corrected calorimetric signal.

Once the baseline correction and integration results are accepted by the user, the program computes the start (T_s) and finish (T_f) phase transition temperatures, estimated from the transformed fraction as the temperatures where the phase transition is completed at 5 % and 95 %, respectively. Additionally, after the introduction of the sample mass, the transition entropy (ΔS_t) and enthalpy (ΔH_t) changes per mass unit are computed.

Finally, a data file consisting of four columns (the temperature (T), the corrected calorimetric signal $\left(\frac{dQ(T)}{dT}\right)$, the baseline ($\zeta(T)$) and the transformed fraction ($\chi(T)$)) is created and stored.

For further details on the computation of the different parameters, the code of this Python program is included in the following pages of this appendix.

```
# ------------------------------------------------------------------------ #
#                                                                          #
#                                CALATO 1.0                                #
#      Improved version of CALATO9.BAS, version 6.0 (January 2001)         #
#                                                                          #
# Signal treatment and thermodynamic calculations on thermograms           #
# corresponding to thermally-induced martensitic transformations.          #
#                                                                          #
# This program automatically ccomputes and corrects the base-line          #
# of the signal.                                                           #
#                                                                          #
# INPUT: Two-columns file containing the temperature (K) and               #
#        the calorimetric signal (V)                                       #
#                                                                          #
# OUTPUT: The program can create the following plotting files:             #
#               1. Temperature (K) vs. time (s)                            #
#               2. Thermogram (V) vs. temperature (K)                      #
#               3. Thermogram and baseline (J/K) vs. temperature (K)       #
#               4. Transformed fraction vs. temperature (K)                #
#                                                                          #
# ------------------------------------------------------------------------ #

#  Import the necessary libraries
import numpy as np
import scipy.integrate as sp_int
import scipy.signal as sp_sig
import scipy.optimize as sp_opt
import pandas as pd
import matplotlib.pyplot as plt
from matplotlib.widgets import Cursor
import sys

sys._enablelegacywindowsfsencoding()

# ----------------------------FUNCTIONS------------------------------- #

# ------------------------------------------------------------------------ #
#                                                                          #
#                             Single plot                                  #
#                                                                          #
# ------------------------------------------------------------------------ #

def single_plot(file1, file2, title, label_1, label_2, col_1x, col_1y, col_2x, col_2y):
    """This function displays a plot with two curves"""

    # We obtain the headers list of the two files
    header1 = list(file1)
    header2 = list(file2)

    single_fig = plt.figure()
    plt.plot(file1[header1[col_1x]], file1[header1[col_1y]], color='k', label=label_1)
    plt.plot(file2[header2[col_2x]], file2[header2[col_2y]], color='r', label=label_2)
    plt.title(title)
    plt.legend()
    plt.ylabel(header1[col_1y])
    plt.xlabel(header1[col_1x])

    return plt.show(single_fig)
```

```
# ------------------------------------------------------------------------ #
#                                                                          #
#                              Double plot                                 #
#                                                                          #
# ------------------------------------------------------------------------ #

def double_plot(file1, file2, title, pl_1_x, pl_1_y, pl_2_x, pl_2_y):
    """This function displays a double plot with two curves per plot"""

    # We obtain the headers list of the two files
    header1 = list(file1)
    header2 = list(file2)

    double_fig = plt.figure()

    plt.subplot(211)
    top_plot = plt.plot(file1[header1[pl_1_x]], file1[header1[pl_1_y]],
                        file2[header2[pl_1_x]], file2[header2[pl_1_y]])
    plt.title(title)
    plt.setp(top_plot[0], color='k', label='Raw data')
    plt.setp(top_plot[1], color='r', label='Smoothed data')
    plt.legend(['Raw data', 'Smoothed data'])
    plt.ylabel(header1[pl_1_y])
    plt.xlabel(header1[pl_1_x])
    plt.subplots_adjust(hspace=0.3)

    plt.subplot(212)
    bottom_plot = plt.plot(file1[header1[pl_2_x]], file1[header1[pl_2_y]],
                           file2[header2[pl_2_x]], file2[header2[pl_2_y]])
    plt.setp(bottom_plot[0], color='k', label='Raw data')
    plt.setp(bottom_plot[1], color='r', label='Smoothed data')
    plt.legend(['Raw data', 'Smoothed data'])
    plt.ylabel(header1[pl_2_y])
    plt.xlabel(header1[pl_2_x])

    return plt.show(double_fig)

# ------------------------------------------------------------------------ #
#                                                                          #
#                           Smoothing routine                              #
#                                                                          #
# ------------------------------------------------------------------------ #

def smoothing_function(file, file_length: int, columns: list):
    """
    This function performs a smoothing onto a desired file.
    The user can choose between five different smoothing methods:
        1. No smoothing
        2. Moving average
        3. Savitzky-Golay
        4. Frequency filter
        5. Percentile filter
    INPUT: File (data frame), file length (integer), file columns to smooth (list)
    OUTPUT: Smoothed file (data frame), file length (integer)
    """

    print("There are five available smoothing methods:"
          "\n\t 1. No smoothing"
          "\n\t 2. Moving average"
```

```
        "\n\t 3. Savitzky-Golay"
        "\n\t 4. Frequency filter"
        "\n\t 5. Percentile filter")

answer = input("Introduce the smoothing method you want to use [1,2,3,4,5]:")

while answer not in ['1', '2', '3', '4', '5']:
    print('\nPlease introduce a suitable answer [1,2,3,4,5]')
    answer = input("Select a suitable smoothing method number [1,2,3,4,5]:")

i = int(answer)

while i != 1 and i != 2 and i != 3 and i !=4 and i != 5:
   i = int(input("Please, select a suitable smoothing method number [1,2,3,4,5]:"))

# We get the headers list of the file we import with this function
header_f = list(file)

if i == 1:
    # No smoothing is performed to the data
    # Creation of the smoothed file
    smoothed_file = pd.DataFrame()
    # Iteration to perform the smoothing method onto the desired columns
    for j in columns:
        smoothed_file[j] = file[header_f[j]]
    NS = int(len(smoothed_file))  # Calculation of the file length

    return smoothed_file, NS

elif i == 2:
    # NX is the window size to perform the temperature and data smoothing
    NX = int(input("\nIntroduce the half window size to perform the moving average"
                   " smoothing"
                   "\n[Recommended values range: 10 - 100]:"))
    # Total window size to perform the smoothing. Always an odd number
    ws = 2 * NX + 1

    # We assure that the introduced window size is smaller than the file length
    while ws > file_length:
        NX = int( input("The selected window size is bigger than the file length."
                        "\nPlease, select a new half window size to perform the "
                        "smoothing:"))
        ws = 2 * NX + 1

    # Creation of the smoothed file
    smoothed_file = pd.DataFrame()
    # Iteration to perform the smoothing method onto the desired columns
    for j in columns:
        smoothed_file[j] = file[header_f[j]].rolling( window=ws, center=True ).mean()
    NS = int(len(smoothed_file))  # Calculation of the file length

    return smoothed_file, NS

elif i == 3:
    # NX is the window size to perform the temperature and data smoothing
    NX = int(input("\nIntroduce the half window size to perform the Savitzky-Golay"
                   " smoothing"
                   "\n[Recommended values range: 50-200]:"))
    # Total window size to perform the smoothing. Always an odd number
```

```
        ws = 2 * NX + 1

        # We assure that the introduced window size is smaller than the file length
        while ws > file_length:
            NX = int( input("The selected window size is bigger than the file length."
                            "\nPlease, select a new half window size to perform the"
                            " smoothing:"))
            ws = 2 * NX + 1

        # Polynomial order to perform the smoothing. It must be smaller than the length
        # of the window
        pol = int( input("Introduce the order of the polynomial to perform the "
                         "Savitzky-Golay smoothing"
                         "\n[Recommended values range: 3-4]:"))

        # Creation of the smoothed file
        smoothed_file = pd.DataFrame()
        # Iteration to perform the smoothing method onto the desired columns
        for j in columns:
            smoothed_file[j] = sp_sig.savgol_filter(file[header_f[j]], ws, pol)
        NS = int(len(smoothed_file))  # Calculation of the file length

        return smoothed_file, NS

    elif i == 4:
        # The Butterworth filter has the following default values
        print( "\nThe default values used for the Butterworth filter are:"
               "\n\tOrder of the filter: 8"
               "\n\tNormalized critical frequency: 0.02 Hz")

        # The default values of the filter are specified here
        par_1 = 8
        par_2 = 0.02

        # The default values of the filter can be modified here
        answer2 = input("\nDo you want to use alternative parameters? [Y/N]:")

        # Loop to filter the possible wrong inputs introduced by the user
        while answer2 not in ['Y', 'y', 'yes', 'Yes', 'YES', 'N', 'n', 'no', 'No', 'NO']:
            print('\nPlease introduce a suitable answer [Y/N]')
            answer2 = input("Do you want to use alternative parameters? [Y/N]:")

        if answer2 in ['Y', 'y', 'yes', 'Yes', 'YES']:
            # We introduce the new parameter values for the Butterworth filter
            par_1 = int(input("Introduce the order of the Butterworth filter:"))
            par_2 = float(input("Introduce the normalized critical frequency of the"
                                " filter [0-1 Hz]:"))

            # This while loop assures that the introduced normalized frequency is in the
            # range 0-1 Hz
            loop = 0
            while loop == 0:
                if par_2 <= 0 or par_2 >= 1:
                    print("The normalized critical frequency introduced is not in the"
                          " specified range")
                    par_2 = float(input("Please, introduce a new value for this parameter"
                                        " [0-1 Hz]:"))
                else:
                    loop = 1
```

```
        else:
            print("The default parameters will be used")

        #  Create a low pass Butterworth filter
        b, a = sp_sig.butter(par_1, par_2, btype='low', analog=False)

        #  Creation of the smoothed file
        smoothed_file = pd.DataFrame()
        #  Iteration to perform the smoothing method onto the desired columns
        for j in columns:
            smoothed_file[j] = sp_sig.filtfilt(b, a, file[header_f[j]])
        NS = int(len(smoothed_file))  # Calculation of the file length

        return smoothed_file, NS

    elif i == 5:
        # The Percentile filter has the following default values
        print("\nThe default values used for the Percentile filter are:"
              "\n\tWindow size: 50"
              "\n\tPercentile: 0.5")

        # The default values of the filter are specified here
        percent = 0.5
        ws = 50

        # The default values of the filter can be modified here
        answer3 = input("\nDo you want to use alternative parameters? [Y/N]:")

        # Loop to filter the possible wrong inputs introduced by the user
        while answer3 not in ['Y', 'y', 'yes', 'Yes', 'YES', 'N', 'n', 'no', 'No', 'NO']:
            print('\nPlease introduce a suitable answer [Y/N]')
            answer3 = input("Do you want to use alternative parameters? [Y/N]:")

        if answer3 in ['Y', 'y', 'yes', 'Yes', 'YES']:
            # NX is the window size to perform the temperature and data smoothing
            NX = int(input("\nIntroduce the half window size to perform the"
                           " percentile filter"
                           "\n[Recommended values range: 10 - 100]:"))
            # Total new window size to perform the smoothing. Always an odd number
            ws = 2 * NX + 1

            # We assure that the introduced window size is smaller than the file length
            while ws > file_length:
                NX = int(input("The selected window size is bigger than the file length."
                               "\nPlease, select a new half window size to perform the"
                               " smoothing:"))
                ws = 2 * NX + 1

            percent = float(input("Introduce the percentile to compute with the filter"
                                  " [0-1]"))

        # Creation of the smoothed file
        smoothed_file = pd.DataFrame()
        # Iteration to perform the smoothing method onto the desired columns
        for j in columns:
            smoothed_file[j] = file[header_f[j]].rolling(window=ws, center=True)\
                .quantile(percent)
        NS = int(len(smoothed_file))  # Calculation of the file length
```

```
        return smoothed_file, NS

# ------------------------------------------------------------------------ #
#                                                                          #
#                              Sensitivity                                 #
#                                                                          #
# ------------------------------------------------------------------------ #

def sensitivity(temp: float):
    """Calculates and returns the sensitivity of the Strain-DSC calorimeter"""

    # The sensitivity is calculated in units of mV/W.

    #  Calibration from 2019 (range: 250 K < T < 360 K)
    sens = -2.0E-3 * temp ** 2 + 1.20626 * temp - 87.71754

    return sens

# ------------------------------------------------------------------------ #
#                                                                          #
#                          Signal correction                               #
#                                                                          #
# ------------------------------------------------------------------------ #

def signal_correction(signal, sens, temp_deriv):
    """
    Performs the signal correction for the sensitivity (mV/W)
     and the dT/dt (K/s) value
     """

    #  The factor 1E6 comes from two sides:
    # 1. Signal: V to mV conversion
    # 2. corr_value: J to mJ conversion
    corr_value = 1E6 * ((signal / sens) / temp_deriv)
    return corr_value

# ------------------------------------------------------------------------ #
#                                                                          #
#                          Indexing function                               #
#                                                                          #
# ------------------------------------------------------------------------ #

def indexing(file, column, temp, tol):
    """
    This function returns the row index of the temperature point
    closest (with a certain margin of tolerance) to the temperature
    value introduced by the user
    """

    k = 0
    l = 0
    dist = abs(temp - file.loc[k, column])
    while l == 0:
        if dist > tol:
            k = k + 1
            dist = abs(temp - file.loc[k, column])
        else:
            break
```

```
    return k

# ------------------------------------------------------------------------ #
#                                                                          #
#                       Picking points function                            #
#                                                                          #
# ------------------------------------------------------------------------ #

def select(num_points):
    """
    This function shows the dQ/dT (mJ/K) vs T (K) plot and
    allows the user to select a certain number of data points
    """

    # ---------------Plot of dQ/dT (mJ/K) vs Temperature(K)---------------- #

    header_s = list(smoothed_thermogram)
    #  We display the plot of the Corrected signal vs Temperature
    corrected_fig = plt.figure()
    ax = corrected_fig.add_subplot(111)
    plt.plot(smoothed_thermogram[header_s[0]], smoothed_thermogram[header_s[6]],
             color='k', label='dQ/dT (mJ/K)', picker=5)

    plt.legend()
    plt.title('Corrected data plot')
    plt.ylabel('dQ/dT (mJ/K)')
    plt.xlabel('Temperature (K)')
    #  We define the cursor properties
    cursor = Cursor(ax, useblit=True, color='k', linewidth=1)
    print('Click once on the plot with the right mouse button to select a point')
    print('We have to select {} points in total'.format(num_points))
    #  lists to store the x and y values of the selected points
    temp = list()
    signal = list()
    #  Necessary indexes for the while loop
    n = 0
    #  Loop to select the number of points desired
    loop = 0
    while loop == 0:
        if n < num_points:
            #  We allow the user to zoom in or out in the plot
            zoom = False
            print('Pres any kayboard to select a new data point')
            while not zoom:
                zoom = plt.waitforbuttonpress()
            #  This returns a list (x,y) of the data point clicked with the mouse
            data_point = plt.ginput(1)
            one_point = pd.DataFrame(data_point)
            #  We just keep both temperature and signal of the point selected
            temp_point = one_point.loc[0,0]
            signal_point = one_point.loc[0,1]
            #  We append it to create a list with the temperatures and signals selected
            temp.append(temp_point)
            signal.append(signal_point)
            if n == 0:
                #  We plot the data point selected
                plt.plot(temp[n], signal[n], marker='v', color='r',
                         label='First temperature range')
                plt.legend()
```

```
                plt.draw()
            elif 0 < n < 2:
                plt.plot( temp[n], signal[n], marker='v', color='r')
                plt.draw()
            elif n == 2:
                #  We plot the data point selected
                plt.plot(temp[n], signal[n], marker='^', color='r',
                         label='Second temperature range')
                plt.legend()
                plt.draw()
            else:
                plt.plot( temp[n], signal[n], marker='^', color='r')
                plt.draw()
            n = n + 1
        else:
            break
    plt.show()

    return temp

# ------------------------------------------------------------------------ #
#                                                                          #
#                        Background regression                             #
#                                                                          #
# ------------------------------------------------------------------------ #

# We define the equation for a line
def lin_funct(x,a,b):
    return a*x + b

# We define the equation for a 3rd order polynomial
def poly_funct(x,a,b,c,d):
    return a*x**3 + b*x**2 + c*x + d

def regression_fit(file, i_start, i_end, col_x, col_y, index):
    """
    This function calculates a linear or a 3rd order polynomial regression to the
     specified x and y data and returns the regression coefficients and their covariances
    """
    header = list(file)

    #  We define the x and y ranges to fit the linear regression
    x = file.loc[i_start:i_end, header[col_x]]
    y = file.loc[i_start:i_end, header[col_y]]

    if index == 1:
        #  We perform the linear regression
        popt,pcov = sp_opt.curve_fit(lin_funct, x, y)
    else:
        #  We perform the 3rd order polynomial regression
        popt, pcov = sp_opt.curve_fit(poly_funct, x, y)

    return popt, pcov

# ------------------------------------------------------------------------ #
#                                                                          #
#                        Background point values                           #
#                                                                          #
# ------------------------------------------------------------------------ #
```

```
def regression_calc(xdata, popt, index):
    """This function calculates the y = f(x,*parameters), where x and the parameters
     are given. The function can be a linear regression or a 3rd order polynomial"""

    if index == 1:
        # We have a linear regression
        ydata = lin_funct(xdata, *popt)
    else:
        # We have a 3rd order polynomial regression
        ydata = poly_funct(xdata, *popt)

    return ydata

# ---------------------------------------------------------------------- #
#                                                                        #
#                          Signal correction                             #
#                                                                        #
# ---------------------------------------------------------------------- #

def dS_computation(temp, signal, background):
    """
    Performs the signal (dQ/dT) correction fot the
    background and the temperature, to compute entropy changes
     """

    corr_value = (1/temp * (signal - background))
    return corr_value

# ---------------------------------------------------------------------- #
#                                                                        #
#                Transition temperatures determination                   #
#                                                                        #
# ---------------------------------------------------------------------- #
def transition_temp_1(file, start_count, end_count, X_value, step):
    """This function identifies the start and end temperatures of the
    transition once a certain tolerance (from 0 to 1) on the transformed
     fraction is specified"""

    count = start_count
    while count <= end_count:
        X = file.loc[count, header_s[10]]
        X_diff = abs(X - X_value)
        if X_diff <= 0.005:
            T_1 = file.loc[count,header_s[0]]
            break
        else:
            count = count + step

    return T_1

def transition_temp_2(file, start_count, end_count, X_value, step):
    """This function identifies the start and end temperatures of the
    transition once a certain tolerance (from 0 to 1) on the transformed
    fraction is specified"""

    # We start from the other side
    count = start_count
    while count >= end_count:
```

```
        X = file.loc[count, header_s[10]]
        X_diff = abs(X - X_value)
        if X_diff <= 0.005:
            T_2 = file.loc[count,header_s[0]]
            break
        else:
            count = count + step

    return T_2

# ------------------------------------------------------------------------ #
#                                                                          #
#                    Transformed fraction tolerance                        #
#                                                                          #
# ------------------------------------------------------------------------ #
def tolerance_function(tolerance):
    """This function checks if the transformed fraction is inside the tolerance margin.
    If not, a backup tolerance is taken and the iterative calculation keeps going"""

    count = i_temp[1]
    while count <= i_temp[2]:
        X = smoothed_thermogram.loc[count, header_s[10]]
        if X <= (-tolerance):
            smoothed_thermogram[header_s[10]] = backup['Transformed fraction']
            print( 'X < {}. We took the backup Transformed fraction'.format(-tolerance))
            break
        elif X >= (1 + tolerance):
            smoothed_thermogram[header_s[10]] = backup['Transformed fraction']
            print( 'X > {}. We took the backup Transformed fraction'.format(1+tolerance))
            break

        count = count + 1
    return smoothed_thermogram[header_s[10]]


# -------------------------------SCRIPT-------------------------------- #

# ------------------------------------------------------------------------ #
#  Package 1: Introduction of the parameters to read the file properly  #
# ------------------------------------------------------------------------ #

print("Welcome to CALATO 1.0!"
      "\nI will guide you through all the steps to properly analyse your thermogram")
# Directories to read the data to analyse and to storage the results obtained

data_DR = "< data directory path >"
storage_DR = "< storage directory path >"

FN = input("Write the name and the extension (e.g: .dat) of the data file: ")
dt = str(input("Introduce the sampling period (s): "))  # dt is a float here

# If the decimal delimiter is a comma, it is replaced by points, else the program
# continues.
if dt.__contains__(',') is True:
    print('The decimal separator is a comma, and will be replaced to points')
    dt = float(dt.replace(',','.'))
else:
    dt = float(dt)
```

```
# ------------------------Opening the data file------------------------ #
path = data_DR + FN

# We define the variable that controls the smoothing loop
loop = 0
while loop == 0:
    try:
        # Read the file. The spacer between columns is a tab, and the first row
        # is the header
        thermogram_file = pd.read_csv(path, sep=None, header=0, engine='python',
                                      keep_default_na=False)
        break
    except IOError:
        print('\nThere is no file with this name in the current data directory')
        print('Please introduce a suitable file name!')
        # We introduce the new file name and we define again the file path
        FN = input( '\nWrite the name and the extension (e.g: .dat) of the data file:')
        path = data_DR + FN
        loop = 0

# We get the number of rows we have in the file
N = int(len(thermogram_file))

print('The imported file has {} rows in total.'.format(N))

# ------------------------------------------------------------------------ #
#    Package 2: Plot of the raw data and computing the smoothed file    #
# ------------------------------------------------------------------------ #

# ----------------------Creating the time axis------------------------ #
header = list(thermogram_file)  # We get the headers list
length = len(header)  # We get the headers list length

# We identify the delimiter from the first element of the first column
element = str(thermogram_file.loc[0,header[0]])
# If the decimal delimiter is a comma, it is replaced by points, else the program
# continues.
if element.__contains__(',') is True:
    print('The decimal separator is a comma, and will be replaced to points')
    thermogram_file = thermogram_file.apply(lambda x: x.str.replace(',','.').
                                            astype(float))
else:
    print('The decimal separator are points')

# If the column separator is a tab, an extra column is created when reading a file
# and we replace it for the time. While if the separator is a space, the imported
# file has only two columns and the third one will be the time.
if length > 2:
    #  We create the column Time(s), taking into account the sampling period
    thermogram_file[header[2]] = pd.Series(np.arange(0, dt * N, dt))
    thermogram_file.rename(columns={header[2]:'Time (s)'}, inplace=True)
    header = list(thermogram_file)  # We get the headers list

elif length <= 2:
    # We create the column Time(s), taking into account the sampling period
    thermogram_file['Time (s)'] = pd.Series(np.arange(0, dt * N, dt))
    header = list(thermogram_file)  # We get the headers list
```

```
# -------------Temperature(K) and Signal(mV) vs t(s) plot-------------- #

fig = plt.figure()

plt.subplot(211)
plt.plot(thermogram_file[header[2]], thermogram_file[header[0]], color='k',
         label='Temperature (K)')
plt.title('Raw imported data of file {}'.format(FN))
plt.ylabel('Temperature (K)')
plt.xlabel('Time (s)')
plt.legend()
plt.subplots_adjust(hspace=0.3)

plt.subplot(212)
plt.plot(thermogram_file[header[2]], thermogram_file[header[1]], color='k',
         label='Signal (V)')
plt.ylabel('Signal (V)')
plt.xlabel('Time (s)')
plt.legend()

plt.show(fig)

# -------------Smoothing both Temperature(K) and Signal(V)------------- #

print('\nNow we will perform a smoothing to both Temperature (K) and Signal (V) columns')
# We define the variable that controls the smoothing loop
loop = 0
while loop == 0:

    answer_loop = input("Do you want to do the same smoothing procedure to both "
                        "Temperature (K) and Signal (V)? [Y/N]:")
    while answer_loop not in ['Y', 'y', 'yes', 'Yes', 'YES', 'N', 'n', 'no', 'No', 'NO']:
        print('\nPlease introduce a suitable answer [Y/N]')
        answer_loop = input("Do you want to do the same smoothing procedure to both"
                            "Temperature (K) and Signal (V)? [Y/N]:")

    # We create a new matrix to store the smoothed variables computed by this function
    smoothed_thermogram = pd.DataFrame()

    if answer_loop in ['Y', 'y', 'yes', 'Yes', 'YES']:
        # We call the smoothing function. It smooths the Temperature(K)
        # and Signal(V) columns
        smoothed_file, NS = smoothing_function(thermogram_file, N, columns=[0, 1])

        # Creation of the Smoothed Temperature column
        smoothed_thermogram['Temperature (K)'] = smoothed_file[0]
        # Creation of the Smoothed Signal column
        smoothed_thermogram['Signal (V)'] = smoothed_file[1]

    elif answer_loop in ['N', 'n', 'no', 'No', 'NO']:
        print('\nWe will start with the Temperature (K) smoothing')
        # We call the smoothing function. It smooths the Temperature (K) column
        smoothed_file, NS = smoothing_function(thermogram_file, N, columns=[0])

        print('\nWe will continue with the Signal (V) smoothing')
        # Creation of the Smoothed Temperature column
        smoothed_thermogram['Temperature (K)'] = smoothed_file[0]

        # We call the smoothing function. It smooths the Signal (V) column
```

```
        smoothed_file, NS = smoothing_function(thermogram_file, N, columns=[1])

        # Creation of the Smoothed Signal column
        smoothed_thermogram['Signal (V)'] = smoothed_file[1]

    # Creation of the time axis for the smoothed file
    smoothed_thermogram['Time (s)'] = pd.Series(np.arange(0, dt * NS, dt))

    # We call the plotting function to display the results of the smoothing
    title = 'Comparison of raw and smoothed temperature and signal'
    double_plot(thermogram_file, smoothed_thermogram, title, pl_1_x=2, pl_1_y=0,
                pl_2_x=2, pl_2_y=1)

    # Loop to filter the wrong inputs introduced by the user
    answer_loop = input("\nDo you want to repeat the smoothing procedure? [Y/N]:")

    while answer_loop not in ['Y', 'y', 'yes', 'Yes', 'YES', 'N', 'n', 'no', 'No', 'NO']:
        print('\nPlease introduce a suitable answer [Y/N]')
        answer_loop = input("Do you want to repeat the smoothing procedure? [Y/N]:")

    if answer_loop in ['Y', 'y', 'yes', 'Yes', 'YES']:
        loop = 0
    elif answer_loop in ['N', 'n', 'no', 'No', 'NO']:
        break

# ------------------------------------------------------------------------ #
#          Package 3: Computation of dT/dt (K/s) and smoothing             #
# ------------------------------------------------------------------------ #

# ----------------------Calculation of dT/dt(K/s)---------------------- #

# We get the headers list of the smoothed file
header_s = list(smoothed_thermogram)

# We compute the derivative of the smoothed temperature using the gradient function
smoothed_thermogram['dT/dt (K/s)'] = np.gradient(smoothed_thermogram[header_s[0]], dt)

# Creation of a dataframe to compare the different smoothings of dT/dt (K/s)
comparison_file = pd.DataFrame()

# Creation of the Temperature and raw smoothed dT/dt columns
comparison_file['Time (s)'] = smoothed_thermogram['Time (s)']
comparison_file['Temperature (K)'] = smoothed_thermogram['Temperature (K)']
comparison_file['Raw dT/dt (K/s)'] = smoothed_thermogram['dT/dt (K/s)']
# We get the number of rows we have in the file
N = int(len(comparison_file))

# ----------------Smoothing the dT/dt(K/s) calculation----------------- #

print('\nNow we will perform a smoothing to dT/dt (K/s)')

# We define the variable that controls the smoothing loop
loop = 0
while loop == 0:
    # We call the smoothing function. It smooths the dT/dt (K/s) column of the
    # comparison file
    smoothed_file, NS = smoothing_function(comparison_file, N, columns=[2])

    # Creation of the 1st smoothed dT/dt column
```

```
comparison_file['1st smoothed dT/dt (K/s)'] = smoothed_file[2]

# We call the plotting function to display the results of the first smoothing
title = 'Comparison of raw and 1st smoothed Temperature derivatives'
label_1 = 'raw dT/dt (K/s)'
label_2 = '1st smoothed dT/dt (K/s)'
label_3 = 'Temperature (K)'

#  We obtain the headers list of the comparison file
header_c = list(comparison_file)

# ------------------Identifying a cooling or a heating----------------- #

# We get the index of the first element of the file
i_startfile = smoothed_thermogram.index[0]
t_start = smoothed_thermogram.loc[i_startfile, header_s[0]]
# We get the index of the last element of the file
i_endfile = smoothed_thermogram.index[-1]
t_end = smoothed_thermogram.loc[i_endfile, header_s[0]]

if t_start > t_end:
    # The data file is a Cooling
    ymax = 0.995 * comparison_file[header_c[3]].max()
    ymin = 1.005 * comparison_file[header_c[3]].min()

elif t_start < t_end:
    # The data file is a Heating
    ymax = 1.005*comparison_file[header_c[3]].max()
    ymin = 0.995*comparison_file[header_c[3]].min()

fig, ax1 = plt.subplots()
plt.plot(comparison_file[header_c[0]], comparison_file[header_c[2]], color='k',
         label=label_1)
plt.plot(comparison_file[header_c[0]], comparison_file[header_c[3]], color='r',
         label=label_2)
ax1.set_ylim([ymin,ymax])
plt.legend()

ax2 = ax1.twinx()
plt.plot(comparison_file[header_c[0]], comparison_file[header_c[1]], color='b',
         label=label_3)
ax2.tick_params(axis='y', labelcolor='b')
plt.legend()

plt.title(title)
ax1.set_ylabel('dT/dt (K/s)')
ax2.set_ylabel('Temperature (K)', color='b')
ax1.set_xlabel('Time (s)')

plt.show()

# -------------------Second smoothing of dT/dt(K/s)-------------------- #

# We give the possibility to perform a second smoothing on the Temperature derivative
answer_loop = input("\nDo you want to perform a second smoothing on dT/dt (K/s)?"
                    " [Y/N]:")

# Loop to filter the wrong inputs introduced by the user
while answer_loop not in ['Y', 'y', 'yes', 'Yes', 'YES', 'N', 'n', 'no', 'No', 'NO']:
```

```
        print('\nPlease introduce a suitable answer [Y/N]')
        answer_loop = input("Do you want to perfotm a second smoothing on dT/dt (K/s)?"
                            " [Y/N]:")

    if answer_loop in ['Y', 'y', 'yes', 'Yes', 'YES']:
        # We call the smoothing function. It smooths the dT/dt (K/s) column
        smoothed_file, NS = smoothing_function(comparison_file, N, columns=[3])

        # Creation of the 2nd smoothed dT/dt column
        comparison_file['2nd smoothed dT/dt (K/s)'] = smoothed_file[3]

        # We copy this smoothed curve to the smoothed thermogram data frame
        smoothed_thermogram['Smoothed dT/dt (K/s)'] = \
            comparison_file['2nd smoothed dT/dt (K/s)']

        # We call the plotting function to display the results of the second smoothing
        title = 'Comparison of 1st and 2nd smoothed Temperature derivatives'
        label_1 = 'raw dT/dt (K/s)'
        label_2 = '1st smoothed dT/dt (K/s)'
        label_3 = '2nd smoothed dT/dt (K/s)'
        label_4 = 'Temperature (K)'

        #  We obtain the headers list of the comparison file
        header_c = list(comparison_file)

        fig, ax1 = plt.subplots()
        plt.plot(comparison_file[header_c[0]], comparison_file[header_c[2]], color='k',
                 label=label_1)
        plt.plot(comparison_file[header_c[0]], comparison_file[header_c[3]], color='r',
                 label=label_2)
        plt.plot(comparison_file[header_c[0]], comparison_file[header_c[4]],
                 color='deepskyblue', label=label_3)
        ax1.set_ylim([ymin, ymax])
        plt.legend()

        ax2 = ax1.twinx()
        ax2.plot(comparison_file[header_c[0]], comparison_file[header_c[1]], color='b',
                 label=label_4)
        ax2.tick_params(axis='y', labelcolor='b')
        plt.legend()

        plt.title(title)
        plt.legend()
        ax1.set_ylabel('dT/dt (K/s)')
        ax2.set_ylabel('Temperature (K)', color='b')
        ax1.set_xlabel('Time (s)')

        plt.show()

    elif answer_loop in ['N', 'n', 'no', 'No', 'NO']:
        print("No additional smoothing will be performed")

        smoothed_thermogram['Smoothed dT/dt (K/s)'] = \
            comparison_file['1st smoothed dT/dt (K/s)']

    answer_loop = input("\nDo you want to repeat the smoothing procedure? [Y/N]:")

    # Loop to filter the wrong inputs introduced by the user
    while answer_loop not in ['Y', 'y', 'yes', 'Yes', 'YES', 'N', 'n', 'no', 'No', 'NO']:
```

```
        print('\nPlease introduce a suitable answer [Y/N]')
        answer_loop = input("Do you want to repeat the smoothing procedure? [Y/N]:")

    if answer_loop in ['Y', 'y', 'yes', 'Yes', 'YES']:
        loop = 0
    elif answer_loop in ['N', 'n', 'no', 'No', 'NO']:
        break

# ---------------------------------------------------------------------- #
#               Package 4: Calculation of the Sensitivity                #
# ---------------------------------------------------------------------- #

print('\nNow we can perform the correction of the Signal(V)'
      '\nwith the calorimeter sensitivity S(mV/W). There are two options:'
      '\n\t1. Strain-DSC sensitivity'
      '\n\t2. No sensitivity correction (S = 1 mV/W)')

i = int(input("Introduce the sensitivity correction you want to perform [1,2]:"))

while i != 1 and i != 2:
    i = int(input("Please, select a suitable option number [1,2]:"))

if i == 1:
    # We calculate the sensitivity column
    smoothed_thermogram['sensitivity (mV/W)'] = smoothed_thermogram.apply(
        lambda x: sensitivity(x[header_s[0]]), axis=1)

else:
    print('The sensitivity is set to 1 mV/W. Therefore, no correction on the data'
          ' will be performed')
    # We calculate the sensitivity column
    smoothed_thermogram['sensitivity (mV/W)'] = smoothed_thermogram.apply(
        lambda x: 1, axis=1)

# ---------------------------------------------------------------------- #
#          Package 5: Correction for the Sensitivity and dT/dt           #
# ---------------------------------------------------------------------- #

# We get the headers list of the smoothed file
header_s = list(smoothed_thermogram)

smoothed_thermogram['dQ/dT (mJ/K)'] = smoothed_thermogram.apply(
        lambda x: signal_correction(x[header_s[1]], x[header_s[5]], x[header_s[4]]),
    axis=1)

# ---------------------------------------------------------------------- #
#            Package 6: Base-line correction and integration             #
# ---------------------------------------------------------------------- #

print('\nNow we will perform the base-line correction')

# We define the variable that controls the full integration loop
loop_int = 0
# This loop allows to repeat all the integration procedure
while loop_int == 0:

    # We define a variable to control the loop for the first background
    loop_background = 0
    # This loop allows to repeat the background selection before starting the
```

```
# integration routine
while loop_background == 0:

    print('\nPlease, select two points on the dQ/dT vs T plot before and'
       ' two more after the transition peak to perform the background correction')

    # We call the function to select four temperature points
    num_points = 4
    temp_values = select(num_points)

    # ----------------Indexing the introduced temperatures----------------- #

    # We define a temperature tolerance, in K units
    tolerance = 5e-2
    # We define an empty index list
    i_temp = list()
    # We compute the indexes of the temperature values introduced by the user
    for i in range(num_points):
        i_point = indexing(smoothed_thermogram, header_s[0],temp_values[i],tolerance)
        i_temp.append(i_point)
        print('Data point index: {}'.format(i_temp[i]))

    # We sort the index values of the index list to order them
    i_temp = sorted(i_temp)



    # We find the temperatures corresponding to the indices found
    # First temperature range before the peak
    t1s = smoothed_thermogram.loc[i_temp[0],header_s[0]]
    t1e = smoothed_thermogram.loc[i_temp[1], header_s[0]]
    # Second temperature range after the peak
    t2s = smoothed_thermogram.loc[i_temp[2], header_s[0]]
    t2e = smoothed_thermogram.loc[i_temp[3], header_s[0]]

    print('\nThe temperatures selected on the corrected file are:')
    print('First temperature range: {} K, {} K'.format(t1s, t1e))
    print('Second temperature range: {} K, {} K'.format(t2s, t2e))

    # ------------------Computing the linear regressions------------------- #

    print('Which type of function do you want to fit for the background?'
          '\n\t 1. Two linear functions (before and after the peak)'
          '\n\t 2. One 3rd order polynomial function for the full data range')

    i = int(input("Introduce the function type you want to use [1,2]:"))

    while i != 1 and i != 2:
        i = int(input("Please, select a suitable function type number [1,2]:"))

    header_s = list(smoothed_thermogram)
    # We save the index value in order to distinguish between linear and polynomial
    # background functions
    index = i

    if index == 1:
        # We calculate the first regression in the index range [i_start:i_end]
        popt_1, pcov_1 = regression_fit(smoothed_thermogram, i_temp[0], i_temp[1],
                                        col_x=0, col_y=6, index=i)
```

```
        print('Fit parameters 1st regression:',popt_1)

        # We calculate the second regression in the index range [i_start:i_end]
        popt_2, pcov_2 = regression_fit(smoothed_thermogram, i_temp[2], i_temp[3],
                                        col_x=0, col_y=6, index=i)
        print('Fit parameters 2nd regression:',popt_2)

    elif index == 2:
        # We calculate a single background for all the points selected as background
        background_polyfit = pd.DataFrame()

        # We add the data of the first background range i_start_1:i_end_1
        bg = pd.DataFrame()
        bg['Temperature (K)'] = smoothed_thermogram.loc[i_temp[0]:i_temp[1],
                                header_s[0]]
        bg['Background (mJ/K)'] = smoothed_thermogram.loc[i_temp[0]:i_temp[1],
                                  header_s[6]]

        background_polyfit = background_polyfit.append(bg, ignore_index=True)

        bg = pd.DataFrame()
        # We add the data of the second background range i_start_2:i_end_2
        bg['Temperature (K)'] = smoothed_thermogram.loc[i_temp[2]:i_temp[3],
                                header_s[0]]
        bg['Background (mJ/K)'] = smoothed_thermogram.loc[i_temp[2]:i_temp[3],
                                  header_s[6]]

        background_polyfit = background_polyfit.append(bg, ignore_index=True)

        # We get the start and end index of the background file
        i_poly_start = background_polyfit.index[0]
        i_poly_end = background_polyfit.index[-1]

        # We calculate the background regression in the full index range
        popt_poly, pcov_poly = regression_fit(background_polyfit, i_poly_start,
                                              i_poly_end, col_x=0, col_y=1, index=i)
        print('Fit parameters of the polynomial regression:', popt_poly)

    # ------------------Identifying a cooling or a heating----------------- #

    # We get the index of the first element of the file
    i_startfile = smoothed_thermogram.index[0]
    t_start = smoothed_thermogram.loc[i_startfile,header_s[0]]
    # We get the index of the last element of the file
    i_endfile = smoothed_thermogram.index[-1]
    t_end = smoothed_thermogram.loc[i_endfile, header_s[0]]

    if t_start > t_end:
        data_type = 'Cooling'
        print('The data file is a Cooling')
    else:
        data_type = 'Heating'
        print('The data file is a Heating')

    # ----------------------Background calculation----------------------- #

    if index == 1:
        print('\nPlease, select the peak position of the the dQ/dT vs T plot')
```

```
        # We get the headers list of the smoothed file
        header_s = list(smoothed_thermogram)

        # We call the function to select four temperature points
        num_points = 1
        temp_values = select(num_points)

        # -----------------Indexing the introduced temperature----------------- #

        # We define a temperature tolerance, in K units
        tolerance = 5e-2

        # We compute the index of the peak position introduced by the user
        i_peak = indexing(smoothed_thermogram, header_s[0], temp_values, tolerance)

        # We find the temperature corresponding to the index found
        # First temperature range before the peak
        t_peak = smoothed_thermogram.loc[i_peak, header_s[0]]

        print('\nThe thermogram peak position selected is:')
        print('Index: {}, Temperature: {} K'.format(i_peak, t_peak))

        # We define the initial background with the two linear regressions calculated
        count = 0
        while count <= i_endfile:
            xdata = smoothed_thermogram.loc[count, header_s[0]]

            if count < i_peak:
                # Background function before the peak position
                smoothed_thermogram.loc[count, 'Background (mJ/K)'] =\
                    regression_calc(xdata, popt_1, index)

            else:
                # Background function after the peak position
                smoothed_thermogram.loc[count, 'Background (mJ/K)'] =\
                    regression_calc(xdata, popt_2, index)

            count = count + 1
    elif index == 2:
        # We define the background with the 3rd order polynomial regression
        count = 0
        while count <= i_endfile:
            xdata = smoothed_thermogram.loc[count, header_s[0]]
            # Polynomial background function
            smoothed_thermogram.loc[count, 'Background (mJ/K)'] =\
                regression_calc(xdata, popt_poly, index)

            count = count + 1

    # Plot of the signal with the first background
    title = 'Plot of the corrected signal and background'
    label_1 = 'dQ/dT (mJ/K)'
    label_2 = 'Background (mJ/K)'
    single_plot(smoothed_thermogram, smoothed_thermogram, title, label_1, label_2,
                col_1x=0, col_1y=6, col_2x=0, col_2y=7)

    answer_loop = input( "\nDo you want to repeat the background selection? [Y/N]:" )
    # Loop to filter the wrong inputs introduced by the user
    while answer_loop not in ['Y', 'y', 'yes', 'Yes', 'YES', 'N', 'n', 'no', 'No',
```

```
                                'NO']:
            print( '\nPlease introduce a suitable answer [Y/N]' )
            answer_loop = input( "Do you want to repeat the the background selection?"
                                 " [Y/N]:" )

        if answer_loop in ['Y', 'y', 'yes', 'Yes', 'YES']:
            loop_background = 0
        elif answer_loop in ['N', 'n', 'no', 'No', 'NO']:
            break

    # We get the headers list of the smoothed file
    header_s = list(smoothed_thermogram)

    # We correct the signal with the initial signal background
    smoothed_thermogram['1/T dQ/dT (mJ/K^2)'] = smoothed_thermogram.apply(
        lambda x: dS_computation(x[header_s[0]], x[header_s[6]], x[header_s[7]]), axis=1)

    # -------------------------First integration------------------------- #

    # We get the headers list of the smoothed file
    header_s = list(smoothed_thermogram)

    # We perform an integration using the trapezoidal rule between the end point
    # of the first temperature range and the start point of the second range.
    integration = pd.DataFrame()
    integration['Integral (mJ/K)'] = \
        sp_int.cumtrapz(smoothed_thermogram.loc[i_temp[1]:i_temp[2], header_s[8]],
                        smoothed_thermogram.loc[i_temp[1]:i_temp[2], header_s[0]],
                        initial=0)

    # We modify the index labels of the integration file
    new_index = list(range( i_temp[1], i_temp[2] + 1, 1))
    integration.index = new_index

    # We assign values to the integral before and after the defined
    # integration range [i_temp1e:i_temp2s]
    count = 0
    while count <= i_endfile:
        if count < i_temp[1]:
            smoothed_thermogram.loc[count,'Entropy integration (mJ/K)'] = float(0)

        elif i_temp[1] <= count <= i_temp[2]:
            smoothed_thermogram.loc[count,'Entropy integration (mJ/K)'] =\
                integration.loc[count,'Integral (mJ/K)']

        else:
            header_s = list(smoothed_thermogram)
            smoothed_thermogram.loc[count,'Entropy integration (mJ/K)'] = \
                smoothed_thermogram.loc[i_temp[2], header_s[9]]
        count = count + 1

    # We store the value of the first integration
    S_0 = smoothed_thermogram.loc[i_temp[2], header_s[9]]
    print('Transition entropy change: {} mJ/K \n'.format(S_0))

    # We define the transformed fraction as the normalized portion of
    # sample that has transformed at that temperature
    smoothed_thermogram['Transformed fraction'] = smoothed_thermogram.apply(
        lambda x: 1 - (x[header_s[9]] / S_0), axis=1)
```

```
header_s = list(smoothed_thermogram)
# We create a backup of the transformed fraction
backup = pd.DataFrame()
backup['Temperature (K)'] = smoothed_thermogram[header_s[0]]
backup['Transformed fraction'] = smoothed_thermogram[header_s[10]]

# Plot of the transformed fraction
plt.plot(smoothed_thermogram[header_s[0]], smoothed_thermogram[header_s[10]],
         color='k', label='Transformed fraction', picker=5)
plt.legend()
plt.title('Plot of the transformed fraction')
plt.ylabel('Transformed fraction (normalized)')
plt.xlabel('Temperature (K)')
plt.show()

# ------------------------Iterative integration------------------------ #

if index == 1:
    loop_num = 0
    cond = 0
    # We start the iterative calculation of the integral
    while cond == 0:
        S_1 = 0
        # We get the headers list of the smoothed file
        header_s = list(smoothed_thermogram)

        # We define the new background in the integration region
        # [i_temp1e:i_temp2s] using the transformed fraction calculated
        count = i_temp[1]
        while count <= i_temp[2]:
            # We define the variables temperature (temp) and
            # martensite transformed fraction (X) to simplify
            temp = smoothed_thermogram.loc[count, header_s[0]]
            X = smoothed_thermogram.loc[count, header_s[10]]

            # We define the new background
            smoothed_thermogram.loc[count, 'Background (mJ/K)'] = \
                                    regression_calc(temp, popt_1, index) * X + \
                                    regression_calc(temp, popt_2, index) * (1 - X)
            count = count + 1

        # We correct the signal with the new signal background
        smoothed_thermogram['1/T dQ/dT (mJ/K^2)'] = smoothed_thermogram.apply(
            lambda x: dS_computation(x[header_s[0]], x[header_s[6]], x[header_s[7]]),
            axis=1)

        # We perform a new integration of the corrected signal
        integration['Integral (mJ/K)'] = \
            sp_int.cumtrapz(smoothed_thermogram.loc[i_temp[1]:i_temp[2], header_s[8]],
                            smoothed_thermogram.loc[i_temp[1]:i_temp[2], header_s[0]],
                            initial=0)
        # We modify the index labels of the integration file
        integration.index = new_index

        count = i_temp[1]
        while count <= i_endfile:
            if count <= i_temp[2]:
                smoothed_thermogram.loc[count, header_s[9]] =\
```

```
                    integration.loc[count, 'Integral (mJ/K)']

            else:
                smoothed_thermogram.loc[count, header_s[9]] = \
                    smoothed_thermogram.loc[i_temp[2], header_s[9]]
            count = count + 1

        # We store the value of the iterative integration
        S_1 = smoothed_thermogram.loc[i_temp[2], header_s[9]]

        smoothed_thermogram['Transformed fraction'] = smoothed_thermogram.apply(
            lambda x: 1 - (x[header_s[9]] / S_1), axis=1)

        if loop_num < 100:
            convergence = 0.00000001
            smoothed_thermogram[header_s[10]] = tolerance_function(tolerance=0.01)
        elif 100 < loop_num < 250:
            convergence = 0.0000001
            smoothed_thermogram[header_s[10]] = tolerance_function(tolerance=0.02)
        elif 250 < loop_num < 450:
            convergence = 0.000001
            smoothed_thermogram[header_s[10]] = tolerance_function(tolerance=0.03)
        elif loop_num > 450:
            convergence = 0.00001
            smoothed_thermogram[header_s[10]] = tolerance_function(tolerance=0.04)

        # We define the integral difference as:
        integ_diff = abs(1 - abs(S_1/S_0))

        # The iterative background calculation and integration goes on until
        # the result between two successive integrations converges.
        if integ_diff > convergence:
            S_0 = S_1
            print('Loop {}, Transition entropy change: {} mJ/K'.format(loop_num, S_0))
            loop_num = loop_num + 1
        else:
            break

    print('\nThe integration has converged!!')

elif index == 2:
    # As no iterative integration is done for a polynomial baseline, the final
    # integration value is set equal to the first one.
    S_1 = S_0
    print('\nNo iterative integration was done')

# ---------------------Enthalpy change calculation--------------------- #

# We correct the dQ/dT (mJ/K) data with the background
smoothed_thermogram['dQ/dT corrected (mJ/K)'] = smoothed_thermogram.apply(
    lambda x: x[header_s[6]] - x[header_s[7]], axis=1)

# We get the headers list of the smoothed file
header_s = list(smoothed_thermogram)

# We calculate the Enthalpy change of the transition
H_integ_trapz = \
    sp_int.trapz(smoothed_thermogram.loc[i_temp[1]:i_temp[2], header_s[11]],
                 smoothed_thermogram.loc[i_temp[1]:i_temp[2], header_s[0]])
```

```
# -------------------Display the integration results------------------- #

print('\nTne transition entropy change is {} mJ/K'.format(S_1))
print('Alternative calculations of this integral:')

# We calculate the integral by the trapezoidal method
S_integ_trapz = \
    sp_int.trapz(smoothed_thermogram.loc[i_temp[1]:i_temp[2], header_s[8]],
                 smoothed_thermogram.loc[i_temp[1]:i_temp[2], header_s[0]])

print('\t 1. Trapeziodal integration: {} mJ/K'.format(S_integ_trapz))

# We calculate the integral by the Simpsons method
S_integ_simp = \
    sp_int.simps(smoothed_thermogram.loc[i_temp[1]:i_temp[2], header_s[8]],
                 smoothed_thermogram.loc[i_temp[1]:i_temp[2], header_s[0]])

print('\t 2. Simpsons integration: {} mJ/K'.format(S_integ_simp))

print('\nWe will plot the results obtained with the integration performed')
#  We call the plotting function to display the results of the integration
title = 'Plot of the corrected signal and background'
label_1 = 'dQ/dT (mJ/K)'
label_2 = 'Background (mJ/K)'
single_plot(smoothed_thermogram, smoothed_thermogram, title, label_1, label_2,
            col_1x=0, col_1y=6, col_2x=0, col_2y=7)

# ------------------------Transformed fraction------------------------- #

# Now we will distinguish between the heating and cooling cases to compute
# the martensite transformed fraction. So far, we have only considered the
# heating case.

if data_type == 'Cooling':
    smoothed_thermogram['Transformed fraction'] = smoothed_thermogram.apply(
        lambda x: 1 - (x[header_s[10]]), axis=1)

# Plot of the transformed fraction
plt.plot(smoothed_thermogram[header_s[0]], smoothed_thermogram[header_s[10]],
         color='k', label='Transformed fraction (mJ/K)', picker=5)
plt.legend()
plt.title('Plot of the transformed fraction')
plt.ylabel('Transformed fraction (normalized)')
plt.xlabel('Temperature (K)')
plt.show()

answer_loop = input("\nDo you want to repeat the integration procedure? [Y/N]:")
# Loop to filter the wrong inputs introduced by the user
while answer_loop not in ['Y', 'y', 'yes', 'Yes', 'YES', 'N', 'n', 'no', 'No', 'NO']:
    print('\nPlease introduce a suitable answer [Y/N]')
    answer_loop = input("Do you want to repeat the integration procedure? [Y/N]:")

if answer_loop in ['Y', 'y', 'yes', 'Yes', 'YES']:
    loop_int = 0
elif answer_loop in ['N', 'n', 'no', 'No', 'NO']:
    break
```

```
# ------------------------------------------------------------------- #
#            Package 7: Display the results and data storage          #
# ------------------------------------------------------------------- #

# --------------------Show the main results obtained------------------ #

# We print the main results obtained with the signal integration
print('Yay! The integration was OK. The main results are printed below:\n')

print('Transition temperatures:')

if data_type == 'Heating':
    T_As = transition_temp_1(smoothed_thermogram, i_temp[1], i_temp[2],
                             X_value=0.95, step=1)
    T_Af = transition_temp_2(smoothed_thermogram, i_temp[2], i_temp[1],
                             X_value=0.05, step=-1)

    print('Austenite start (As): {} K \t Austenite finish (Af): {} K\n'.
          format(T_As,T_Af))

elif data_type == 'Cooling':
    T_Ms = transition_temp_1(smoothed_thermogram, i_temp[1], i_temp[2],
                             X_value=0.05, step=1)
    T_Mf = transition_temp_2(smoothed_thermogram, i_temp[2], i_temp[1],
                             X_value=0.95, step=-1)

    print('Martensite start (Ms): {} K \t Martensite finish (Mf): {} K\n'.
          format(T_Ms,T_Mf))

print('Entropy and enthalpy:')
mass = str(input('Please introduce the sample mass (mg):'))

# If the decimal delimiter is a comma, it is replaced by points,
# else the program continues.
if mass.__contains__(',') is True:
    print('The decimal separator is a comma, and will be replaced to points')
    sample_mass = float(mass.replace(',','.'))
else:
    sample_mass = float(mass)

# The factors 1000 are for the g to kg conversion
H_mass = 1000 * H_integ_trapz/sample_mass
S_mass = 1000 * S_1/sample_mass

print('Enthalpy change: {} J/kg'.format(H_mass))
print('Entropy change: {} J/K kg'.format(S_mass))

# --------------------Creation of the corrected file------------------ #

# We create a file to store the corrected signal
corrected_thermogram = pd.DataFrame()

# We create the Temperature column
corrected_thermogram['Temperature (K)'] = smoothed_thermogram[header_s[0]]
# We cretate the corrected signal column
corrected_thermogram['dQ/dT (mJ/K)'] = smoothed_thermogram[header_s[6]]
# We create the background signal column
corrected_thermogram['Background (mJ/K)'] = smoothed_thermogram[header_s[7]]
# We create the transformed fraction column
```

```
corrected_thermogram['Transformed fraction (normalized)'] = \
    smoothed_thermogram[header_s[10]]

# ----------------------Storing the corrected file---------------------- #

# We distinguish in the file name between the type of background that we have chosen
if index == 1:
    bg = 'lin_bg_'
elif index == 2:
    bg = 'pol_bg_'

# We define the file path of the corrected file
corrected_path = storage_DR + 'corrected_' + bg + FN
# We store the corrected file at the same location as the imported file
corrected_thermogram.to_csv(corrected_path, sep='\t', index=False, mode='a')

# ---------------------Storing the dT/dt data file---------------------- #

# We define the file path of the corrected file
comparison_path = storage_DR + 'temperature_' + bg + FN
# We store the corrected file at the same location as the imported file
comparison_file.to_csv(comparison_path, sep='\t', index=False, mode='a')
```

Appendix B

Ni-Mn-In: Single caloric thermal response under the influence of a secondary field

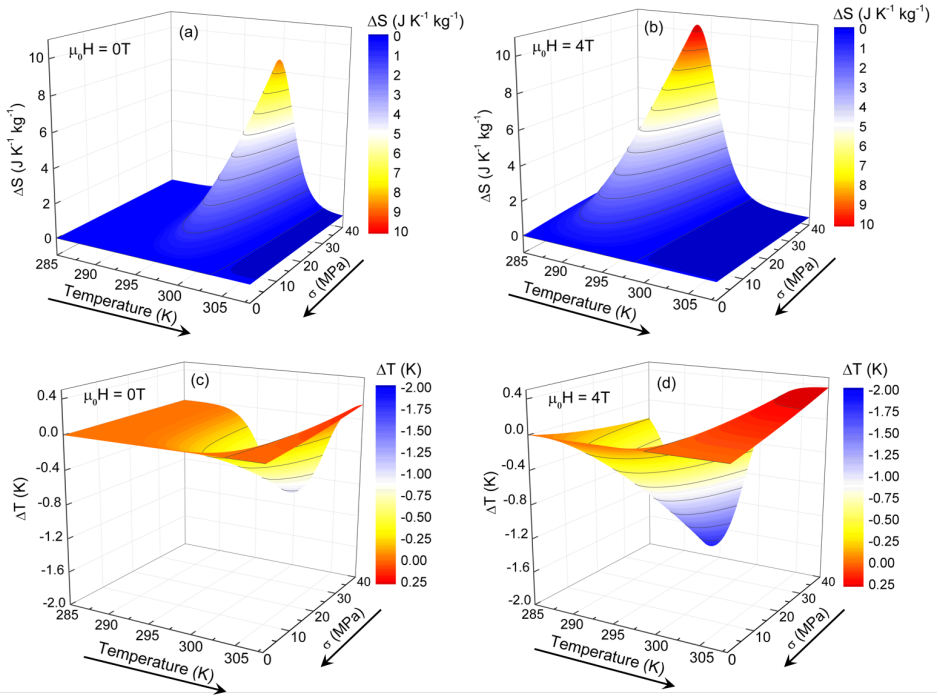

Figure B.1: *Three-dimensional plots of the elastocaloric isothermal entropy (panels (a) and (b)) and adiabatic temperature (panels (c) and (d)) changes under the removal of uniaxial stress ($\sigma' \rightarrow 0\,MPa$) as a function of temperature. Left side panels ((a) and (c)) correspond to the elastocaloric thermal response in the absence of magnetic field, whereas right side panels ((b) and (d)) to data under an applied magnetic field of $\mu_0 H = 4\,T$. Arrows along the axis indicate the direction of the temperature and uniaxial stress changes.*

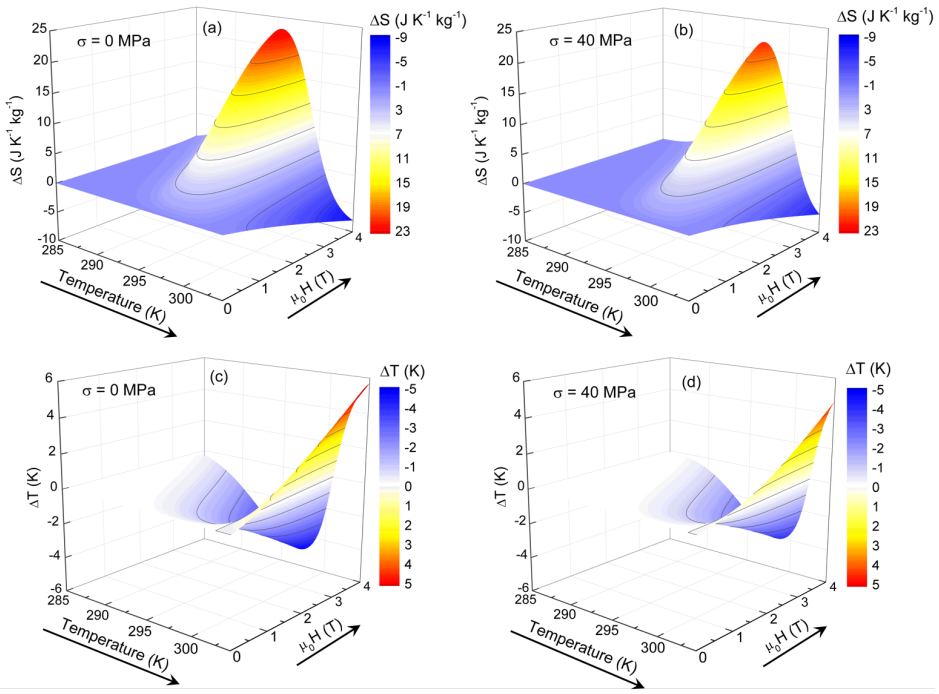

Figure B.2: *Three-dimensional plots of the magnetocaloric isothermal entropy (panels (a) and (b)) and adiabatic temperature (panels (c) and (d)) changes under the application of magnetic field ($0\ T \rightarrow \mu_0 H'$) as a function of temperature. Left side panels ((a) and (c)) correspond to the magnetocaloric thermal response in the absence of stress, whereas right side panels ((b) and (d)) to data under an applied stress of $\sigma = 40\ MPa$. Arrows along the axis indicate the direction of the temperature and magnetic field changes.*

Appendix C

Ni-Mn-Ga-Cu: Single caloric thermal response under the influence of a secondary field

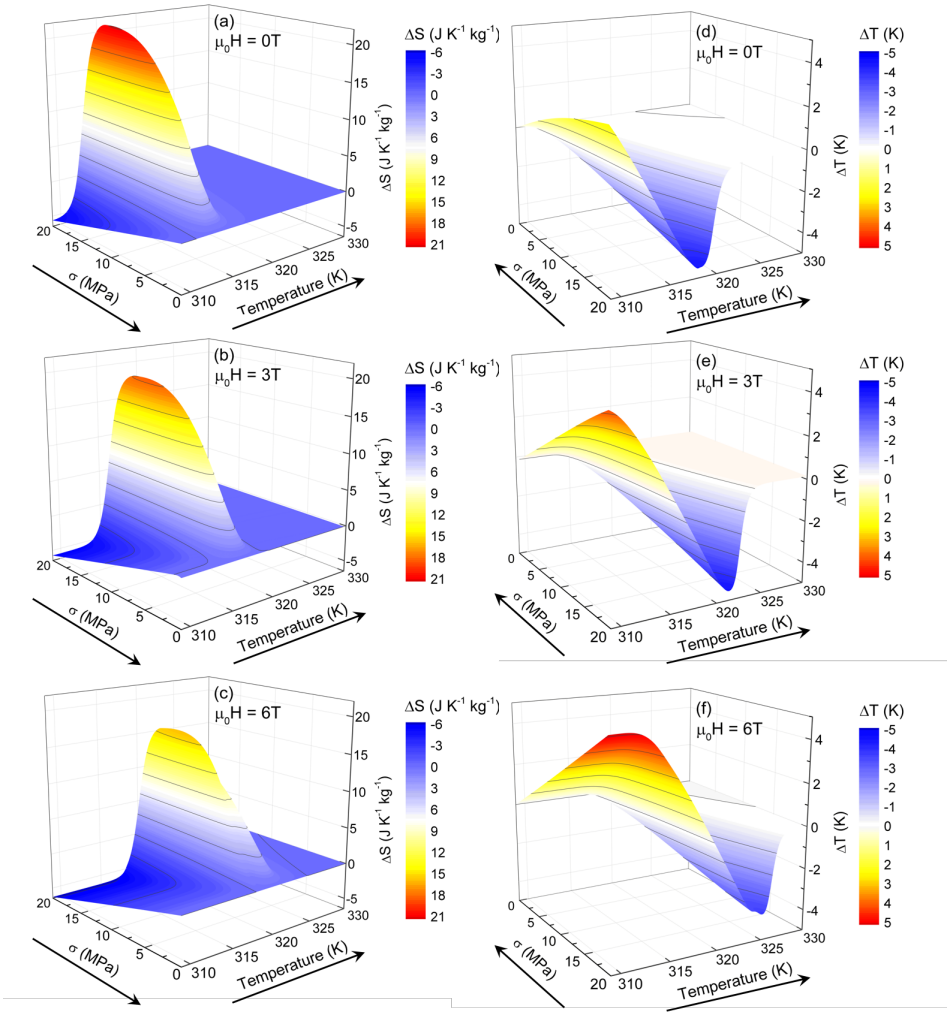

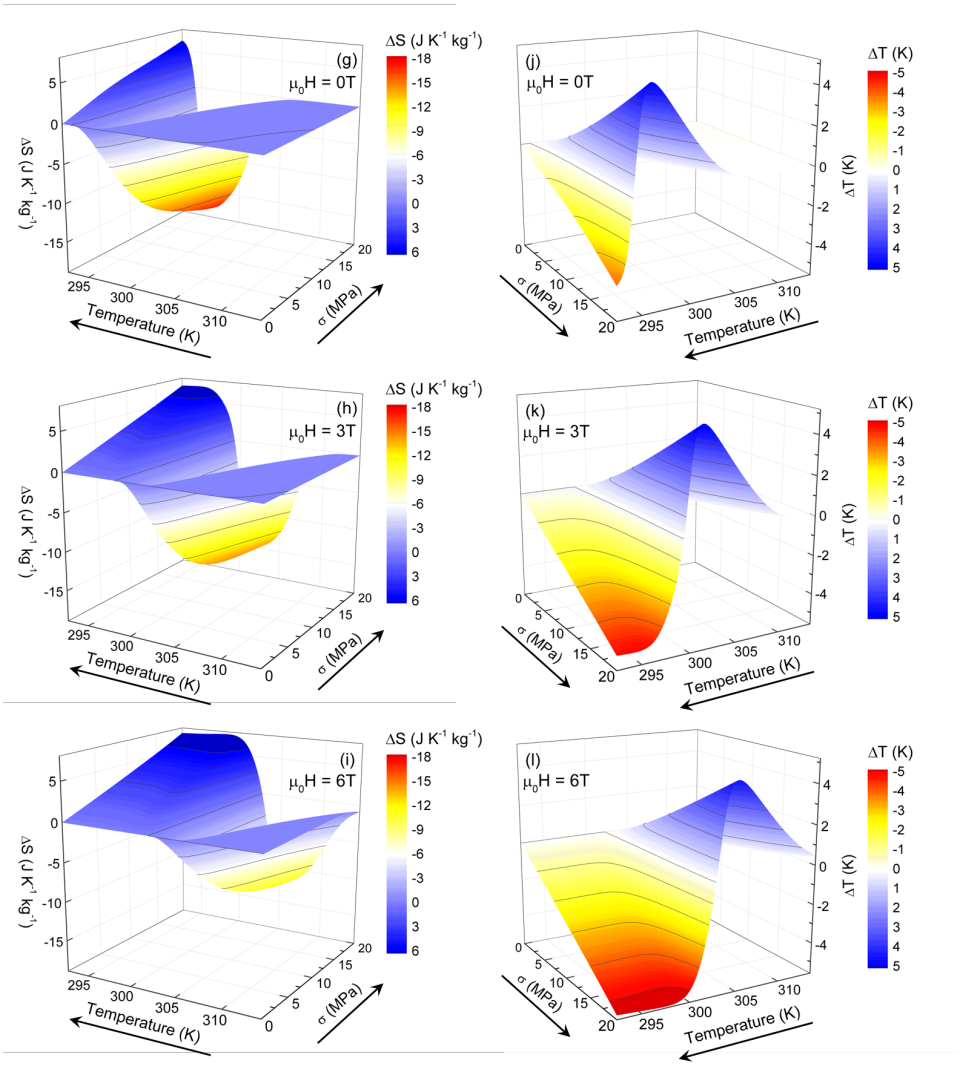

Figure C.1: *Three-dimensional plots of the elastocaloric isothermal entropy (left side) and adiabatic temperature (right side) changes computed from the entropy curves upon heating (panels (a)-(f)) and cooling (panels (g)-(l)) as a function of temperature at selected values of magnetic field* $\{\mu_0 H_j\} = \{0, 3, 6\}$ *T. Arrows along the axis indicate the direction of the temperature and uniaxial stress changes.*

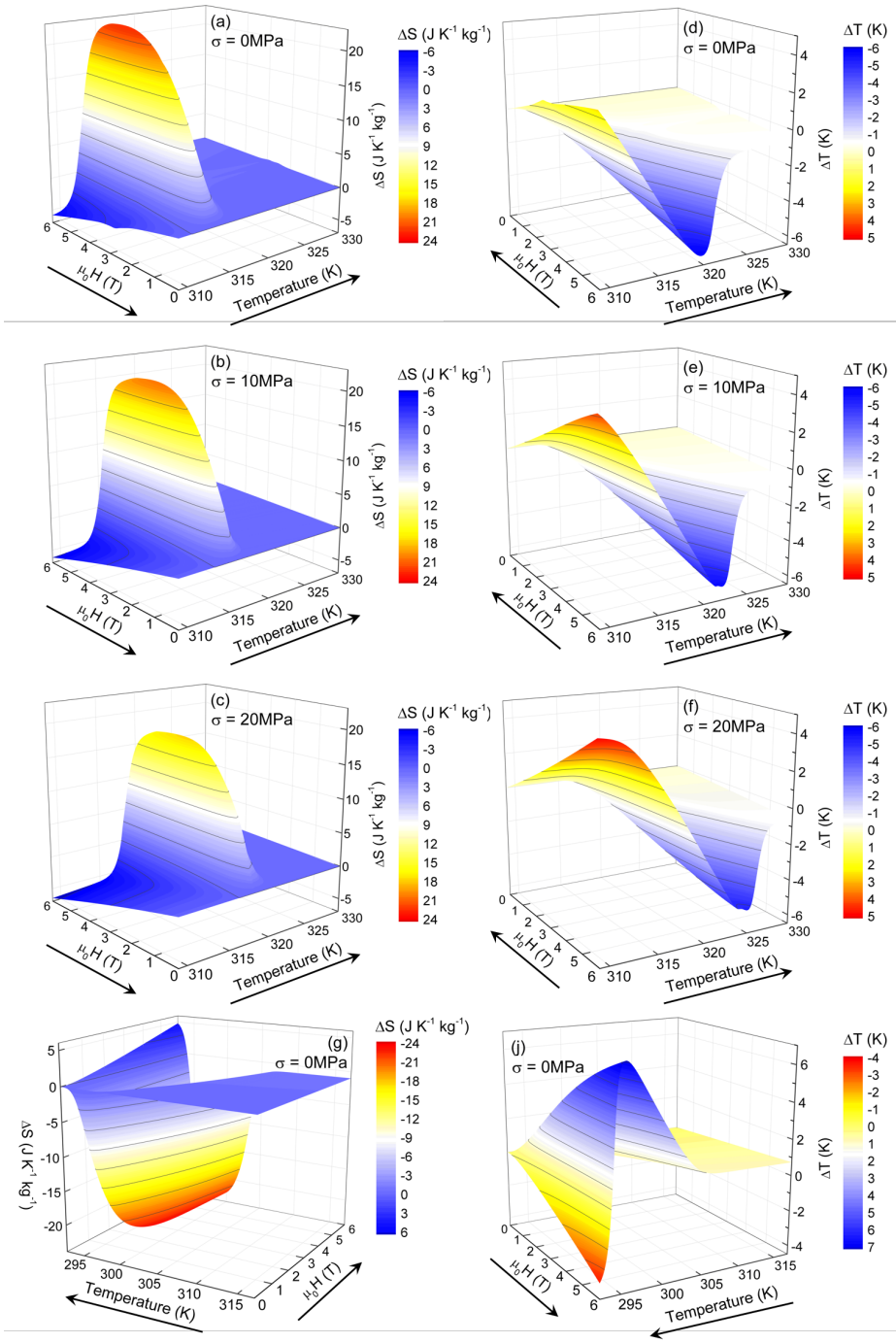
(a)
σ = 0MPa
(b)
σ = 10MPa
(c)
σ = 20MPa
(d)
σ = 0MPa
(e)
σ = 10MPa
(f)
σ = 20MPa
(g)
σ = 0MPa
(j)
σ = 0MPa
ΔS (J K-1 kg-1)
ΔT (K)
μ0H (T)
Temperature (K)

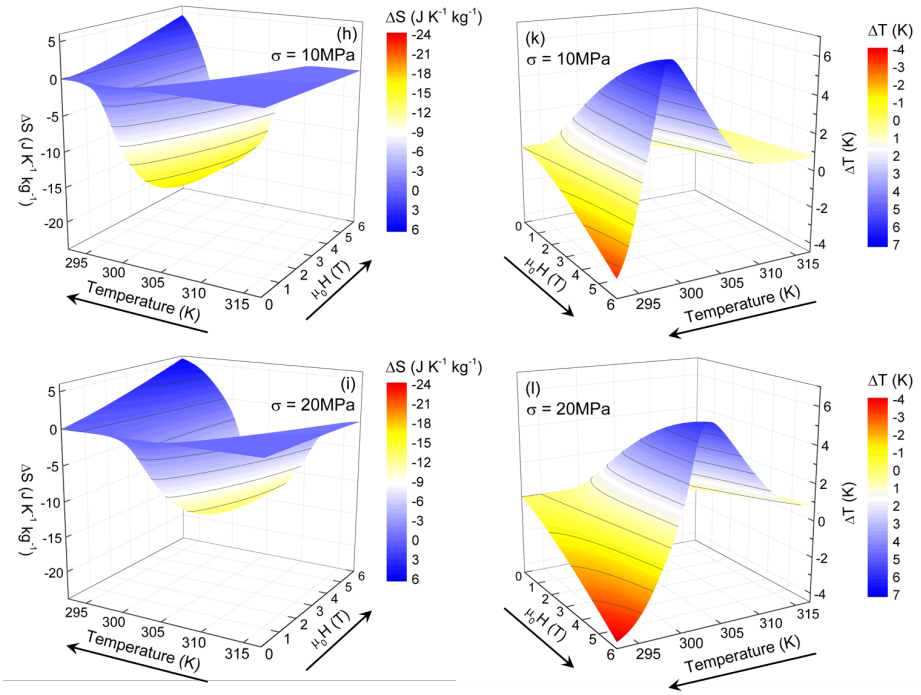

Figure C.2: *Three-dimensional plots of the magnetocaloric isothermal entropy (left side) and adiabatic temperature (right side) changes computed from the entropy curves upon heating (panels (a)-(f)) and cooling (panels (g)-(l)) as a function of temperature at selected values of applied stress* $\{\sigma_i\} = \{0, 10, 20\}$ *MPa. Arrows along the axis indicate the direction of the temperature and magnetic field changes.*